Fatigue Behaviour of Steel Fibre Reinforced Concrete Pavements

by

Iman Munadhil Abbas Al-Damad

A thesis submitted in fulfilment of

the requirements for the degree of

Doctor of Philosophy

School of Civil and Environmental Engineering

The University of New South Wales

Sydney, Australia

February 2020

THESIS/DISSERTATION SHEET

Surname/Family Name	:	**AL-DAMAD**
Given Name/s	:	**Iman Munadhil Abbas**
Abbreviation for degree as give in the University calendar	:	**PhD**
Faculty	:	**Engineering**
School	:	**Civil and Environmental Engineering**
Thesis Title	:	**Fatigue Behaviour of Steel Fibre Reinforced Concrete Pavements**

Abstract

The design of rigid pavements subjected to increasing heavy wheel loads and high traffic volumes necessitates, over time, the design of thicker pavements. With the advent of steel fibre reinforced concrete (SFRC), there exist the possibilities of enhancing fatigue performance of rigid pavements by including fibres in concrete and bridging cracks once they form. In the first part of this investigation, a material level of study was undertaken to investigate the performance of three different types of SFRC. Testing on round panels was undertaken to determine fatigue resistance; several varying load levels were applied at constant amplitude. A series of matched direct uniaxial tension and prism bending tests were also undertaken to provide comprehensive material characterisation data. It was concluded that fibres improve the fatigue life of concrete and a design model was developed. The model was validated against a large pool of experimental data obtained through the course of this study and is shown to correlate well with the test data. Also in this dissertation, the development of a constitutive model is presented for SFRC for post-cracking fatigue damage during cyclic loops. Comparing the results of the model with test data shows that the model is capable of accurately predicting the overall cyclic fatigue loading response of SFRC. The model is also able to capture the change in the COD, the stiffness changes with increasing load cycles and the number of load cycles to failure. In the final part of this study, a novel experimental program was developed to investigate the performance of large scale plain and SFRC slabs tested under static and cyclic loading – the SFRC slabs were 20% thinner than plain concrete slabs. The results show that the thinner SFRC pavements can carry higher numbers of load repetitions compared to those of currently constructed of plain concrete, with excellent serviceability performance in terms of crack width propagation and deflection development.

ORIGINALITY STATEMENT

'I hereby declare that this submission is my own work and to the best of my knowledge it contains no materials previously published or written by another person, or substantial proportions of material which have been accepted for the award of any other degree or diploma at UNSW or any other educational institution, except where due acknowledgement is made in the thesis. Any contribution made to the research by others, with whom I have worked at UNSW or elsewhere, is explicitly acknowledged in the thesis. I also declare that the intellectual content of this thesis is the product of my own work, except to the extent that assistance from others in the project's design and conception or in style, presentation and linguistic expression is acknowledged.'

Signed .....

Date 28/02/2020.....

INCLUSION OF PUBLICATIONS STATEMENT

UNSW is supportive of candidates publishing their research results during their candidature as detailed in the UNSW Thesis Examination Procedure.

Publications can be used in their thesis in lieu of a Chapter if:

- The candidate contributed greater than 50% of the content in the publication and is the "primary author", i.e. the candidate was responsible primarily for the planning, execution and preparation of the work for publication
- The candidate has approval to include the publication in their thesis in lieu of a Chapter from their supervisor and Postgraduate Coordinator.
- The publication is not subject to any obligations or contractual agreements with a third party that would constrain its inclusion in the thesis

Please indicate whether this thesis contains published material or not:

☒ This thesis contains no publications, either published or submitted for publication
(if this box is checked, you may delete all the material on page 2)

☐ Some of the work described in this thesis has been published and it has been documented in the relevant Chapters with acknowledgement
(if this box is checked, you may delete all the material on page 2)

☐ This thesis has publications (either published or submitted for publication) incorporated into it in lieu of a chapter and the details are presented below

CANDIDATE'S DECLARATION

I declare that:

- I have complied with the UNSW Thesis Examination Procedure
- where I have used a publication in lieu of a Chapter, the listed publication(s) below meet(s) the requirements to be included in the thesis.

Candidate's Name	**Signature**	**Date (dd/mm/yy)**
Iman Munadhil Abbas Al-Damad		28/02/20

This dissertation is dedicated to my family

ACKNOWLEDGEMENTS

The research presented in this thesis was carried out at the School of Civil and Environmental Engineering at the University of New South Wales. The presented work would not be possible without the support and dedication of numerous people.

First, I wish to express my deep gratitude and appreciation to my supervisor, Professor Stephen J. Foster, for the opportunity to undertake this research, and also for his invaluable guidance, continued advice, encouragement and constant support over the course of this research. It has been an absolute privilege to study under his supervision and mentorship.

Work on this thesis would not have been possible without the time and dedication provided by the school's technical and administrative staff. A very special thank you to Dr Zhen-Tian Chang, Mr. Ronald Moncay, Mr Greg Worthing and Mr Sanjeewa Herath for their assistance in manufacturing and testing the specimens. Appreciations are also given to Associate Professor Hamid Valipour and Professor Nasser Khalili.

The support provided by BOSFA towards the project and the provision of fibres is thankfully acknowledged. Special thanks to Dr Tian Sing Ng for his support and guidance.

I also wish to thank my friends and colleagues in the school for helping to make this adventure an enjoyable one.

Lastly, my sincerest gratitude extends to my family for their constant support, encouragement, patience, consistent inspiration and motivation. To my parents particularly, thank you for being unwaveringly supportive and believing in my abilities to overcome any obstacle; all the work presented herein is without a doubt the fruit of your support and patience.

ABSTRACT

The design of rigid pavements subjected to increasing heavy wheel loads and high traffic volumes necessitates, over time, the design of thicker pavements. With the advent of steel fibre reinforced concrete (SFRC), there exist the possibilities of enhancing fatigue performance of rigid pavements by including fibres in concrete and bridging cracks once they form. In the first part of this investigation, a material level of study was undertaken to investigate the performance of three different types of SFRC. Testing on round panels was undertaken to determine fatigue resistance; several varying load levels were applied at constant amplitude. A series of matched direct uniaxial tension and prism bending tests were also undertaken to provide comprehensive material characterisation data. It was concluded that fibres improve the fatigue life of concrete and a design model was developed. The model was validated against a large pool of experimental data obtained through the course of this study and is shown to correlate well with the test data. Also in this dissertation, the development of a constitutive model is presented for SFRC for post-cracking fatigue damage during cyclic loops. Comparing the results of the model with test data shows that the model is capable of accurately predicting the overall cyclic fatigue loading response of SFRC. The model is also able to capture the change in the COD, the stiffness changes with increasing load cycles and the number of load cycles to failure. In the final part of this study, a novel experimental program was developed to investigate the performance of large scale plain and SFRC slabs tested under static and cyclic loading – the SFRC slabs were 20% thinner than plain concrete slabs. The results show that the thinner SFRC pavements can carry higher numbers of load repetitions compared to those of currently constructed of plain concrete, with excellent serviceability performance in terms of crack width propagation and deflection development.

TABLE OF CONTENTS

LIST OF TABLES

LIST OF FIGURES

NOTATION

A	=	factor
A_c	=	area of concrete
A_f	=	cross sectional area of individual fibre
a	=	shear span
B	=	factor
b	=	width of the section
c_1	=	a coefficient accounting for the beneficial effect of the fibres to the tensile strength of the matrix
c_2	=	a factor controlling the steepness of the matrix tensile softening relationship
C	=	factor
D	=	total depth of section; a factor
d_f	=	diameter of steel fibre
d_g	=	maximum size of aggregate particle
d_n	=	depth of neutral axis
E	=	factor
E_c	=	elastic modulus of concrete
E_i	=	unloading modulus at cycle number i
E_t	=	tensile secant modulus of concrete
F	=	applied force; a factor
f'	=	static strength

$f_{0.5}$	=	residual tensile strength calculated at a COD = 0.5 mm
f_1	=	first-peak strength used in prism bending tests
$f_{1.5}$	=	residual tensile strength calculated at a COD = 1.5 mm
f_{150}^{D}	=	residual strength at net deflection of L/150 used in prism bending tests
f_{600}^{D}	=	residual strength at net deflection of L/600 used in prism bending tests
f_c'	=	characteristic compressive strength of concrete
f_{cf}	=	modulus of rupture
f_{cm}	=	mean compressive strength of concrete
f_{ct}	=	tensile strength of concrete matrix
$f'_{ct.fm}$	=	mean flexural tensile strength of concrete
$f_{ct,L}^{f}$	=	limit of proportionality
f_P	=	peak strength used in prism bending tests
$f_{R,j}$	=	residual flexural tensile strength of SFRC corresponding to a Crack Mouth Opening Displacement (CMOD) = $CMOD_j$
f_{sp}	=	split-cylinder concrete tensile strength
f_w	=	average tensile strength carried by fibres
h	=	thickness of a slab
h_{sp}	=	depth of section minus notch depth
k	=	notation for the total number of stress levels of fatigue loading; mean flexural tensile strength coefficient; a factor; ratio of length of a line drawn normal to the nearest axis of rotation in round panel test

$k_{3D,b}$	=	three-dimensional fibre orientation factor used in uniaxial tension test
k_b	=	fibre orientation factor used in prism bending tests
k_c	=	casting factor
k_n	=	notch coefficient
k_w	=	Westergaard modulus of subgrade reaction; Winkler constant
L	=	loading span
l_f	=	length of steel fibre
m	=	moment of resistance per unit length of fracture line
N	=	number of cycles
N_f	=	number of cycles to failure
N_{fi}	=	number of cycles applied to failure at a specific stress level i
$N_{f,exp}$	=	observed number of fibres crossing failure plane
$N_{f,theory}$	=	theoretical number of fibres crossing failure plane
N_i	=	number of cycles applied at a specific stress level i
n	=	number of stabilised cracks
P	=	corrected peak load used in round panel tests; applied central load
P'	=	measured peak load used in round panel tests
P_1	=	first-peak load used in prism bending tests
P_{150}^D	=	residual load at net deflection of $L/150$ used in prism bending tests
P_{600}^D	=	residual load at net deflection of $L/600$ used in prism bending tests

P_{max}	=	peak load
P_P	=	peak load used in prism bending tests
P_{upper}	=	load at the upper load level during cyclic test
R	=	stress ratio; radius of the panel and P is the applied central load
R_{150}^{D}	=	flexural strength ratio at net deflection of L/150 used in prism bending tests
r	=	radius from the centre of the panel to the support
S	=	stress level; loading span
SR	=	stress ratio
S_{max}	=	maximum stress level
S_{min}	=	minimum stress level
T	=	period of repetitive loads in seconds per cycle
T_{150}^{D}	=	flexural toughness at net deflection of L/150 used in prism bending tests
t	=	thickness of round panel
W	=	corrected energy absorption used in round panel tests
W'	=	measured energy absorption used in round panel tests
W_E	=	external work
W_I	=	internal work
w	=	Crack Opening Displacement (COD)
w_i	=	crack opening displacement at cycle number i
w_{max}	=	crack opening displacement at upper limit of applied cyclic load

w_T	=	crack opening displacement in which steel fibres have achieved maximum effectiveness
y	=	distance from the centre to the crack line
z	=	lever arm
α	=	fibre engagement constant; a factor
α_i	=	angles (i = …6)
β	=	a function of the depth of the neutral axis; a factor; material constant
γ	=	frequency distribution; a factor
δ	=	mid-span deflection; a factor
δ_1	=	net deflection at first-peak load used in prism bending tests
δ_{150}^{D}	=	net deflection of L/150 used in prism bending tests
δ_{600}^{D}	=	net deflection of L/600 used in prism bending tests
δ_P	=	net deflection at peak load used in prism bending tests
ε	=	factor
ε_t	=	cracking strain of matrix
ϵ	=	factor
θ	=	rotation of fracture line
$\xi(w)$	=	transition function
ρ_f	=	theoretical steel fibre volumetric ratio
$\sigma_{applied}$	=	fatigue stress
σ_{max}	=	maximum applied stress in fatigue models
σ_{min}	=	minimum applied stress in fatigue models

σ_{fu}	=	ultimate tensile stress carried by steel fibres
$\sigma(w)$	=	stress of fibre reinforced concrete for crack width w
$\sigma_c(w)$	=	strength of unreinforced cementitious matrix
$\sigma_f(w)$	=	post-cracking residual stress of fibre reinforced concrete for crack width w
ω	=	function of loading parameters

ABBREVIATIONS

AASHO	American association of state highway officials
ACPA	American concrete pavement association
AFGC	association Française de Génie civil
CBR	California bearing ratio
CMOD	crack mouth opening displacement
COD	crack opening displacement
COE	corps of engineering
COV	coefficient of variation
CRCP	continuously reinforced concrete pavement
FD	fatigue damage
FRC	fibre reinforced composite; fibre reinforced concrete
FSB	fully supported beam
FSS	fully supported slab
HBM	Hottinger Baldwin Messtechnik
JPCP	jointed plain concrete pavement
JRCP	jointed reinforced concrete pavement
LSCT	linear strain conversion transducer
LVDT	linear variable displacement transformer
MOR	moment of rupture
N.A.	neutral axis
PCA	Portland cement association

PM	Palmgren-Miner
RCCP	roller compacted concrete pavement
RPT	round panel test
SAP	superaccelerated pavement
SFRC	steel fibre reinforced concrete
SG	strain gauge
SR	stress ratio
SSB	simply supported beams
SSD	stationary dynamic deflectomer
UTM	universal testing machine

Chapter 1 INTODUCTION

1.1. Introduction

This section provides a brief introduction about the research topic, followed by a list of the main objectives to be achieved. Finally, a description of the organisation of the thesis is presented.

1.2. General

Portland cement concrete is a widely utilised material in construction such as industrial pavements, roadways, parking areas, airport runways and bridge projects (Krstulovic-Opara et al., 1995; Sorelli et al., 2006). Tensile stresses are developed in concrete pavements due to traffic loadings, moisture and temperature gradient. Traffic axel loadings mainly lead to flexure and shear of concrete member; these loads are repetitive for millions of cycles throughout the structure's service life. This continuous flexing of the concrete pavement results in the development of microcracks, which continue to grow over time, due to repetitive loading, resulting in fatigue damage and failure (Cachim, 1999; Saleh et al., 2012).

Fatigue damage is a concern because a material designed to withstand a safe load once may fail when this same load is applied repeatedly. This cyclically applied load causes cracks to initiate and propagate with time from the areas of highest stress concentrations in the concrete layer of the pavement. The influence of these stresses can be manifested through temperature gradients, moisture gradients, external loads, as well as a combination of these, at any time during the service life of the pavement. The material eventually fails when the crack grows to a sufficient width so that applied load causes a stress that exceeds the ultimate strength of the material (Roesler, 1998; Titus-Glover et al., 2005).

In the last decades, the utilisation of fibre reinforced concrete has been increasing. The results of experimental tests indicate that the addition of fibres to concrete enhance the following properties of plain concrete: tensile splitting, flexural strength, first cracking strength, toughness, stiffness, durability, impact resistance, deflection, crack width, resistance to shrinkage and creep, and fatigue properties (Johnston, 1985; Johnston and Zemp, 1991; Banthia et al., 1995; Khaloo and Kim, 1997; Elsaigh and Kearsley, 2002; Kwan et al., 2002). The improvement in the mechanical properties of steel fibre reinforced concrete (SFRC) is attributed to the controlling of the cracking mechanism. The concept of fatigue performance of concrete and fibre reinforcement has been studied by several researchers, but there are still some unanswered questions about the fatigue behaviour of fibre reinforced structures, as well as the influence of various design parameters.

Several studies were carried out to evaluate the fatigue performance of SFRC at the material level. In addition, numerous experimental testing has been undertaken for SFRC slabs on ground under static loading. However, the failure of pavements occurs at much lower stresses due to fatigue and the fatigue behaviour of SFRC pavements, at the structural level, has not received much attention. The purpose of this research is to investigate the fatigue behaviour of SFRC pavements and to test the hypothesis that thinner SFRC pavements can carry the same load repetition of currently constructed plain concrete pavements with minimum maintenance requirement in terms of deflection and crack widths. Attention and consideration are given to the method of applying the fatigue load in an attempt to simulate the crack patterns, due to load sequence, and failure mode of pavements in practice.

1.3. Research Objectives

The expected outcomes of this research project are:

- investigate the performance of SFRC pavements under simulated cyclic wheel loading;
- compare the obtained results with those of plain concrete pavements;
- understand the mechanism of fatigue fracture failure of SFRC pavements;
- examine the fatigue serviceability performance of SFRC pavements;
- assess the post-peak fatigue performance of various fibre types; and
- test the hypothesis that thinner SFRC pavements can carry the same or higher load repetition than that of plain concrete pavements constructed using contemporary methods while maintaining a minimum maintenance requirement.

1.4. Scope of the Work and Thesis Organisation

This research considers the behaviour of thinner SFRC pavements under fatigue loading. Experimental and numerical analysis programmes are developed to determine the entire behaviour of the SFRC pavements including failure mechanisms and life expectancy under fatigue. The results of this study can be used to evaluate the failure cycle as well as deflection and crack widths of SFRC pavements.

This thesis consists of seven chapters and four appendices. Chapter 2 is a review of the literature. It starts with a general background of different types of concrete pavements, where their distress modes are briefly reviewed. The state of the art of the fatigue performance of concrete generally is presented as well as the characterisation of fibre reinforced concrete under cyclic loading. The literature review is then extended to describe the major studies of slabs under static and cyclic loading; this is followed by a comparison of cracks patterns between tested specimens and observed ones in practice. The review is completed by a section illustrating various concrete fatigue models.

Following this, a discussion pertaining to the limitation of the literature review is presented.

Chapter 3 describes the experimental program undertaken to investigate the material characterisation of SFRC under monotonic and cyclic loading. The fatigue test results of three series of round panel tests are also discussed in details in this chapter.

In Chapter 4, a simple and efficient inverse analysis procedure capable of converting the results from notched and un-notched prism bending tests to uniaxial stress is developed for strain softening SFRC. The model is validated against a large pool of experimental data obtained through the course of this study.

In Chapter 5, a post-cracking fatigue model of round panel determinate supported panels is developed. The model is capable of predicting the fatigue damage during cyclic loops. The model is verified against available test data with a framework developed for further calibration as new data becomes available.

Chapter 6 reports the fatigue behaviour of large scale plain and SFRC pavements. It includes a discussion pertaining to the materials used and the testing regime adopted. Major conclusions and future research recommendations drawn from this study are highlighted in Chapter 7.

Appendices A to D contain raw and processed data collected from the laboratory testing programmes over the course of this study.

Chapter 2 LITERATURE REVIEW

2.1. Rigid Pavements

The aim of this section is to provide a clear understanding and description of several types of rigid pavements used in practice. This is extended to provide information about the subgrade and subbase of pavement. Eventually distinct distress categories are briefly presented.

2.1.1. Introduction

Road pavements are used to directly support the traffic induced stresses and transfer them to the founding soils; or earthworks. A typical road pavement consists usually of several layers. The upper layer of the roadway absorbs the tangential stresses induced by the traffic while the base and subbase layers do the degradation of the vertical loads (Cachim, 1999).

In practice, pavements have been mainly divided into flexible and rigid pavements based on the way that they degrade stresses to the foundation layers. In flexible pavements, high stresses are induced into the soil because the loads are degraded through small area. On the other hand, in rigid pavements, usually made of concrete slabs, the stresses induced on the founding soils are smaller because the pavement slab stiffness is higher than that of the soil. Therefore, the performance of concrete pavements is mainly, but not entirely, dependent on the performance of the concrete slab. This means that developing comprehensive understanding of concrete behaviour is important to correctly analyse and design concrete road pavements (Cachim, 1999). The components of flexible and rigid road pavement structures are shown in Figures 2.1 and 2.2, respectively.

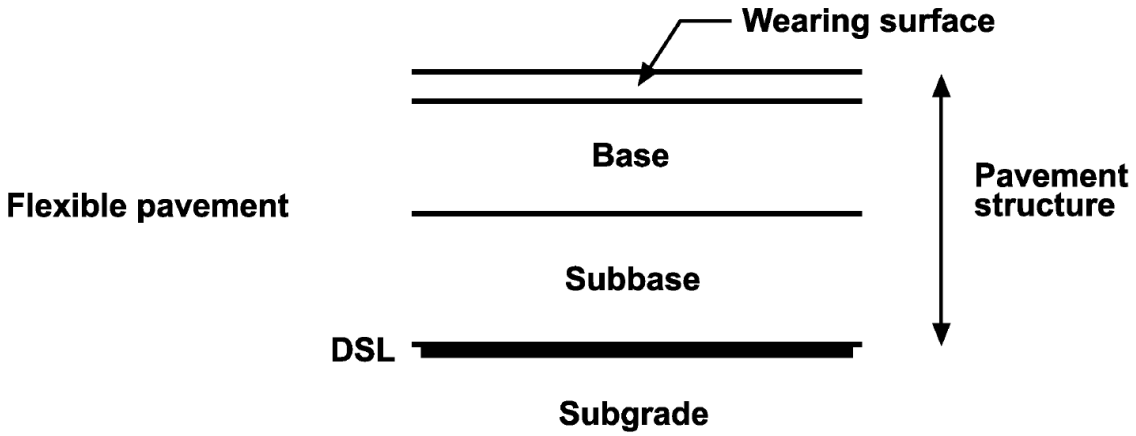

Figure 2.1 – Components of flexible road pavement structures (Austroads, 2009).

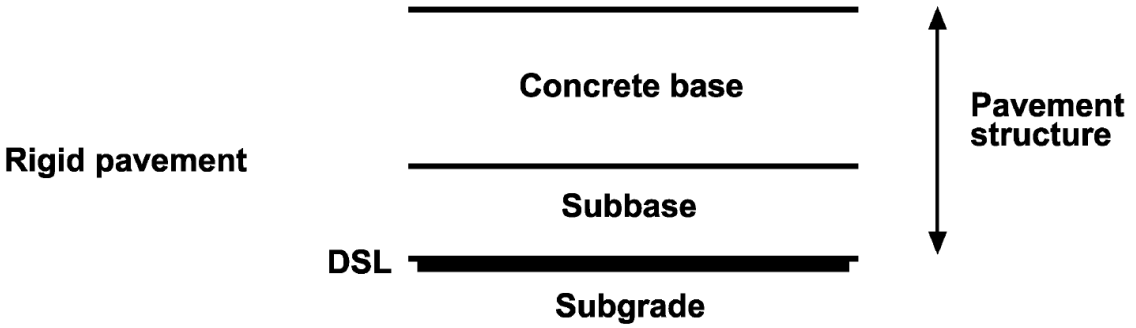

Figure 2.2 – Components of rigid road pavement structures (Austroads, 2009).

Concrete usually has a high initial cost compared to asphalt; however, it lasts longer and generally has low associated maintenance costs. The choice of pavement type varies with the function of the road, traffic loading, availability of materials, and environment. The main reasons to adopt a concrete pavement are its high strength, good durability performance and reduced maintenance requirements. Therefore, concrete pavements are usually utilised for high traffic situations where maintenance works are expensive for road users. Concrete pavements should have a lifetime ranging from 30 to 40 years of low maintenance.

A significant feature of concrete is its brittle behaviour in tension; this is one of the main drawbacks in the performance of concrete pavements. Therefore, some actions need to be taken to overcome this drawback and to control the crack formation to ensure

its performance while maintaining low maintenance, particularly at joints. To this end, reinforcement or/and addition of fibres may be used to increase serviceability (Cachim, 1999; Hoel and Short, 2006; Austroads, 2012).

2.1.2. Types of Rigid Pavements

Various types of concrete pavements are currently in use, depending on the required function. The length of concrete pavement slabs can be short (3.6 m – 6 m), long (7.5 m – 9 m) or continuous. The pavement thickness is dependent on the foundation type and traffic density but usually ranges from 20 cm to 30 cm. This section presents the most conventionally concrete pavements used in practice such as jointed plain concrete pavement (JPCP), jointed reinforced concrete pavement (JRCP), continuously reinforced concrete pavement (CRCP) and roller compacted concrete pavements (RCCP). In addition, some of the other less common concrete pavements are also described (Cachim, 1999; Austroads, 2012; Delatte, 2014).

Jointed Plain Concrete Pavement (JPCP)

Jointed plain concrete pavement (JPCP) is usually the cheapest to build and the easiest to construct. It consists of short plain (unreinforced) concrete slabs with transverse contraction joints spaced between 3.6 m and 6.0 m. The joints are spaced closely enough to avoid crack formation in the slab during the pavement's lifetime. The spacing of transverse joints is sometimes not uniform to avoid the resonance. Loads need to be transferred across the joints and this is usually achieved by aggregate interlock and dowels (Cachim, 1999; Austroads, 2012; Delatte, 2014). Dowel bars have mainly two functions (Delatte, 2014); the first is to prevent differential vertical movement of adjacent slabs (faulting), and the second is to allow horizontal movement, so that joints can open and close without building up stress.

JPCP construction usually uses tie bars to connect between the traffic lanes and to avoid longitudinal cracking. The ties are made of steel bars. Unlike the transverse joints where

movements of the edge slabs are allowed; however, in the longitudinal joints, the movement between the two faces of the joint should be prevented and, accordingly, good bonding between the bars and concrete must exist. Tie bars are used to separate lanes for highway pavements while dowel bars are used in the direction of the traffic movement (ACPA, 1999; Cachim, 1999; Delatte, 2014). JPCP is illustrated in Figure 2.3.

During the construction of JPCP, concrete is continuously poured with a slipform paver. The transverse joints are usually made later by saw cutting the concrete slab; this needs to be performed before the appearance of the first shrinkage cracking which is usually about 12 hours after placing the concrete. The joint grove depth is usually about 25% of the slab thickness (Cachim, 1999; Austroads, 2012; Delatte, 2014).

Jointed Reinforced Concrete Pavement (JRCP)

Jointed reinforced concrete pavements (JRCPs) are similar to JPCP, except the slabs are longer and light reinforcement is added. This reinforcement is usually used only as shrinkage and temperature steel. The reinforcement ratio in the longitudinal direction is usually in the range of 0.1% to 0.25% of the cross sectional area. A lower volume of steel is used in the transverse direction. The steel bars are placed at the neutral axis of the slab (mid-depth); accordingly, the reinforcement has negligible influence on the flexural performance of concrete, with its main function to control the cracks and keep them together. Due to the addition of steel reinforcement, larger spacing between joints is allowed. The spacing between concrete slabs typically ranges from 7.5 m to 9 m, although slab lengths of up to 30 metres have been used in practice (ACPA, 1999; Cachim, 1999; Delatte, 2014).

Even though the joints in JRCP slabs are spaced further apart than for JPCP slabs, the cracks will still form within the same interval as JPCP. Thus, the main advantage of JRCP over JPCP is fewer joints. However, this is generally outweighed by the cost of

steel and poor performance of the joints and the cracks as the joints are spaced further apart, compared with JPCP (Cachim, 1999; Delatte, 2014). JRCP is presented in Figure 2.4.

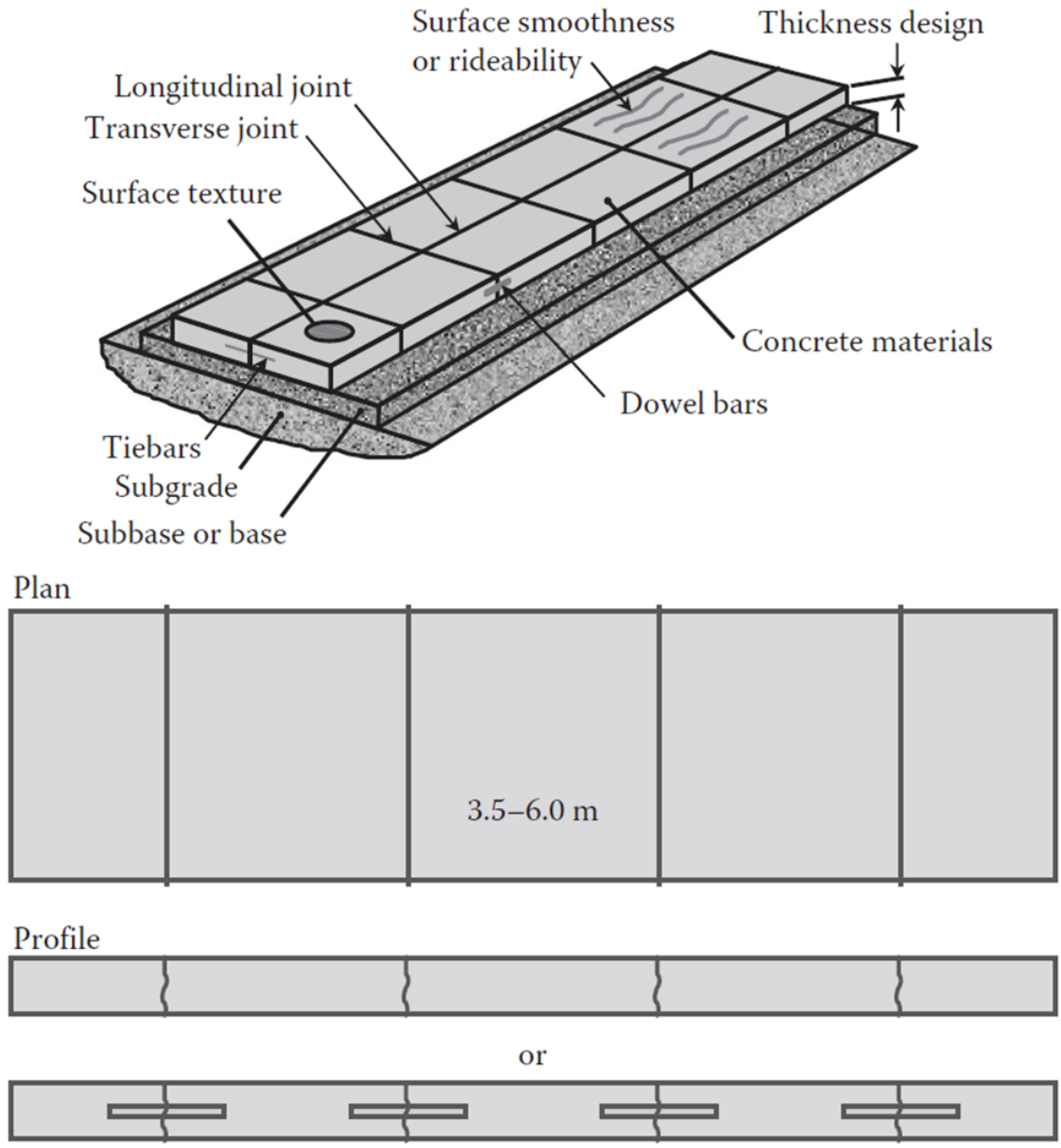

Figure 2.3 – Jointed plain concrete pavement (Delatte, 2014).

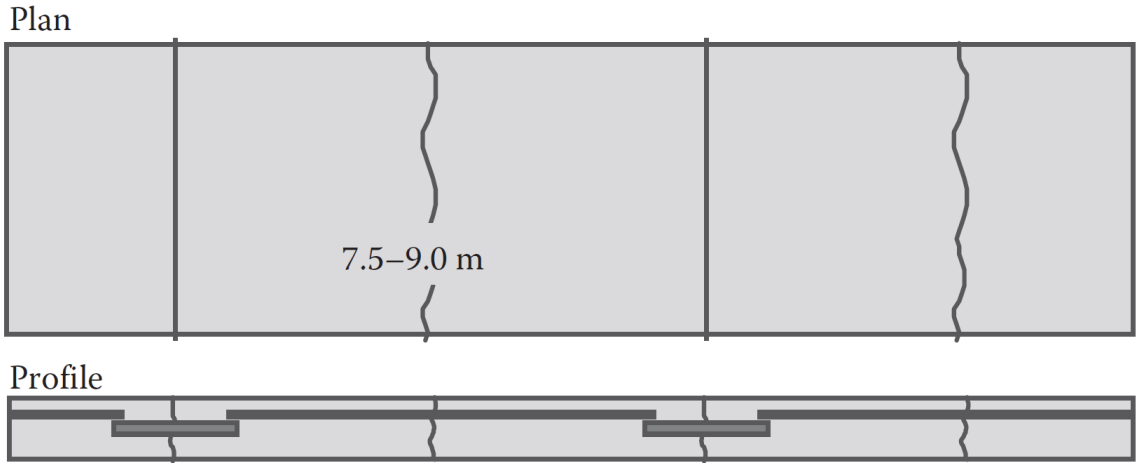

Figure 2.4 – Jointed reinforced concrete pavement (Delatte, 2014).

Continuously Reinforced Concrete Pavement (CRCP)

A continuously reinforced concrete pavement (CRCP) is usually used when heavy and a high volume of traffic is expected and is characterised by the absence of transverse joints over considerable lengths. Cracks are controlled by the addition of heavy longitudinal steel reinforcement at ratios typically of 0.4% to 0.8% of the cross sectional area. Lower percentage of reinforcement is provided in the transverse direction as it only serves as temperature steel.

The reinforcing steel holds the cracks tightly together. Consequently, the cracks in CRCP are closely spaced, approximately 0.6 m – 2 m apart (see Figure 2.5), and are of small width (around 0.3 mm). CRCP is expected to have a lifetime of 40 years with almost no maintenance. Building of CRCP is expensive; however, the maintenance cost is minimal, provided that the slab is well constructed (Cachim, 1999; Rasmussen et al., 2011; Delatte, 2014).

There are two execution methods to place the steel reinforcement in CRCP. The reinforcement is placed in advance laying on supports and the concrete is placed afterwards. Or, alternatively, the steel bars can be placed simultaneously with concrete

by the aid of trumpets. No transverse reinforcement is used in the latter case (Cachim, 1999; Rasmussen et al., 2011).

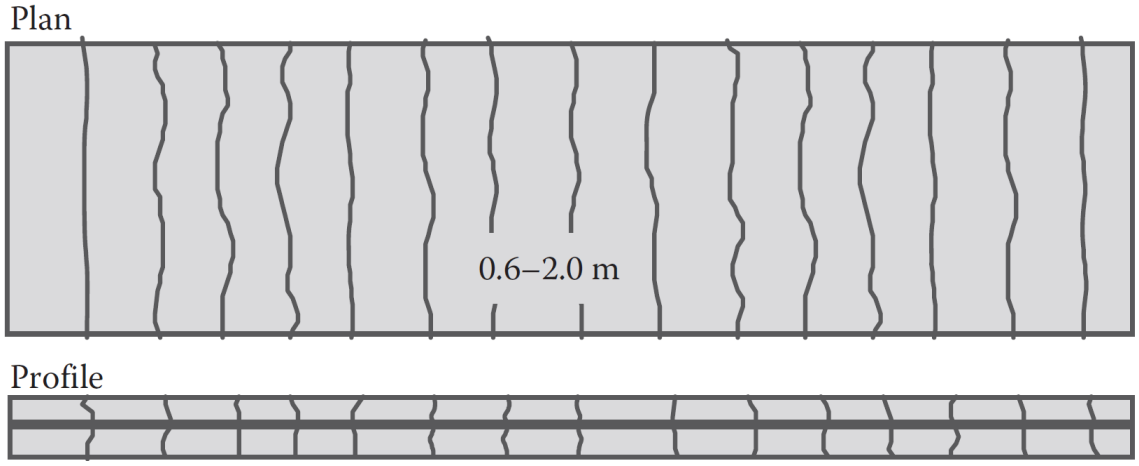

Figure 2.5 – Continuously reinforced concrete pavement (Delatte, 2014).

Roller Compacted Concrete Pavement (RCCP)

Roller compacted concrete pavements (RCCPs) are characterised by their low water content mix; consequently, the pavements shrink less and the cracks or joints are further apart than those for JPCP. The dry mix concrete is compacted by a roller instead of the traditional vibration. A two-step compaction is typically performed; a vibrated rolling followed by rubber-tyre (Delatte, 2014).

Due to the construction process, the surface of RCCP is usually rough, which is not ideal for high speed traffic. Therefore, a bituminous surface layer must be used if RCCP is applied for high speed traffic. Whenever RCCP is used in strengthening works, these pavements can be quickly open to traffic (Cachim, 1999).

RCCPs are economical to construct, do not require forms, dowel or tie bars and there is no need for the labour for texturing and finishing. This means that construction costs are lower than JPCP (Cachim, 1999; Delatte, 2014).

Other Types of Concrete Pavements

There are various other types of concrete pavements available such as prestressed concrete pavements, recycled concrete pavements and cellular rigid pavements. A brief illustration of these pavements is presented.

Prestressed concrete pavements

Prestressed concrete pavements are generally expensive and, therefore, not often used in road construction. The length of concrete slabs can reach 300 meters while the thickness of the slab typically ranges from 120 mm to 200 mm. The major benefits of prestressed concrete pavements are their reduced number of joints, reduced thickness and reduced numbers and widths of cracks. The main disadvantages are their cost and the difficulties in applying the prestress (Cachim, 1999; Tayabji et al., 2013; Delatte, 2014).

Recycled concrete pavements

As there is an increasing volume of demolition waste from the construction industry, including concrete fragments, it is seen as necessary to utilise these wastes in a safe and environmentally acceptable manner. Accordingly, herein in pavements seems as a promising solution. Some experimental investigations have been undertaken on studying recycled concrete pavements and the results seem encouraging (Cachim, 1999).

Cellular rigid pavements

Cellular rigid pavements are constructed by using waste plastic for forms to create cells. This technique allows a reduction by about 25% of concrete, compared with conventional concrete pavements. These pavements may typically be used for parking areas, walks, revetments, slabs on ground and similar construction applications (Bright and Mays, 1996).

2.1.3. Subgrade and Subbase

For concrete pavement design, the support given to concrete slab by the subgrade and the subbase, where used, are of significant importance. The quality of the support provided to the pavement, the moisture susceptibility, and the frost susceptibility should be considered in design (Austroads, 2012; Delatte, 2014).

The quality of support is generally characterized in terms of the Westergaard modulus of subgrade reaction, k_w, in units of MPa/m or N/mm^3. This modulus represents the spring constant of an imaginary spring or dense liquid foundation supporting the slab. It is assumed that the subgrade reaction increases linearly with the deflection of the slab (PCA, 1984; Delatte, 2014). California bearing ratio (CBR) is another parameter that can be used to determine the quality of the subgrade. CBR is typically a measurement of strength, a plate bearing test is used to compare the bearing capacity of a material with that of a well-graded crushed stone (Austroads, 2012).

Following Austroads (2012) guidelines, the thickness of the concrete pavement is determined based on the strength of the subgrade that is assessed in terms of CBR. All materials within one metre depth below the subbase materials must be assessed to determine the design subgrade CBR. The subgrade materials should be consisted of a uniform volumetric stable material that would be constant for the entire projected life of the pavement with a minimum CBR value of 5%. Table 2.1 shows typical presumptive values of the subgrade design CBR. Table 2.2 shows the approximate relationship between CBR and modulus of subgrade reaction (k_w) values of some typical soil type (Knapton, 1999).

Table 2.1 – Typical presumptive subgrade design CBR values (Austroads, 2012).

Description of subgrade		**Typical CBR values (%)**	
Material	**Unified Soil Classification**	**Excellent to good drainage**	**Fair to poor drainage**
Highly plastic clay	CH	4	2 – 3
Silt	ML	5	2
Silty-clay	CL	5 – 6	3 – 4
Sandy-clay	CL		
Sand	SW, SP	10 – 18	10 – 18

Table 2.2 – Typical values of modulus of subgrade reaction, k_w, related to soil type (Knapton, 1999).

Soil type	**CBR (%)**	**k_w value (N/mm^3)**
Humus soil or peat	< 2	Unacceptable
Recent embankment	2	0.01 – 0.02
Fine or slightly compacted sand	3	0.015 – 0.03
Well compacted sand	10 – 25	0.05 – 0.10
Very well compacted sand	25 – 50	0.10 – 0.15
Loam or clay (moist)	3 – 15	0.03 – 0.06
Loam or clay (dry)	30 – 40	0.08 – 0.10
Clay with sand	30 – 40	0.08 – 0.10
Crushed stone with sand	25 – 50	0.10 – 0.15
Coarse crushed stone	80 – 100	0.20 – 0.25
Well compacted crushed stone	80 – 100	0.20 – 0.30

Subbase is generally defined as one or more layers of compacted materials that are located between the subgrade and concrete pavement slab. Subbase is used for the following reasons (AASHTO, 1993):

- ensure uniform, permanent and stable support;
- increase the subgrade reaction modulus;
- reduce the damaging effects from the frost actions;
- stop the pumping of subgrade materials through the joints, cracks and edges of the rigid pavement; and
- provide a platform for construction equipment.

Using the subbase only to increase the subgrade reaction modulus is not economical, without consideration of the other reasons.

2.1.4. Distress Modes in Pavements

The main function of a pavement is to support the applied traffic loading and environmental effects over its projected life. The applied wheel load typically tends to spread through a slab resulting in significant tensile stresses at the bottom of the layer. Flexible pavement deforms (bends and deflects) under applied loads and horizontal tensile strains are developed (Figure 2.6(a)). In rigid pavement, a relatively uniform distribution of strains on the subgrade is produced by the applied wheel load as shown in Figure 2.6(b) (Austroads, 2009).

In concrete pavement structures, failure can occur due to cracking, joint deficiencies, surface defects and/or miscellaneous distress (Miller and Bellinger, 2003). However, faulting at transverse joints (in JPCP and JRCP) and fatigue cracking is the major distress modes concerned in rigid pavement design (Kabir, 2015). The topic of faulting of transverse joints is beyond the scope of this research.

In road pavements, repeated traffic loading can result in stresses that cause fatigue damage. Cyclically applied load can cause cracks to initiate and propagate with time

from the areas of highest stress concentration. The material eventually fails when the crack grows to a sufficient width so that applied load causes a stress that exceeds the ultimate strength of the material (Titus-Glover et al., 2005). The repeated occurrence of traffic stresses can lead to structural cracks propagating through the concrete layer of the pavement. The influence of these stresses can be manifested through temperature gradients, moisture gradients, external loads, as well as a combination of these, at any time during the service life of the pavement (Roesler, 1998). The fatigue loading can result in micro-cracks that propagate in the concrete pavement resulting in transverse cracks, longitudinal cracks and/or corner cracks as shown in Figure 2.7 (Kabir, 2015).

Transverse cracks occur perpendicular to traffic direction (Miller and Bellinger, 2003). This crack type can propagate and lead to a shattered slab, causing slab replacement (Delatte, 2014). The main reason to the occurrence of transverse cracks is the combination of heavy traffic load repetitions and stresses due to drying shrinkage, moisture and temperature gradients (Huang, 2004).

Longitudinal cracks are those parallel to the direction of the traffic (Miller and Bellinger, 2003). These cracks occur due to combinations of heavy load repetitions, loss of supports, wrapping and curling stresses and/or improper construction of longitudinal joints (Delatte, 2014).

Corner cracks occur only in the corners of JPCP and JRCP (Miller and Bellinger, 2003). The main reasons for corner breaks, as stated by Huang (2004), can be poor load transfer through the joints, repetition of load with loss of support, thermal curling and moisture warping stresses. Two criteria are required for a crack to be classified as a corner break. The first one is that the crack should extend vertically through the concrete pavement thickness. Secondly, the crack must intersect with both the transverse and longitudinal joints/edge at less than 1.8 m from the corner of the pavement (Huang, 1993).

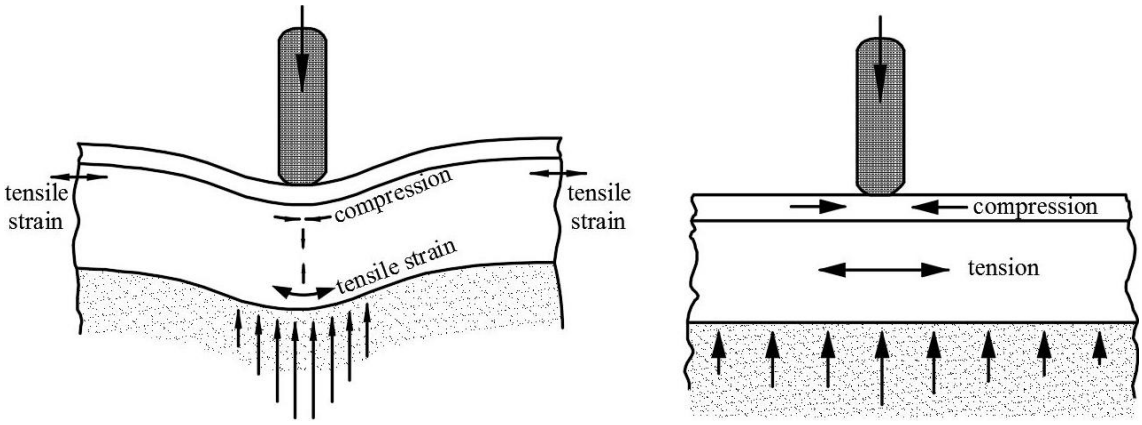

(a) (b)

Figure 2.6 – Responses of (a) flexible and (b) rigid pavements types to load (Austroads, 2009).

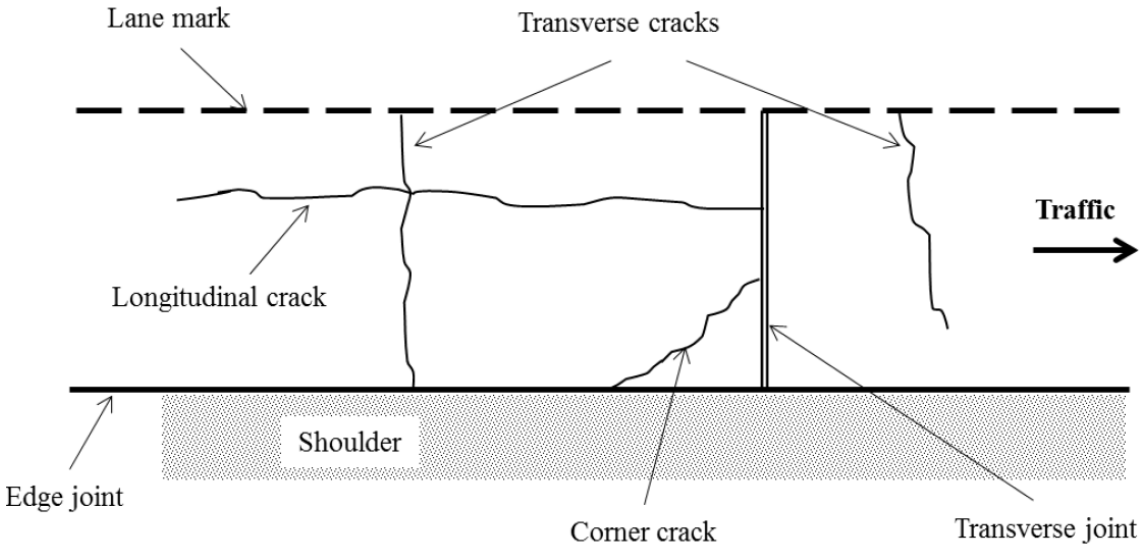

Figure 2.7 – Distresses that develop in the rigid pavement under traffic loading (Kabir, 2015).

Cracks can either propagate from the bottom surface to the upper one or vice versus. Typically for fatigue distress analyses, the stresses/strains of the bottom surface of the concrete slab are considered for analysis purposes as it is predicted that the maximum tensile stresses exist at the bottom layer due to the traffic loading near the mid-point of the longitudinal edge of the pavement (Heath et al., 2003). It is assumed that the curling stress due to negative thermal gradients is negligible at the mid-slab edge and that the positive thermal gradients add to the stress caused by traffic loading (Jiang and Tayabji, 1998).

Another case that should be considered is when moisture and temperature gradients are high. In this case, the maximum tensile stresses exist at the upper surface and the cracks accordingly are developed at the top surface of concrete and propagate to the bottom surface with the traffic load being applied near the transverse joint along the longitudinal edge of the slab (Heath et al., 2003; Hiller, 2007).

To evaluate the stresses induced into a structure, information about loads, structural geometry, boundary conditions and material constitutive relationships are required. In rigid pavements, stresses are mainly developed due to traffic, temperature and moisture gradients. Such types of loading can be repeated thousands or millions of times during the life of concrete pavement. Consequently fatigue is an important consideration in the design of road pavements. Stresses induced due to temperature and moisture gradients are beyond the scope of this research and; thus, only the fatigue induced by traffic loading is discussed further.

2.2. Fatigue of Concrete

In this section, background knowledge about fatigue is provided. This is followed by a brief description of the fatigue failure mechanism of concrete. After that, several factors influence the fatigue performance of concrete as well as the effect of strain hardening are discussed.

2.2.1. Background Knowledge

Concrete structures in Australia are mostly subjected to static loads. However, some structures such as highway pavement and bridges projects might be subjected to repetitive cyclic loading, which may give a rise to fatigue problems. Fatigue is a process of progressive and localized structural damage due to internal structural changes in the material. In concrete, these changes are mainly attributed to a progressive process of micro-crack initiation and propagation, leading to macro-cracks that grow to a stage in which failure occurs. These internal structural changes lead to changes in the mechanical properties of the materials, where an increase in the permanent strain is obtained as well as steady decrease in the stiffness of the structure and, eventually, can lead to a fatigue failure. This means that fatigue failure does not occur due to applying a large isolated load but by the repeated occurrence of loads that, individually, cannot cause failure. Even if fatigue failure does not occur, fatigue loading can promote to problems such as aggravating crack widths, deflection and reduced stiffness. Consequently, the structure might be no longer able to carry the loads that it was designed for (Holmen, 1982; Lee and Barr, 2004; Parvez and Foster, 2014).

Fatigue loading is mainly divided into two components; low cycle and high cycle loadings. Low cycle loading involves applying high stress levels for a few load cycles; i.e. from 1 to 10^3 cycles. While high cyclic loading is characterised by applying low stress levels for large number of cycles, approximate range from 10^3 to 10^7. Table 2.3 outlines the classification of fatigue loading as described by Hsu (1981).

Table 2.3 – Classification of fatigue loading (Hsu, 1981).

Low cycle fatigue			**High cycle fatigue**				**Super high cycle fatigue**		
1	10	10^2	10^3	10^4	10^5	10^6	10^7	10^8	10^9
Structures subject to earthquakes			Airport pavements and bridges		Highway and railway bridges, highway pavements		Mass rapid transit structure		Sea structures

Fatigue strength is generally expressed as the maximum stress level of a cyclic load, presented usually as a friction of the monotonic strength. Stress level, S, is generally defined as:

$$S = \frac{\sigma_{applied}}{f'} \tag{2.1}$$

where $\sigma_{applied}$ is the applied fatigue stress and f' is the static strength (compressive or tensile).

Generally, fatigue models for concrete pavement design incorporate both the stress induced in the concrete by the applied loading and the flexural strength of concrete, or moment of rupture (MOR), evaluated from prism bending tests under a third point load configuration, and expressed in terms of stress ratio (SR):

$$SR = \frac{\sigma_{applied}}{MOR} \tag{2.2}$$

The term stress ratio in concrete pavement design is used to describe the critical bending stress over the flexural strength of concrete, and is different from the stress ratio, R, which is defined as:

$$R = \frac{S_{min}}{S_{max}} \tag{2.3}$$

where S_{max} and S_{min} are the maximum and minimum stress levels, respectively.

Several approaches have been used to assess the fatigue strength of structural members. The most accepted and utilised method in engineering is the empirically derived Whöler curve, also known as the *S-N* curve. The *S-N* curve is the relationship between the fatigue strength, S, and the number of repeated loading cycles, N and is usually plotted in a semi-log representation, with S usually plotted on the y-axis and N is plotted on the x-axis. *S-N* curves are generally plotted for a given constant minimum stress level or a constant stress ratio, R. As stated above, the stress level is obtained by non-dimensionalising the applied fatigue stress by the static strength of an identical specimen, as shown in Equation 2.1. Accordingly, this non-dimensionalised curve is independent of the specimen shape, the concrete strength, curing conditions, the moisture and the age conditions at loading (Hsu, 1981; Lee and Barr, 2004).

A series of Whöler curves for different stress ratios are demonstrated in Figure 2.8. As can be noticed from the figure, a higher minimum stress (σ_{min}) leads to higher fatigue strength; this means that smaller fatigue life is obtained when a greater stress range is applied (CEB, 1988).

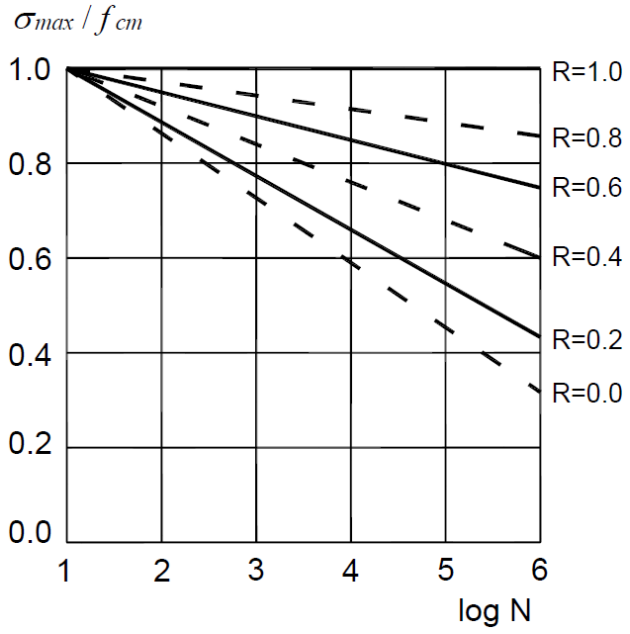

Figure 2.8 – *S-N* curves for concrete for different values of R (CEB, 1988).

2.2.2. Mechanism of Fatigue in Plain Concrete

Concrete is non-homogenous material and has inherent flaws. For example, pores, air voids, shrinkage cracks and lenses of bleed water under coarse aggregates. Fatigue damage begins at the microscopic level and is associated with crack growth and, ultimately, reduction in the stiffness of the materials (Zhang, 1998). Gao and Hsu (1998) described the fatigue failure mechanism of concrete in three stages. Stage I is termed as flaw initiation, where flaws are developed within the weak regions of concrete. This stage typically occurs during the hardening process of fresh concrete where flaws and microcracks are formed. Stage II is typically termed micro-cracking. In this stage, the flaws gradually propagate to the critical size. This stage occurs at a micro-meso level where the internal structural degeneration is characterised by the evaluation of the micro-defects. At the final stage, Stage III, continuous or macro-cracks are formed as well as sufficient numbers of unstable cracks; which leads eventually to failure. During this macro-level stage, the strength and the stiffness of the structure decrease with increasing numbers of loading cycles. The development of these stages is schematically illustrated in Figure 2.9.

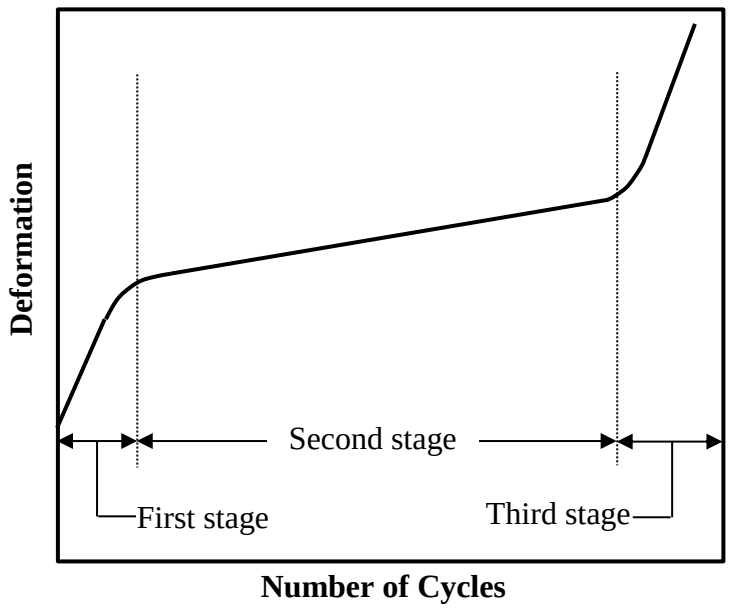

Figure 2.9 – Graphical presentation of deformation development during fatigue loading.

As observed in Figure 2.9, each of the first and third stages makes up approximately 10% of the total fatigue life curve. The middle stage accounts approximately to the remaining 80% of the curve (Cornelissen and Reinhardt, 1984). Hordijk and Reinhardt (1993) found that the slope of the second stage is correlated to the fatigue life. This indicates that fatigue failure criterion for concrete is based on ultimate strain or deformation, as it appears that there is a strong relationship between the increase of strain per cycle in the secondary branch of the cyclic creep curve and the number of cycles to failure.

Similar crack patterns are observed under both static and fatigue loading. However, unlike cracks that occur as a result of monotonically increasing statically applied loads, fatigue crack growth can be divided into two stages, the deceleration and acceleration stages. During the deceleration stage, the crack growth rate decreases as the crack is growing, while during the acceleration stage, there is a steady increase in the rate of crack growth to failure (Su and Hsu, 1988; Horii et al., 1992; Kim and Kim, 1996; Kolluru et al., 2000). Hsu (1984) found that different loading cycle types result in different mechanism changes within the concrete matrix. For high cycle loading (e.g. traffic loadings), cracks are formed in a slow and gradual process. However, in low cycle loadings, mortar cracks result in the formation of networks of continuous cracks. Additionally, it was found that concrete fracture toughness under fatigue conditions is higher than that under monotonic loading and crack length increases with increasing the number of loading cycles (Perdikaris et al., 1986). Originally, it was believed that concrete has an endurance or fatigue limit but Saito (1983) found that plain concrete subjected to repeated uniaxial tensile stresses exhibit no fatigue limit under 2×10^6 cycles. This indicates that there is no known stress level below which fatigue life of concrete can be infinite. However, some researchers agree that the fatigue strength of concrete in tension, compression and bending at 10^7 cycles is approximately equivalent to 55% of the static strength of concrete (Van Ornum, 1903; Van Ornum, 1907; Crepps, 1923; Hatt, 1925; Williams, 1943; Kesler, 1953; Saito, 1983; Lee and Barr, 2004).

2.2.3. Factors Influencing Fatigue Behaviour

The fatigue strength of concrete is influenced by several parameters. Some of these parameters are:

- matrix composition;
- loading frequency;
- amplitude cyclic loading;
- stress ratio;
- loading conditions;
- boundary conditions;
- stress level;
- number of cycles; …. etc.

However, the agreement on the influence of these parameters on the fatigue performance of concrete is not yet confirmed in the literature. The influence of some of these parameters is presented below.

Matrix Composition

The influence of mixture composition such as type of aggregates, water-cement ratio, air entrainment, curing conditions, cement type and age at loading is not yet finalised in the literature. However, it is indicated that fatigue performance of concrete is not significantly influenced by these parameters provided the fatigue strength is presented in terms of the ultimate static strength (Raithby and Galloway, 1974; Raithby, 1979; Klcriber, 1982; RILEM, 1984).

Researchers found the specimen's moisture content or curing conditions does not influence the fatigue behaviour of concrete when adopting a stress ratio concept (Raithby and Galloway, 1974). However, fatigue test results are generally characterised by a large amount of scatter due to the heterogeneity of the material. This scatter of data

is attributed to the uncertainty in determination of the reference static strength (Cornelissen and Reinhardt, 1984). Accordingly, it is expected that the scatter of static strength results in increasing the scatter of fatigue test results as fatigue stresses do not become non-dimensionalised by the static strength of the same specimen; instead, normalisation is by a second specimen of the same mix (Mallet, 1991).

Loading Frequency

Many researchers have indicated that the loading rate has an effect on the monotonic strength of concrete; accordingly, the frequency of cyclic loading has a large impact on fatigue test results. Accelerated fatigue testing procedures tend to increase the true fatigue resistance of the specimen and overestimate the fatigue life of the structure, especially in case of structures that carry high stress ratios at low cycles (Mallet, 1991). However, this influence is less prevalent when the maximum stress level is below 75% of the monotonic stress. Studies have shown that the influence of loading frequency within the range from 1 Hz to 15 Hz, is considered insignificant for a stress level below 75% (Kesler, 1953; Raithby and Galloway, 1974; Cornelissen, 1984). For stress levels above 75%, however, it has been observed that the fatigue life increases with higher loading frequency (McCall, 1958; Sparks and Menzies, 1973; Cornelissen and Reinhardt, 1984).

Zhang et al. (1996) claimed that higher loading frequency results in longer fatigue life due to less damage occurrence in concrete at high loading frequencies. However, testing at high frequency can result in undesirable heating issues. It was suggested to limit the frequency of cyclic loading for beams under fatigue bending tests to no more than 3 Hz to avoid any heating influencing the results (Mallet, 1991).

Amplitude Cyclic Loading

The loading patterns also influence the fatigue life of concrete. The fatigue behaviour of concrete structures under constant amplitude loading regimes is different from that under variable amplitude loading (RILEM, 1984). However, most studies on the fatigue behaviour of concrete have been restricted to constant amplitude loading. Loading frequency and stress ratio have substantial impact on the fatigue life of concrete.

Oh (1991) indicated that both the magnitude and the sequence at which the variable amplitude loading is applied have a great influence on the fatigue performance of concrete. Moreover, it was found that the fatigue resistance of concrete is reduced by stress reversals (Cornelissen, 1984; Zhang et al., 1996).

Stress cycles can largely vary in magnitude, number and order. Consequently, it was found that there is a need to account for the sequence of loading because, for instance, applying high loads at early stages can reduce the fatigue resistance of concrete (Miner, 1945; CEB, 1988). To consider the effect of different load levels on the fatigue strength of concrete, Palmgren-Miner's (PM) hypothesis is generally applied. This hypothesis assumes that failure is independent of load sequence and that the accumulation of fatigue damage is linear and is equal to one at failure, at a particular stress level. The accumulated fatigue damage (FD) for a number of cycles is presented mathematically as the sum of the damage contributions from each individual cycle as shown in Equation 2.4 (Miner, 1945):

$$FD = \sum_{i=1}^{k} \frac{N_i}{N_{fi}} = 1 \qquad (2.4)$$

where N_i is the number of cycles applied at a specific stress level i, N_{fi} is the number of cycles to failure at the stress level i and k is the notation for the total number of stress levels of fatigue loading. This relationship is called cumulative damage theory.

A number of tests were conducted with multi-stage loading to investigate the validity of PM hypothesis. However, this rule does not accurately describe the behaviour of concrete material. The weakness of PM rule that it does not take into account the impact of the order of applying various stress levels. Additionally, the damage accumulation is assumed to be at the same rate of a given stress level and the past stress history is not taken into account (Holmen, 1982). Some researchers claimed that PM rule is conservative and safe to use in most cases (Cornelissen, 1984; Cornelissen and Reinhardt, 1984). Others showed that the total cumulative damage has been found to be greater than one; this means that PM hypothesis in not conservative and unsafe (Holmen, 1982; Oh, 1991; Zhang et al., 1997). A study conducted by Grzybowski and Meyer (1993) found that for a stress level beyond 75%, the fatigue damage increases nonlinearly; indicating that PM rule is unsafe in most cases. To overcome this limitation of the PM rule, Oh (1991) used a nonlinear cumulative damage theory to describe the fatigue life of specimen with variable amplitude loads. This model describes the damage occurring in the specimen by utilising the shape of the total strain versus the number of cycle.

Holmen (1982) indicated that variable amplitude loading is more damaging than what is predicted by PM rule; consequently, a modified PM rule was proposed:

$$\sum_{i=1}^{k} \frac{N_i}{N_{fi}} = \omega \qquad (2.5)$$

where ω is a function of loading parameters.

Stress Ratio

Many investigations have been carried out to examine the influence of stress range on the fatigue performance of concrete (Murdock and Kesler, 1958; Aas-Jakobsen, 1970; Awad, 1971; Tepfers, 1979; Tepfers and Kutti, 1979). Murdock and Kesler (1958) are considered the first to formally report the influence of stress ratio on the fatigue performance of concrete beams. Aas-Jakobsen (1970) examined the influence of the minimum stress (σ_{min}) on the fatigue strength of concrete. The result shows that the relationship between S_{max} and S_{min} is linear for fatigue failure at $N = 2 \times 10^6$ cycles; this means that the relationship between S_{max} and R is linear as well. A fatigue equation was developed by Aas-Jakobsen (1970) to account for both minimum and maximum stress levels applied to the specimen; this equation was further validated by Tepfers and Kutti (1979) and Tepfers (1979):

$$S = 1 - \beta(1 - R)\log N \qquad (2.6)$$

where β is a material constant representing the slope of the *S-N* curve. This equation was found to be valid for concrete in compressive or split tensile fatigue as well as for flexural fatigue testing of concrete beams. The value of β was experimentally determined to be 0.064 by Aas-Jakobsen (1970). Tepfers and Kutti (1979) suggested a value of β = 0.0684 to take into account for the variations of in-service pavements that are not considered in laboratory testing type. These variations can include the stresses due to environment, different rest periods in the field, variety of concrete properties such as strength and thickness.

Domenichini and Marchionna (1981) were one of the first researchers to propose using of the applied tensile stress ratio and stress range in the design of concrete pavements. However, every fatigue cycle can have different maximum and minimum stress levels due to the variation in temperature and moisture effects; accordingly, the implantation of stress ratio into pavement fatigue design can be challenging (Roesler et al., 2005).

Hsu (1981) mentioned that Equation 2.6 has two main drawbacks. Firstly when R reaches unity, the repeated load becomes a sustained load. Sustained loads are time dependent; accordingly, time should be included in the equation. Secondly, the relationship does not take into account the rate of loading as a variable. To overcome these weaknesses, a period term, T, was introduced into the fatigue Equation 2.6 and the relationship becomes:

$$S = 1 - 0.0662(1 - 0.556R)logN - 0.0294logT \quad (2.7)$$

where T is the period of repetitive loads in seconds per cycle. This allows considering the influence of low loading rate and high cycle fatigue testing.

Another model was developed by Stemland et al. (1990) to evaluate the relationship between maximum and minimum stress levels for compression fatigue:

$$logN = (12 + 16S_{min} + 8S_{min}^2)(1 - S_{max}) \quad (2.8)$$

Loading Waveform

Sinusoidal waveform has been used in most fatigue tests to load a specimen. Such type of loading waveform reflects the conditions of structures subjected to wind or wave loading. However, there are cases were sinusoidal waveform is neither representative nor appropriate, such as the case of machine foundations. In such situations, other types of wave profiles are suggested; for example, triangular or rectangular loading waveforms. It has been found that rectangular wave profiles are more critical to the fatigue performance of structures in comparison than the triangular wave types (RILEM, 1984).

The study of Roesler et al. (2005) included various stress ratios and ranges for both a single and tridem load pulse. The results show that stress pulse type, peak stress and stress range have influence on the fatigue behaviour of concrete slabs.

2.2.4. Strain Hardening Influence

The fatigue strength of concrete, at a given number of cycles, is generally expressed in terms of the static strength. Cyclic loading can result in strain hardening; in turn, an increase in the stiffness due to the compaction of the material. This means that the material, as a result, becomes more homogenous and more brittle. Consequently, the subsequent static strength of concrete, after which it has been subjected to cyclic loading, is not representative to the quantity of damage that the specimen has undergone (Ballatore and Bocca, 1997).

2.3. The Properties of Fibre Reinforced Concrete under Fatigue Loading

In the last decades, the utilisation of fibre reinforced concrete has been significantly increasing. Several types of fibres have been utilised in concrete research and practice, but steel fibres seem to be the most popular. There are four main parameters that mainly influence the properties of fibre reinforced concrete, which are type, content, aspect ratio and the orientation within the concrete matrix.

The results of experimental tests indicate that the addition of fibres to concrete enhance the following properties of plain concrete: tensile splitting, flexural strength, first cracking strength, toughness, stiffness, durability, impact resistance, deflection, crack width, resistance to shrinkage and creep, and fatigue properties (Johnston, 1985; Johnston and Zemp, 1991; Banthia et al., 1995; Khaloo and Kim, 1997; Elsaigh and Kearsley, 2002; Kwan et al., 2002; Schäfer et al., 2019). The improvement in the mechanical properties of SFRC is attributed to the controlling of the cracking mechanism. According to Bekaert (1999), steel fibres play two main mechanisms to reduce the intensity of the stress in the vicinity of the crack; these mechanisms include:

- higher loads are resisted at the crack tip due to the greater Young's modulus of steel fibre compared to surrounding concrete; and
- bridging of the crack and redistribution of the stress across the crack through the steel fibres.

The ability of the steel fibres to control crack propagation is mainly dependent on the fibre distribution as well as the bond between the concrete and fibres (Elsaigh, 2008; Schäfer et al., 2019). The post-peak behaviour of fibre reinforced concrete is dependent on the fibre distribution as well as the number of fibres present in the critical regions of the crack (Komloš et al., 1995). The bond between the concrete and fibres is the mechanism of stress transformation from the concrete matrix to the steel fibres. Several factors are involved in determining the ability of steel fibres to develop sufficient stress transformation, which are (Elsaigh, 2008):

- the steel fibre characteristics (surface texture, end shape and yield strength);
- the orientation of the steel fibre within the concrete; and
- the properties of the concrete itself.

The fatigue behaviour of concrete seems to be reasonably understood as shown in Section 2.2. The utilisation of fibres to control the growth of cracks is steadily increasing. Understanding the concept of fatigue performance of concrete and fibre reinforcement is not very comprehensive in comparison to metals.

Various studies have been done on fibre reinforced concrete to obtain the fatigue characteristics, which mostly consist of fatigue life predictions, fatigue creep rate values, etc. Both empirical and analytical fatigue models are reported in literature. The experimental models have the drawback that the testing methods vary significantly due to the lack of standardized testing procedures for fatigue loading and so a comparison may not be always appropriate. However, these models are more easily adoptable than the numerical models due to their simplicity.

The major differences in the testing configurations in the literature are in the type of loading, test control parameters (load/displacement), specimen shape and size, loading frequency, loading range, definition of endurance limit and the type of concrete itself (i.e., high strength, normal strength, fibre type and dosage, etc.) (Batson et al., 1972; Cornelissen and Reinhardt, 1984; Johnston and Zemp, 1991; Oh, 1991; Chang and Chai, 1995; Wei et al., 1996; Pasakova and Meyer, 1997; Naaman and Hammoud, 1998; Singh and Kaushik, 2003; Singh et al., 2004; Germano and Plizzari, 2012; Schäfer et al., 2019). In spite of the differences, a few definite conclusions regarding the performance of FRC with reference to plain concrete can be drawn and discussed below.

As stated in Subsection 2.2.2, the mechanism of fatigue failure in concrete can be divided into 3 stages. The first stage is the structural behaviour without any damage. The second one is the damaged response up to maximum applied load. The last stage is structural collapse (post-peak behaviour). By the addition of closely spaced and randomly dispersed fibres, it is aimed to retard and inhibit the crack growth in the second stage. Energy is dissipated in the region of the crack tip by the action of fibre bridging and fibre poll-out in fibre reinforced concrete. This results in crack growth control and increases the load carrying capacity of fibre reinforced concrete structures. In addition, the fatigue performance of fibre reinforced concrete (FRC) is better with longer or more slender fibres (i.e., with higher aspect ratio), though a definite relationship with the shape of fibres could not be drawn. The improvement in fatigue performance, especially in bending, is related to the fibre volume, with more significance for low cycle loading (Batson et al., 1972; Chang and Chai, 1995; Wei et al., 1996; Naaman and Hammoud, 1998; Zhang et al., 1999; Lee and Barr, 2004).

In general, it is expected that higher fibre content of a given fibre design results in better fatigue resistance. With a larger fibre volume, there would be more fibres available to

control the cracks as well as to increase ductility and energy adsorption capacity. Higher level of loads can be transferred by having larger numbers of fibres resulting in delay in the pull-out process and, consequently, improving the composite performance under cyclic loading. However, from the literature, there are conflicting conclusions and it seems that the addition of fibre has double sided influence on the fatigue characterisation of concrete. Some studies showed that fibre can bridge the cracks and slow down their propagation and accordingly improves the composite's behaviour under fatigue loading. Other studies indicate that the addition of fibres can result in additional initial presence of flaws leading to a reduction in strength. Defining which of these two effects would govern is determined by fibre size and content (Grzybowski and Meyer, 1993). This highlights that there may be an optimum fibre dosage to obtain the most benefit of fibres in enhancing fatigue behaviour.

Most of the investigations indicate that the addition of steel fibres has significantly improved the bending fatigue characterisation of concrete (Johnston and Zemp, 1991; Grzybowski and Meyer, 1993; Zhang and Stang, 1998; Schäfer et al., 2019). Paskova and Meyer (1997) stated that the addition of fibres substantially increased the fatigue performance of concrete considering all fibre volumes. However, Grzybowski and Meyer (1993) reported that for fibre content above 25%, the fatigue life of fibre reinforced concrete is reduced comparing with plain concrete. Furthermore, the results of the tests performed by Cachim (1999) showed fibre addition result in marginal benefits under flexural fatigue tests. For uniaxial compression, it was found that the fatigue life increase with 30 mm fibres, while it decreases with 60 mm fibres. Cachim et al. (2002) claimed that the addition of fibre resulted in additional flaws which outweighed the benefits for some of the conducted tests. Zhang and Stang (1998) found that 1% is the optimum fibre content and that a larger fibre volume result in negative effects.

A study by Chang and Chai (1995) found that increasing fibre content and aspect ratio increase the amount of energy dissipated during crack propagation under fatigue loading. This indicates that various variables such as fibre content, fibre geometry and type play an important role in the extent of the fatigue resistance improvement. Different fatigue behaviours are obtained by various combinations of these factors. The addition of fibres has added a further dimension to the fatigue study of concrete and increased the level of complexity of the analysis.

Studies have been conducted to examine if fibre reinforced concrete has a fatigue limit. Hsu (1981) indicated that such a limit does not exist, while Li and Matsumoto (1998) showed that a fatigue limit exists for fibre reinforced concrete. Ramakrishnan and Lokvik (1992) claimed that fibre reinforced concrete has an endurance limit of 2×10^6 loading cycles; Johnston and Zemp (1991) argued that experimental tests should be conducted up to 2×10^6 loading cycles to confirm this hypothesis. Yin and Hsu (1995) proposed that the presence of fibre is beneficial in fatigue only in low number of cycles (< 1000) and it does not provide any improvement for higher cycle regions. This is explained by the differentiation between mortar and bond cracking as suggested by Hsu (1984). Fibres can increase the fatigue resistance in the region of mortar cracking (low cycle fatigue) but the action of fibres stops when bond cracking starts (high cycle fatigue). This indicates that fibres are unable to increase the fatigue life of concrete. Additionally, tests performed by Paskova and Meyer (1997) showed that more energy is dissipated at lower stress levels compared to higher stress levels in fibre reinforced concrete. The debate regarding fatigue life of fibre reinforced concrete remains unresolved.

2.4. Static Testing of SFRC Slabs on Ground

Several researchers have investigated the performance of steel fibre reinforced concrete slabs on grade (Beckett, 1990; Falkner and Teutsch, 1993; Falkner et al., 1995; Bischoff et al., 1996; Roesler and Barenberg, 1999a; Roesler and Barenberg, 1999b; Elsaigh, 2001; Bischoff et al., 2003; Kearsley and Elsaigh, 2003; Chen, 2004; Meda and Plizzari, 2004; Roesler et al., 2006; Sorelli et al., 2006; Alani et al., 2012; Alani et al., 2014; Øverli, 2014). These projects examined the behaviour of SFRC under static loading applied at the centre, edge and/or corner. The behaviour of SFRC and plain concrete slabs on grade were analysed and compared. Major finding of these studies that the addition of steel fibre increases the load carrying capacity of concrete slabs on ground significantly.

Various explanations have been suggested in the literature for the increase in the load carrying capacity of SFRC slabs on ground. It has been proposed that the structural ductility of statically indeterminate slab and the post-cracking strength of SFRC are the main reasons for the increased bearing capacity; where partial stress redistribution occurs due to the statically indeterminate nature. Additionally, the punching shear resistance has a significant role in increasing the capacity of the slabs (Falkner and Teutsch, 1993; Kearsley and Elsaigh, 2003). Some of the above cited studies are presented and discussed.

In the study of Falkner et al. (1995), plain and SFRC slabs with dimension of 3 m × 3 m × 0.15 m were tested under static loading at their centre. The slabs were placed on top of 3.5 m × 3.5 m × 0.06 m subbase. The subbase was either constructed out of cork or rubber, giving two different moduli of subgrade reaction values k_w = 0.025 N/mm^3 and 0.005 N/mm^3, respectively. Two types of steel fibres were used, mill cut (length of 32 mm) and end-hooked fibres (length of 60 mm and diameter of 0.8 mm). From the observations of this study, it was found that the deformation characterisations of SFRC can be divided into three states:

- State 1: the un-cracked state, where the behaviour of the slab is linear elastic.
- State 2: occurrence of the first radial crack at the centre of the slab, gradual development until the main crack can be seen at the edge of the slab.
- State 3: the state of stress redistribution and the formation of plastic hinge lines along the main cracks where eventually collapse occurs.

In the study of Falkner et al. (1995), the major difference in the behaviour between plain and SFRC slabs is observed in State 3 where the significant effect is found on the SFRC slab's toughness after the formation of the main cracks. While the plain concrete slab fails by punching, for the SFRC slab, the stresses are redistributed within the slab after the formation of main cracks; this allows the slab to maintain its function due to the formation of plastic hinges along the main transverse cracks. Eventually failure occurred by punching or destruction of the subbase. This means that plain concrete slabs fail at an early age, while the SFRC slabs last longer due to the redistribution of the stresses. The typical load-displacement response of SFRC slab in presented in Figure 2.10.

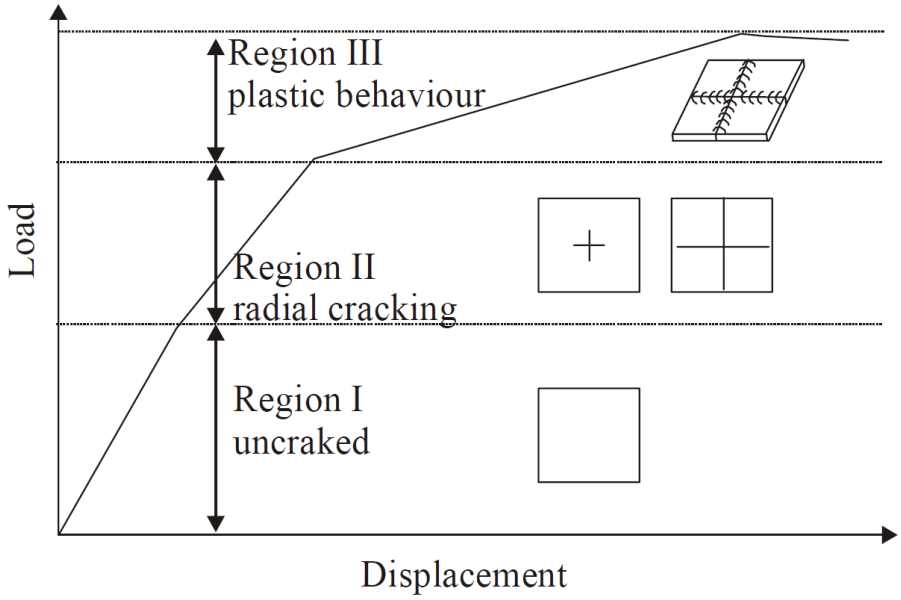

Figure 2.10 – Typical load – displacement response of SFRC slab on ground (Falkner and Teutsch, 1993).

An experimental test was carried out by Beckett (1999) to examine the corner and edge loadings of SFRC slabs using single and double loading plates. In this project, two slabs were built together and then separated with a sawn joint. The slab had a dimension of 11 m × 3 m × 0.15 m before separation; while after separation the dimensions become 5.5 m × 3 m × 0.15 m. End-hooked steel fibres were used. It was found that beside the increased corner load capacity of SFRC slab by increasing the fibre content, the vertical deformation was reduced with increasing fibre quantity. Additionally, it was observed that increasing the plane dimension of the tested slabs from the typical tested dimension of 3 m × 3 m to 11 m × 3 m, it is possible to observe the negative partial circumference yield lines in the upper surface of the slab. It was also found that the double loading plates centred 300 mm apart did not have any significant effect on the cracking load, when comparing with a single load plate. The results obtained from the study were not compared with those of plain concrete slabs.

Kearsley and Elsaigh (2003) examined the effect of ductility on the load carrying capacity of SFRC slabs on ground and compared the deformation behaviour of SFRC to that of plain concrete slabs and the applicability of reducing the thickness of SFRC slabs. The performance of plain concrete slabs of plan dimension 3 m × 3 m by 150 mm thick was compared against SFRC slabs of the same plane dimension but with a reduced thickness of 125 mm. The thickness of SFRC was 16.6% less than the plain concrete one. A dosage of 15 kg/m^3 of end-hooked steel fibres of length 60 mm and tensile strength of 1100 MPa were used. The subgrade modulus of reaction used in this project was 0.25 N/mm^3. The load was applied at the centre of the slab through a 100 mm × 100 mm plate.

The results of the Kearsley and Elsaigh (2003) test showed that the failure load for both slabs (plain concrete and SFRC) was approximately equal. Accordingly, the thickness of SFRC slabs can be reduced to carry the same load as those of plain concrete slabs. The load carrying capacity of concrete can be nominalised by the content of steel fibres.

Additionally, it was found that thinner SFRC results in higher deflections than for the plain concrete ones. This means that the deflection of SFRC slabs needs to be limited to acceptable values.

Chen (2004) tested four full scale concrete ground slabs of 2 m × 2 m × 0·12 m. The specimens were loaded statically at their centre. The slabs were cast and tested on a 2.5 m × 2.5 m × 0·06 m subbase constructed of a cork, giving a subgrade modulus of reaction, k_w, between 0.044 N/mm^3 and 0.055 N/mm^3. Two types of steel fibres (end hooked and mill cut) were used with fibre contents of 20 kg/m^3 and 30 kg/m^3. It was found that the load carrying capacity of slabs on ground increases remarkably with the addition of steel fibres. In addition, the flexural toughness, which is an indicator of the energy absorption capacity of SFRC specimens, can be used in assessing the effect on the load-carrying capacity of SFRC ground slabs. The friction between the slab and supporting layer results in a horizontal thrust, which increases the load-carrying capacity of the ground slab.

In an effort to compare the structural response between plain and fibre reinforced concrete (FRC) slabs, Roesler et al. (2006) tested large scale slabs with dimensions of 2.2 m × 2.2 m by 127 mm thick under monotonic loading. The FRC slabs contained 0.32% and 0.48% volume of synthetic fibres with length of 40 mm, aspect ratio of 0.92 and average tensile strength of 600 MPa. The slabs were placed on top of 200 mm of compacted, low plasticity clay contained inside a containment box of plan dimension 5.08 m × 2.44 m by 310 mm. The subgrade modulus of reaction was 0.103 N/mm^3. The load was applied through a steel plate at the centre of the slab and its edge. The results show that synthetic fibres significantly changed the failure response of plain concrete slabs and increased the collapse loading. For the centre loading configuration, the flexural cracking load is increased by 32% and 25% for fibre volume of 0.48% and 0.32%, respectively. The flexural cracking load was increased by 28% with 0.48% of synthetic fibres under the edge loading. However, the tensile cracking loads of both

plain concrete and FRC slabs were found to be the same (Roesler et al., 2004; Roesler et al., 2006).

In a study reported by Meda and Plizzari (2004) and Sorelli et al. (2006) slabs on grade were tested under static loading to examine the structural behaviour of SFRC slabs. To reproduce a Winkler soil 64, steel supports were placed under the slab at centres of 375 mm in each direction. These supports are steel plates on a square base having a side dimension of 100 mm. A layer of high-strength mortar, a few millimetres thick, was placed on each spring to provide the contact between the spring and the bottom face of the slab. The average spring stiffness was determined by compression tests performed on each spring and the result was equal to 11 kN/mm. Considering the influence area of each spring as 375 mm × 375 mm, the average subgrade constant k_w is 0.0785 N/mm^3, which is representative of a uniform graded sand soil according to ACI classification (ACI, 1992). Moreover, the load was applied as a concentrated point load in the middle of the slab. The results indicated that a relatively low content of steel fibres effectively increase the load-carrying capacity of slabs on ground and makes the structural response more ductile.

In the project of Alani et al. (2012) SFRC slabs of 6 m × 6 m by 150 mm thick were cast and tested on soil subbase which gave an average of modulus of reaction, k_w, of 0.05 N/mm^3. The test was conducted at different locations (centre, edges and corners) under static loading. The obtained results were compared against those theoretical values derived by using the design codes. Significant difference was found as the calculations showed that the theoretical failure loads are substantially lower than the test values.

2.5. Cyclic Testing of Concrete Slabs

Limited research has been undertaken to examine the performance of full scale plain concrete slabs under cyclic or fatigue loading (Falkner et al., 1997; Roesler, 1998; Roesler and Barenberg, 1999a; Roesler and Barenberg, 1999b; Roesler et al., 2005; Suh et al., 2005; Sivagamasundari and Kumaran, 2011). One pilot study was undertaken to examine the cyclic performance of SFRC slabs on ground (Falkner et al., 1997).

Understanding the fatigue relationship between simply supported beams (SSB) and fully supported slabs (FSS) would allow predicting the fatigue performance of rigid pavements in the field based on the laboratory results of SSB. To determine the differences in the fatigue resistance of slabs and beams, Roesler and Barenberg (1999b) tested simply supported beams and fully supported slabs under static and cyclic loading. To simulate a pavement slab and to maintain the same deflection profile along the slab edges, the FSS was partially restrained through connecting the edges of the slab to an external steel structure (dowels). Ideally, an infinite FSS needs to be tested; however, Roesler and Barenberg (1999b) believed that a partially restrained finite slab performs in a similar manner as infinite slab. Figure 2.11 illustrates the configuration of FSS. Dimensions of 1.2 m × 1.2 m × 152 mm were chosen to simulate infinite conditions; the decision was made based on the deflection and stress profile analyses of the slab using a model developed by ILLI-SLAB software.

Roesler and Barenberg (1999b) found from theoretical stress analysis and field observations that the edge of the slab is the most critical location for the development of fatigue cracking in roadway pavements and, accordingly, an edge loaded slab configuration was selected. The loading was applied by a steel plate located symmetrically at the edge of the slab. The frequency of loading was 1 Hz or 2 Hz including no rest periods. The cyclic loading for the slabs was chosen to provide a bending stress with an approximate percentage of the average concrete modulus of rupture obtained from SSB testing. The maximum cyclic load required to provide a

certain stress in the slab was determined by analyses performed through ILLI-SLAB software. The minimum load was 10% of the maximum applied load. The slab was placed on top of soil containment box; the steel box served as the container for all the foundation materials and was a self-contained reaction frame. The dimensions of the steel box were 1.8 m × 1.8 m × 1.3 m size. Layers of crushed stone, sand and soil were compacted into the box. Polyethylene sheet was placed between the slab and the foundation materials to prevent moisture evaporation. Figure 2.12 presents the soil containment structure and the loading frame system.

Two slabs were tested under static loading. The bending stresses at the flexural cracking load were 6.33 MPa and 7.35 MPa for FSS; however, using SSB configuration stresses of 4.99 MPa and 5.09 MPa were obtained. This implies that FSS had a greater cracking resistance than SSB. Furthermore, a crack at the edge of the slab was observed before reaching the full depth cracking load. This indicates that the concrete modulus of rupture obtained from testing SSB is not corresponding to the concrete modulus of rupture based on FSS testing. Roesler and Barenberg (1999b) claimed that the main reasons for this discrepancy are:

- specimen size (beam versus slab);
- boundary conditions (fully supported versus simply supported); and
- load configuration (distributed load versus point load).

Before reaching the first cracking load, the slab deflection profile was smooth and continuous. After first cracking, the slab behaved as two cantilever beams with loads on their free ends.

Ten FSS were tested under cyclic loading. The failure of the slabs was determined by the substantial increase in deflection from the previous cycle (30% to 100%). This jump in the deflection of FSS was always in conjunction with observing visual cracks in the loading edge. After the failure of each slab, beams 152 mm × 152 mm × 533 mm were

extracted from the slab using a concrete chainsaw. These extracted beams were tested in SSB configuration to determine the modulus of rupture. The obtained values were then used in calculating the stress ratio instead of the cast SSB.

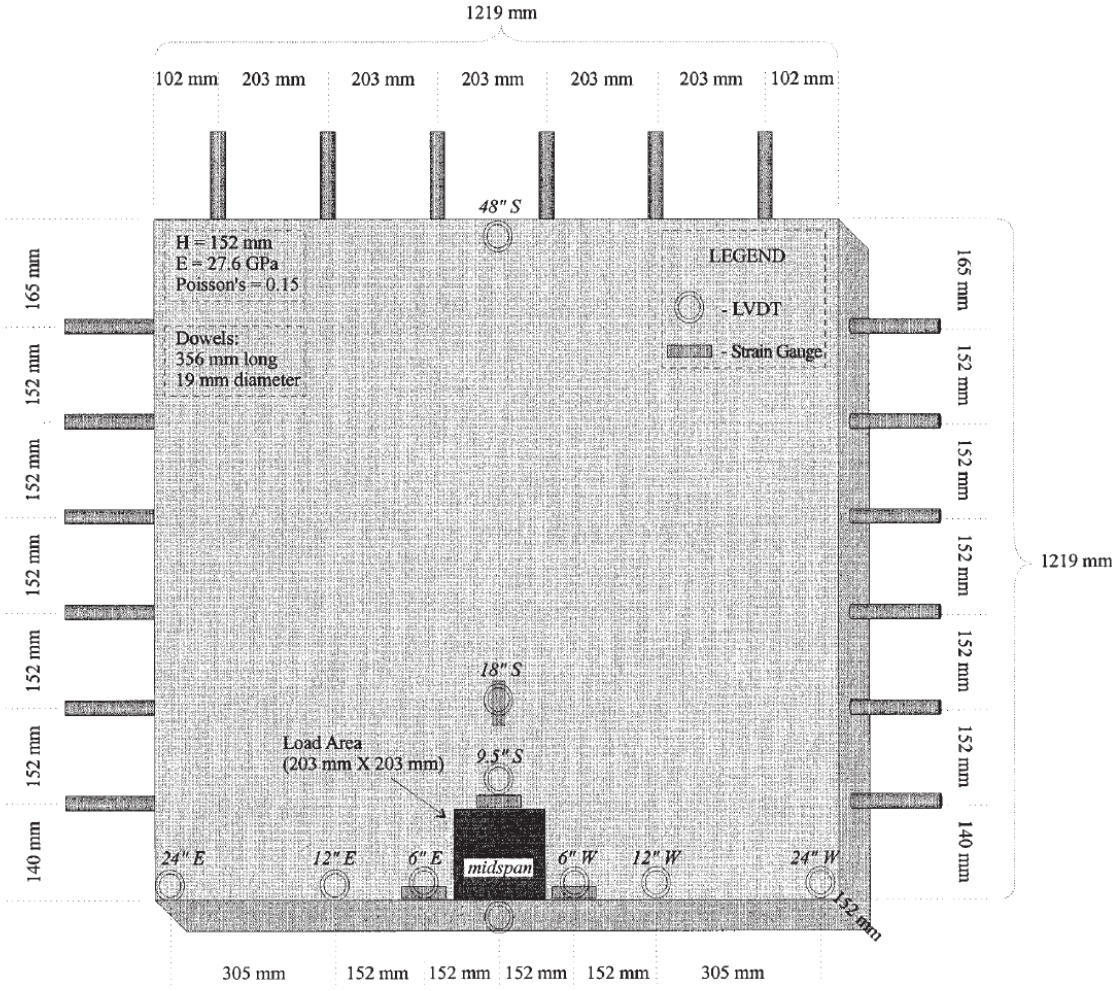

Figure 2.11 – The dimensions and configuration of fully supported slab (Roesler and Barenberg, 1999b).

A comparison between the fatigue curves of FSS and SSB is shown in Figure 2.13. As can be seen from the figure, the fatigue capacity of the slab was approximately 30% higher than that of SSB tests. This implies that the slab can sustain 30% higher stress level than beams for the same load repetition to failure. The fatigue curve for FSS (shown in Figure 2.13) was obtained based on the assumption that the concrete modulus

of rupture of SSB is representative of the true strength of FSS, but this assumption is flawed. The flexural strength of FSS, under static loading, is 30% higher than SSB. This discrepancy is because FSS, unlike beams, has the ability for plastic deformation and stress redistribution in more than one direction. Accordingly, the static strength of the slab was used to obtain the corrected stress ratio of FSS and the fatigue curves are presented in Figure 2.14. FSS and SSB seemed to have the same fatigue resistance after correcting the stress level of the FSS.

Roesler and Barenberg (1999b) claimed that testing laboratory FSS under repeated loading gives an extensive insight about the mechanism of slab fatigue failure where data and visual observations about the crack pattern and slab failure mode are obtained.

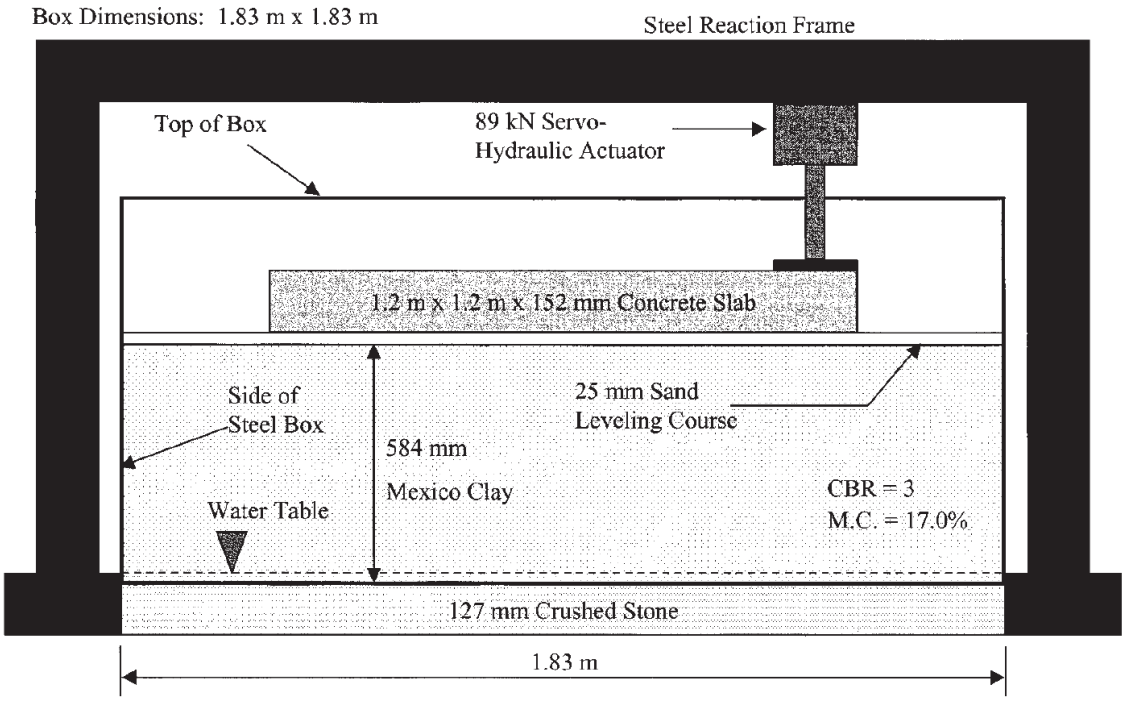

Figure 2.12 – The soil containment box and the loading frame system for fully supported slab testing (Roesler and Barenberg, 1999b).

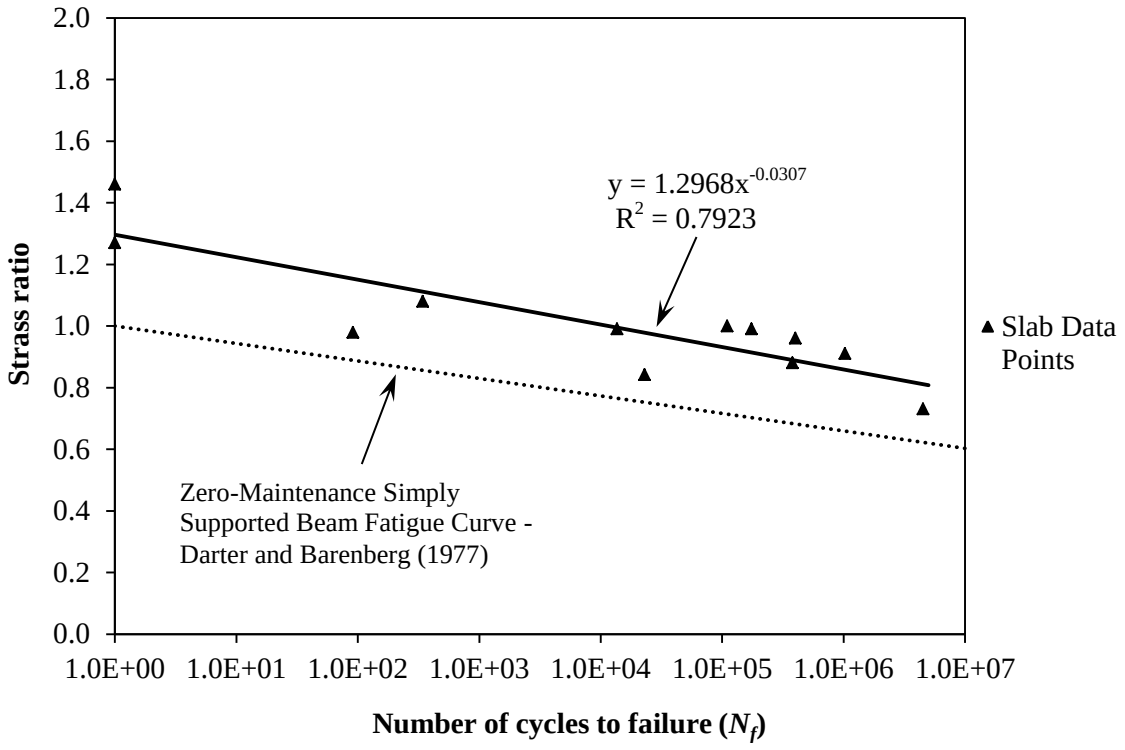

Figure 2.13 – Comparison between SSB and FSS fatigue curves (Roesler and Barenberg, 1999b).

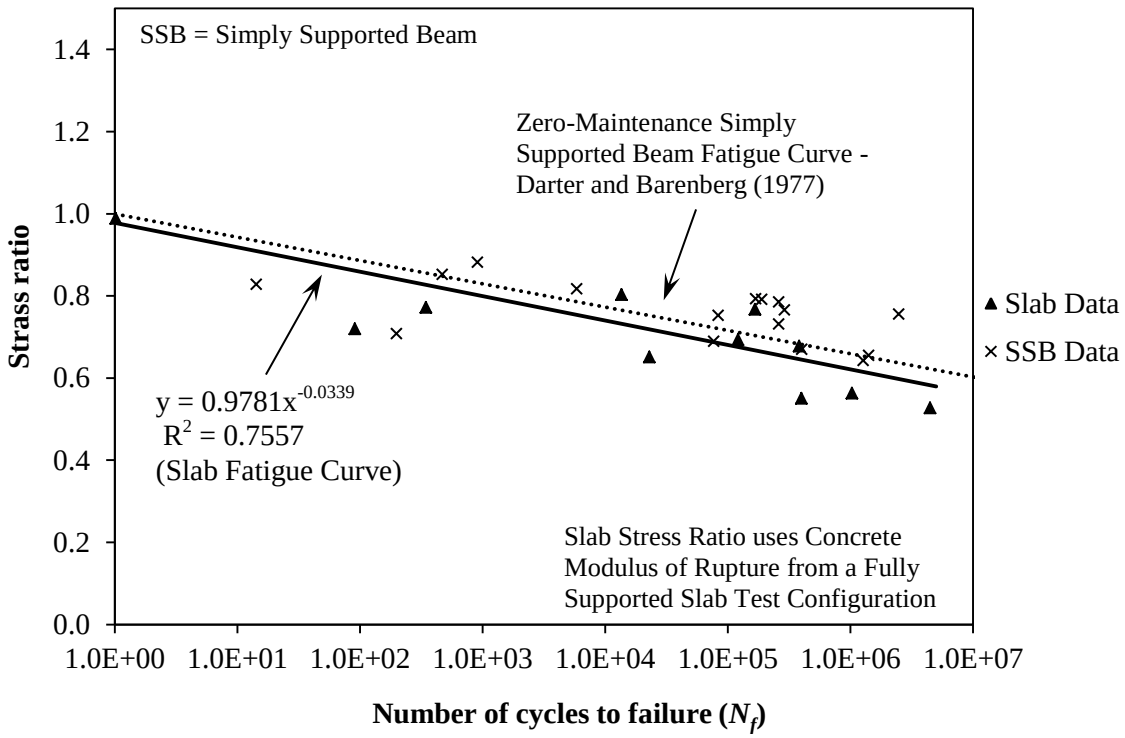

Figure 2.14 – FSS fatigue curve using slab static strength in the stress ratio (Roesler and Barenberg, 1999b).

Falkner et al. (1997) investigated the possibility of using steel fibres to improve the load bearing capacity and maintenance of reduced thickness plain concrete pavements. An experimental program was carried out to compare the deformation and the load bearing capacity of plain and steel fibre reinforced concrete under cyclic loading. The slabs contained 40 kg/mm^3 of end hooked steel fibres with a length of 50 mm, a diameter of 0.6 mm and minimum tensile strength of 1100 MPa. The size of the slab was 3 m × 3 m and the depth of the plain concrete slab was 270 mm (Fa-P1-1). The total depth of SFRC slab was 220 mm with the thickness of SFRC layer being 170 mm (Fa-P1-2) or 160 mm (Fa-P1-3) – see Figure 2.15. The SFRC slab was covered with a layer (50 mm or 60 mm) of plain concrete, as presented in Figure 2.15. The tested slab was supported by an elastic subbase with dimensions of 3.5 m × 3.5 m × 0.06 m. The subbase consisted of a 60 mm cork layer and a rubber sheet in the loading application area. The dimensions of the rubber sheet were 1.25 m × 1.25 m × 0.06 m, as shown in Figure 2.16. The subbase materials were compacted to k_w = 0.05 N/mm^3 as specified for industrial pavements in iBMB tests. This value was roughly representative of moderately compacted sand.

The deformation in the elastic subbase for the Falkner et al. (1997) test specimens is presented in Figure 2.17. As can be seen from the figure, the compaction value of the cork was dependent on its deformation while the value of the rubber remained unchanged. The testing load was applied at the centre of the slab through a 150 mm × 150 mm steel plate. A variable applied loading was used in this experiment. For the first 10,000 cycles, the maximum applied load was set to be 200 kN during dynamic loading while the minimum load was 20 kN. The maximum and minimum loads were increased by 20 kN after reaching 10^4 cycles as can be seen from Figures 2.18 to 2.20. The frequency of applied loading was 0.5 Hz.

The load versus number of cycles for specimens Fa-P1-1, Fa-P1-2 and Fa-P1-3 are presented in Figures 2.18 to 2.20, respectively. For the plain concrete, the test stopped

after 605,508 cycles with an ultimate load of 340 kN. For SFRC specimen (Fa-P1-2), the maximum load was 460 kN for maximum load cycles of 1,215,767. The load increased up to 360 kN for specimen Fa-P1-3 and stopped after 1.9×10^6 cycles. From these results, it can be seen that although SFRC slabs were thinner than the plain concrete ones, they sustained a considerably higher number of load repetitions showing higher fatigue resistance. This is possibly due to the variable loading applied and such type of loading had a higher influence on the crack formation in plain concrete slab comparing with SFRC ones. This implies that the steel fibres in the thinner SFRC slabs compensated for the reduced thickness of the slab. Moreover, it was found that the addition of steel fibres in the slab increased the moment carrying capacity.

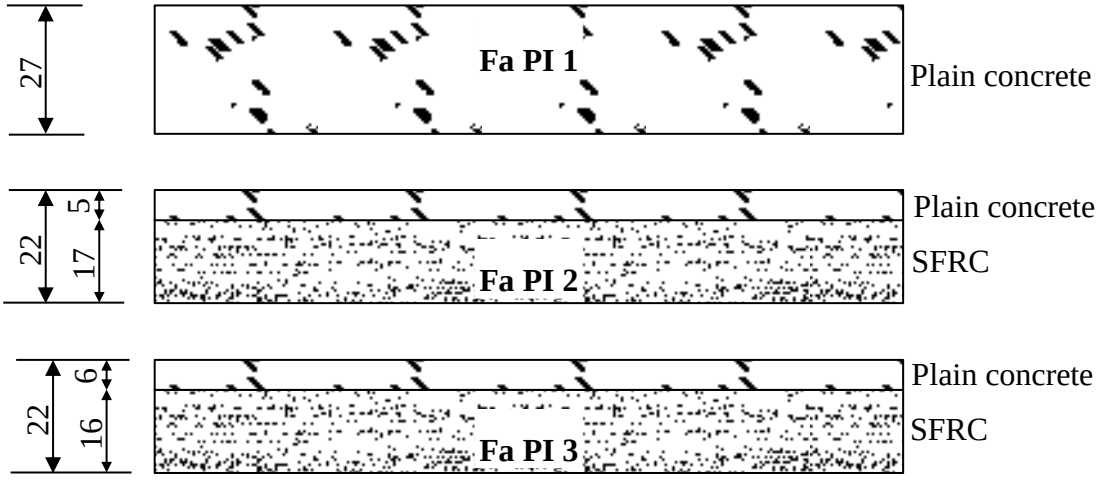

Figure 2.15 – Cross section of the experimental slabs, dimensions in cm (Falkner et al., 1997).

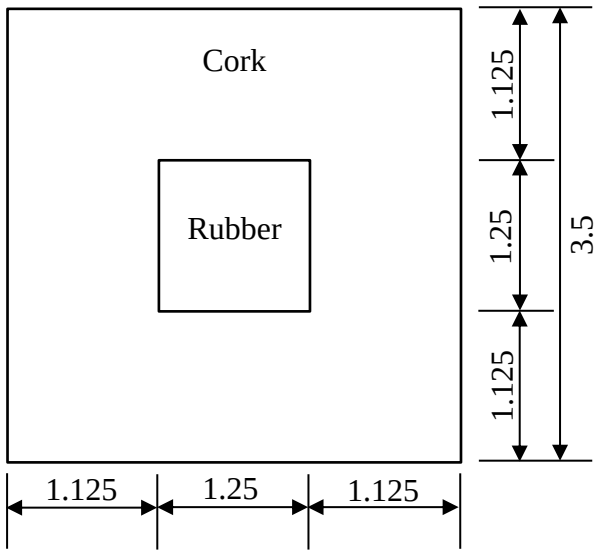

Figure 2.16 – Elastic subbase of concrete slabs, dimensions in metre (Falkner et al., 1997).

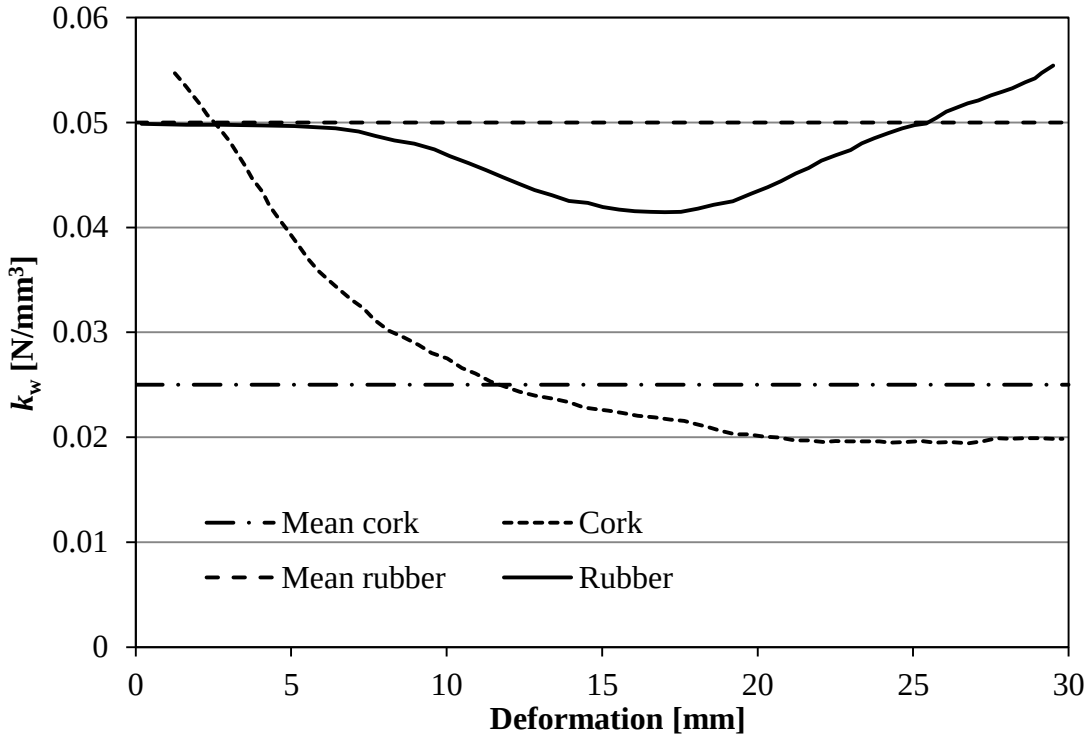

Figure 2.17 – Compaction value of cork and rubber in relation to deformation (Falkner et al., 1997).

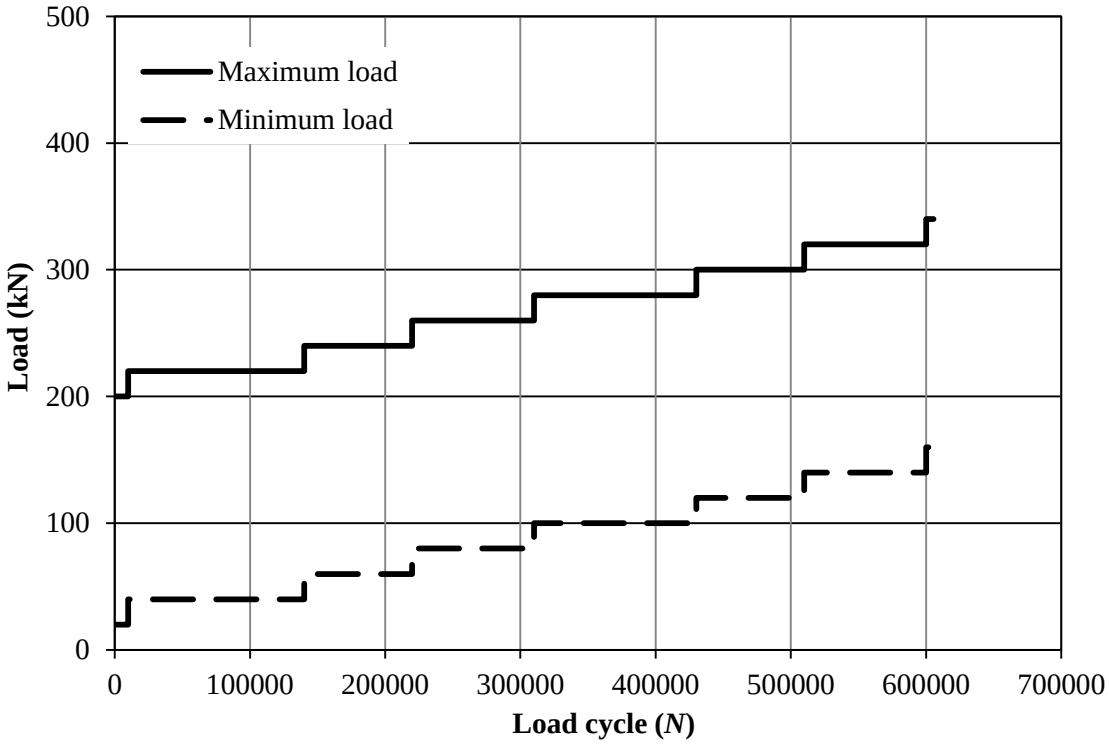

Figure 2.18 – Cyclic loading test for plain concrete specimen (Fa-P1-1) (Falkner et al., 1997).

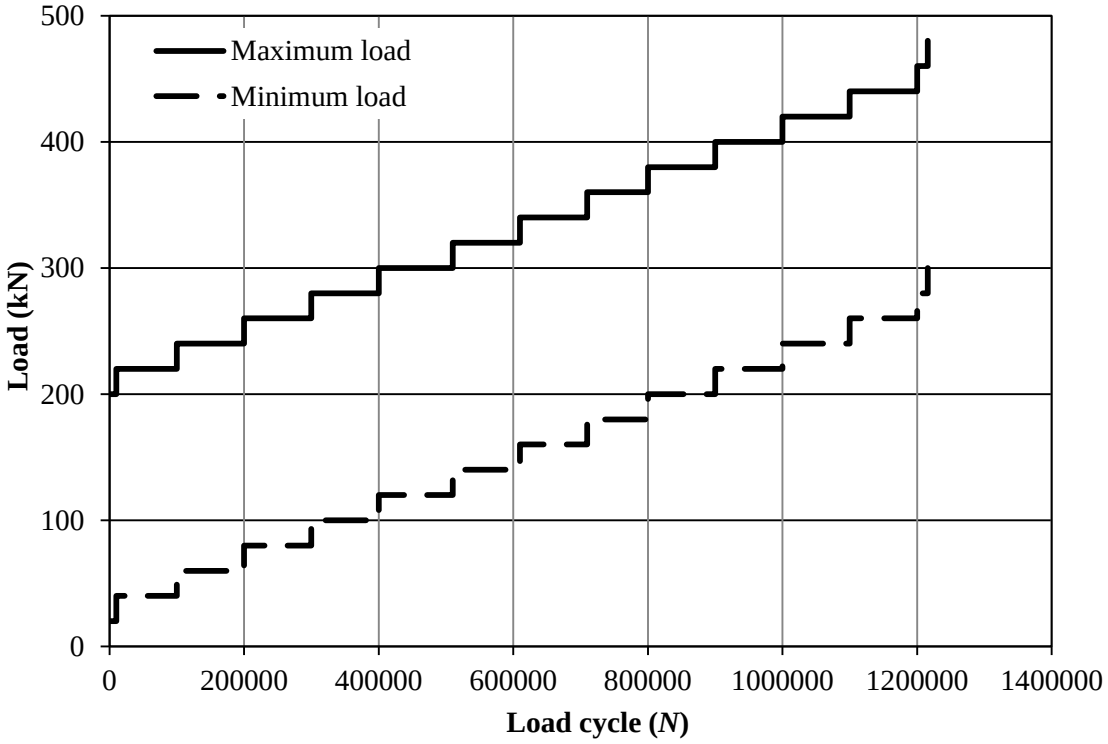

Figure 2.19 – Cyclic loading test for specimen (Fa-P1-2) (Falkner et al., 199

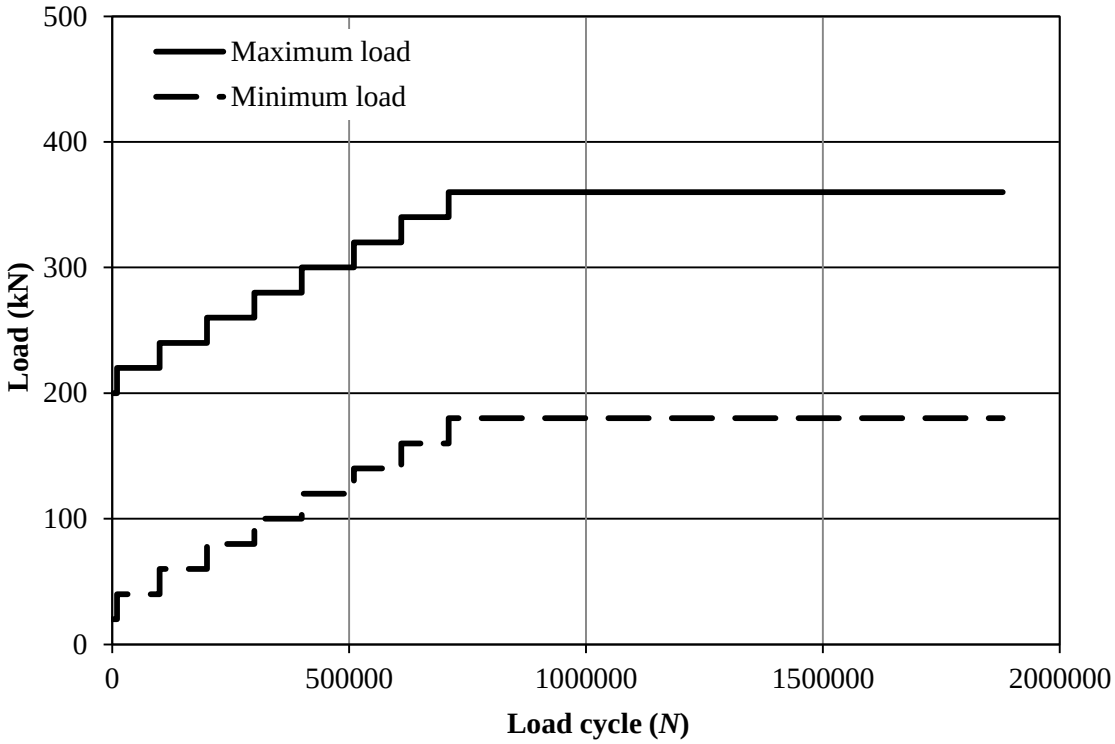

Figure 2.20 – Cyclic loading test for specimen (Fa-P1-3) (Falkner et al., 1997).

In the study of Roesler et al. (2005), large scale concrete slabs were tested to evaluate the effect of multiple wheel gears on the fatigue life of plain concrete slabs. The concrete slabs were fully supported by 200 mm natural clay subgrade placed within a laboratory test frame. The CBR value of the soil was 5 at 17% moisture content. Slabs of plan dimension 2 m × 2 m and 150 mm thick were tested statically and cyclically at their edge. The test plan included various stress ratios and ranges for both a single and tridem load pulse (Figure 2.21). The single pulse was applied at a frequency of 2 Hz with no unloading between pulses as can be seen from Figure 2.21, while the tridem pulse was applied at 3 Hz frequency. For the tridem pulse, the unloaded stress was 10% of the maximum load.

The results of Roesler et al. (2005) tests show that stress pulse type, peak stress and stress range have influence on the fatigue behaviour of concrete slabs. For low cycle fatigue, the applied peak stress controlled the allowable number of load repetition, while

stress range effect was not significant. Both the peak stress and stress range had impact on the number of load repetition in high cycle fatigue.

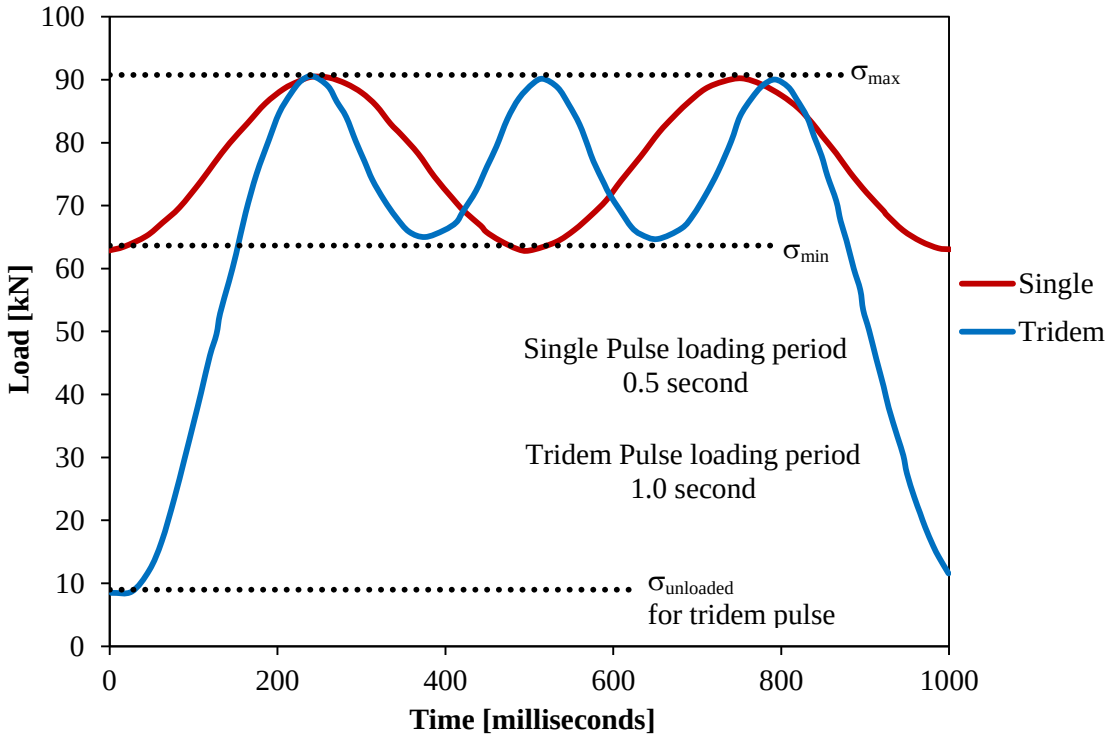

Figure 2.21 – Example of single and tridem load pulses (R = 0.70) (Roesler et al., 2005).

Suh et al. (2005) conducted an experimental study to examine the fatigue resistance of both laboratory beams and in-field full scale plain concrete slabs. In addition, this investigation evaluated the feasibility of superaccelerated pavement (SAP) testing method for cyclic loading of full scale concrete pavement in real field scenario, through utilising the stationary dynamic deflectomer (SDD). In this experimental program, Suh et al. (2005) tested several beams and full scale concrete slabs. In the laboratory fatigue testing procedure, beams of size 152 mm × 152 mm × 914 mm were tested under third load pointing configuration. The stress ratio of cyclic loading was kept constant at a value of 0.1. The loading frequency was 5 Hz with no rest period. Regarding the SAP

testing, both static and fatigue tests were performed by applying a load at the centre of the concrete slab. Figures 2.22 and 2.23 illustrate the set-up for SDD technique.

In the study of Suh et al. (2005), the rigid pavement system consisted of three layers; a natural subgrade, an asphalt stabilized base and concrete slab. Tests were performed to determine the properties of the natural subgrade before placing the asphalt base; afterwards, a 100 mm thick asphalt stabilized base was built on the top of the subgrade materials. Eventually, full scale slabs 3.66 m × 3.66 m by 150 mm thick were placed on the asphalt stabilised base. The load applied was at a frequency of 20 Hz; the stress ratio was 0.4.

The fatigue failure of filed concrete slabs was determined by the occurrence of the first visible crack, which was usually accompanied by the abrupt changes in the displacement. To examine the stress redistribution and crack propagation under fatigue loading, the cyclic loading was applied until the occurrence of full depth cracking at the edges of the concrete slab. Figure 2.24 is a conceptual diagram representing the slab behaviour. For all concrete slabs, the first visible crack was observed near the loading point at the top surface as presented in Figure 2.25. After applying significant number of cycles, edge cracks were clearly observed at the bottom of the slab, which then propagated to the top surface. This implies that concrete field slabs showed stress redistribution during the crack propagation period. Moreover, both the laboratory beams and concrete slabs had almost identical *S-N* relationships after applying equivalent fatigue life concept (correction of the stress ratio discrepancy).

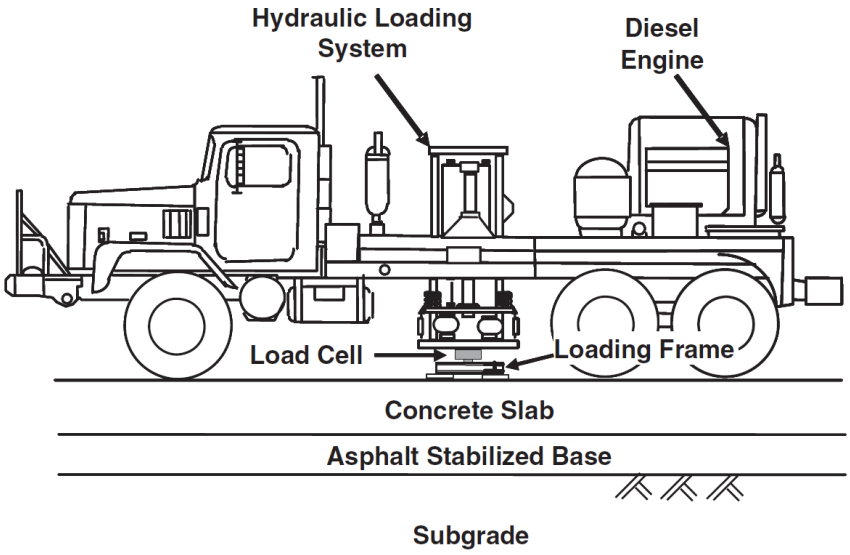

Figure 2.22 – General SDD testing arrangement (Suh et al., 2005).

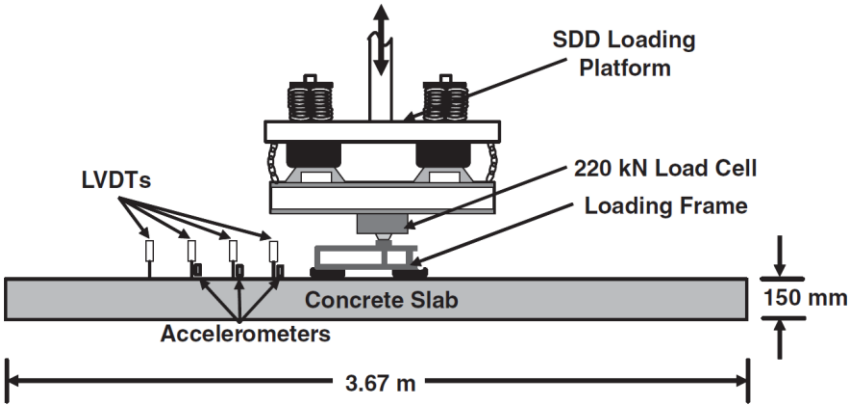

Figure 2.23 – Expanded view of SDD loading system and layout of sensors (Suh et al., 2005).

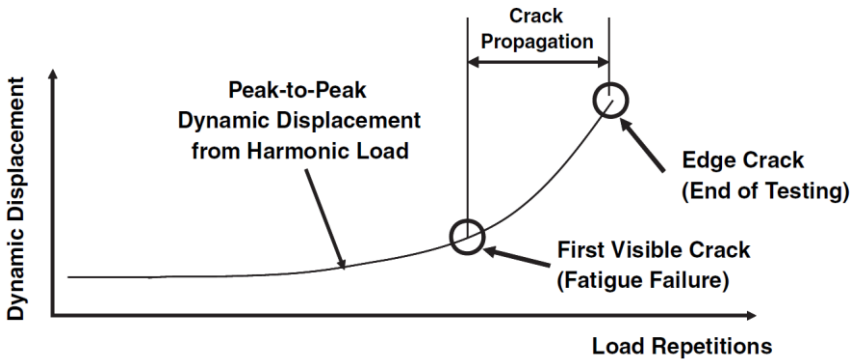

Figure 2.24 – Illustration of the changes of the dynamic displacement with the increase in load repetitions (Suh et al., 2005).

Figure 2.25 – Plane view of failed slab after fatigue testing (Suh et al., 2005).

2.6. Comparison of Crack Patterns

The deterioration of concrete pavements under traffic loading is a critical concept in civil engineering research. Studies have been carried out to characterise the fatigue performance of concrete slabs; however, most of these simulate fatigue loading by a fixed load, not a running load. Consequently, the deterioration of the slabs can be different due to different loading process. Based on several survey reports, Matsui et al. (1986) demonstrated that the deterioration process in slabs under repeated loading first involves the development of one-way cracks in the perpendicular direction to the traffic flow, as displayed in Figure 2.26(a). Following, two-way cracking is formed in a grid shape, as illustrated in Figure 2.26(b). These grid type patterns of cracks are further developed by the repeated occurrence of traffic flow (Figure 2.26(c)). After that, the cracks at the bottom of the slab are jointed with those on the top surface. The continuous utilisation of the cracked slab results in repeated opening and closing of the cracks due to the repetition of bending moments. As a result, the cracks grow up to form slits, which can lead to partial sinking of the pavement surface, as shown in Figure 2.26(d), which is the final stage of the deterioration process (Maeda et al., 1980a; Maeda et al., 1980b; Maeda et al., 1981; Matsui et al., 1986).

Figures 2.27 and 2.28 display the cracking pattern of the bottom surface of a tested specimen under concentrated point load and actual crack pattern of the slab in reality, respectively. As can be seen from the figures, the crack pattern developed by the fatigue loading during testing is not representative of the reality. The deterioration of the actual concrete slabs cannot be accurately evaluated from such experimental studies, where the testing procedure involves simulating traffic volume by a load at a fixed point on the slab.

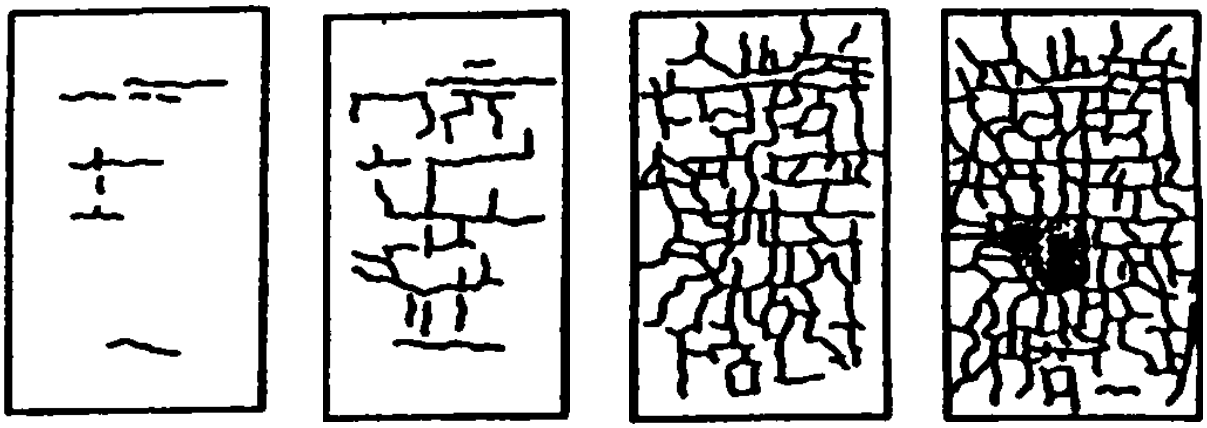

(a) One-way cracks (b) Two-way cracks (c) Grid-like pattern (d) Final stage

Figure 2.26 – Deterioration process of slabs (Matsui et al., 1986).

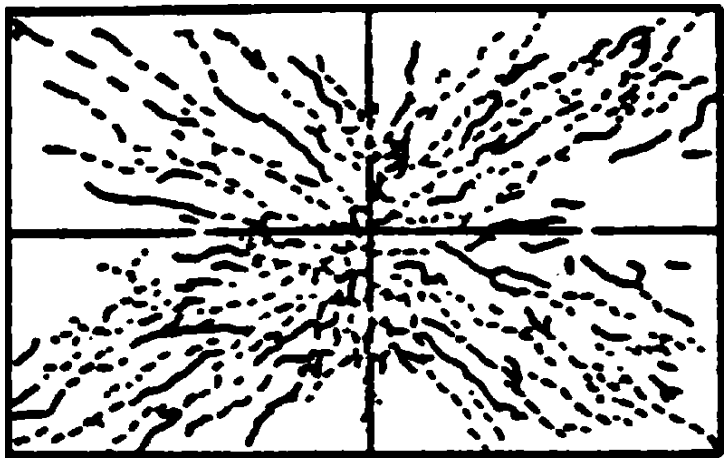

Figure 2.27 – Cracking pattern of test slab (Matsui et al., 1986).

Figure 2.28 – Cracking pattern of actual slab (Matsui et al., 1986).

2.7. Concrete Fatigue Models

For concrete pavements, most of the design procedures are based on developing sufficient slab's thickness to resist fatigue cracking. Typically in concrete pavements, the critical stresses are considered to be the flexural stresses at the bottom surface of the slab under an edge loading condition (bottom-up cracking), given that some other investigations indicated that critical bending stresses can be developed at the upper surface of the slab under corner loading conditions (top-down cracking) as illustrated in Section 2.1.4. The focus of this section is on the development of fatigue models themselves and not extended to the development of concrete pavement design procedures, in which they may be a part of.

In this discussion, a summary of the some common fatigue models is presented. A brief background for the development of each model is described, indicating the limitations and the assumption behind their development. The concrete pavement fatigue models presented in this section are designed based on the information obtained from concrete beam fatigue testing and field testing of concrete slabs. Also, some fatigue models of fatigue laboratory testing of concrete slab and of SFRC are presented.

2.7.1. Fatigue Models of Concrete Beams

There are several fatigue models developed for plain concrete mainly based on the results of concrete beams; for example, Portland Cement Association (PCA) Model and Zero-Maintenance Design Fatigue Model. A brief description of some of these models is provided.

The PCA fatigue model assumes that there is no endurance limit for stress ratio below 0.45; this means that the fatigue life of concrete is infinite if stress remains sufficiently low. One of the weaknesses with the PCA fatigue model is that it assumes that the fatigue behaviour of a simply supported beam is equivalent to a fully supported slab in the field. Packard and Tayabji (1985) describes the PCA model as:

$$For\ SR \leq 0.45 \qquad N_f = Unlimited \qquad (2.9a)$$

$$For\ 0.45 < SR < 0.55 \qquad N_f = \left[\frac{4.2577}{SR - 0.4325}\right]^{3.268} \qquad (2.9b)$$

$$For\ SR \geq 0.55 \qquad logN_f = 11.737 - 12.077SR \qquad (2.9c)$$

where SR is stress ratio and given by Equation 2.2 and N_f is number of cycles to failure.

The design guide for jointed plain concrete highway pavements of the Illinios Department of Transportation also uses the *S-logN* beam fatigue model based on the zero-maintenance report by Darter (1977):

$$logN_f = 17.61 - 17.61S \qquad (2.10)$$

This beam fatigue model provides the allowable number of load repetition with a 50% failure probability.

Darter (1977) found that the highest tensile stresses occur within the pavement midway between the transverse joints, along the longitudinal joints. These observations correlate with the field studies performed by AASHO Road Test (HRB, 1962) where the critical failure point was found mainly to be at the longitudinal edge. However, the results of Bates Road Test (Older, 1924) and Michigan Road Test (Finney and Oehler, 1959) found that the critical location is at the transverse joints for thin slabs (below 200 mm).

2.7.2. Fatigue Models of Field Concrete Slabs

The U.S. Corps of Engineering (COE) developed a fatigue model based on the data of 51 full scale field sections tested between 1943 and 1973 (Smith and Roesler, 2003). The results of the COE fatigue tests are provided by Parker et al. (1979). The COE tests only considered the influence of the applied traffic load in the stress calculation and did not quantify the environmental stresses such as temperature curling and moisture warping of slabs. The fatigue failure in the COE test was defined as the point where

50% of the slab in the trafficked area had cracked. The strength of concrete used in the development of fatigue models is defined as the modulus of rupture obtained from third point loading tests. The COE stated that the edge and the corner loading conditions produce the greater stresses in pavements (Smith and Roesler, 2003). The COE fatigue models changed over time; consequently, there are several versions of the fatigue models developed by COE. Only a few of them, which present the fatigue life versus stress levels, are presented.

Darter (1988) developed a fatigue model as shown in Equation 2.11 using the airfield pavement fatigue results of tests conducted by COE. A summary of these results can be found in (Parker et al., 1979; Barker, 1981). This model was originally evaluated for airport pavements but it seems that it shows good correlation in other applications.

$$logN_f = 2.13SR^{-1.2} \qquad (2.11)$$

A nonlinear fatigue model to predict the fatigue performance of in-situ concrete slabs was developed by Thompson and Barenberg (1992) based on the COE test (Barker, 1981) and AASHO test data (HRB, 1962). In order to account for temperature curling in the stress calculation, a weighted average annual temperature differential was determined for each test section based on measure data. The following fatigue models were developed (Equation 2.12):

for $SR > 1.25$ $\qquad LogN_f = -1.7136SR + 4.284 \qquad (2.12a)$

for $SR \leq 1.25$ $\qquad LogN_f = 2.8127(SR)^{-1.2214} \qquad (2.12b)$

2.7.3. Comparison between Different Fatigue Models

As seen in the previous sections, a variety of fatigue models are available to use for concrete pavement design, however, each of them provide different results. Figure 2.29 demonstrates the scatter in the results of the fatigue models obtained from beam tests and actual field data. The beam based models are more conservative in low cycle fatigue (less than 1000 cycles) but less conservative in high cycle fatigue. A large scatter in the predicted fatigue life is obtained depending on the model's selection. This can be attributed to the differences in the way that each model was developed. Accordingly, one fatigue model cannot simply be used in place of another in a given design procedure. As can also be seen from the figure, the maximum stress ratio for concrete beam developed models is 1.0, while for field slab developed model, it can exceed 1.0, as per definition of stress ratio, SR, in Section 2.2.1.

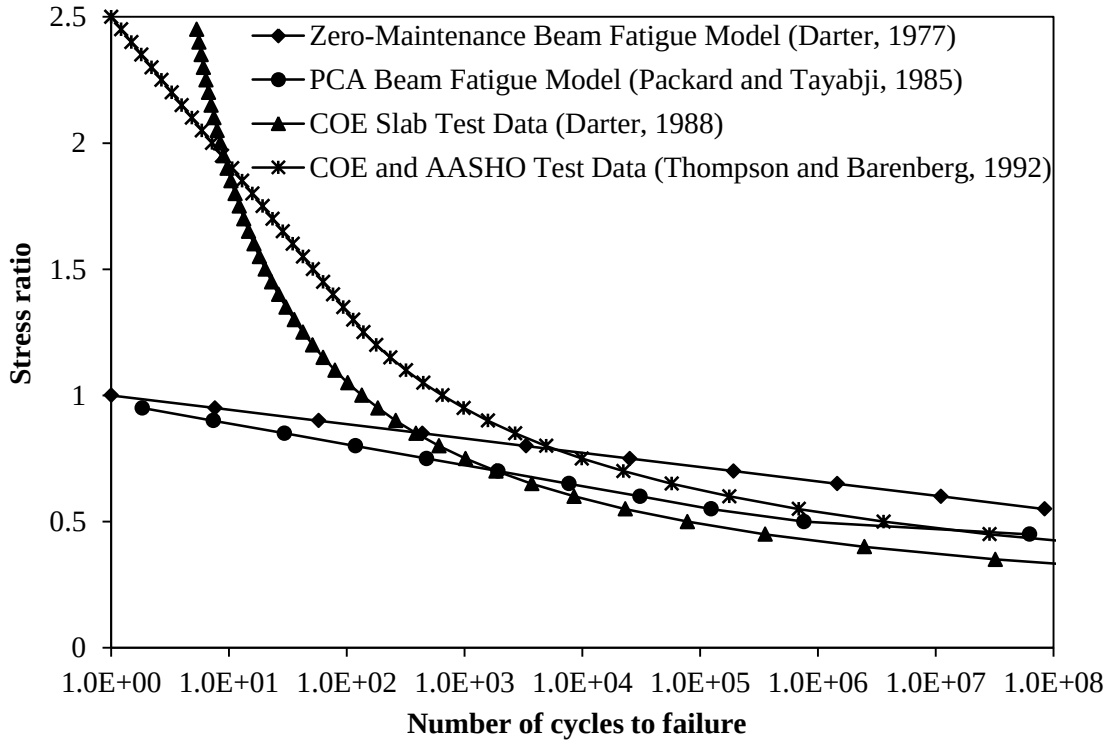

Figure 2.29 – Comparison of several existing concrete fatigue curves.

2.7.4. Fatigue Models of Laboratory Concrete Slabs

Roesler (1998) investigated experimentally and under laboratory conditions the influence of various support and boundary conditions on the fatigue performance of concrete. Three types of specimens were tested: simply supported beams, fully supported beams and fully supported slabs. The fully supported slab was tested at its edge.

The results of simply and fully supported beams of Roesler (1998) were similar to those presented by the Zero-Maintenance Design Fatigue Model. However, the results of the fully supported slabs showed higher fatigue life compared to the predicted ones using the beam fatigue models. Accordingly, in an attempt to account for the difference between slab and beam fatigue results, Roesler (1998) replaced the ultimate flexural strength of the slab with the modulus of rupture of a beam and a fatigue equation was developed, based on the obtained results, to present 50% probability of fatigue failure as:

$$N_f = \left[\frac{1.2968}{\sigma_{max}/MOR_{beam}}\right]^{32.57} \quad (2.13)$$

where σ_{max} is maximum applied stress and MOR_{beam} is moment of rupture of a beam.

Roesler (1998) found that a stress ratio ($\sigma_{max}\ /MOR_{beam}$) of around 1.30 is required to cause flexural cracking after one fatigue cycle. This means that the results of simply supported beams underestimate the strength of concrete slab by 30%. Accordingly, to accurately predict the fatigue life of concrete slab, the flexural strength of the slab should be known. The strength of concrete slab is dependent on boundary conditions, loading configuration, thickness and geometry of the slab.

2.7.5. Fatigue Models of SFRC

The available guidelines and methods for designing rigid pavement are based on conventional concrete and are not modified to consider fibre influence. There is a need to examine the influence of steel fibre addition on the fatigue behaviour of concrete and accordingly adjust the existing concrete fatigue models.

Several fatigue models, in terms of stress ratio-fatigue life (*S*-*N* curves), have been reported for FRC (Chang and Chai, 1995; Wei et al., 1996; Pasakova and Meyer, 1997; Cachim, 1999; Singh and Kaushik, 2003; Lee and Barr, 2004; Germano and Plizzari, 2012). The models indicated that the addition of fibres tends to shift the fatigue life curves towards the right of those of plain concrete; consequently, the FRC indicates a higher value of allowable load repetitions for the same stress level in comparison to plain concrete. However, these models were evaluated from fatigue tests on uncracked specimens.

A study on the fatigue performance of uncracked FRC specimen may be insufficient to draw significant conclusions about the effect of cyclic loading on the toughness due to the fact that the fibres mainly influence the response in the fracture process zone. Therefore, a few studies were conducted on pre-cracked specimens (Naaman and Hammoud, 1998; Plizzari et al., 2000; Germano and Plizzari, 2012). For pre-cracked specimens, the fatigue performance corresponds to the crack initiation and propagation stages and can be taken to be governed by the toughness of the FRC. These results are more representative of the fatigue response of FRC, as considered in inelastic design. It is noted that, even in comparison to the model for uncracked plain concrete, the FRC specimens show high fatigue resistance. It is worth to mention that the study by Naaman and Hammoud (1998) is on high early strength concrete with high dosages of fibres (above 1%) resulting in a strain hardening type of response, which is not directly comparable to the study being discussed here.

Based on the literature review and model comparisons, it is inferred that the incorporation of fibres results in the enhancement of fatigue life of concrete by about 20–25% in the pre-cracked stage. After cracking, the plain concrete is not expected to have any further life as failure will occur almost simultaneously with the first crack appearance, whereas FRC can endure cyclic loading at least at low stress levels for an appreciable number of cycles and this phenomenon can be related to the toughening due to the fibres. However, a conclusive quantitative estimate of the relationship between the fatigue life and toughness of FRC could not be obtained.

2.8. Concluding Remarks

This chapter provides a review about the main findings of research regarding the fatigue performance of plain and steel fibre reinforced concrete and the approaches to determine of the fatigue life of concrete pavements. Several limitations were found and they are listed and described briefly below.

Heavy wheel loads and high traffic volumes over time have required the design of thicker pavements. In rigid pavements, the thickness is frequently governed by the applied traffic loads, rather than the stresses due to temperature and moisture gradients. The structural design of rigid concrete pavements subjected to traffic loading is, generally, based on results of loading tests, experimental experience and empirically or semi-empirically approaches using the theoretical analyses. One of the main assumptions in the analyses of rigid pavements is that a concrete slab behaves as a rigid-elastic layer resting on top of an elastic subgrade and subjected to various loading and boundary conditions. However, the fatigue fracture mechanism of concrete, generally, and SFRC, specifically, is highly nonlinear and non-elastic, raising the influence of size effect. Currently, the flexural strength is used to characterise the fatigue performance of concrete pavements, it is recognised, however, that flexural strength of concrete is size dependent.

It is seen in the literature that the modulus of rupture obtained from prism tests is used in concrete pavements design to obtain the fatigue life of the structure. However, the static strength of fully supported slab can be higher than that obtained from simply supported beams. Additionally, some of the existing fatigue models used in pavements design are based on the fatigue performance of beams, where the fatigue resistance of a rigid pavement is assumed to be similar to that for a concrete beam. This raises the question on the adequately and the suitability of using the Wohler curve or the static strength obtained from a small scale beam as an indicator of the structural fatigue performance of full scale pavements under cyclic loading.

Studies on statically tested large scale SFRC slabs on ground have found that the load carrying capacity of SFRC is significantly larger than that obtained for plain concrete slabs. However, the existing design methods that are used to design SFRC slabs on grade are the same as those used to design plain concrete slabs. The design procedure for plain concrete slabs on ground or pavements is generally based on an elastic analysis where un-cracked concrete section is assumed. However, this method tends to underestimate the load carrying capacity of SFRC slabs on ground, as the utilisation of these approaches in the design SFRC slabs does not take into account the post-cracking contribution that SFRC can make for both the flexural strength and post-cracking strength of SFRC slab. Accordingly, the improved strength properties due to the addition of steel fibres are not appropriately considered. Moreover, the design methods that have been adapted based on the established techniques used for slabs on grade is a major drawback, since the failure of slabs on grade is predominantly caused by static loading, whereas the failure of pavements, more often than not, occurs at much lower stresses due to fatigue. This indicates that there is lack of studies specific to pavements.

As mentioned above, there has been significant research on SFRC under static loading but very limited under cyclic loading and only one pilot study was found in the literature where SFRC slabs on ground were tested under cyclic loading. In this study

the load was simulated by a fixed point under cyclic loading; this resulted in deterioration process, crack pattern and failure mode that are unrepresentative of the actual observed results in reality. Accordingly, there is a need to consider the influence of load sequence to obtain a representative crack patterns and failure mode; afterwards, the effect of steel fibres in controlling the cracks need to be simulated.

Plain concrete pavements are designed in a way that the tensile stress are limited in the slab to such a level of fatigue cracking will not occur for the projected number of stress repetitions. As a result, the number of cycles until the initial cracking is used to determine the fatigue life of plain concrete pavements. However, in SFRC pavements, cracks are going to occur but their propagation is controlled by the fibres and higher loading capacity can be utilized in the post-cracking phase. Accordingly, the fatigue failure mechanism of SFRC is completely different from those plain concrete ones. This indicates that testing small scale specimens or statically testing SFRC slabs on grade, or cyclically testing SFRC slabs on grade by a fixed point, does not provide information about the fatigue life of indeterminate SFRC pavements, and definitely will not provide details and insight into the crack patterns and the mechanism of fatigue fracture failure of SFRC pavements.

The present study relates mainly to the thickness design of concrete slab in rigid pavements. The hypothesis is that thinner SFRC pavement slabs can replace thicker plain concrete slabs. The aim is to provide experimental results that demonstrate the addition of fibres can result in reduction in the thickness of concrete pavements with minimum maintenance requirement in terms of deflection and crack width. Attention and consideration is to be given to the method of applying the fatigue load in an attempt to more correctly simulate the crack patterns and failure mode of pavements in practice.

Chapter 3 MATERIAL CHARACTERISATION OF STEEL FIBRE REINFORCED CONCRETE UNDER STATIC AND FATIGUE LOADING

3.1. Introduction

In this chapter, the results of an experimental study on the characterisation of steel fibre reinforced concrete under fatigue and static loading are presented. Tests were conducted on eighteen dog-bones, thirty six prisms and twenty seven round panels. In Section 3.2, the experimental program undertaken in this study is presented. The experimental results and observations are presented in Sections 3.3 to 3.8 and conclusions presented in Section 3.9.

3.2. Experimental Program

3.2.1. Fibres and Compressive Properties

An experimental program was conducted to investigate the post-cracking and fatigue behaviour of steel fibre reinforced concrete round panels. A series of matched direct uniaxial tension and prism bending tests were undertaken in conjunction with the round panel tests (RPT) to provide comprehensive material characterisation data. A total twenty seven round panels were cast and tested using three different SFRC mix designs. The SFRC mixes were fabricated using three types of commercially available steel fibres:

(i) Double End-Hooked (Series A) Dramix® 5D 65/60 BG fibres;

(ii) End-Hooked (Series B) Dramix® 4D 65/35 BG fibres; and

(iii) End-Hooked (Series C) Dramix® 4D 55/60 BG fibres.

The fibres were manufactured by Bekaert and supplied to the project by BOSFA Pty Ltd Australia. The specimens were cast and tested at the University of New South Wales Heavy Structures Laboratory. The fibre dimensions and material properties are provided in Table 3.1. The SFRC tests are categorised in three series, Series A, B and C. The target fibre dosage used in this study was 30 kg/m^3.

The seventy two specimens produced in this investigation were cast in three batches of nine panels, together with twelve prisms and six dog-bone tension specimens. The concrete mix design was obtained from a local ready mix supplier and it was nominally identical for all three batches. The concrete was provided to the testing laboratory without the fibres in the mix; the specified target concrete compressive strength was 40 MPa and the coarse aggregate used was basalt with a maximum particle size of 20 mm. The workability of the fresh SFRC was measured by means of a slump test and was found to be 80 mm. For the pours that had specimens without fibres, these specimens were cast first. The calculated weight of the fibres was then added, on-site, and mixed in the agitator for a minimum of 10 minutes; when fully mixed, the SFRC specimens were cast.

For Series A and B, the actual fibre content was determined by extracting three cylinders (150 mm diameter by 300 mm high) at the start of the pour and a further three cylinders at the end of the pour. For Series C, additional three cylinders were extracted at the middle of the pour as this series was casted with the large scale slabs and larger volume of concrete was ordered. The cylinders were emptied, the cement content washed out and the fibres extracted using a magnet. The fibres were then dried and their weight measured. The average fibre dosage and coefficient of variation (COV) are given in Table 3.2. External vibration was used for all SFRC specimens. Photograph of specimens after casting are shown in Figure 3.1.

Table 3.1 – Properties of steel fibres.

Property	**A**	**B**	**C**
Length, l_f [mm]	60	35	60
Diameter, d_f [mm]	0.9	0.55	1.05
Aspect ratio, l_f/d_f	65	65	55
Tensile strength, σ_{fu} [MPa]	2300	1850	1450
Strain at ultimate strength	6.0%	0.8%	0.8%
Minimum dosage [kg/m^3]	15	15	18
Fibre Shape	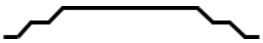	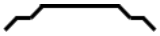	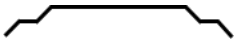

Handling and placing is a major drawback of the ASTM C1550 (2012) round panel test due to the large size of the specimen and, consequently, high weight (91 kg). To facilitate the handling process, 75 mm long lifting ferrules were attached to the steel moulds using an elastic glue to ensure smooth demoulding. As the inclusion of these ferrules can result in micro-cracks formation leading to a weak region within the specimen, subsequently affecting the flexural performance of the material, the lifting ferrules were placed in line with the pre-planned location of the supports during testing. This ensured that the lifting ferrules were not placed within the expected region of crack formation. Additionally, the lifting ferrules were located 100 mm away from the edge of the support to avoid any potential of punching shear failure. This is shown in Figure 3.2.

The specimens were moist cured for a period of 28 days, after which they were cleaned, dried and measured prior to testing. The specimens were tested at least 180 days after casting to minimise any change in strength due to aging.

Figure 3.1 – Round panel test specimens after casting.

Figure 3.2 – Round panel mould with lifting ferrules.

Table 3.2 – Fibre content taken from cylinders during casting.

Series	Start of pour			Mid of pour			End of Pour			Average kg/m^3	COV
	Cylinder 1 (kg/m^3)	Cylinder 2 (kg/m^3)	Cylinder 3 (kg/m^3)	Cylinder 1 (kg/m^3)	Cylinder 2 (kg/m^3)	Cylinder 3 (kg/m^3)	Cylinder 1 (kg/m^3)	Cylinder 2 (kg/m^3)	Cylinder 3 (kg/m^3)		
A	23.6 (-4.8%)	22.3 (-10.1%)	27.3 (+10.2%)	-	-	-	24.3 (-1.8%)	23.7 (-4.4%)	27.5 (+10.9%)	24.8	0.09
B	29.1 (+4.8%)	29.7 (+6.7%)	29.5 (+6.1%)	-	-	-	25.2 (-9.2%)	25.9 (-6.7%)	27.3 (-1.8%)	27.8	0.07
C	34.7 (+15.1%)	28.5 (-5.4%)	32.1 (+6.3%)	28.0 (-7.1%)	31.0 (+2.8%)	30.6 (+1.6%)	27.4 (-9.2%)	31.2 (+3.3%)	27.9 (-7.4%)	30.2	0.08

The compression strength of the concrete used in this study was determined from 150 mm diameter by 300 mm high cylinders. The results are summarised in Table 3.3. The mean compressive strength (f_{cm}) was determined from two to five cylinders tested under load control at a rate of 20 MPa per minute, as per AS1012.9 (1999). The Young's modulus of elasticity (E_c) was obtained in accordance with AS1012.17 (1997).

Table 3.3 – Compressive properties of SFRC mixes.

Series	f_{cm} **[MPa]**		E_c **[GPa]**
	28 days*	**At time of testing***	
A	44.6 (3)	56.0 (5)	31.8 (2)
B	35.7 (3)	51.5 (5)	28.0 (2)
C	48.6 (2)	55.7 (5)	30.3 (2)

Note: * Number in ( ) equals number of cylinders tested.

3.2.2. Uniaxial Tension Test Preparation and Procedure

The uniaxial tension tests were conducted on hour glass shaped "dog-bone" specimens in accordance with AS3600 (2018). The sample geometry, being approximately 40% narrower in the midsection than at its ends, permits for failure to occur within a reasonably well defined region. Furthermore, no notches are required and therefore the dominant crack does not pass through a pre-determined plane. Prior to casting, four 16 mm 8.8 grade threaded rods were placed 100 mm within each end of the formwork. The level and alignment of the threaded rods were checked from the inside of the form and then locked in place using a nut on either side of the wall of the formwork.

The dogbone specimens were tested in a 1 MN capacity Instron servo-hydraulic universal testing machine (UTM). The threaded rods protruding from the specimens were bolted to end plates and connected to the UTM. One end was fixed while the other was fitted with a universal joint to eliminate any residual tension that may develop during the gripping process. To measure the crack opening displacement (COD), displacement transducers (LVDTs and LSCTs) were attached to the North, South, East and West faces of the specimen. The gauges were centred on the specimen and had a gauge length of 230 mm (Figure 3.3). Loading was applied using displacement control, initially at a rate of 0.12 mm/min until the formation of the dominate crack. After cracking, the rate was increased to 0.2 mm/min with additional rate increases introduced as the test progressed. Following the conclusion of testing of uniaxial specimens, the number of fibres crossing the fracture plane was recorded.

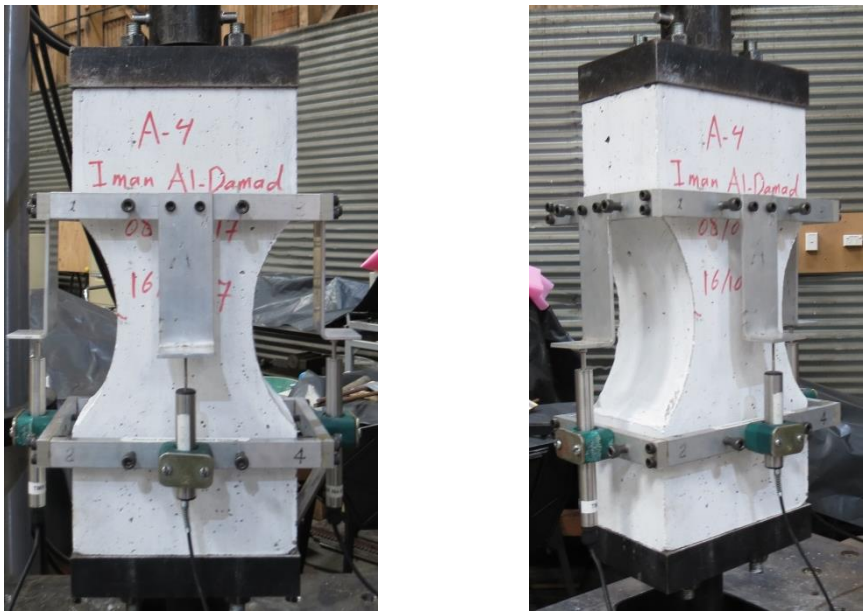

Figure 3.3 – Uniaxial tension test showing displacement transducers.

3.2.3. Prism Bending Test Preparation and Procedure

Bending tests can be performed on notched or un-notched prisms. The use of un-notched specimens enables the crack to initiate at the weakest section of a member; however, this becomes problematic when trying to measure the crack mouth opening displacement (CMOD). On the other hand, the failure plane in a notched specimen is not necessarily the weakest cross section of the member per unit cross-sectional area as a large number of fibres could cross the section, and a large scatter of results has been reported (Parmentier et al., 2008; di Prisco et al., 2009; Foster et al., 2013; Amin et al., 2017). For un-notched specimens tested in a four-point arrangement, the first crack will appear at the weakest cross-section between the two loading points. As the location of the crack cannot be predicted, it is difficult to measure the CMOD and often results are presented in terms of load versus mid-span deflection.

In this study and for each series, the prism bending tests were conducted on twelve samples of 150 mm square in cross-section and 600 mm long. Three different prism bending test procedures were followed: EN 14651 (2007), ASTM C1609 (2006) and JCI-S-002 (2003).

Three to five specimens of each series were notched 25 mm at their mid-span using a diamond blade saw and tested in a three point arrangement spanning 500 mm (as per EN 14651, 2007) to measure the flexural tensile strength. The specimens were tested in a closed loop test system by fixing a clip gauge to the underside of the prism at the notch to measure and control the crack mouth opening displacement at the extreme tensile fibre. Testing was conducted by increasing the CMOD at a rate of 0.05 mm/min until the CMOD reached 0.10 mm; this rate was then increased to 0.20 mm/min until the CMOD reached 5 mm, at which point testing was concluded.

The flexural toughness of the specimens was evaluated by testing four specimens of each series according to ASTM C1609 (2006). The specimens were placed on two roller

supports over a span of 450 mm. The prism midspan deflection was measured by a pair of linear potentiometers attached to a frame such that a net midspan deflection would be measured, according to ASTM C1609 (2006). The prisms were loaded at a rate of 0.05 mm/min until the net deflection reached 0.50 mm; this rate was then increased to 0.20 mm/min. The test was terminated at a deflection of 5 mm.

The fracture energy was obtained from testing two to five notched specimens of each series according to Japanese Concrete Institute Standard JCI-S-002 (2003). The 45 mm length notch was formed by a 3 mm wide saw cut across the full width of the specimen. The specimens were placed on two roller supports over the span of 450 mm. The loading was controlled using CMOD at a rate of 0.075 mm/min. The test was terminated at a CMOD of 5 mm.

For Series B and C, ASTM C1609 (2006) and EN 14651 (2007) tests, concrete strain was measured as the applied deflection or CMOD increased to determine the location of neutral axis. Each specimen was instrumented with five 60 mm electronic strain gauges fixed through the depth of the prism, at the mid-span, as shown in Figures 3.4 and 3.5 for the notched and un-notched prism bending tests, respectively.

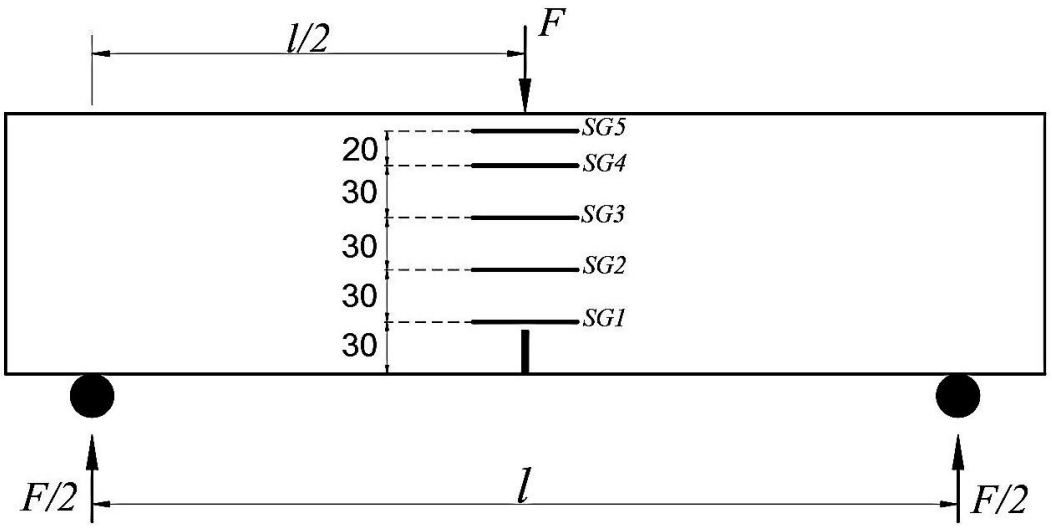

Figure 3.4 – Location of strain gauges for notched prism bending test (dimensions in mm).

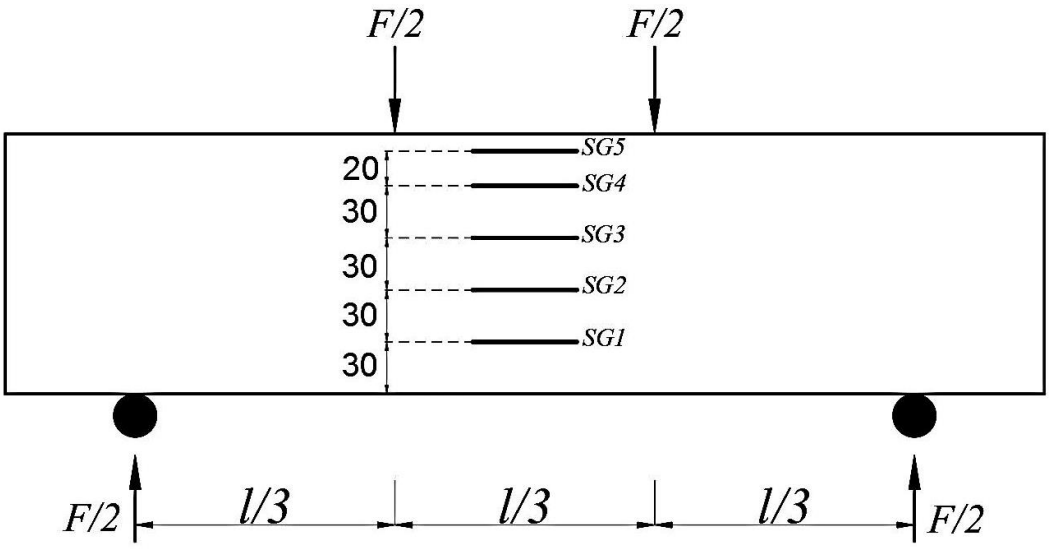

Figure 3.5 – Location of strain gauges for un-notched prism bending test (dimensions in mm).

3.2.4. Round Panel Test Preparation and Procedure

The determinate round panel specimens were produced with nominal diameter of 800 mm and nominal thickness of 75 mm and tested to ASTM C1550 (2012). Before testing, the diameter of the panel was measured at three places and the thickness of the panel was measured at six points around the edge. The average measured dimensions of each specimen are given in Table 3.4. Table 3.4 shows that the mean coefficient of variation in diameter and thickness of the panels is small. Full data are presented in Appendix A.

The RPTs are designated using the notation U-VW-X-Y-Z, where 'U' is the series name indicating the type of fibre used, 'V' is the specimen number of the series (i.e. same specimen type under the same loading conditions), 'W' refers to static (S) or cyclic (C) applied loading, 'X' indicates plain (P) or fibre reinforced (F) concrete, 'Y' represents whether the specimen was pre-cracked (C) or uncracked (U) before the application of the cyclic (fatigue) loading and 'Z' is the percentage of the maximum load level during fatigue loading. For example, specimen A-1C-F-C-60 represents a pre-cracked SFRC round panel specimen of Series A with 5D 65/60 steel fibres, cycled up to 60% of its static capacity and is the first specimen of this test type.

The panels were supported on three symmetrically arranged pivot points giving a loading radius, r, of 375 mm (Figure 3.6). Each specimen was instrumented with an LSCT, placed underneath the loading point, to measure the central deflection. To provide crack opening measurements, three PI-gauges and three draw wire gauges were placed at 120^{o} angles and 150 mm and 300 mm, respectively, away from the edge of the specimen (Figure 3.7). A 100 kN capacity load cell was placed between the loading head and the actuator to measure applied load.

All round panel specimens were loaded at their centres by an Instron 500 kN capacity actuator mounted on a stiff testing frame. The test machine was servo-controlled with

fully digital control and data acquisition. Depending on the test type, displacement-control or load-control mode was used. In the static load test, the test was controlled via ram displacement control, initially at a rate of 0.3 mm/min until the formation of the three fracture lines and then increased to 3 mm/min. Testing concluded at a central displacement of at least 45 mm.

Two types of fatigue test were performed, the first on an uncracked specimen and the second on a pre-cracked specimen. The test program for the RPTs is outlined in Table 3.4. For the uncracked specimens, the load range for the fatigue tests was selected based on the mean peak cracking load observed in the static tests. The load ranges are presented as a percentage of mean static peak load. During the test, the load was applied monotonically up to the lower load level of the range under deflection control at a rate of 0.3 mm/min. The cyclic load was then applied using a sine waveform under load control at frequency of 3 Hz until failure was imminent, or until predetermined cyclic limit was reached. The point of imminent failure was marked by a large increase in the measured central deflection. For all uncracked specimens, the cycle limit was 3 million cycles. At the conclusion of the applied fatigue loading, a displacement controlled monotonic load was applied until a central deflection of at least 45 mm was reached. If the specimen reached the cycle limit without failure, the specimen was then loaded statically to failure to determine its residual strength.

For the pre-cracked specimens, three stages of loading were planned with the aim of monitoring the crack growth development in the concrete subjected to cyclic loads. In the first stage, a static load was applied until, at a rate of 0.3 mm/min, a crack width of 0.5 mm was reached; the specimen was then unloaded to the chosen value of preset lower limit of the following cyclic stage. This first initial quasi-static load was planned in order to form a microcracked zone placed at the crack's tip to better assess the fatigue behaviour of SFRC in flexure (Slowik et al., 1996; Plizzari et al., 2000; Germano et al., 2016). In the second stage, fatigue testing was carried out. The cyclic load was applied

using a sine waveform under load control at a frequency of 3 Hz. The load ranges for the fatigue tests of the pre-cracked specimens were selected as a percentage of the peak load (P_{max}), which was measured for each specimen in the initial monotonic stage. Since the scope of this research work is to investigate the fatigue behaviour of SFRC, two different load levels were planned for Series A and B and three load levels for Series C. It is worth mentioning that the choice of referring the fatigue load levels to the actual peak load (P_{max}, measured during the initial monotonic loading of each specimen), instead of the average cracking load obtained from all the monotonic tests previously carried out, is to reduce the experimental scatter of fatigue results, which is related, to a great extent, to variations in the ultimate loads of similar specimens. In the final stage, as the envelope curve is being approached, the specimen is no longer able to sustain the upper limit value and a sudden rapid increase in both the central deflection and crack opening displacement occurs from one cycle to the subsequent one. At this stage, the cyclic loading is stopped and a monotonic increase in deflection at rate of 3 mm/min is imposed until a central deflection of at least 45 mm is reached. If testing reached the 3 million cycles without failure, the specimen was then loaded statically to failure – expect for the specimens cycled with a maximum load level of 50%. In specimens loaded to 50% maximum load, cyclic loading continued up to 10 million cycles or failure, whichever occurred first.

Prior to testing, the specimens were lightly painted white to facilitate the crack detection process.

Table 3.4 – Test program of round panel specimens and their dimensions.

Specimen ID	Diameter	Thickness	Test type	Pre-cracked	Max load
	[mm]	[mm]			
A-1S-P	799	77.0	Static	-	-
A-1S-F	799	77.7	Static	-	-
A-2S-F	798	76.9	Static	-	-
A-1C-F-U-60	798	78.4	Fatigue	No	60%
A-1C-F-U-70	799	77.5	Fatigue	No	70%
A-1C-F-C-60	798	75.0	Fatigue	Yes	60%
A-2C-F-C-60	799	76.1	Fatigue	Yes	60%
A-1C-F-C-40	798	79.3	Fatigue	Yes	40%
A-2C-F-C-40	799	76.7	Fatigue	Yes	40%
B-1S-F	799	77.7	Static	-	-
B-2S-F	799	78.4	Static	-	-
B-1C-F-U-70	799	82.3	Fatigue	No	70%
B-2C-F-U-70	799	79.2	Fatigue	No	70%
B-1C-F-C-60	799	80.9	Fatigue	Yes	60%
B-2C-F-C-60	799	80.7	Fatigue	Yes	60%
B-3C-F-C-60	799	76.9	Fatigue	Yes	60%
B-1C-F-C-40	798	76.0	Fatigue	Yes	40%
B-2C-F-C-40	799	77.6	Fatigue	Yes	40%
C-1S-F	800	78.4	Static	-	-
C-2S-F	800	77.3	Static	-	-
C-1C-F-U-70	799	79.4	Fatigue	No	70%
C-2C-F-U-70	799	80.7	Fatigue	No	70%
C-1C-F-C-60	799	79.5	Fatigue	Yes	60%
C-2C-F-C-60	799	75.4	Fatigue	Yes	60%
C-1C-F-C-50	799	81.0	Fatigue	Yes	50%
C-2C-F-C-50	800	80.2	Fatigue	Yes	50%
C-1C-F-C-40	800	77.6	Fatigue	Yes	40%
Mean	**799**	**78.3**			
COV	**0.07%**	**2.39%**			

Figure 3.6 – Photograph of test set-up for round panel specimens.

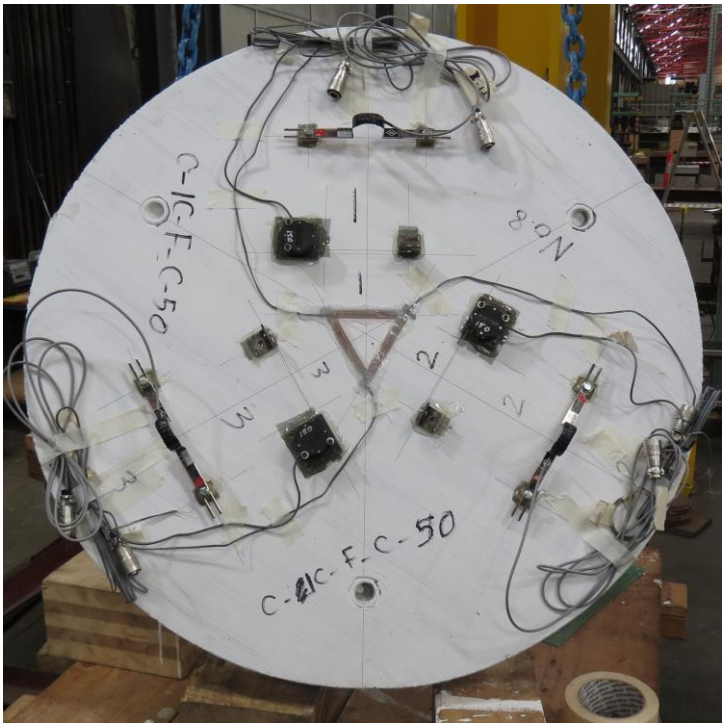

Figure 3.7 – Instrumentation details of test set-up (bottom side).

3.3. Uniaxial Tension Test Results

In this section, the results and test observations of the uniaxial tension test specimens are reported. For each series, six dog-bone specimens were cast and tested. The raw experimental results for the uniaxial tests are presented in Figure 3.8. The points plotted on the axes of the figures are the tensile strengths of the matrix (f_{ct}), with the average for each series given in Table 3.5. In Table 3.5, E_t refers to the tensile secant modulus of the concrete, ε_t is the cracking strain of the matrix and $f_{0.5}$ and $f_{1.5}$ are the average stresses at a CODs of 0.5 mm and 1.5 mm, respectively. To determine the crack opening displacement, the average of the four transducers is taken. All cracking occurred within the gauged length (see Appendix B). The tensile stresses presented in the analysis are in terms of equivalent tensile stress, which is the resultant of the applied tensile load divided by the cross sectional area at the most narrow cross-section. It is worthy of note that the response of SFRC structural elements is typically concerned with the behaviour of members with small crack widths (i.e. $w < 2$ mm); the response at significantly large crack widths ($w > 2$ mm) is mainly of academic interest. The full test data are given in Appendix B.

Table 3.5 – Summary of raw uniaxial tension test results.

Series	**Fibre Type**	f_{ct}	$f_{0.5}$	$f_{1.5}$	E_t	ε_t ($\times 10^{-4}$)
		[MPa]	**[MPa]**	**[MPa]**	**[GPa]**	**[mm/mm]**
A	5D 65/60 BG	2.98	1.45	1.08	29.8	1.22
B	4D 65/35 BG	2.31	0.91	0.89	23.4	1.23
C	4D 55/60 BG	3.77	-	1.16	31.2	1.33

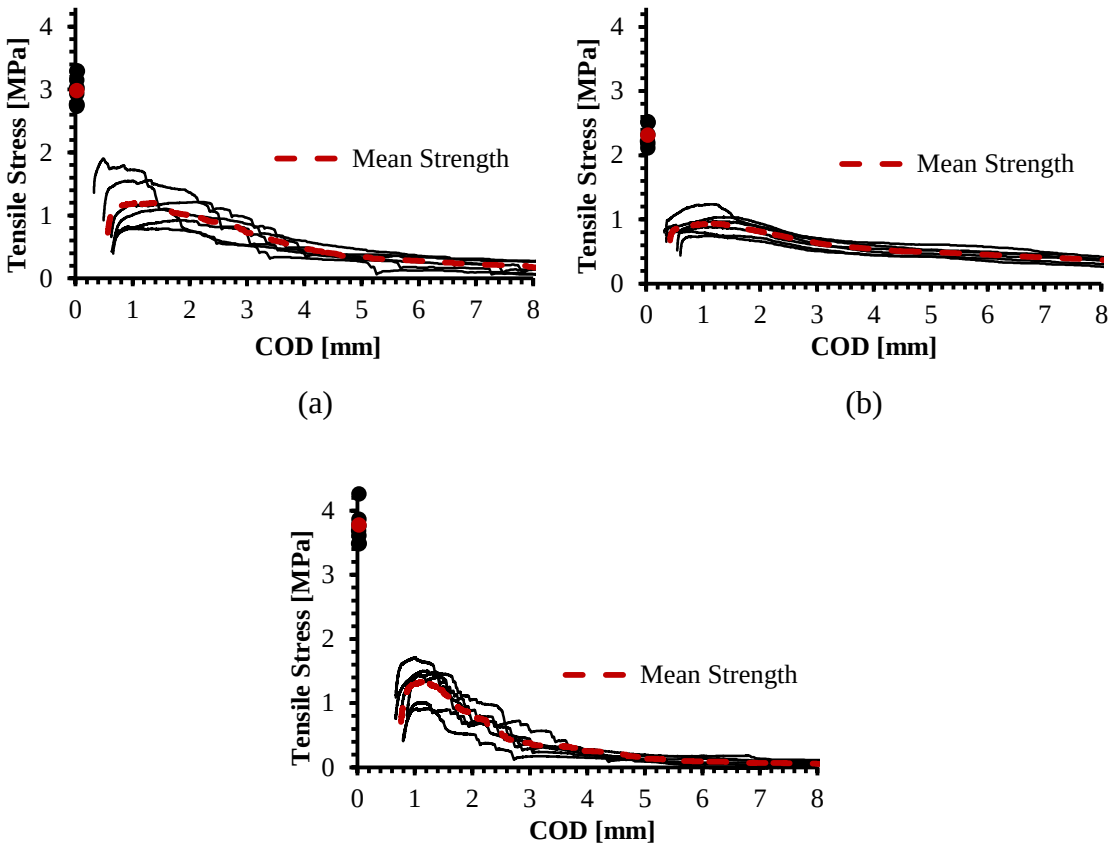

Figure 3.8 – Uniaxial tension test results: (a) Series A; (b) Series B; (c) Series C.

Initially upon loading, the specimens behaved approximately linear elastically and it was assumed that the deformation was uniformly distributed over the gauged length. Close to the peak stress, the overall response became softer due to micro-cracking (see Appendix B). The fracture processes of all specimens consisted of three main stages. The first stage involved the formation of a meso-crack of less than 0.05 mm width. This defined the end of the linear elastic range of the tensile stress-strain response, and corresponded to a significant reduction in stiffness. Once initiated, the dominant crack propagated along the weakest cross section along a surface (see Figure 3.9). At this stage, the peak stress had been achieved. This was shortly followed by a sharp reduction in load, coinciding with a significant opening of the crack, as the elastic strain energy stored in the specimen and testing rig was recovered. No displacement data is available between the peak load and that corresponding to the stabilised crack.

Soon after cracking had stabilised, it was clear that the concrete provided no direct contribution to the tensile strength of the dog-bone specimens and that the strength was due to the fibres alone. That is, no tensile stresses were transmitted through the concrete matrix. At this stage, the tensile strength of the specimen is derived through the bond and development of interfacial shear stresses between the fibres and surrounding concrete matrix. The long tail of the curves reflects the progressively smooth residual capacity of the specimens.

The fracture plane of the specimens was relatively flat, even when low fibre dosages were used. There was no evidence of local damage to the concrete surrounding the fibres (Appendix B).

Figure 3.9 – Formation of dominant crack.

Following the conclusion of testing of uniaxial tension specimens, the number of fibres crossing the fracture plane was recorded. The average number of fibres crossing the failure plane, $N_{f,exp}$, for each series are presented in Table 3.6. Full data can be found in Appendix B.

For fibres randomly orientated in three dimensions, Aveston and Kelly (1973) showed that the number of fibres crossing a plane of unit area is $\rho_f / 2A_f$, where ρ_f is the volumetric ratio of fibres and A_f is the cross sectional area of an individual fibre. The expression of Aveston and Kelly (1973) for the total number of fibres crossing a certain failure plane may be expressed as:

$$N_{f,theory} = \frac{\rho_f A_c}{2k_{3D,b}A_f} \tag{3.1}$$

where $N_{f,theory}$ is the number of fibres crossing the failure plane, A_c is the cross sectional area of the failure crack and $k_{3D,b}$ is a three-dimensional fibre orientation factor; to correct for the "*wall effect*", and is included based on the observations of Ng et al. (2012) and Foster et al. (2013).

In Series A and C, where fibres have a length of 60 mm, the wall effect can be pronounced, as can be seen from Figure 3.10. The number of fibres crossing the failure plane of the dog-bones is presented alongside the theoretical number of fibres calculated from the Equation 3.1, with A_c taken at the most narrow cross section of the specimen.

Considering the actual fibre volume for each series, it can be seen that the theoretical number of fibres crossing the failure crack ($N_{f,theory}$) is consistently greater than the actual number of fibres crossing the failure crack ($N_{f,exp}$). The explanation for this is that failure occurred on the weakest plane of the dogbone, this would imply that the number of fibres at the crack is statistically lower than the prescribed mean value. For the specimens tested in this study, the mean value and the coefficient of variation are 0.81 and 0.11, respectively. This is consistent with previous research (Htut, 2010; Foster et al., 2013) and observed in Amin et al. (2017). Number of fibres crossing the failure crack versus the tensile stress at COD = 1.5 mm is presented in Figure 3.11.

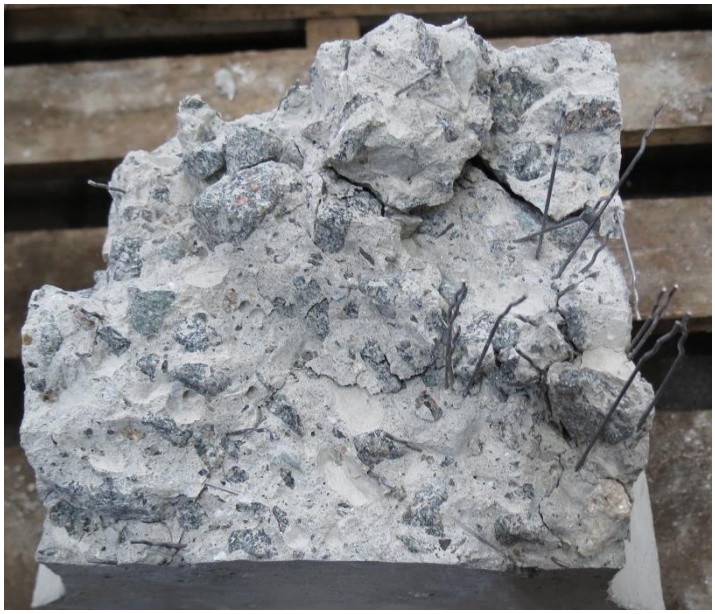

Figure 3.10 – Fibres distribution along a failure plane of uniaxial tension test.

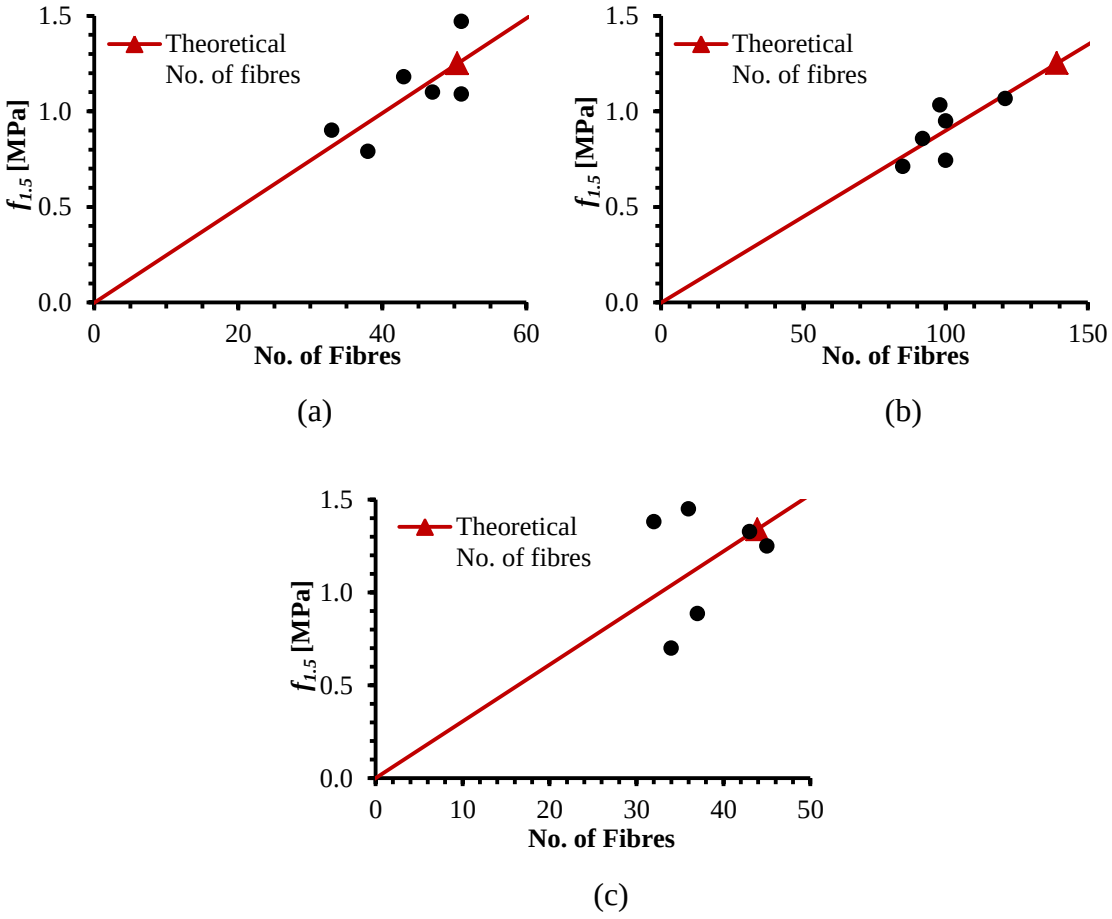

Figure 3.11 – Residual tensile stress vs number of fibres crossing failure plane of uniaxial tension tests: (a) Series A; (b) Series B; (c) Series C.

Table 3.6 – Number of fibres crossing failure plane of uniaxial tension test.

Series	$N_{f,exp}$	$N_{f,theory}$	$N_{f,exp}/N_{f,theory}$	f_{ct} **[MPa]**	$f_{1.5}$ **[MPa]**
A	44	51	0.87	2.98	1.08
B	99	139	0.71	2.31	0.89
C	38	44	0.86	3.77	1.16
Mean			**0.81**		
COV			**0.11**		

In this study, all end hooked fibres had pulled out of the matrix; no fibres were observed to have fractured. Furthermore, it was noticed that not all the end hooked fibres had straightened. This was particularly true for fibres near the edge of the fracture plane (see Figure 3.10) and for those fibres that were near parallel to the fracture surface (Figure 3.12). The ends of the majority of the double hooked fibres (Series A) had not straightened. This is due to the increased mechanical bond of the fibre coupled with their high tensile strength (2300 MPa).

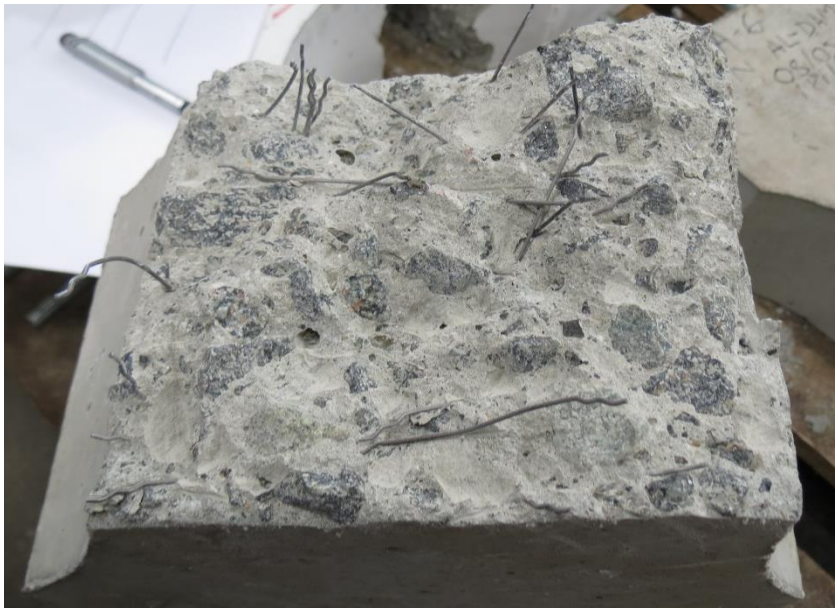

Figure 3.12 – Un-straightened fibres near parallel to the fracture surface.

A comparison between Series A, B and C is presented in Figure 3.13. As can be seen, for a crack opening displacement ranging from zero to 2 mm, the three series show approximately the same toughness. However, after a crack width of 4 mm approximately being reached, Series B showed a higher performance. It is worth to mention that the response of SFRC structural elements is typically concerned with the behaviour of members with small COD ($w < 2$ mm); however, the response at larger COD ($w > 2$ mm) is reported for the academic interest mainly.

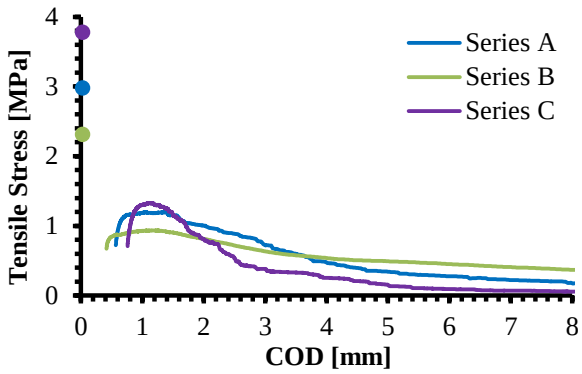

Figure 3.13 – Comparison between Series A, B and C dog-bone test results.

To determine the tensile strength of concrete using uniaxial tension test and to investigate the progression of cracking within each specimen, it is important to consider the readings obtained from each transducer and transfer them to equivalent readings at the corners of the specimen. The centre to centre distance between the North (w_2) and South (w_1) transducers is 210 mm, and the centre to centre distance between East (w_4) and West (w_3) transducers is 310 mm. The readings obtained from the transducers were adjusted to determine the elongation at the edge of the specimen. A linear variation of crack widths between the North and South, and the East and West transducers over the centre to centre distance between the transducers is assumed. The readings of each individual transducer at the cracking strength of each specimen are presented in Table 3.7, along with the calculated in and out plane rotations. The readings of the

transducers can be linearly interpolated to determine the elongation at the four corners of the specimen.

From a mathematical analysis, three non-collinear points are needed to determine a unique fracture plane in geometry. However, four transducer readings are available. This means that the system is overdetermined and there is no unique solution. To overcome this, four cases are considered, each of them with three transducer readings. These four cases are then averaged to determine the average elongation at each corner. The extension at each corner can be determined:

$$w_{c1} = 0.75(w_2 + w_3) - 0.25(w_1 + w_4) \quad (3.2a)$$

$$w_{c2} = 0.75(w_2 + w_4) - 0.25(w_1 + w_3) \quad (3.2b)$$

$$w_{c3} = 0.75(w_1 + w_4) - 0.25(w_2 + w_3) \quad (3.2c)$$

$$w_{c4} = 0.75(w_1 + w_3) - 0.25(w_2 + w_4) \quad (3.2d)$$

Figure 3.14 shows the location of the four transducer readings in addition to the calculated measurements at the four corners of the specimen. Table 3.8 presents the cracking strain at the corners of each specimen, along with the cracking strain corresponding to the location of each transducer. The cracking strain is obtained from diving the transducer reading by the gauges length. The tensile strength is evaluated by multiplying the strain at each location by the elastic Young's modulus as shown in Table 3.9 and Figures 3.15 to 3.17. As observed in Tables 3.8 and 3.9, the maximum tensile strength occurs at one corner of each specimen, as expected. This is the true tensile strength of the material, as concrete is considered a brittle material. Also, it can be seen from the figures that the maximum tensile strength across the cracking plane for each specimen approximately equals to the theoretically expected mean tensile strength.

Equation 3.2 can also be used to determine the progression of the fracture line within the specimen at different crack widths. Table 3.10 presents the variation in crack opening displacement across the cracking plane at an average COD = 1.5 mm for each specimen. As can be seen from the table, some cracks widen while in other instances they close. This is strongly related to the variation in the number of fibres crossing the cracking plane at different edges (see Figure 3.10). This implies that greater force passes through the specimen at the locations with more fibres, and at these locations the cracks are expected to be narrower. This means that the post-peak strength is not uniformly distributed across the cracking plane of the specimen. This also leads to in and out of plane rotations.

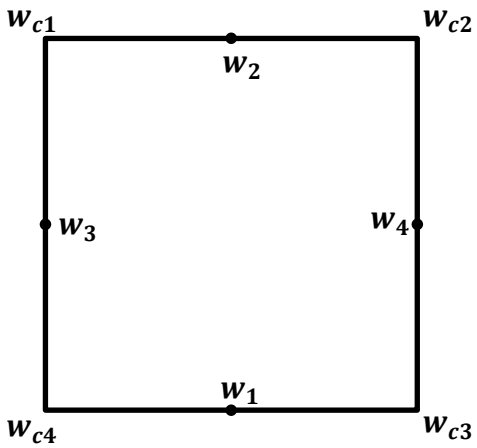

Figure 3.14 – Cross section displaying the location of the strain values.

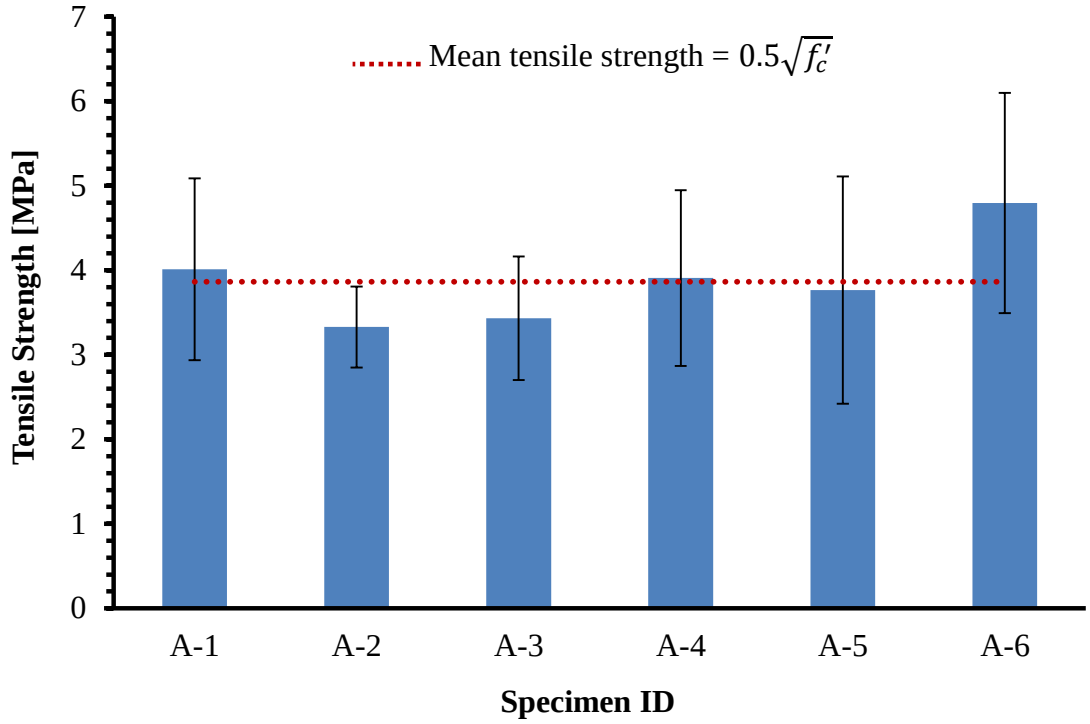

Figure 3.15 – Variation in tensile strength of Series A.

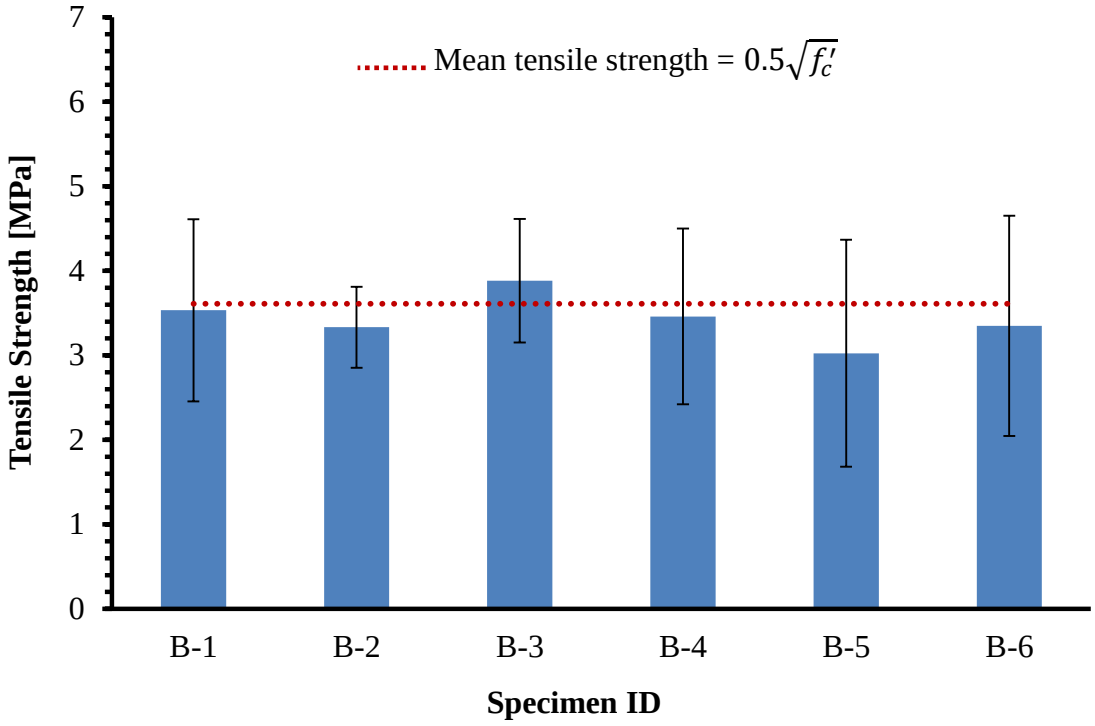

Figure 3.16 – Variation in tensile strength of Series B.

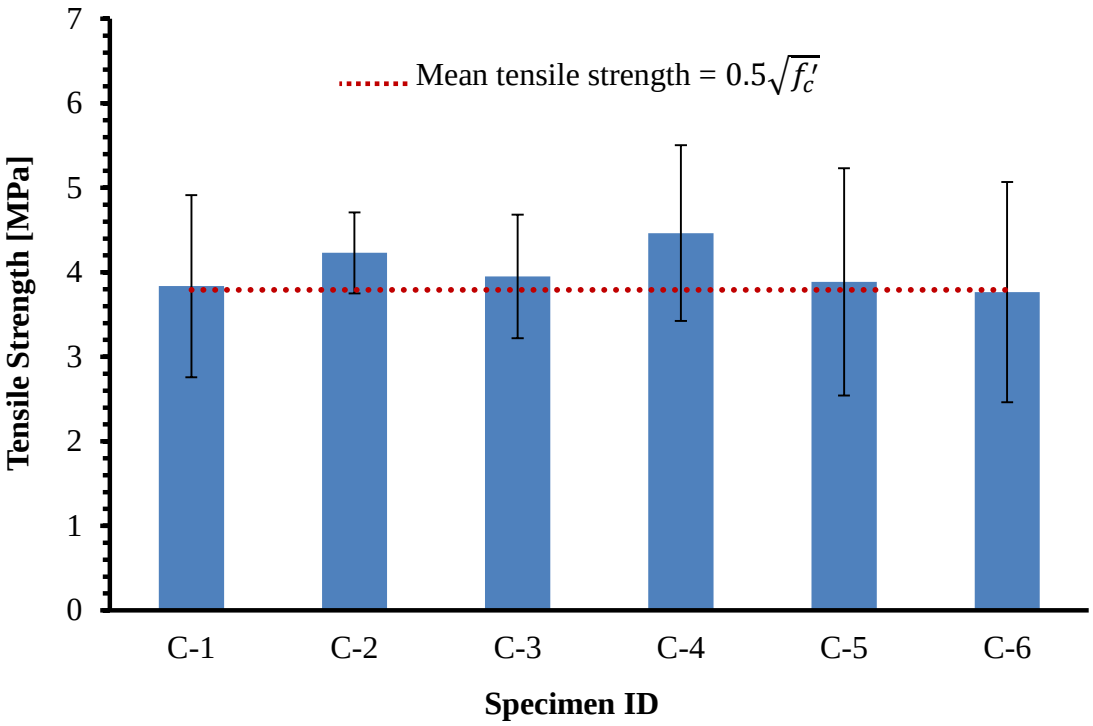

Figure 3.17 – Variation in tensile strength of Series C.

Table 3.7 – LSCT/LVDT readings from uniaxial tension tests at the peak load.

Specimen ID	w_1 [mm]	w_2 [mm]	w_3 [mm]	w_4 [mm]	out of plane rotation (mrad)	in plane rotation (mrad)
A-1	0.033	0.024	0.011	0.048	-0.043	0.122
A-2	0.018	0.030	0.022	0.027	0.057	0.017
A-3	0.033	0.018	0.016	0.032	-0.071	0.052
A-4	0.024	0.030	0.011	0.048	0.029	0.121
A-5	0.015	0.039	0.011	0.043	0.114	0.104
A-6	0.024	0.045	0.016	0.054	0.100	0.121
B-1	0.030	0.027	0.043	0.016	-0.014	-0.087
B-2	0.036	0.009	0.005	0.059	-0.129	0.173
B-3	0.015	0.048	0.027	0.038	0.157	0.035
B-4	0.027	0.033	0.000	0.054	0.029	0.173
B-5	0.039	0.012	0.011	0.038	-0.129	0.086
B-6	0.036	0.015	0.043	0.016	-0.100	-0.087
C-1	0.019	0.040	0.040	0.018	0.023	-0.017
C-2	0.014	0.050	0.026	0.038	0.040	0.009
C-3	0.026	0.034	0.032	0.029	0.009	-0.002
C-4	0.038	0.028	0.029	0.041	-0.011	0.009
C-5	0.018	0.040	0.022	0.037	0.024	0.011
C-6	0.024	0.032	0.040	0.018	0.008	-0.016

Table 3.8 – Variation in cracking strain across the cracking plane at the peak load for each specimen.

Specimen ID	$\varepsilon_1 \times 10^{-3}$	$\varepsilon_2 \times 10^{-3}$	$\varepsilon_3 \times 10^{-3}$	$\varepsilon_4 \times 10^{-3}$	$\varepsilon_{c1} \times 10^{-3}$	$\varepsilon_{c2} \times 10^{-3}$	$\varepsilon_{c3} \times 10^{-3}$	$\varepsilon_{c4} \times 10^{-3}$
A-1	0.135	0.112	0.094	0.163	0.080	0.149	0.172	0.103
A-2	0.089	0.120	0.100	0.110	0.115	0.125	0.094	0.084
A-3	0.130	0.091	0.090	0.120	0.073	0.104	0.143	0.112
A-4	0.110	0.125	0.094	0.163	0.097	0.165	0.149	0.081
A-5	0.086	0.148	0.086	0.153	0.116	0.183	0.121	0.054
A-6	0.123	0.177	0.117	0.187	0.143	0.213	0.159	0.089
B-1	0.128	0.120	0.154	0.103	0.147	0.097	0.105	0.155
B-2	0.133	0.063	0.092	0.189	0.035	0.132	0.203	0.106
B-3	0.093	0.181	0.131	0.150	0.173	0.192	0.105	0.085
B-4	0.122	0.138	0.067	0.167	0.081	0.182	0.166	0.066
B-5	0.146	0.076	0.080	0.130	0.048	0.098	0.168	0.118
B-6	0.139	0.083	0.154	0.103	0.117	0.067	0.122	0.172
C-1	0.101	0.155	0.146	0.104	0.175	0.133	0.078	0.121
C-2	0.093	0.187	0.127	0.151	0.174	0.198	0.105	0.081
C-3	0.120	0.140	0.134	0.128	0.144	0.137	0.117	0.123
C-4	0.157	0.130	0.140	0.162	0.122	0.145	0.172	0.150
C-5	0.099	0.156	0.115	0.143	0.143	0.170	0.114	0.086
C-6	0.112	0.132	0.147	0.106	0.154	0.114	0.094	0.135

Table 3.9 – Variation in tensile strength across the cracking plane for each specimen.

Specimen ID	$f_{ct,1}$ [MPa]	$f_{ct,2}$ [MPa]	$f_{ct,3}$ [MPa]	$f_{ct,4}$ [MPa]	$f_{ct,c1}$ [MPa]	$f_{ct,c2}$ [MPa]	$f_{ct,c3}$ [MPa]	$f_{ct,c4}$ [MPa]	$f_{ct,Max}$
A-1	4.31	3.57	2.98	5.19	2.54	4.75	5.48	3.28	**5.48**
A-2	2.82	3.81	3.19	3.49	3.67	3.98	2.99	2.68	**3.98**
A-3	4.15	2.91	2.85	3.82	2.33	3.30	4.54	3.57	**4.54**
A-4	3.49	3.98	3.00	5.17	3.07	5.24	4.75	2.58	**5.24**
A-5	2.74	4.72	2.74	4.86	3.69	5.82	3.84	1.71	**5.82**
A-6	3.91	5.63	3.71	5.94	4.55	6.77	5.05	2.82	**6.77**
B-1	3.58	3.36	4.30	2.89	4.13	2.72	2.94	4.35	**4.35**
B-2	3.73	1.75	2.56	5.29	0.98	3.71	5.68	2.96	**5.68**
B-3	2.61	5.06	3.66	4.21	4.83	5.38	2.94	2.39	**5.38**
B-4	3.43	3.87	1.87	4.67	2.28	5.09	4.64	1.83	**5.09**
B-5	4.09	2.12	2.24	3.65	1.34	2.75	4.71	3.30	**4.71**
B-6	3.88	2.33	4.30	2.90	3.28	1.87	3.43	4.83	**4.83**
C-1	3.05	4.70	4.44	3.16	5.30	4.02	2.38	3.65	**5.30**
C-2	2.83	5.65	3.86	4.58	5.28	6.00	3.18	2.46	**6.00**
C-3	3.62	4.23	4.07	3.88	4.35	4.16	3.55	3.74	**4.35**
C-4	4.76	3.94	4.24	4.92	3.71	4.39	5.22	4.53	**5.22**
C-5	3.00	4.72	3.50	4.33	4.33	5.16	3.44	2.61	**5.16**
C-6	3.39	3.99	4.46	3.22	4.68	3.44	2.85	4.09	**4.68**

Table 3.10 – Variation in crack opening displacement across the cracking plane at an average COD = 1.5 mm for each specimen.

Specimen ID	w_1 [mm]	w_2 [mm]	w_3 [mm]	w_4 [mm]	w_{c1} [mm]	w_{c2} [mm]	w_{c3} [mm]	w_{c4} [mm]
A-1	1.62	1.33	1.28	1.76	1.11	1.59	1.88	1.40
A-2	1.35	1.61	1.15	1.89	1.26	2.00	1.75	1.00
A-3	2.30	0.67	1.15	1.86	0.33	1.04	2.67	1.96
A-4	1.58	1.40	1.22	1.80	1.12	1.70	1.87	1.30
A-5	1.42	1.53	1.28	1.77	1.31	1.80	1.69	1.20
A-6	1.81	1.15	1.86	1.18	1.51	0.84	1.49	2.16
B-1	1.74	1.23	1.43	1.61	1.16	1.33	1.84	1.67
B-2	1.83	1.11	1.34	1.74	0.94	1.34	2.07	1.67
B-3	1.20	1.77	1.38	1.66	1.65	1.92	1.35	1.08
B-4	1.26	1.71	1.35	1.67	1.56	1.89	1.44	1.11
B-5	1.57	1.40	1.35	1.67	1.25	1.58	1.75	1.42
B-6	1.47	1.49	1.62	1.42	1.61	1.41	1.39	1.59
C-1	0.86	2.13	2.40	0.60	3.03	1.23	-0.04	1.76
C-2	0.78	2.22	1.32	1.69	2.03	2.40	0.97	0.60
C-3	2.17	0.83	1.92	1.07	1.25	0.40	1.74	2.59
C-4	2.40	0.61	1.12	1.86	0.24	0.98	2.76	2.02
C-5	1.10	1.91	1.72	1.27	2.13	1.68	0.87	1.32
C-6	2.35	0.64	1.99	1.03	1.13	0.17	1.87	2.83

3.4. Bending Test Results

3.4.1. EN 14651 Prism Bending Test Results

Flexural tensile tests were undertaken according to EN 14651 (2007) with a three-point bending set-up on three to five notched prisms. The specimens were 600 mm long, 150 mm deep and 150 mm wide; the span was 500 mm and the notch depth was 25 mm. The resulting stresses $f_{ct,L}^{f}$ and f_{Ri}, $i = 1, 4$, are described in Figure 3.18 (EN 14651, 2007). Load – CMOD results and the parameters obtained from the notched prism bending tests are presented in Figure 3.19 and are summarised in Table 3.11. The response of the three-point notched bending test can be described by three distinct phases: (i) an elastic phase up to cracking; (ii) a flexural hardening response up to the post-cracking peak load; and (iii) a reduction of load with increasing CMOD.

In general the prism specimens exhibited some degree of scatter and variability, as is expected from this type of test (Parmentier et al., 2008; di Prisco et al., 2009; Foster et al., 2013; Amin et al., 2017). Two cracking forms characterised the failure modes of the prisms. The first was one in which failure occurred over a single localised dominant crack that propagated directly from the notch toward the loading point. In this case no secondary cracks developed from the primary crack (see Figure 3.20 and Appendix C).

The second cracking form was one where multiple cracks occurred and significant branching from the primary crack occurred, or sometimes the nucleation of new cracks (Figure 3.21). This type of cracking was observed in the mix with 5D 65/60 BG steel fibre. In this case, most specimens displayed residual flexural tensile stresses much higher than that required for elastic cracking.

A comparison between Series A, B and C is presented in Figure 3.22. As can be seen, Series A and C have higher flexural toughness than Series B. This is because hardening behaviour was noted with some prisms of Series A and C.

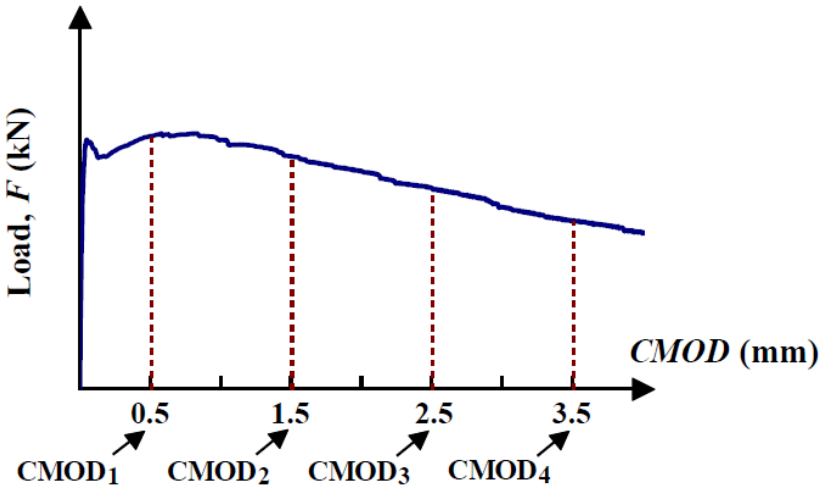

Figure 3.18 – Definition of key points on the applied force versus crack mouth opening displacement (CMOD) curve for flexural testing of prisms (EN 14651, 2007).

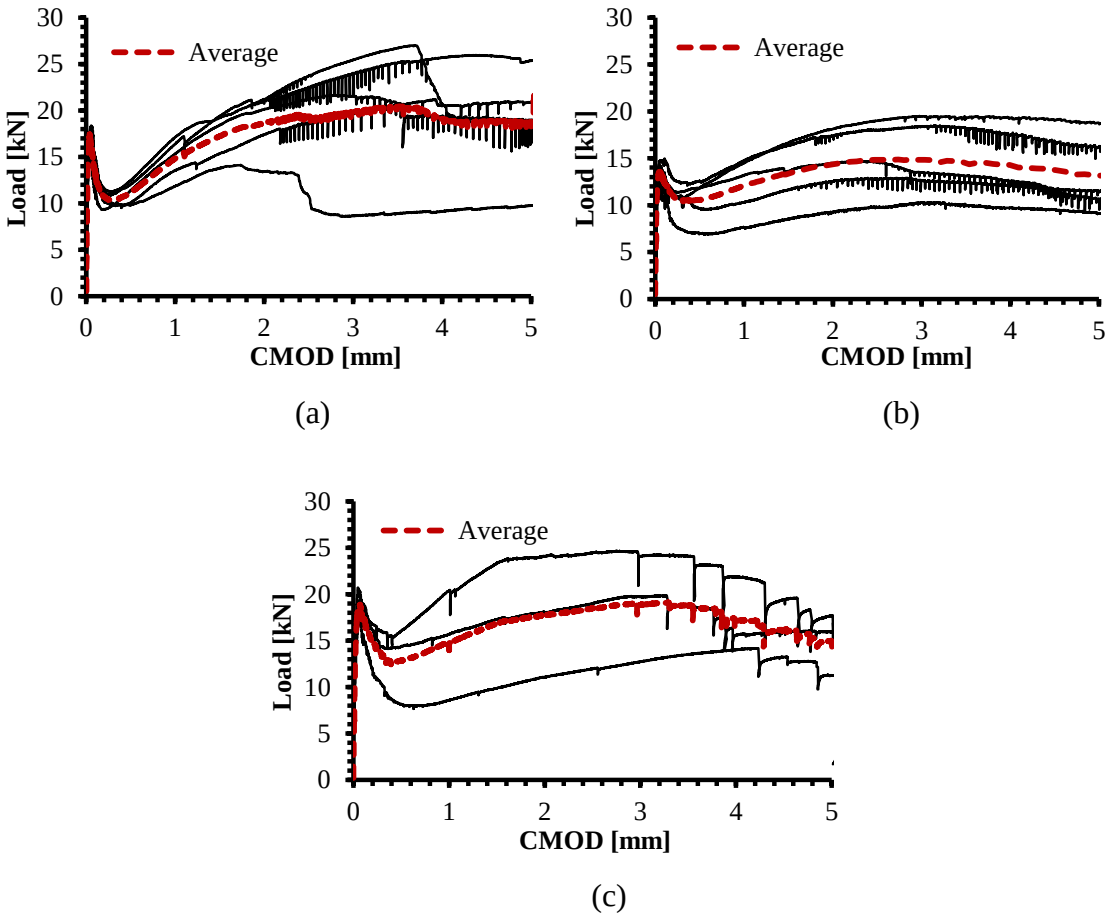

Figure 3.19 – EN 14651 prism bending test results: (a) Series A; (b) Series B, (c) Series C.

(a) Series B (b) Series C

Figure 3.20 – Single dominant cracking in EN 14651 prism bending test.

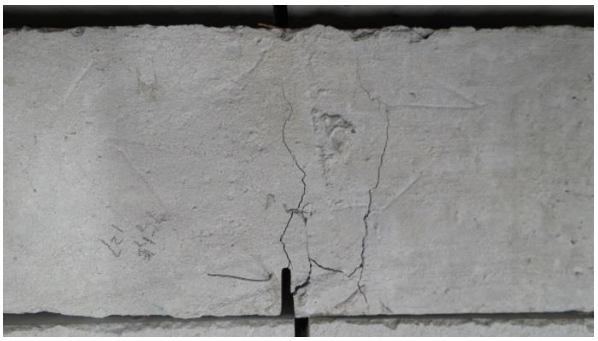

Figure 3.21 – Multiple cracking in EN 14651 prism bending test – Series A.

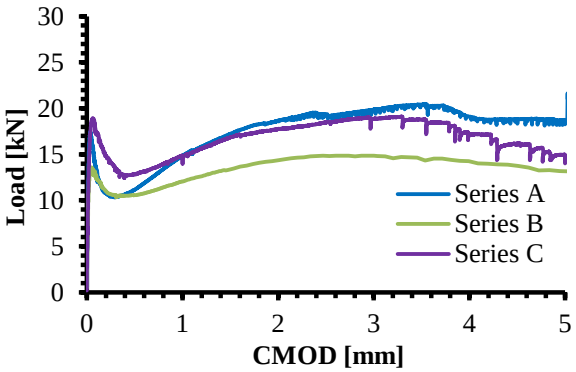

Figure 3.22 – Comparison between Series A, B and C EN 14651 prism bending test results.

Table 3.11 – Summary of EN 14651 prism bending test results.

Series	Fibre Type	$f^{f}_{ct,L}$	f_{R1}	f_{R2}	f_{R3}	f_{R4}
		[MPa]	[MPa]	[MPa]	[MPa]	[MPa]
A	5D 65/60 BG	5.45	3.43	5.30	5.96	6.29
B	4D 65/35 BG	4.10	3.15	3.98	4.42	4.33
C	4D 55/60 BG	5.65	3.84	4.99	5.50	5.60

3.4.2. ASTM C1609 Prism Bending Test Results

Flexural toughness tests were carried out according to ASTM C1609 (2006) with a four-point bending set-up on four un-notched prisms. The prisms were 600 mm long, 150 mm deep and 150 mm wide; the span was 450 mm. The resulting forces are defined in Figure 3.23 and converted to stresses, assuming linear elastic behaviour (ASTM C1609, 2006). The experimental results for the tests are presented in Figure 3.24 and are summarised in Table 3.12. From Figure 3.24, it can be seen that the load versus midspan deflection relationship is approximately linear up to first structural cracking, typically followed by a sudden drop in load. After this point, the specimen may behave in two different ways. In the first case, the prism gains some strength prior to steadily dropping load again. In the second case, the load drops continuously without any hardening. Important points of the load-deflection relationship are: (i) first-crack load; (ii) post-cracking peak load; and (iii) a reduction of load with increasing deflection. If a specimen does not exhibit deflection hardening after the initial load drop, the load corresponding to the first point after cracking is considered to be the post-cracking peak load. These important loads are listed in Table 3.12. It can be seen from Table 3.12 that both Series A and B exhibited a deflection hardening after the initial load drop, while Series C showed a minor hardening.

Some degree of scatter and variability can be seen from prism testing. Two cracking methods characterised the failure modes of the prisms. The first was one in which failure occurred over a single localised dominant crack that initiated from the weakest plane under the loading point. However, this was sometimes associated with the propagation of small cracks at the top section of the prisms (see Figure 3.25). The second was one where multiple cracks had formed and significant branching from the primary crack occurred, or sometimes the nucleation of new cracks (see Figure 3.26). This type of cracking was observed in the mix with 5D 65/60 BG steel fibre. The full test data and the location of flexural cracks when the test was stopped can be found in Appendix C.

A comparison between Series A, B and C is presented in Figure 3.27. As can be seen, Series A and B have a similar flexural toughness, while Series C shows lower toughness. However, the toughness of the three mixes within a smaller deflection range ($\delta \leq 1.5$) is approximately the same.

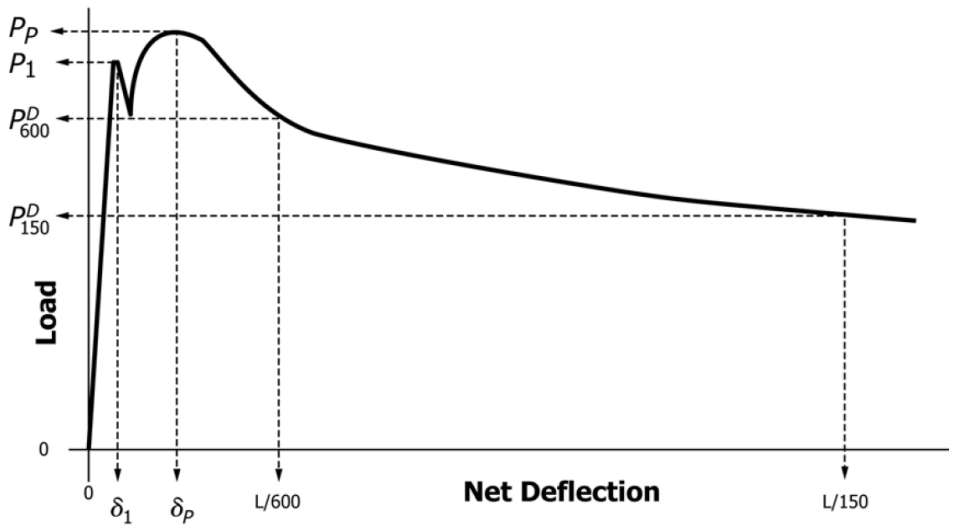

Figure 3.23 – Definitions of key points on the applied force versus deflection curve for flexural toughness testing of prisms (ASTM C1609, 2006).

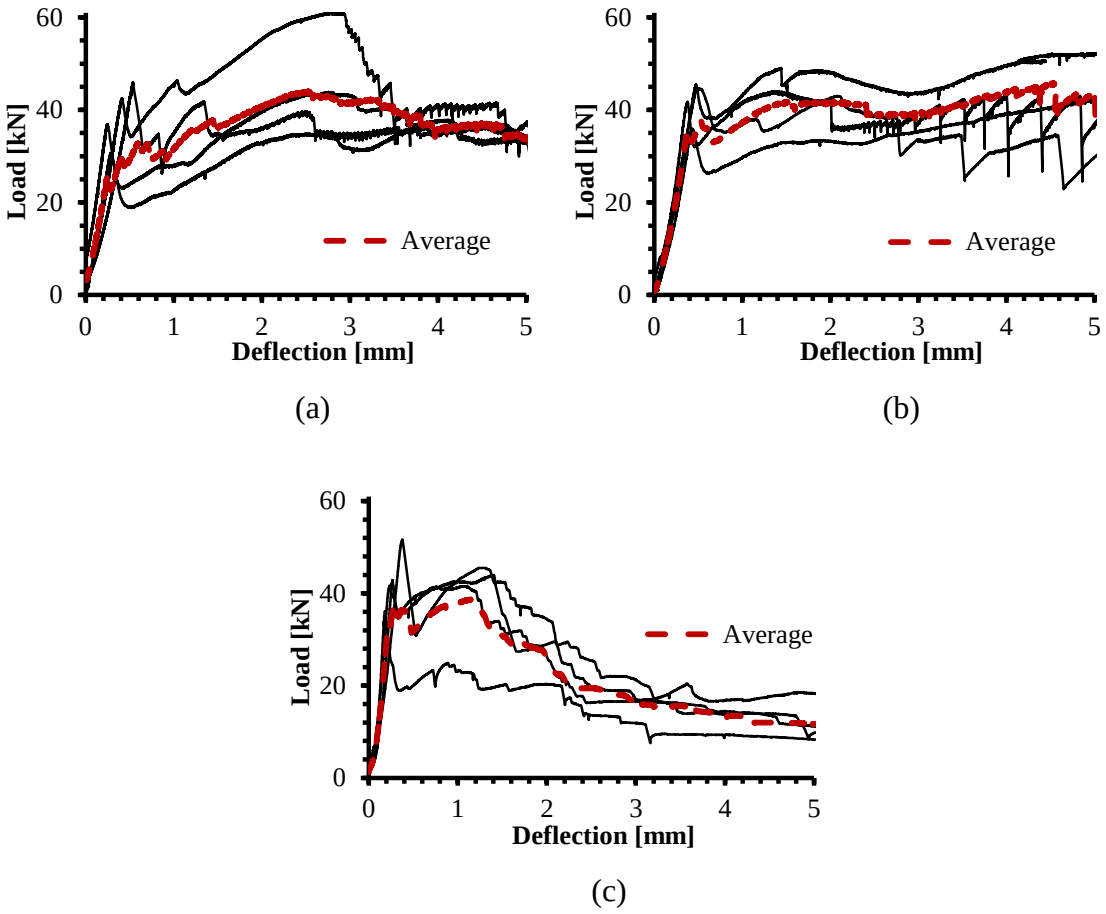

Figure 3.24 – ASTM C1609 prism bending test results: (a) Series A; (b) Series B, (c) Series C.

Figure 3.25 – Single dominant cracking in ASTM C1609 prism bending test.

Figure 3.26 – Multiple cracking in ASTM C1609 prism bending test.

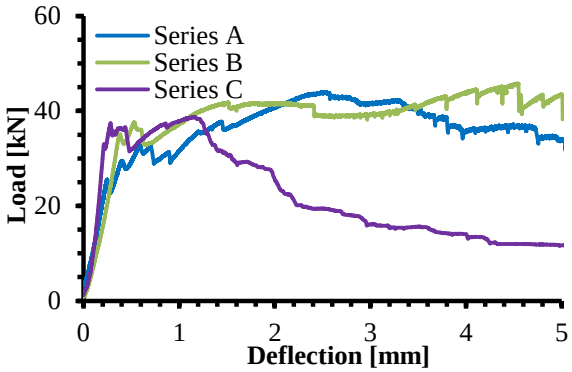

Figure 3.27 – Comparison between Series A, B and C ASTM C1609 prism test results.

Table 3.12 – Summary of ASTM C1609 prism bending test results.

Series	Fibre Type	P_P	δ_P	P_1	δ_1	P_{600}^D	P_{150}^D	f_P	f_1	f_{600}^D	f_{150}^D	T_{150}^D	R_{150}^D
		[kN]	**[mm]**	**[kN]**	**[mm]**	**[kN]**	**[kN]**	**[MPa]**	**[MPa]**	**[MPa]**	**[MPa]**	**[J]**	**%**
A	5D 65/60 BG	47.0	2.65	39.0	0.37	30.3	41.6	5.8	4.9	3.8	5.2	105.9	0.09
B	4D 65/35 BG	46.0	3.08	41.9	0.45	34.8	37.4	5.6	5.2	4.3	4.6	107.7	0.09
C	4D 55/60 BG	43.4	0.55	43.1	0.27	35.1	16.7	5.5	5.5	4.4	2.1	83.3	0.06

3.4.3. JCI-S-002 Prism Bending Test Results

In addition to the other methods, the fracture energy of SFRC was obtained from notched three point bending test according to the Japan Concrete Institute Standard JCI-S-002 (2003). The prisms were 600 mm long, 150 mm high and 150 mm wide; the span was 450 mm and the notch depth was 45 mm. Load – CMOD results obtained from the notched prism bending tests are presented in Figure 3.28. The response of the three-point notched bending test can be described by three distinct phases: (i) an elastic phase up to cracking; (ii) a flexural hardening response up to the post-cracking peak load; and (iii) a reduction of load with increasing CMOD.

In general the prism specimens exhibited some degree of scatter and variability. Mainly a single crack characterised the failure mode of the prisms, in which failure occurred over a localised dominant crack that propagated directly from the notch toward the loading point and no major no secondary cracks developed from the primary crack (see Appendix C).

A comparison between Series A, B and C is presented in Figure 3.29. As can be seen, the three series show approximately consistent results with slightly better performance for Series A.

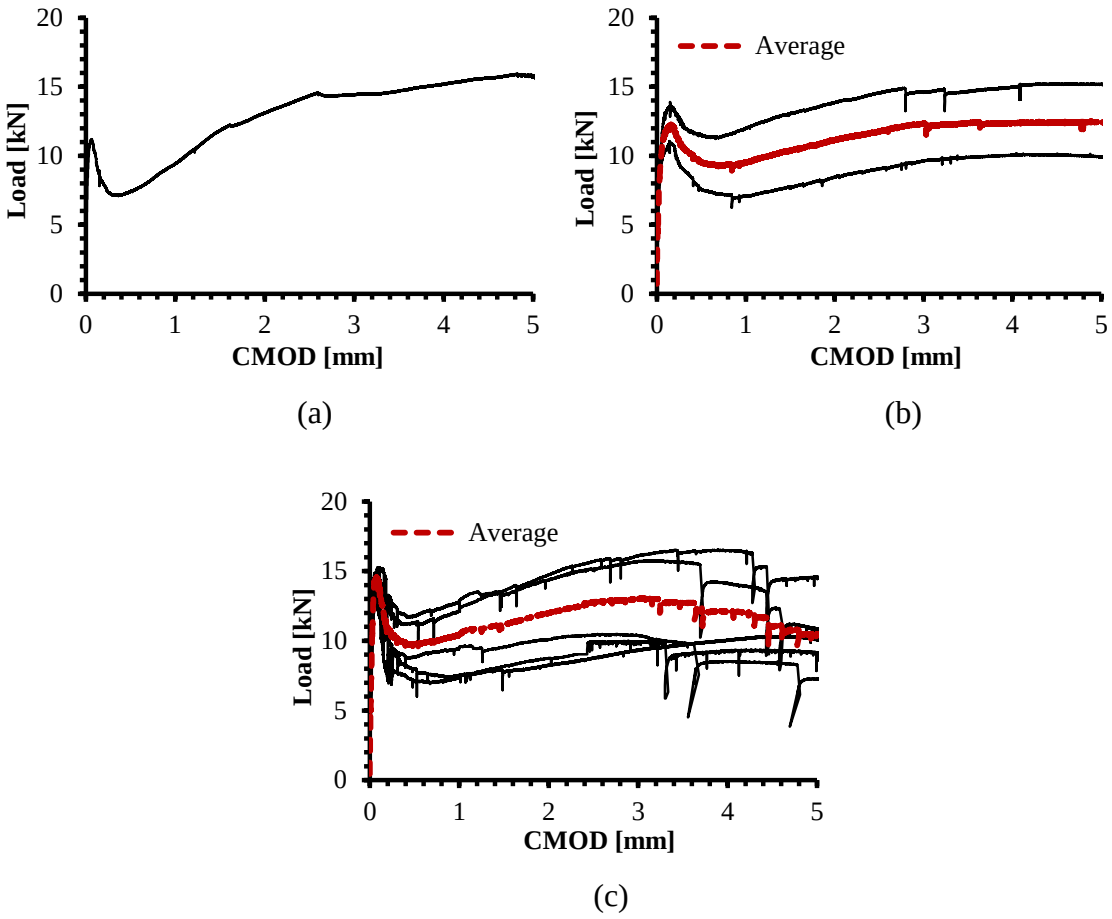

Figure 3.28 – JCI-S-002 prism bending test results: (a) Series A; (b) Series B, (c) Series C.

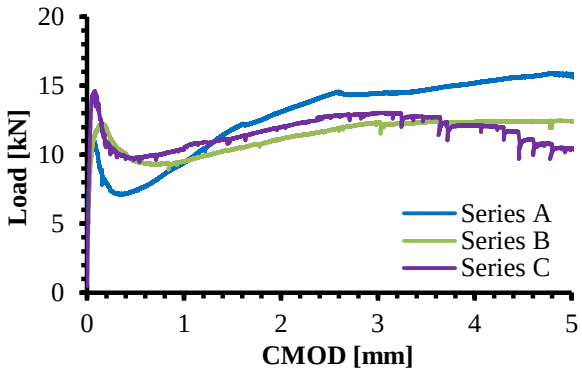

Figure 3.29 – Comparison between Series A, B and C JCI-S-002 prism test results.

3.4.4. Strain Development

To examine the change in the neutral axis depth as the deflection or CMOD increases, concrete strain gauges were placed across the depth of the prisms at the mid-section, as described in Section 3.2.3, for both notched and un-notched prism bending specimens of Series B and C. Presented in Figures 3.30 and 3.31 the results for the load-strain curve for one of the notched and un-notched prism bending tests, respectively. Full data can be seen in the Appendix C. As can be seen from the figures, three main behaviours are observed. For strain gauges placed near the bottom fibres of the prism – beneath $h_{sp}/2$ or $D/2$ for notched and un-notched prisms, respectively, i.e. SG1 and SG2, the concrete strain remains in the tensile side and only positive strain is observed, as expected, until a cracking concrete strain of 150 μm/mm to 250 μm/mm is reached signalling that the concrete matrix has cracked.

For the two strain gauges fixed on the top fibres – above $h_{sp}/2$ or $D/2$ for notched and un-notched prisms, respectively, i.e. SG4 and SG5, the negative strain indicates that the concrete is uncracked at the top fibres. As the test continues, the absolute value of the concrete strain in top fibres decreases until it reaches zero. This indicated the location of the neutral axis at that specific deflection or CMOD. After that, the strain value becomes positive until failure of the gauge.

For strain gauge (SG3), which is located almost at the mid-section of the prism – specifically for notched prisms, at the initial stage of the test, it has very minor compressive strain. Soon after, a zero value is reached as expected. Following that, similar to SG4 and SG5, tensile strain is noticed until the failure of the strain gauge.

As only three strain gauges are located on the compressive side of the prisms, accordingly, only three exact values indicating the location of the neutral axis can be obtained as presented in Tables 3.13 to 3.16 and in Figures 3.32 and 3.33.

The average crack opening displacement between the root of the notch and the crack tip, presented in Tables 3.13, 3.14 and Figure 3.34, is obtained from the geometry as shown in Figure 3.35 for notched prisms:

$$w = \frac{CMOD}{2} \times \frac{(h_{sp} - d_n)}{(D - d_n)} \tag{3.3}$$

To determine the location of the neutral axis during the test, interpolation between the compressive and tensile strains was performed assuming that Euler-Bernoulli beam theory is valid where plane section before bending remains plane after bending. As a result, the strain distribution is linear and the value of zero strain can be obtained by interpolation. All the interpolated values were obtained with regression coefficient higher that 97%. Plotted in Figures 3.36 to 3.38, the interpolated neutral axis value along with the exact obtained value demonstrated in Tables 3.13 to 3.16.

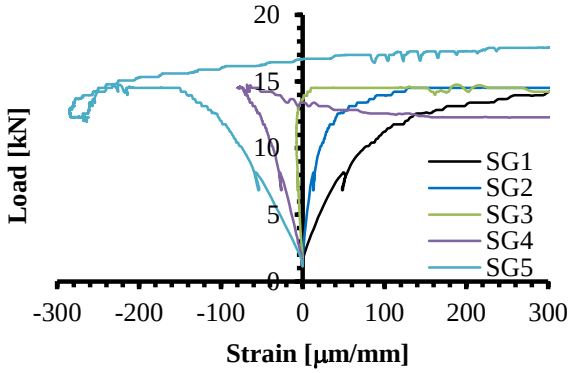

Figure 3.30 – Load-strain curve for EN 14651 notched prism bending test, specimen B-1.

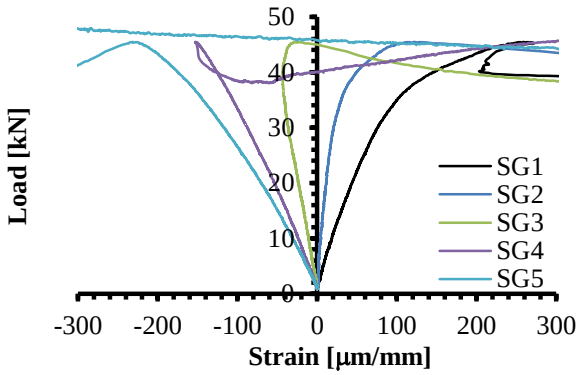

Figure 3.31 – Load-strain curve for ASTM C1609 un-notched prism bending test, specimen B-3.

Table 3.13 – Progression of neutral axis depth during Series B notched prism bending test.

Specimen ID	d_n = 60 mm			d_n = 30 mm			d_n = 10 mm		
	Load	**CMOD**	**COD**	**Load**	**CMOD**	**COD**	**Load**	**CMOD**	**COD**
	[kN]	**[mm]**	**[mm]**	**[kN]**	**[mm]**	**[mm]**	**[kN]**	**[mm]**	**[mm]**
B-1	13.7	0.03	0.01	13.4	0.17	0.07	16.7	1.70	0.70
B-3	12.1	0.03	0.01	8.5	0.17	0.07	7.1	0.87	0.36
B-4	10.3	0.01	0.01	13.1	0.09	0.04	12.7	0.67	0.28
B-5	2.0	0.00	0.00	13.1	0.08	0.03	12.9	0.91	0.38
Mean	**9.5**	**0.02**	**0.01**	**12.0**	**0.13**	**0.05**	**12.4**	**1.03**	**0.43**
COV	**0.55**	**0.78**	**0.78**	**0.20**	**0.37**	**0.37**	**0.32**	**0.44**	**0.44**

Table 3.14 – Progression of neutral axis depth during Series C notched prism bending test.

Specimen ID	d_n = 60 mm			d_n = 30 mm			d_n = 10 mm		
	Load	**CMOD**	**COD**	**Load**	**CMOD**	**COD**	**Load**	**CMOD**	**COD**
	[kN]	**[mm]**	**[mm]**	**[kN]**	**[mm]**	**[mm]**	**[kN]**	**[mm]**	**[mm]**
C-1	18.7	0.05	0.02	16.4	0.17	0.07	15.3	0.86	0.36
C-2	2.4	0.00	0.00	16.7	0.20	0.10	24.2	2.23	0.96
C-3	14.7	0.03	0.01	13.2	0.17	0.07	8.0	0.59	0.24
Mean	**11.9**	**0.03**	**0.01**	**15.5**	**0.18**	**0.08**	**15.8**	**1.23**	**0.52**
COV	**0.71**	**0.86**	**0.86**	**0.13**	**0.09**	**0.22**	**0.51**	**0.72**	**0.74**

Table 3.15 – Progression of neutral axis depth during Series B un-notched prism bending test.

Specimen ID	d_n = 60 mm		d_n = 30 mm		d_n = 10 mm	
	Load	Deflection	Load	Deflection	Load	Deflection
	[kN]	[mm]	[kN]	[mm]	[kN]	[mm]
B-2	44.5	0.53	36.1	0.68	31.1	2.79
B-3	44.8	0.49	40.1	0.85	45.7	2.36
B-4	35.6	0.44	29.1	0.52	30.7	1.10
Mean	**41.7**	**0.49**	**35.1**	**0.68**	**35.8**	**2.08**
COV	**0.13**	**0.09**	**0.16**	**0.24**	**0.24**	**0.42**

Table 3.16 – Progression of neutral axis depth during Series C un-notched prism bending test.

Specimen ID	d_n = 60 mm		d_n = 30 mm		d_n = 10 mm	
	Load	Deflection	Load	Deflection	Load	Deflection
	[kN]	[mm]	[kN]	[mm]	[kN]	[mm]
C-1	40.0	0.22	35.5	0.34	41.4	1.11
C-2	35.1	0.19	24.9	0.26	23.4	0.72
C-3	40.5	0.28	36.0	0.43	40.3	1.58
C-4	50.4	0.39	40.6	0.87	28.5	1.64
Mean	**41.5**	**0.27**	**34.3**	**0.47**	**33.4**	**1.26**
COV	**0.16**	**0.32**	**0.19**	**0.58**	**0.27**	**0.34**

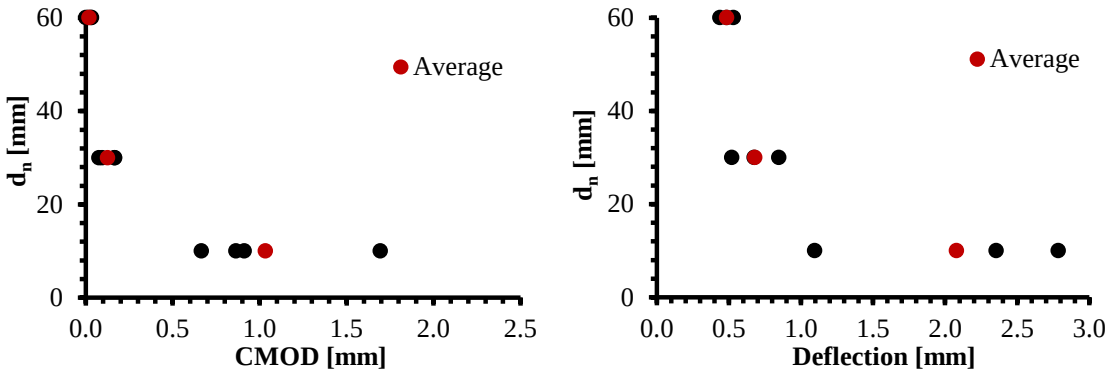

(a) (b)

Figure 3.32 – Change in neutral axis depth during Series B testing: (a) EN 14651 notched prism bending test; (b) ASTM C1609 un-notched prism bending test.

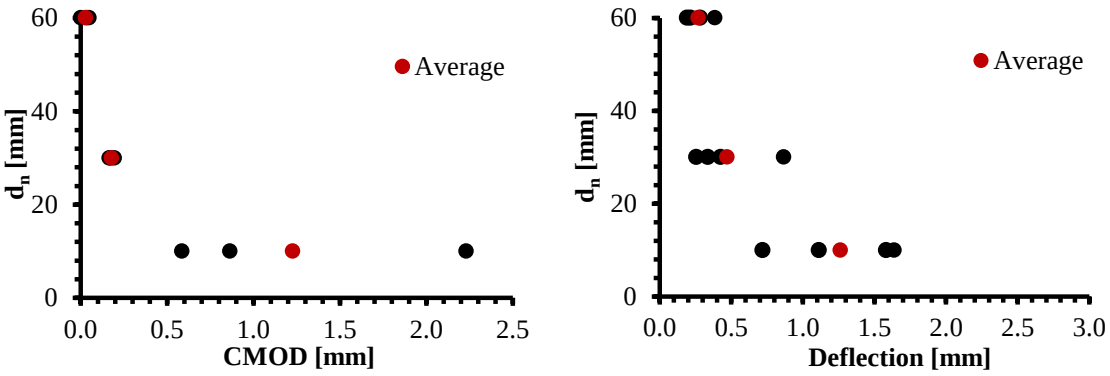

(a) (b)

Figure 3.33 – Change in neutral axis depth during Series C testing: (a) EN 14651 notched prism bending test; (b) ASTM C1609 un-notched prism bending test.

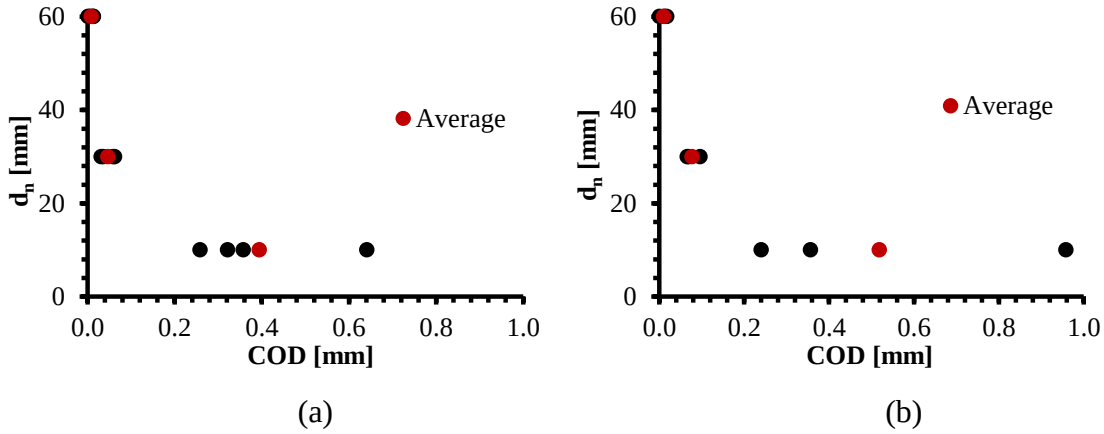

Figure 3.34 – Neutral axis depth versus the COD during EN 14651 notched prism bending test: (a) Series B; (b) Series C.

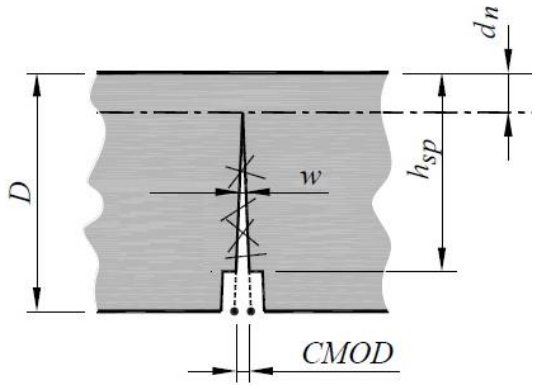

Figure 3.35 – Cracked section in SFRC prism in bending.

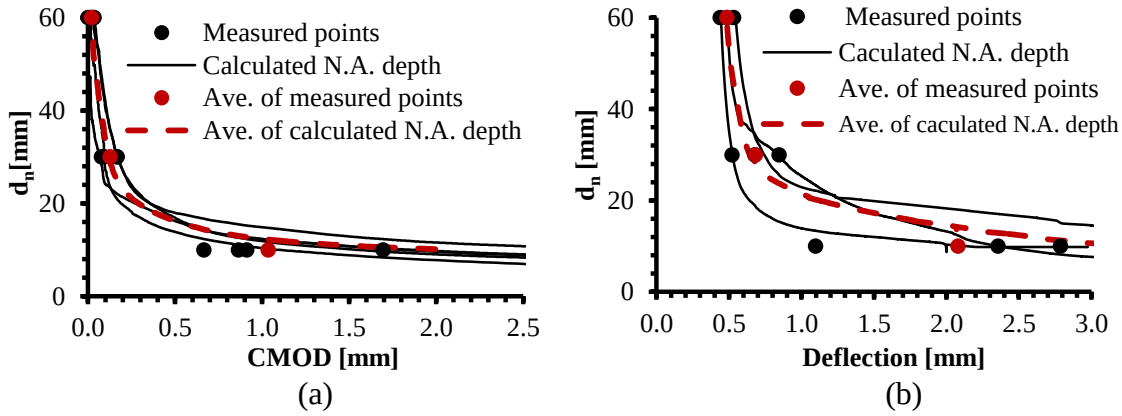

Figure 3.36 – The development of neutral axis depth during Series B testing: (a) EN 14651 notched prism bending test; (b) ASTM C1609 un-notched prism bending test.

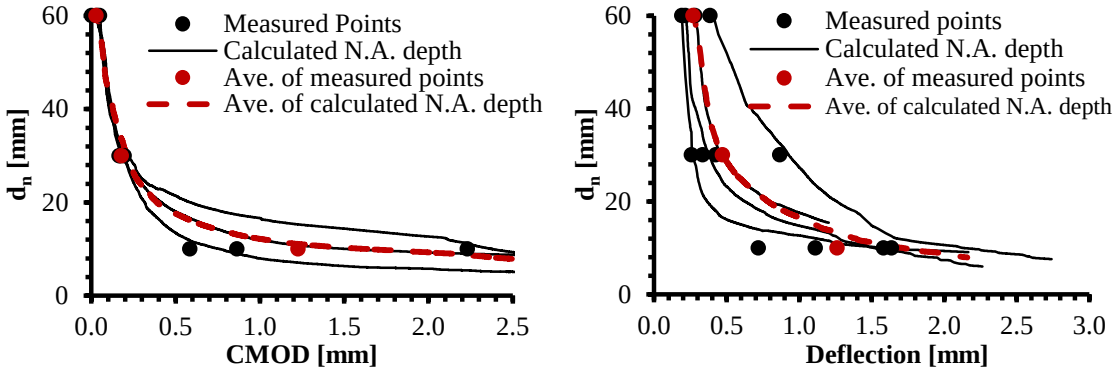

(a) (b)

Figure 3.37 – The development of neutral axis depth during Series C testing: (a) EN 14651 notched prism bending test; (b) ASTM C1609 un-notched prism bending test.

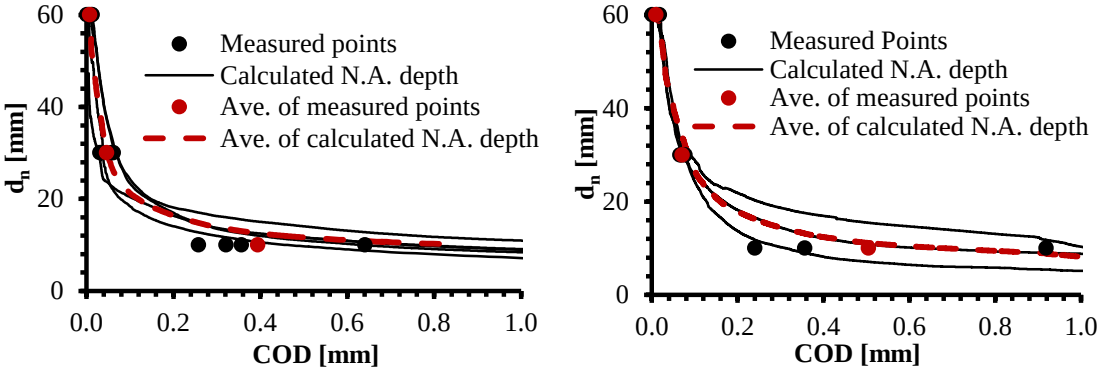

(a) (b)

Figure 3.38 – The development of neutral axis depth versus the COD during notched prism bending test: (a) Series B; (b) Series C.

3.5. Specimen to Specimen Variability

Of interest to researchers is the variability of the experimentally obtained parameters that are then used in design. Figures 3.39 and 3.40 present the coefficient of variation for different values of COD or deflection, respectively, for each series with at least four tested specimens. The coefficient of variation of tensile stress or load, for different values of COD, CMOD or deflection is displayed in Figures 3.41 to 3.43, respectively.

It can be seen that the different tests offer varying degrees of variation. The cracking strain of the matrix obtained from the uniaxial tension test shows low variation (see Figure 3.39). Correlations can be made between the number of fibres crossing the cracking plane and the residual tensile strength provided by the fibres. The degree of the scatter as represented by the coefficient of variation, (COV), may be related to the probability of fibre dispersion. For the direct tension test, the mean of the coefficients of variation taken at COD = 1.5 mm was 0.09. A greater variability can be seen with the un-notched prism bending test, specifically, in the initial stage of the deflection curve. The mean of the coefficient of variation taken at a deflection of 3.0 mm (δ_{150}^{D}) was 0.14.

The coefficient of variation of tensile stress in uniaxial tension test results is 0.50 and 0.14 for Series A and B, respectively, taken at a COD of 0.5 mm (see Figure 3.41). However, the COV is 0.25, 0.20 and 0.31 at COD equals to 1.5 mm for Series A, B and C, respectively. This indicates that the utilisation of long and strong fibres, such as 5D fibres, results in higher scatter in the tensile strength during crack stabilisation stage. However, soon after cracking had stabilised, the variation is reduced. For the prism bending test, again, greater variability in noted for Series A compared with Series B and C. For notched prisms, the coefficient of variation of load taken at CMOD equals to 3.5 mm ($CMOD_4$) was 0.34, 0.27 and 0.27 for Series A, B and C, respectively; while, the coefficients were 0.31, 0.10 and 0.09 for Series A, B and C, respectively, taken at a deflection of 3.0 mm (δ_{150}^{D}).

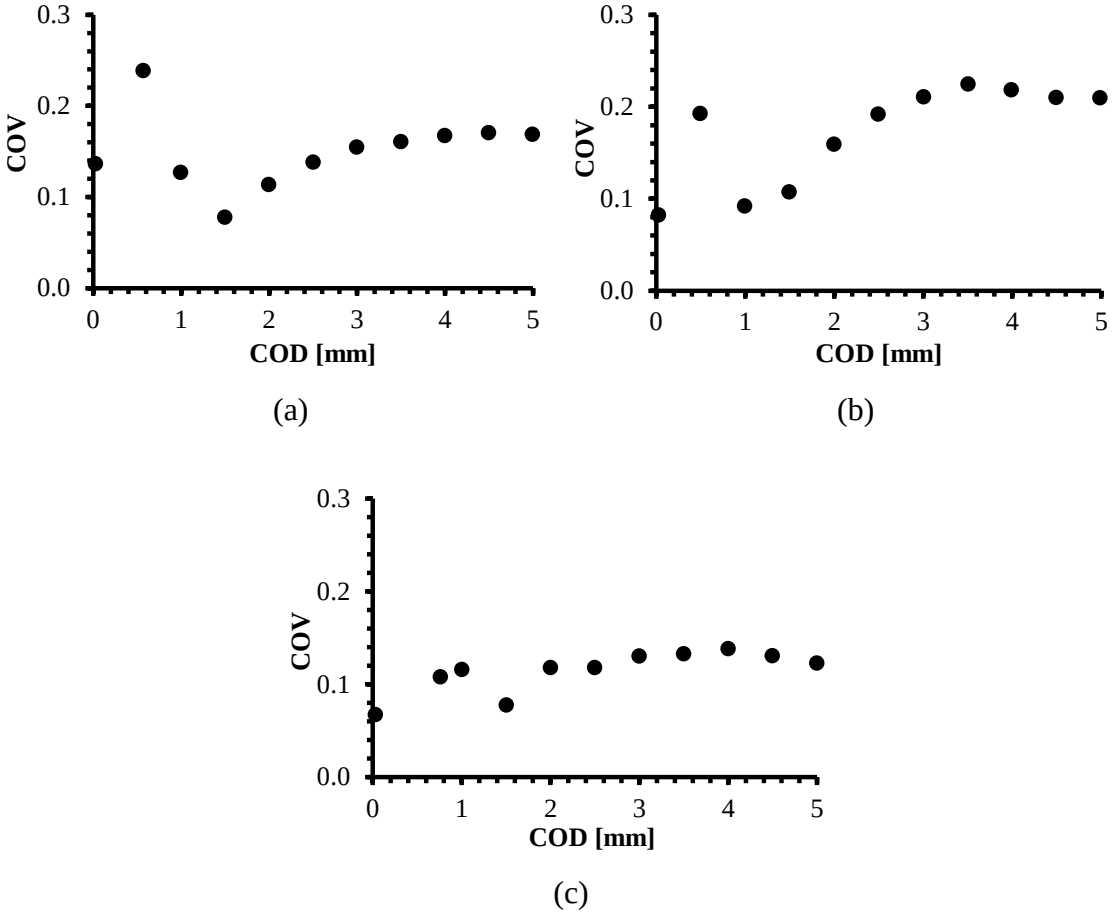

Figure 3.39 – Uniaxial tension test results coefficient of variation: (a) Series A; (b) Series B; (c) Series C.

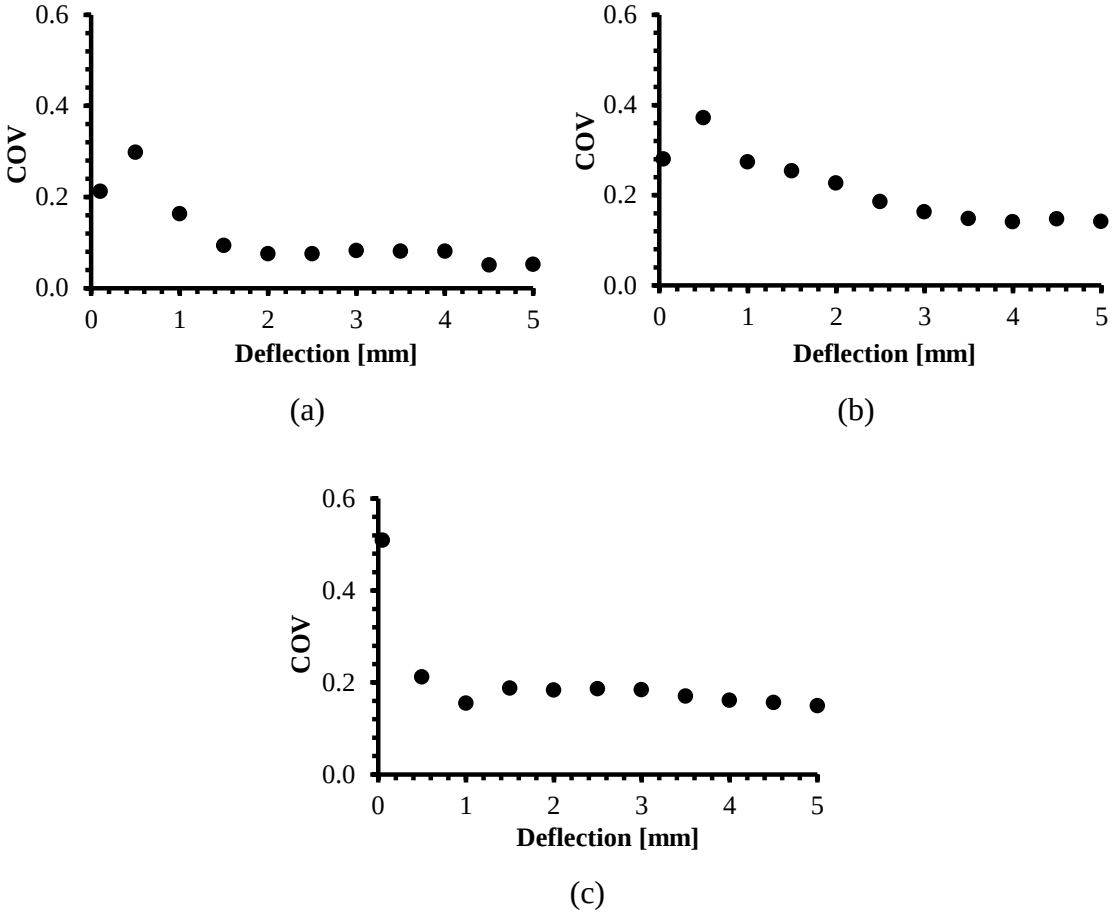

Figure 3.40 – Un-notched prism bending test results coefficient of variation: (a) Series A; (b) Series B; (c) Series C.

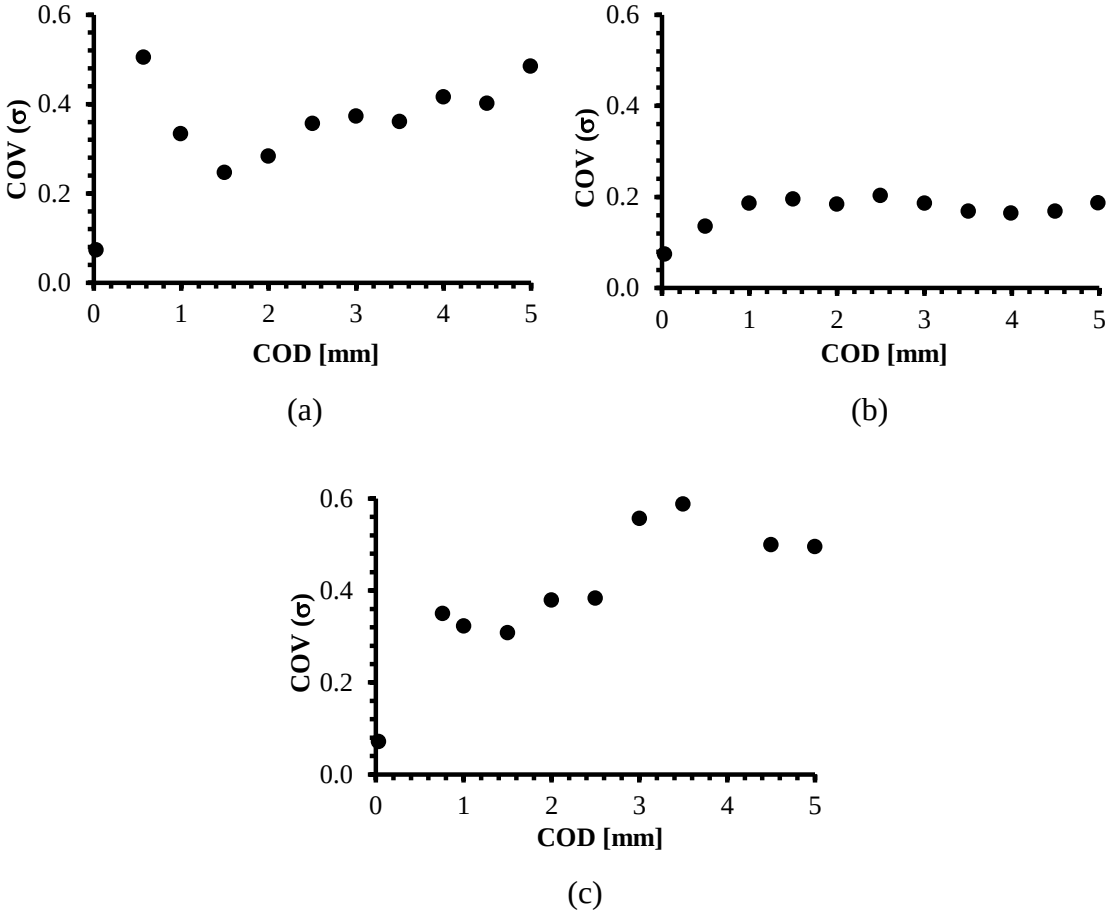

Figure 3.41 – Coefficient of variation of tensile stress for different values of COD: (a) Series A; (b) Series B; (c) Series C.

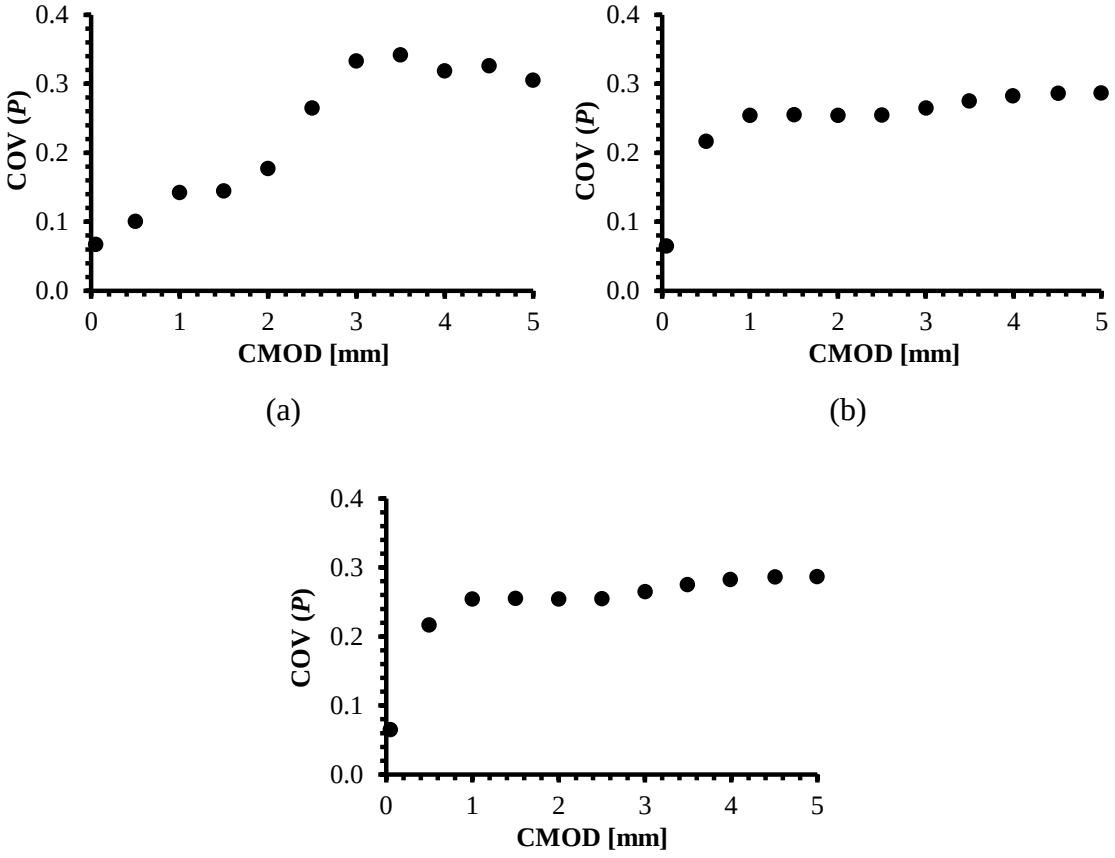

Figure 3.42 – Coefficient of variation of applied load for different values of CMOD: (a) Series A; (b) Series B; (c) Series C.

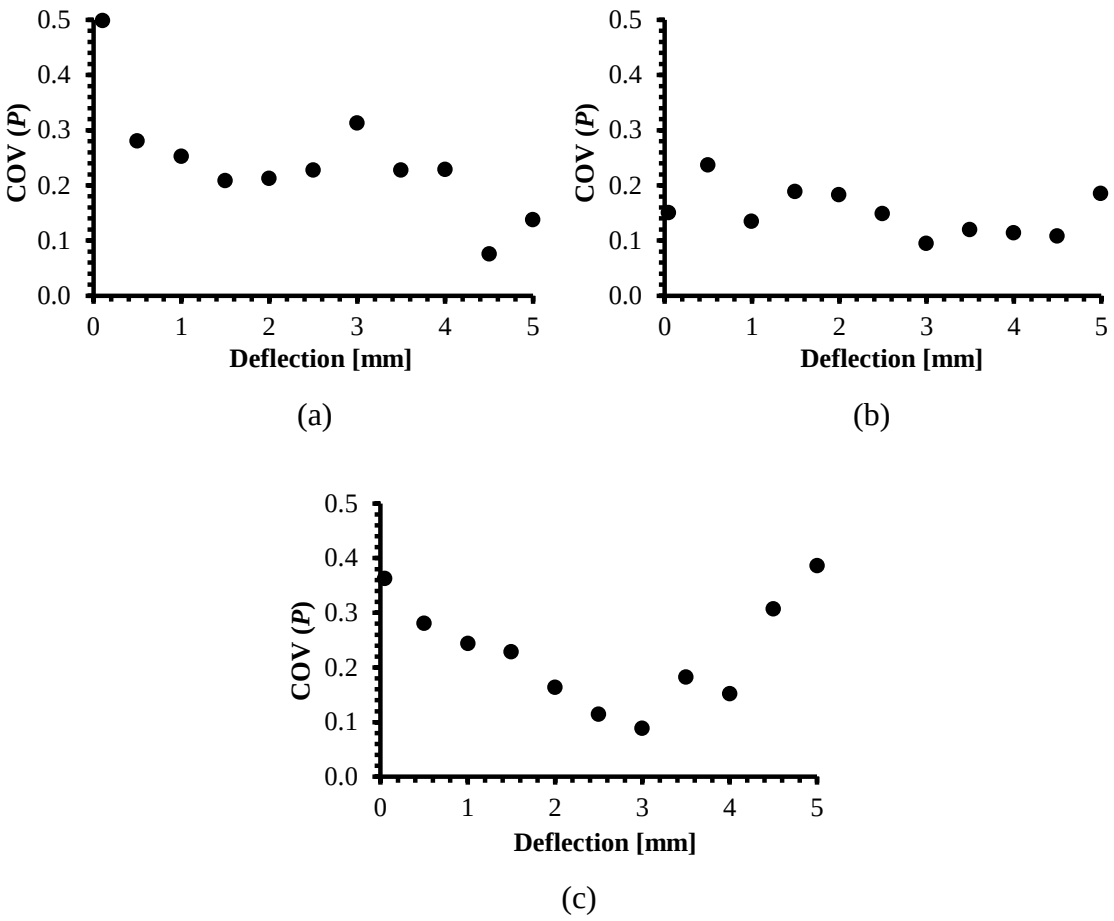

Figure 3.43 – Coefficient of variation of applied load for different values of deflection: (a) Series A; (b) Series B; (c) Series C.

3.6. Round Panel Static Test Results

Flexural toughness tests were carried out according to ASTM C1550 (2012) on round panels supported on three symmetrically arranged supports and subjected to a central point load. During the test, the crack width and central deflection of the specimens were measured and recorded. The raw experimental results for the static tests are presented in Figures 3.44 to 3.46 and are summarised in Table 3.17. The residual tensile strength of round panel test specimens has been expressed in Joules, represented by the area under the load versus central displacement curve up to 40 mm central deflection. The peak load, *P'*, of a specimen was corrected for actual specimen dimensions as well as the calculated energy absorption, *W'*, as per ASTM C1550 (2012). The corrected peak load, *P*, and corrected energy absorption, *W*, are shown in Table 3.17. Plotted too in Figures 3.44 to 3.46 is the mean response associated with each test.

As can be seen from the results, the curve is approximately linear before the crack formation. Three dominant radial cracks formed in most specimens and this coincides with a reduction in capacity of the panels. After cracking, it was clear that the concrete provided little direct contribution to the flexural strength of the round panel specimens and that the strength was primarily due to the fibres. The long tail of the curves reflects the progressively smooth residual capacity of the specimens. With the exception of specimen C-2S-F, the specimens failed by the formation of three fracture lines. Panel C-2S-F failed with a single fracture line (Appendix A).

In some circumstances, such as in Series A with 5D steel fibres and Series C with 4D 60 mm fibres, secondary crack(s) propagated out of a primary crack as the deflection increased (see Figure 3.47). Interestingly, the primary crack width did not propagate further due to fibre engagement but the width of the secondary crack developed with increased deflection to contribute to the failure of the specimen.

A comparison between plain concrete as well as Series A, B and C is presented in Figure 3.48. It is be observed that the effect of fibres on peak load is negligible; however, the load after cracking initially dropped below that of the peak residual strength for the SFRC panels; the load increased later as the fibres became engaged. Notice that all the SFRC specimens had a softening post-cracking behaviour in flexure.

Interestingly, all three series had similar toughness up to a deflection of around 7 mm – equivalent to a surface crack width of about 3 mm. Following that, a noticeable difference is observed; this is mainly due to the number of fibres crossing the failure surface. For the same target fibre content of 30 kg/m^3 and as demonstrated in Table 3.18, it is clear that Series B had the highest number of fibres crossing the failure surface resulting in larger flexural toughness, while Series C had the lowest number of fibres. It is evident that Series A with 7,498 fibres per cubic metre of concrete, corresponding to a dosage of 30 kg/m^3 of fibres, had a higher performance than Series C with 5,551 fibres; this is likely due to the increased mechanical bond of the double hooked fibre coupled with their high tensile strength (2300 MPa). The crack distribution and failure mode of the statically tested specimens are shown in Appendix A.

Table 3.17 – Summary of ASTM C1550 round panel static tests.

Series	**Fibre Type**	***P'***	***P***	***W'***	***W***
		[kN]	**[kN]**	**[J]**	**[J]**
A	5D 65/60 BG	29.7	28.0	498	477
B	4D 65/35 BG	28.3	26.2	533	503
C	4D 55/60 BG	32.7	30.4	344	325

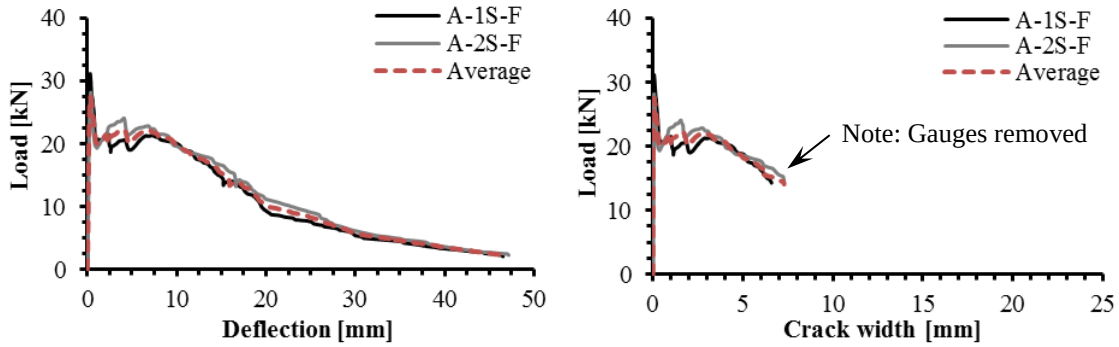

(a) (b)

Figure 3.44 – Results of static load test for Series A: (a) load versus deflection; (b) load versus crack width.

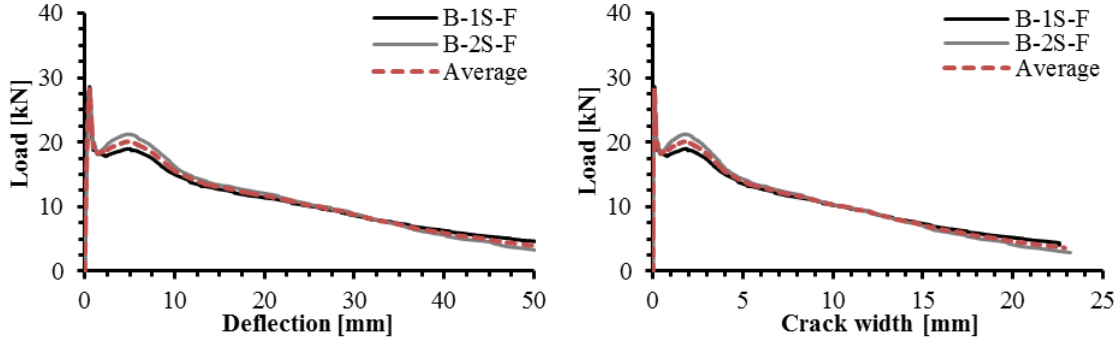

(a) (b)

Figure 3.45 – Results of static load test for Series B: (a) load versus deflection; (b) load versus crack width.

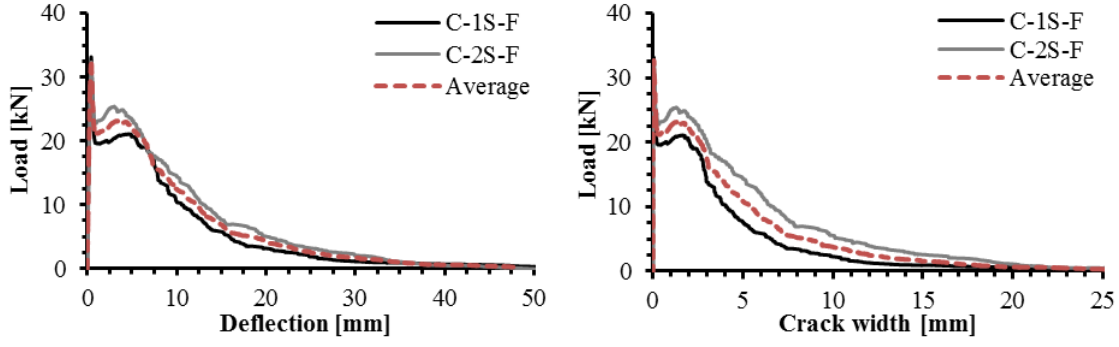

(a) (b)

Figure 3.46 – Results of static load test for Series C: (a) load versus deflection; (b) load versus crack width.

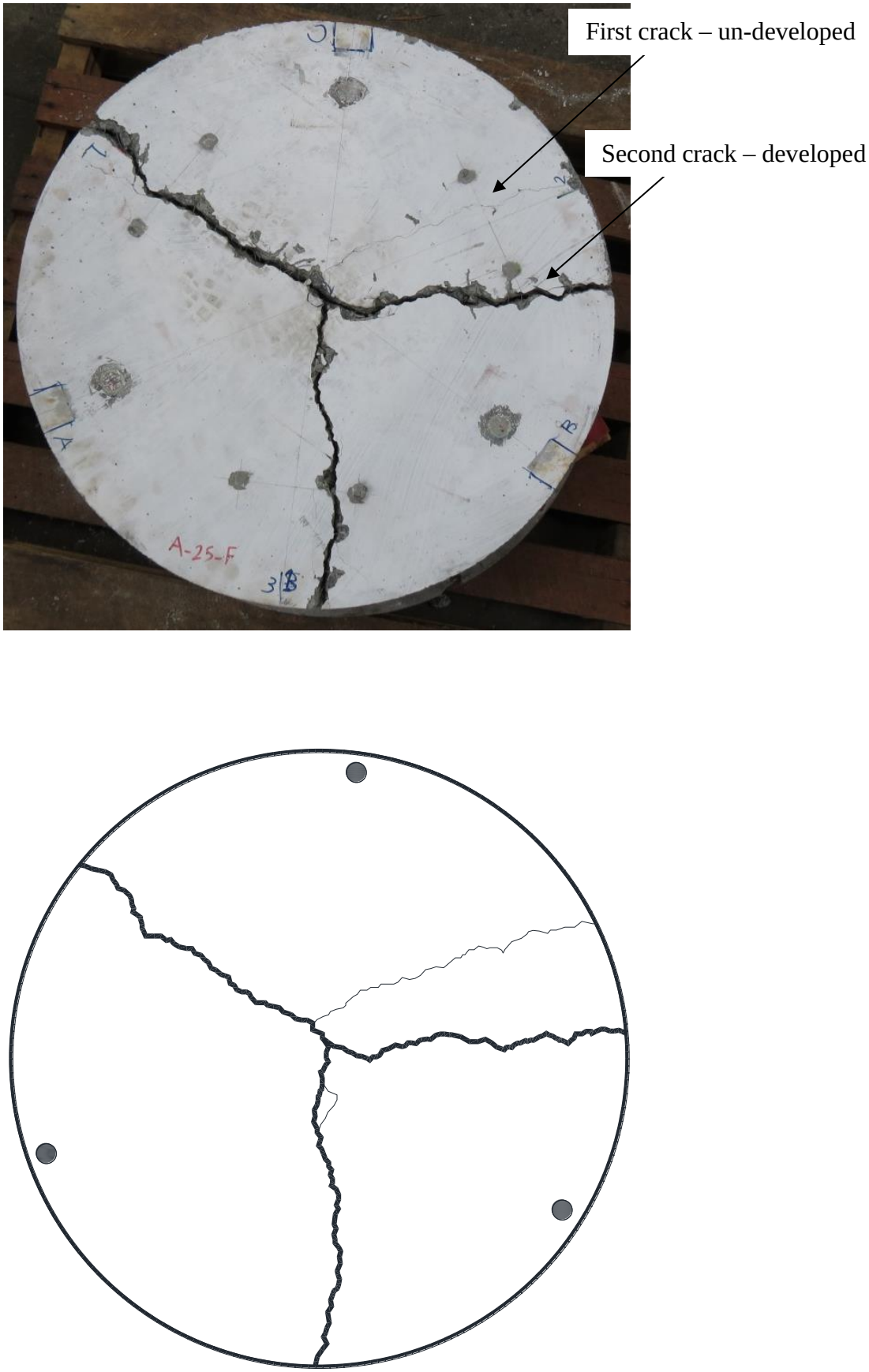

Figure 3.47 – Multiple cracking in round panel test – Specimen A-2S-F.

Table 3.18 – Number of fibres per 1.0 m^3 of concrete in a dosage of 30 kg/m^3.

Series	Fibre Type	Length [mm]	Diameter [mm]	No. of fibres
A	5D 65/60 BG	60	0.9	7,498
B	4D 65/35 BG	35	0.55	34,157
C	4D 55/60 BG	60	1.05	5,551

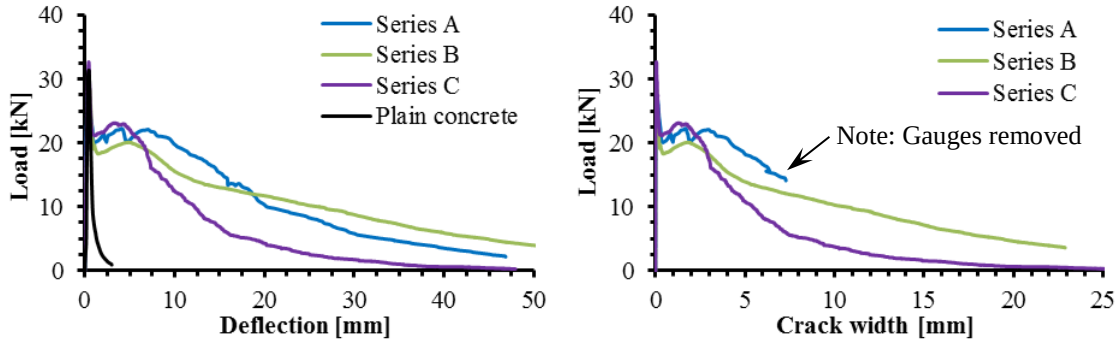

Figure 3.48 – Comparison between plain concrete and Series A, B and C round panel test results.

The mean flexural tensile strength coefficient is evaluated based on the results of the static round panel tests of this study. From fracture line analysis, assuming that the angles between fracture lines are 120° and considering small rotations (θ); and hence displacements, the resisting moment per unit length is Tran (2003):

$$m = \frac{p}{3\sqrt{3}}\frac{r}{R} \qquad (3.4)$$

where r is the radius from the centre of the panel to the supports, R is the radius of the panel and P is the applied central load. For the tests of this study r = 375 mm and R = 400 mm.

From a sectional stress block, we write:

$$m = 0.25\ z\ t\ k\ \sqrt{f_c'} \qquad (3.5)$$

where z is the internal lever arm, t is the thickness of the panel, f_c' is the characteristic compressive strength and k is the mean flexural tensile strength coefficient shown in Table 3.19 for each series. AS3600 (2018) suggests that the mean flexural tensile strength for Australian concretes is 1.4 times its characteristic strength; thus:

$$f'_{ct.fm} = 1.4 \times 0.6\sqrt{f_c'} = 0.84\sqrt{f_c'} \qquad (3.6)$$

The results show that the measured flexural tensile strengths are within expectations.

Table 3.19 – Mean flexural tensile strength coefficient.

Series	Plain Concrete	A	B	C
$\boldsymbol{f'_{ct.fm}}$	$0.88\sqrt{f_c'}$	$0.80\sqrt{f_c'}$	$0.77\sqrt{f_c'}$	$0.83\sqrt{f_c'}$
$\boldsymbol{k}$	0.88	0.80	0.77	0.83

3.7. Round Panel Fatigue Test Results

3.7.1. Fatigue Lives and Failure Modes

The fatigue lives and modes of failure for the twenty tested round panels are presented in Table 3.20. Six specimens of Series A were tested and seven of Series B and C under cyclic (fatigue) loading. In total, six specimens were uncracked prior to fatigue testing while fourteen of them were pre-cracked with a surface crack width of 0.5 mm.

All pre-cracked specimens with a maximum load level of 40% did not fail after 3 million cycles and were then loaded statically to failure. Cyclic testing continued with one pre-cracked round panel, C-1C-F-C-50, from Series C with a maximum load level of 50% up to 10 million cycles without the occurrence of failure. On the other hand, round panel C-1C-F-C-60 from Series C, as well but tested with a maximum load level of 60%, failed during loop tuning and before one load cycle was completed. Consequently, fatigue live of pre-cracked specimens can differ significantly for a small change in load level; for example, from a 50% to a 60% load level. The reason for the high fatigue life of C-1C-F-C-50 is discussed in details in Section 3.7.2. In addition, significant scatter is noticed between specimens tested repetitively under the same circumstances. Noticeable scatter is recorded for the fatigue life of uncracked specimens as well.

Table 3.20 – Fatigue lives and modes of failure for tested specimens.

Specimen ID	Max load	Pre-cracked	No. of cycles	Failure mode
A-1C-F-U-60	60%	No	> 3 Million	Loaded monotonically up to failure
A-1C-F-U-70	70%	No	> 3 Million	Loaded monotonically up to failure
A-1C-F-C-60	60%	Yes	98,386	One fracture line
A-2C-F-C-60	60%	Yes	96,743	Three fracture lines
A-1C-F-C-40	40%	Yes	> 3 Million	Loaded monotonically up to failure
A-2C-F-C-40	40%	Yes	> 3 Million	Loaded monotonically up to failure
B-1C-F-U-70	70%	No	646,246	Three fracture lines
B-2C-F-U-70	70%	No	399,743	Three fracture lines
B-1C-F-C-60	60%	Yes	388,975	Three fracture lines
B-2C-F-C-60	60%	Yes	460	One fracture line
B-3C-F-C-60	60%	Yes	12,431	Three fracture lines
B-1C-F-C-40	40%	Yes	> 3 Million	Loaded monotonically up to failure
B-2C-F-C-40	40%	Yes	> 3 Million	Loaded monotonically up to failure
C-1C-F-U-70	70%	No	243,158	Three fracture lines
C-2C-F-U-70	70%	No	1,375,127	Three fracture lines
C-1C-F-C-60	60%	Yes	Nill	Failed during loop tuning
C-2C-F-C-60	60%	Yes	5,868	Three fracture lines
C-1C-F-C-50	50%	Yes	> 10 Million	Loaded monotonically up to failure
C-2C-F-C-50	50%	Yes	1,617,982	Three fracture lines
C-1C-F-C-40	40%	Yes	> 3.5 Million	Loaded monotonically up to failure

3.7.2. Individual Round Panel Fatigue Test Results

Specimen A-1C-F-U-60

Specimen A-1C-F-U-60 was uncracked and cycled between 15% (4.5 kN) and 60% (17.9kN) of the determined average static cracking load. The central deflection of the round panel at both maximum and minimum loads is shown Figure 3.49. The load-deflection curves during fatigue loading are presented in Figure 3.50. A deflection of 0.06 mm and 0.18 mm was measured at minimum and maximum loads, respectively, at the first cycle; the specimen then experienced a slow steady increase in deflection through the test. After 3 million cycles, the minimum and maximum deflections of the round panel A-1C-F-U-60 were 0.15 mm and 0.30 mm, respectively. At about two million cycles, a slight reduction in deflection was observed. This is determined to be due to thermal change and its influence on the supporting system from which the LSCT was secured. Temperature effect became noticeable due to the small central deflection and long-time testing. No flexural cracks were observed after the completion of 3 million cycles.

The specimen did not fail after 3 million cycles of testing. The specimen was then tested under static loading to determine its residual strength. The load-displacement response of failed specimen and crack width development during the static test are shown in Figure 3.51. The crack pattern at the conclusion of the static test is shown in Figure 3.52. The failure mode is represented by the development of a single fracture line.

At the start of the static test, three cracks developed, as shown in Figure 3.51(b). After that and due to fibres engagement, secondary cracks propagated out of the primary cracks (cracks 1 and 3) as the displacement increased and multiple cracking were observed (see Figures 3.51(b) and 3.52). This explains the fluctuation at the beginning

of load-displacement curve (Figure 3.51(a)). The secondary branch of crack 3 and crack 2 developed further to form the fracture line.

The result of the static test of the panel after 3 million load cycles is shown in Figure 3.51. Also shown is the average for the static tests of specimens A-S-F (Figure 3.51). It is observed that the residual strength of specimen A-1C-F-U-60 after 3 million cycles loading between 15% and 60% of the static capacity did not result in any significantly observable damage. The long tail of the curve reflects the progressively smooth residual capacity of the specimen. Figures 3.51(b) and 3.52 show that the failure cracks passed through the gauged region of crack 2 but not of cracks 1 and 3 (noting that the crack gauges were located for the expected three crack failure mechanism).

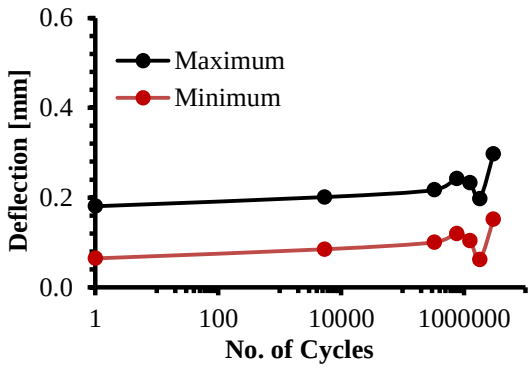

Figure 3.49 – Central deflection versus number of cycles for round panel A-1C-F-U-60.

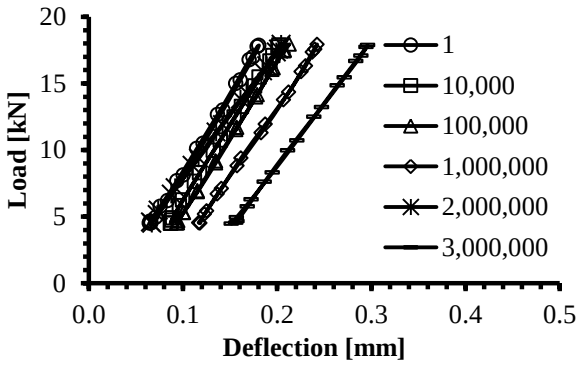

Figure 3.50 – Load-deflection curves of round panel A-1C-F-U-60 during cyclic loading.

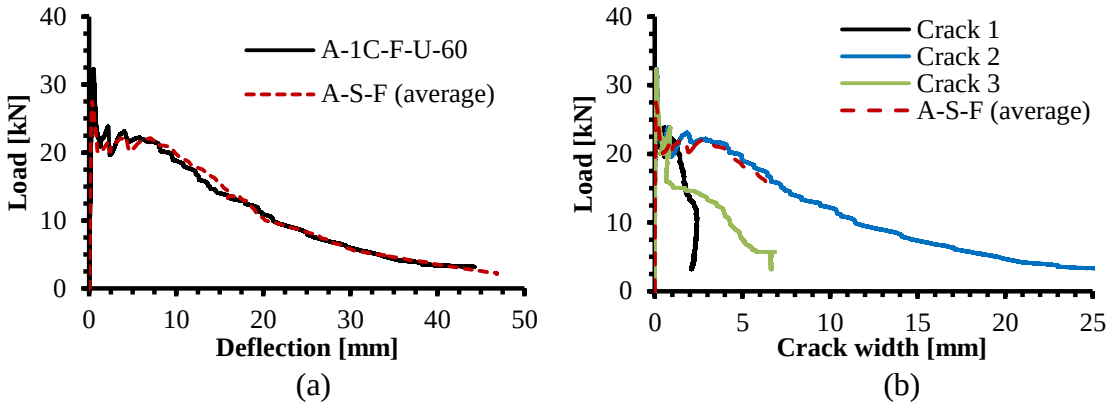

Figure 3.51 – Static test result for round panel A-1C-F-U-60 after 3 million load cycles: (a) load versus deflection; (b) load versus crack width.

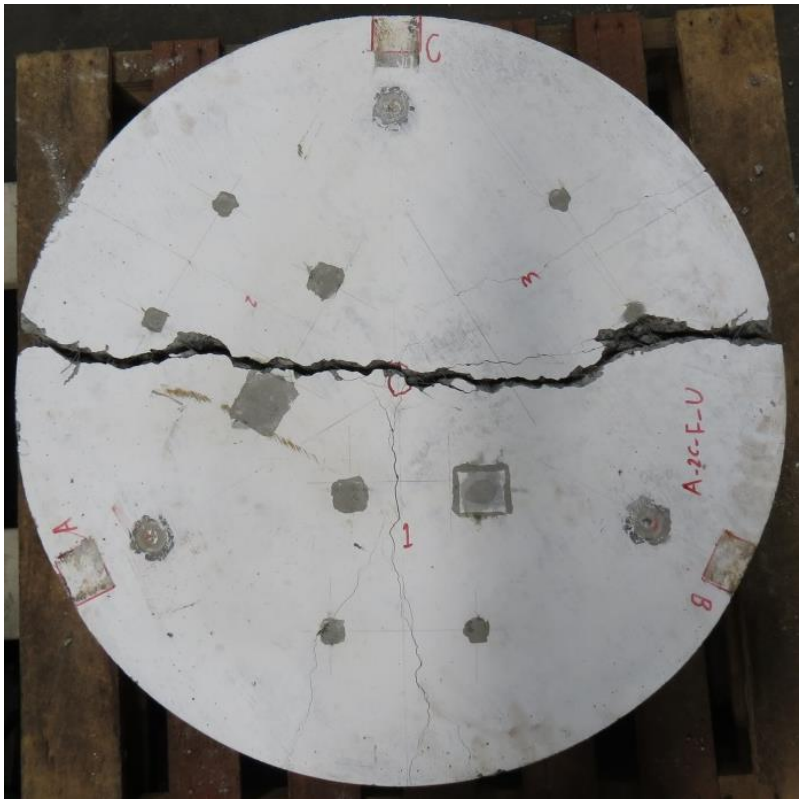

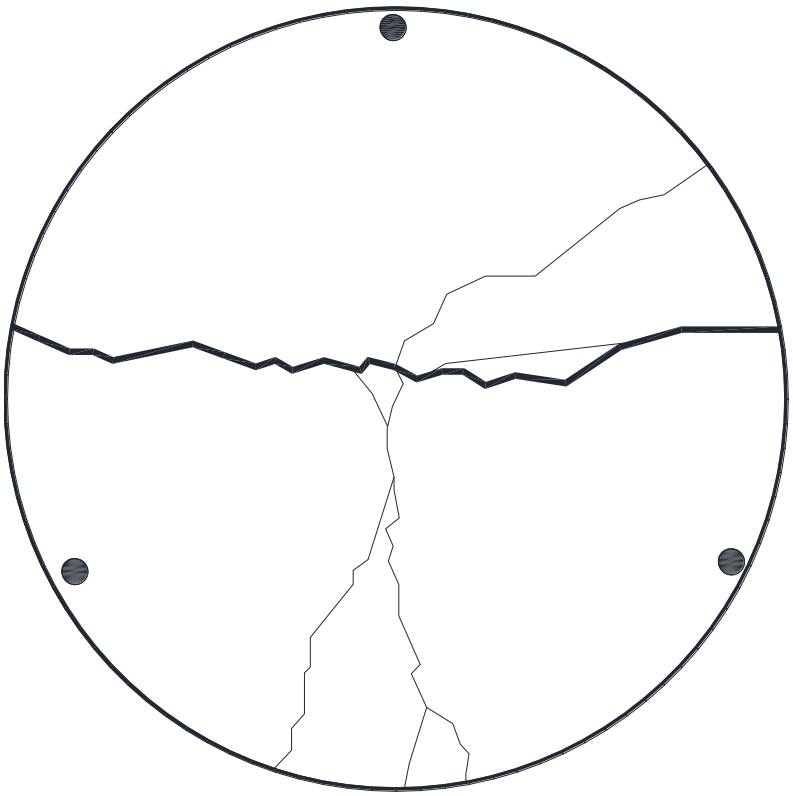

Figure 3.52 – Fracture line of A-1C-F-U-60.

Specimen A-1C-F-U-70

Specimen A-1C-F-U-70 was uncracked and cycled between 15% (4.6 kN) and 70% (20.9 kN) of the average static cracking load. Figure 3.53 demonstrates the central deflection of the round panel at both maximum and minimum loads and Figure 3.54 presents the load-displacement response recorded during the cyclic loading. At the first load cycle, specimen A-1C-F-U-70 had maximum and minimum deflections of 0.26 mm and 0.10 mm, respectively. This was followed by almost constant deflection for the first 10,000 cycles as shown in Figures 3.53 and 3.54. After this, a steady increase in deflection was observed up to 0.53 mm at 3 million cycles at the maximum load and 0.30 mm at the minimum load. No failure occurred until the completion of 3 million cycles and no flexural cracks were visibly observed.

A static test was then performed to determine the residual strength. Figure 3.55 presents the load-displacement response of the failed specimen and crack width development during the static test. The crack pattern at the conclusion of the static test is shown in Figure 3.56. The failure mode is represented by the development of a single fracture line.

Also plotted in Figure 3.55 are the average results obtained from the static tests (Figure 3.44). It is seen only little damage is observed from the 3 million cycles loads of 70% of the cracking capacity. Similarly to specimen A-1C-F-U-60, at the start of the static test, three cracks were developed. However, as the applied deflection increased, secondary cracks were developed (see Figure 3.56). The secondary branch of crack 1 and crack 2 continued to increase in their width to form the fracture line, as shown in Figures 3.55(b) and 3.56 (note that the failure line did not pass through the gauge zone for crack 3). Local damage to the concrete surrounding the fibres can be noticed in Figure 3.56.

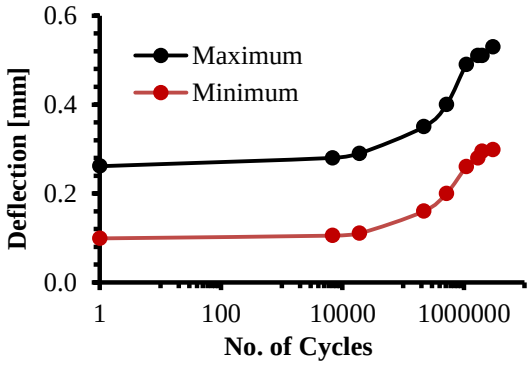

Figure 3.53 – Central deflection versus number of cycles for round panel A-1C-F-U-70.

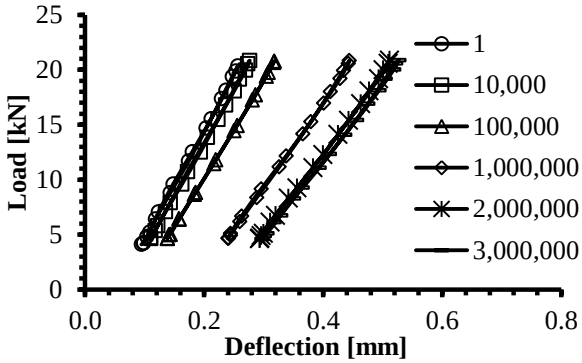

Figure 3.54 – Load-deflection curves of round panel A-1C-F-U-70 during cyclic loading.

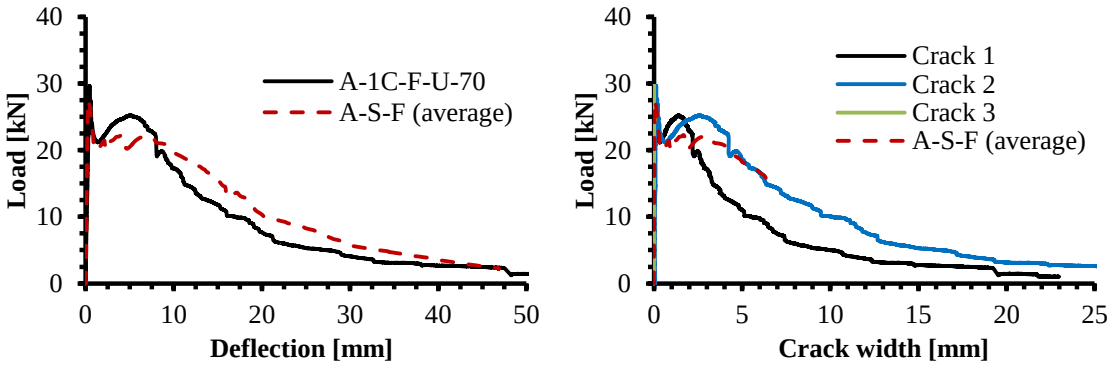

(a) (b)

Figure 3.55 – Static test result for round panel A-1C-F-U-70 after 3 million load cycles: (a) load versus deflection; (b) load versus crack width.

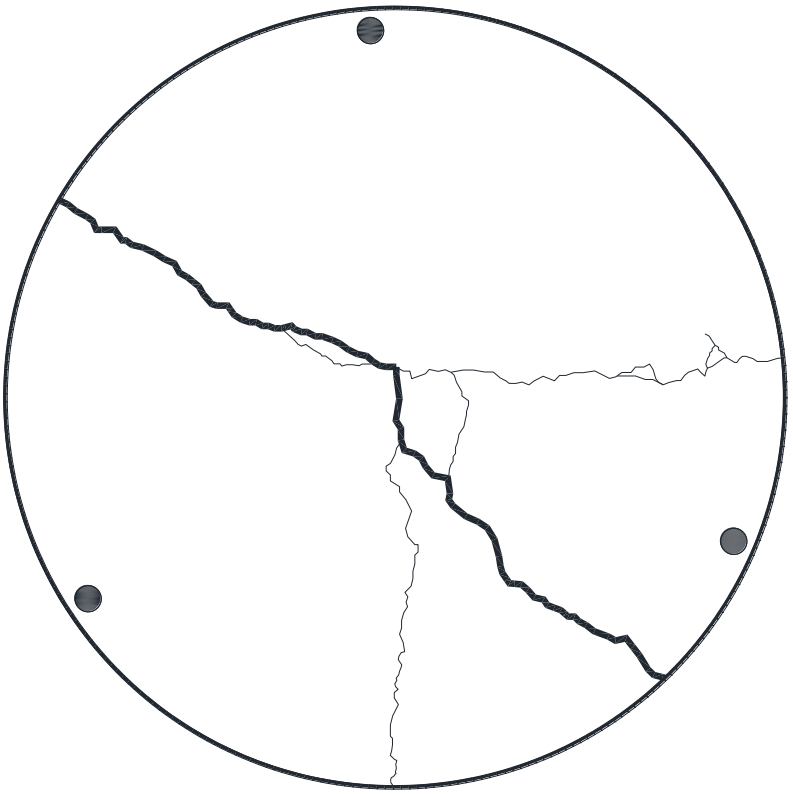

Figure 3.56 – Fracture line of A-1C-F-U-70.

Specimens A-1C-F-C-60 and A-2C-F-C-60

Specimens A-1C-F-C-60 and A-2C-F-C-60 were loaded monotonically until a crack width of 0.5 mm was developed, after which cyclic loading between 15% and 60% of their own static capacity (from 4.9 kN to 18.3 kN and 4.7 kN to 17.7 kN for specimens A-1C-F-C-60 and A-2C-F-C-60, respectively) was applied at 3 Hz to determine the residual fatigue resistance. The fatigue lives for the pre-cracked test panels were 98,386 and 96,743 cycles for specimens A-1C-F-C-60 and A-2C-F-C-60, respectively. Figures 3.57 and 3.58 show the deflection and average crack width of the round panels at their maximum and minimum loads. The load versus deflection and average crack width taken at different loading cycles are shown in Figures 3.59 and 3.60 for panels A-1C-F-C-60 and A-2C-F-C-60, respectively.

For specimen A-1C-F-C-60, the deflection was initially 1.48 mm at the maximum load. The deflection increased at a steady rate to 3.93 mm at about 90,000 cycles. Similarly, the deflection at minimum load began at 1.07 mm and increased to 3.01 mm at about 90,000 cycles. After 90,000 cycles, the deflection increased dramatically signalling the impending failure.

At the first load cycle, specimen A-2C-F-C-60 had minimum and maximum deflections of 0.86 mm and 1.22 mm, respectively. Similar to specimen A-1C-F-C-60, the deflection increased steadily for the first 85,000 cycles to reach 2.74 mm and 3.53 mm minimum and maximum deflections, respectively. This was followed by a substantial increase in central deflection resulting in failure.

For the crack width, specimen A-1C-F-C-60 had a maximum crack width of 0.50 mm at the first cycle and 0.46 mm minimum crack width. Following the deflection performance, a steady increase in crack width was observed for the first 90,000 cycles with 1.43 mm and 1.76 mm minimum and maximum crack widths, respectively. After that, a sudden increase in crack enlarging was observed.

The maximum and minimum average crack widths for specimen A-2C-F-C-60 at the first cycle were 0.34 mm and 0.30 mm, respectively. Consistent with the increase in deflection, the average crack width increased steadily throughout the test until a rapid increase was observed from 85,000 load cycles onwards, signally imminent failure.

The sudden rapid increase of central deflection and average crack width enlarging from one cycle to the subsequent one indicated the impending failure, meaning that the specimen was no longer capable to sustain the maximum load level and the envelope curve was almost approached. At this stage, the fatigue testing was stopped and monotonic loading was applied. The load-displacement response of failed specimens and crack width development of the static tests are presented in Figures 3.61 and 3.62 for specimens A-1C-F-C-60 and A-2C-F-C-60, respectively.

The crack distribution and failure mode of the specimens A-1C-F-C-60 and A-2C-F-C-60 at the conclusion of the static test is shown in Figures 3.63 and 3.64. The failure mode is represented by the development of a single (curved) fracture line for A-1C-F-C-60 (see Figures 3.61(b) and 3.63). Figures 3.61(b) and 3.63 show that the failure crack passed through the gauged region of crack 2 but not of cracks 1 and 3 (noting that the crack gauges were located for the expected three crack failure mechanism). On the other hand, specimen A-2C-F-C-60 failed by the development of three fracture lines (see Figures 3.62(b) and 3.64). For both specimens, some secondary cracks propagated out of primary cracks as the number of cycles increased, and multiple cracking was observed.

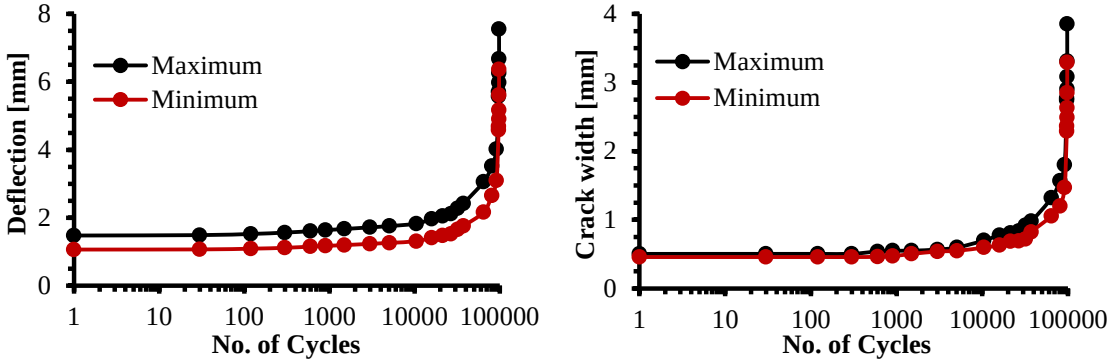

(a) (b)

Figure 3.57 – Specimen A-1C-F-C-60: (a) load versus deflection; (b) load versus crack width.

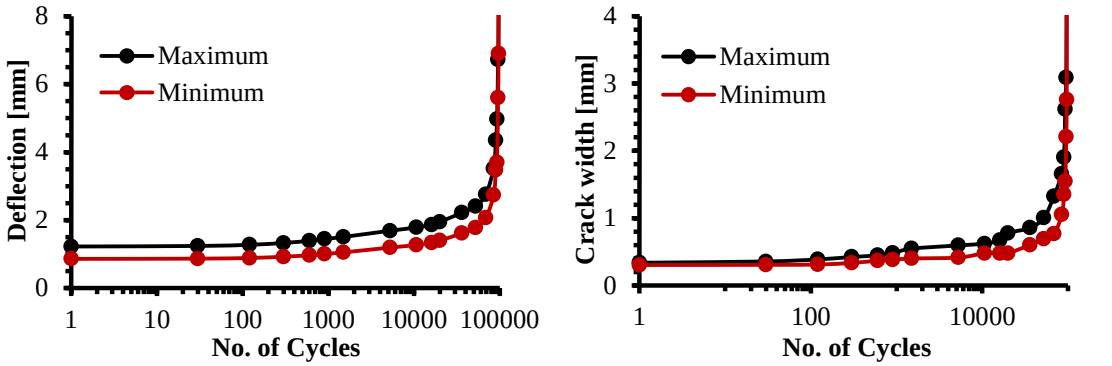

(a) (b)

Figure 3.58 – Specimen A-2C-F-C-60: (a) load versus deflection; (b) load versus average crack width.

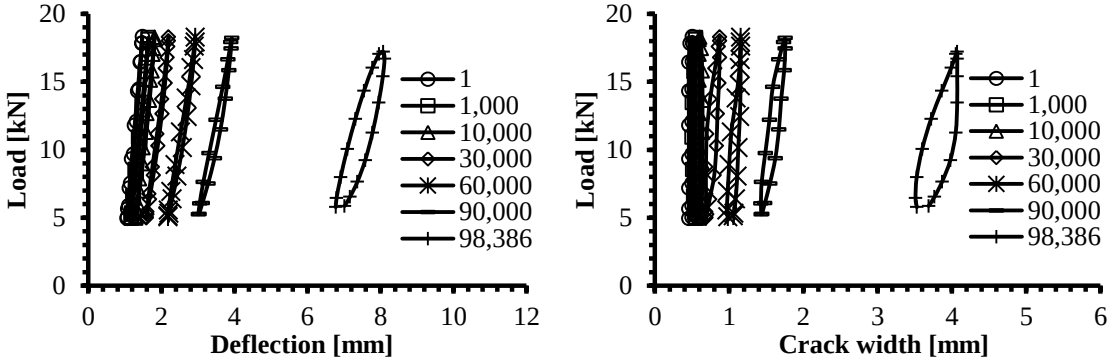

(a) (b)

Figure 3.59 – Load versus (a) deflection and (b) crack width at various cycle intervals for specimen A-1C-F-C-60.

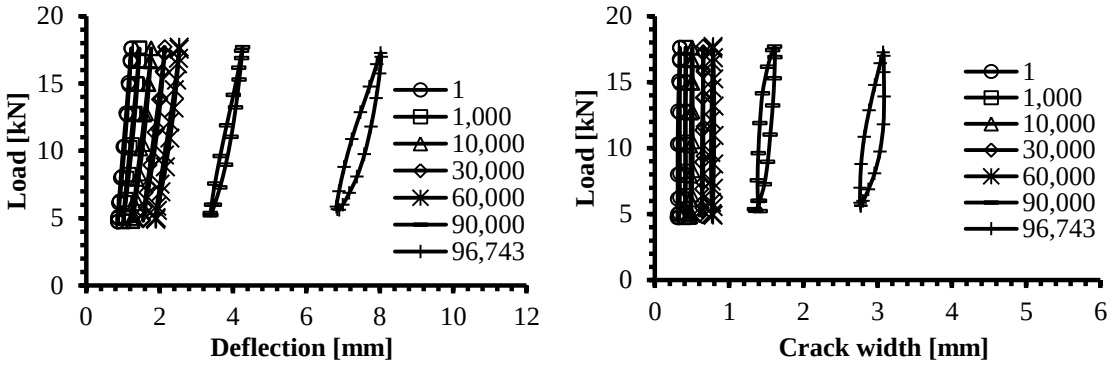

(a) (b)

Figure 3.60 – Load versus (a) deflection and (b) average crack width at various cycle intervals for specimen A-2C-F-C-60.

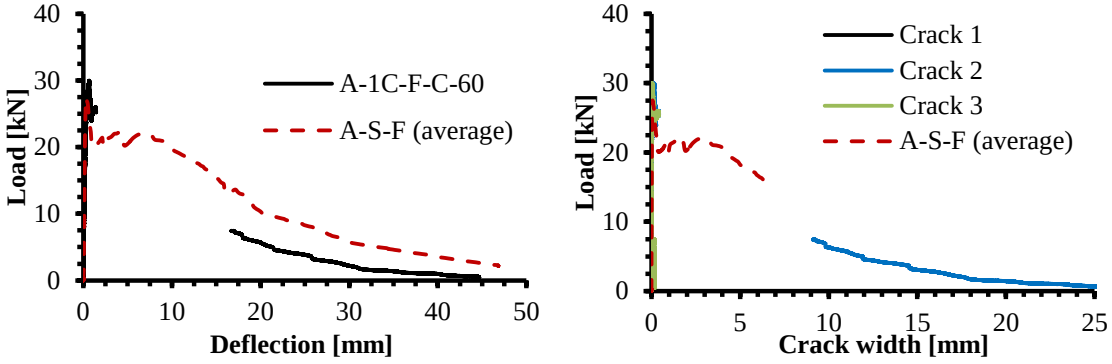

(a) (b)

Figure 3.61 – Static test result for round panel A-1C-F-C-60.

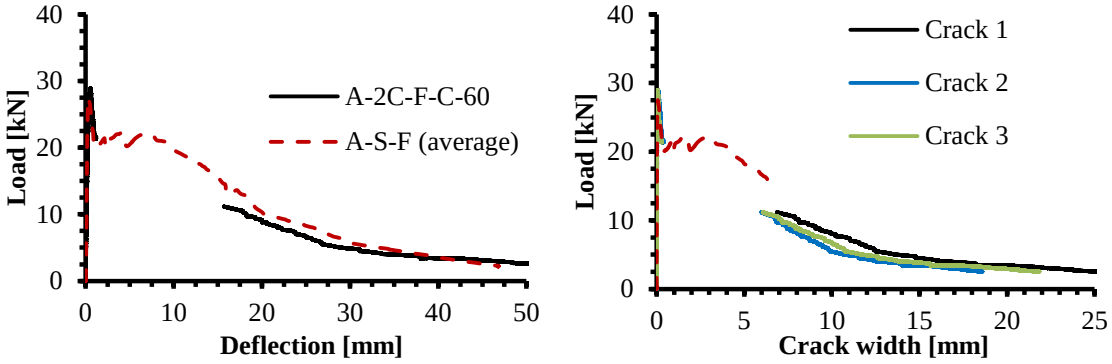

(a) (b)

Figure 3.62 – Static test result for round panel A-2C-F-C-60.

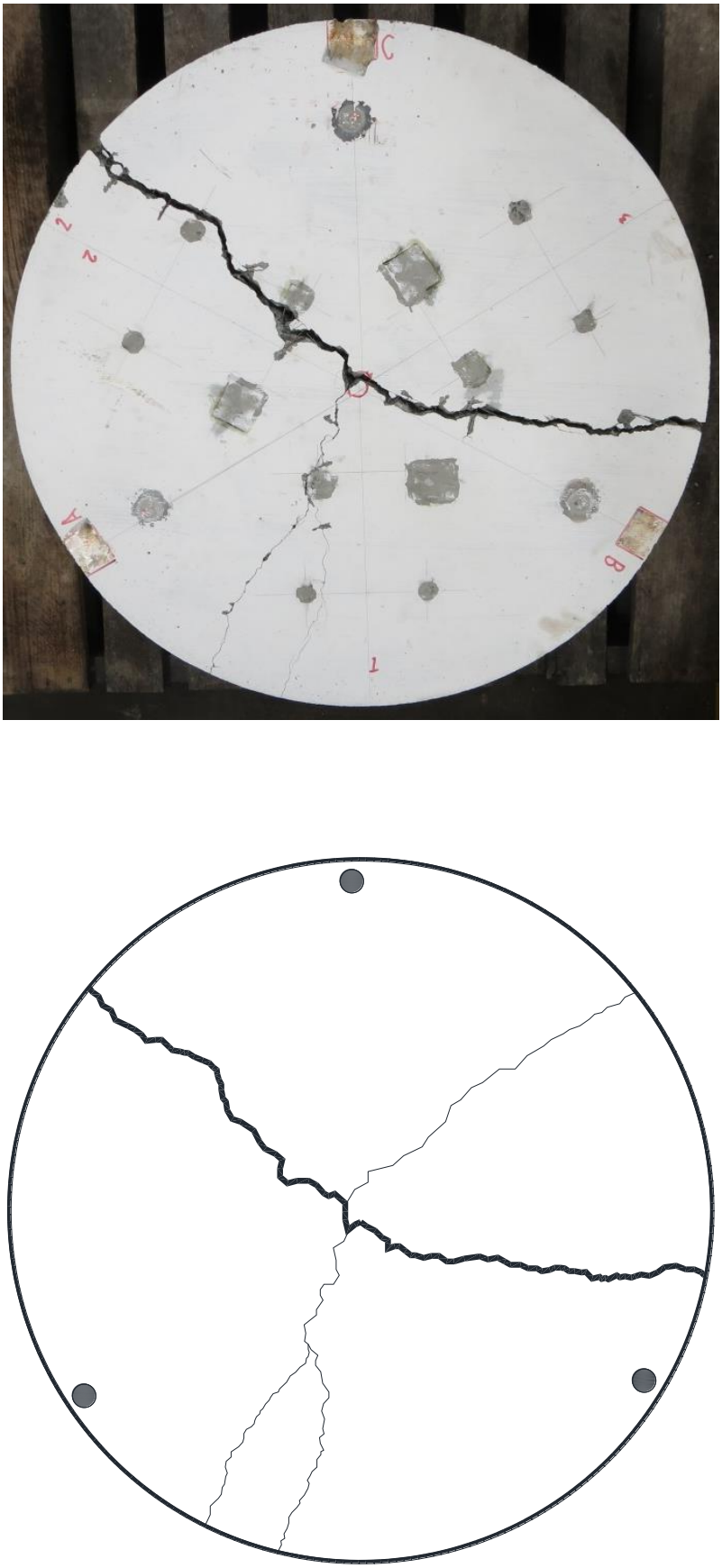

Figure 3.63 – Fracture line of A-1C-F-C-60.

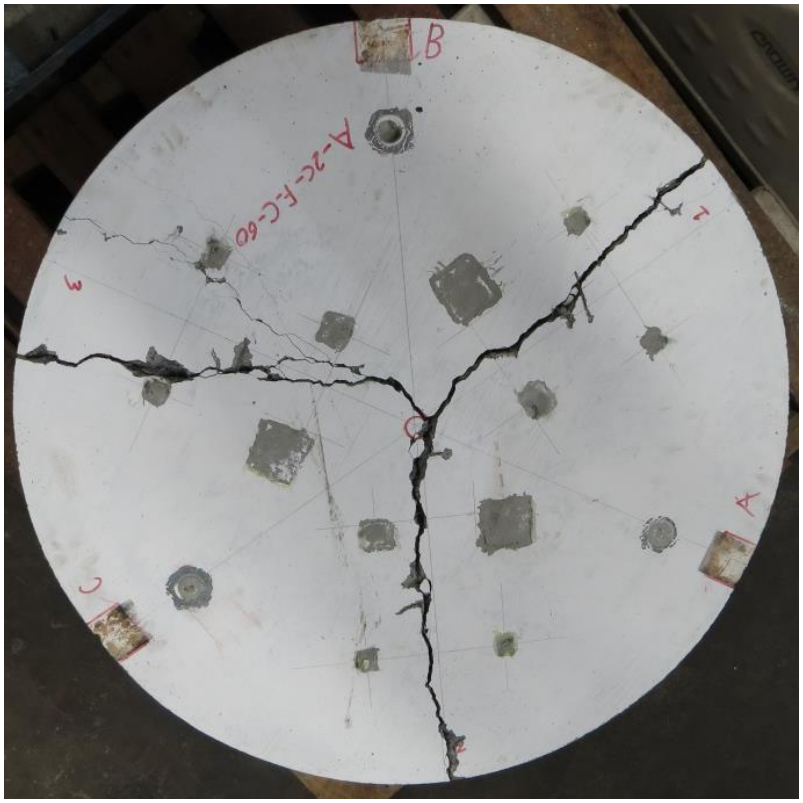

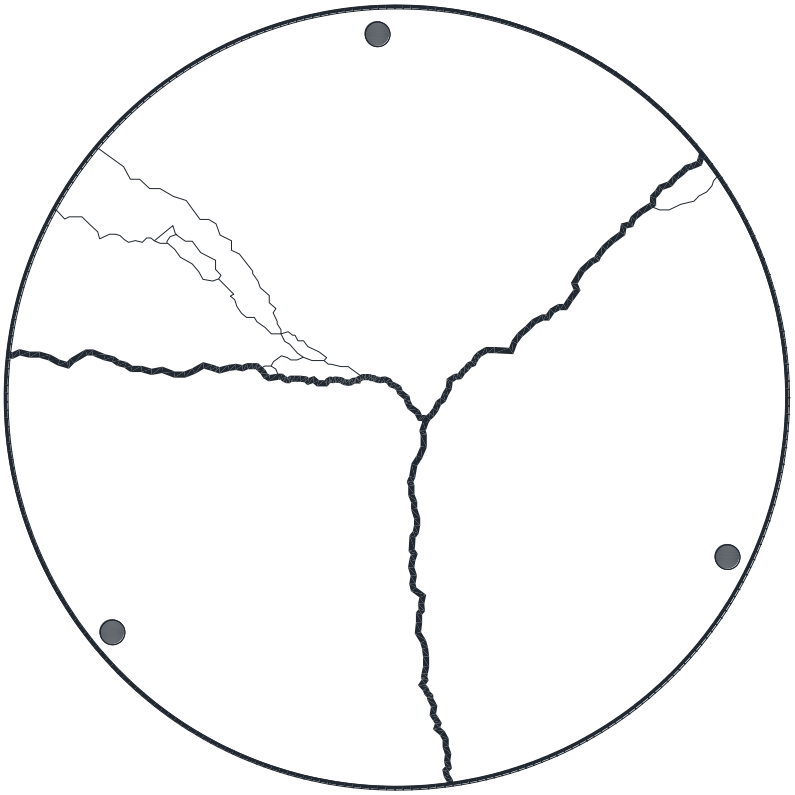

Figure 3.64 – Fracture lines of A-2C-F-C-60.

Specimens A-1C-F-C-40 and A-2C-F-C-40

Specimens A-1C-F-C-40 and A-2C-F-C-40 were loaded monotonically until a crack width of 0.5 mm was developed. After that, cyclic loading was applied at 3 Hz between 15% and 40% of their static capacity (loads from 5.3 kN to 13.7 kN and 4.5 kN to 11.8 kN for panels A-1C-F-C-40 and A-2C-F-C-40, respectively) to determine the post-cracking fatigue performance. The deflection and average crack width of the round panels A-1C-F-C-40 and A-2C-F-C-40 at both maximum and minimum loads are presented in Figures 3.65 and 3.66, respectively. Figures 3.67 and 3.68 show the load versus deflection and average crack width taken at different loading cycles.

At the first cycle, the minimum and maximum deflections were 0.79 mm and 0.97 mm, respectively, for specimen A-1C-F-C-40. This was followed by almost constant deflection for the first 1,000,000 cycles. After this, a steady increase in deflection was observed up to 0.83 mm and 1.04 mm at the minimum and maximum loads at the completion of 3 million cycles.

For specimen A-2C-F-C-40, the minimum and maximum deflections were 0.79 mm and 0.97 mm, at the first cycle, respectively. Similarly to specimen A-1C-F-C-40, constant deflection was observed for the first 1,000,000 cycles. This was followed by a steady increase in deflection to reach 0.91 mm and 1.12 mm, at 3 million cycles, at the minimum and maximum loads, respectively.

For the crack width, specimen A-1C-F-C-40 had a minimum and maximum average crack width of 0.26 mm and 0.30 mm at the first cycle. After this, a steady increase in average crack width development was observed up to 0.30 mm and 0.34 mm at the minimum and maximum loads at 10,000 cycles. Then, no further increase in average crack width was observed until the completion at 3 million cycles.

The maximum and minimum average crack widths for specimen A-2C-F-C-40 at the first cycle were 0.36 mm and 0.34 mm, respectively. No further development in average

crack width was observed until 250,000 cycles. This was followed by a noticeable increase in average crack width at 800,000 cycles to reach 0.38 mm and 0.43 mm at minimum and maximum loads, respectively. Then, no further increase in average crack width was observed after 3 million cycles of testing.

Neither specimen A-1C-F-C-40 nor A-2C-F-C-40 failed after 3 million cycles of testing. The specimens were then tested under static loading to determine their residual strength. The load-displacement response of the failed specimens and crack width development of the static test are shown in Figures 3.69 and 3.70 (note that the failure line did not pass through the gauge zone for crack 3 for both specimens). The crack pattern at the conclusion of the static test is shown in Figures 3.71 and 3.72. In each case the failure mode is represented by the development of three fracture lines. Interestingly in specimen A-1C-F-C-40, the load induced within the engaged fibres exceeded the previously attained peak matrix load observed (see Figure 3.69) and multiple cracking was observed (see Figure 3.71). Furthermore, local damage to the concrete surrounding the fibres can be noticed in Figure 3.71. This explains the fluctuation at the beginning of load-displacement curve in Figure 3.69(a) resulting in softening followed by hardening behaviour as more critical load paths are defined through the cracking process.

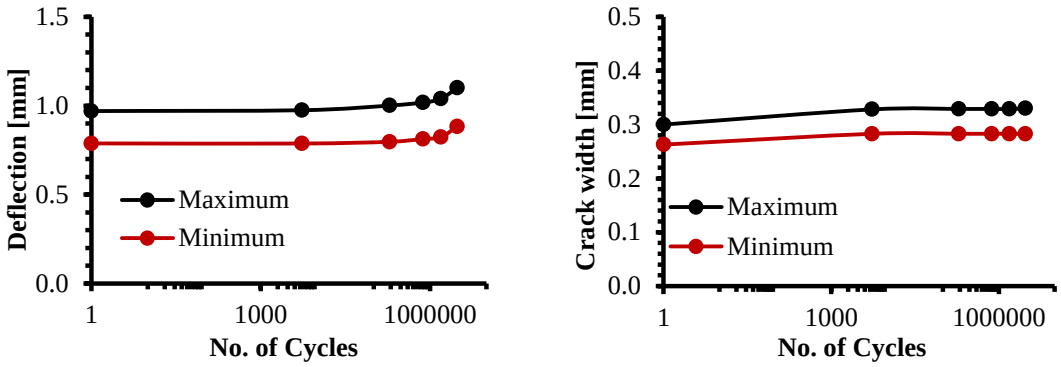

Figure 3.65 – Specimen A-1C-F-C-40: (a) load versus deflection; (b) load versus average crack width.

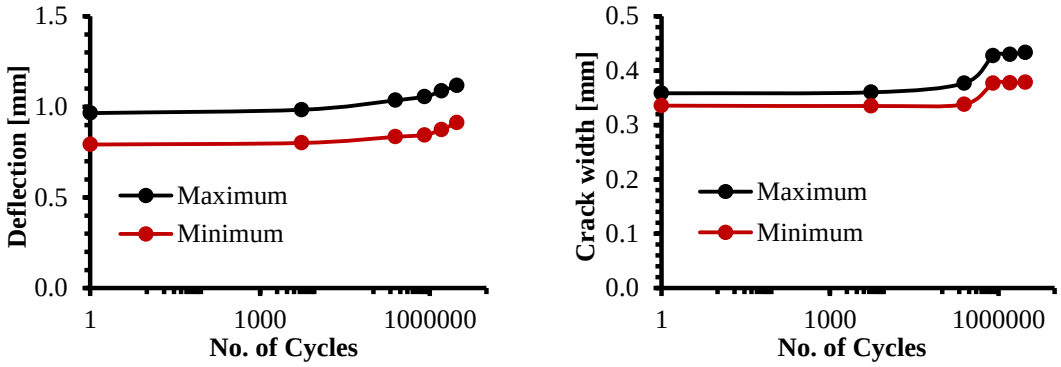

Figure 3.66 – Specimen A-2C-F-C-40: (a) load versus deflection; (b) load versus average crack width.

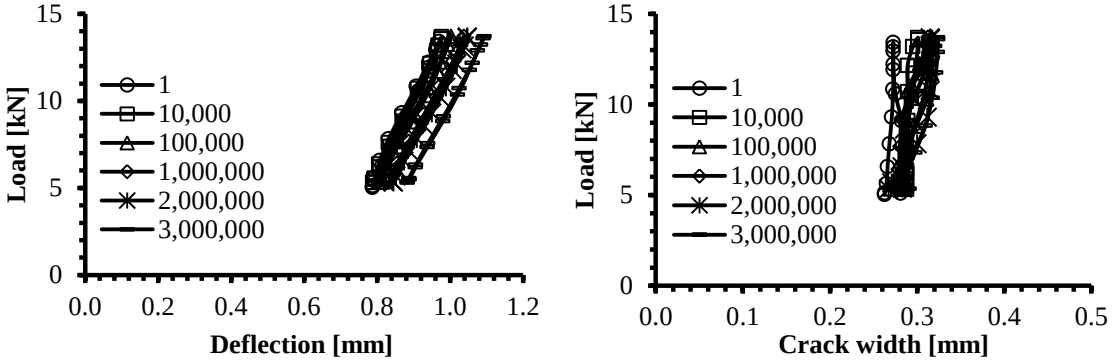

Figure 3.67 – Load versus (a) deflection and (b) average crack width at various cycle intervals for specimen A-1C-F-C-40.

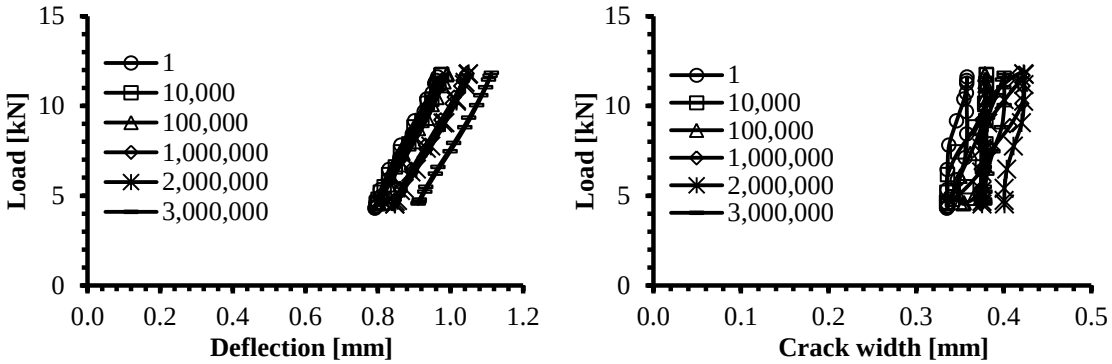

Figure 3.68 – Load versus (a) deflection and (b) average crack width at various cycle intervals for specimen A-2C-F-C-40.

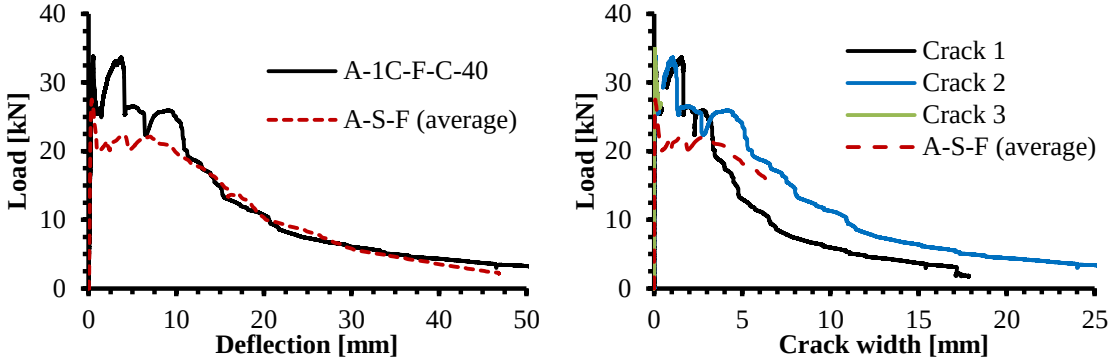

(a) (b)

Figure 3.69 – Static test result for round panel A-1C-F-C-40.

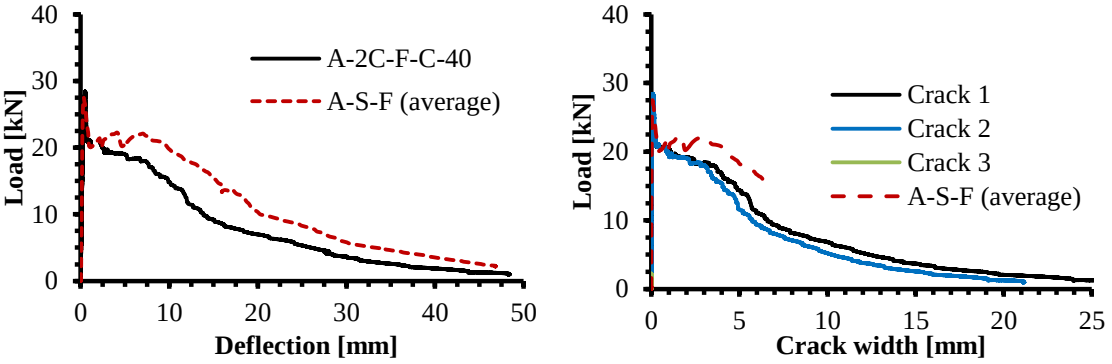

(a) (b)

Figure 3.70 – Static test result for round panel A-2C-F-C-40.

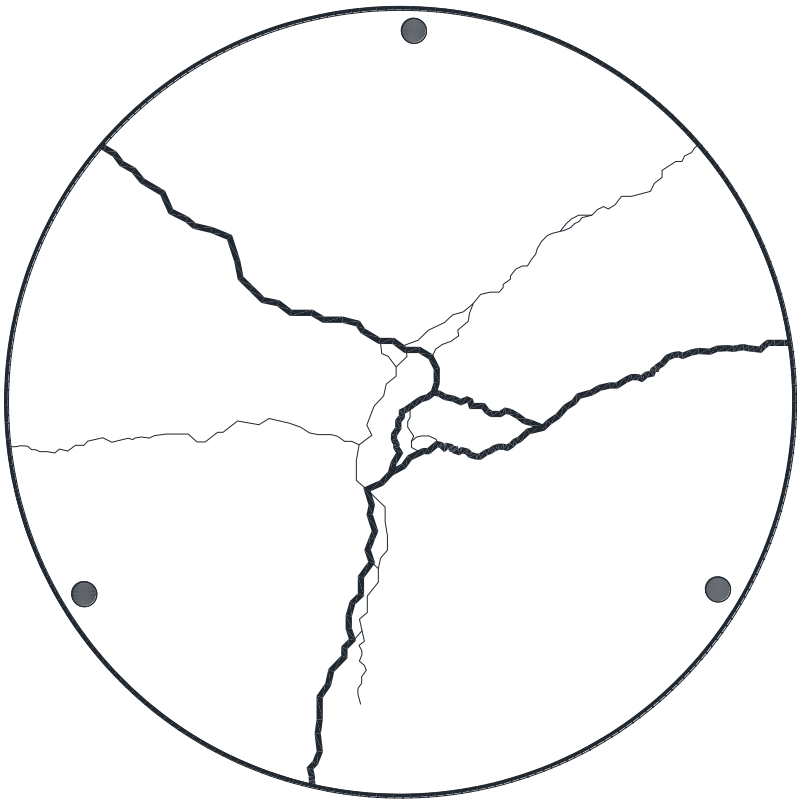

Figure 3.71 – Fracture lines of A-1C-F-C-40.

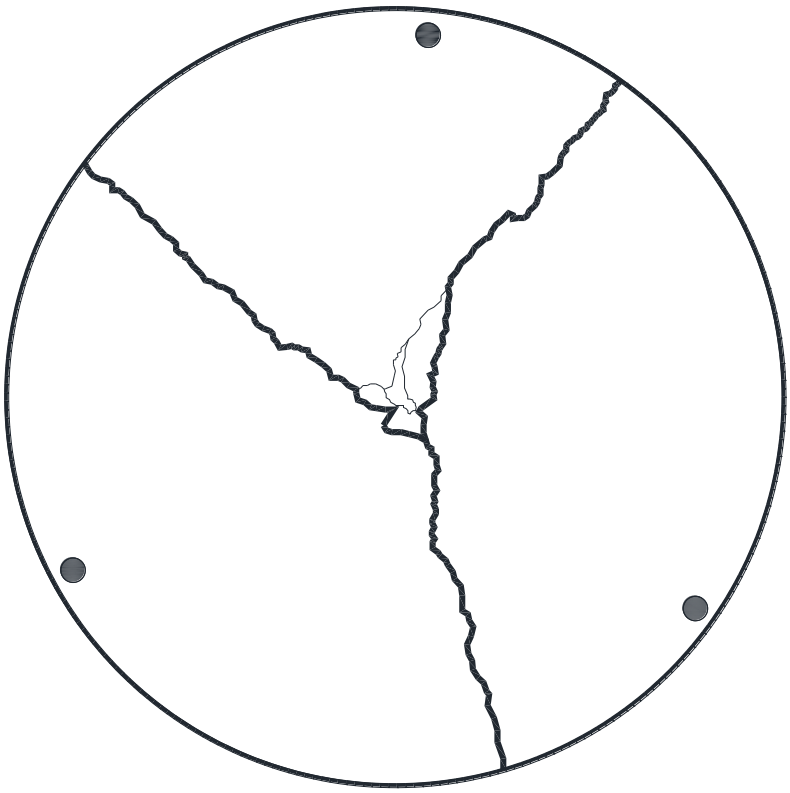

Figure 3.72 – Fracture lines of A-2C-F-C-40.

Specimens B-1C-F-U-70 and B-2C-F-U-70

Specimens B-1C-F-U-70 and B-2C-F-U-70 were uncracked and cycled between 15% (4.3 kN) and 70% (19.9 kN) of the average static cracking load at 3 Hz. The fatigue lives for the uncracked test panels were 646,246 and 399,743 cycles for specimens B-1C-F-U-70 and B-2C-F-U-70, respectively. The central deflection and average crack width development of the round panels at both maximum and minimum loads are shown Figures 3.73 and 3.74. Load versus deflection and average crack width taken at different loading cycles are displayed in Figures 3.75 and 3.76.

The central deflection of specimen B-1C-F-U-70 was 0.13 mm and 0.25 mm at minimum and maximum loads, respectively, and then increased steadily for the first 230,000 cycles to reach 0.16 mm and 0.31 mm at minimum and maximum loads, respectively. An accelerated increase in deflection was subsequently observed indicating a reduction in the flexural strength of the specimen possibly due to the formation of cracks. The minimum and maximum deflections at 646,100 cycles were 0.39 mm and 0.67 mm, respectively. After that and within 146 cycles, the deflection increased dramatically to reach 5.59 mm and 6.79 mm at the minimum and maximum loads, respectively, signalling the impending failure.

At the first cycles, round panel B-2C-F-U-70 had a minimum and maximum deflection of 0.07 mm and 0.22 mm, respectively. This was followed by a very slow steady increase in deflection for the first 238,000 cycles to reach 0.16 mm and 0.34 mm at the minimum and maximum loads, respectively. After that, and in a similar manner to specimen B-1C-F-U-70, the rate of deflection increase accelerated to reach 0.46 mm and 0.75 mm at 398,900 cycles possibly due to cracking. The last recorded minimum and maximum deflections were 6.57 mm and 7.37 mm at 399,743 cycles, just prior to failure.

For specimen B-1C-F-U-70, flexural cracks were not recorded by the instrumentations for the first 230,000 cycles. After that, and consistent with the observed increase in deflection, three flexural cracks had appeared. The average crack width was 0.01 mm and 0.02 mm at the minimum and maximum loads, respectively, as demonstrated in Figures 3.73 and 3.75. Cracks grew in length up until 646,100 cycles with the measured average crack width been 0.18 mm at the maximum load level. At 646,246 cycles, the crack had grown and on average widened to 2.58 mm and 3.06 mm at the minimum and maximum loads, respectively.

As can be seen from Figures 3.74 and 3.76, no flexural cracks were noted in specimen B-2C-F-U-70 for the first 238,000 cycles, and then three radial cracks were formed. The cracks grew slowly and steadily up to 398,900 cycles to reach an average crack width of 0.12 mm and 0.18 mm at the minimum and maximum loads, respectively. After 398,900 cycles, the average crack growth was rapid. The measured average crack widths, at 399,743 cycles, at the minimum and maximum loads were 2.69 mm and 2.95 mm, respectively.

The sudden rapid increase of central deflection and average crack width enlarging from one cycle to the subsequent one indicated the impending failure, meaning that the specimen was no longer capable to sustain the maximum load level and the envelope curve was almost approached. At this stage, the fatigue testing was stopped and monotonic loading was applied. Figures 3.77 and 3.78 demonstrate the load-displacement response of failed specimens and crack width development during the static test for specimens B-1C-F-U-70 and B-2C-F-U-70, respectively.

The crack distribution and failure mode of the specimens B-1C-F-U-70 and B-2C-F-C-70 at the conclusion of the static test are shown in Figures 3.79 and 3.80. The failure mode is represented by the development of three fracture lines for both panels. No major secondary cracks were observed.

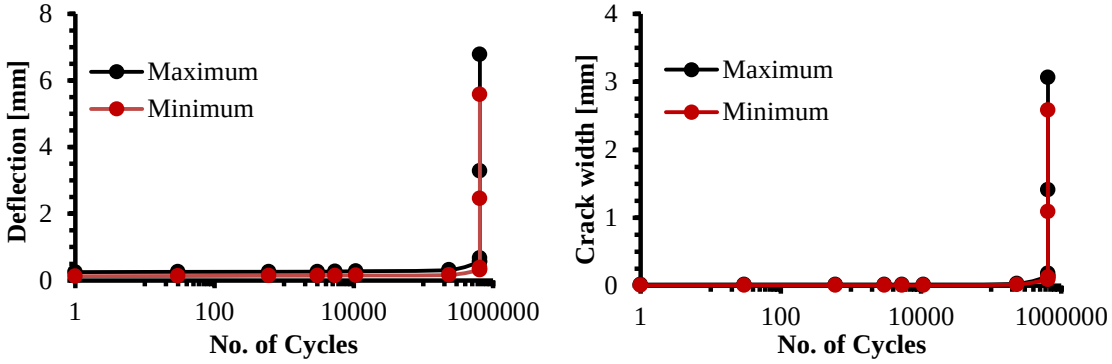

(a) (b)

Figure 3.73 – Specimen B-1C-F-U-70: (a) load versus deflection; (b) load versus average crack width.

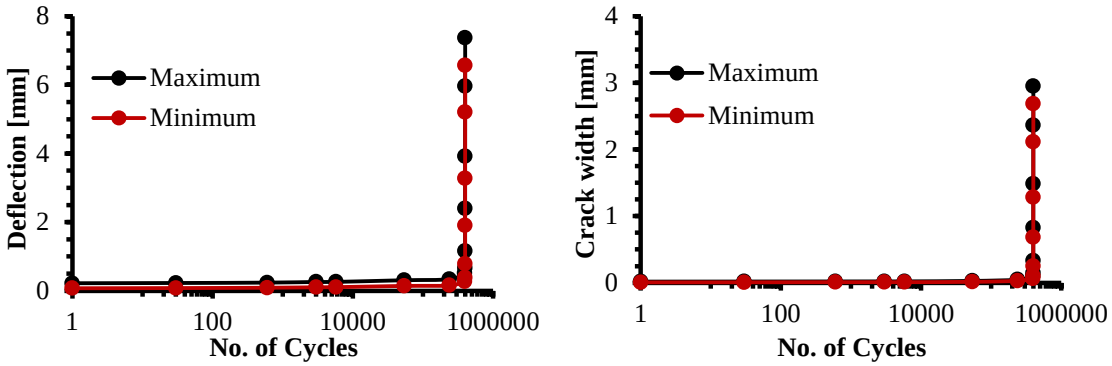

(a) (b)

Figure 3.74 – Specimen B-2C-F-U-70: (a) load versus deflection; (b) load versus average crack width.

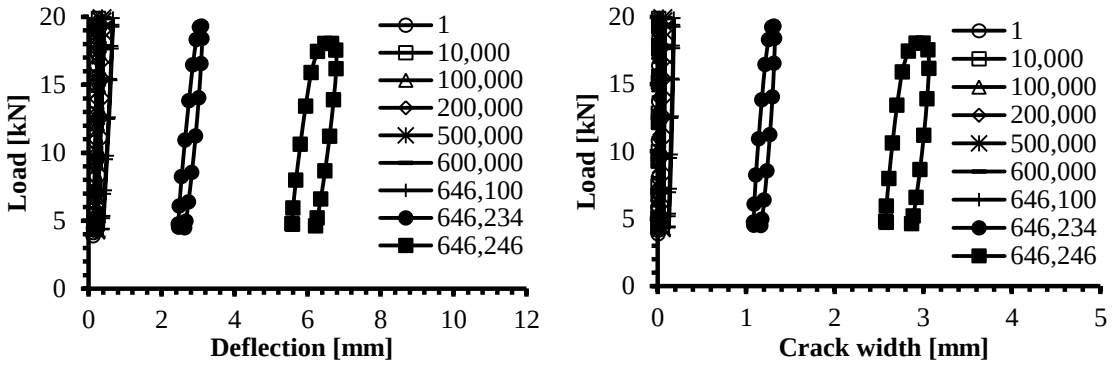

Figure 3.75 – Load versus (a) deflection and (b) average crack width at various cycle intervals for specimen B-1C-F-U-70.

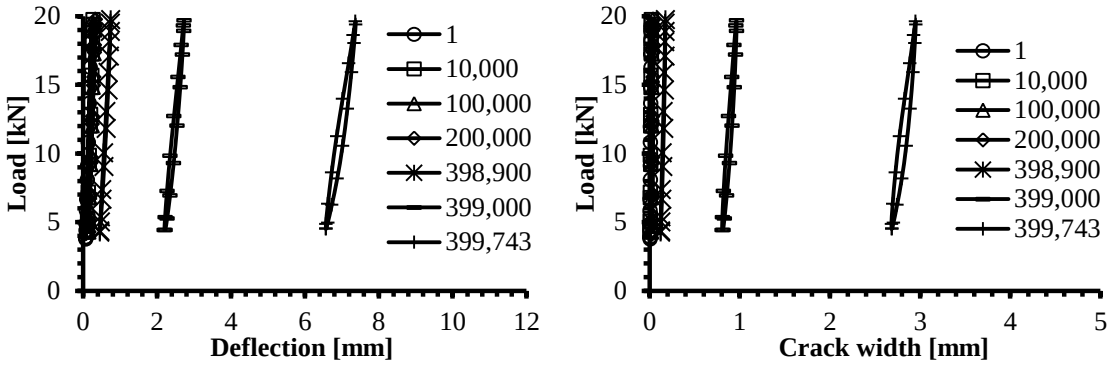

Figure 3.76 – Load versus (a) deflection and (b) average crack width at various cycle intervals for specimen B-2C-F-U-70.

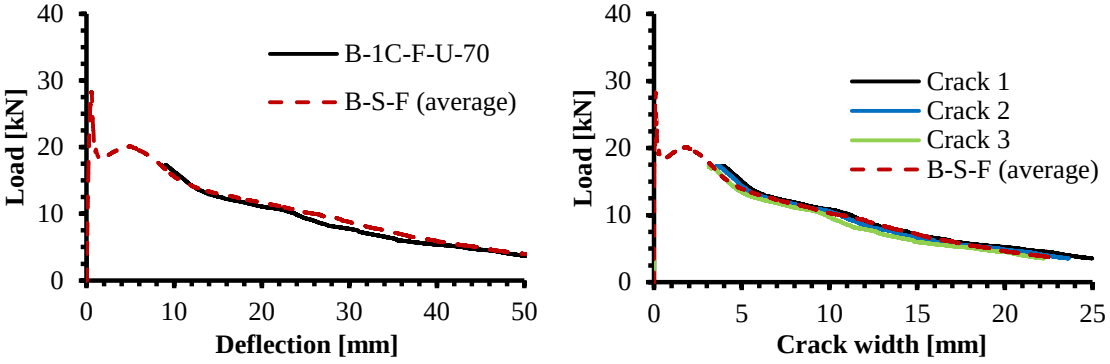

(a) (b)

Figure 3.77 – Static test result for round panel B-1C-F-U-70.

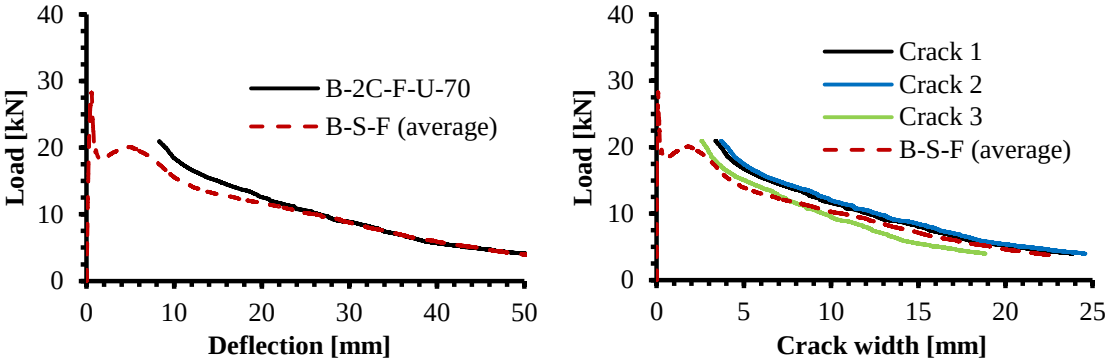

(a) (b)

Figure 3.78 – Static test result for round panel B-2C-F-U-70.

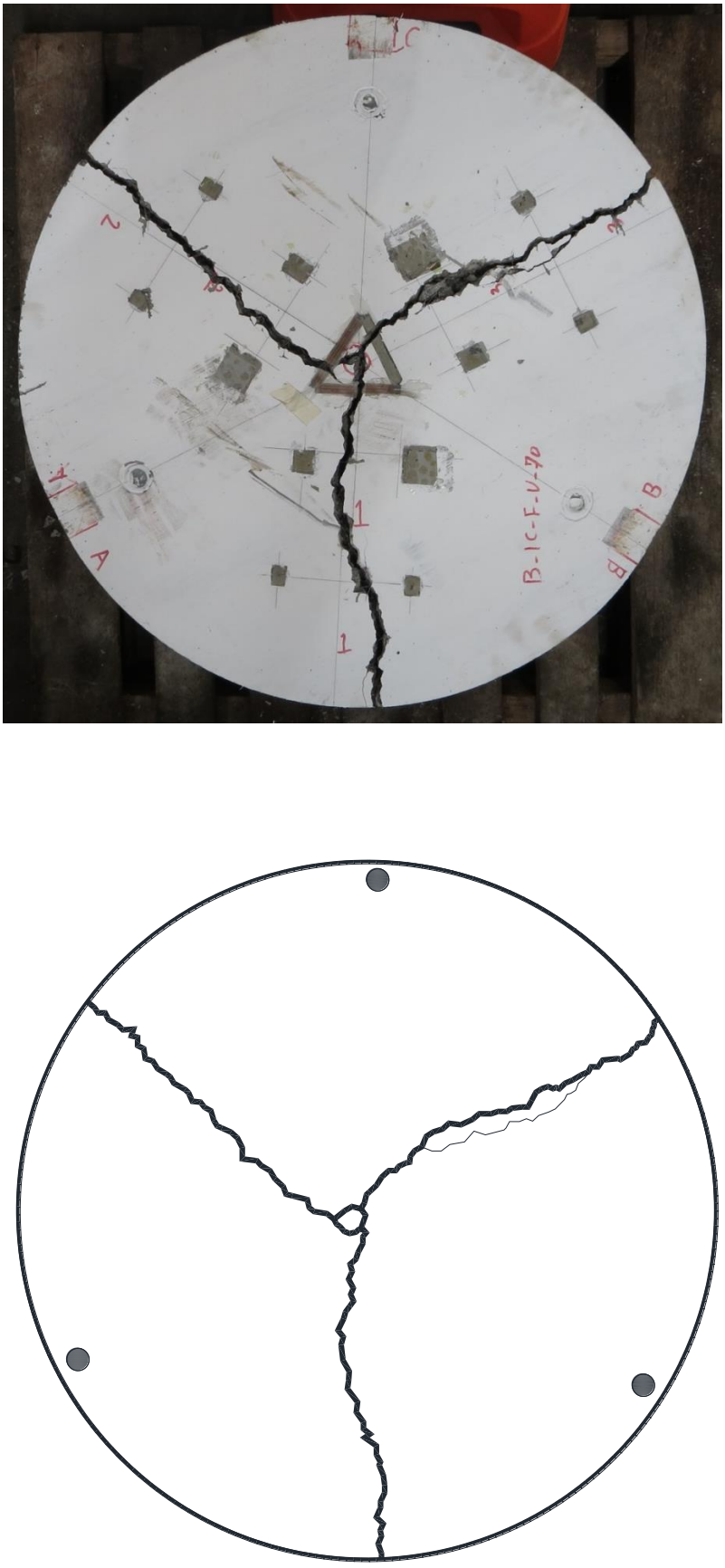

Figure 3.79 – Fracture lines of B-1C-F-U-70.

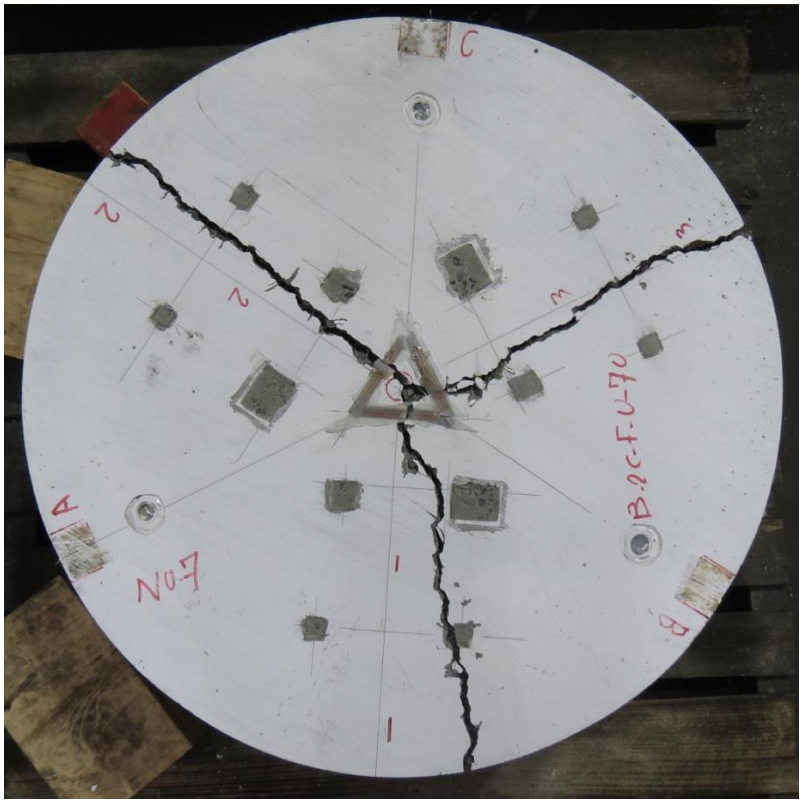

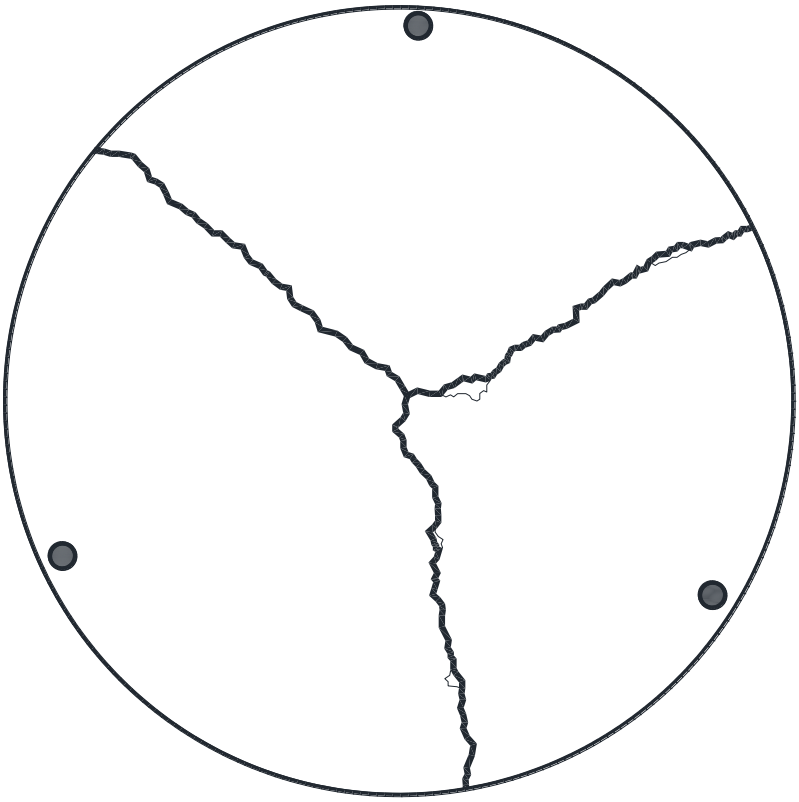

Figure 3.80 – Fracture lines of B-2C-F-U-70.

Specimens B-1C-F-C-60, B-2C-F-C-60 and B-3C-F-C-60

Specimens B-1C-F-C-60, B-2C-F-C-60 and B-3C-F-C-60 were loaded monotonically until a crack width of 0.5 mm was developed, after which cyclic loading between 15% and 60% (from 4.1 kN to 17.7 kN, 4.3 kN to 17.5 kN and 4.2 kN and 17.3 kN for panels B-1C-F-C-60, B-2C-F-C-60 and B-3C-F-C-60, respectively) of their own static capacity was applied at 3 Hz to determine the residual fatigue resistance. The fatigue lives for the pre-cracked test panels were 388,975, 460 and 12,431 cycles for specimens B-1C-F-C-60, B-2C-F-C-60 and B-3C-F-C-60, respectively. Figures 3.81 to 3.83 show the deflection and average crack width development of the round panels at both maximum and minimum loads. Figures 3.84 to 3.86 display the load versus deflection and average crack width taken at various loading cycles.

For specimen B-1C-F-C-60, the deflection was 1.46 mm at the maximum load. The deflection increased at a steady rate to 4.2 mm at about 350,000 cycles. Similarly, the deflection at minimum load began at 1.13 mm and increased to 3.68 mm at about 350,000 cycles. After 350,000 cycles, the deflection increased dramatically signalling the impending failure.

At the first load cycle, specimen B-2C-F-C-60 had minimum and maximum deflections of 0.87 mm and 1.09 mm, respectively. After that, the deflection increased steadily for the first 300 cycles to reach 1.52 mm and 1.85 mm minimum and maximum deflections, respectively. This was followed by a rapid increase in central deflection resulting in failure.

The central deflection of specimen B-3C-F-C-60 was 0.88 mm and 1.23 mm at minimum and maximum loads, respectively, and then increased at an accelerated rate for the first 11,000 cycles to reach 4.42 mm and 5.19 mm at minimum and maximum loads, respectively. A rapid deflection increase was then followed indicating the impending failure.

For the crack width development, specimen B-1C-F-C-60 had a maximum average crack width of 0.56 mm at the first cycle and 0.46 mm minimum average crack width. Following the deflection performance, a steady increase in average crack width was observed for the first 350,000 cycles with 1.69 mm and 1.86 mm minimum and maximum average crack widths, respectively. After that, a sudden increase in average crack width was observed.

The maximum and minimum crack widths for specimen B-2C-F-C-60 at the first cycle were 0.48 mm and 0.41 mm, respectively. Consistent with the observed increase in deflection, the crack width grew and widened steadily throughout the test. A rapid increase was observed from 300 load cycles onwards, signally imminent failure.

For specimen B-3C-F-C-60, the initial average crack width was 0.32 mm and 0.41 mm at the minimum and maximum loads, respectively, as demonstrated in Figure 3.83(b). Cracks grew in length up until 11,000 cycles with the measured average crack width been 2.17 mm at the maximum load level. A significant increase in average crack width was observed prior to failure.

After the completion of fatigue testing, monotonic loading was applied. The load-displacement response of failed specimen and crack width development during the static test are presented in Figures 3.87 and 3.88 for specimens B-2C-F-C-60 and B-3C-F-C-60, respectively. Due to an instrument error, the tail of the curve of specimen B-1C-F-C-60 was not captured.

The crack distribution and failure mode of the specimens B-1C-F-C-60, B-2C-F-C-60 and B-3C-F-C-60 at the conclusion of the static test are shown in Figures 3.89 to 3.91, respectively. The failure mode is represented by the development of three fracture lines for round panels B-1C-F-C-60 and B-3C-F-C-60, while only one fracture line was developed for specimen B-2C-F-C-60 in addition to the development of some secondary cracks (see Figures 3.87(b) and 3.90). Figures 3.87(b) and 3.90 show that the failure

crack passed through the gauged region of crack 1 but not of cracks 2 and 3 for panel B-2C-F-C-60 (noting that the crack gauges were located for the expected three crack failure mechanism).

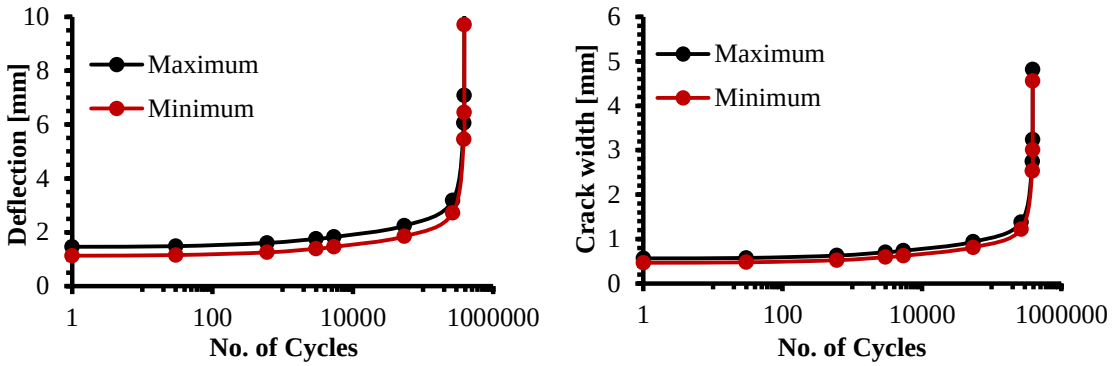

(a) (b)

Figure 3.81 – Specimen B-1C-F-C-60: (a) load versus deflection; (b) load versus average crack width.

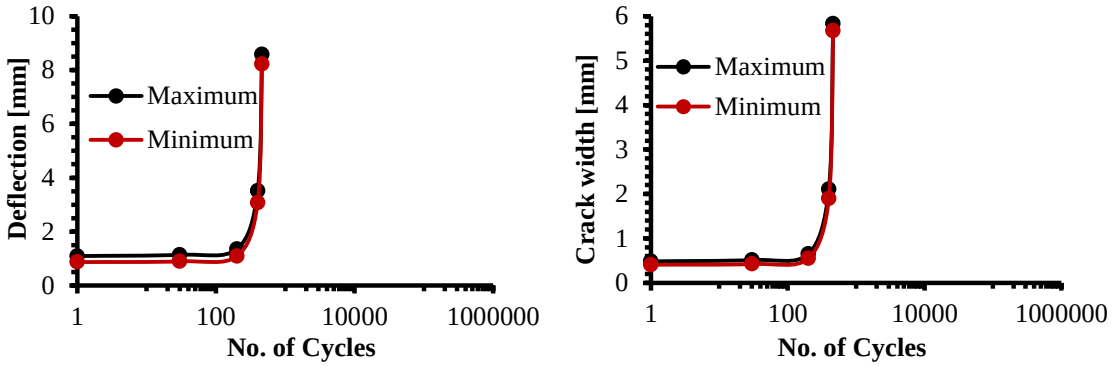

(a) (b)

Figure 3.82 – Specimen B-2C-F-C-60: (a) load versus deflection; (b) load versus crack width.

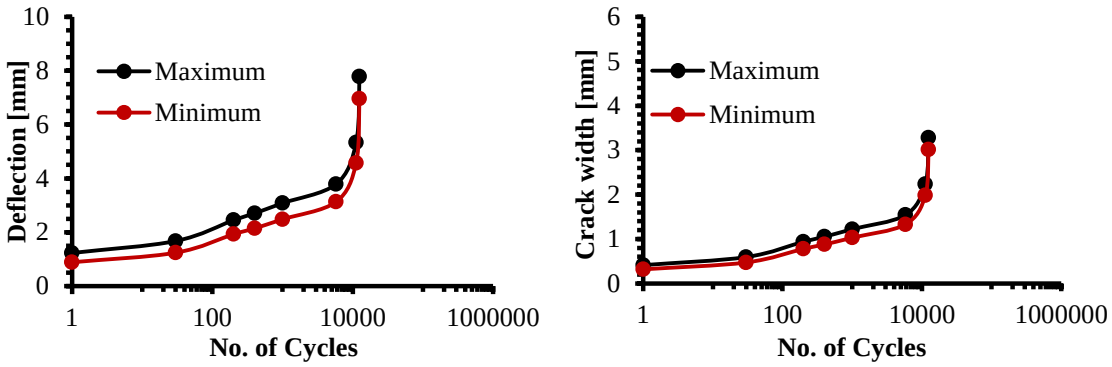

(a) (b)

Figure 3.83 – Specimen B-3C-F-C-60: (a) load versus deflection; (b) load versus average crack width.

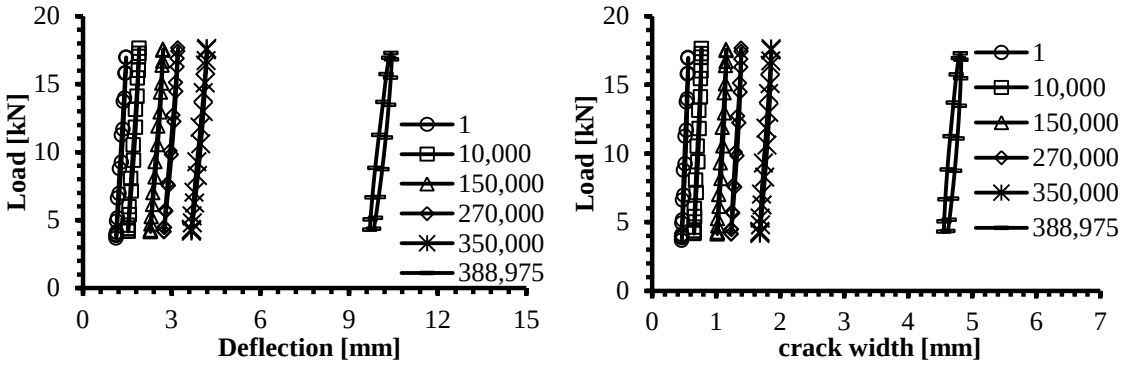

(a) (b)

Figure 3.84 – Load versus (a) deflection and (b) average crack width at various cycle intervals for specimen B-1C-F-C-60.

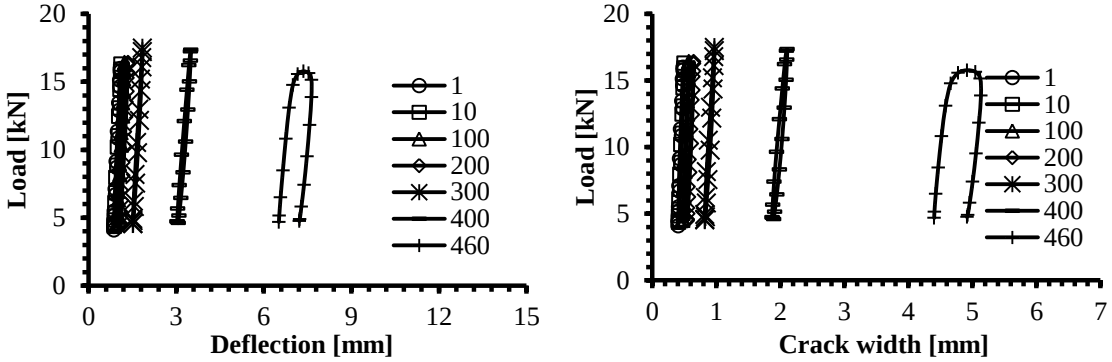

Figure 3.85 – Load versus (a) deflection and (b) crack width at various cycle intervals for specimen B-2C-F-C-60.

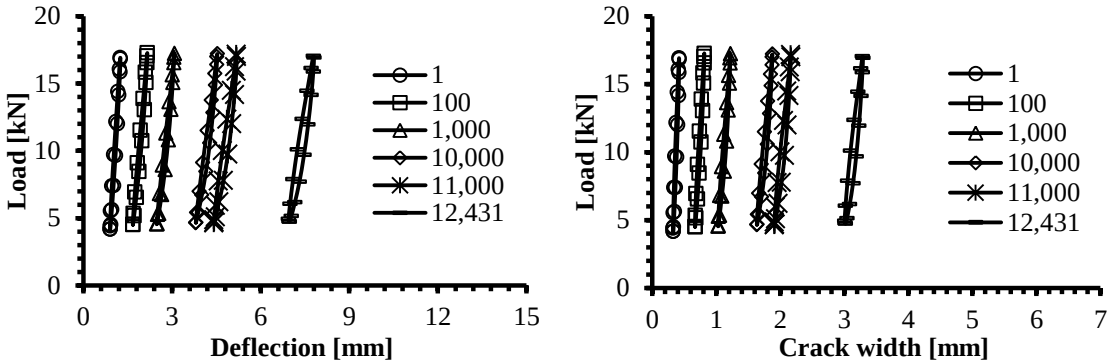

Figure 3.86 – Load versus (a) deflection and (b) average crack width at various cycle intervals for specimen B-3C-F-C-60.

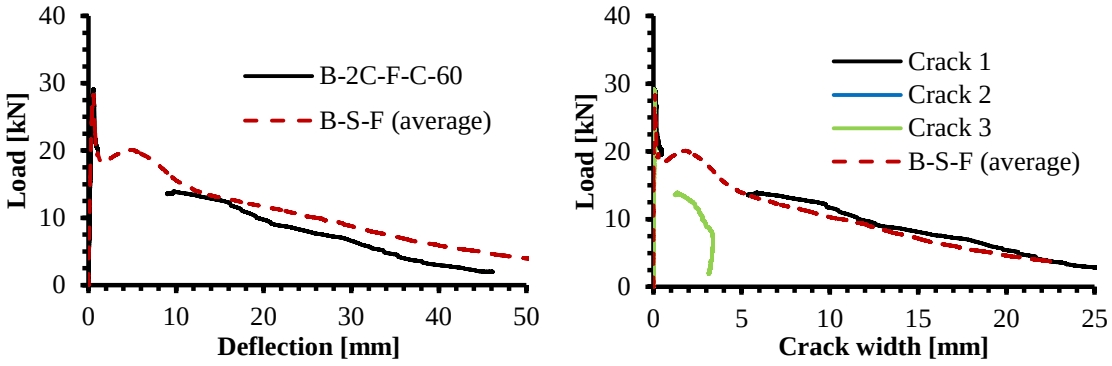

(a) (b)

Figure 3.87 – Static test result for round panel B-2C-F-C-60.

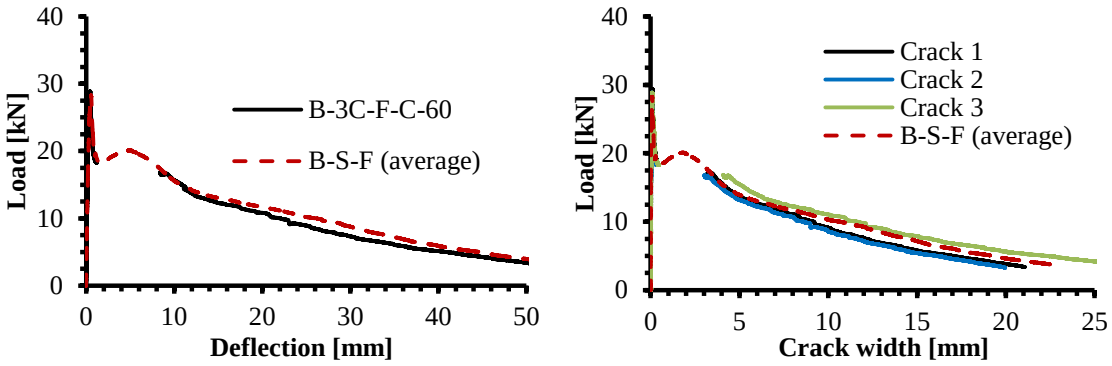

(a) (b)

Figure 3.88 – Static test result for round panel B-3C-F-C-60.

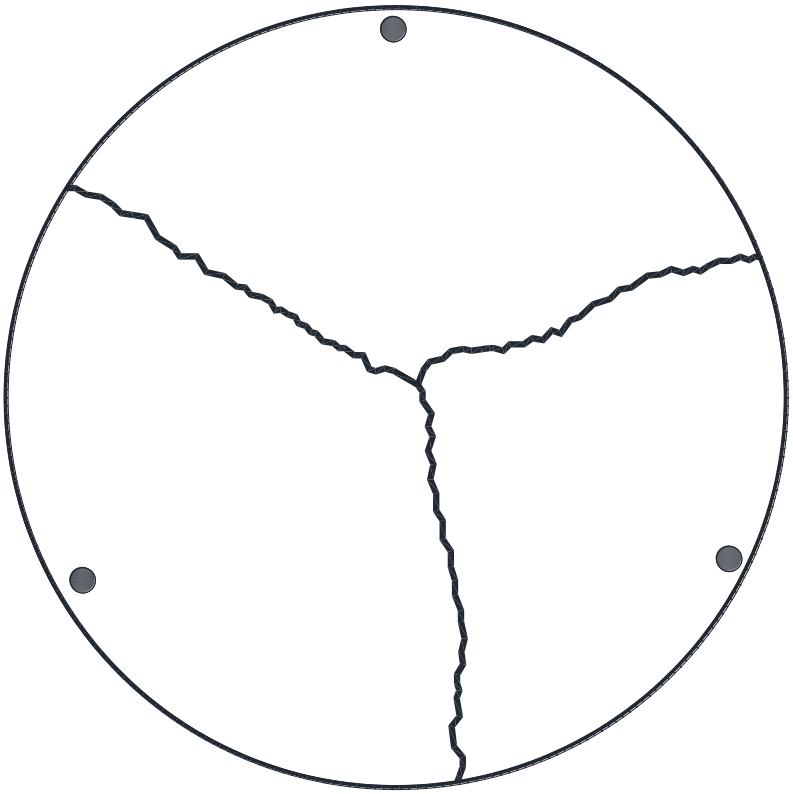

Figure 3.89 – Fracture lines of B-1C-F-C-60.

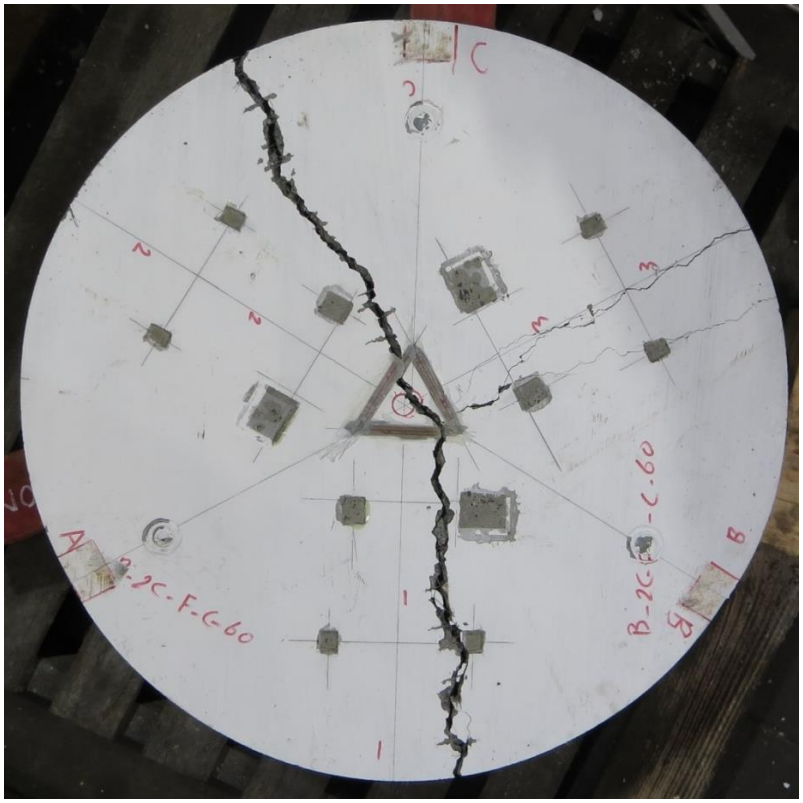

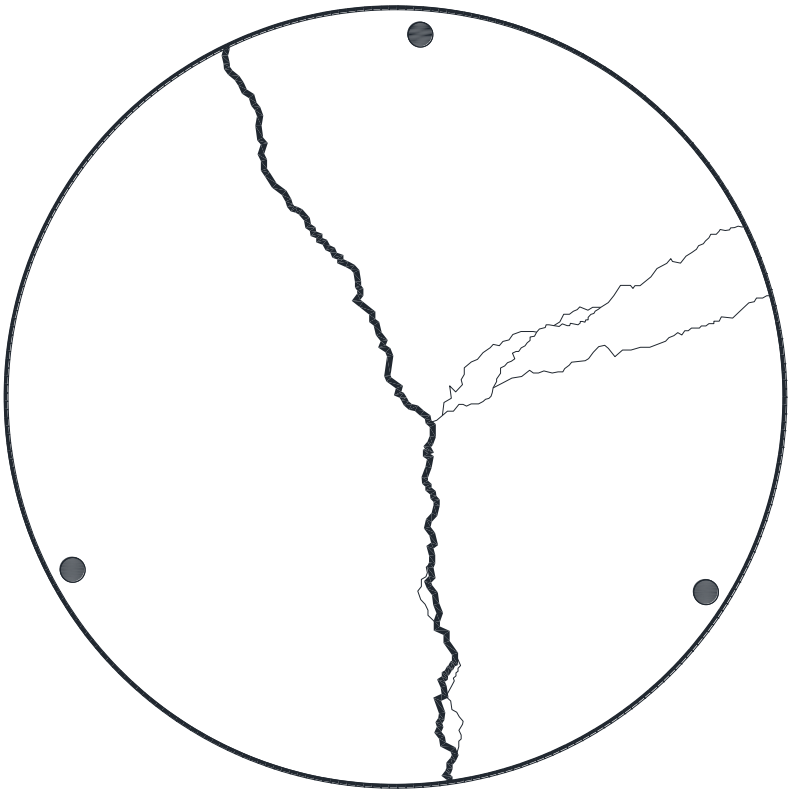

Figure 3.90 – Fracture line of B-2C-F-C-60.

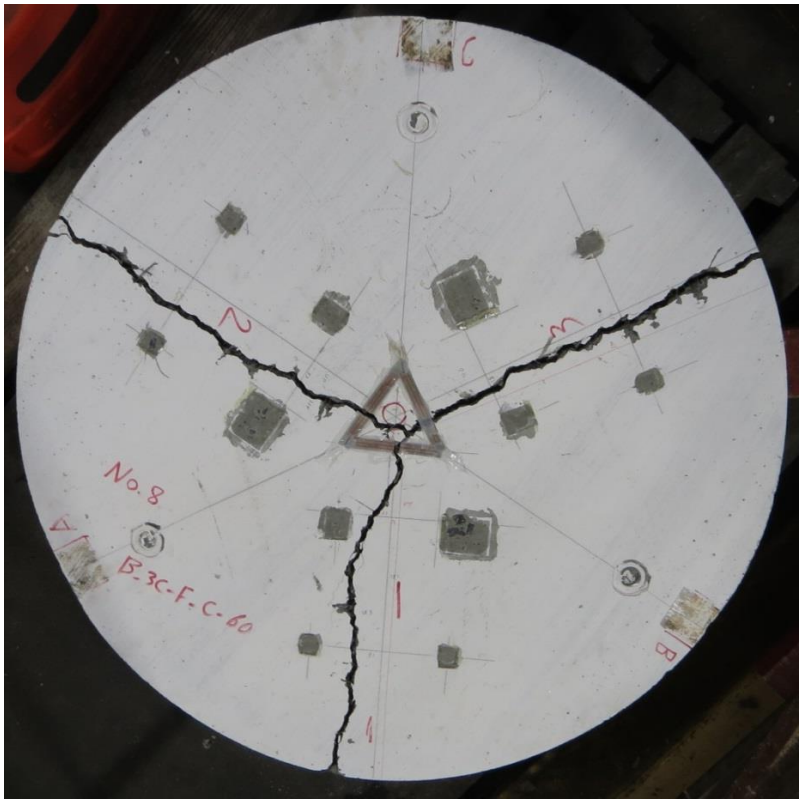

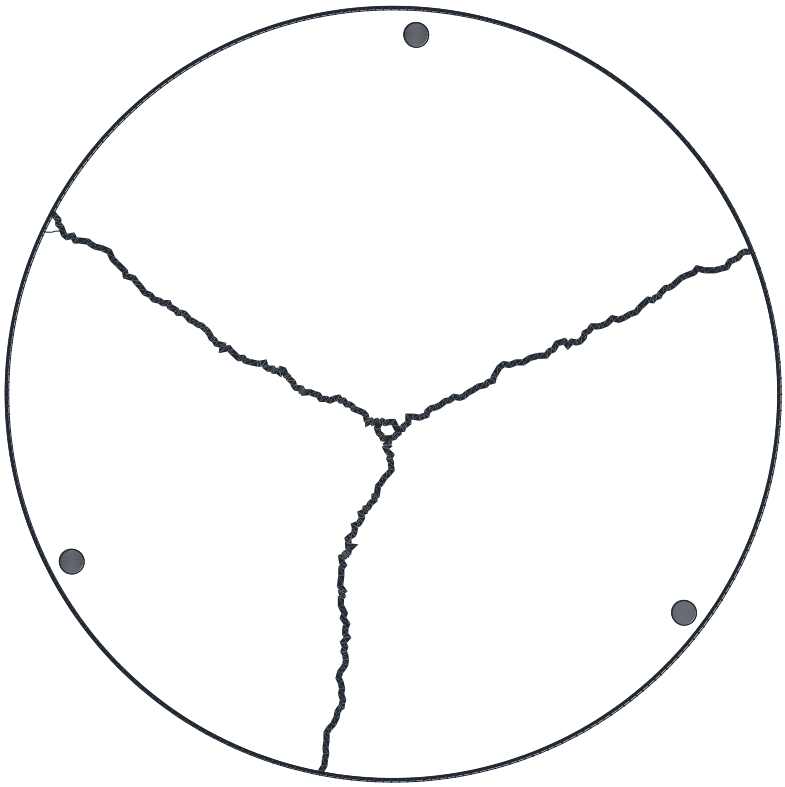

Figure 3.91 – Fracture lines of B-3C-F-C-60.

Specimens B-1C-F-C-40 and B-2C-F-C-40

Specimens B-1C-F-C-40 and B-2C-F-C-40 were loaded monotonically until a crack width of 0.5 mm was developed. Cyclic loading was then applied at a frequency of 3 Hz between 15% and 40% (from to 3.9 kN to 10.5 kN and from 4.2 kN to 11.3 kN for panels B-1C-F-C-40 and B-2C-F-C-40, respectively) of their own static capacity to determine the post-peak fatigue performance. The deflection and average crack width development of the round panels B-1C-F-C-40 and B-2C-F-C-40 at both maximum and minimum loads are presented in Figures 3.92 and 3.93, respectively. Load versus deflection and average crack width taken at different loading cycles are presented in Figures 3.94 and 3.95.

Round panel B-1C-F-C-40 experienced a deflection of 0.99 mm and 1.16 mm at the minimum and maximum loads at the first cycle then the specimen experienced a very slow steady increase of deflection through the test. At 3 million cycles, the minimum and maximum deflections of the round panel B-1C-F-C-40 were 1.08 mm and 1.29 mm. No failure occurred after 3 million cycles of testing specimen B-1C-F-C-40.

At the first load cycle, specimen B-2C-F-C-40 had a minimum and maximum deflection of 0.96 mm and 1.13 mm, respectively. This was followed by almost constant deflection for approximately the first 600,000 cycles. After this, a steady increase in deflection was observed up to 1.31 mm at the maximum load and 1.10 mm at the minimum load at, 3 million cycles. Specimen B-2C-F-C-40 did not fail after the completion of 3 million cycles of testing.

For the crack width, specimen B-1C-F-C-40 had a minimum and maximum average crack width of 0.30 mm and 0.34 mm, at the first cycle, respectively. After this, a steady increase in average crack width development was observed up to 0.39 mm and 0.44 mm at the minimum and maximum loads at 3 million cycles.

The minimum and maximum average crack widths for specimen B-2C-F-C-40 at the first cycle were 0.34 mm and 0.39 mm, respectively. No further development in average crack width was observed until 100,000 cycles. This was followed by a sharp increase in average crack width at 500,000 cycles to reach 0.41 mm and 0.47 mm at minimum and maximum loads, respectively. At 3 million cycles of testing, the cracks negligibly reduced in width to reach 0.40 and 0.46 at the minimum and maximum loads, respectively.

Both specimens, B-1C-F-C-40 and B-2C-F-C-40, did not fail after 3 million cycles of testing. Each specimen was then tested under static loading to determine its residual strength. The load-displacement response of failed specimen and crack width development of the static test are shown in Figures 3.96 and 3.97. The crack pattern at the conclusion of the static test is shown in Figures 3.98 and 3.99. The failure mode is represented by the development of three fracture lines for both panels. For specimen B-2C-F-C-40, some secondary cracks propagated out of primary cracks as the applied deflection increased.

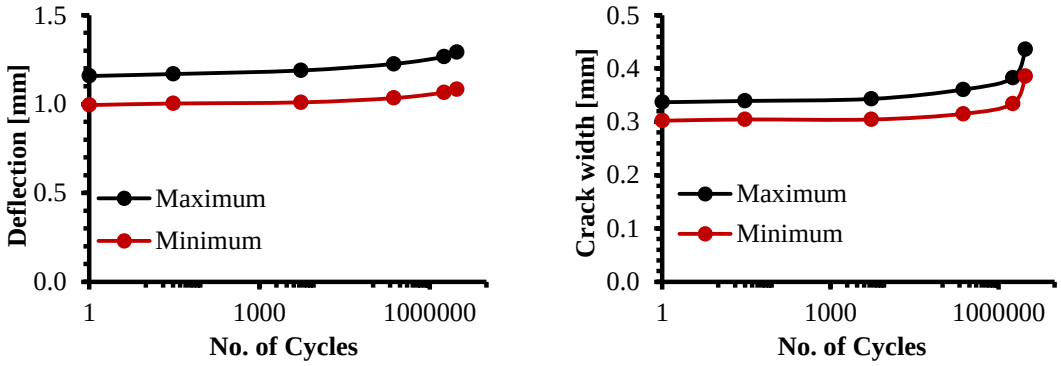

Figure 3.92 – Specimen B-1C-F-C-40: (a) load versus deflection; (b) load versus average crack width.

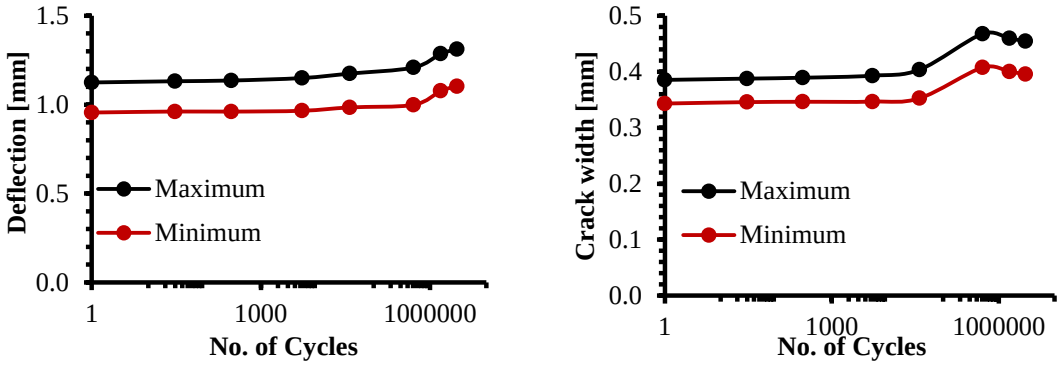

(a) (b)

Figure 3.93 – Specimen B-2C-F-C-40: (a) load versus deflection; (b) load versus average crack width.

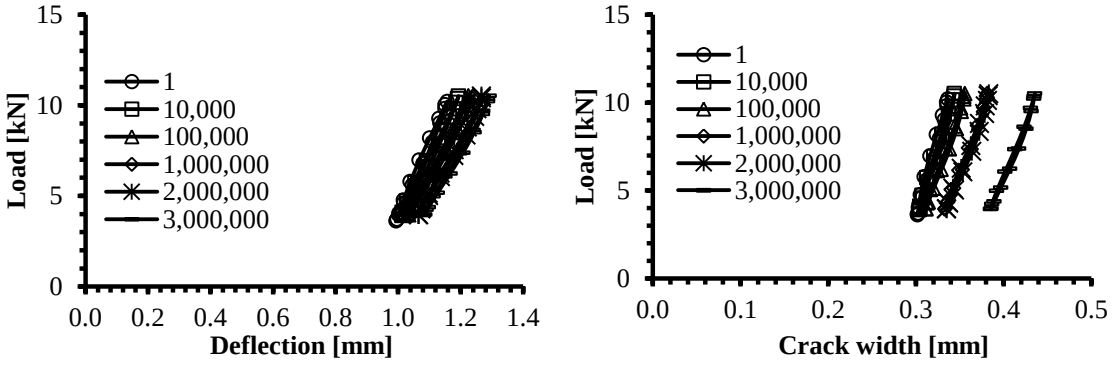

(a) (b)

Figure 3.94 – Load versus (a) deflection and (b) average crack width at various cycle intervals for specimen B-1C-F-C-40.

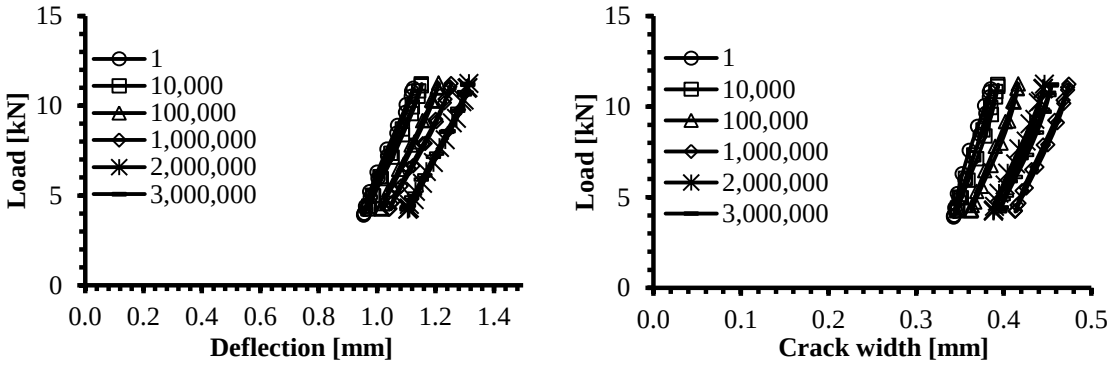

(a) (b)

Figure 3.95 – Load versus (a) deflection and (b) average crack width at various cycle intervals for specimen B-2C-F-C-40.

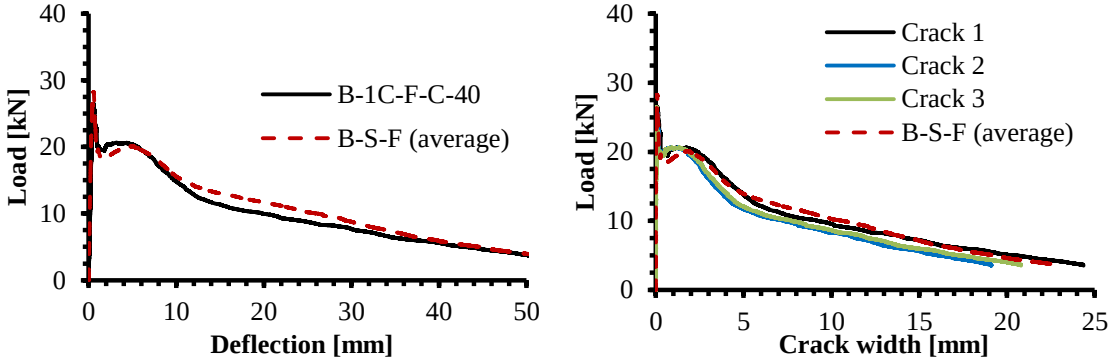

(a) (b)

Figure 3.96 – Static test result for round panel B-1C-F-C-40.

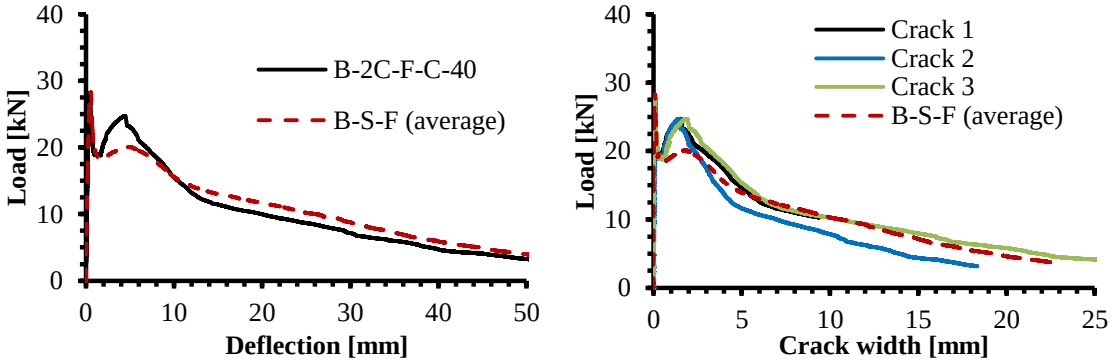

(a) (b)

Figure 3.97 – Static test result for round panel B-2C-F-C-40.

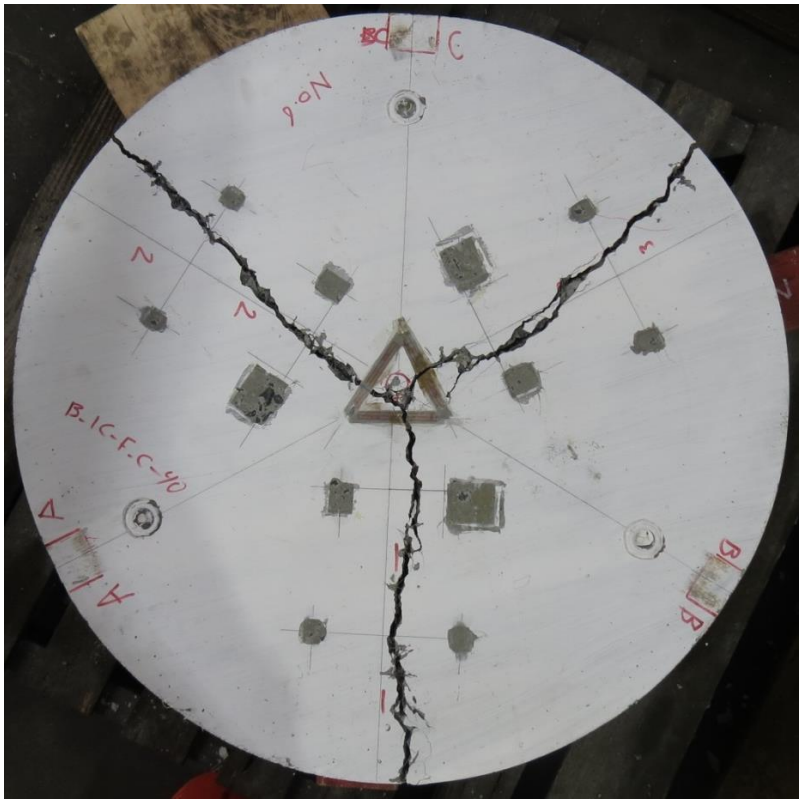

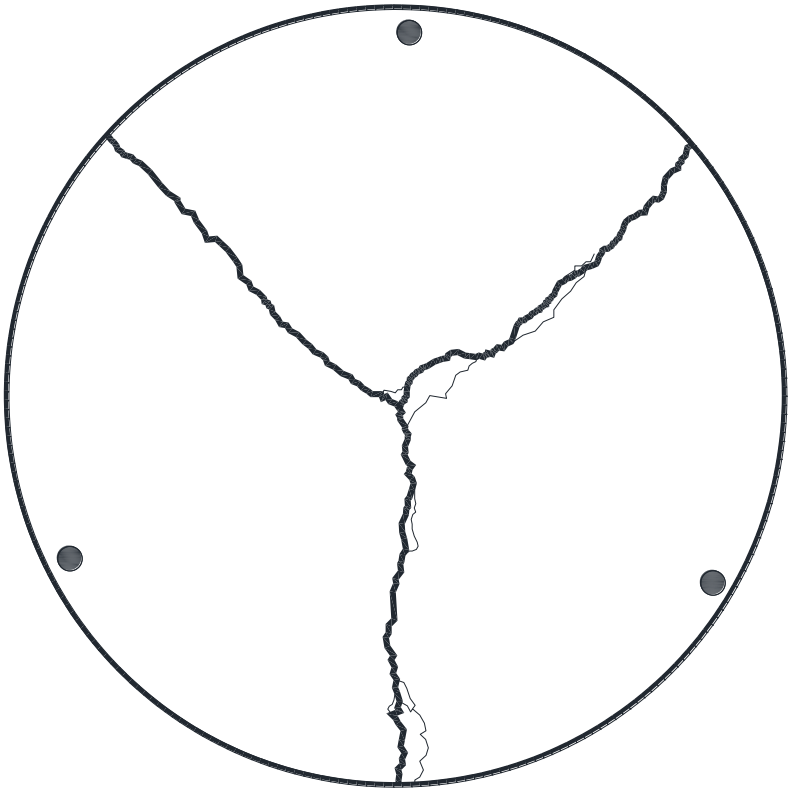

Figure 3.98 – Fracture lines of B-1C-F-C-40.

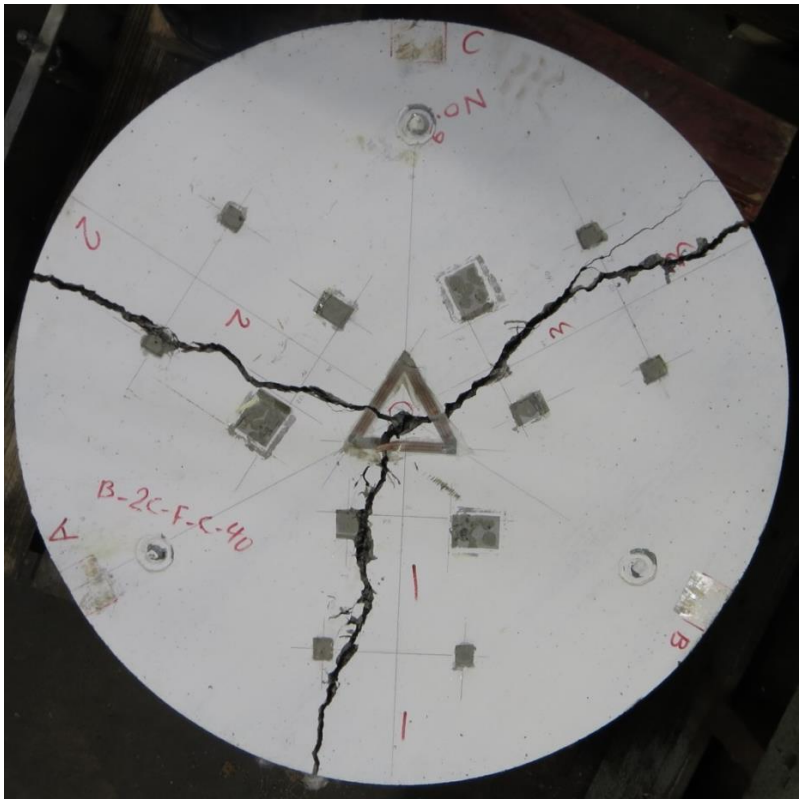

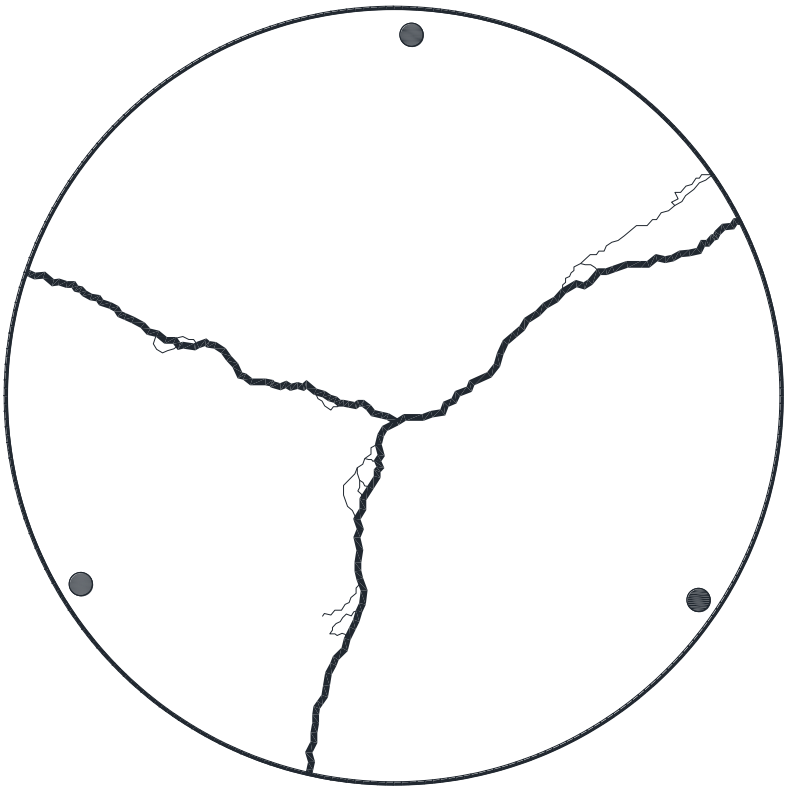

Figure 3.99 – Fracture lines of B-2C-F-C-40.

Specimens C-1C-F-U-70 and C-2C-F-U-70

Specimens C-1C-F-U-70 and C-2C-F-U-70 were uncracked and cycled between 15% (4.6 kN) and 70% (22.7 kN) of the average static cracking load at 3 Hz. The fatigue lives for the uncracked test panels were 243,158 and 1,375,127 cycles for specimens C-1C-F-U-70 and C-2C-F-U-70, respectively. The central deflection and average crack width development of the round panels at both maximum and minimum loads are shown Figures 3.100 and 3.101. Load versus deflection and average crack width taken at different loading cycles are presented in Figures 3.102 and 3.103.

At the first cycles, round panel C-1C-F-U-70 had a minimum and maximum deflection of 0.11 mm and 0.26 mm, respectively. This was followed by a slow steady increase in deflection for the first 150,000 cycles to reach 0.20 mm and 0.40 mm at the minimum and maximum loads, respectively. After that, the rate of deflection increase accelerated to reach 0.33 mm and 0.61 mm at 243,100 cycles, possibly due to cracking. The last recorded minimum and maximum deflections were 2.26 mm and 2.97 mm, respectively, at 243,158 cycles, just prior to failure.

The central deflection of specimen C-2C-F-U-70 was initially 0.06 mm and 0.20 mm at minimum and maximum loads, respectively, and then increased steadily for the first 715,000 cycles to reach 0.20 mm and 0.39 mm at minimum and maximum loads, respectively. In a similar manner to specimen C-1C-F-U-70, an accelerated rate of deflection increase was subsequently observed indicating a reduction in the flexural strength of the specimen due to the formation of cracks. The minimum and maximum deflections at 1,375,000 cycles were 0.46 mm and 0.67 mm, respectively. After that and within 127 cycles, the central deflection increased dramatically to reach 2.31 mm and 3.05 mm during minimum and maximum loads, respectively, signalling the impending failure.

For specimen C-1C-F-U-70, no flexural cracks were recorded by the instrumentations for the first 75,000 cycles. After that, one flexural crack formed as shown in Figure 3.104, while the other two cracks appeared at 150,000 cycles. This deviation in crack formation reduced the flexural rigidity of the panel resulting in earlier failure comparing with specimen C-2C-F-U-70. At 75,000 cycles, the crack width was 0.03 mm and 0.06 mm at the minimum and maximum loads, respectively, as demonstrated in Figures 3.100 and 3.102. Cracks grew in length up until 243,100 cycles with the measured average crack width been 0.24 mm and 0.17 mm at the maximum and minimum load level, respectively. At 243,158 cycles, the average crack width have grown and widened to 1.20 mm and 1.49 mm at the minimum and maximum loads, respectively.

As can be seen from Figures 3.101 and 3.103, no flexural cracks were observed in specimen C-2C-F-U-70 for the first 715,000 cycles. After that, and consistent with the increase in deflection observed, three radial cracks were formed. The cracks grew slowly and steadily up to 1,375,000 cycles to reach an average crack width of 0.14 mm and 0.21 mm at the minimum and maximum loads, respectively. After 1,375,000 cycles, the average crack growth was rapid. The measured average crack width at 1,375,127 cycles at the minimum and maximum loads was 1.02 mm and 1.27 mm, respectively.

The fatigue life of the round panels due to the contribution of concrete component (before cracking) is 75,000 and 715,000 cycles for C-1C-F-U-70 and C-2C-F-U-70, respectively. After cracking, the post-peak fatigue life of round panels C-1C-F-U-70 and C-2C-F-U-70 were 168,158 and 660,127 cycles, respectively. This indicates that the expected scatter due to uneven fibre distribution is with the range of expected scatter for concrete. The degree of scatter is attributed to the material variability of concrete tensile strength and fibre distribution. The difference of fatigue performance of both concrete and fibre components are accumulated, and this should be considered in design codes.

The sudden rapid increase of deflection and average crack width enlarging from one cycle to the subsequent one indicated the impending failure, meaning that the specimen was no longer capable to sustain the maximum load level and the envelope curve was approached. At this stage, the fatigue testing was stopped and monotonic loading was applied. Figures 3.105 and 3.106 demonstrate the residual load-displacement response of the failed specimens and crack width development after the completion of the cyclic load stage for specimens C-1C-F-U-70 and C-2C-F-U-70, respectively, with the static results of the non-cyclically loaded specimens.

The crack distribution and failure mode of the specimens C-1C-F-U-70 and C-2C-F-U-70 at the conclusion of the static test is shown in Figures 3.107 and 3.108, respectively. The failure mode is represented by the development of three fracture lines for round panel C-1C-F-U-70 and no major secondary cracks were observed. For specimen C-2C-F-U-70, it is observed from Figures 3.106(b) and 3.108 that cracks 1 and 3 were wider than crack 2. However, due to the small difference in crack width, it was concluded that the failure mode for this panel was by the development of three fracture lines as well.

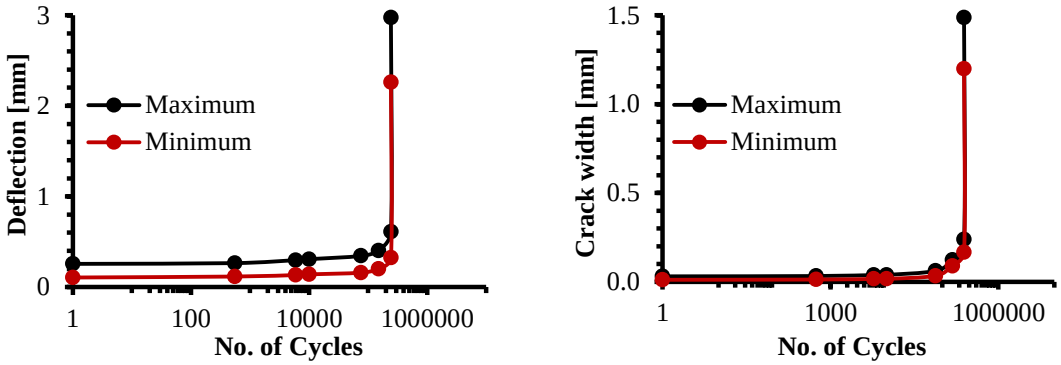

Figure 3.100 – Specimen C-1C-F-U-70: (a) load versus deflection; (b) load versus average crack width.

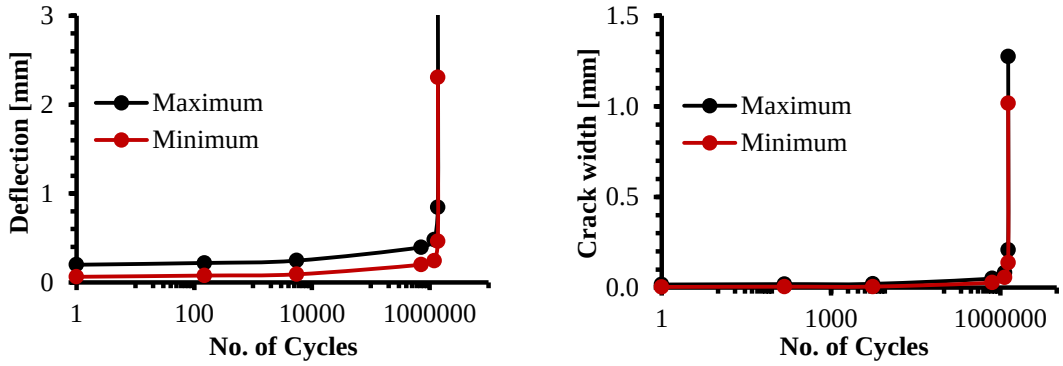

(a) (b)

Figure 3.101 – Specimen C-2C-F-U-70: (a) load versus deflection; (b) load versus average crack width.

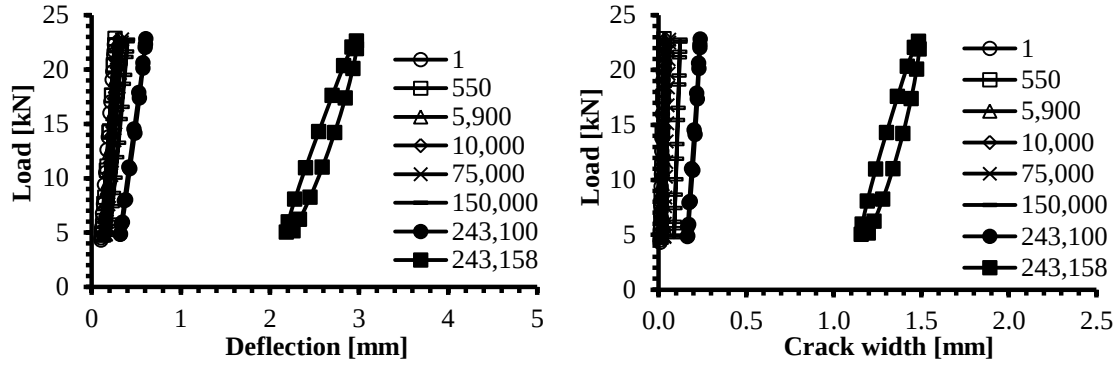

(a) (b)

Figure 3.102 – Load versus (a) deflection and (b) average crack width at various cycle intervals for specimen C-1C-F-U-70.

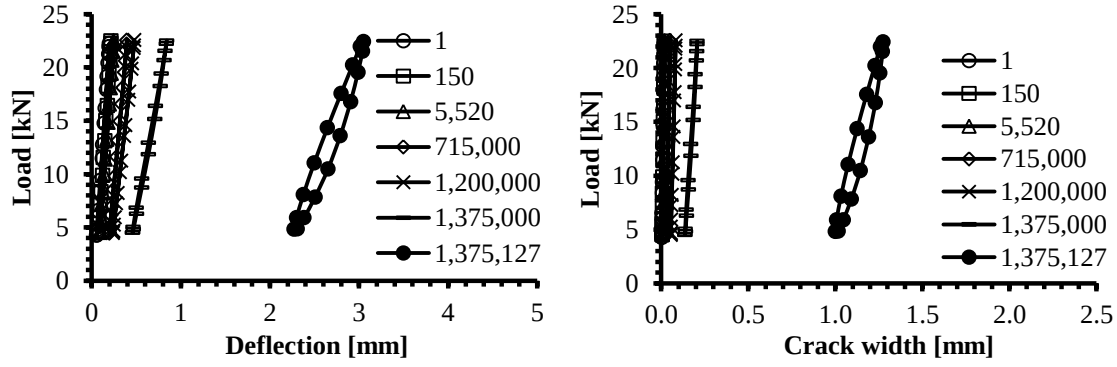

(a) (b)

Figure 3.103 – Load versus (a) deflection and (b) average crack width at various cycle intervals for specimen C-2C-F-U-70.

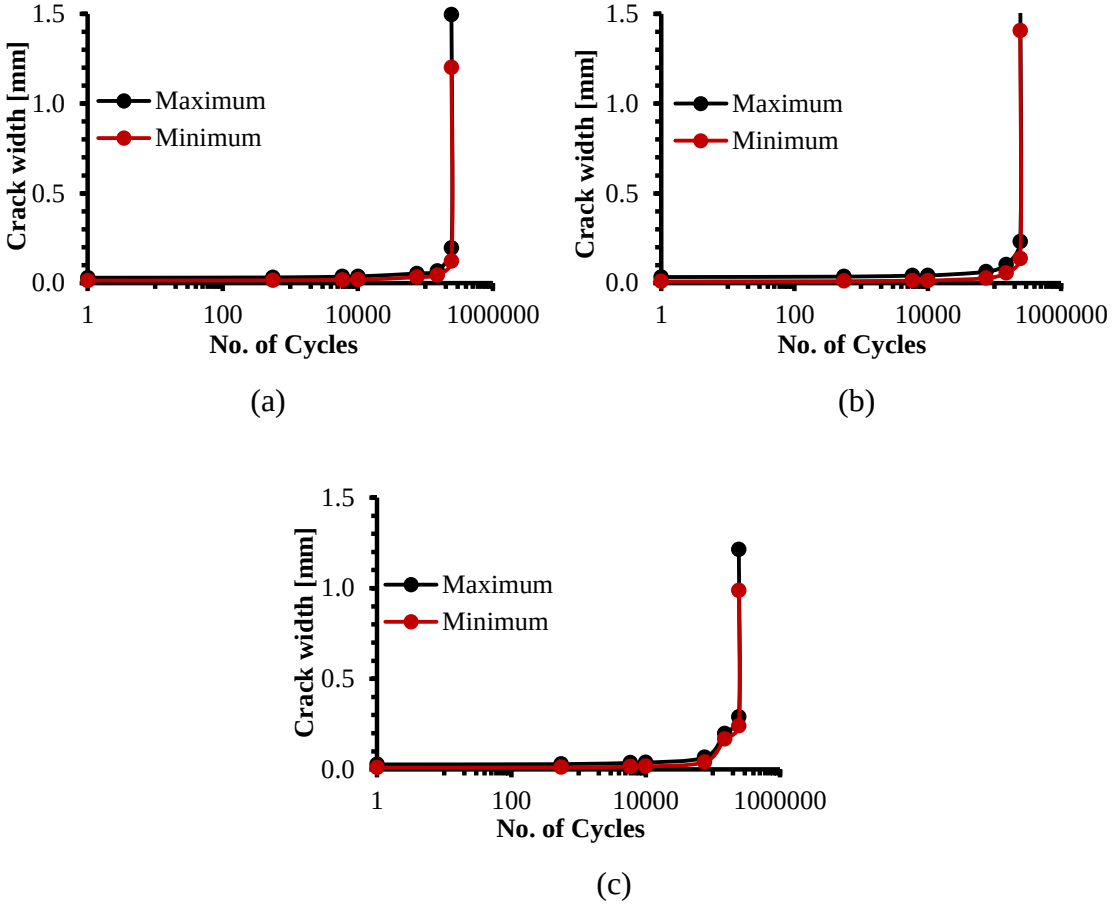

Figure 3.104 – Crack width versus number of cycles for round panel C-1C-F-U-70 (a) crack 1; (b) crack 2; (c) crack 3.

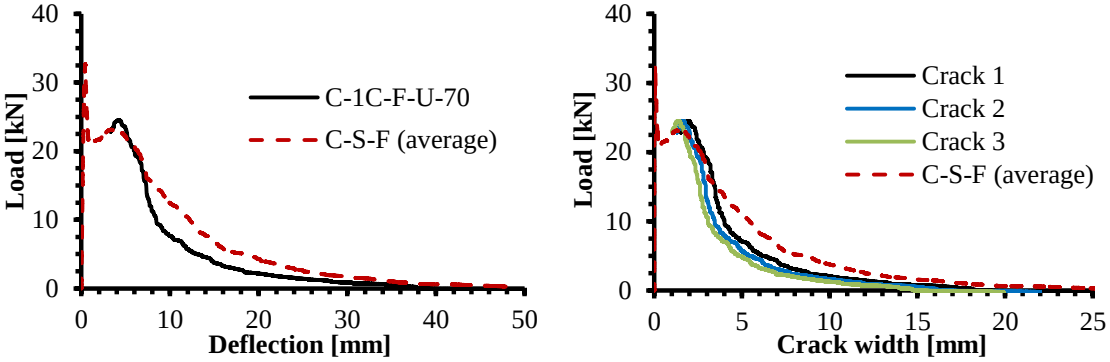

(a) (b)

Figure 3.105 – Static test result for round panel C-1C-F-U-70.

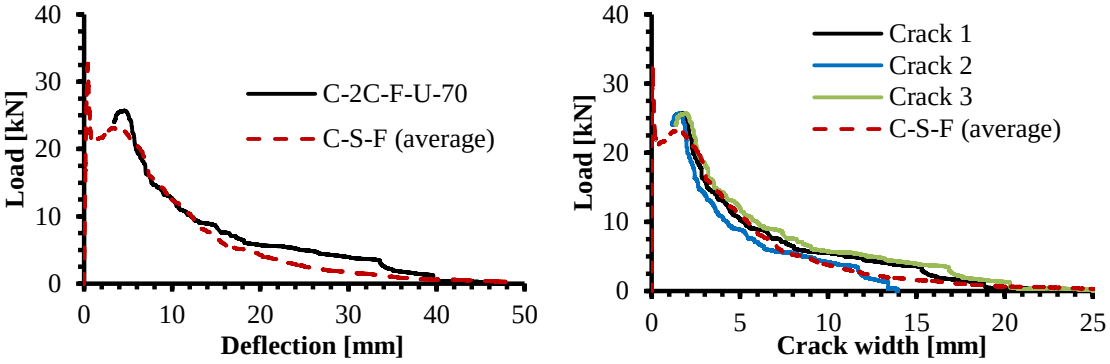

(a) (b)

Figure 3.106 – Static test result for round panel C-2C-F-U-70.

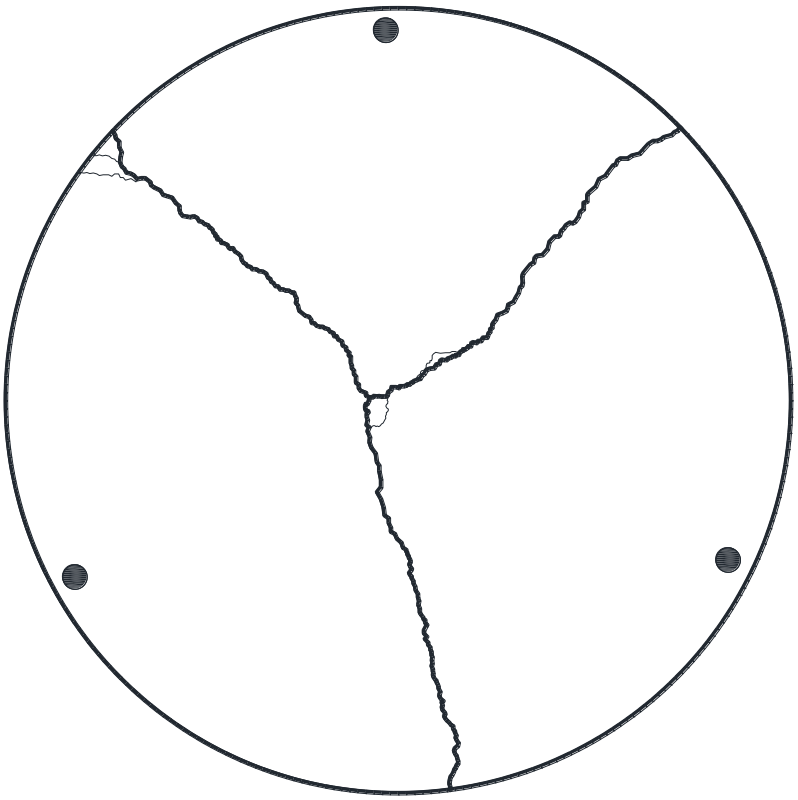

Figure 3.107 – Fracture lines of C-1C-F-U-70.

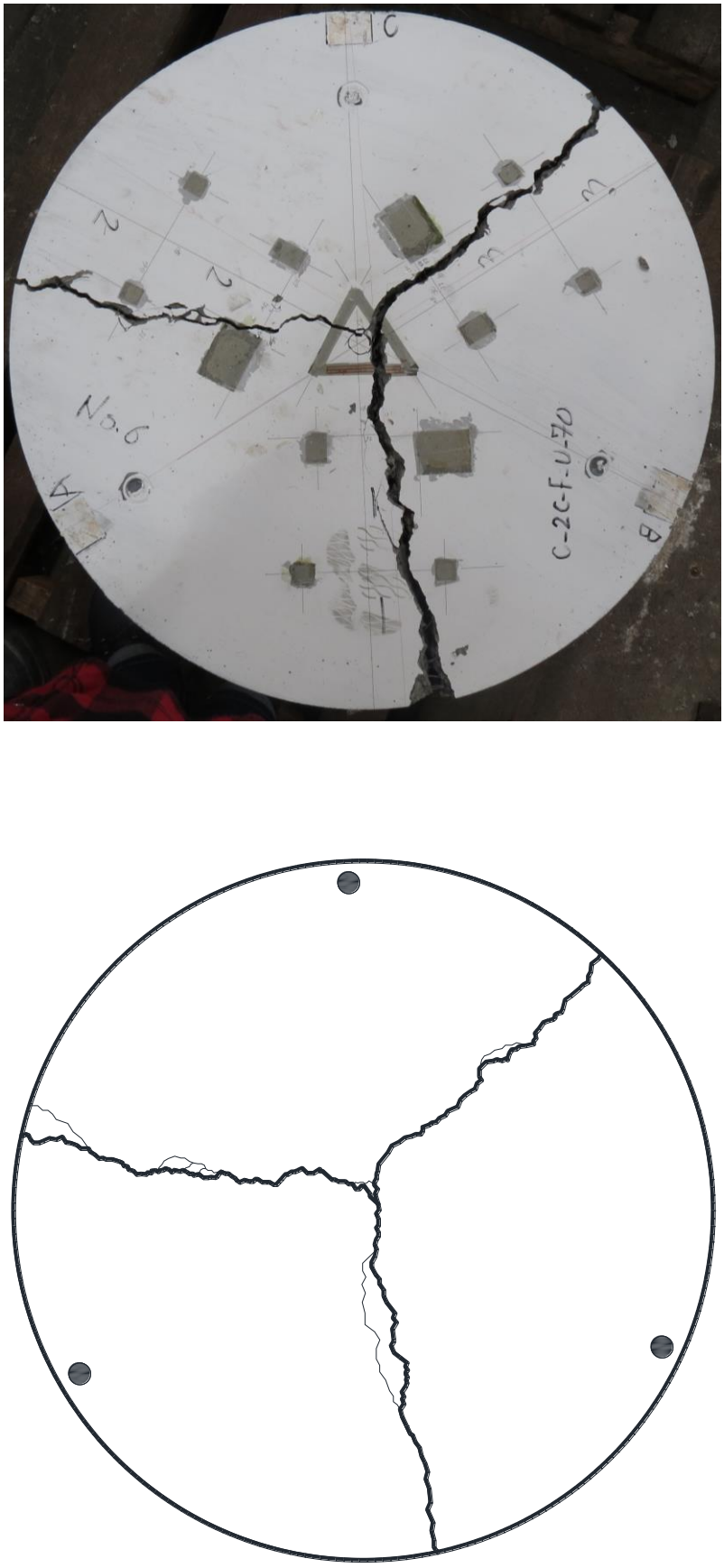

Figure 3.108 – Fracture lines of C-2C-F-U-70

Specimens C-1C-F-C-60 and C-2C-F-C-60

Specimens C-1C-F-C-60 and C-2C-F-C-60 were loaded monotonically until a crack width of 0.5 mm was developed, after which cyclic loading between 15% and 60% (from 4.1 kN to 17.5 kN for panel C-2C-F-C-60) of their own static capacity was applied at 3 Hz to determine the residual fatigue resistance. The fatigue life for the pre-cracked tested panel C-2C-F-C-60 was 5,868, while specimen C-1C-F-C-60 failed during loop tuning. This indicates that the specimen had negligible flexural capacity to withstand even a few cycles. Figure 3.109 shows the deflection and the average crack width development of the round panel C-2C-F-C-60 at both the maximum and minimum loads. Figure 3.110 shows load versus displacement and average crack width at various cycle intervals for specimen C-2C-F-C-60.

The central deflection of specimen C-2C-F-C-60 was 1.35 mm and 1.92 mm at minimum and maximum loads, respectively, and then increased at a steady rate for the first 4,000 cycles to reach 2.92 mm and 3.70 mm at minimum and maximum loads, respectively. A rapid deflection increase then followed indicating the impending failure.

The maximum and minimum average crack widths for specimen C-2C-F-C-60 at the first cycle were 0.68 mm and 0.51 mm, respectively. Following the deflection performance, a steady increase in average crack width was observed for the first 4,000 cycles with 1.13 mm and 1.41 mm minimum and maximum average crack widths, respectively. After that, a sudden increase in average crack enlarging was observed.

The sudden rapid increase of central deflection and average crack width enlarging from one cycle to the subsequent one indicated the impending failure, meaning that the specimen was no longer capable of sustaining the upper load level as the envelope curve was approached. The specimen failed very quickly and could not be saved to conduct a monotonic test.

The crack distribution and failure mode of the specimens C-1C-F-C-60 and C-2C-F-C-60 at the conclusion of the test is shown in Figures 3.111 and 3.112, respectively. The failure mode is represented by the development of three fracture lines for both round panels. No major secondary cracks were observed.

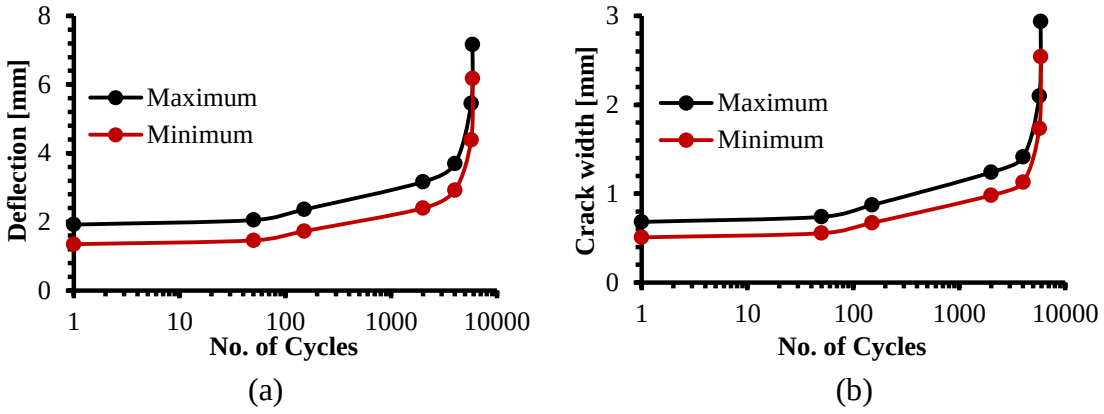

(a) (b)

Figure 3.109 – Specimen C-2C-F-C-60: (a) load versus deflection; (b) load versus average crack width.

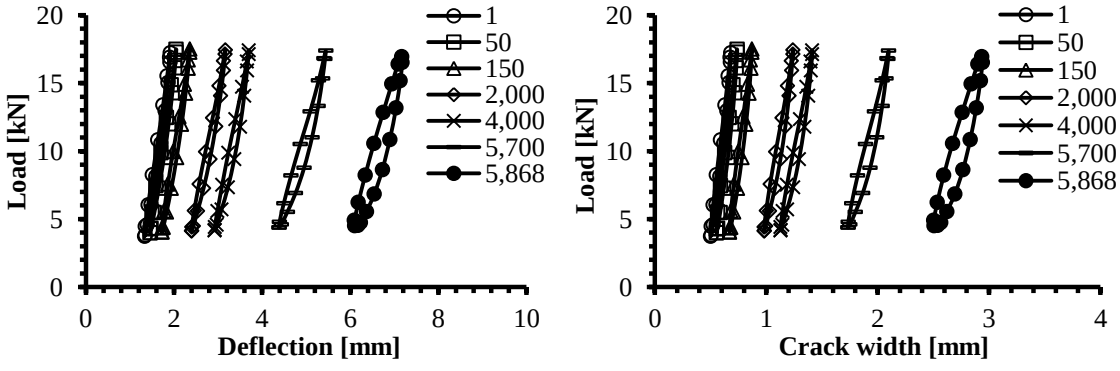

(a) (b)

Figure 3.110 – Load versus (a) deflection and (b) average crack width at various cycle intervals for specimen C-2C-F-C-60.

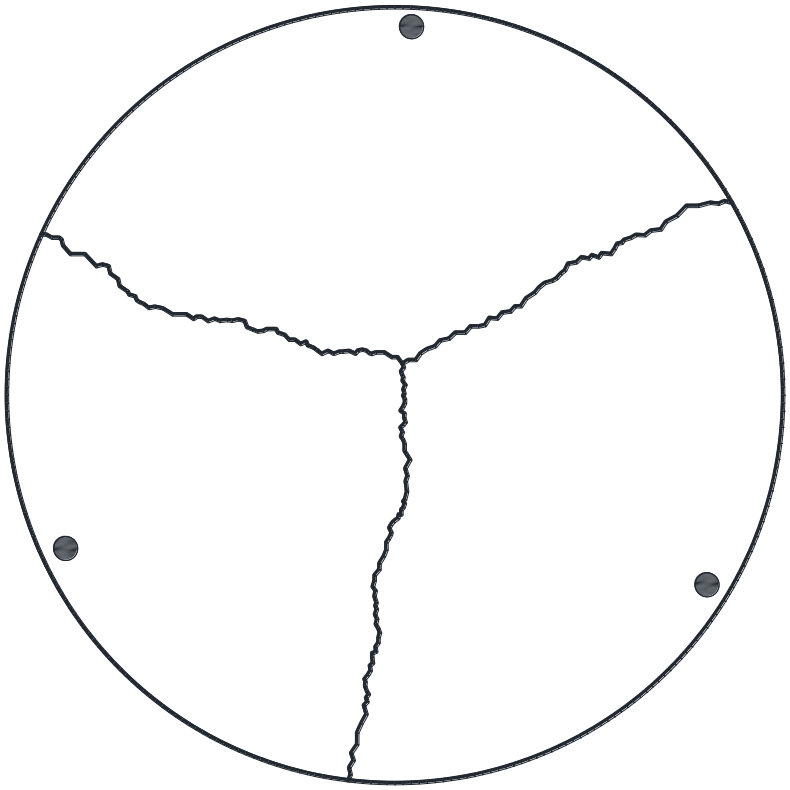

Figure 3.111 – Fracture lines of C-1C-F-C-60.

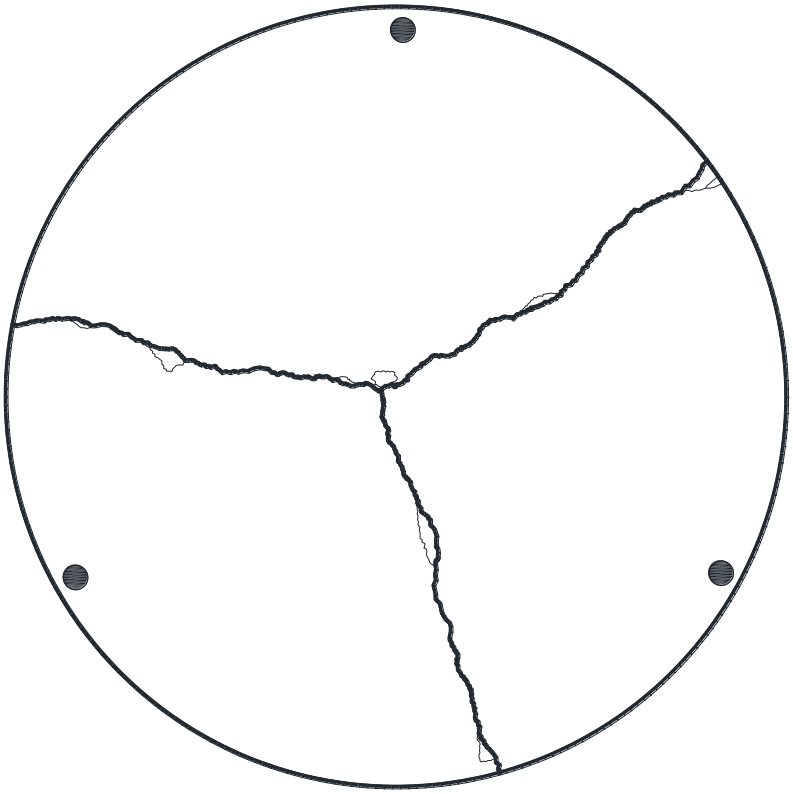

Figure 3.112 – Fracture lines of C-2C-F-C-60.

Specimen C-1C-F-C-40

Specimen C-1C-F-C-40 was loaded monotonically until a crack width of 0.5 mm was developed. Cyclic loading was then applied at a frequency of 3 Hz between 15% (4.4 kN) and 40% (11.3 kN) of its static capacity to determine the post-cracking fatigue performance. The central deflection and the average crack width development of the round panel at the maximum and minimum loads are presented in Figure 3.113. Load versus deflection and average crack width at various load cycles are displayed in Figure 3.114.

At the first cycle, the minimum and maximum deflections were 0.73 mm and 0.93 mm, respectively. This was followed by almost constant deflection for the first 100,000 cycles. After this, a steady increase in deflection was observed up to 0.93 mm and 1.17 mm at the minimum and maximum loads, respectively, at the completion of 3 million cycles.

For the average crack width development, specimen C-1C-F-C-40 had a minimum and maximum average crack width of 0.24 mm and 0.29 mm, respectively, at the first cycle. A negligible increase in average crack width was observed up to 100,000 cycles, after which a steady increase in the average crack width was observed, up to 0.31 mm and 0.38 mm at the minimum and maximum loads at 3 million cycles, respectively.

The specimen did not fail after 3 million cycles of testing. The specimen was then tested under static loading to determine its residual strength. The load-displacement response of failed specimen and crack width development of the static test are shown in Figure 3.115. The crack pattern at the conclusion of the static test is shown in Figure 3.116. The failure mode is represented by the development of three fracture lines; note that the failure line did not pass through the gauge zone for crack 2, as shown in Figure 3.115(b).

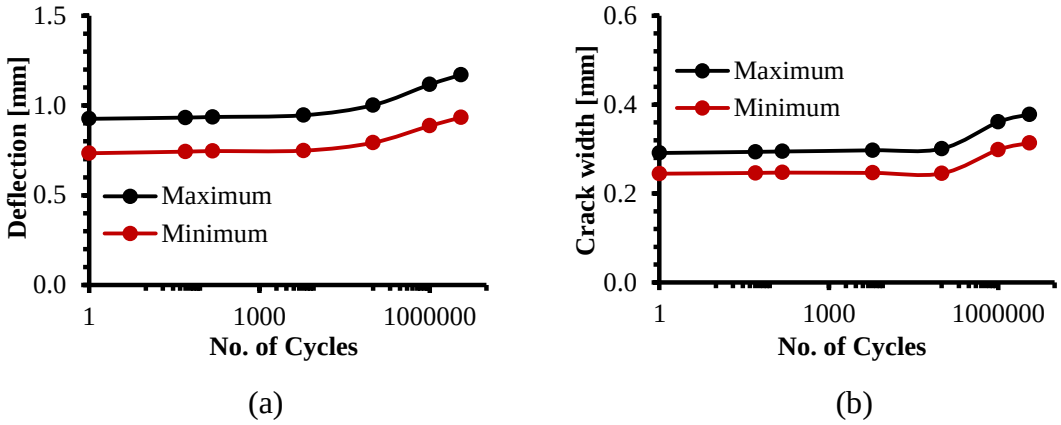

(a) (b)

Figure 3.113 – Specimen C-1C-F-C-40: (a) load versus deflection; (b) load versus average crack width.

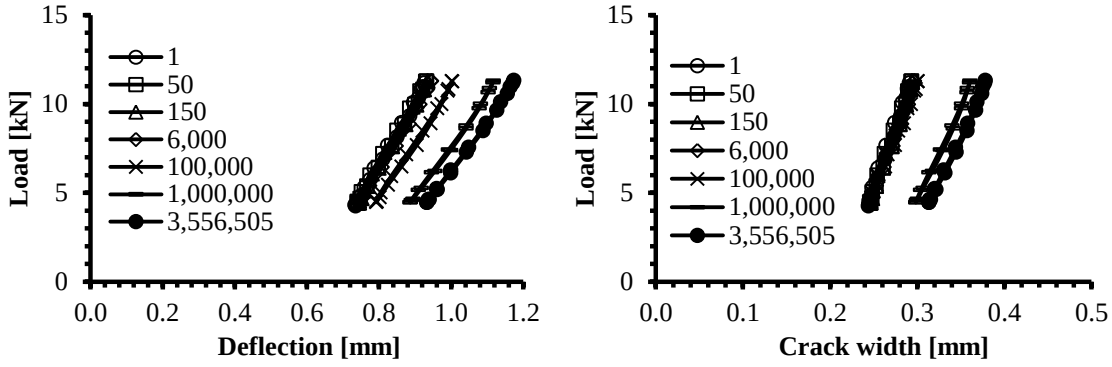

(a) (b)

Figure 3.114 – Load versus (a) deflection and (b) average crack width at various cycle intervals for specimen C-1C-F-C-40.

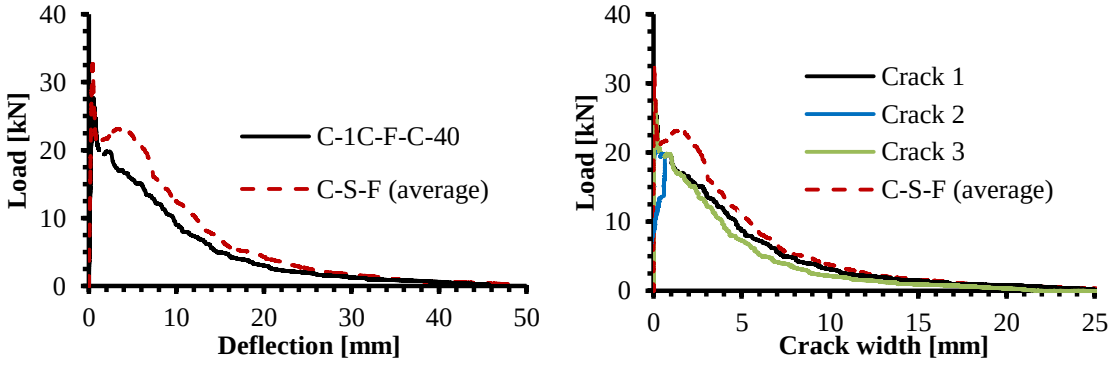

(a) (b)

Figure 3.115 – Static test result for round panel C-1C-F-C-40.

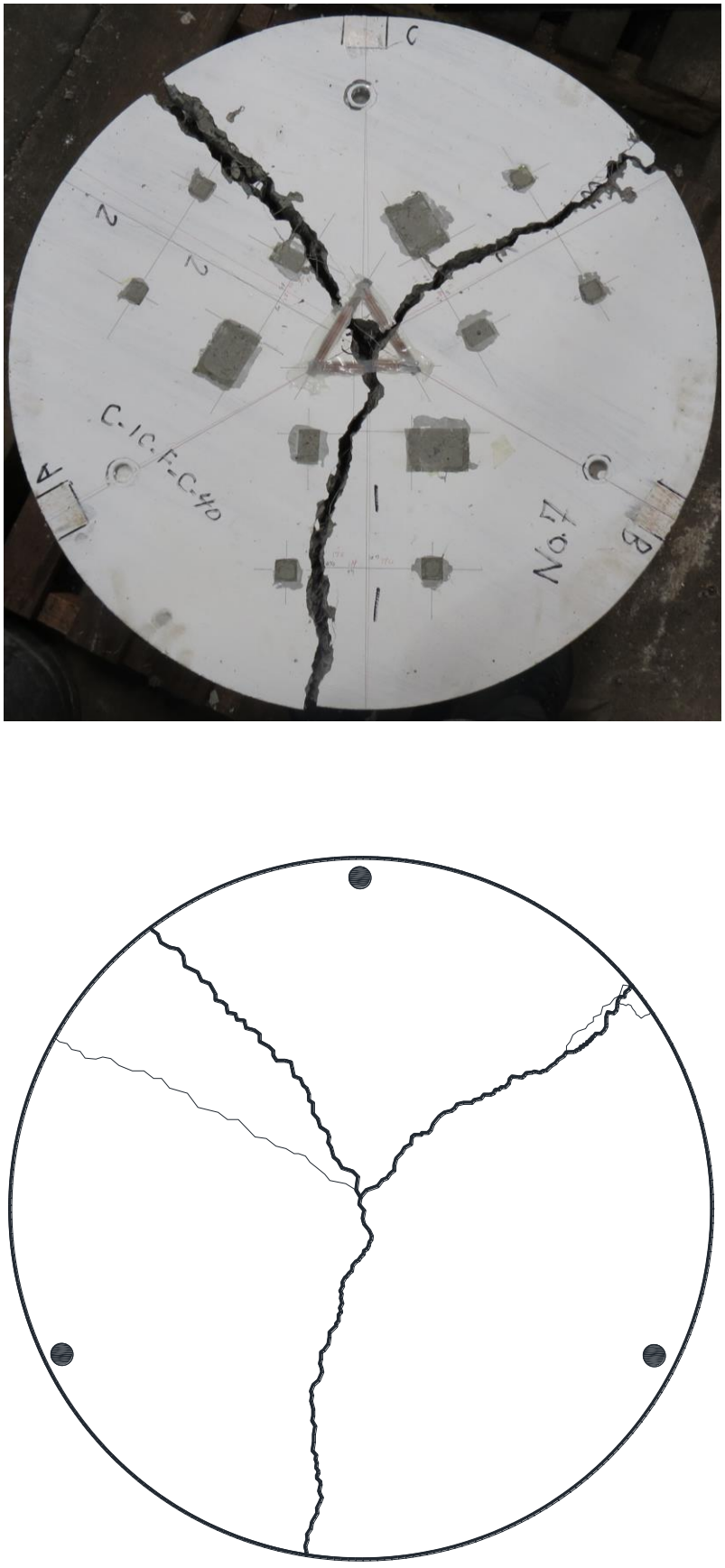

Figure 3.116 – Fracture lines of C-1C-F-C-40.

Specimens C-1C-F-C-50 and C-2C-F-C-50

Specimens C-1C-F-C-50 and C-2C-F-C-50 were loaded monotonically until a crack width of 0.5 mm was developed, after which cyclic loading between 15% and 50% (from 5.4 kN to 17.0 kN and from 4.8 kN to 15.7 kN for specimens C-1C-F-C-50 and C-2C-F-C-50, respectively) of their own static capacity was applied at 3 Hz to determine the residual fatigue resistance. A maximum load level of 50% was selected for these last two specimens due to the fact that pre-cracked specimens loaded with maximum load level of 60% had a very short life (< 6,000 cycles); the pre-cracked round panel with a maximum load level of 40% did not fail after three million cycles. Accordingly, it was expected that fatigue life of pre-cracked specimens, with a maximum load level of 50% would be somewhere between one and three million cycles. Specimen C-1C-F-C-50 did not fail after 10 million cycles; while the fatigue life for panel C-2C-F-C-50 was 1,617,982 cycles. Figures 3.117 and 3.118 show the deflection and the average crack width development of the round panels C-1C-F-C-50 and C-2C-F-C-50, respectively, at both maximum and minimum loads. Load versus deflection and average crack width at various load cycles are displayed in Figures 3.119 and 3.120, respectively.

At the first load cycle, specimen C-1C-F-C-50 had a minimum and maximum deflection of 0.77 mm and 1.03 mm, respectively. This was followed by almost constant deflection for the first 200,000 cycles, approximately. After this, a steady increase in deflection was observed up to 1.80 mm at the maximum load and 1.38 mm at the minimum load at 10 million cycles. Specimen C-1C-F-C-50 did not fail after the completion of 10 million cycles.

The central deflection of specimen C-2C-F-C-50 was 1.00 mm and 1.21 mm at minimum and maximum loads, respectively, this was followed by almost a constant deflection for the first 100,000 cycles, approximately. After that, the deflection increased steadily to reach 1.99 mm and 2.47 at minimum and maximum loads,

respectively, at 1,250,000 cycles (see Figure 3.120(a)). The deflection then increased at an accelerated rate to reach 4.01 mm and 4.63 mm at minimum and maximum loads, respectively, at 1,613,000 cycles. Within approximately another 5,000 cycles, the deflection increased dramatically to reach 6.37 mm and 6.90 mm during minimum and maximum loads, respectively, signalling the impending failure.

The minimum and maximum average crack widths for specimen C-1C-F-C-50 at the first cycle were 0.28 mm and 0.35 mm, respectively. No further development in average crack width was observed until 200,000 cycles. Consistent with the observed increase in deflection, the average crack width grew and widened steadily throughout the test to reach 0.56 mm and 0.68 mm at the minimum and maximum loads, respectively, at 10 million cycles (Figures 3.117(b) and 3.119(b)).

For specimen C-2C-F-C-50, the minimum and maximum average crack widths at the first cycle were 0.36 mm and 0.41 mm, respectively. After this, negligible increase in average crack width was observed up to 100,000 cycles. A steady increase in average crack width was then observed up to 0.77 mm and 0.92 mm at the minimum and maximum loads at 1,250,000 cycles. After that, and as shown in Figures 3.118(b) and 3.120(b), the rate on enlarging of average crack width accelerated to reach minimum and maximum average crack widths of 1.66 mm and 1.86 mm, respectively, at 1,613,000 cycles. This was followed by a rapid increase in average crack width to reach 2.70 mm and 2.88 mm at minimum and maximum loads, respectively, at 1,617,982, cycles signally imminent failure.

As outlined above round panel C-1C-F-C-50 did not fail after 10 million cycles of testing. The specimen was then tested under static loading to determine its residual strength. The load-displacement response of failed specimen and crack width development during the static test are shown in Figure 3.121. It is observed from Figure 3.121 that although the maximum applied load of 17.0 kN represented 60% of that of the static test, it had a significantly higher post-peak strength in the range of zero

to 6 mm of displacement. This explains the higher cyclic capacity, and the post-cracking peak strength is an important parameter for design. For panel C-2C-F-C-50, static load was applied at the conclusion of cycle 1,617,982. The load-displacement response of failed specimen and crack width development of the static test are presented in Figure 3.122 for specimen C-2C-F-C-50. Figure 3.122(b) shows that the failure cracks passed through the gauged region of crack 1 and 3 but not of 2.

The crack distribution and failure mode of the specimens C-1C-F-C-50 and C-2C-F-C-50 at the conclusion of the static test is shown in Figures 3.123 and 3.124, respectively. The failure mode is represented by the development of three fracture lines for both round panels with no major secondary cracks observed.

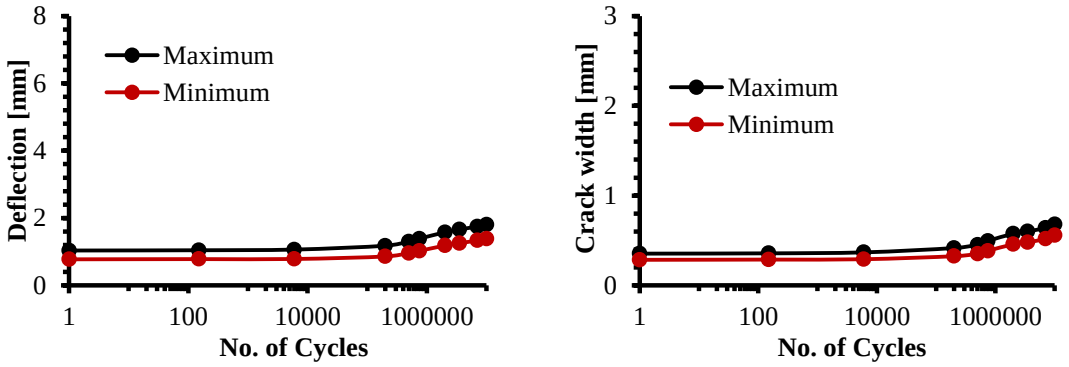

Figure 3.117 – Specimen C-1C-F-C-50: (a) load versus deflection; (b) load versus average crack width.

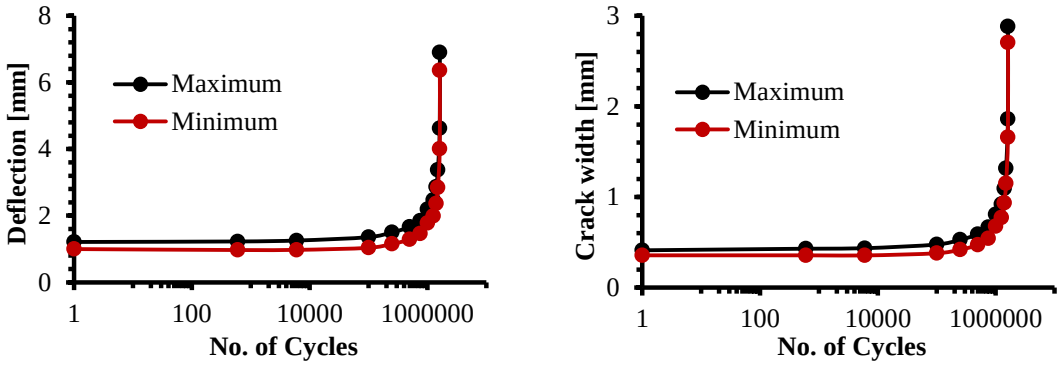

(a) (b)

Figure 3.118 – Specimen C-2C-F-C-50: (a) load versus deflection; (b) load versus average crack width.

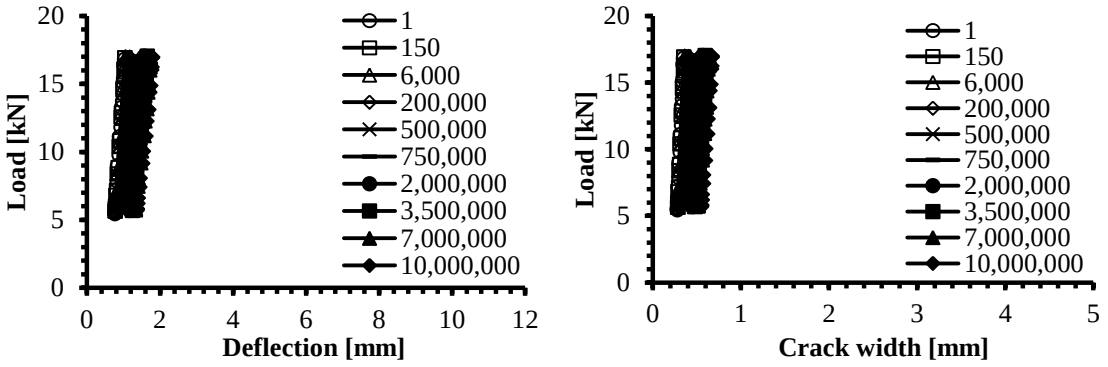

(a) (b)

Figure 3.119 – Load versus (a) deflection and (b) average crack width at various cycle intervals for specimen C-1C-F-C-50.

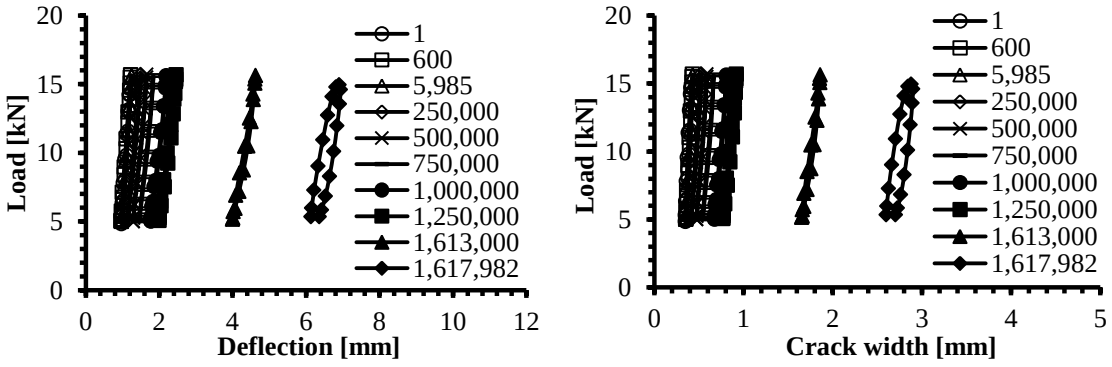

(a) (b)

Figure 3.120 – Load versus (a) deflection and (b) average crack width at various cycle intervals for specimen C-2C-F-C-50.

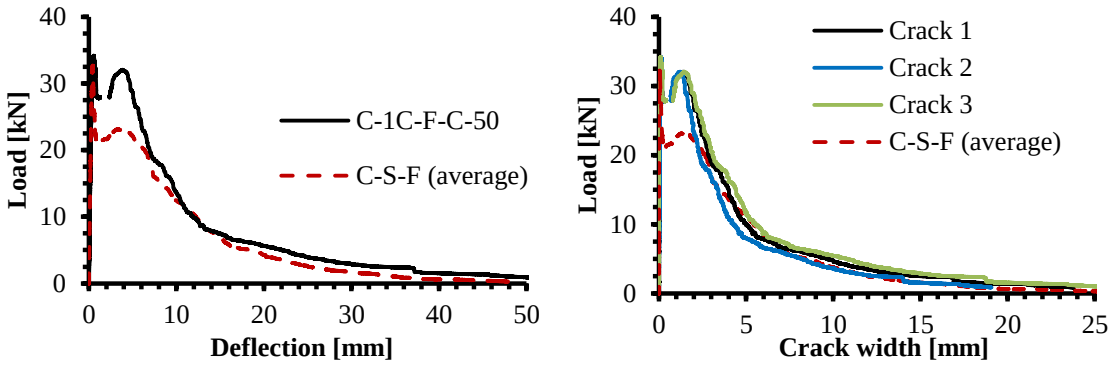

Figure 3.121 – Static test result for round panel C-1C-F-C-50.

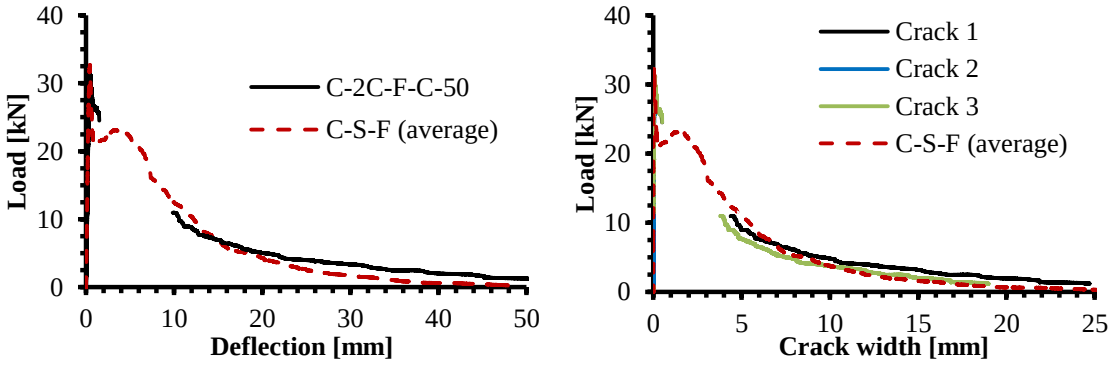

Figure 3.122 – Static test result for round panel C-2C-F-C-50.

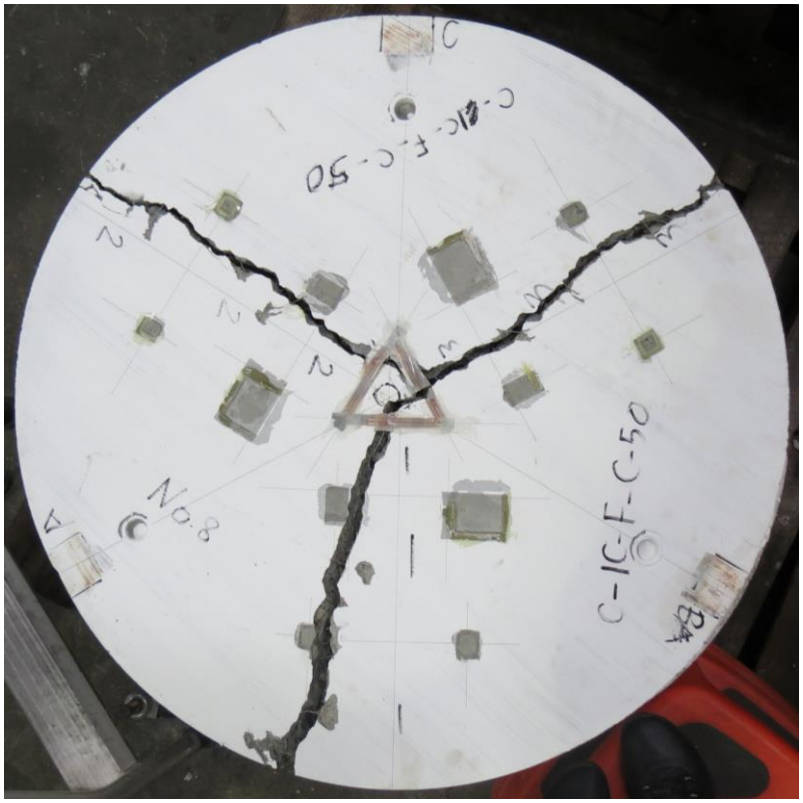

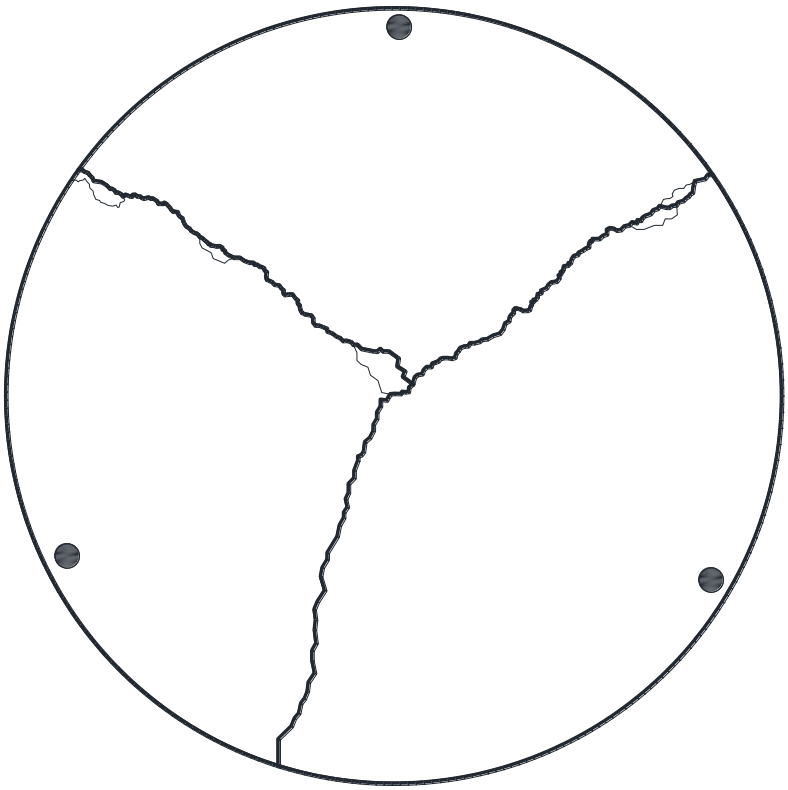

Figure 3.123 – Fracture lines of C-1C-F-C-50.

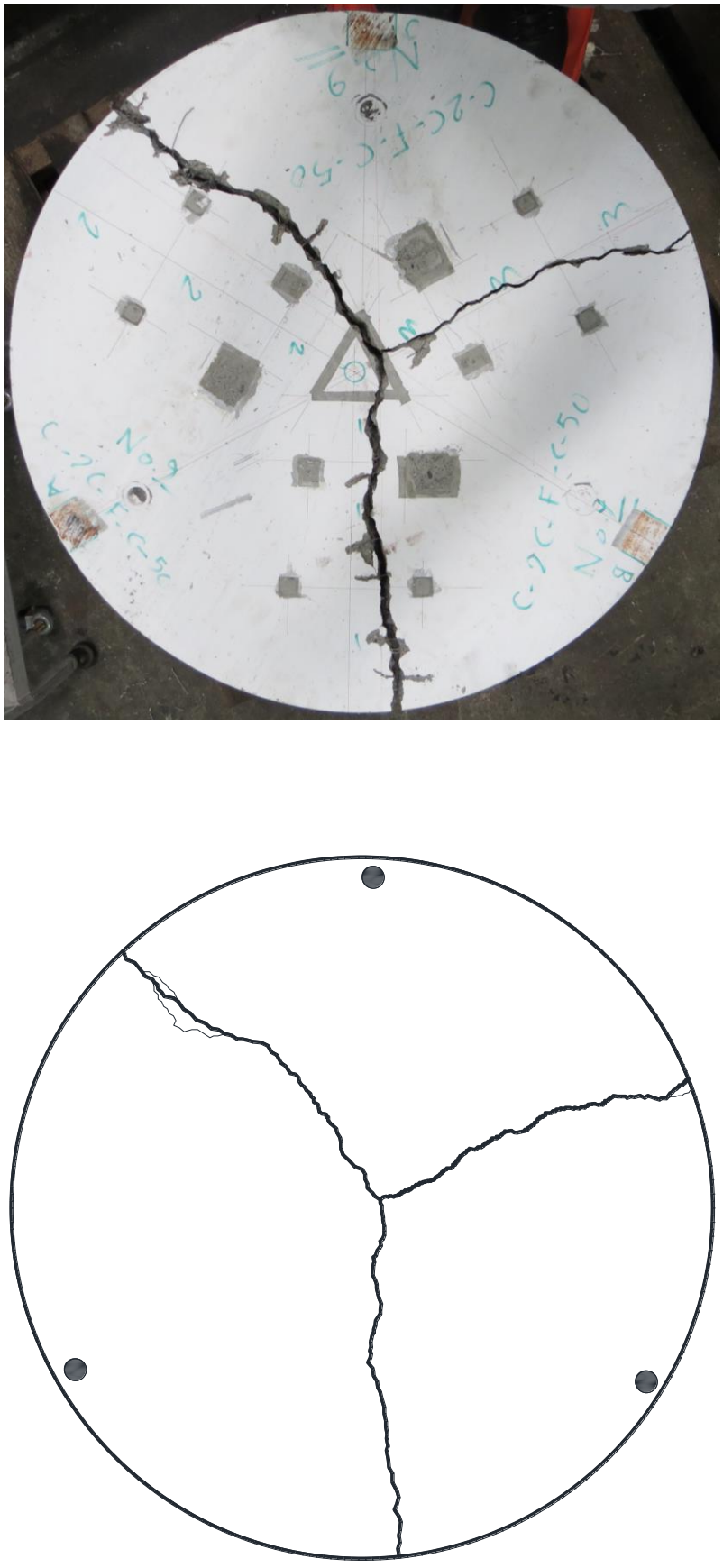

Figure 3.124 – Fracture lines of C-2C-F-C-50.

3.8. Envelope Curves

All un-failed specimens during fatigue loading were loaded monotonically to determine their residual strength. The load-displacement envelopes, of both failed and un-failed specimens, of the static test are shown in Figures 3.125 to 3.127 for Series A, B and C, respectively. The results are consistent for all series with higher scatter seen for Series A compared with Series B and C. This means that the post-fatigue static tests match the monotonic curves with a good agreement. As a result, it is concluded that the static load – displacement backbone curve is not influenced (i.e. not weakened) by the cyclic loading.

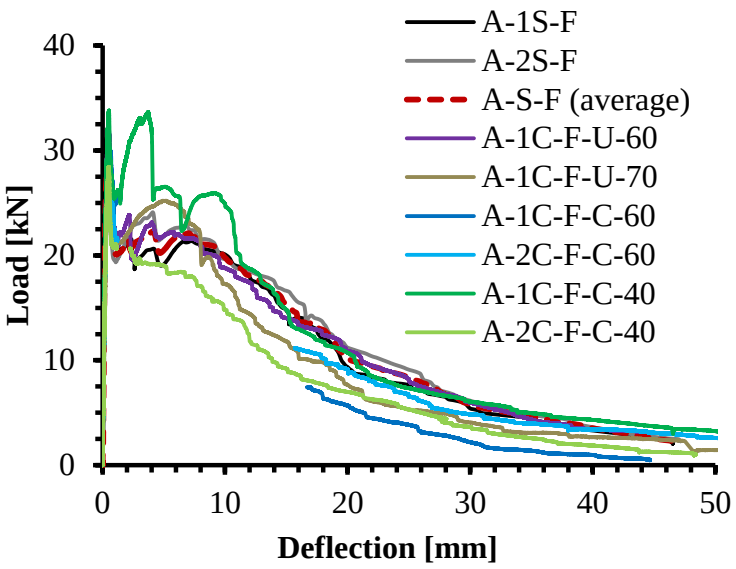

Figure 3.125 – Summary of the static envelope of Series A.

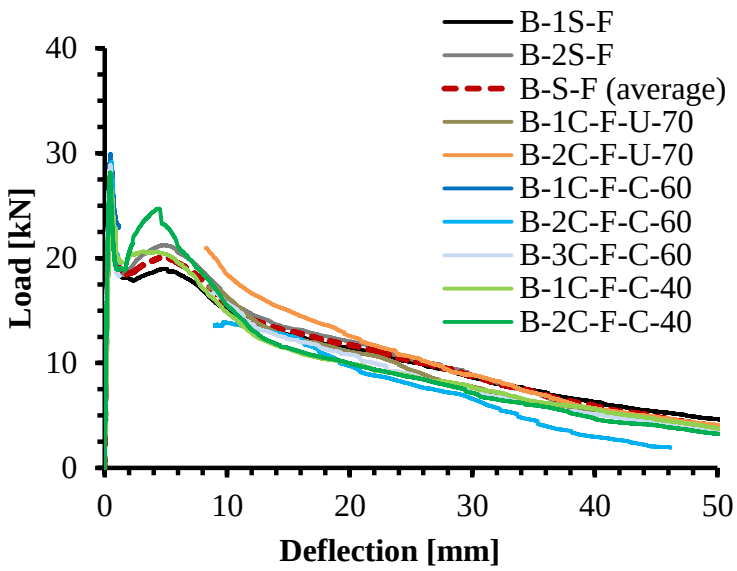

Figure 3.126 – Summary of the static envelope of Series B.

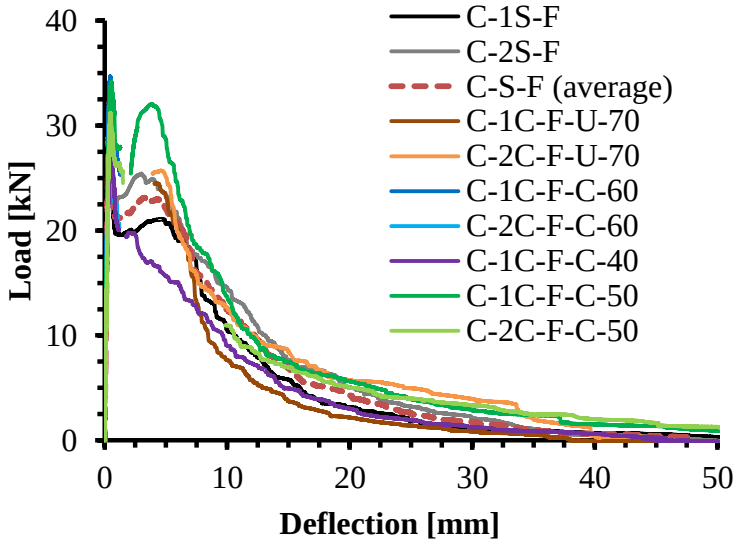

Figure 3.127 – Summary of the static envelope of Series C.

3.9. Summary and Concluding Remarks

A total of 27 round panels were cast and tested using three different SFRC mix designs to investigate the post-cracking and fatigue behaviour of steel fibre reinforced concrete, together with a series of matched direct uniaxial tension and prism bending tests were also undertaken to provide comprehensive material characterisation data. Two types of fatigue test were performed, the first on an uncracked specimen and the second on a pre-cracked specimen. The round panels were tested with different load levels. Experimental results show that the post-fatigue static test results match the monotonic curves with a good agreement. It is concluded that fibres improve the fatigue life of concrete and result in higher energy dissipation for all the load levels and fibre types considered in this study.

The predominately flexural failures in Series B and C were characterised by the formation of three radial cracks dividing the specimen into pie-shaped segments. Based on fracture line analysis, these flexural cracks correspond to the critical lines. However, the failure modes for Series A were inconsistent, where a varying number of cracks were produced. It is evident that the performance of the material is dependent on the fibre dispersion, particularly for the case of cyclic loading. In many cases a theoretically lower fracture energy line governed, assuming uniform fibre distribution. In addition, there is a tendency for a crack to propagate around the fibres as opposed to passing through them. This occasionally resulted in the propagation of secondary cracks emanating from primary cracks as the displacement or number of cycles increased, and multiple cracking was observed. This resulted in fluctuations in the beginning of load-displacement curve of some specimens.

In a specimen of 75 mm thick containing 60 mm long steel fibres, fibres can have a tendency to orientate in the direction of the plan of the specimen resulting in a 2D bias in the distribution. This reflects the limitations of this round panel test when long fibres

are used and a 3D orientation correction factor is required when considering thick applications.

Although multiple cracking was often observed, the ends of the majority of double hooked fibres had not straightened at the completion of testing. This is attributed to the increased mechanical bond of the 5D steel fibres coupled with their high tensile strength (2300 MPa). In addition, localised crushing of the concrete was observed around the fibres. The implication of this is that the increased anchorage of the fibre within the matrix induces high interfacial shear stresses between the fibres and the concrete matrix, especially where 20 mm aggregates are used.

Chapter 4 STRESS – COD MODEL FOR SFRC

4.1. Model for SFRC Material – Prism Bending

One of the difficulties in the development of reliable design models for SFRC structures is in establishing the characteristic tensile properties of the composite. The most important property when considering the design of a structural member manufactured with SFRC is its post cracking, or residual, tensile strength.

Before cracking, the representative behaviour of SFRC is generally represented by the tensile stress-strain response. After cracking, the behaviour is expressed in terms of the nominal stress versus crack opening displacement ($\sigma - w$) relationship (Figure 4.1). This relationship for SFRC can be directly obtained from a uniaxial tensile test. However, tensile testing is complex to perform and expensive.

Indirect methods have been proposed over the last three decades as an alternative to conducting uniaxial tensile testing to obtain the $\sigma - w$ relationship of SFRC, with three or four point prism bending tests typically adopted. One such method is the inverse analysis procedure and this approach has been investigated by a number of researchers (Uchida et al., 1995; Kooiman, 2000; de Oliveira e Sousa et al., 2002; di Prisco et al., 2009; Prisco et al., 2013; Amin et al., 2015; Foster et al., 2018).

For prism bending tests on strain softening materials, a single crack should occur to definitively characterise the flexural tensile behaviour of either notched or un-notched specimens, while applying load. Together with applied load either CMOD or mid-span deflection is recorded. From the results a tensile $\sigma - w$ curve is then inferred by means of an inverse analysis (Roelfstra and Wittmann, 1986; Uchida et al., 1995; Kitsutaka, 1997; Planas et al., 1999; de Oliveira e Sousa et al., 2002; Löfgren, 2005; di Prisco et al., 2009; Prisco et al., 2013; Amin et al., 2015; Foster et al., 2018). These inverse analysis procedures determine a theoretical softening curve that may be compared to

direct tension test data. Researchers have postulated multi-linear and exponential softening curves and determined their parameters by optimum fitting of load-deflection curves measured from stable tests of notched and un-notched specimens.

In this chapter, an enhanced model is developed for determining the $\sigma - w$ relationship for SFRC. The model is developed from Amin et al. (2015) and Foster et al. (2018) and enhanced by determining more accurately the depth to the neutral axis from the extreme compressive fibre. In this approach, the strength of a fibre reinforced composite (FRC), $\sigma(w)$, for a given crack opening displacement, COD, is obtained by a summation of its individual components (Figure 4.1); that is, the overall response of FRC is due to the combination strength of the unreinforced matrix, $\sigma_c(w)$, and the strength contribution of each individual fibre crossing the failure plane, $\sigma_f(w) = \sum_{i-1}^{n} \sigma_{fi}(w)$ where n is the number of fibre crossing the fracture surface. That is:

$$\sigma(w) = \sigma_c(w) + \sigma_f(w) \qquad (4.1)$$

In the development of this model, the following assumptions are made (Ng et al. 2012):

1. for fibres centred at more than one-half a fibre length away from a boundary, the geometric centres of the fibres are uniformly dispersed in space and all fibres have an equal probability of being oriented in any direction;
2. fibres centred at less than one-half a fibre length from a boundary are influenced by wall effects;
3. fibres that pulled out do so from the side of the crack with the shorter embedded length while the longer side of the fibre remains rigidly embedded in the matrix;
4. displacements due to elastic strains taking place within the fibres are small in comparison to the displacements arising from movement occurring between the fibres and the matrix; and
5. the energy expended by bending of fibres compared to that of pull-out of the fibres is small and can be neglected.

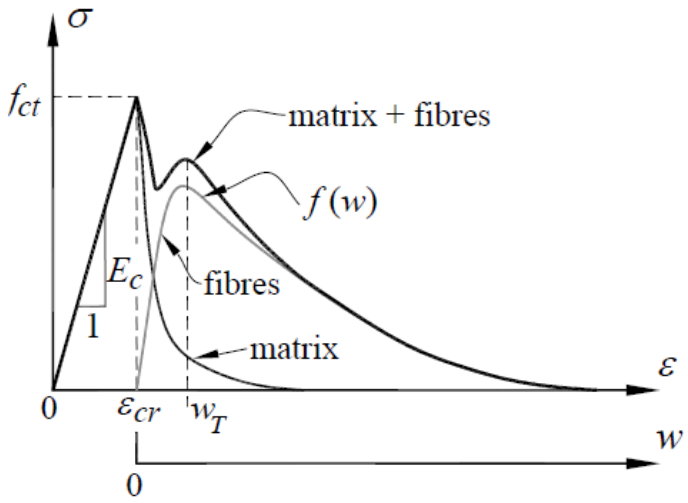

Figure 4.1 – Stress versus crack COD(w) for SFRC (Htut and Foster, 2010).

4.1.1. Matrix Component

For unreinforced concrete, the tension softening stress can be taken as (Voo and Foster, 2004; Lee and Foster, 2007; Lee and Foster, 2008, Voo and Foster, 2009; Htut and Foster, 2010):

$$\sigma_c(w) = c_1 f_{ct} e^{-c2w} \qquad (4.2)$$

where f_{ct} is the tensile strength of the concrete without fibre reinforcement and c_1 and c_2 are coefficients. The coefficient c_1 accounts for the beneficial effect of the fibres on the peak matrix strength while c_2 is a factor that controls the steepness of the descending branch and is influenced by the volume of fibres, the cementitious matrix composition, as well as the strength of the unreinforced matrix. For Mode I fracture, Voo and Foster (2003, 2004, 2009), Htut (2010), Htut and Foster (2010) and Lee et al. (2011) adopted c_1 as unity. In contrast, c_1 is taken as $1 + 72\rho_f$ for Mode II fracture (Lee and Foster, 2007; Lee and Foster, 2008; Htut, 2010; Htut and Foster, 2010).

The c_2 coefficient is dependent on the fibre volume concentration in the composite. Ng et al. (2012) proposed that:

$c_2 = 30/(1 + 100\rho_f)$ …. for mortar and concrete with $d_g \leq 10$ mm (4. 3a)

$c_2 = 20/(1 + 100\rho_f)$ …. for concrete with $d_g > 10$ mm (4.3b)

where d_g is the maximum size of the aggregate particles.

4.1.2. Fibre Component

Figures 4.2 and 4.3 illustrate the cross-section for a notched and un-notched SFRC prisms cracked in bending, respectively, where D is the total depth of the prism, h_{sp} is the depth minus the notch depth, d_n is the depth from the extreme compressive fibre to the neutral axis and b is the width of the prism. On the compressive side, the neutral axis rises in the section as the crack opens. On initial cracking, the stress block is linear and becomes increasingly more non-linear as the crack mouth opening displacement (CMOD) or deflection increases. The lever arm, z, is insensitive to the shape of the compressive stress block; however, it is sufficiently accurate to assume the stress block to be linear throughout the analysis.

For a small length on the tensile side of the neutral axis, the concrete is uncracked and carries tension. At greater distances from the neutral axis, the concrete is cracked and the steel fibres carry a tensile stress, f_w, which corresponds to a direct tensile stress for a crack opening, w, at the level in the section under consideration.

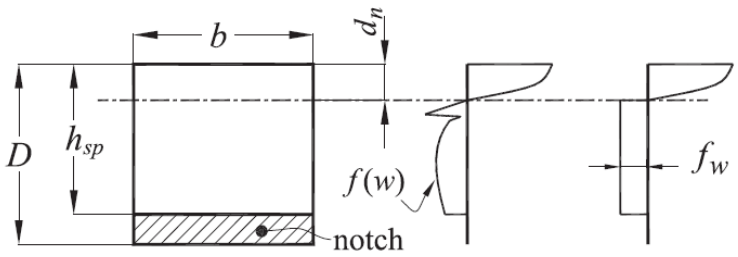

(a) Section (b) Sectional Stresses (c) Simplified Model

Figure 4.2 – Model for inverse analysis of $\sigma - w$ curve from notched prism bending tests (Amin et al., 2015).

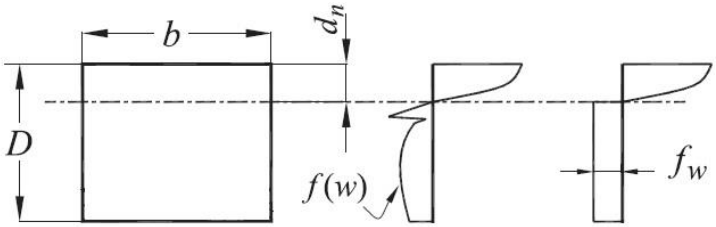

(a) Section (b) Sectional Stresses (c) Simplified Model

Figure 4.3 – Model for inverse analysis of $\sigma - w$ curve from un-notched prism bending tests.

For notched prisms, Amin et al. (2015) denoted the stress on the $\sigma - w$ curve for the average crack opening displacement between the root of the notch and the crack tip as f_w, and may be calculated from:

$$f_w = \frac{kFa}{h_{sp}^2 b} \tag{4.4}$$

where k is a function of d_n/h_{sp}, F is the externally applied force and a is the shear span (see Figure 4.4). The value k is determined from:

$$k = \frac{3}{[3.9 - (0.85 + \alpha)\beta]\beta} \tag{4.5}$$

where $\beta = 1 - d_n/h_{sp}$ and α is a factor. Amin et al. (2015) suggested taking $\alpha = 0.2$.

For un-notched prisms, Foster et al. (2018) denoted the stress on the $\sigma - w$ curve for the average crack opening displacement between the base of the prism and the crack tip as, f_w, and is calculated as:

$$f_w = \frac{Fa}{b[D - d_n][D + 0.2d_n]} \tag{4.6}$$

To determine the crack opening displacement corresponding to the calculated value of, f_w, the following assumptions are made:

(i) rigid body rotations of the two prism halves centred about the crack tip; and

(ii) failure of the prism occurs along a single dominant crack – as is the case for strain softening materials.

The COD(w) for the proposed $\sigma - w$ curve relationship is obtained from the measured crack mouth opening displacement as demonstrated in Equation 4.7 and shown in Figure 4.5. For notched prisms:

$$w = \frac{CMOD}{2} \times \frac{(h_{sp} - d_n)}{(D - d_n)} \qquad (4.7)$$

For un-notched prisms, the method of Vandewalle and Dupont (2003) is used to convert the vertical displacement, measured at mid-span, to the CMODs, then to w as shown below:

$$w = \frac{CMOD}{2} = \frac{2\delta}{L}(D - d_n) \qquad (4.8)$$

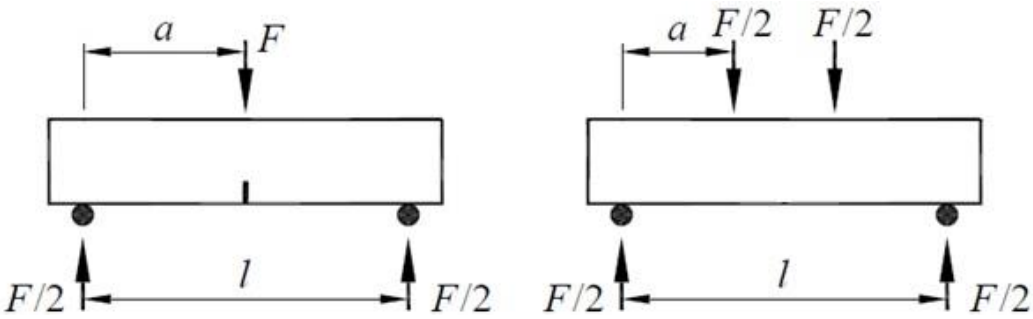

3-point bending 4-point bending

Figure 4.4 – Forces applied to three-point and four-point bending prism specimens.

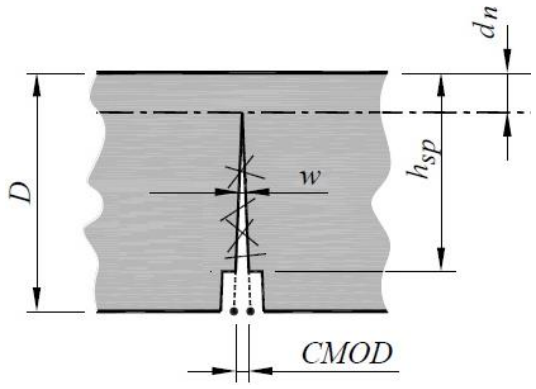

Figure 4.5 – Cracked section in SFRC prism in bending.

In the prism tests, it is important to recognize that at the early stages of the test after the matrix has cracked, the matrix component is significant when interpreting the resulting moment versus COD response. At later stages of the test, the neutral axis rises higher up the cross section and the influence of the matrix component is less significant and the stress carried by the fibres may be obtained from Equation (4.1) taking $\sigma_f(w) = f_w$ for the COD(w) given by Equation (4.7) or (4.8). This response is depicted in Figure 4.6, with a transition zone taken between the cracking point, COD_0, and a point COD_T where the influence of the uncracked concrete on the moment-COD response may be considered as insignificant.

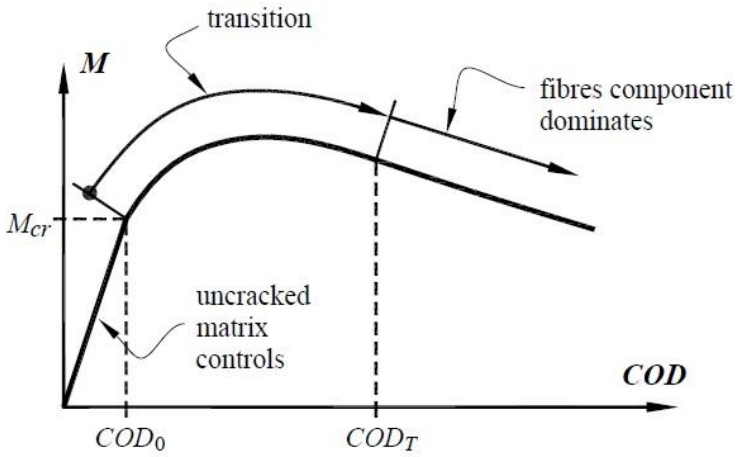

Figure 4.6 – Simplified approach for the transition in the moment-COD response of the prism test being influenced by the uncracked concrete component to the stress block to the point where the uncracked concrete component is non-significant (Amin et al., 2015).

Voo and Foster (2004) and Foster et al. (2006) observed that the take-up, or engagement, of fibres is delayed from the initial point of cracking, with the length of the delay dependent on the angle of a fibre with respect to the cracking plane and with the complete response determined by integrating the individual fibre responses over a given area. The result of this is a progressive take up of the fibres component from the initial point of cracking to a peak, as shown in Figure 4.1. To develop the first part of the curve, the fibres component can be taken as:

$$\sigma_f(w) = \xi(w) f_w \qquad (4.9)$$

where f_w is obtained from Equations (4.4) or (4.6) and $\xi(w)$ is a transition function. Amin et al. (2015) proposed an elliptical transition function for the transition:

$$\xi(w) = \begin{cases} \sqrt{1 - \dfrac{(w_T - w)^2}{w_T^2}}, & w < w_T \\ 1 \quad , & w \geq w_T \end{cases} \qquad (4.10)$$

where w_T (see Figure 4.1) is the point on the $\sigma - w$ curve where the fibres have achieved their maximum effectiveness. It is noted that this transition influences only the initial part of the response after cracking and is not overly significant in the development of a design approach for the determination of the residual direct tensile strength from prism bending tests.

4.1.3. Fibre-Boundary Influence Factor

Before comparing the results from the inverse analysis of the bending tests, both the uniaxial and prism bending test data need to be compensated for the boundary (wall) effect. In terms of three dimensions, the presence of a boundary restricts a fibre from being freely orientated and limits the fibre angle. This is referred to as the boundary effect and is portrayed in Figure 4.7 (Romualdi and Mandel, 1964; Aveston and Kelly, 1973; Stroeven, 2009; Lee et al., 2011; Ng et al., 2012).

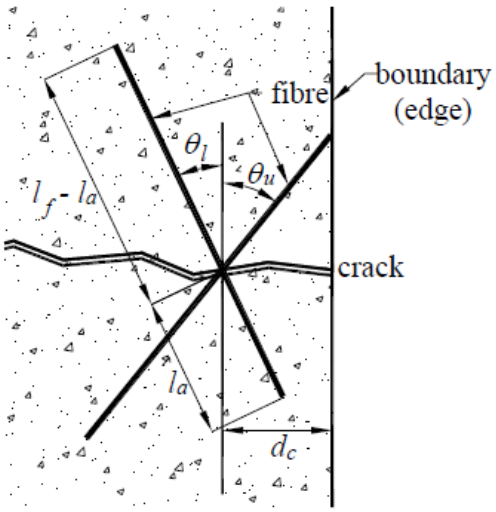

Figure 4.7 – The effect of a boundary on the fibre inclination angle (Voo and Foster, 2009).

An orientation factor, $k_{3D,b}$, may be applied to the uniaxial tension test results to remove this influence, thus converting the results to that of an equivalent 3D fibre distribution free of boundary factors. For an element approximately square in section and tested in tension, as is the case in this study, the boundary influence found in Lee et al. (2011) can be approximated as:

$$k_{3D,b} = 0.5 \leq \frac{1}{0.94 + 0.6\, l_f / b} \leq 1.0 \qquad (4.11)$$

Limits on the orientation that fibres may take when located near a specimen's boundary influences the test's performance, and this is the case whether testing in direct tension or indirect tension and applying inverse analysis. Fibres located within a distance of one-half of their length from the boundary have a restricted orientation. However, design models largely assume a 3D random orientation for fibres; whereas, in the immediate vicinity of a planar boundary, or wall, fibres are orientated in two-dimensions (2D). An orientation factor, k_b, is to be applied to the prism test results to remove this influence, converting the results to that of an equivalent 3D fibre distribution free of boundary influence.

For the notched prism tests, the wall effect is largely mitigated by the influence of the notch at the bottom and by the compressive region at the top; in this case only the side walls provide significant influence and the wall effect can be approximated as a 2D problem (Figure 4.8). For the case of notched prism tests, provided that $l_f/b \leq 1$, the boundary influence factor may be adapted from the 2D approximation of Ng et al. (2012) as:

$$k_b = \frac{\pi}{3.1 + 0.6\, l_f/b} \leq 1.0 \qquad (4.12)$$

For the case of prism bending tests conducted to ASTM C1609 (2006), the boundary at the extreme tensile fibre influences not just the force but also the internal moment, due to its effect on the moment lever arm (Figure 4.9). For $l_f/b \leq 1$ and $b = D$, the boundary factor is thus determined by Foster et al. (2018) as:

$$k_b = \frac{\pi}{3.1 + 1.1\, l_f/b} \leq 1.0 \qquad (4.13)$$

4.1.4. Notch Effect

It is well understood that the presence of dominant notch influences the behaviour of prism bending result (Foster et al., 2013). In this context a notch coefficient (k_n) is introduced that is determined through testing (Foster et al., 2013). The coefficient k_n accounts for the influence of the notch on defining the crack path and the resulting influence on the measured tensile strength, as described in Foster et al. (2013). For the case of un-notched specimens, the critical crack will find a path of least resistance and failure occurs at sections where fibre distributions are at their lowest and, thus, the equivalent fibre dosage at the failure section is less than the average fibre dosage for the specimen. Whereas for notched specimens, the location of the failure plane is predefined by the location of the notch. In this case the fibre volume fraction at the failure section will, on average, equal the supplied fibre dosage for the specimen. Foster et al. (2013) suggested $k_n = 1.0$ for un-notched prism tests (e.g., ASTM C1609 2006), whereas; to convert the results of notched prism tests to that of un-notched uniaxial tensile tests, Htut (2010) and Foster et al. (2013) found $k_n = 0.82$.

4.1.5. Influence of Casting Bias

It is well accepted that the orientation of steel fibres is influenced by the direction of flow of fresh concrete within the specimens (Barnett et al., 2010). Previous research showed that distribution and orientation of the steel fibres in SFRC can have a considerable effect on its mechanical properties (Ferrara and Meda, 2006; Kim et al., 2008; Pansuk et al., 2008). These effects must be addressed for structural applications where variation of fibre distribution in large sections may result in considerable variability in mechanical properties within the section (AFGC, 2002). Specimen size indirectly affects the orientation of fibres since they are forced to align along moulded surfaces (Dupont and Vandewalle, 2005). Consequently, the coefficient k_c represents the horizontal bias in the orientation of fibres due to casting of small scale specimens (prisms). Foster et al. (2018) recommended taking the casting factor $k_c = 0.8$, assuming

a light degree of fibre alignment with the longitudinal axis of the specimens during vibration.

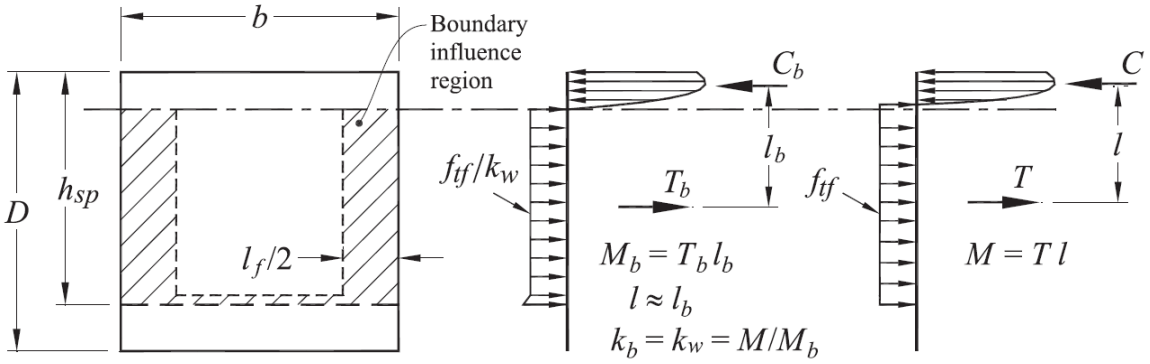

(a) Section (b) Sectional Stresses (c) Simplified Model

Figure 4.8 – Determination of boundary influence factor for notched prism bending tests (Foster et al., 2018).

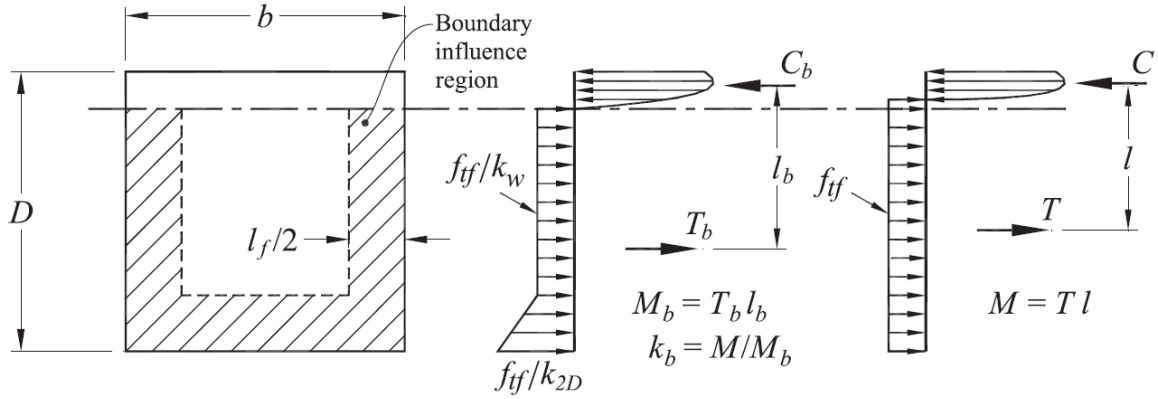

(a) Section (b) Sectional Stresses (c) Simplified Model

Figure 4.9 – Determination of boundary influence factor for prism bending tests without notches (Foster et al., 2018).

4.1.6. Neutral Axis Location

Figures 4.10 to 4.13 show the propagation of the neutral axis for both notched and un-notched prisms. As can be seen from the figures, the neutral axis depth starts with a value equal to one half of the cross section depth; $0.5h_{sp}$ for notched prism bending tests and $0.5D$ for un-notched prism bending tests. This is followed with a gradual decrease until a plateau, of $0.07h_{sp}$ for notched prism bending tests and $0.07D$ for un-notched prism bending tests, is reached. These values represent the asymptotes of the curves.

DataFit software (Oakdale Engineering) was used to develop equation for the development of the neutral axis from test measurements with emphasis on the following conditions:

For notched prisms (Figures 4.10 and 4.11):

$$d_n = 0.5h_{sp} \text{ when } CMOD = 0 \text{ and} \tag{4.14a}$$

$$d_n \to 0.07h_{sp} \text{ as } CMOD \to \infty \tag{4.14b}$$

accordingly;

$$d_n = 0.5h_{sp} \times e^{\frac{-\alpha CMOD}{CMOD+\beta}} \tag{4.15}$$

For un-notched prisms (Figures 4.12 and 4.13):

$$d_n = 0.5D \text{ when } \delta \leq \delta_1 \text{ and} \tag{4.16a}$$

$$d_n \to 0.07\text{D as } \delta \to \infty \tag{4.16b}$$

accordingly;

$$d_n = \begin{cases} 0.5D & , \quad \delta < \delta_1 \\ 0.5D \times e^{\frac{-\alpha(\delta-\delta_1)}{\delta-\beta}} & , \quad \delta \geq \delta_1 \end{cases} \tag{4.17}$$

where α and β are coefficients. The coefficient α accounts towards the asymptote value of the curve and it contributes towards the neutral axis depth at failure, while β is a factor that controls the steepness of the descending branch and is influenced by the volume of fibres, the cementitious matrix composition, as well as the strength of the unreinforced matrix. The asymptote factor may be taken as $\alpha = 2.2$, assuming a neutral axis depth of 7% of the depth of the notched or un-notched specimen, i.e. $0.07h_{sp}$ for notched prism bending tests and $0.07D$ for un-notched prism bending tests. The factor β can be taken as 0.25 and 0.1 for EN 14651 (2007) and ASTM C1609 (2006) prism bending tests, respectively.

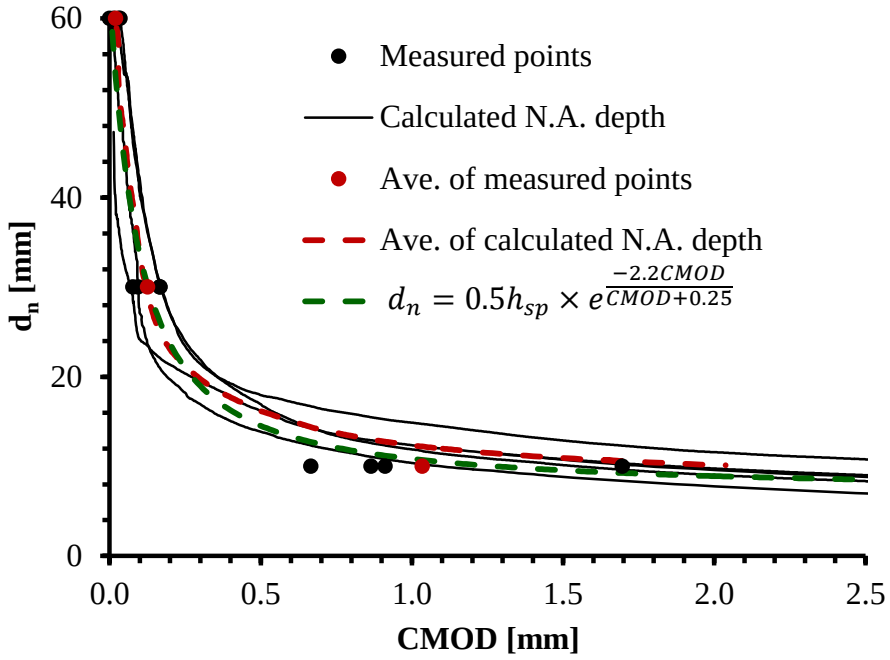

Figure 4.10 – The development of neutral axis depth for Series B notched prism bending test.

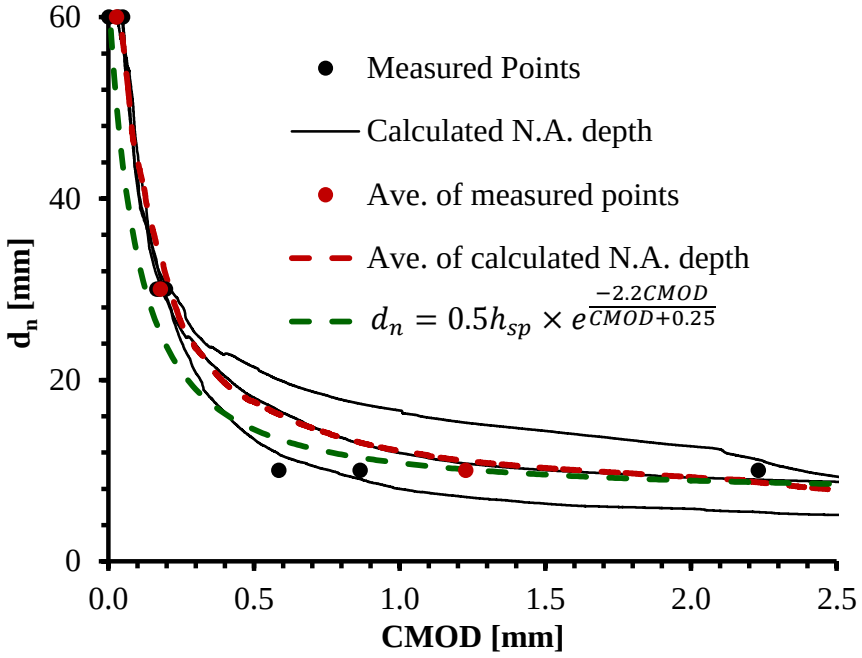

Figure 4.11 – The development of neutral axis depth for Series C notched prism bending test.

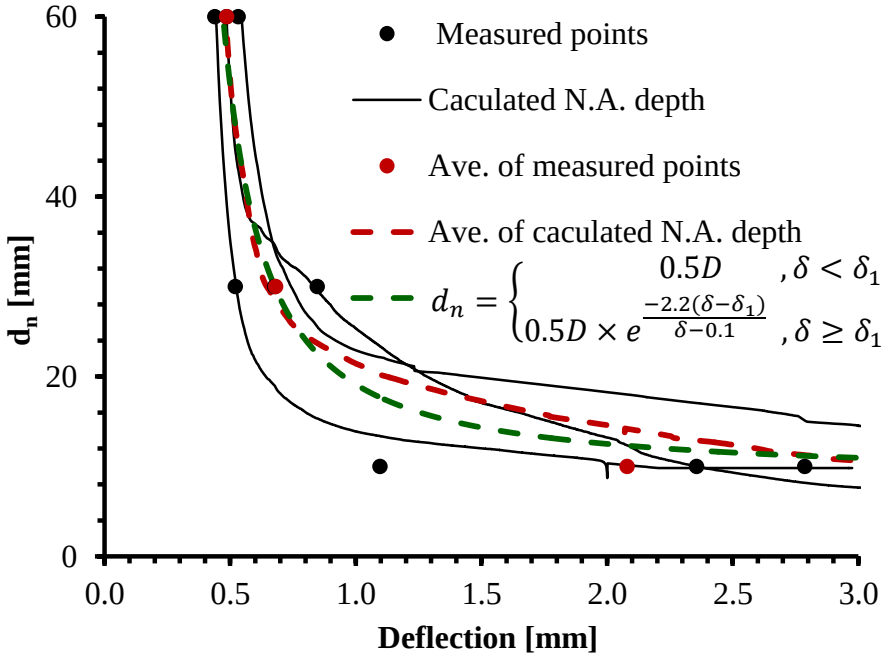

Figure 4.12 – The development of neutral axis depth for Series B un-notched prism bending test.

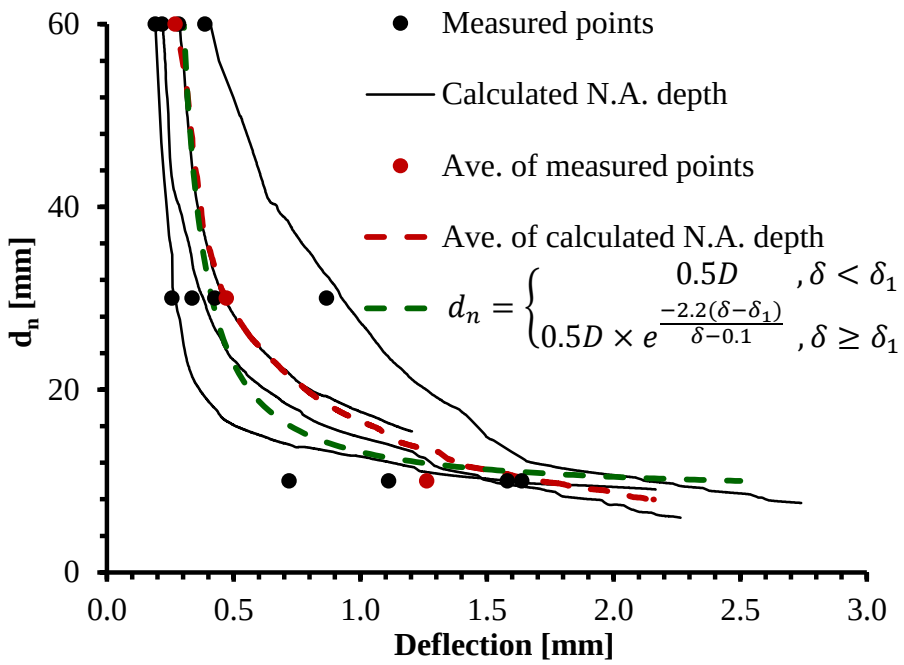

Figure 4.13 – The development of neutral axis depth for Series C un-notched prism bending test.

4.2. Model Validation

4.2.1. Introduction

The model presented in this study is compared with the specimens tested and presented in Chapter 3 and the outcomes are discussed in the following sub-sections.

4.2.2. Inverse Analysis for EN 14651 Prism Bending Tests

The application of the inverse analysis technique for a notched softening SFRC prism in bending described by Equations (4.1), (4.7) and (4.15) is illustrated in Figure 4.14 for w_T = 0.3 mm to the experiments described in Chapter 3. It can be seen that, when compensated for the wall effect and the horizontal bias in the orientation of fibres due to casting, the proposed model fits reasonably within the data obtained from the uniaxial tension tests for Series B and C. For Series A; however, the suggested model slightly overestimates the tensile strength. This is due to the fact that the failure mode of the majority of the notched prisms of Series A (and some of Series C) was characterised

with the formation of multiple cracks; where significant branching from the primary crack occurred, or sometimes the nucleation of new cracks (see Figure 3.21 and Appendix C). Accordingly, most specimens displayed residual flexural tensile stresses higher than that of the cracking.

In addition to the effect of the development of multiple cracks, described above, and as can be seen from Table 3.11 and Figure 3.19(a), the load resisted by the specimens at CMOD = 3.5 mm ($CMOD_4$) was greater than that required for elastic cracking, and that load occurred at a CMOD of about 1.5 mm (see Table 3.11 and Figure 3.19(a)). This implies that the behaviour of the material, through prism bending tests, is transitioning between strain softening to strain hardening and it is outside the bounds of the model developed in Section 4.1, where a primary assumption of the model is violated. On the other hand, the material behaviour, through uniaxial tension tests, reflects strain softening material. This raises the question about the accuracy of the prism bending tests in reflecting the actual behaviour of the material under these conditions. Indeed, the transition from strain softening to strain hardening behaviour depends on many factors such as specimen geometry, fibre geometry, and distribution in the matrix, and is not always a representation of the mechanical properties of the fibre–matrix composite. Without consideration of this transition, inverse analysis from a prism bending test may significantly overestimate the tensile stress for a given crack opening displacement, should multiple cracking occur, as observed in this study.

To overcome this, a correction limit has been raised in this model, the residual stress, at a crack opening displacement beyond 0.5 mm ($w > 0.5$), must be smaller or equal to that at COD = 0.5 mm ($f_{0.5}$) and the post-cracking (or residual) tensile is limited to the tensile strength of the matrix without fibres (f_{ct}). Figure 4.15 presents the proposed model with the correction limit and compared with the results of uniaxial tension test. It can clearly be seen from the figure that the proposed model fits reasonably within the data obtained from the uniaxial tension tests. The full analysed data are given in Appendix D.

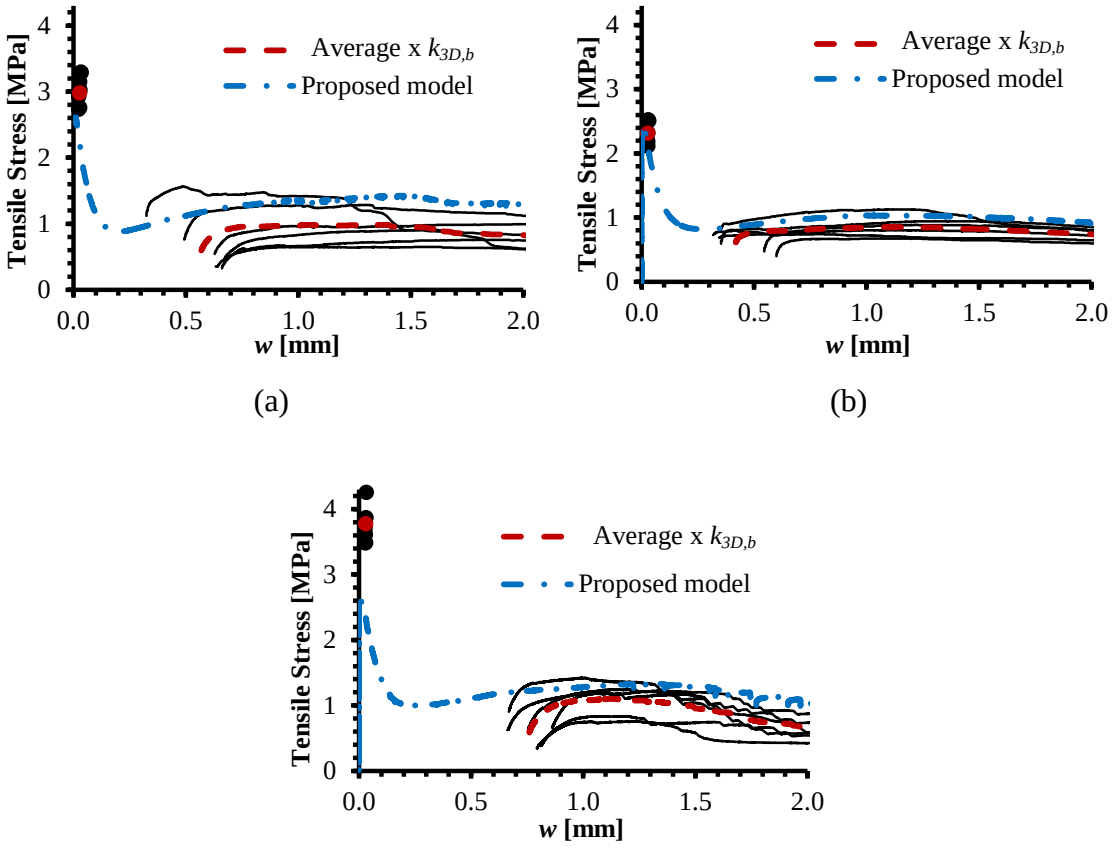

Figure 4.14 – Comparison of predicted uniaxial $\sigma - w$ curves obtained from inverse analysis of notched prism bending tests with uniaxial tension test data: (a) Series A; (b) Series B; (c) Series C.

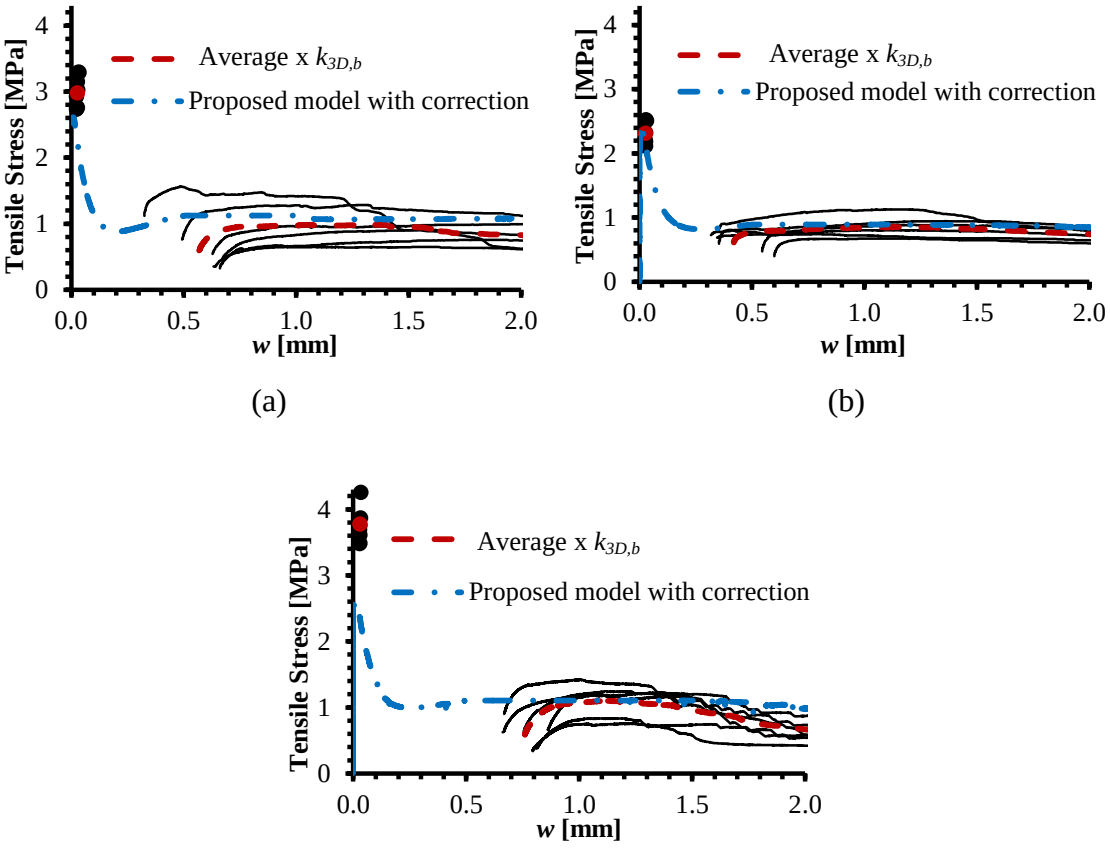

Figure 4.15 – Comparison of predicted uniaxial $\sigma - w$ curves obtained from inverse analysis of notched prism bending tests with uniaxial tension test data: (a) Series A; (b) Series B; (c) Series C.

4.2.3. Inverse Analysis for ASTM C1609 Prism Bending Tests

The inverse analysis for un-notched SFRC prisms tested in bending is performed by Equations (4.1), (4.8) and (4.17) and illustrated in Figure 4.16 for w_T = 0.3 mm to the experiments described in Chapter 3. The proposed model fits reasonably within the data obtained from the uniaxial tension for Series C. However, it can be seen that the proposed model overestimates the data obtained from the uniaxial tension tests even when compensated for the wall effect and the horizontal bias in the orientation of fibres due to casting for Series A and B. This is due to the fact that the majority of the prisms of Series A and B had residual flexural tensile stresses higher than that of the cracking. In addition to that, and as can be seen from Figure 3.24 and Table 3.12, the load resisted by the specimens at a deflection of 3.0 mm (δ_{150}^{D}) was greater than that required for elastic cracking, and that the peak load occurred at deflection of about 0.75 mm (δ_{600}^{D}). This means that some of specimens of Series A and B showed deflection hardening behaviour. However for Series C, the residual strength at deflection of 3.0 mm was well below that of elastic cracking and the post-cracking strength of deflection of 0.75 mm indicating deflection softening material behaviour and this is consistent with the uniaxial tension results obtained for Series C.

Similarly to the notched prism bending tests, more attention is needed to investigate the difference in material behaviour obtained from different test procedures for the same material; while some tests indicated hardening behaviour, others showed softening. Again a correction limit has been raised in this model, the residual stress, at a crack opening displacement beyond 0.5 mm ($w > 0.5$), must be smaller or equal to that at COD = 0.5 mm ($f_{0.5}$) and the post-cracking (or residual) tensile is limited to the tensile strength of the matrix without fibres (f_{ct}). Figure 4.17 presents the proposed model with the correction limit and compared with the results of uniaxial tensile test. It can clearly be seen from the figure that the proposed model fits reasonably within the data obtained from the uniaxial tension tests. The full analysed data are given in Appendix D.

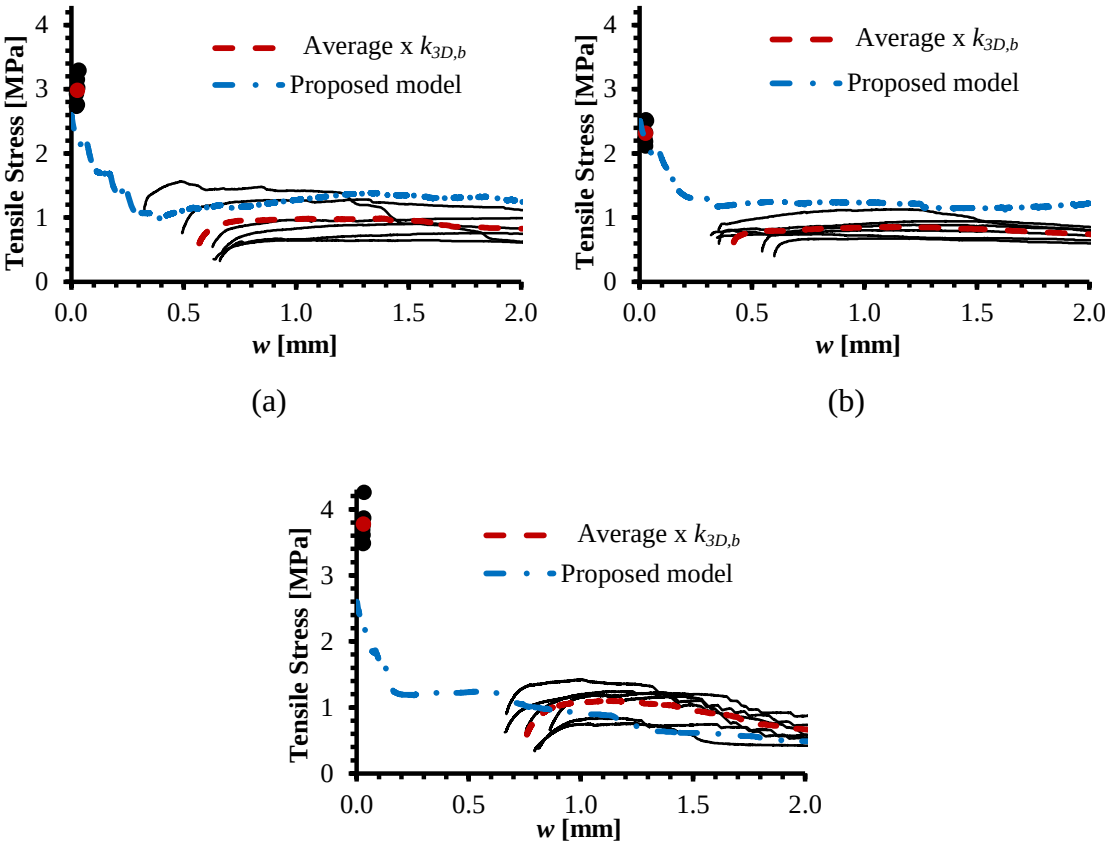

Figure 4.16 – Comparison of predicted uniaxial $\sigma - w$ curves obtained from inverse analysis of un-notched prism bending tests with uniaxial tension test data: (a) Series A; (b) Series B; (c) Series C.

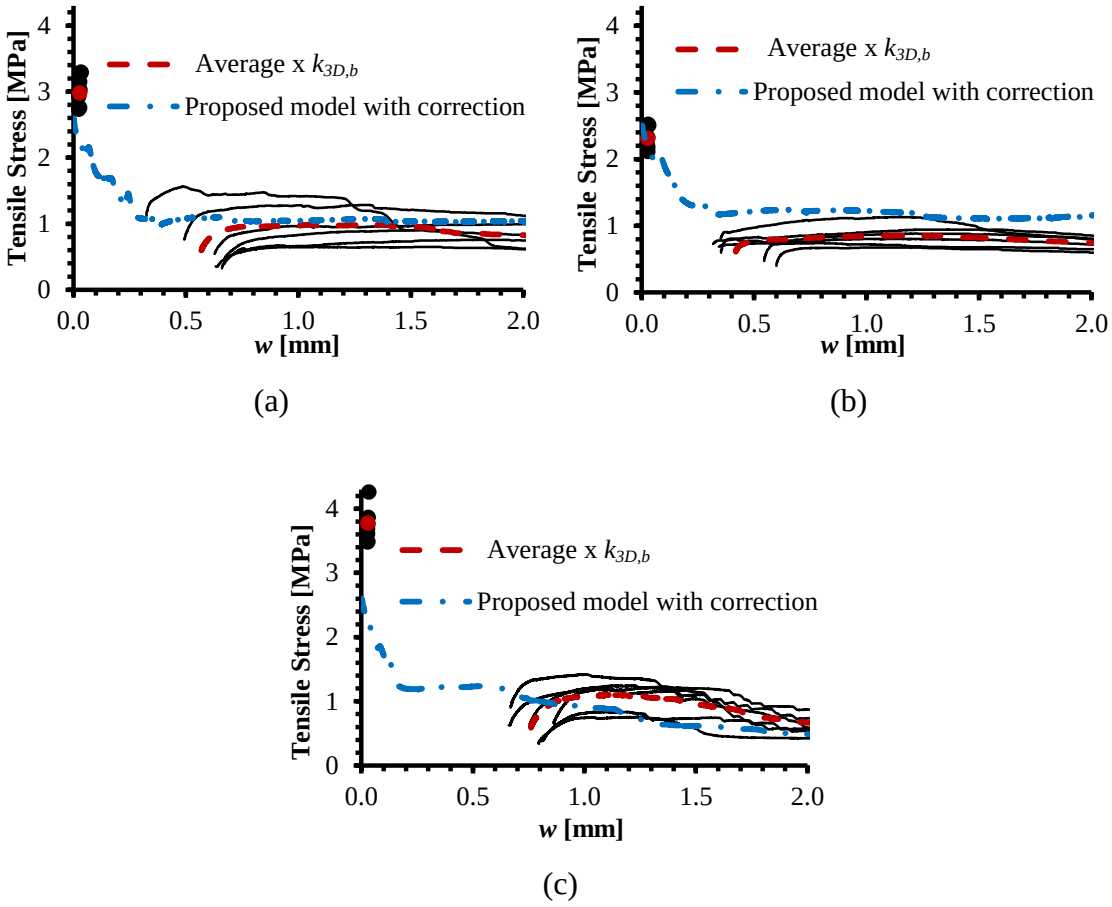

Figure 4.17– Comparison of predicted uniaxial $\sigma - w$ curves obtained from inverse analysis of un-notched prism bending tests with uniaxial tension test data: (a) Series A; (b) Series B; (c) Series C.

4.2.4. Comparison between EN 14651 and ASTM C1609 Inverse Analysis Models

Noting the limited number of bending and/or direct tension tests (three to six specimens for each case), the full model reasonably captures the post-cracking behaviour of the specimens reported in the this study. It is observed that the model works well in the case of both notched and un-notched prisms, as can be seen from Figure 4.18.

Significantly higher scatter is observed with the inverse analysis of un-notched prism bending test as can be seen in Tables 4.1 to 4.4, the results are summarised at w = 0.5 mm and w = 1.5 mm for both tests conducted in this study. For the EN 14651 prism bending test, at w = 0.5 mm the mean predicted to test ratio is 1.15 with a COV = 0.16 and at w = 1.5 mm the mean predicted to test ratio is 1.02 with a COV = 0.02. For ASTM C1609 prism bending test, at w = 0.5 mm the mean predicted to test ratio is 1.00 with a COV = 0.45 and at w = 1.5 mm the mean predicted to test ratio is 1.23 with a COV = 0.51. This is because the central deflection is being measured during ASTM C1609 prism bending test; however, the crack appears at the weakest cross-section between the two loading points, which is not necessarily the mid-span of the prism. In addition to that, with ASTM C1609 prism bending test set-up, it is possible for multiple cracks to develop in this region. This can explain the higher scatter with the inverse analysis of un-notched prism bending test.

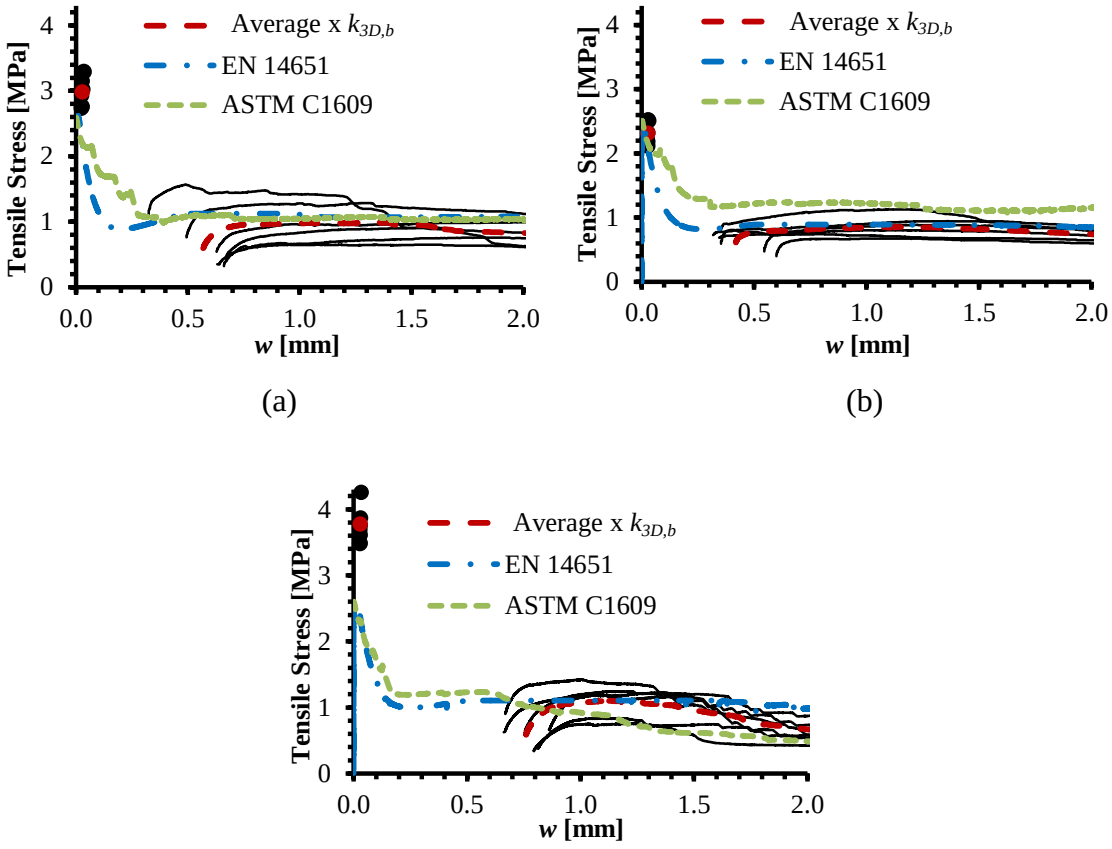

Figure 4.18 – Comparison of predicted uniaxial $\sigma - w$ curves obtained from inverse analysis of notched and un-notched prism bending tests with uniaxial tension test data: (a) Series A; (b) Series B; (c) Series C.

Table 4.1 – Comparison of residual tensile strength at a COD of 0.5 mm from inverse analysis of notched prisms.

Series	**$\sigma(w)$ at w = 0.5 mm**		
	Experimental -A-	**Proposed model -B-**	**A/B**
Series A	1.45	1.13	1.28
Series B	0.91	0.89	1.02
Series C	-	1.10	-
Mean			**1.15**
COV			**0.16**

Table 4.2 – Comparison of residual tensile strength at a COD of 1.5 mm from inverse analysis of notched prisms.

Series	**$\sigma(w)$ at w = 1.5 mm**		
	Experimental -A-	**Proposed model -B-**	**A/B**
Series A	1.08	1.07	1.01
Series B	0.89	0.88	1.01
Series C	1.16	1.10	1.05
Mean			**1.02**
COV			**0.02**

Table 4.3 – Comparison of residual tensile strength at a COD of 0.5 mm from inverse analysis of un-notched prisms.

Series	**$\sigma(w)$ at w = 0.5 mm**		
	Experimental -A-	**Proposed model -B-**	**A/B**
Series A	1.45	1.10	1.32
Series B	0.91	1.33	0.68
Series C	-	1.23	-
Mean			**1.00**
COV			**0.45**

Table 4.4 – Comparison of residual tensile strength at a COD of 1.5 mm from inverse analysis of un-notched prisms.

Series	**$\sigma(w)$ at w = 1.5 mm**		
	Experimental -A-	**Proposed model -B-**	**A/B**
Series A	1.08	1.04	1.04
Series B	0.89	1.22	0.73
Series C	1.16	0.60	1.93
Mean			**1.23**
COV			**0.51**

4.3. Simplified Model for Design

The stress – COD model for a SFRC material was developed in Section 4.1 from prism bending tests for the inclusion of the neutral axis location and validated in Section 4.2. From the model, it is evident that the location of neutral axis is sufficiently high in the cross-section after the occurrence of sufficient cracking; accordingly, uncracked concrete has negligible contribution to the bending moment capacity in comparison to that provided by fibres.

For the determination of a simple model for design, the flexural strength corresponding to CMODs of 1.5 mm and 3.5 mm are adopted (Amin et al., 2015; Foster, 2017; Foster et al., 2018) for the conversion of prism bending test data to $\sigma - w$. These points are corresponding to $CMOD_2$ and $CMOD_4$ according to EN 14651 (2007) and shown in Figure 3.18. The point $CMOD_2$ is sufficiently distant from initial cracking, such that the uncracked concrete has little to negligible contribution to the section capacity of the prism. The selection of sufficiently separated points provides reasonable coverage to model the most significant region of the $\sigma - w$ curve for both strength and serviceability.

The basis of the simplified model of Amin et al. (2015) and Foster et al. (2018) is adapted in this study for conversion of prism bending test data to $\sigma - w$, and is:

$$f_w = 0.4f_{R2} + 1.2(f_{R4} - f_{R2})\xi(w) \tag{4.18}$$

$$\xi(w) = \frac{w}{3}\frac{(D - d_n)}{(h_{sp} - d_n)} - \frac{1}{4} \tag{4.19}$$

where f_{R2} and f_{R4} are stresses obtained from the prism bending test that correspond to crack mouth opening displacements (CMODs) of 1.5 mm and 3.5 mm (see Figure 3.18), respectively, w is the uniaxial tensile crack width, D is the depth of the prism (see Figures 4.2 and 4.3), d_n is the neutral axis depth, h_{sp} is the depth measured from the

extreme compressive fibre to the notch root, and f_w is post-cracking residual tensile strength determined from inverse analysis.

For the test configuration of EN 14651 (2007), an equation is evaluated for the development of the neutral axis through notched prism bending test, as previously discussed in sub-section 4.1.6, and shown below (Figures 4.19 and 4.20):

$$d_n = 0.5h_{sp} \times e^{\frac{-\alpha w}{w+\beta}} \qquad (4.20)$$

where α and β are coefficients. The coefficient α determines towards the asymptote value of the curve and it contributes towards the neutral axis depth at failure, while β is a factor that controls the steepness of the descending branch. The asymptote factor may be taken as $\alpha = 2.2$. The factor β can be taken as 0.1.

For tests conducted according to the ASTM C1609 (2006), the method of Vandewalle and Dupont (2003) was used to convert the vertical displacement, measured at mid-span, to the CMODs needed to determine f_{R2} and f_{R4}. In this method:

$$CMOD = \frac{4\delta}{L}(D - d_n) \qquad (4.21)$$

where L is the loading span, δ is the mid-span deflection, and d_n is the neutral axis depth. For the determination of the neutral axis depth, Equation (4.17) is used. Equation (4.21) is only applicable to post-cracking stage and, accordingly, the elastic component should be subtracted from the total deflection.

Equations (4.18) and (4.19) do not include other influencing factors, such as the wall effect, casting bias and the existence of the notch. The effect of these factors are extracted and considered separately. Consequently, the post-cracking strength with compensation for various influencing effects is:

$$\sigma_f(w) = k_b k_c k_n f_w \qquad (4.22)$$

For a strain softening concrete, with failure controlled by fracture processes, for which the model in this study is derived for, the post-cracking (or residual) tensile strength at a given crack opening displacement, beyond COD = 0.5, is limited to the tensile strength of the matrix without fibres (f_{ct}) and should not exceed the residual strength of ($f_{0.5}$). This ensures that the inverse analysis from prism bending tests is not overestimating the tensile stress at a given COD, specifically over multiple cracking occurs (see Figure 3.21) and a transition from strain softening to strain hardening behaviour is observed.

The simplified model is compared to the direct tension test data of this study and presented in Figures 4.21 and 4.22 for notched and un-notched prism bending tests, respectively, for the domain $w \in [0, 2.0]$ mm. It is seen that the proposed simplified model reasonably predicts the residual tensile strength of the SFRC, except for Series B with un-notched prism bending tests. The full analysed data are given in Appendix D. A comparison between notched and un-notched simplified models is presented in Figure 4.23. It is observed that the simplified inverse analysis design procedure for notched prisms is predicting results closer to the measured direct tensile test data than that of the un-notched tests. This requires further investigation.

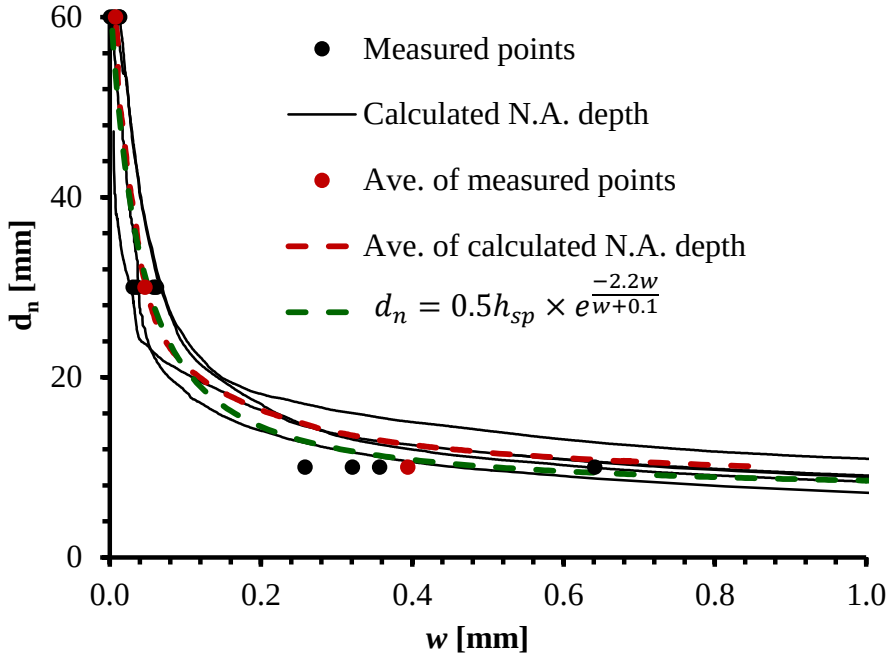

Figure 4.19 – Neutral axis depth versus COD for Series B notched prism bending test.

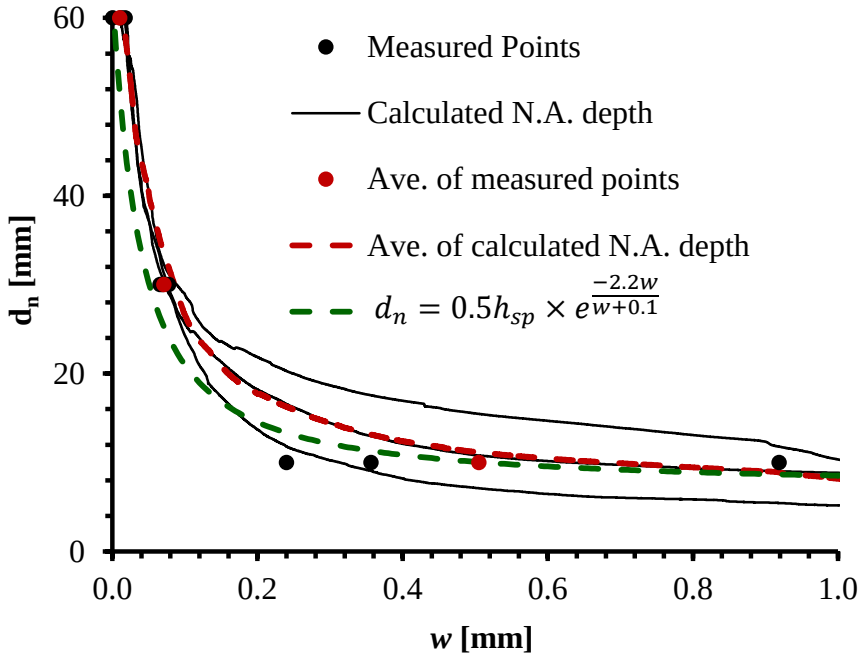

Figure 4.20 – Neutral axis depth versus COD for Series C notched prism bending test.

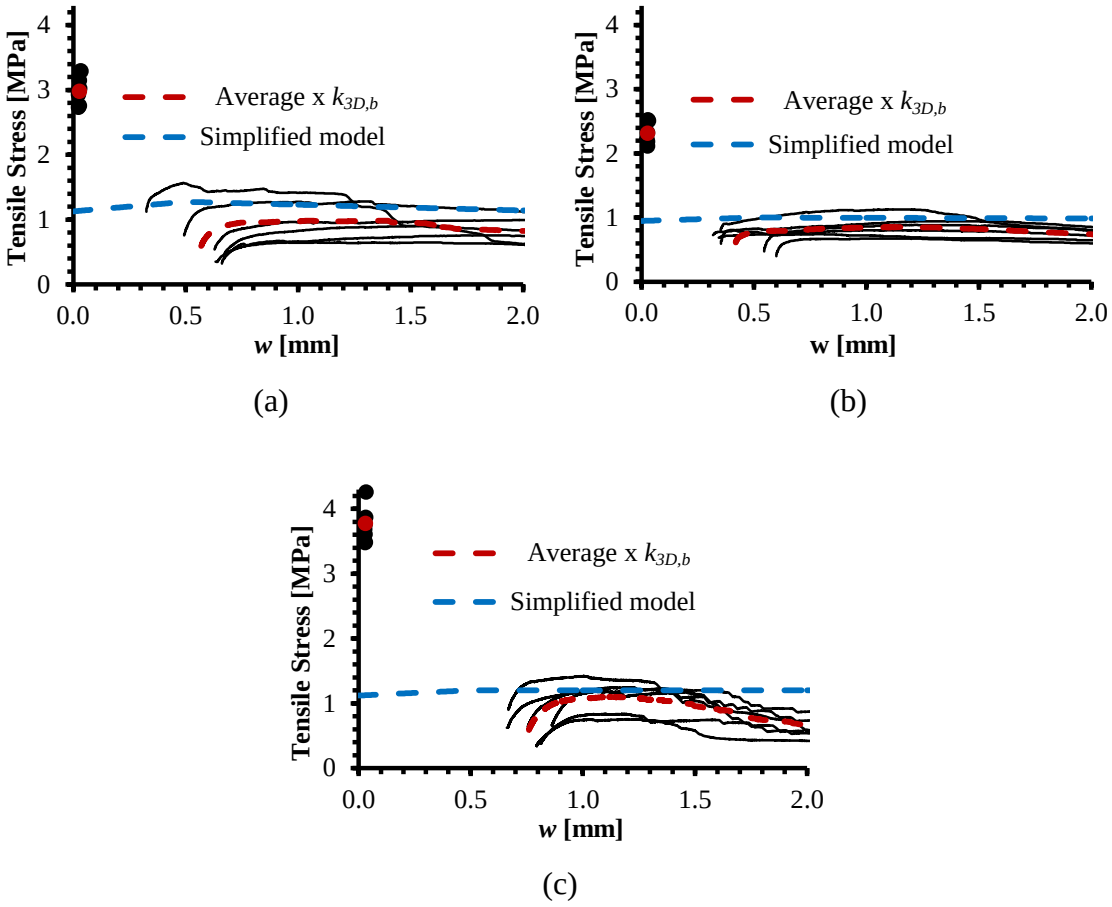

Figure 4.21 – Comparison of simplified design model of notched prism bending tests with uniaxial tension test data: (a) Series A; (b) Series B; (c) Series C.

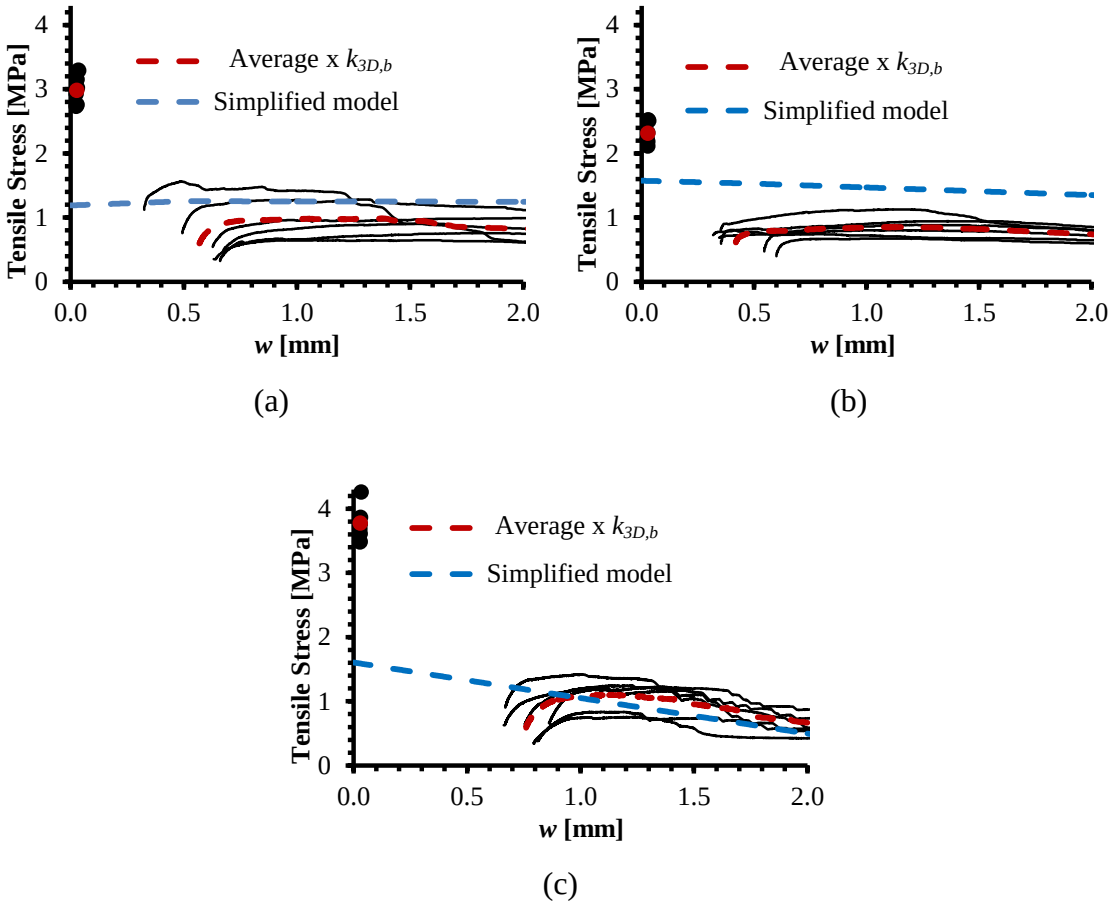

Figure 4.22 – Comparison of simplified design model of un-notched prism bending tests with uniaxial tension test data: (a) Series A; (b) Series B; (c) Series C.

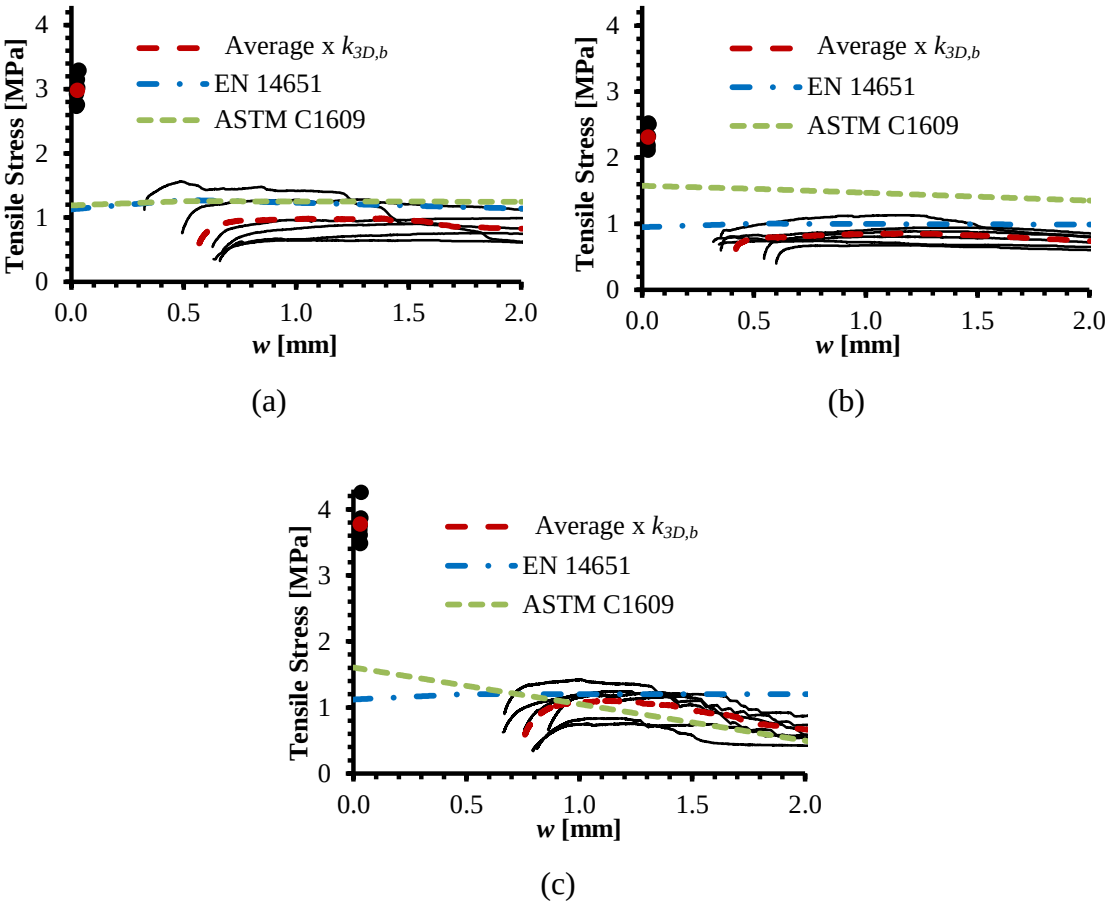

Figure 4.23 – Comparison of predicted uniaxial $\sigma - w$ curves obtained from the simplified inverse analysis model of notched and un-notched prism bending tests with uniaxial tension test data: (a) Series A; (b) Series B; (c) Series C.

4.4. Summary and Concluding Remarks

Reliable methods to acquire the residual behaviour of SFRC are needed to have confidence in the design of SFRC in structural applications. This study presents an approach to establish the post-cracking or residual tensile strength of SFRC. The post-cracking behaviour of SFRC can be obtained directly from uniaxial tension tests, or indirectly following an inverse analysis of notched or un-notched prisms in bending.

Following an experimental investigation of three SFRC mixes that displayed softening behaviour in uniaxial tension testing, an inverse analysis procedure was derived to find the $\sigma - w$ relationship for SFRC from both notched and un-notched prism bending tests. The model considers the influence of fibres on the moment carried by the specimen, as well as the location of neutral axis at a specified CMOD or deflection, depending on the test type.

The model was validated against experimental data obtained from direct tension tests for the three SFRC mixes carried out in this study, the model predicted the results within reasonable bounds and, generally, within the scatter range of the collected data. The model does not apply to the situation where a prism test is in transition from strain softening to strain hardening behaviour, leading to multiple cracking. This may occur due to specimen geometry, fiber geometry, and distribution in the matrix. To capture such cases, limits are applied to the model such that: (i) the residual stress at a crack opening displacement greater than 0.5 mm ($w > 0.5$) must be smaller or equal to that at COD = 0.5 mm ($f_{0.5}$); and (ii) the post-cracking (or residual) tensile is limited to the tensile strength of the matrix without fibres (f_{ct}).

Chapter 5 DAMAGE MODEL FOR FATIGUE IN SFRC ELEMENTS

5.1. Introduction

The experimental results presented in Chapter 3 are analysed and discussed in details in this chapter. The influence of the variety of different failure modes of round panels is discussed in Section 5.2. A relationship between crack opening displacement and central deflection for different failure modes is presented in Section 5.3 and validated against the experimental results. The effectiveness of SFRC on fatigue behaviour is investigated in terms of cyclic creep curves and Wöhler diagrams in Sections 5.4 and 5.5. A constitutive model is developed for SFRC for post-cracking fatigue damage during cyclic loops. The model is verified against available test data in Section 5.6. Finally, concluding remarks are presented in Section 5.7.

5.2. Failure Planes in the Round Panel Test

Theoretically, the cracks of the round determinate supported panel specimens should form midway between the supports where the applied moment is the greatest (Figure 5.1(a)). However, in testing significant deviation was noticed. This deviation from theory is due to the variation of concrete matrix strength within the specimen and the sensitivity of the fracture processes to this variation. After cracking, the material's performance is mainly controlled by the fibre component. However, uneven fibre distribution along the failure planes can lead to a theoretically higher energy in the fracture line pattern to develop (Figure 5.1(b)). Accordingly and in order to undertake fracture and post-cracking analysis, it is important to consider a series of fracture line analyses of possible failure modes in round determinate supported panels.

There are mainly three possible fracture line patterns of failure in the round panel test. The first pattern is the pattern of diametric single crack running through the centre of the round panel specimen. The second failure mode is a single fracture line located off-centre. The last pattern, noticed in this project, is the formation of three radial cracks lines as presented in Figure 5.1(a). Tran (2003) reported the fan yield line pattern; however, this failure can only occur in ductile elements and was not observed in this project, nor in the literature (Bernard, 2000; Tran, 2003; Tran et al., 2005; Bernard and Xu, 2008; Moss, 2008; Barnett et al., 2010; Minelli and Plizzari, 2010; Chao et al., 2011; de Montaignac et al., 2012; Amin et al., 2017). The various failure modes observed in this study are recorded in Table 5.1. Plotted in Figure 5.2 is a frequency distribution of γ for all panel specimens which failed by the formation of three fracture lines.

There are several limitations in determining the fundamental material laws based on the study of round panel tests. These can occur due to the following assumptions (Amin et al., 2017):

1. rigid plastic $\sigma - w$ model to describe the post-cracking response of SFRC;
2. estimated depth of neutral axis;
3. random alignment of fibres;
4. ignoring the tensile membrane actions that occur due to friction imposed supporting arrangements;
5. the 120^{o} theoretical arrangement of fracture lines; and
6. the location of the crack junction being at the centre of the panel.

In this study the last two assumptions are discussed, the remaining assumptions were well discussed by Amin et al. (2017) and it was concluded that these assumptions lead to small errors only.

Deviation of fracture lines from theory (γ_1, γ_2 and γ_3 in Figure 5.1(a)) and the development of one fracture line instead of three, influences the internal work calculations and, as the internal work is a minimum on the 120^o theoretical pattern, the error leads to a non-conservative solution. Bernard and Xu (2008) and Amin et al. (2017) concluded deviation of fracture lines from theory leads to small errors only. In this study, the variation of angles for the panels tested in this study is shown in Figure 5.2 and presented in Table 5.1, together with the resulting sum of the internal work ($\sum W_I$) relative to theory. An accurate calculation for the work (internal and external) based on the experimentally observed fracture lines, is demonstrated in Figure 5.3, where the angles α_i (i = 1 … 6) are dependent on the location of the origin (O') and the deviation of the fracture lines from their theoretical values.

In the fracture line analyses undertaken herein, the value of α are determined from the equations outlined by Tran (2003) assuming that (O') coincides with (O). The results show an average error of just 2.1%, with a maximum error of 5.7% for the failure mode of three fracture lines. This reinforces the conclusions of Amin et al. (2017) as well as Bernard and Xu (2008) that the variations of the crack angles from theory do not significantly influence the derived results. However, whenever one fracture line is developed, the error is significantly higher up to 56.8%. As such this non-conservative error is not small and must be addressed.

Errors can also be introduced in the external work calculation due to the location of the crack junction being away from the centre of the panel for the failure mode of three fracture lines. The locations of the crack junction (O' in Figure 5.1(a)) for the panels tested in this study are presented in Table 5.1. The external work is $W_E = P\ k\ \delta$, where k equals the length of a line drawn normal to the nearest axis of rotation (Figure 5.3) divided by r = 375 mm. However, in this study, whenever one fracture line is developed, it was passing through the centroid of the panel and, accordingly, the error in external work calculation ends up being zero. The average error in the external work

assumption is 3.6%, with a maximum of 11.0%. When the errors in the internal work are combined with those of the external work, noting that the errors are multiplicative, the average error in the determined moment for the panels tested is +7.4% and the maximum is +20.1%.

From a fracture line analysis and the work evaluated from Tran (2003), the required applied load can be evaluated for the main two failure modes observed in this research: one and three fracture lines. For the pattern of one fracture line (Figure 5.1(b)), the external and internal energies can be expressed as (Tran, 2003):

$$W_E = P\delta \tag{5.1}$$

and,

$$W_I = \left(2\sqrt{R^2 - y^2}\right)\theta m \tag{5.2}$$

where R is the radius of the panel, θ is the rotation at the fracture line, m is the moment of resistance per unit length of fracture line, and y is the distance from the centre to the crack line. The total rotation at the fracture line is:

$$\theta = \theta' + \theta" = \delta\left[\frac{3}{r - y}\right] \tag{5.3}$$

where r is the distance from the centre to the support (Figure 5.1), and the failure load for this pattern is:

$$P = 6\left(\frac{\sqrt{R^2 - y^2}}{r - y}\right)m \tag{5.4}$$

Given that $R = 400$ and $r = 375$. Minimum value when $y = 0$:

$$P_{one\ fracture\ line} = 6.4m \tag{5.5}$$

For the mode of failure of three fracture lines, it was presented by Tran (2003) that the minimum load value P occurs for the symmetric case in which all included angles between fracture lines equal 120°, i.e. all midpoint angles, γ, equal zero (Figure 5.1(a)); thus:

$$P_{three\ fracture\ lines} = 3\sqrt{3}m\frac{R}{r} = 5.54m \qquad (5.6)$$

The magnitude of this estimate of P is 13% lower than the value given in Equation (5.5) for the diametral mode of failure, so the three crack symmetric mode of failure will theoretically govern behaviour because it is the lower bound on the fracture line analysis, assuming uniform fibre distribution. However, it can be seen from Appendix B that the coefficient of variations in the post-cracking tensile strength of Series A, B and C were 22%, 16% and 26%, respectively. By simply comparing the difference in load magnitude required to form a diametral mode of failure and the coefficient of variation in post-cracking tensile strength, it can be concluded that the variation in fibre distribution, or the scatter in post-cracking tensile strength, can flip the theoretical statement that the three crack symmetric mode of failure will govern behaviour. Instead only a variation of 13% in residual strength is needed to lead to the occurrence of one fractural line failure mode which results in lower magnitude in failure load P. This is due to the fact that the fibre component mainly controls the material's performance after cracking, and uneven fibre distribution along the failure planes led to a theoretically higher energy in the fracture line pattern to develop but lower magnitude in load in practice. The probability that a failure mode of a single fracture line governs, as opposed to a three fracture line mode, is 10.7%, based on a normal distribution.

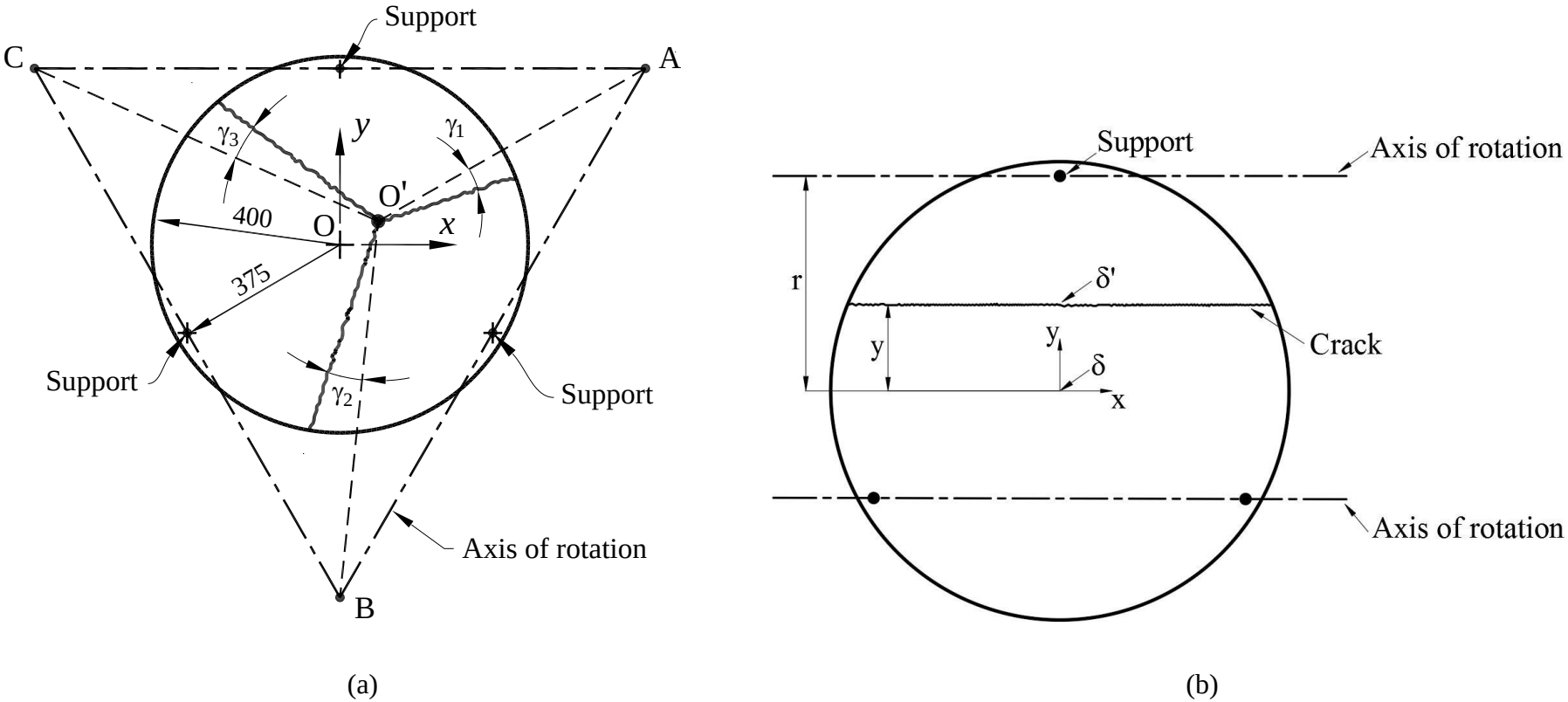

Figure 5.1 – Theoretical failure mechanism of round panel tests (a) fracture lines pattern I (Amin et al., 2017); (b) fracture line pattern II.

Table 5.1 – Cracking angles, cracking centre and comparison of calculated internal and external work relative to theory by fracture line analysis.

Panel ID	No. of fracture lines	Cracking angles			Coords. of crack junction		$\frac{\sum W_I}{\sum W_{I,theory}}$	$\frac{\sum W_E}{\sum W_{E,theory}}$	Overall error [%]
		γ_1 [deg.]	γ_2 [deg.]	γ_3 [deg.]	x [mm]	y [mm]			
A-1S-P	3	-16	-15	-19	-13.4	-2.2	1.044	0.992	5.1%
A-1S-F	3	12	14	-8	23.6	0	1.018	0.9461	10.8%
A-2S-F	3	-5	0	17	0	0	0.995	1.000	4.6%
A-1C-F-U-60	1	-	-	-	-	-	1.433	1.000	0%
A-1C-F-U-70	1	-	-	-	-	-	1.476	1.000	2.2%
A-1C-F-C-60	1	-	-	-	-	-	1.568	1.000	7.9%
A-2C-F-C-60	3	-9	0	-13	-3	-12	1.013	0.975	4.8%
A-1C-F-C-40	3	18	0	24	37.6	10	1.052	0.949	13.9%
A-2C-F-C-40	3	-21.6	0	-26	0	0	1.057	1.000	9.5%
B-1S-F	3	-21	-1	-11	-28	-23	1.031	0.971	9.1%
B-2S-F	3	-15	4	-12	0	0	1.020	1.000	5.2%
B-1C-F-U-70	3	-8	9	0	0	0	1.008	1.000	3.3%
B-2C-F-U-70	3	-11	6	0	14.8	-3.1	1.009	0.921	11.1%

Panel ID	No. of fracture lines	Cracking angles			Coords. of crack junction		$\frac{\sum W_I}{\sum W_{I,theory}}$	$\frac{\sum W_E}{\sum W_{E,theory}}$	Overall error [%]
		γ_1 [deg.]	γ_2 [deg.]	γ_3 [deg.]	x [mm]	y [mm]			
B-1C-F-C-60	3	-1	0	9	22	10	1.004	0.963	5.1%
B-2C-F-C-60	1	-	-	-	-	-	1.433	1.000	0%
B-3C-F-C-60	3	11	-3	-5	13.5	-19	1.008	0.949	8.1%
B-1C-F-C-40	3	0	13	-13	4.6	-13.3	1.015	0.934	11.4%
B-2C-F-C-40	3	12	-10	0	0	0	1.011	1.000	3.6%
C-1S-F	3	-10	9	-4	-3.8	-10.8	1.011	0.978	6.4%
C-2S-F	1	-	-	-	-	-	1.488	1.000	3.0%
C-1C-F-U-70	3	-15	20	-9	-30.4	-16.3	1.042	0.941	20.1%
C-2C-F-U-70	3	0	-19	-14	20	0	1.028	0.980	6.9%
C-1C-F-C-60	3	5	-17	0	17.7	20.5	1.015	0.890	15.0%
C-2C-F-C-60	3	-19	-18	0	-24.4	3.9	1.037	0.930	13.3%
C-1C-F-C-50	3	21	0	-7	28	12	1.018	0.941	14.7%
C-2C-F-C-50	3	0	12	0	26.9	20.6	1.007	0.950	7.1%
C-1C-F-C-40	3	10	22	-4	0	0	1.027	1.000	6.1%

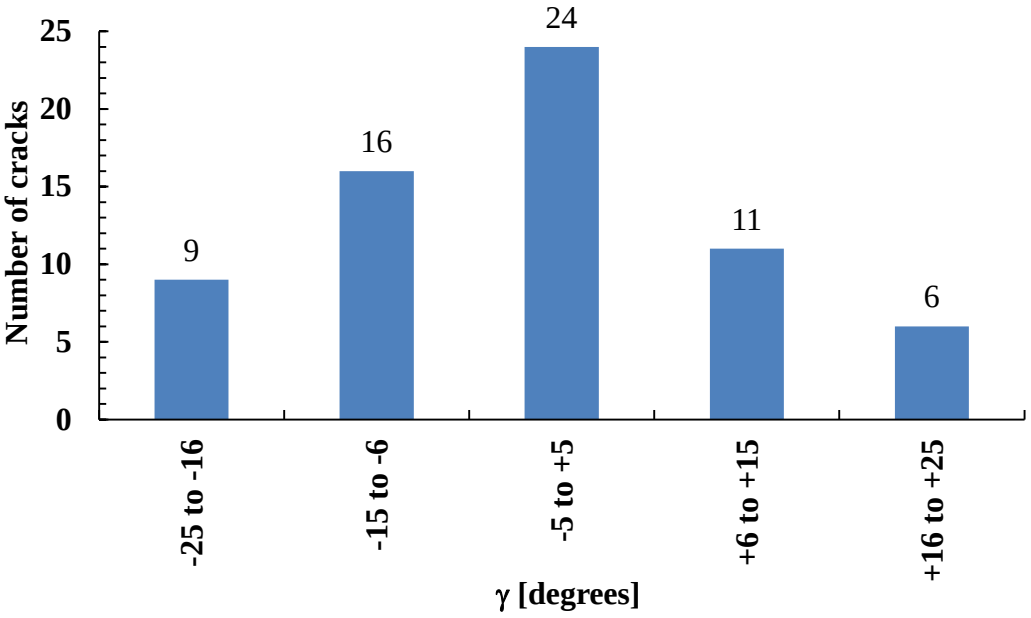

Figure 5.2 – Deviation between theoretical failure plane and actual failure plane in round panel determinate tests.

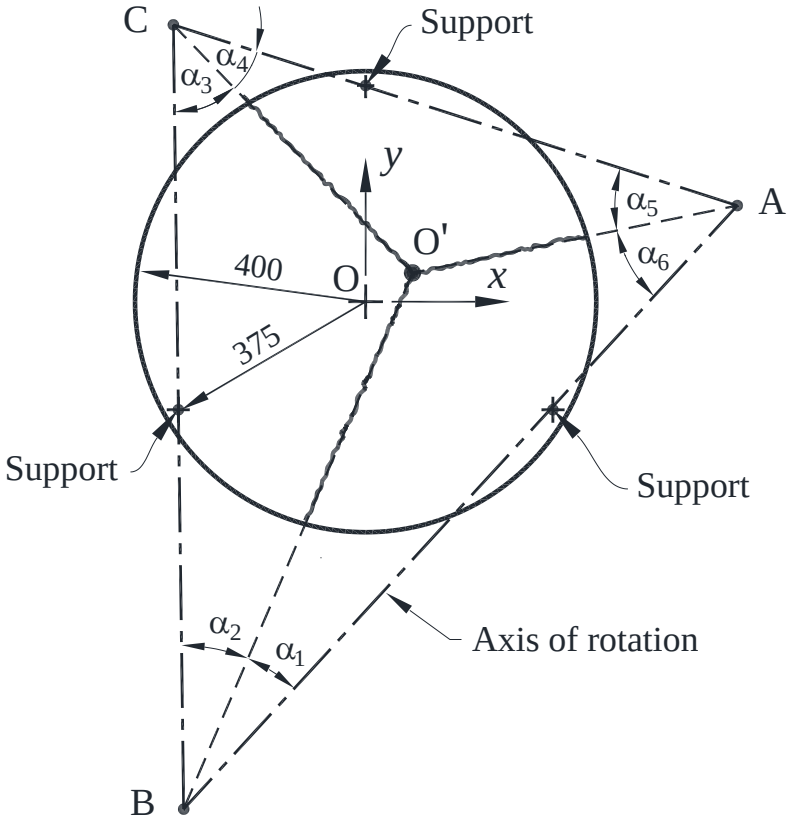

Figure 5.3 – Deviation of fracture lines from theory (Amin et al., 2017).

5.3. Relationship between Crack Opening Displacement and Central Deflection

The rotation of the fracture line has been previously evaluated by Tran (2003) for the three different failure modes mentioned previously. The COD(w) for the round panels can be obtained from the rotation of the yield line and by using the geometrical sectional block for each failure mode.

For the diametral pattern of fracture line, the COD(w) is defined as:

$$w = \tan\left(\frac{1.5\delta}{r}\right)(t - d_n) \cong \left(\frac{1.5\delta}{r}\right)(t - d_n) \tag{5.7}$$

For the off-centre pattern of fracture line, the expression is:

$$w = \tan\left(\frac{1.5\delta}{r - y}\right)(t - d_n) \cong \left(\frac{1.5\delta}{r - y}\right)(t - d_n) \tag{5.8}$$

For the three fracture lines pattern, assuming equal angles between fracture lines, the crack opening displacement is:

$$w = \frac{\sqrt{3}}{2r}\delta(t - d_n) \tag{5.9}$$

where w is the crack opening displacement; δ is the central deflection; r is the radius from the centre of the panel to the support (see Figure 5.1); t is the thickness of the panel; d_n is the depth to the neutral axis and y is the distance from the centre to the crack line.

For the determination of the depth of the neutral axis, d_n, as is required to evaluate Equations (5.7) to (5.9), Amin et al. (2015) and Amin and Foster (2016) showed that the location of d_n had little influence on the $w/CMOD$ ratio. For this reason, the depth of the compressive stress block is fixed and taken as $d_n = 0.1t$.

A comparison between theoretically and experimentally measured COD of Series A to C is presented in Figures 5.4 to 5.6, respectively. The results are consistent for all series with minimal difference. This means that Equations (5.7) to (5.9) provide good estimation of crack opening displacement during static and cyclic loading.

5.4. Cyclic Creep Curves

In fatigue tests, deflection increase at the maximum load level is generally plotted versus the number of cycles for concrete in compression (Holmen, 1979); this curve is known as cyclic creep curve. However, for concrete in tension, it was plotted in terms of crack opening displacement because the deformations tend to localise in cracks (Cornelissen and Reinhardt, 1984; Hordijk, 1991). These curves, when obtained from uncracked specimens, typically consist of three stages. First, a rapid increase of deformation (crack opening) up to about 10% of total life caused by the extension of pre-existing microcracks until a stable situation is reached (1). Next, a uniform increase from 10% to 90% governed by stable crack extension and creep (2). Finally, a rapid increase due to unstable crack propagation until failure is observed (3) (Holmen, 1979; Cornelissen and Reinhardt, 1984; Hordijk, 1991). Figures 5.7 and 5.8 present both the central deflection and average crack width at the maximum load level as a function of the number of cycles (N), respectively. It is clear from the figures that both central deflection and average crack width follow the same pattern.

All uncracked specimens from Series A did not fail or crack before 3 million cycle limit was reached; as a result, the round panels were loaded statically to failure. The static test results of round panels A-1C-F-U-60 and A-1C-F-U-70 showed that fatigue loading did not affect the ultimate load capacity or the toughness for these panels. The uncracked specimens from Series B and C failed during fatigue loading.

All failed uncracked panels followed the same pattern; a very slow steady increase in deflection up to fatigue cracking. After cracking, the rate of deflection and average

crack width increase accelerated. Following that, and within few cycles, the central deflection and average crack width increased dramatically, signalling the impending failure as cyclic load versus displacement curve approaching the corresponding envelope curve. This is generally well approximated by the quasi-static curves from monotonic tests (Hordijk, 1991; Plizzari et al., 1997; Zhang and Stang, 1998; Plizzari et al., 2000; Germano et al., 2016).

All pre-cracked specimens with maximum load level of 60% plus specimen C-2C-F-C-50 demonstrated similar fatigue behaviour, where central deflection and average crack width increased at a steady rate up to around 80% - 90% of the specimen's fatigue life. After that, a dramatic increase in central deflection and average crack width was noted, indicating impending failure. On the other hand, the pre-cracked panels with maximum load level of 40% showed steady increase in deflection and average crack width up to 3 million cycles. Round panel C-1C-F-C-50 experienced almost constant deflection and average crack width for the first 200,000 cycles approximately. After this, a steady increase in deflection and average crack width was observed up 10 million cycles without fatigue failure.

For pre-cracked specimens, only the last two stages of a typical cyclic creep curve (stages 2 and 3 of uncracked specimens) can be observed, since the initial monotonic loading stage already provokes the formation of a fracture process zone. The cyclic creep curves for pre-cracked concrete are characterized by a linear branch followed by a rapid increase of deflection and average crack width until failure. One can observe that the number of cycles to failure is related to the slope of the linear branch; in fact, N_f decreases when the slope of the secondary branch becomes larger (Cornelissen and Reinhardt 1984). It is evident from Figures 5.7 and 5.8 that the addition of fibres resulted in a slower crack growth and this is enforcing the influence of fibres in improving the fatigue behaviour of concrete in all series investigated in this study.

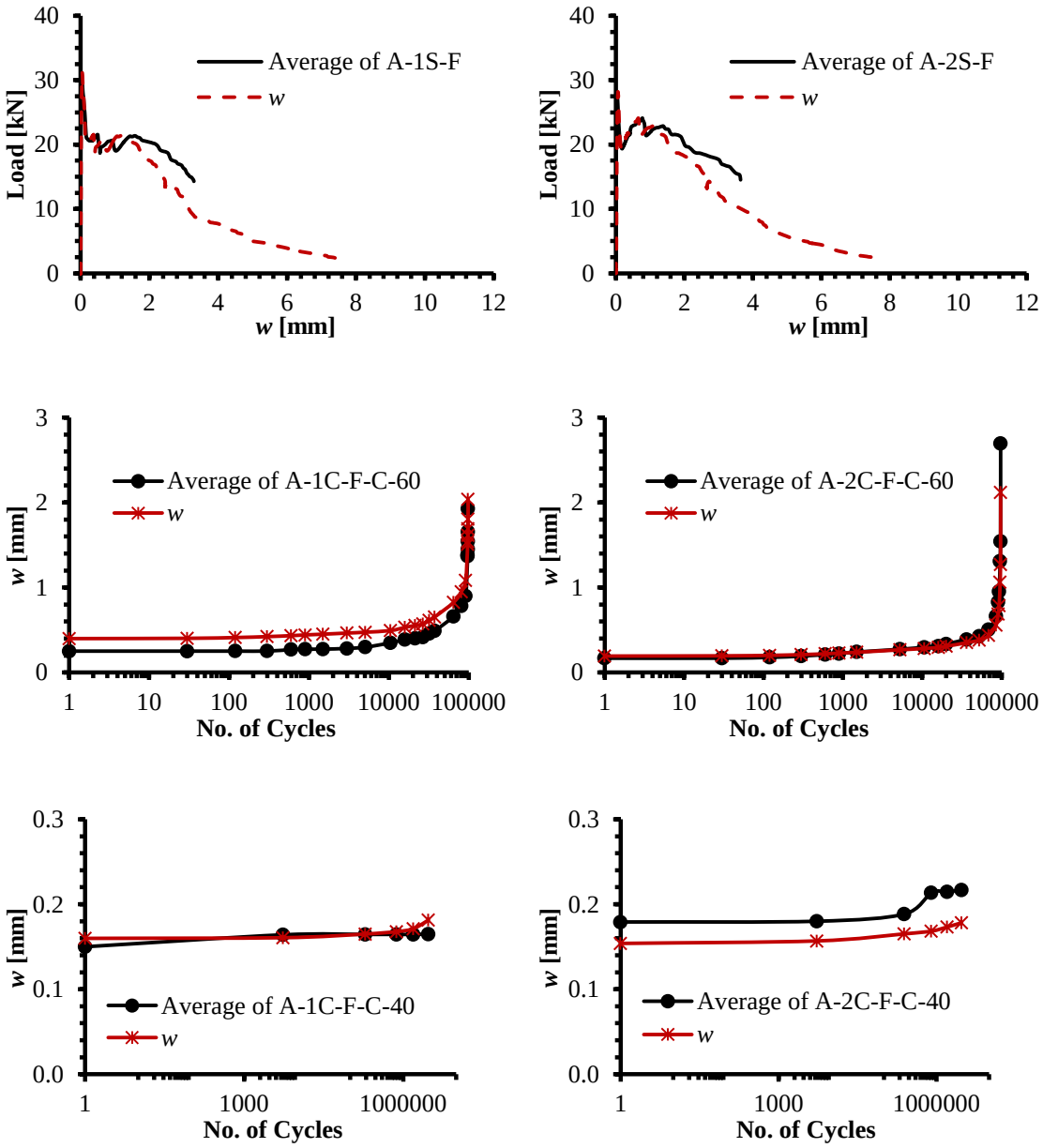

Figure 5.4 – Comparison between theoretically and experimentally measured COD of Series A.

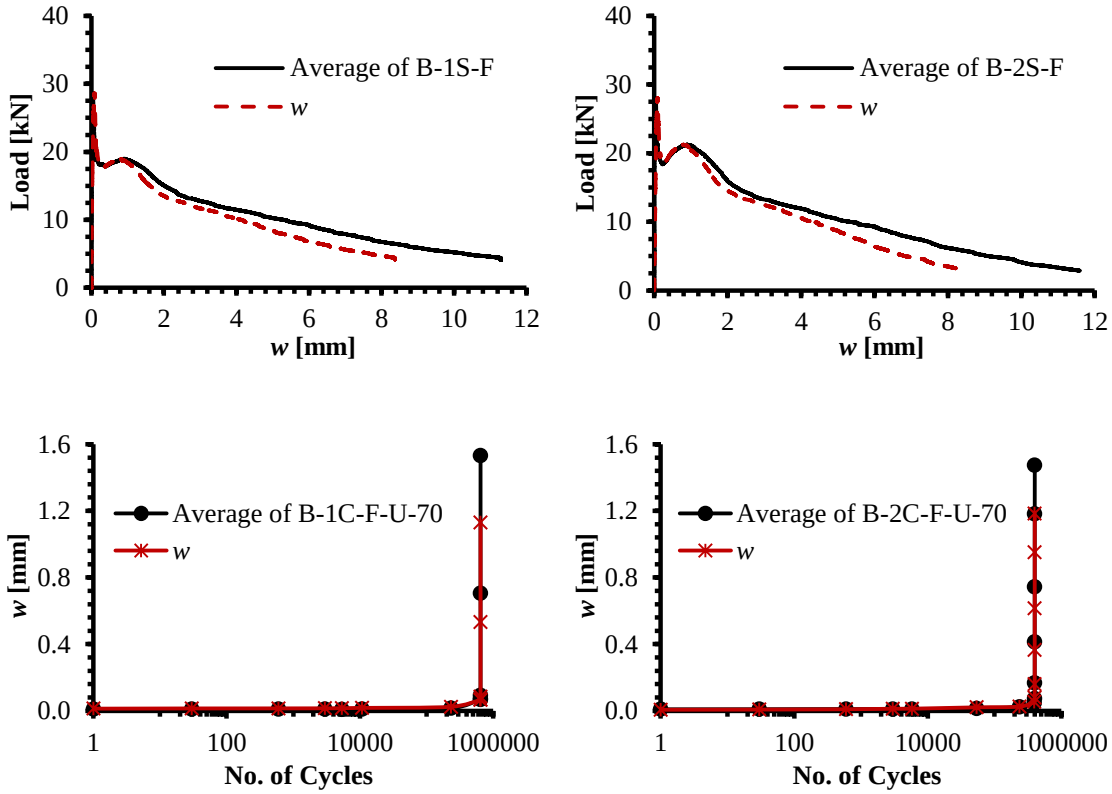

Figure 5.5 – Comparison between theoretically and experimentally measured COD of Series B.

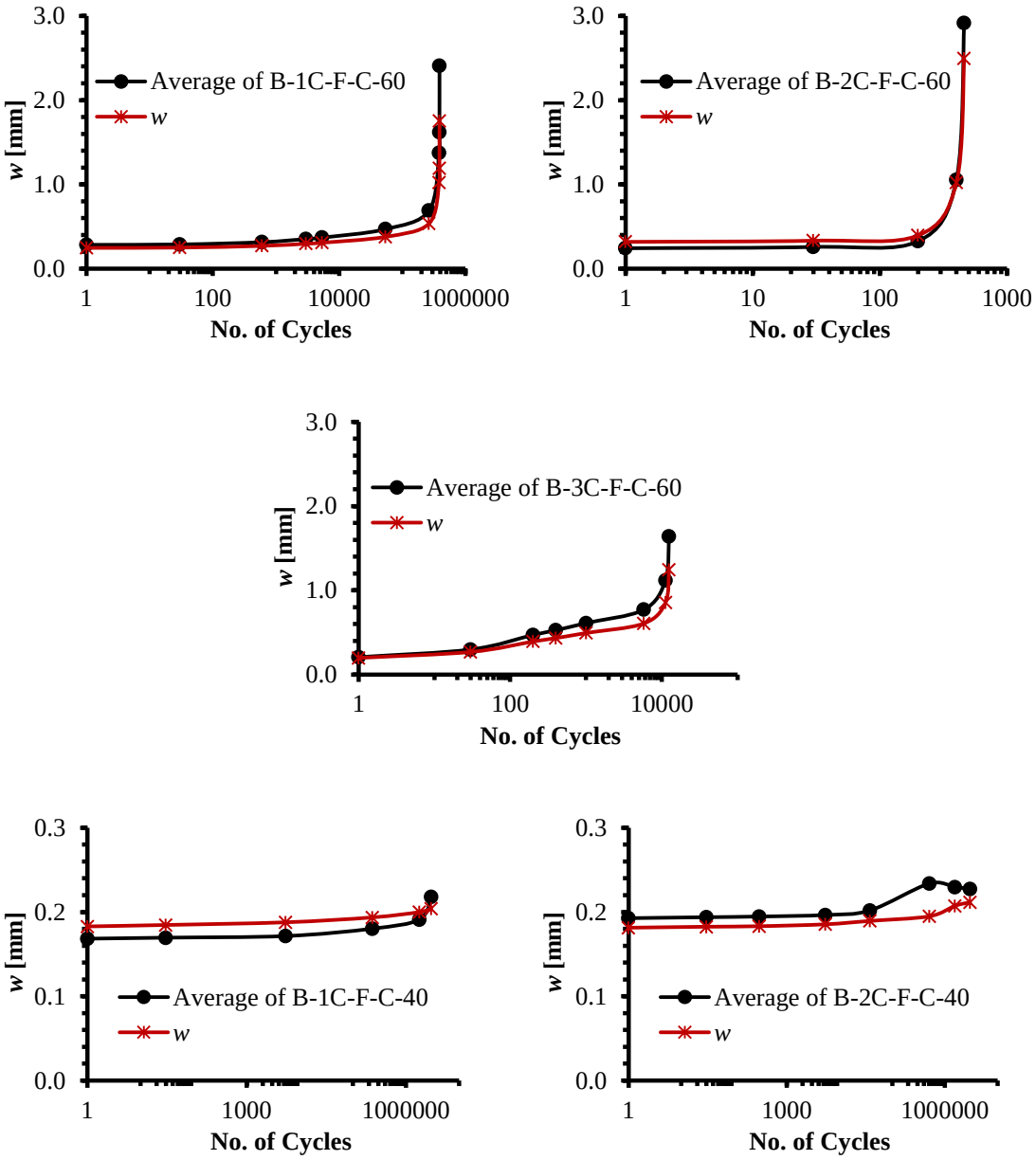

Figure 5.5 (Cont.) – Comparison between theoretically and experimentally measured COD of Series B.

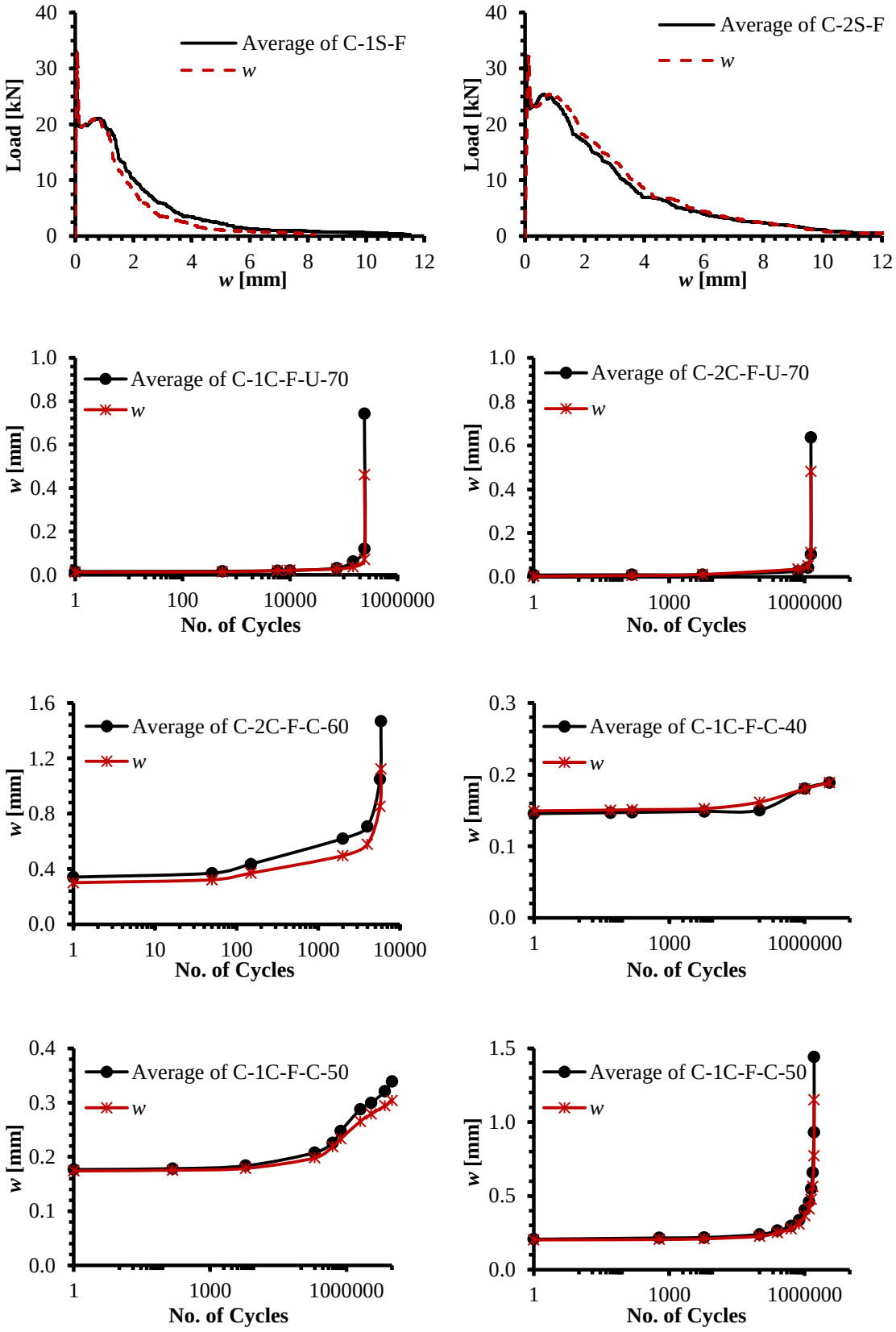

Figure 5.6 – Comparison between theoretically and experimentally measured COD of Series C.

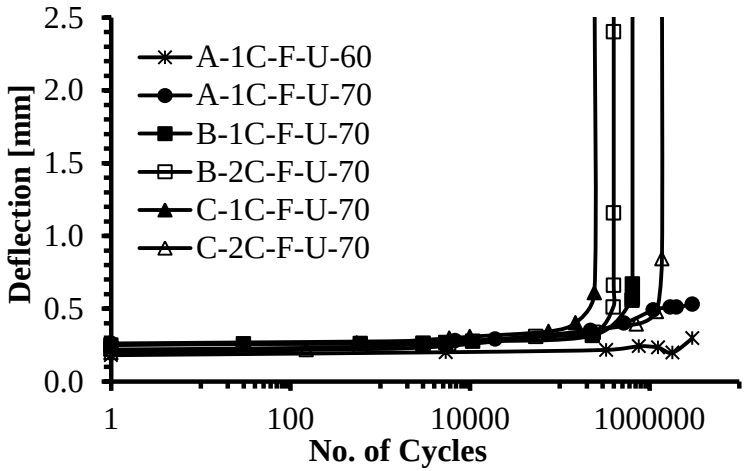

(a)

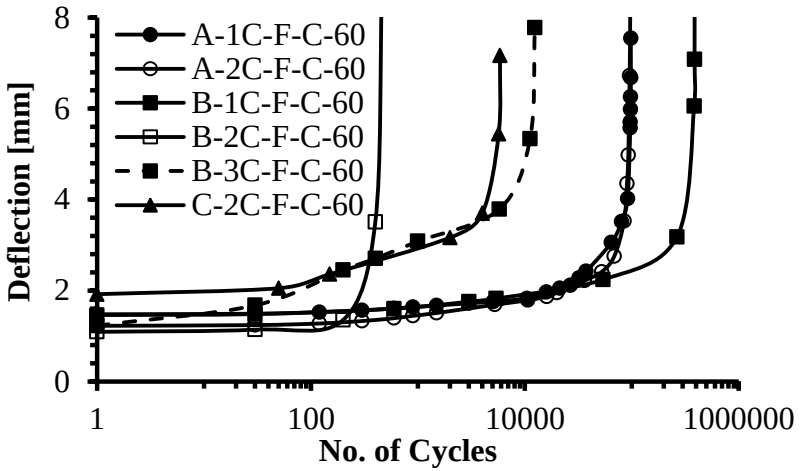

(b)

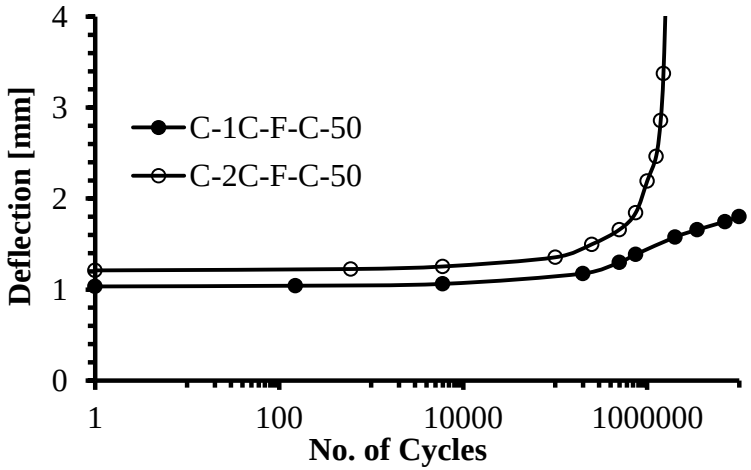

(c)

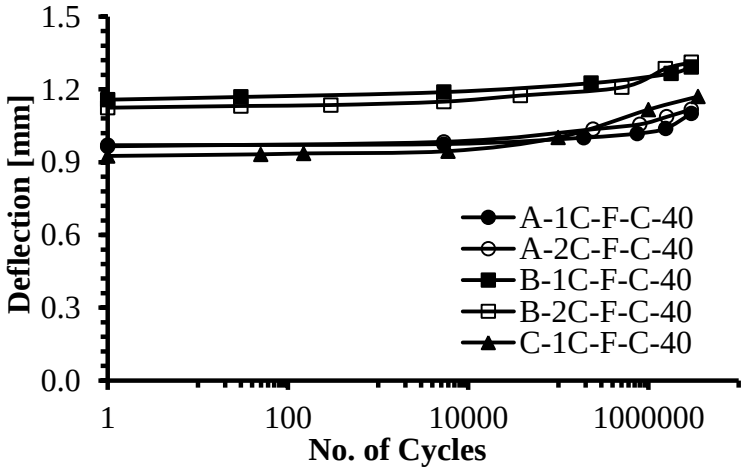

(d)

Figure 5.7 – Deflection versus number of number of cycles during maximum load level for round panels.

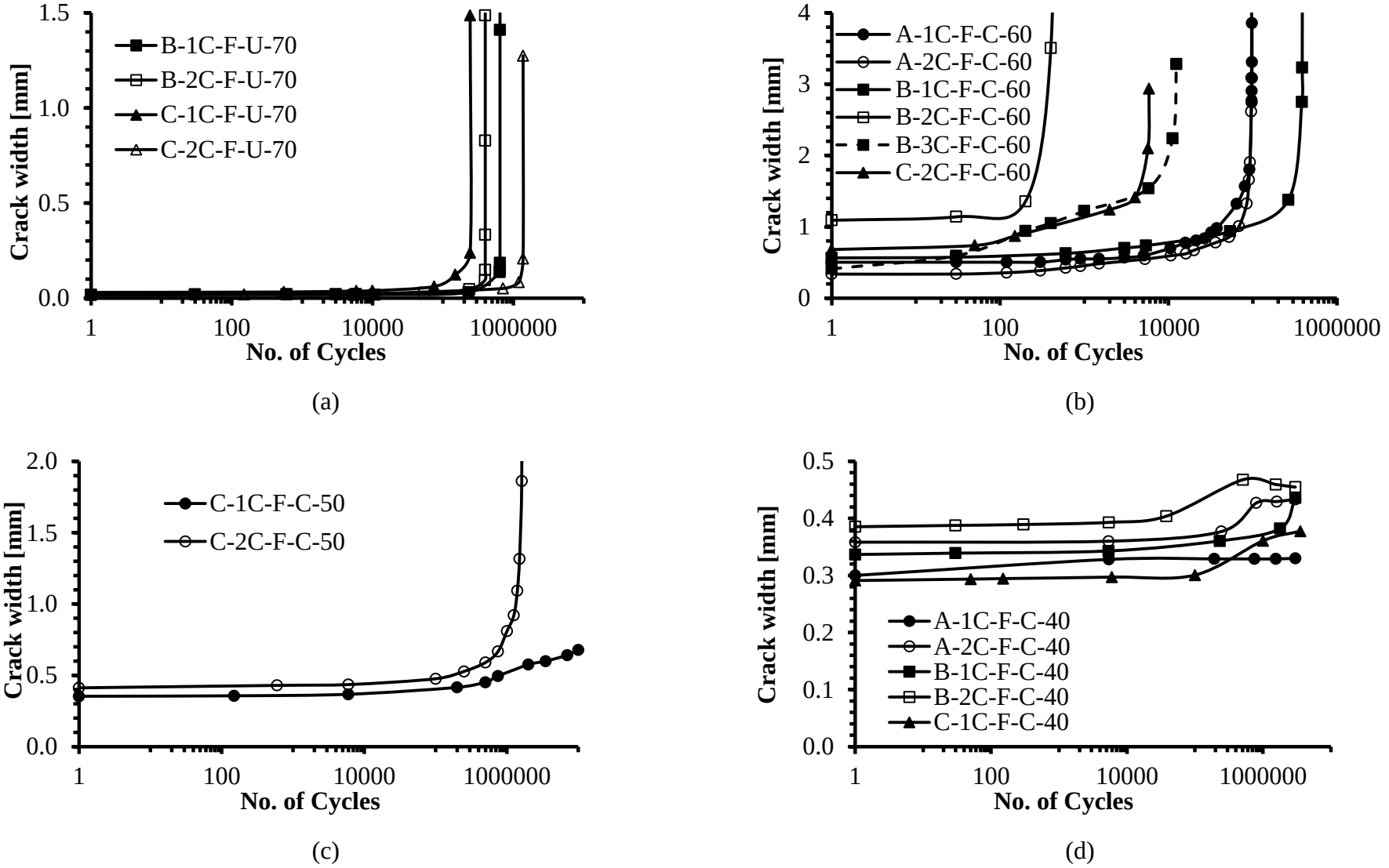

Figure 5.8 – Average crack width versus number of number of cycles during maximum load level for round panels.

5.5. Wöhler Curve

The results of fatigue tests can be summarized by plotting load level versus the number of cycles to failure (N_f); thus adopting the *S-N* (or Wöhler) curves to predict the fatigue performance of materials. For the tests performed in this research (three series), the fatigue lives for pre-cracked round panel, N_f, are shown in Figure 5.9. The load levels for the corresponding fatigue live are presented as a percentage of the peak load (P_{max}), experimentally measured for each specimen in the initial monotonic stage. Plotting *S-N* curves requires fatigue tests to be conducted at different load levels. In this study only two load levels for pre-cracked specimens, expect Series C, were considered. Accordingly, no *S-N* line equations are produced. In any case, the contribution of SFRC to fatigue resistance is evident as it guarantees a higher number of cycles to failure after concrete cracking. Also, it is clear that Figure 5.9 does not establish that a clear threshold of fatigue exists for SFRC; however, it is indicated that in excess of 3 million cycles is possible provided that load level, as percentage of concrete peak load capacity, does not exceed 40%. This disagrees with the statement by Germano et al. (2016) that the addition of fibres seems to be not effective in improving the fatigue behaviour of concrete when performing cyclic test under a 15% - 65% load level. Instead, SFRC seems to be effective for load levels within high cycle fatigue range, which generally involve large number of cycles at lower load levels. SFRC's effectiveness tends to maximise with fatigue load levels of not more than 50% of concrete capacity.

The fatigue life in Figure 5.9 shows significant scatter and is varying by more than two orders of magnitude for a given load level; it has been broadly stated that fatigue data always have wide range of scatter. However, this can also be attributed to the variation in post-cracking residual strength. From Figures 3.125 to 3.127, it is noticed that the residual post-cracking strength in range of zero to 6 mm of displacement varies remarkably, where fibre contribution has the maximum impact on fatigue life. Accordingly, and since the scope of this research work is to investigate the fatigue

behaviour of SFRC, it is worth mentioning that the choice of referring the fatigue load levels to the actual post-cracking peak load, instead of the concrete maximum load obtained from the static tests, can lead to reduce the large experimental scatter of fatigue results. This scatter can be related to a great extent to the dispersion of relating post-cracking strength (where fibre component governs the performance) to that of uncracked strength (where concrete component governs the performance). Accordingly, fatigue lives in Figure 5.10 are plotted versus load levels evaluated as a percentage of the post-cracking peak load. For the round panels that did not fail under cyclic loading, the post-cracking peak load of the specimen itself was used to evaluate the load level, while for failed panels the average post-cracking peak load of non-cyclically loaded specimens was used; this can explain the scatter of the data. It is also evident from Figure 5.10 that a fatigue life exceeding 3 million cycles is expected for a load level of 60% of post-cracking peak load. Consequently, it is clear that fatigue damage accumulated between steel fibres and concrete increases with higher load levels. Also shown in Figure 5.10 is an expression for load level versus failure number of cycles as shown below:

$$S = -0.087 \log(N_f) + 1.21 \qquad (5.10)$$

The model predicts the number of cycles after cracking of the concrete as presented in Table 5.2, where the fatigue limit equals the number of cycles to crack the concrete plus the number of post-cracking cycles. Equation (5.10) provides a reasonable approximation of the experimental results for the few specimens that were tested; more tests are needed to provide better evaluation of Equation (5.10).

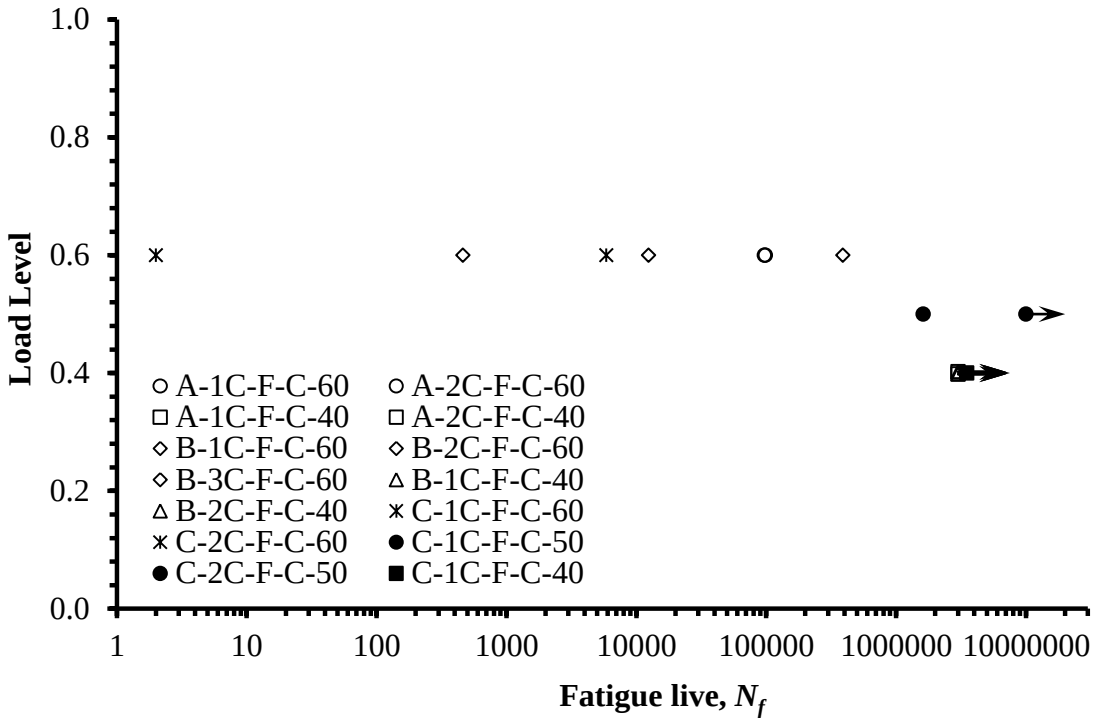

Figure 5.9 – Experimental fatigue lives based on concrete peak load capacity.

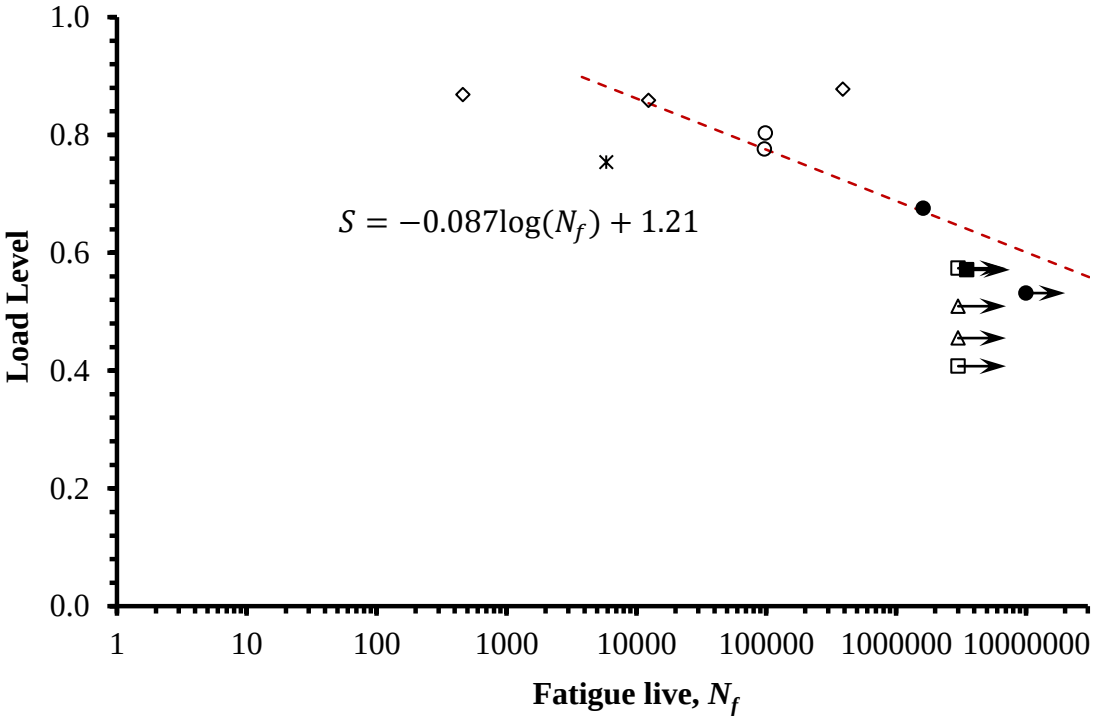

Figure 5.10 – Experimental fatigue lives based on post-cracking peak load capacity.

Table 5.2 – Experimental and model results of the number of cycles to failure.

Specimen ID	**Pre-cracked panels, No. of cycles**	
	$N_{f,Exp}$	$N_{f,Model}$
A-1C-F-C-60	98,386	47,908
A-2C-F-C-60	96,743	97,198
A-1C-F-C-40	> 3 Million	1.6×10^9
A-2C-F-C-40	> 3 Million	20.6×10^6
B-1C-F-C-60	388,975	6,594
B-2C-F-C-60	460	8,466
B-3C-F-C-60	12,431	11,014
B-1C-F-C-40	> 3 Million	113×10^6
B-2C-F-C-40	> 3 Million	473×10^6
C-1C-F-C-60	Nill	-
C-2C-F-C-60	5,868	175,935
C-1C-F-C-50	> 10 Million	62.9×10^6
C-2C-F-C-50	1,617,982	1.3×10^6
C-1C-F-C-40	> 3.5 Million	22.1×10^6

5.6. Constitutive Model for Post-Cracking Fatigue Damage

The load versus deflection and crack opening displacement are reported in Figures 5.11 to 5.17. The crack opening displacement in the figures is evaluated from Equations (5.7) to (5.9), with the elastic component of deflection subtracted. Linear approximation was adopted for the unload/reload path. It is clear that the rate of crack opening increment per cycle strongly affects the fatigue life. In other words, the higher is the crack opening rate, the faster the envelope curve is reached. One can observe that by increasing the load level, the crack increment per cycle increases significantly, as the higher is the upper load, the higher the fatigue demand and the relative damage induced (Sparks, 1982; Germano et al., 2016). In addition, plain concrete has a negligible crack opening rate; consequently, the addition of fibres guarantees a higher number of cycles to reach the envelope curve. Also, it is clear from the figures that as soon as the COD at the upper load during fatigue testing approaches the COD corresponding to the post-cracking peak load, the rate of COD increase accelerates; indicating that fibres are no longer capable of controlling the crack propagation and signalling the impending failure. This means that the extended fatigue resistance by the contribution of fibres is limited to the post-cracking peak load and its corresponding COD.

The unloading/reloading stiffness of the panel during the cyclic loading may be normalised by the modulus of the specimen to facilitate comparison and development of a material model. There are mainly two options, either normalising the unloading/reloading stiffness with the uncracked modulus or by the cracked modulus of the panel. The results of round panel B-2C-F-C-60 were neglected in this analysis since it had only a short fatigue life.

In previous studies of the literature, the performance of SFRC is mainly related to the uncracked concrete. The reduction of secant modulus ratio to the initial modulus of uncracked round panel over the related numbers of cycles to failure is shown in Figure 5.18, together with the evaluation of secant modulus for each series separately. It

is clear from the figure, that the cracked modulus of the specimen is about 40% of the uncracked ones. However, it is of high importance to relate the modulus of cracking cycles during fatigue loading to that of initial cracking stiffness, since the aim of this study is to shed new light on the post-cracking fatigue performance of SFRC where fibres mainly influence of the fatigue response in the fracture process zone and concrete has negligible impact. Accordingly, the modulus of cracked load cycles were normalised by the initial cracked stiffness.

The selection of initial cracked stiffness should be taken after crack stabilisation. This is due to the fact that the fatigue tests were conducted on pre-cracked specimens where cracks had already been initiated; this is followed by a stage of crack stabilisation. Consequently and for the purpose of determining the number of cycles required for crack stabilisation, the evaluation of secant modulus ratio to the modulus of the 1^{st}, 10^{th}, 100^{th} and 1000^{th} cracking cycle over the numbers of cycles to failure is presented in Figures 5.19 to 5.22, respectively, together with the evaluation of secant modulus for each series separately. The development of crack opening minus the 1^{st}, 10^{th}, 100^{th} and 1000^{th} cycle COD during cyclic loading is shown in Figures 5.23 to 5.26, respectively, along with the COD development for each series.

Different fibre types result in different post-cracking stiffness and crack opening displacement. For the purpose of comparison of different fibre types the modulus of cyclic loading were normalised with the initial cracking modulus which should eliminate or at least reduce any differences due to the utilisation of different fibres. For crack opening displacement, it can be seen from Figures 5.23 to 5.26 that the COD within the range of zero to 0.5 mm, approximately (up to post-cracking peak load), are actually contributing to the fatigue life of the SFRC. After that, and for the three series, fatigue failure occurs. It was discussed in Chapter 3, that with a range of COD from zero to about 2.0 mm, the post-cracking toughness is almost equivalent for the three

types of fibres used in this study. Consequently, it is acceptable to compare the development of crack opening displacement of these three series together.

It is clear from the figures that the curves become more coincident as the number of cycles selected as a reference increases. This is also more evident from the coefficient of variation of both the modulus ratio and the initial COD minus the crack opening of different number of cycles shown in Figures 5.27 and 5.28. However, for more a consequential comparison, the modulus ratio and COD development over the related number of cycles along with the corresponding coefficient of variation is plotted in Figure 5.29. It is observed that the coefficient of variation has the lowest percentage with 100 cycles of initial cyclic loading. Accordingly, the modulus ratio of E/E_{N100} and the COD development ($w - w_{100}$) were selected for the proposed model.

From the cyclic loading tests, presented in Figures 5.11 to 5.17, the load – COD(w) relationships have a tension-softening-like curve. It is noticeable that the residual COD(w) remained after the unloading stage, and the unloading/reloading stiffness tended to decrease as the COD(w) at the unloading plateau increased. From Figure 5.21, it is observed that the modulus ratio in pre-cracked SFRC in flexure and under cyclic loading follows three distinct stages, similar to concrete in compression; a rapid stiffness reduction from 0 to about 10 percent of the post-cracking fatigue life (Stage I), a uniform reduction from 10 percent to approximately 90 percent of the post-cracking fatigue life (Stage II) followed by a rapid increase to failure (Stage III). A similar approach is noticed for the crack opening displacement development shown Figure 5.25. Consequently, a model is proposed to represent these stages and is shown in in Figure 5.30.

Based on a regression analysis of the test data, the following relationship is proposed:

Stage I:

$$E_N = E_{N100}\, A e^{-B\frac{N}{N_f}} \qquad (5.11)$$

$$w_{max} = w_{100} + \alpha \ln(\beta \frac{N}{N_f} + 1) \quad (5.12)$$

Stage II:

$$E_N = E_{N100}\, C e^{-D\frac{N}{N_f}} \quad (5.13)$$

$$w_{max} = w_{100} + \gamma e^{\delta\frac{N}{N_f}} \quad (5.14)$$

Stage III:

$$E_N = E_{N100}\, E e^{-F\frac{N}{N_f}} \quad (5.15)$$

$$w_{max} = w_{100} + \varepsilon e^{\epsilon\frac{N}{N_f}} \quad (5.16)$$

The proposed model in Equations (5.11) to (5.16) uses the modulus and COD of one hundred cycles as its basis. The model is defined by twelve empirical parameters; where w_{max} is the crack opening displacement at upper limit of applied cyclic load, w_{100} is the crack opening displacement COD(w) at the 100th cycles, E_N is the unloading modulus at cycle N, E_{N100} is the unloading modulus at the 100th cycle (Figure 5.30), N_f is the number of cycles to failure and the constants A to F and α to ϵ are parameters that depend on the material properties and the load levels to fit experimental data. The parameters for the best fit are given in Table 5.3.

One of the main remaining concepts to establish the number of cycles to fatigue failure, through defining the failure cycle N_f from the static load – COD(w) relationship, is to initiate when the w_{max} at cycle N_f equals the ultimate w obtained from the static test at the target load level; a bilinear curve can be adopted to describe the static load – COD(w) curve as shown in Figure 5.30. Alternatively, failure cycle N_f can be calculated from Equation (5.10).

As can be seen from Figures 5.31 and 5.32, Equations (5.11) to (5.16) provide a reasonable approximation of the experimental results, given that only few specimens were tested. However, more tests will better approximate the values of parameters A to F and α to ϵ for different concrete mixtures.

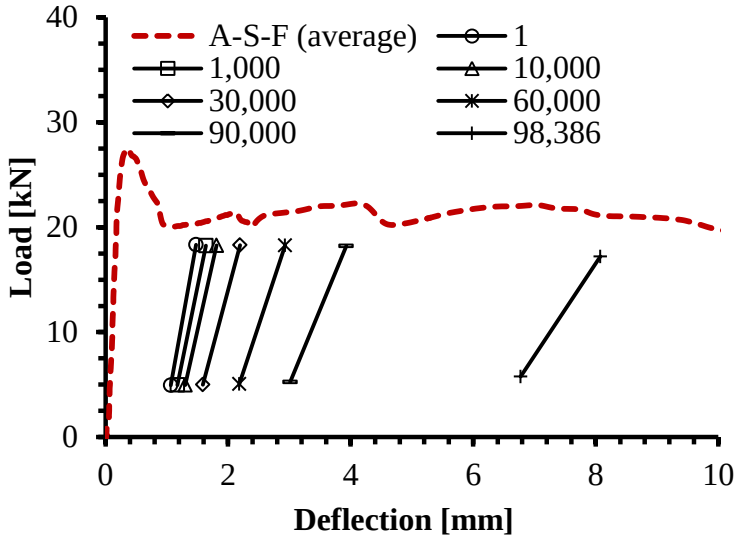

(a)

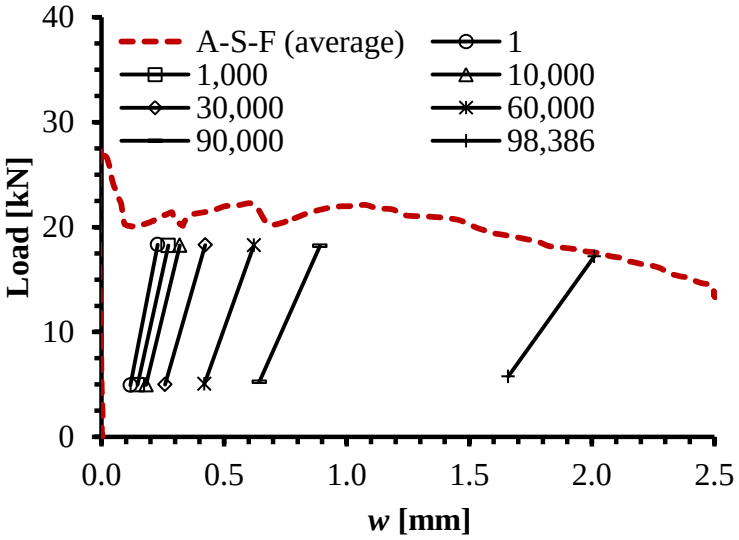

(b)

Figure 5.11 – Fatigue performance of round panel A-1C-F-C-60 (a) load versus deflection, (b) load versus COD.

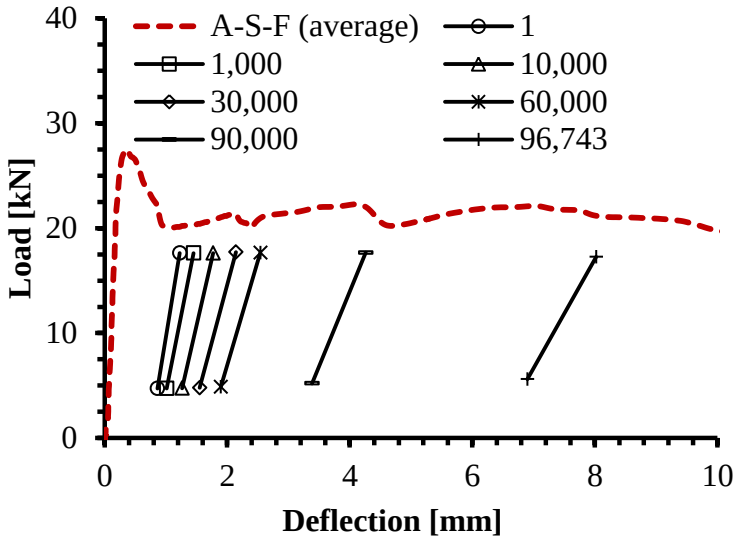

(a)

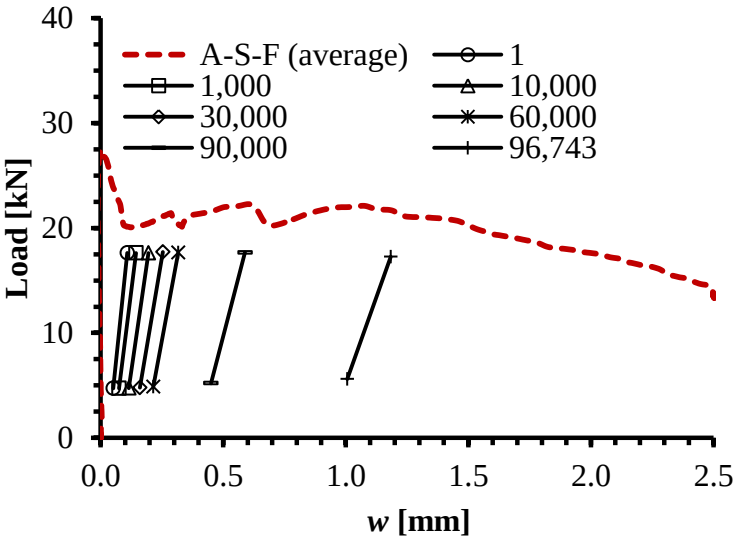

(b)

Figure 5.12 – Fatigue performance of round panel A-2C-F-C-60 (a) load versus deflection, (b) load versus COD.

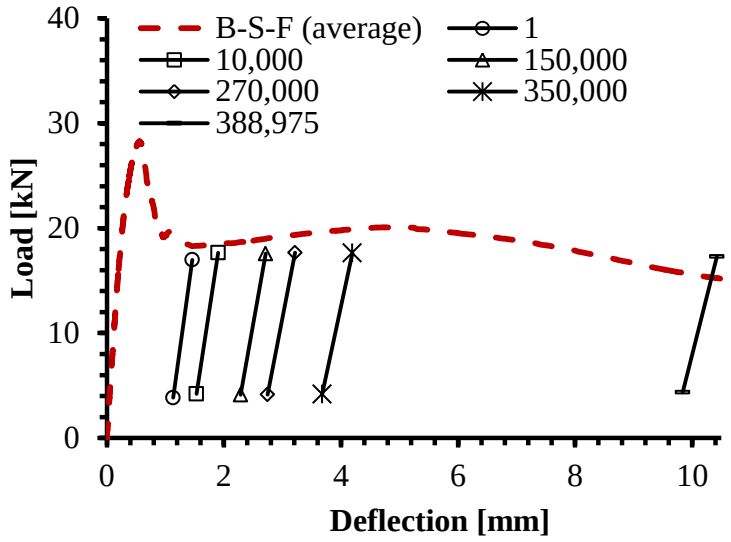

(a)

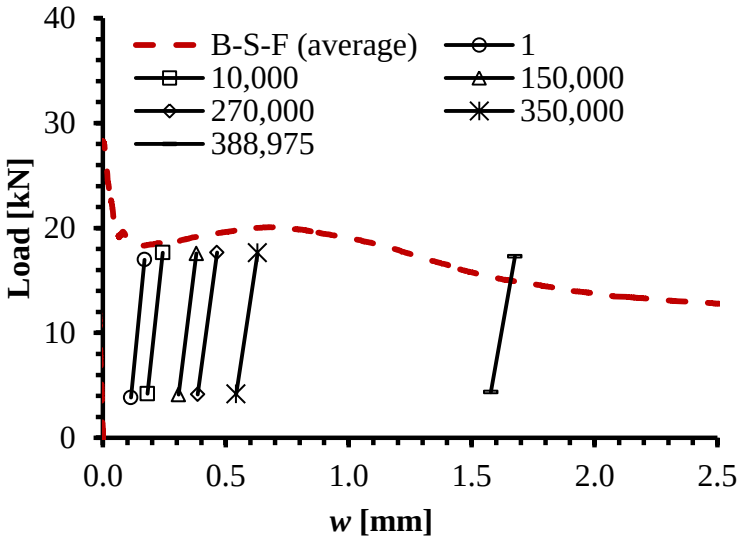

(b)

Figure 5.13 – Fatigue performance of round panel B-1C-F-C-60 (a) load versus deflection, (b) load versus COD.

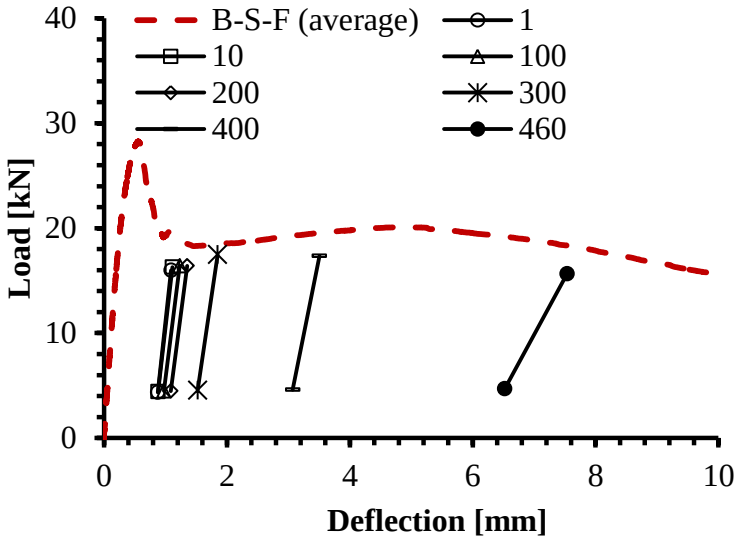

(a)

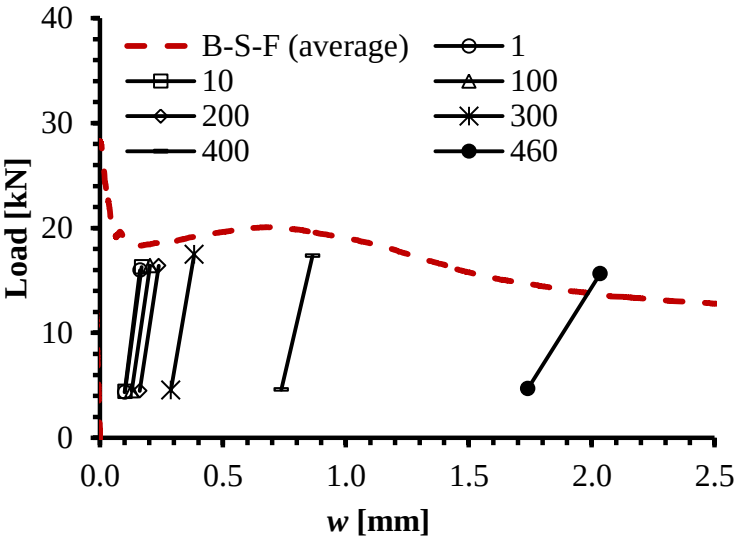

(b)

Figure 5.14 – Fatigue performance of round panel B-2C-F-C-60 (a) load versus deflection, (b) load versus COD.

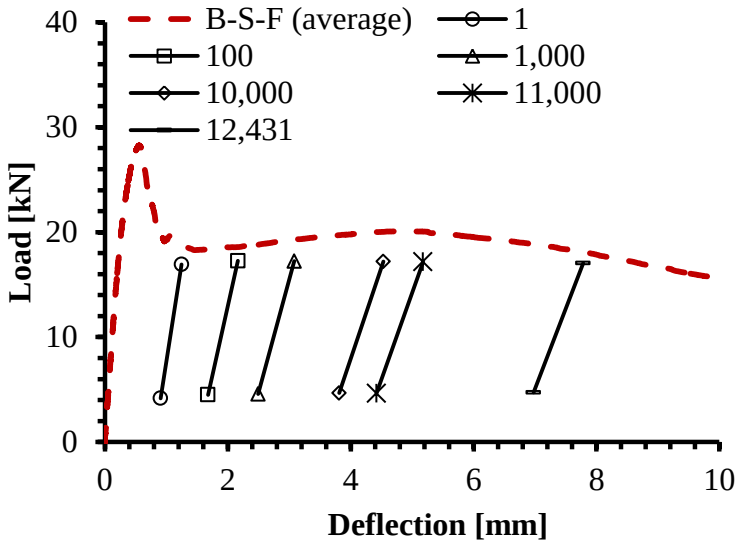

(a)

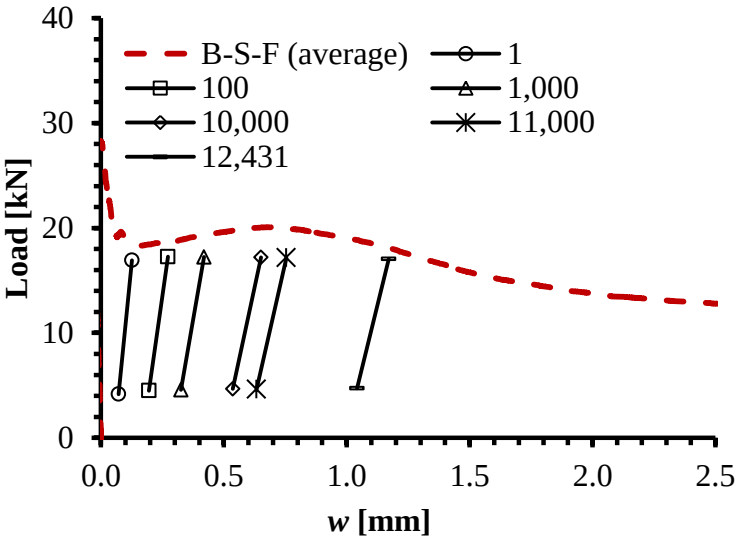

(b)

Figure 5.15 – Fatigue performance of round panel B-3C-F-C-60 (a) load versus deflection, (b) load versus COD.

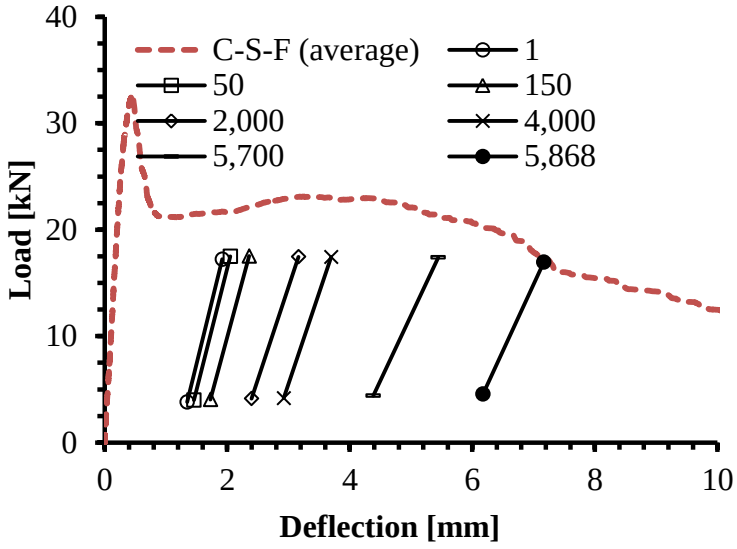

(a)

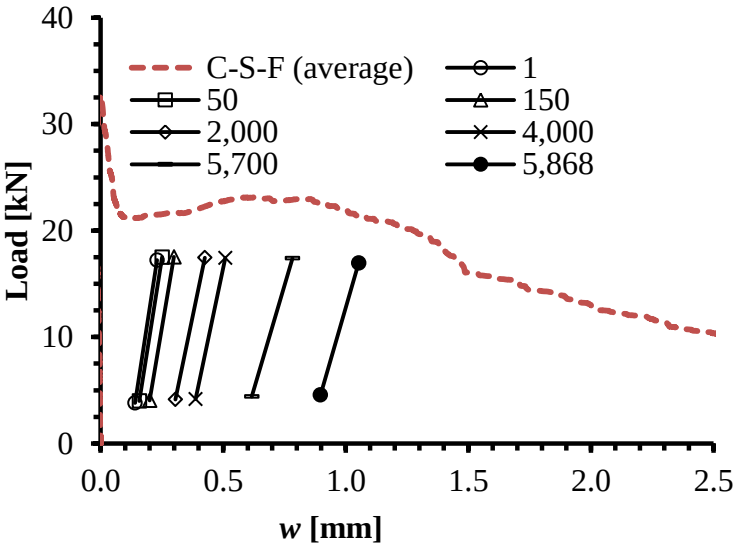

(b)

Figure 5.16 – Fatigue performance of round panel C-2C-F-C-60 (a) load versus deflection, (b) load versus COD.

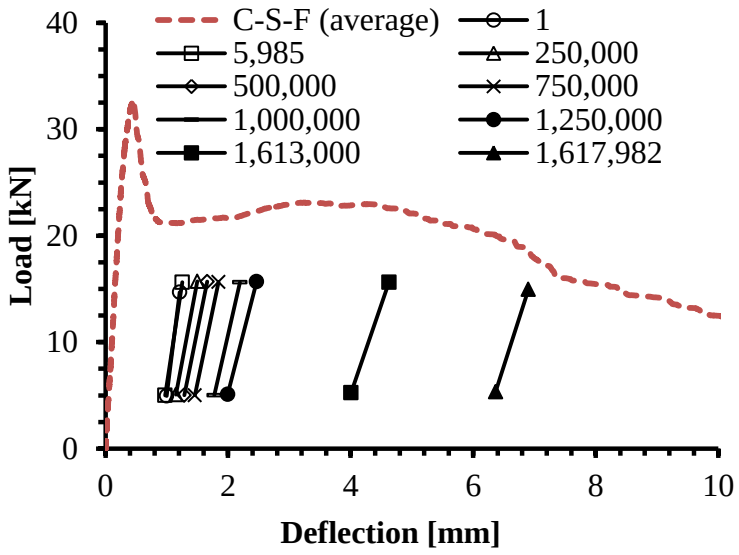

(a)

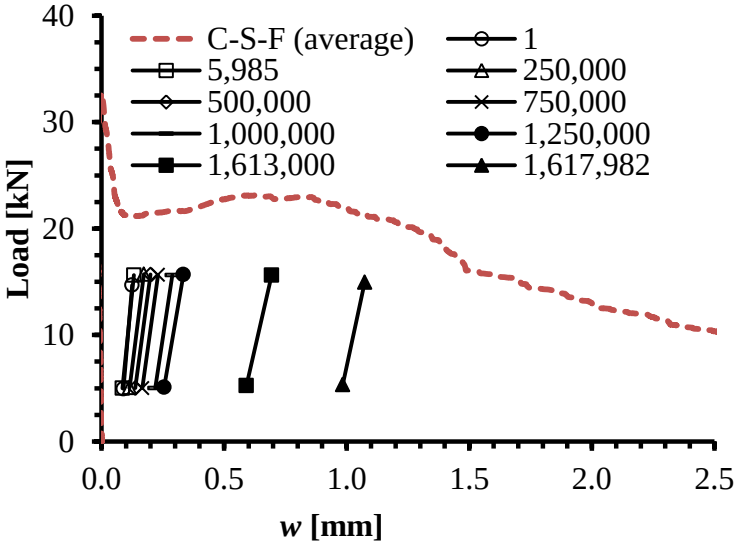

(b)

Figure 5.17 – Fatigue performance of round panel C-2C-F-C-50 (a) load versus deflection, (b) load versus COD.

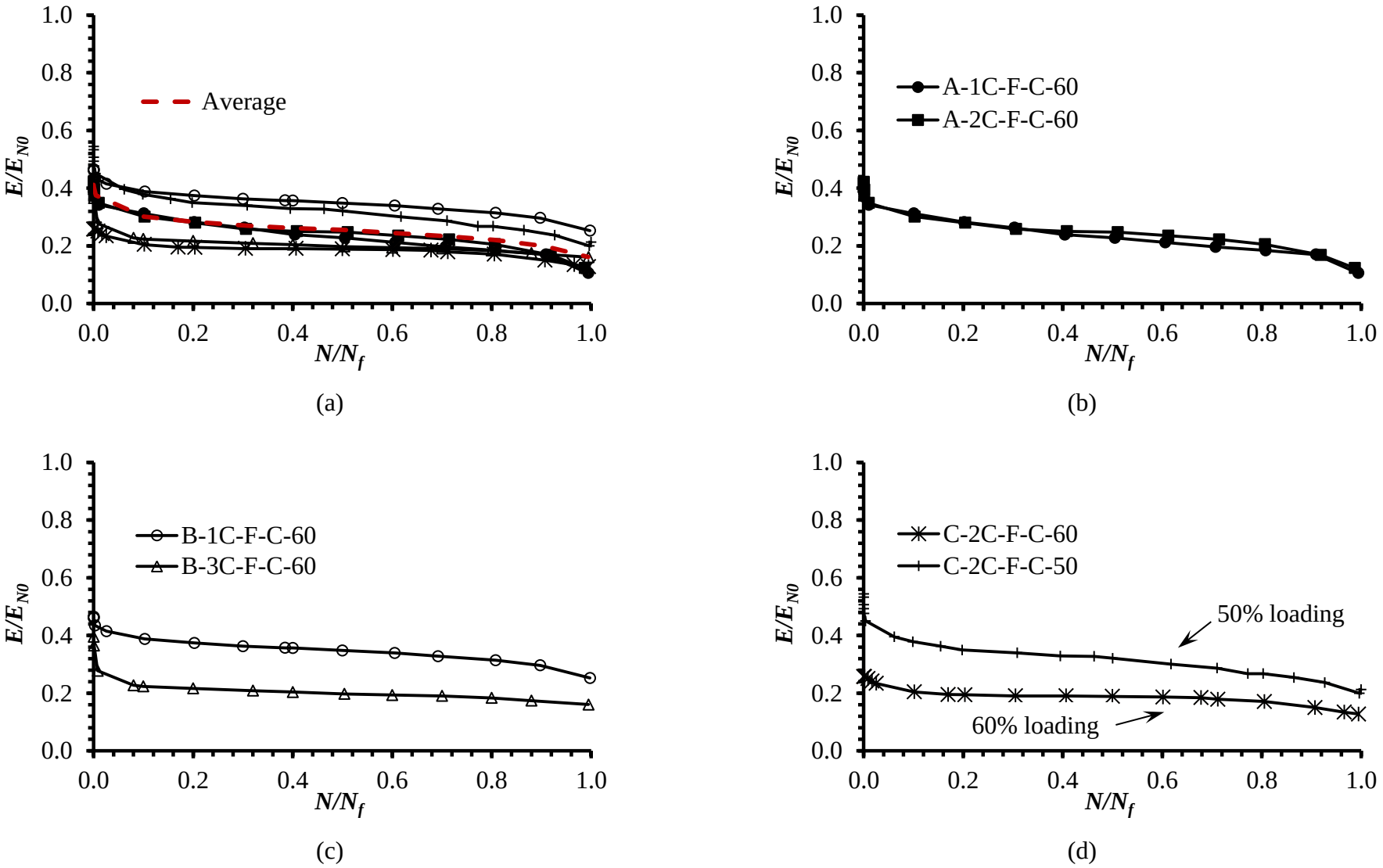

Figure 5.18 – Evaluation of secant modulus ratio to the initial modulus of uncracked round panel over the related numbers of cycles to failure.

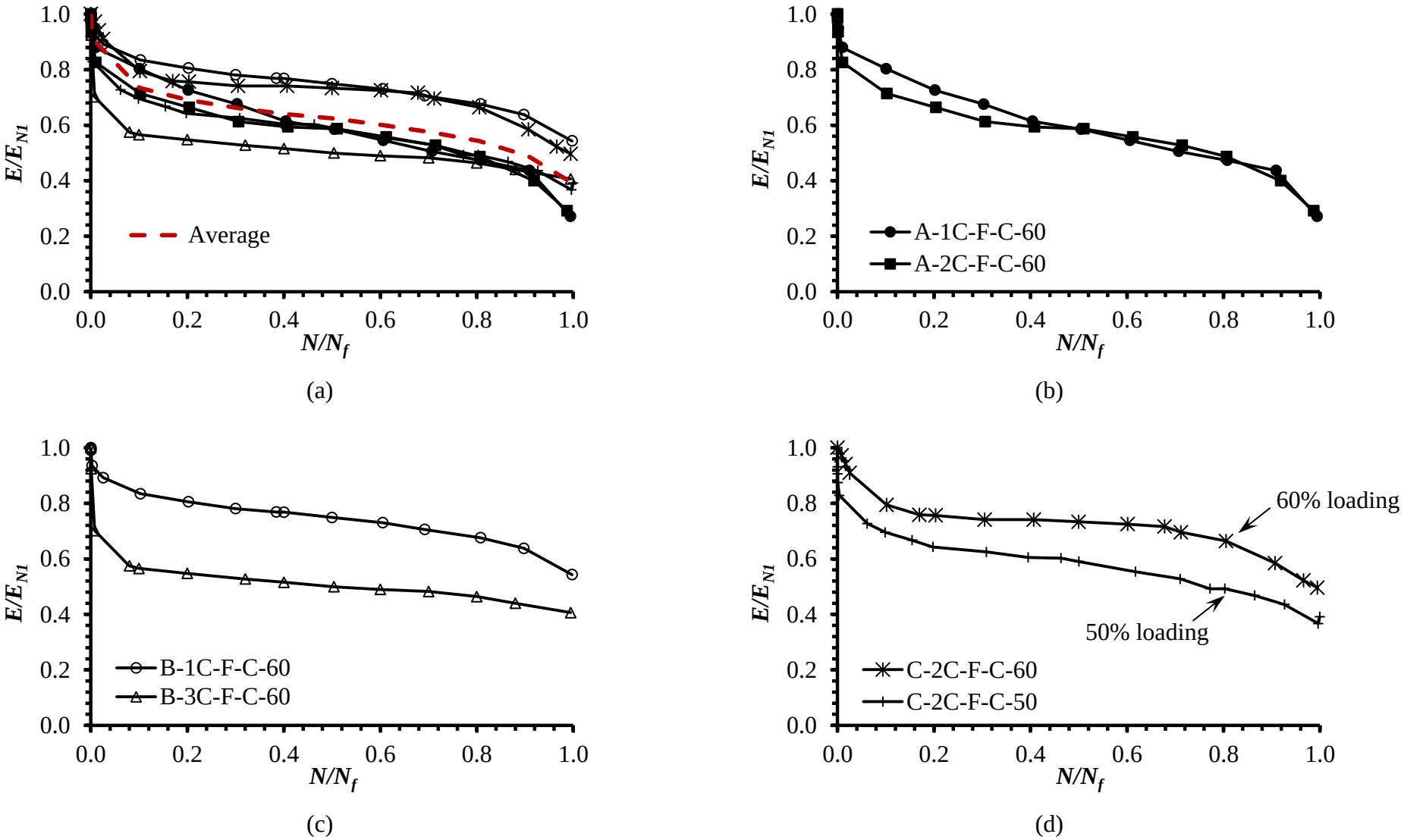

Figure 5.19 – Evaluation of secant modulus ratio to the 1st cracking cycle modulus over the related numbers of cycles to failure.

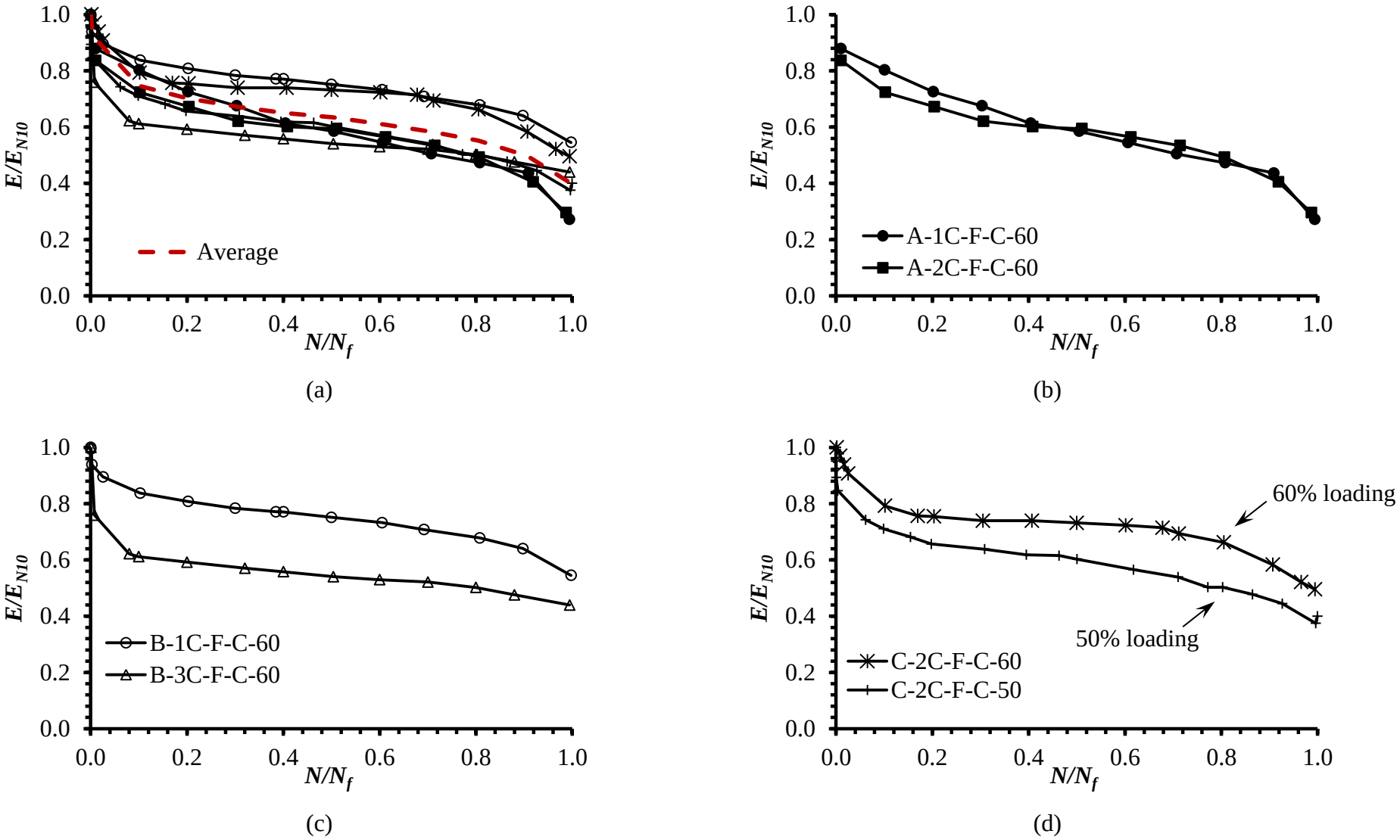

Figure 5.20 – Evaluation of secant modulus ratio to the 10th cracking cycle modulus over the related numbers of cycles to failure.

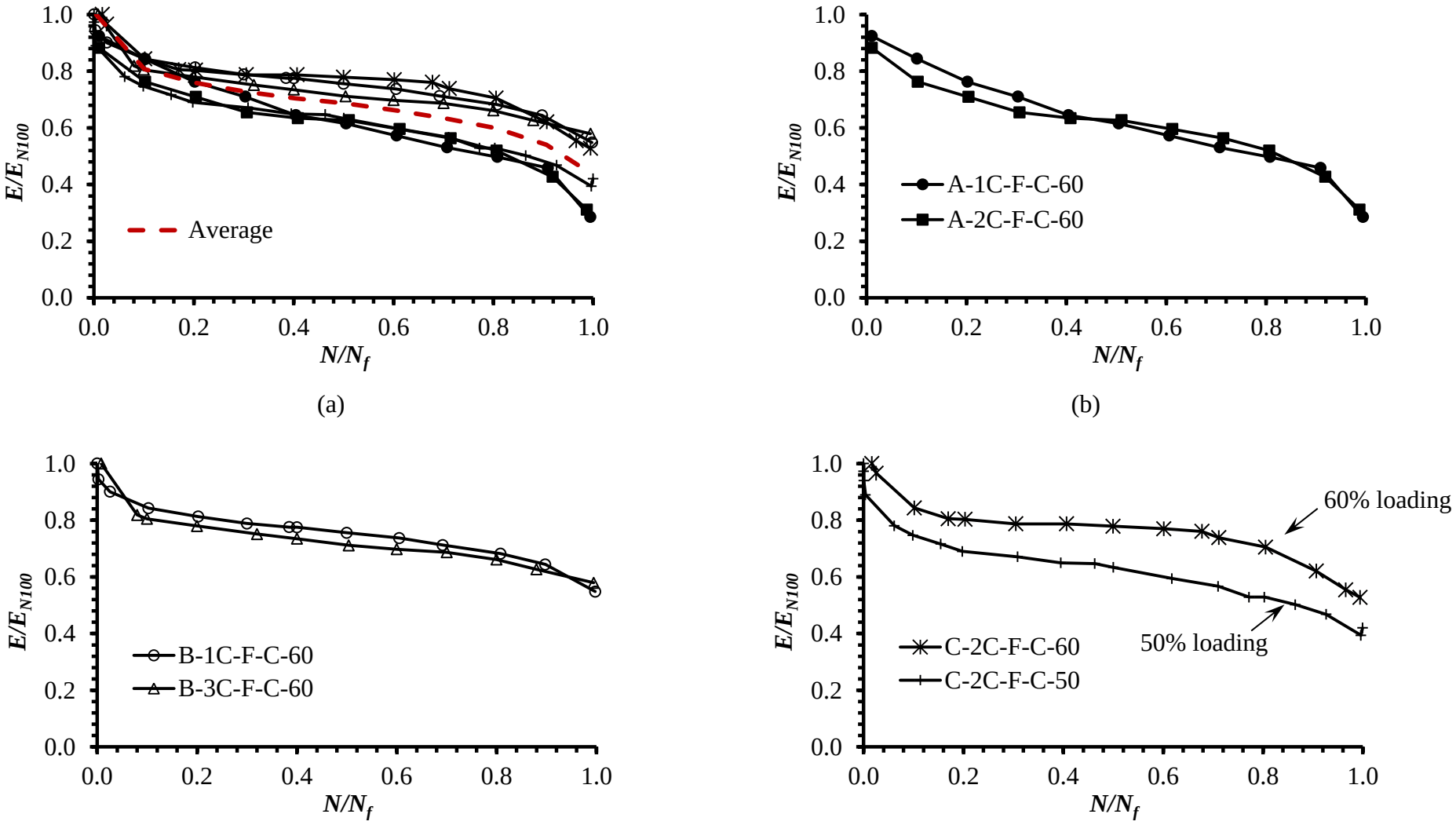

Figure 5.21 – Evaluation of secant modulus ratio to the 100th cracking cycle modulus over the related numbers of cycles to failure.

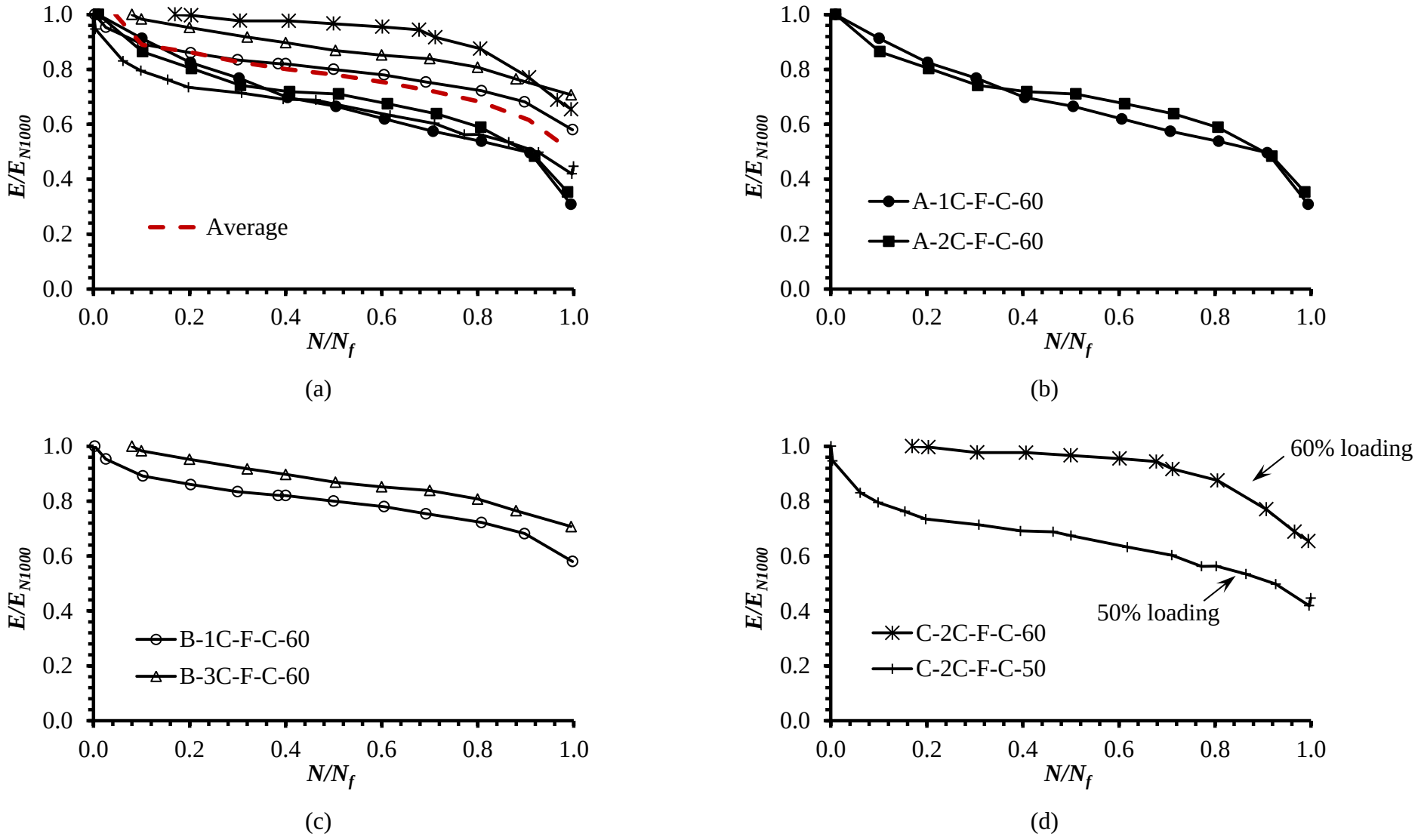

Figure 5.22 – Evaluation of secant modulus ratio to the 1000th cracking cycle modulus over the related numbers of cycles to failure.

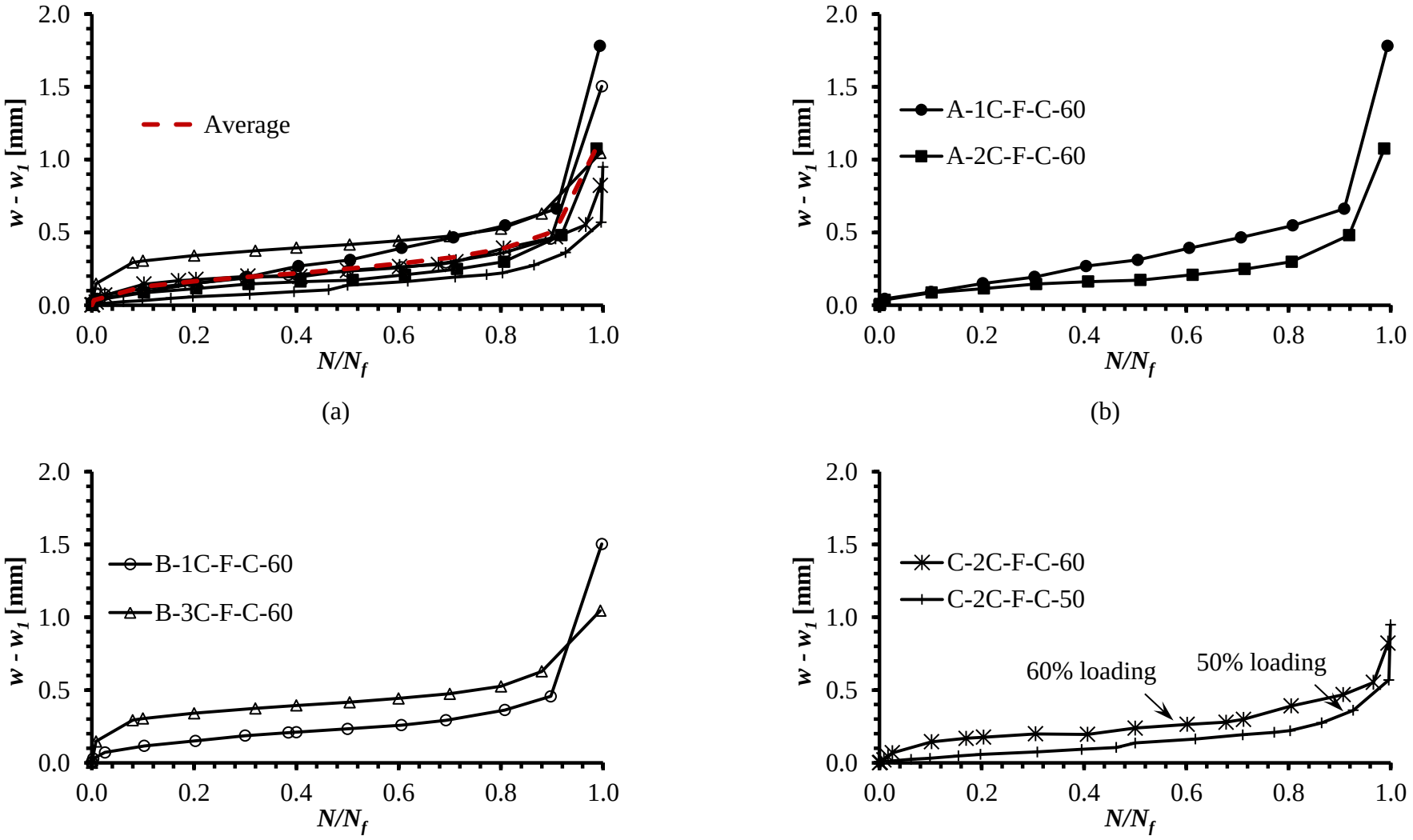

Figure 5.23 – Development of COD minus the 1st cycle COD during cyclic loading.

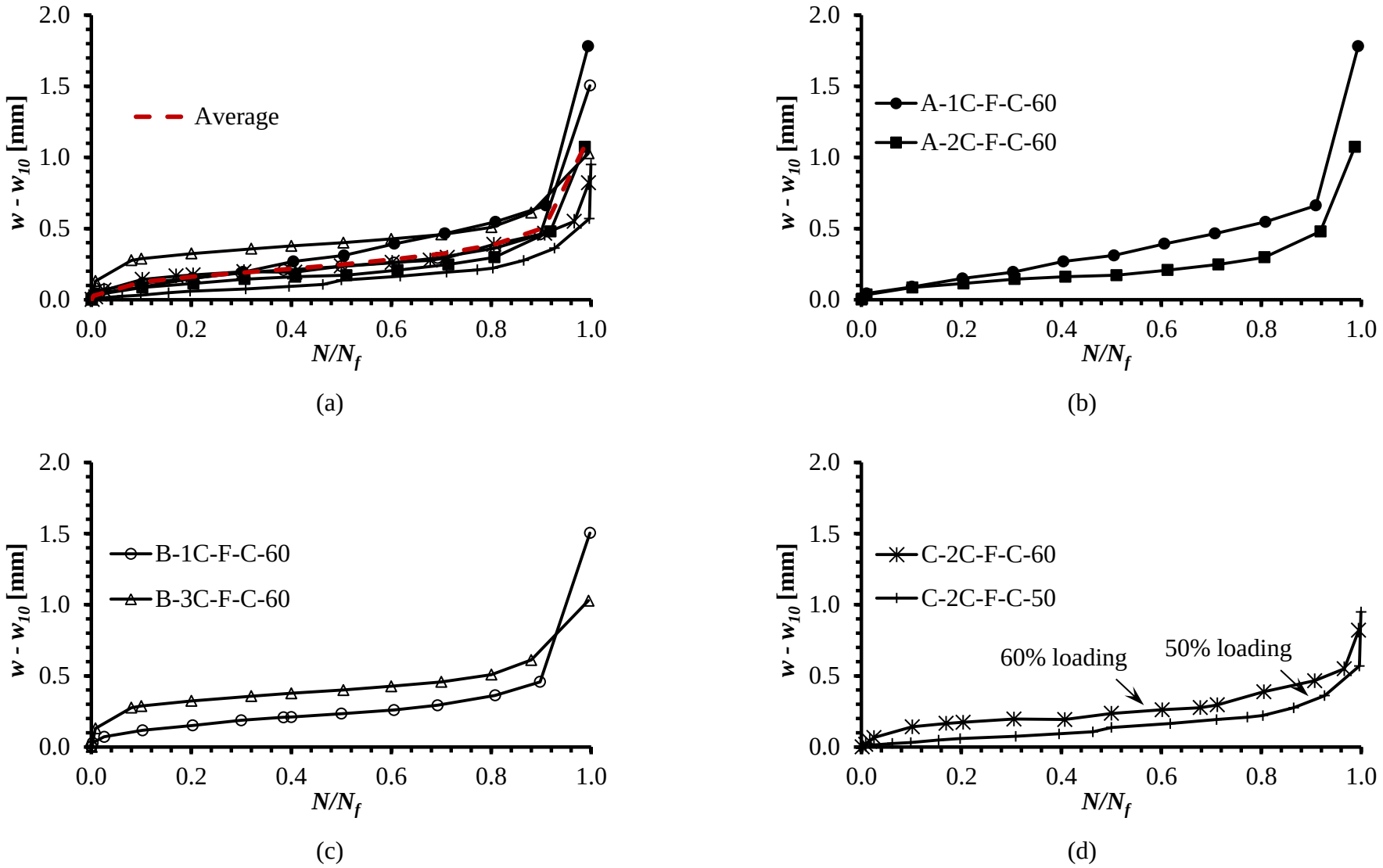

Figure 5.24 – Development of COD minus the 10th cycle COD during cyclic loading.

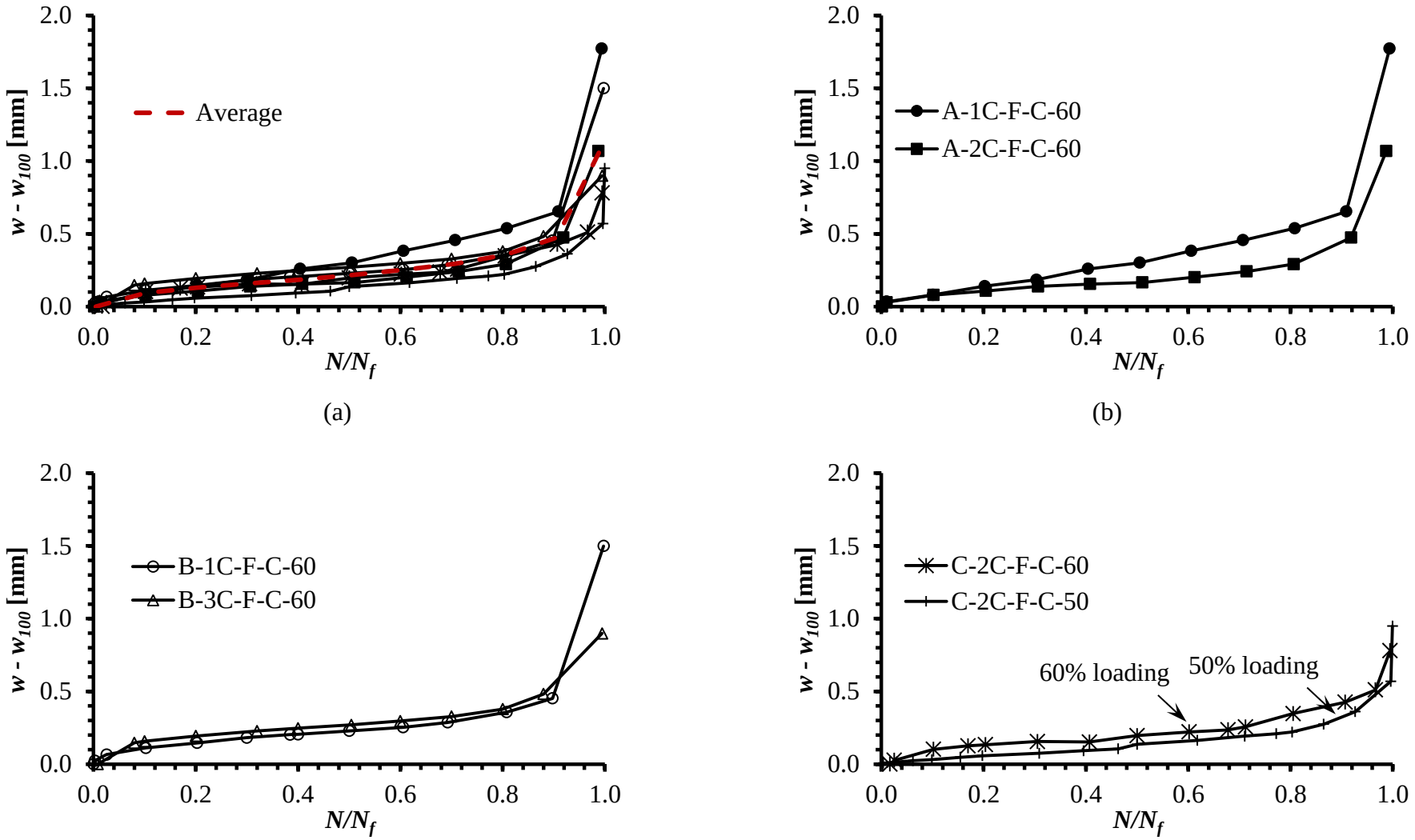

Figure 5.25 – Development of COD minus the 100th cycle COD during cyclic loading.

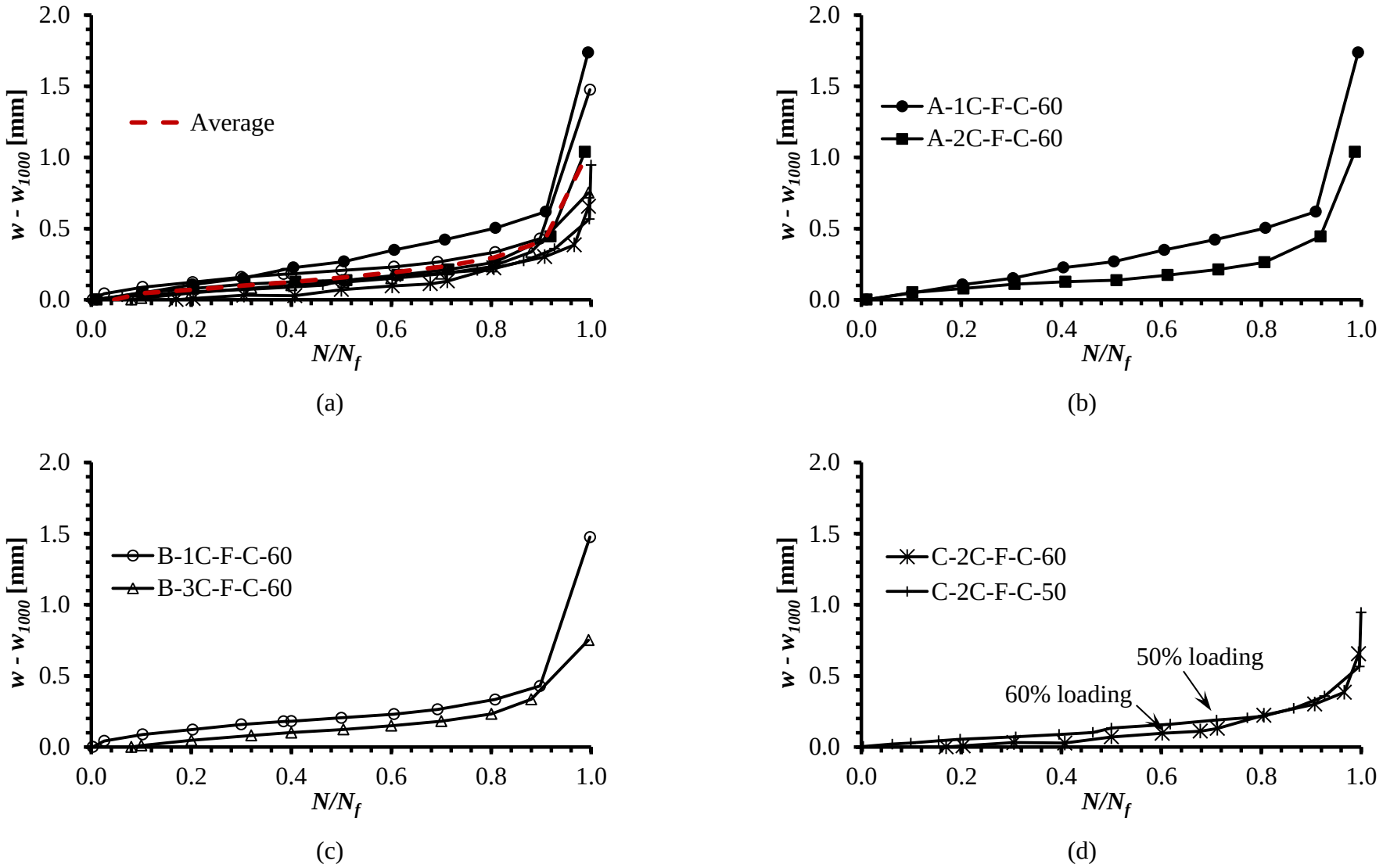

Figure 5.26 – Development of COD minus the 1000th cycle COD during cyclic loading.

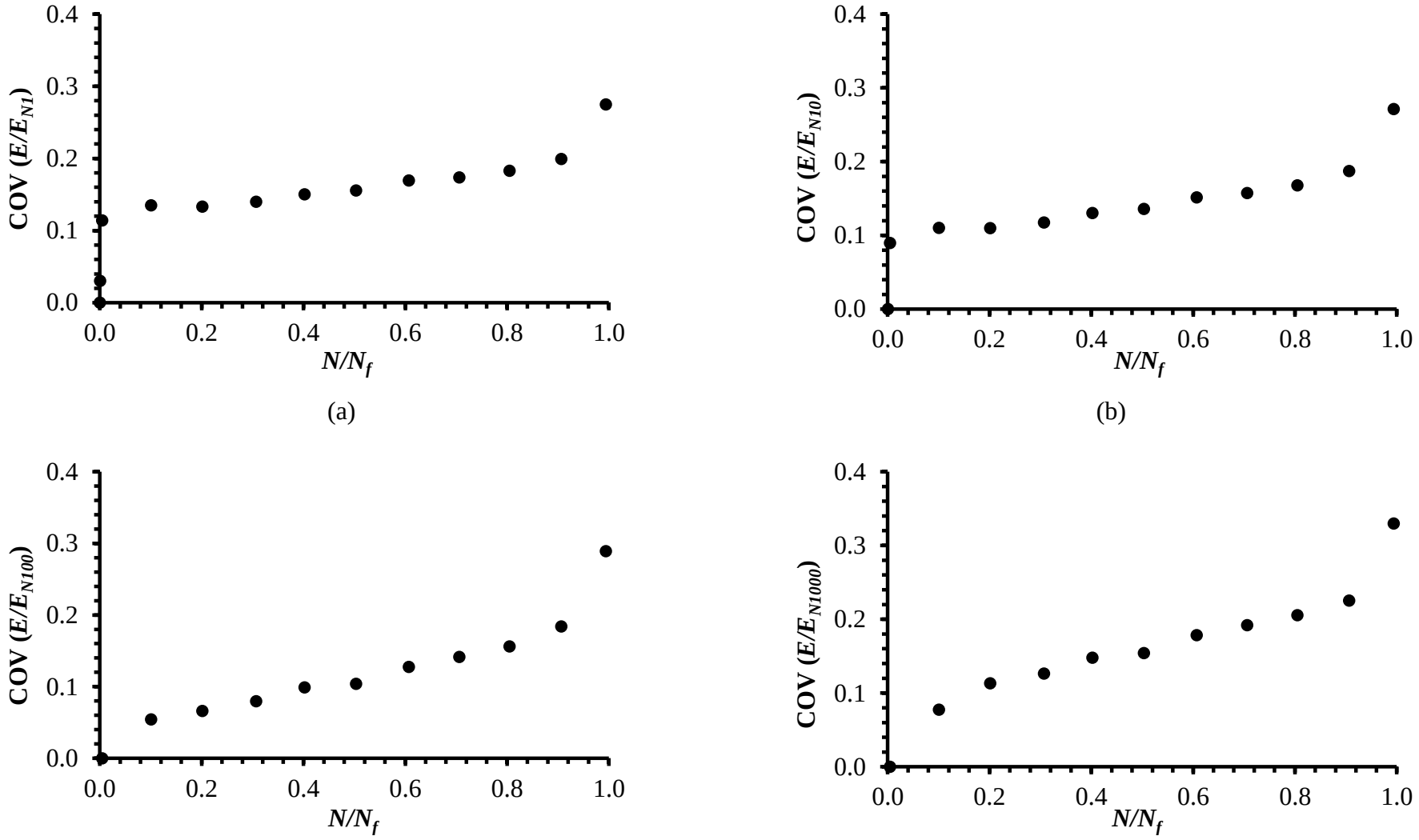

Figure 5.27 – Coefficient of variation of modulus ratio for different number of cycles: (a) E_{N1}; (b) E_{N10}; (c) E_{N100}; (d) E_{N1000}.

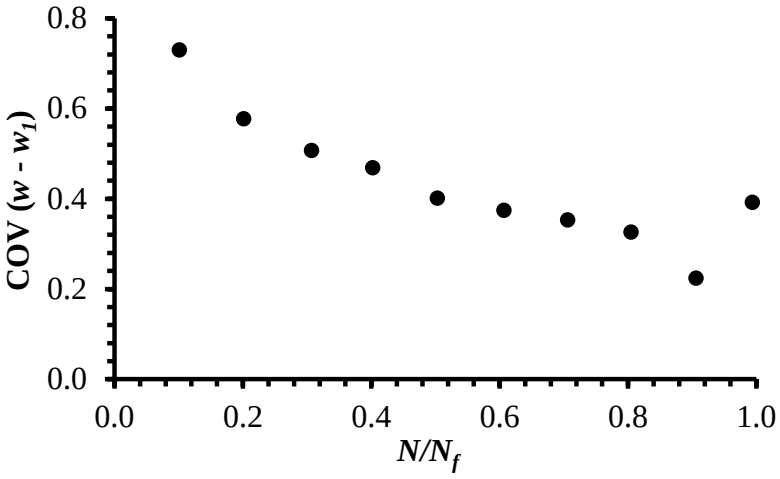

(a)

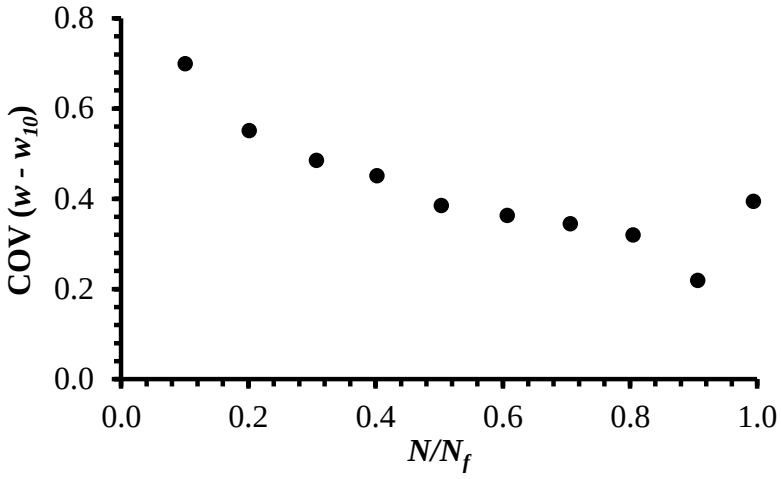

(b)

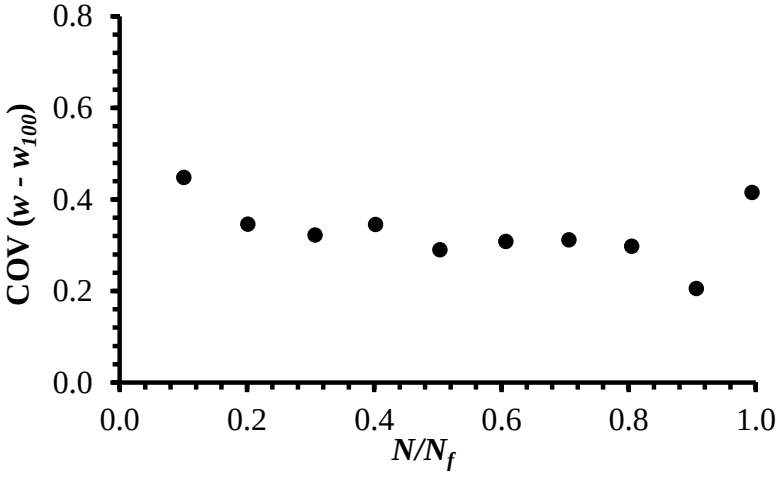

(c)

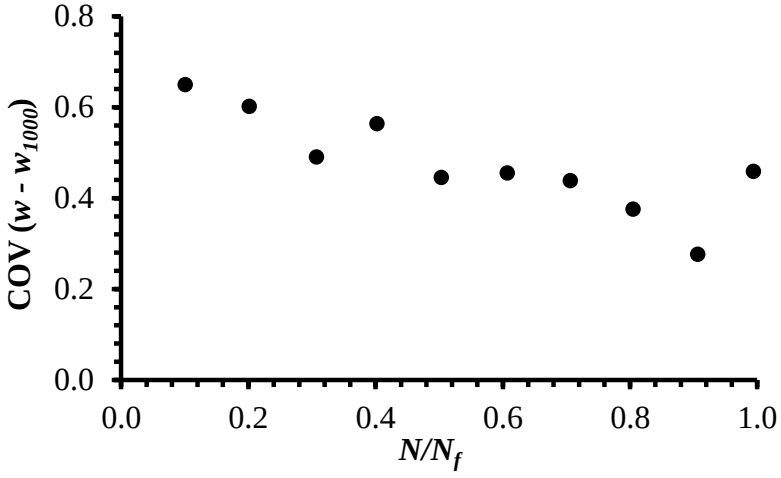

(d)

Figure 5.28 – Coefficient of variation of COD minus the COD of different number of cycles: (a) w_1; (b) w_{10}; (c) w_{100}; (d) w_{1000}.

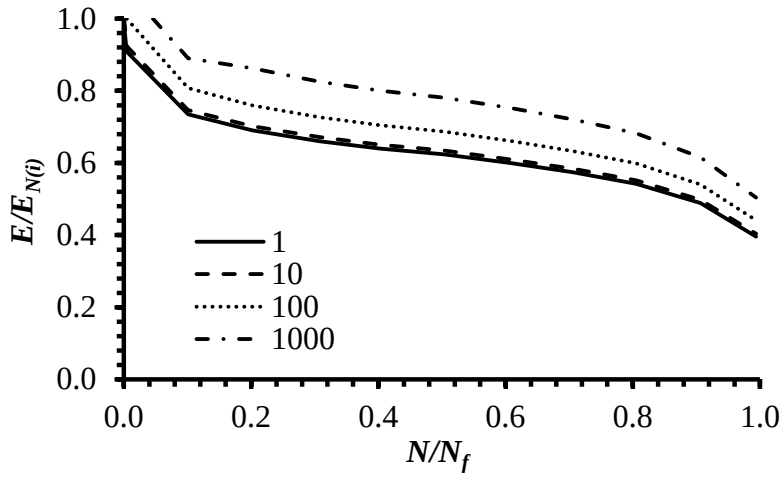

(a)

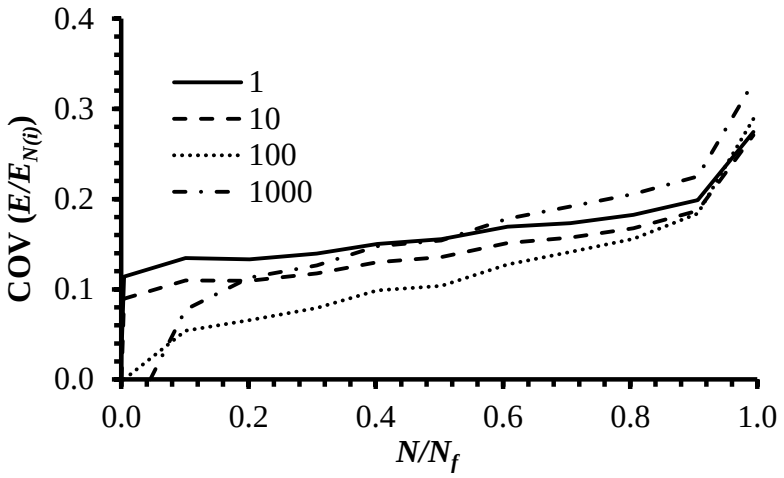

(b)

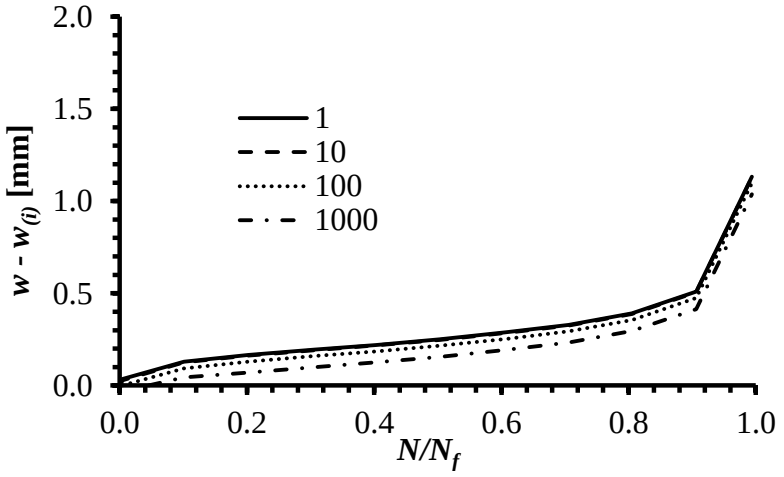

(c)

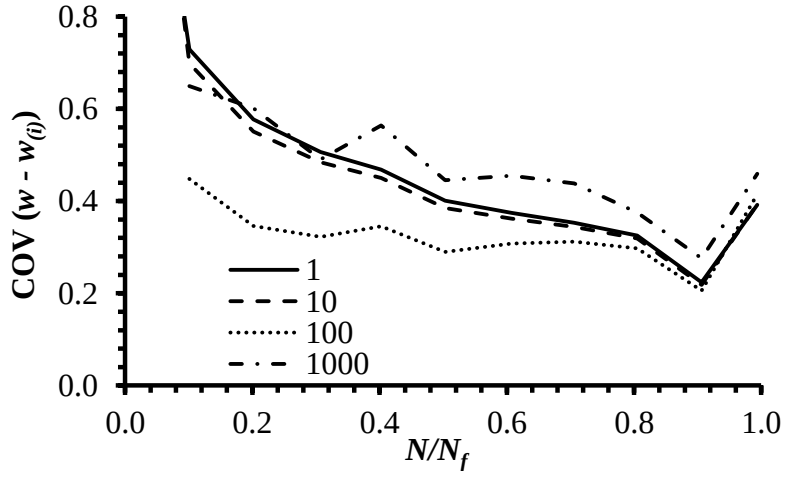

(d)

Figure 5.29 – Comparison of modulus ratio and COD development over the related number of cycles along with the corresponding COV.

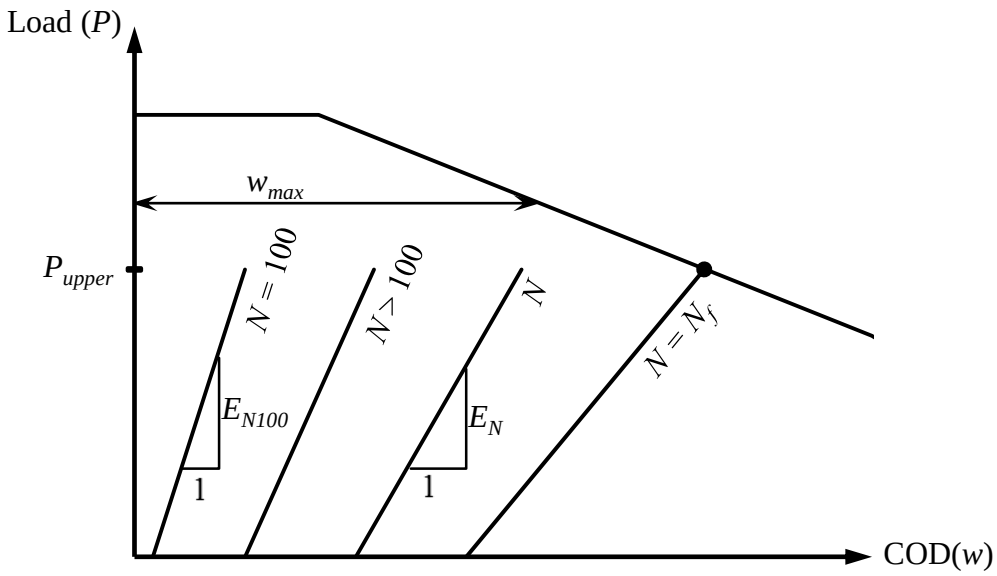

Figure 5.30 – Cyclic hysteresis model for SFRC round panel subjected to fatigue loading.

Table 5.3 – Constants for load – COD(w) relationship

Constant	Value	Constant	Value
A	1.0	α	0.4
B	2.1	β	3.0
C	0.85	γ	0.09
D	0.44	δ	1.8
E	4.5	ε	0.00008
F	2.3	ϵ	9.6

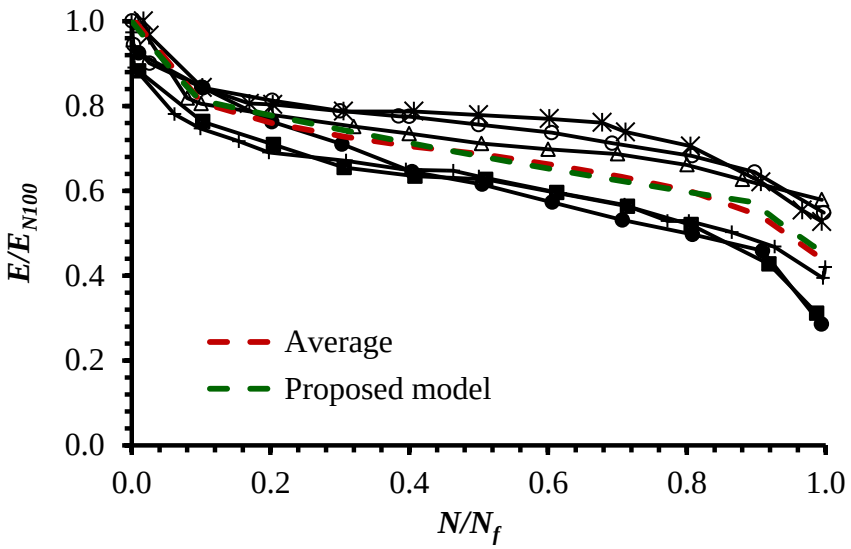

Figure 5.31 – Evaluation of modulus over the related numbers of cycles to failure.

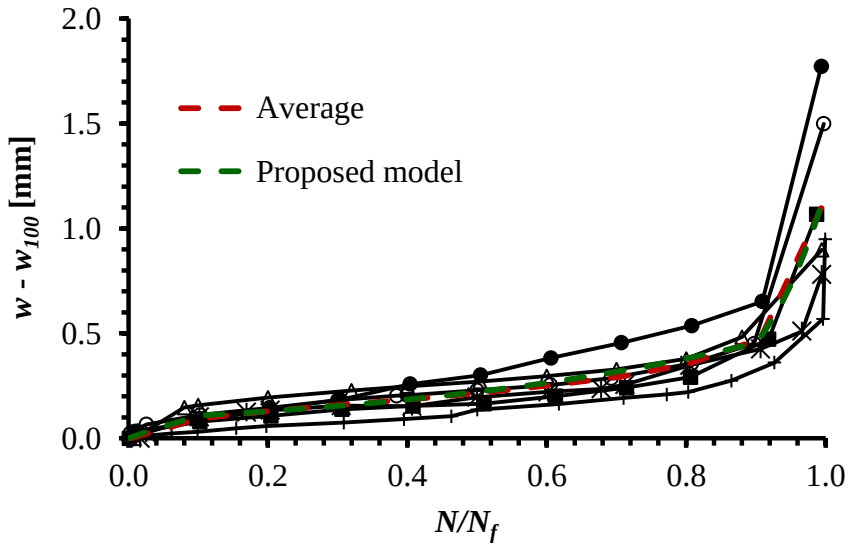

Figure 5.32 – Development of crack opening displacement over the related numbers of cycles to failure.

5.7. Concluding Remarks

In this chapter, the deviation of failure planes in round panel tests was discussed and related to the variation in post-cracking material properties. It was concluded that a variation of 13% in residual strength is needed to lead to one fractural line failure mode which results in lower magnitude in failure load. Based on a normal distribution, the probability that a single fracture line governs, as opposed to a three fracture line mode, is 10.7%.

Fibres control the crack opening range and the crack opening increment per cycle; the combination of these two parameters governs the fatigue life of SFRC and results in greater fatigue resistance. The effectiveness of steel fibres is greater for high cycle fatigue range and tends to maximise with fatigue load level lower than 50% of the specimen capacity. The envelope curves obtained from cyclic tests match well with the curves obtained from the static tests for round panels. The cyclic creep curves for pre-cracked concrete are characterized by a linear branch followed by a rapid increase of deformation and crack growth until failure. The number of cycles to failure is related to the slope of the linear branch. The experimental test results indicated that steel fibres control the crack propagation and increase the fatigue resistance of SFRC up to the post-cracking peak load and its corresponding COD.

A constitutive model is developed for SFRC for post-cracking fatigue damage during cyclic loops. The model is verified against the test data collected in this study with a framework developed for further calibration as new data becomes available. Comparing the results of the model with test data shows that the model is capable of accurately predicting the overall cyclic fatigue loading response of SFRC. The model is also able to capture the change in the COD, the stiffness development with increasing load cycles, and the number of load cycles to failure. The need for more tests on pre-cracked concrete subjected to high cycle fatigue loading is identified.

Chapter 6 PERFORMANCE OF PLAIN AND STEEL FIBRE REINFORCED CONCRETE PAVEMENTS UNDER STATIC AND FATIGUE LOADING

6.1. Introduction

The use of steel fibre reinforced concrete for infrastructure applications is becoming more popular with the introduction of new high performance materials. SFRC is introduced to enhance the overall performance of structures, such as composite bridge decks, beams, bearing walls, road pavements, etc. Concrete is the most used construction material possessing many desirable properties like high compressive strength and durability. At the same time, concrete has some disadvantages. Plain concrete has low tensile strength, low ductility and does not offer much resistance against cracking. The development of micro cracks limits its tensile strength at initially, these cracks do not harm too much, but on propagation the magnitude of loss and severity of damage will be more. Concrete with its brittle nature and low tensile strength is more susceptible to fracture. These problems can be overcome by reinforcing concrete with fibres.

Structural fibres can extend the service life of thin concrete pavements and overlays. These fibres improve the post-crack performance of concrete (Rollins, 1986; Roesler et al., 2003; ACI, 2009; Mulheron et al., 2015) by keeping cracks tight, which helps to reduce the propagation of fatigue cracks. These fibres increase the joint load transfer (Barman, 2014) and decrease the slab deflection at joints or cracks (Barman and Hansen, 2018), which eventually can decrease joint faulting or other joint deteriorations. The higher performance of SFRC provides evidence about the qualitative benefit of structural fibres (Barman and Hansen, 2018); however, those evidences do not provide a comprehensive quantification of the benefits.

Use of fibre reinforced concrete for pavements, though widely established, lacks comprehensive standardization with respect to both design as well as implementation. Most widely used design methods have adopted the established techniques used for slab-on-grade, mostly due to lack of studies specific to pavements. This is a major drawback since the failure of slabs-on-grade is predominantly caused by static loading whereas the failure of pavements, more often than not, occurs at much lower stresses due to fatigue. In this context, a comprehensive experimental methodology is proposed to test the hypothesis that thinner SFRC pavements can carry the same or even higher number of load repetition of those of currently constructed plain concrete ones, with minimum maintenance requirements.

6.2. Experimental Program

The experimental program consists of eight fully supported pavements of which three are plain concrete control specimens and five are SFRC. The main testing parameters are steel fibre content, specimen thickness and load levels. Four (out of eight) slabs were tested under constant amplitude cyclic loading and four specimens were tested under static loading. Two different load levels were used to study the effect of cyclic loading on the fatigue performance of the SFRC slabs. All the specimens were uncracked prior to fatigue testing, but slab B-CF-C was pre-cracked before the cyclic loading was applied. End-hooked steel fibres 4D 55/60 were used in SFRC slabs. The results of the tests are presented and evaluated with particular emphasis on the effects of steel fibres on the fatigue life of the pavements by controlling the propagation of cracks.

6.2.1. Variables and Specimen Dimensions

The specimens were designated using the notation U-VW-X, where 'U' is the series name indicating the loading span as (A), having a loading span of 1.0 metres, and (B) with a loading span of 2.3 metres; 'V' refers to static (S) or cyclic (C) applied loading; 'W' indicates plain (P) or fibre reinforced (F) concrete; and 'X' represents whether the specimen was pre-cracked (C) or uncracked (U) before the application of the cyclic (fatigue) loading. For example, specimen B-CF-C represents a pre-cracked SFRC slab specimen of Series B with 2.3 metres loading span, and cyclic loading is applied.

The specimen dimensions and testing arrangements are shown in Figure 6.1. The pavements were 1.0 metres wide, 3.0 metres long and had an overall depth of 250 mm for the plain concrete slabs and 200 mm for the SFRC ones. The test program for the slabs is outlined in Table 6.1.

Table 6.1 – Test program for pavements.

Specimen ID	**Loading span, *S* [mm]**	**Test type**	**Slab's thickness, *h* [mm]**	**Pre-cracked**	**Fibre content**	**Max load**
A-SP-U	1000	Static	250	No	0	-
A-SF-U	1000	Static	200	No	30 kg/m^3	-
A-CP-U	1000	Fatigue	250	No	0	70%
A-CF-U	1000	Fatigue	200	No	30 kg/m^3	70%
B-SP-U	2300	Static	250	No	0	-
B-SF-U	2300	Static	200	No	30 kg/m^3	-
B-CF-U	2300	Fatigue	200	No	30 kg/m^3	70%
B-CF-C	2300	Fatigue	200	Yes	30 kg/m^3	50%

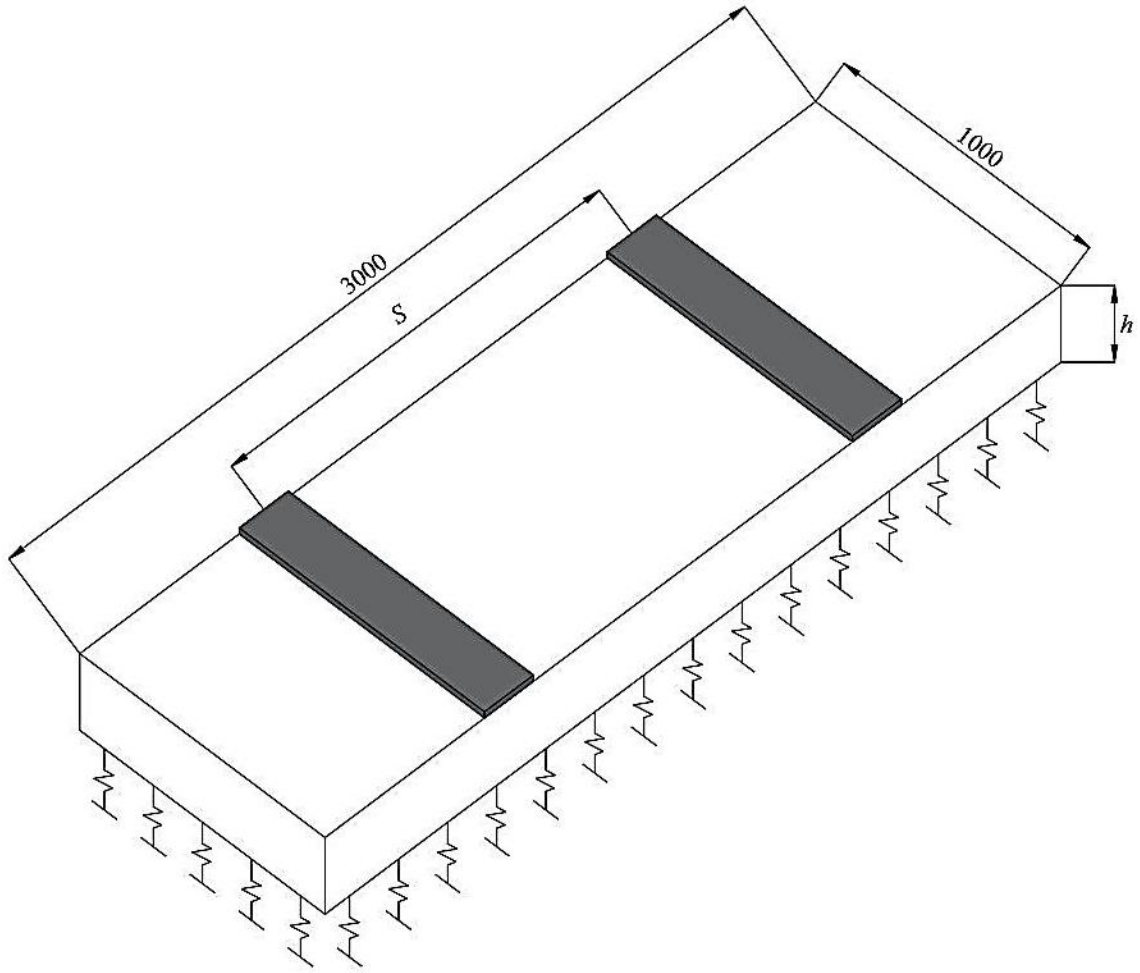

(a)

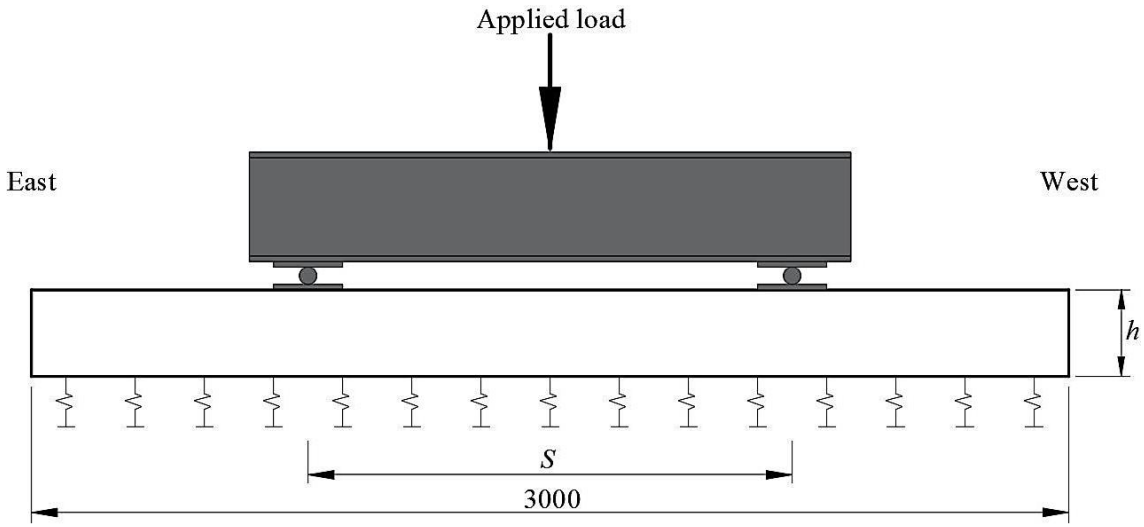

(b)

Figure 6.1 – Experimental arrangement and specimen dimensions: (a) 3D configuration of the test set-up; (b) section view of test specimen.

6.2.2. Construction of Slabs and Materials Properties

Both the SFRC and plain concrete slabs were constructed of plywood. Before casting of the specimens, the forms were cleaned and greased to allow smooth stripping. The slabs were cast along with sets of companion specimens to determine the material properties (see Figure 6.2).

For the plain concrete slabs, the concrete was provided to the testing laboratory by a local ready-mix concrete supplier. The specified target concrete compressive strength was 40 MPa and the coarse aggregate used was basalt with a maximum particle size of 20 mm. The workability of the fresh concrete was measured by means of a slump test and was found to be 95 mm.

The SFRC slabs were cast in two batches; three slabs were cast with Series C of the round panel specimens; while slabs B-SF-U and B-CF-C were casted separately. For slabs B-SF-U and B-CF-C, the concrete without the addition of fibres was ordered from a local concrete supplier, the calculated weight of the fibres was then added, on site, and mixed in the agitator for a minimum of 10 minutes; when fully mixed, the SFRC slabs and companion specimens were cast. The steel fibres used for the SFRC slabs tested in this study were the end-hooked Dramix® 4D 55/60 BG fibre. The fibres were 1.05 mm in diameter and 60 mm long. The fibres had an ultimate tensile strength of 1450 MPa. The target fibre dosage used in this study was 30 kg/m^3.

After casting, the specimens were covered under wet hessian and plastic sheeting. The specimens were moist cured for a period of 28 days, after which they were cleaned, dried and measured prior to testing. The specimens were tested at least 180 days after casting to minimise any change in strength due to aging.

For the plain concrete slabs, tests for compressive strength (f_{cm}), modulus of elasticity (E_c), indirect tensile strength by the Brazil test (f_{sp}) and modulus of rupture (f_{cf}) were performed in accordance with Australian Standards AS 1012.9 (1999), AS 1012.17

(1997), AS 1012.10 (2000), and AS 1012.11 (2000), respectively. The results of the material control tests are summarized in Table 6.2.

The characterisation performance of the SFRC slabs cast with Series C can be found in Chapter 3. The measured short term mechanical properties of the SFRC specimens B-SF-U and B-CF-C are presented in Figures 6.3 to 6.5 and summarised in Table 6.3. The fracture properties of the SFRC were determined directly by obtaining the tensile strength of the concrete matrix, f_{ct}, and the average residual tensile strength, $f_{1.5}$ (taken at a crack width of 1.5 mm), from five uniaxial 'dogbone' specimens (Figure 6.3) tested to the procedure outlined in AS3600 (2018). The tensile properties were also determined indirectly from the residual flexural strength through ten notched and un-notched prisms tested to EN 14651 (2007) and ASTM C1609 (2006), respectively, as presented in Figures 6.4 and 6.5. The mean compressive strength, f_{cm}, and Young's modulus, E_c, at the day of slab testing were determined by testing two to seven 150 mm diameter by 300 mm high cylinders and shown in Table 6.2.

Figure 6.2 – Pavement specimens after casting.

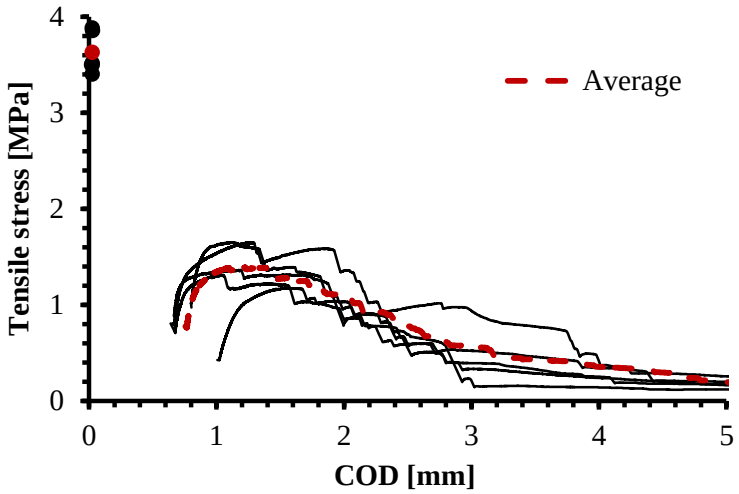

Figure 6.3 – Uniaxial tension test results.

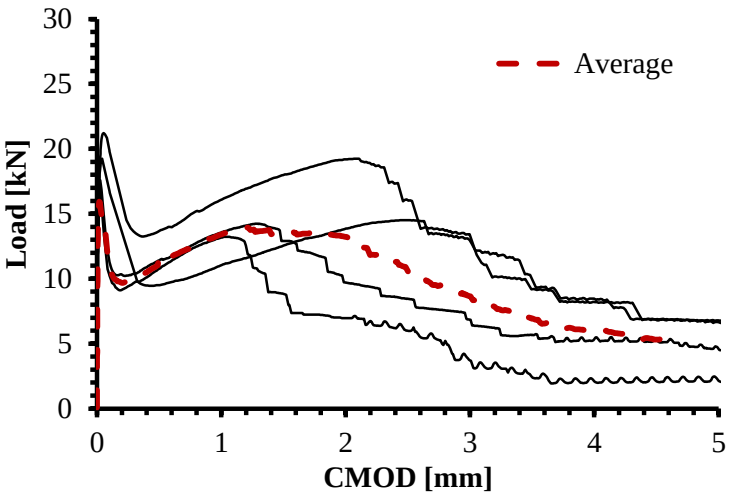

Figure 6.4 – EN 14651 prism bending test results.

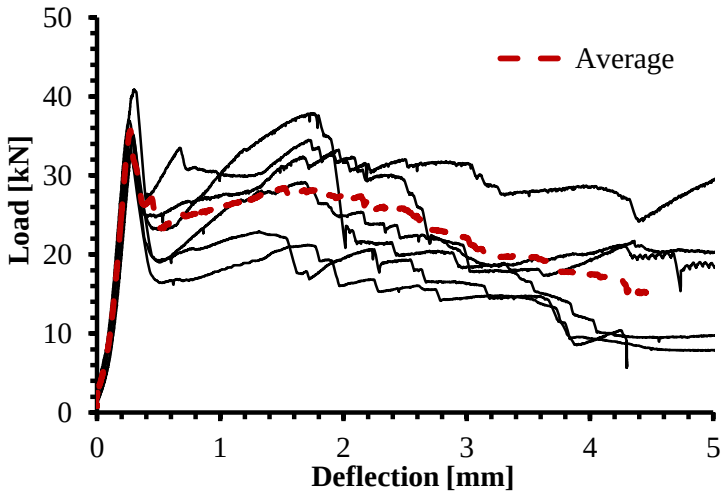

Figure 6.5 – ASTM C1609 prism bending test results.

Table 6.2 – Material properties of control specimens.

Batch type	f_{cm} [MPa]		E_c [GPa]	f_{sp} [MPa]	f_{cf} [MPa]
	28 Days *	At time of testing *			
Plain concrete	43.9 (2)	51.3 (7)	33.0 (2)	4.4 (3)	5.9 (6)
SFRC – batch 1	48.6 (2)	62.0 (4)	30.3 (2)	-	-
SFRC – batch 2	48.5 (3)	57.8 (6)	34.5 (2)	-	-

Note: * Number in ( ) equals number of cylinders or prisms tested.

Table 6.3 – Short term mechanical properties of SFRC.

AS3600 (2018) uniaxial tension test		EN 14651 (2007) prism bending test				ASTM C1609 (2006) prism bending test			
f_{ct} [MPa]	$f_{1.5}$ [MPa]	f_{R1} [MPa]	f_{R2} [MPa]	f_{R3} [MPa]	f_{R4} [MPa]	f_P [MPa]	f_1 [MPa]	f_{600}^D [MPa]	f_{150}^D [MPa]
3.63	1.31	3.15	3.56	3.02	1.99	4.6	4.5	3.0	2.5

6.2.3. Subgrade Preparation

A series of materials were considered to simulate the subgrade beneath the pavement, such as real soil, foam, cork and springs. The main purpose of this test is to compare the performance of plain concrete slabs with those of thinner SFRC specimens. This means that, excluding the specimen thickness and fibre content, the remaining variables should remain constant. One of the most important reasons, to neglect selecting soil to simulate the subgrade, is the fact that the properties of soil change with temperature and humidity. This change to soil properties can result in inappropriate comparison between the performance of plain and SFRC specimens. The other option was the selection of foam or cork similarly to some tests found in the literature (Falkner et al., 1995; Elsaigh

and Kearsley, 2002; Chen, 2004; Øverli, 2014). However, after extensive investigation, it was concluded that the foam layer needs to be changed prior to each test and it is not possible to ensure that all foam layers will have exactly the same thickness and stiffness. Also, it was found that springs were the most economic selection when considering the cost between foam and the springs. As a result, heavy duty springs were selected to simulate the subgrade underneath the specimens.

To reproduce a Winkler soil, a total of 75 heavy duty springs were specifically manufactured for the purpose of this research. The springs were placed under the slab at centres of 200 mm apart in both directions. The average spring stiffness was specified to be 3.2 kN/mm. By considering the influence area of each spring (200 mm × 200 mm), the average Winkler constant, k_w, is equal to 0.08 N/mm^3, which corresponds to a uniform graded sand soil (see Table 2.2).

A base steel plate was designed with 300 threaded holes, 4 threaded holes per a spring, to hold the springs in location by threaded bars, as shown in Figure 6.6. Each spring was placed in its location. A Masonite layer was placed on top of each spring followed by a square steel plate of dimension 195 mm × 195 mm. This is followed by another strip of Masonite on top of five springs in North-South direction as shown in Figure 6.7. Providing a strip of Masonite in the North-South direction allows averaging the height of the springs in the direction of specimen's width.

One of the main issues, associated with installation of springs, is the fact that each spring had a slightly different height, as shown in Figure 6.8. The layout of the springs was arranged to match the slope of the laboratory floor to provide a uniform support to the specimen. The Masonite strips, in the North-South direction, allow averaging the height of the springs in the North-South direction and eliminate the effect of any gaps between the supporting system and the specimen. With the exception of specimen A-

SF-U[1], a layer of high-strength mortar with a few millimetres thickness was placed on each Masonite strip to ensure the contact with the bottom face of the slab so that nothing moves around during testing, specifically when cyclic loading was applied. In addition to that, the mortar layer levelled out as the self-weight of the slab is applied to ensure eliminating any remaining gaps in West-East direction between the supports and the slab. Figure 6.9 presents the mortar layers immediately prior to slab set-up.

6.2.4. Test Instrumentation

The instrumentation set-up involved electrical gauging and monitoring equipment. Loads, displacements and concrete surface strains were measured. A computerised data-logging system was used to obtain these measurements through a Hottinger Baldwin Messtechnik (HBM) system. In addition to these measurements, the development and propagation of cracks were also monitored and traced throughout the test of SFRC specimens. For the SFRC slabs, excluding A-SF-U and A-CF-U, five PI-gauges were used to provide crack opening measurements. Three PI-gauges were placed at depths of 20 mm, 100 mm and 180 mm across the thickness of the slab in addition to two PI-gauges located at the surface of the specimen. To ensure that the crack is passing through the gauges, the gauges were placed during testing and as soon as a crack is formed, the testing was paused at the load which the crack formed at. Then the crack width was measured with an optical microscope, to determine the initial crack width measurements, at the locations of the PI-gauges to be installed. Testing was then resumed. For specimen A-CF-U, no gauges were used to monitor the crack width development during testing. However, the cracks widths were measured with an optical microscope at the end of fatigue testing at upper load level. The crack widths were measured at depths of 20 mm, 60 mm, 100 mm, 120 mm and 180 mm. No gauges were placed to monitor the crack width development for specimen A-SF-U.

[1] Specimen A-SF-U was the first specimen tested. On reflection of the results a high strength mortar layer was added to the following tests to provide a more uniform support condition to the test slab and better distribute the support reactions.

The front surface of the SFRC slabs was painted to facilitate the crack detection process during testing. During different intervals of fatigue testing, crack development was marked using a felt tip pen.

The slabs were instrumented with 18 LVDTs and LSCTs to measure the vertical deflection along the length and the width of the slab during monotonic and cyclic loadings. The transducers were placed in two rows; nine along the centreline of the slab as shown in Figure 6.10 and the remaining nine gauges were located 400 mm away from the centreline.

Extensive strain measurements of the concrete surface were recorded throughout the test. Each slab was instrumented with fifteen to twenty electrical resistance strain gauges attached to the concrete surface, before testing the specimen. The strain gauges were placed at different heights across the depth of the slab (see Figures 6.11 and 6.12). For specimens A-SP-U and A-SF-U, the strain gauges were placed as shown in Figure 6.13.

All specimens were tested with two loading points. In all tests, a 500 kN load cell was placed between the hydraulic jack and the spreader beam and at the mid-span of the specimen to measure the applied load. The load cell was linked to the HBM data acquisition system.

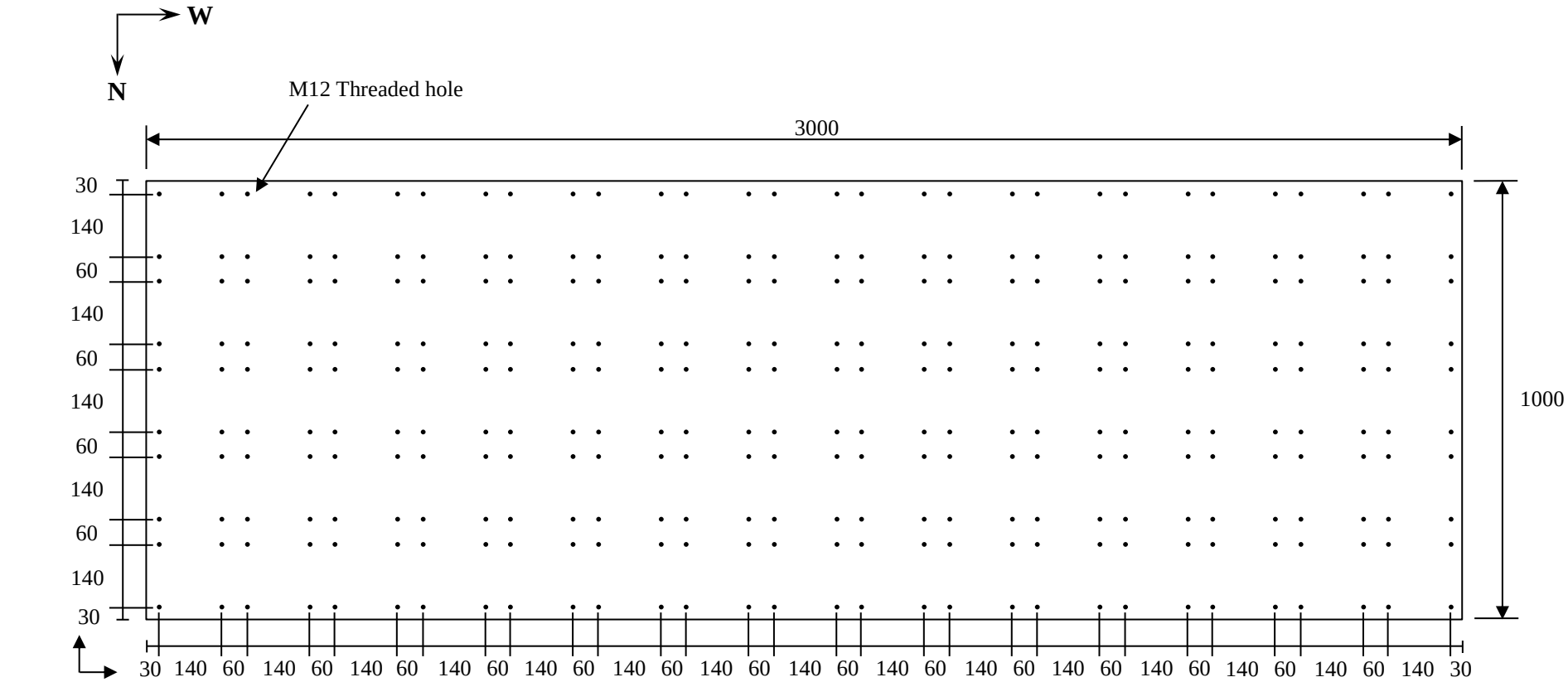

Figure 6.6 – Base plate design (dimensions in mm).

(a)

(b)

Figure 6.7 – Set-up of the support system.

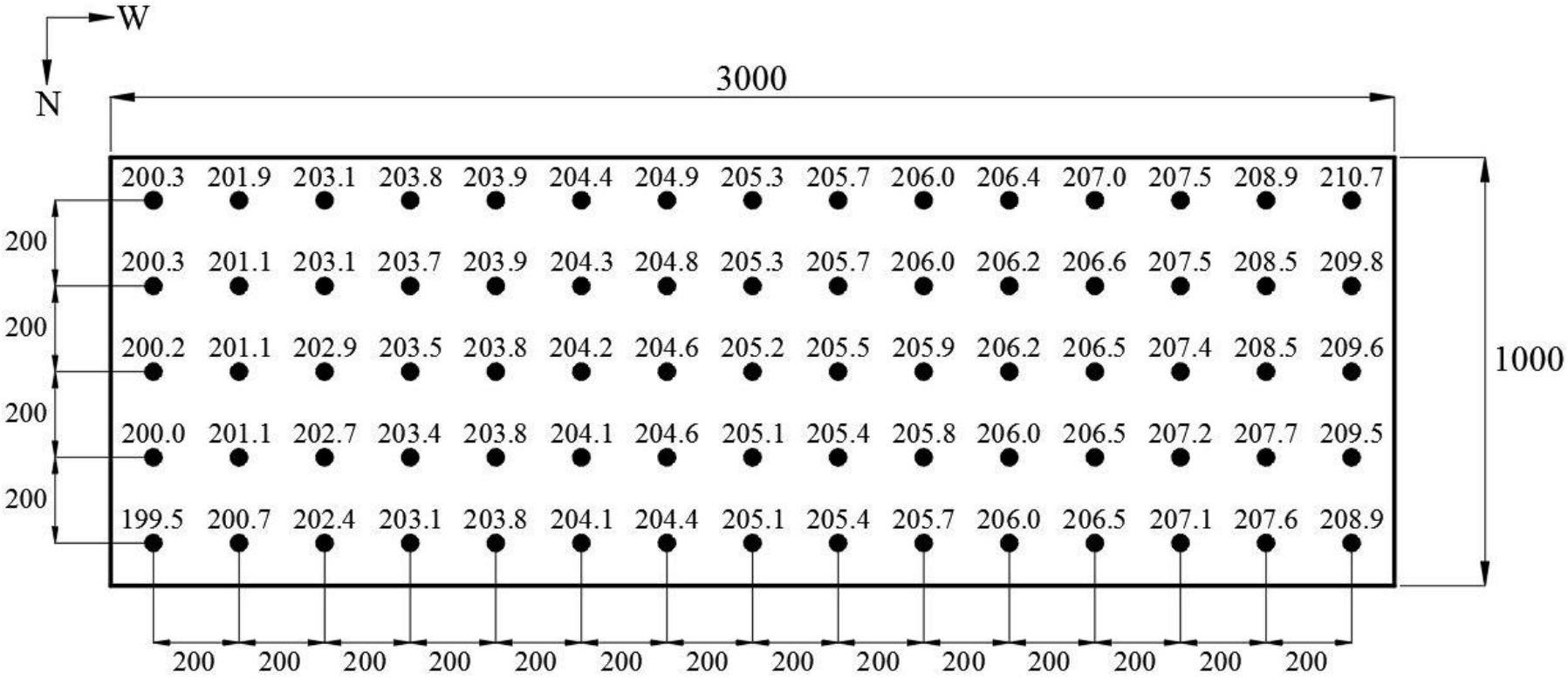

Figure 6.8 – Variation in the height of the springs in both directions (dimensions in mm).

Figure 6.9 – Wet mortar layers on top of Masonite strips, immediately prior to placing slab.

6.2.5. Test Set-up and Testing Procedure

All pavement specimens were fully supported by 75 springs and tested in an Instron 500 kN capacity actuator supported by a stiff testing frame (Figure 6.14). Each of the slab specimens was loaded under two loading points. The load from the hydraulic actuator was transferred to the pavement loading points by a steel spreader beam (Figure 6.1(b)). One end of the spreader beam was pinned supported and the other end had a roller support. To avoid crushing at the loading points, the load was applied through 200 mm by 1000 mm by 16 mm thick steel plates.

The test machine was servo-controlled with fully digital control and data acquisition. Depending on the test type, a displacement-control mode or load-control mode was used. To determine the ultimate capacity of plain concrete pavements, one slab was tested statically from each series. In the static load test and to pre-crack slab B-CF-C, the test was controlled via ram displacement control at a rate of 0.12 mm/min until failure or crack formation, respectively.

During the fatigue tests, the load was applied monotonically up to the minimum load of the load range under deflection control at a rate of 0.12 mm/min. The cyclic load was then applied using a sine waveform under load control at frequencies of 1.25 Hz, 1.5 Hz or 2.5 Hz. The maximum frequency was limited by the maximum applied load and actuator capacity. Testing was undertaken continuously 24 hours a day (including weekends) until failure was imminent, or until predetermined cyclic limit was reached, whichever occurred first. The point of imminent failure was marked by a large increase in the measured central deflection. For all specimens other than B-CF-C, the cycle limit was 3 million cycles. For specimen B-CF-C, it was 5 million cycles.

The load range for fatigue tests was selected based on the cracking load recorded during the static test of plain concrete specimens. Two load ranges were selected as 17 to 70 percent and 17 to 50 percent of the static cracking load. However, for slab B-CF-U and after the completion of 2.0 million cycles of fatigue loading with the specified range shown in Table 6.1, the load range was increased by a factor of two for a further of one million loading cycles.

At the conclusion of the applied fatigue loading, for specimen A-CF-U, a displacement controlled monotonic load, at a rate of 0.12 mm/min, was applied until a load of at least 450 kN was reached.

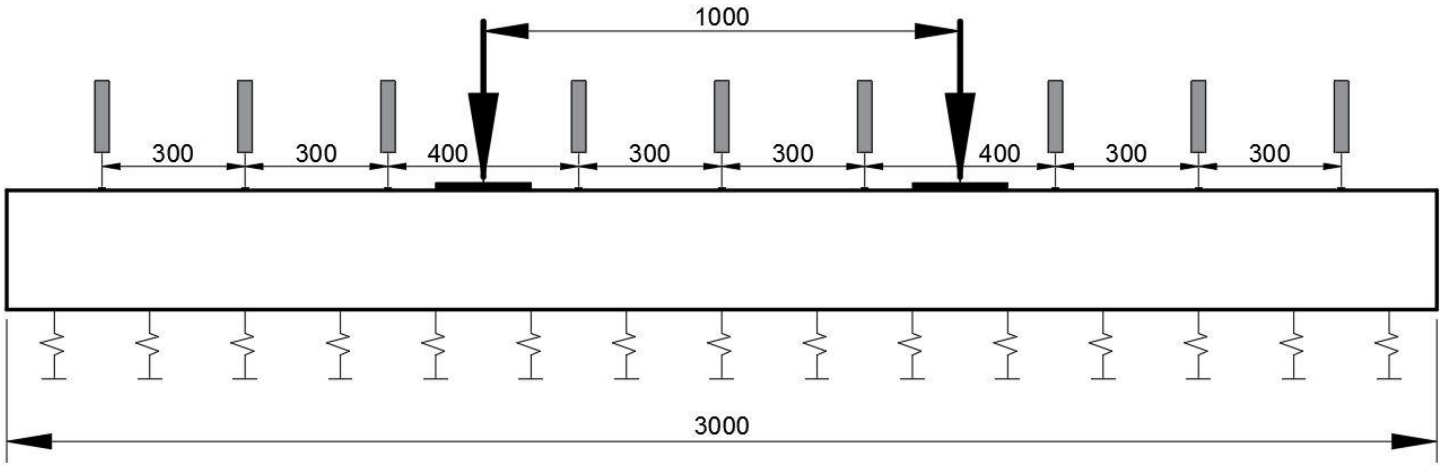

(a)

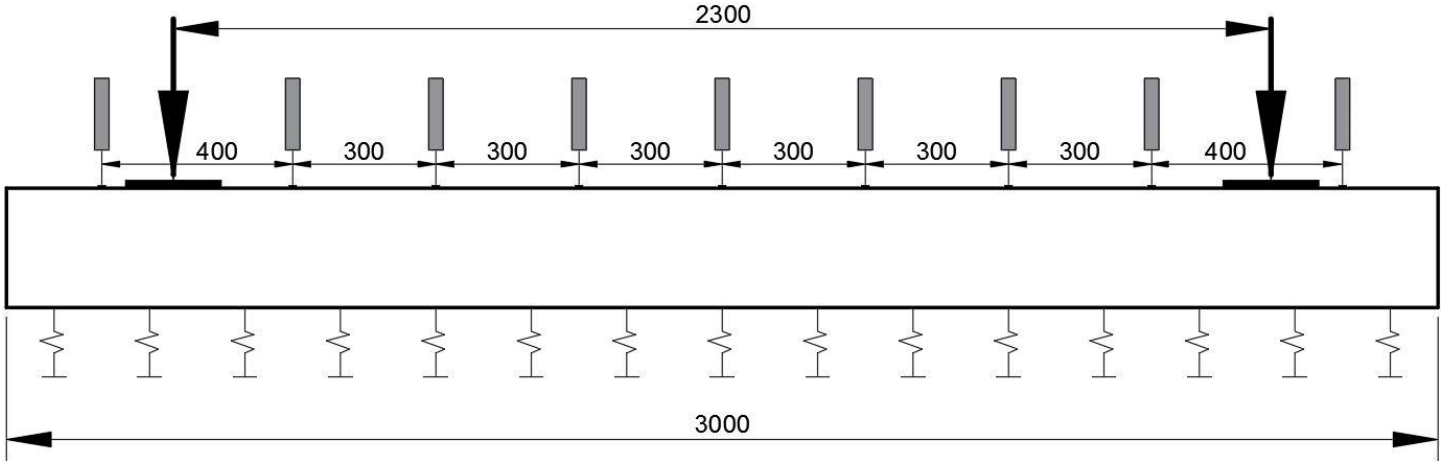

(b)

Figure 6.10 – LVDTs and LSCTs layout along the centreline: (a) Series A; (b) Series B (dimensions in mm).

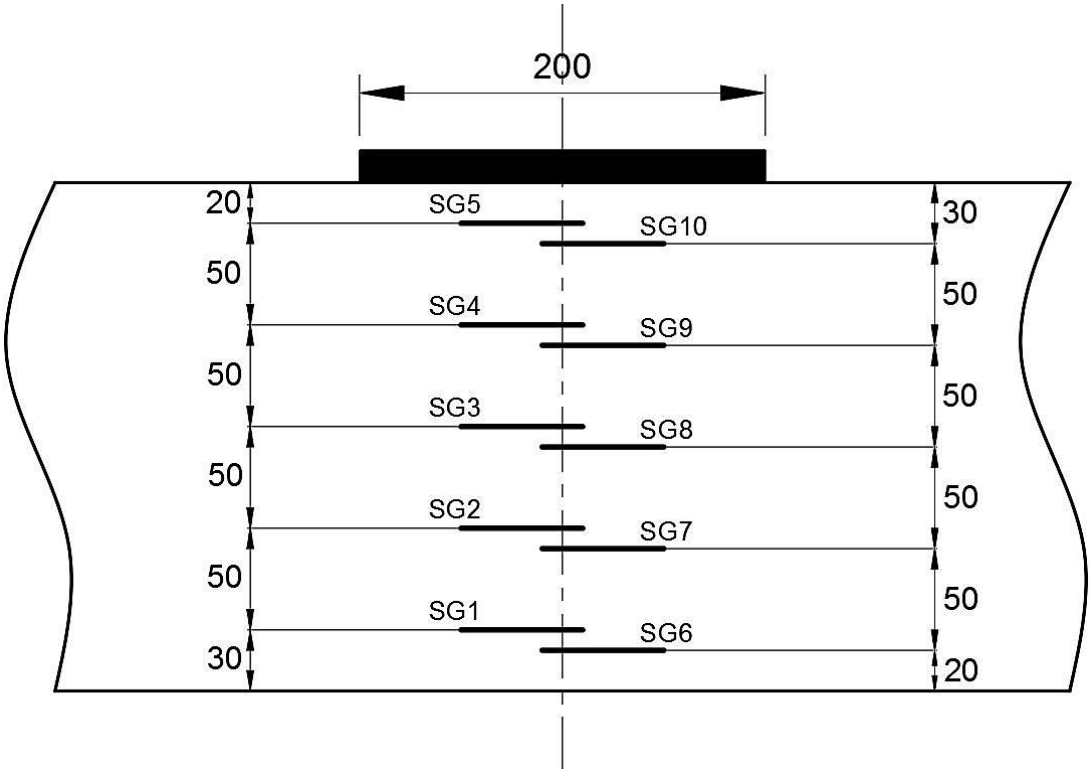

(a)

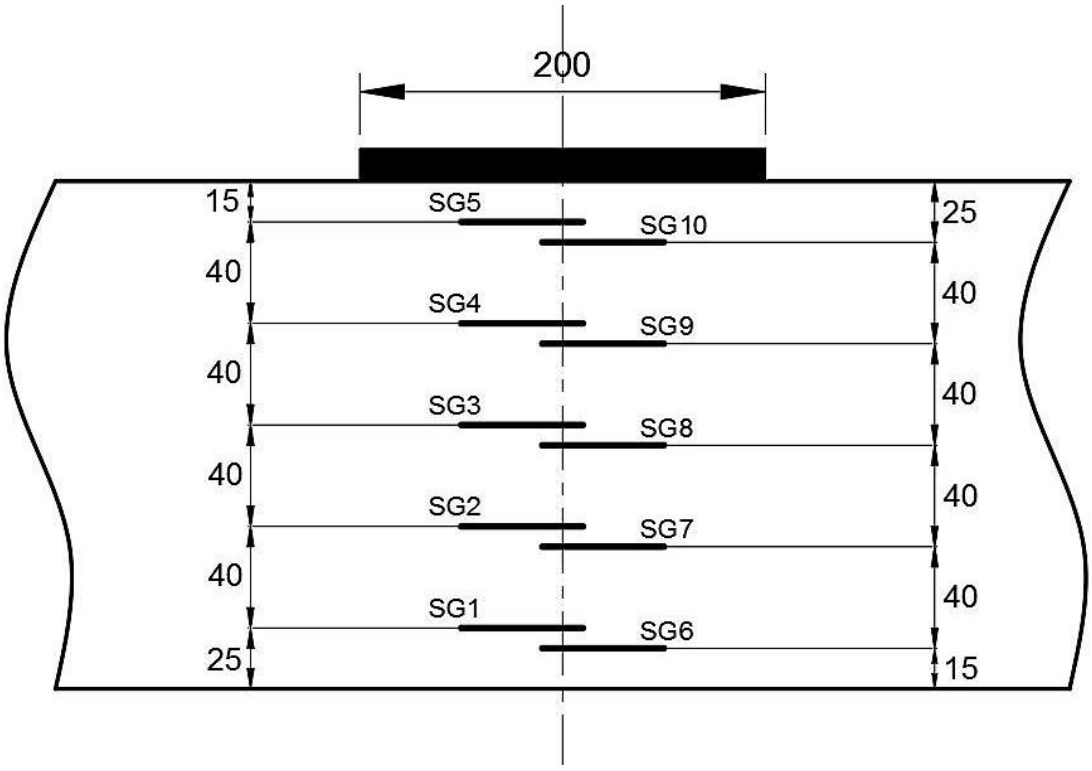

(b)

Figure 6.11 – Location of strain gauges on concrete surface for Series A slabs: (a) plain concrete; (b) SFRC specimens (dimensions in mm).

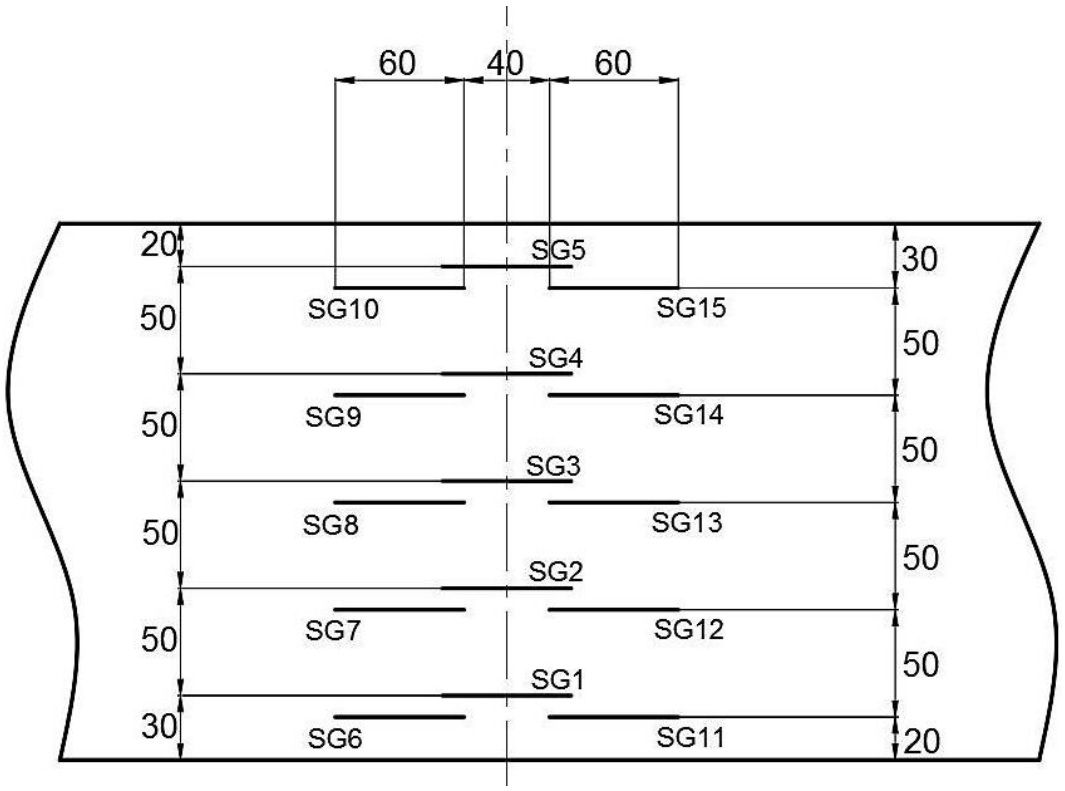

(a)

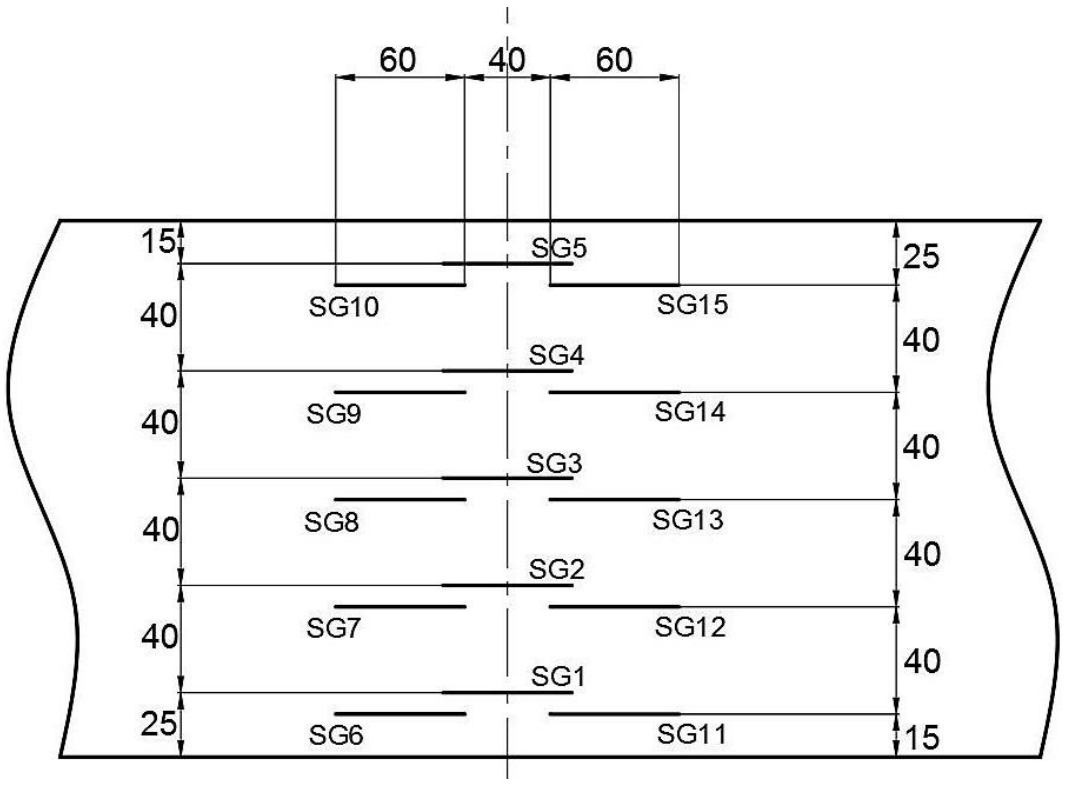

(b)

Figure 6.12 – Location of strain gauges on concrete surface for Series B slabs: (a) plain concrete; (b) SFRC specimens (dimensions in mm).

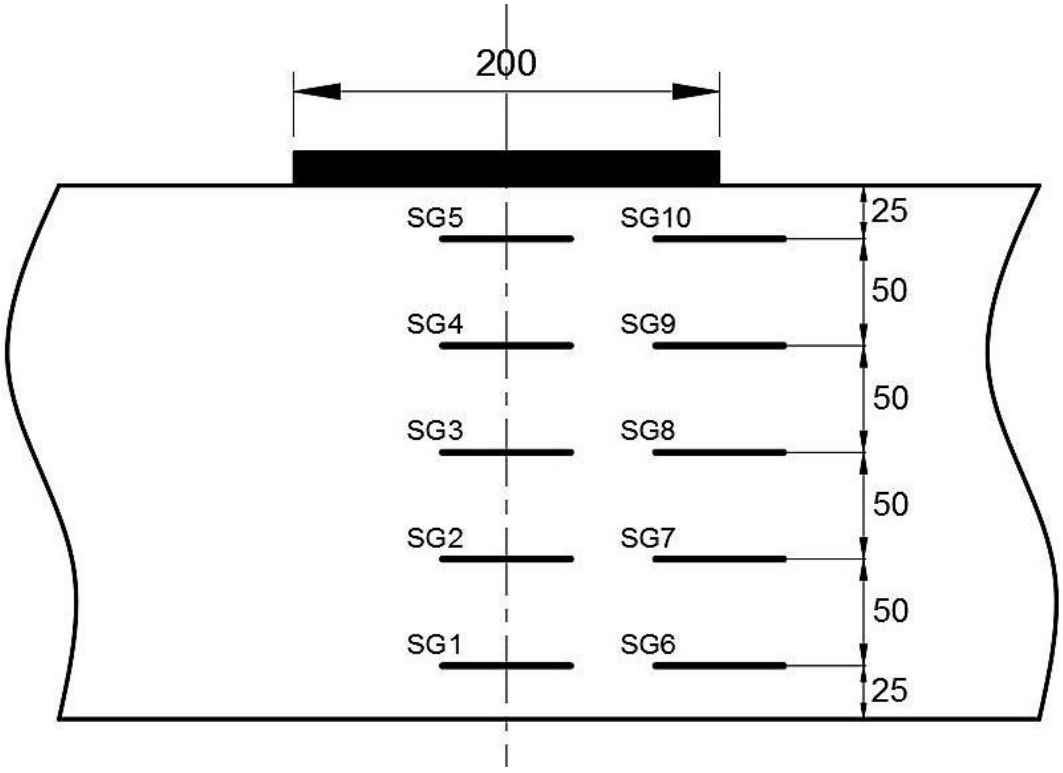

(a)

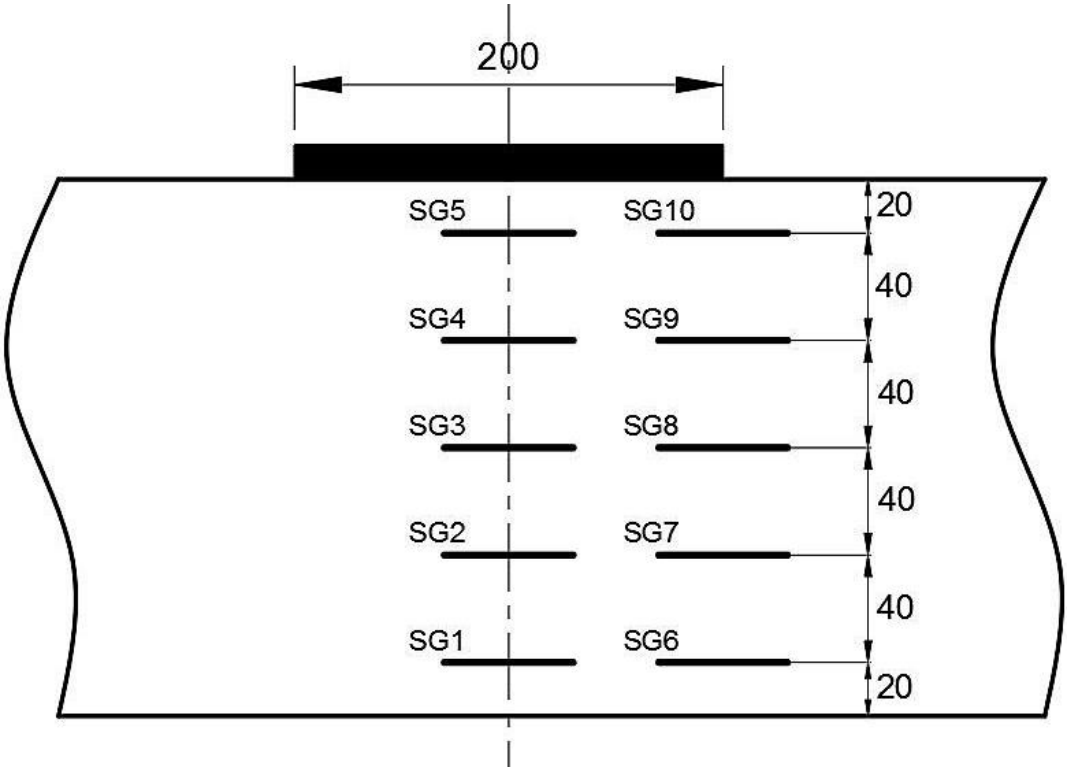

(b)

Figure 6.13 – Location of strain gauges on concrete surface for slabs: (a) A-SP-U; (b) A-SF-U (dimensions in mm).

(a)

(b)

Figure 6.14 – Test set-up for static and fatigue testing: (a) Series A; (b) Series B.

6.3. Static Test Results

In this section, the experimental test results are presented for plain and SFRC slabs tested monotonically from each series. Test results of individual specimen are discussed in details.

Specimen A-SF-U

A SFRC slab was tested statically with a loading span of 1.0 metres and a slab thickness of 200 mm. This specimen was the first one to be tested and no mortar layers were used in the set-up of the support system. After the completion of this test and with the observation made, a layer of high strength mortar was added to the support system to enhance the support of the slabs.

The maximum measured deflection at the West loading line, together with the central deflection, during the static test is presented in Figure 6.15. It is clear from the figure that the stiffness of the specimen and the rate of deflection increase remained unchanged during the test. No reduction in load bearing capacity was observed, given that two cracks formed, at the West loading line, during the test as shown in Figures 6.16 and 6.17 at loads of about 260 kN and 280 kN. This indicates that slab action was maintained after crack formation resulting in higher ultimate bearing capacity and increased toughness. The test was stopped at 476.6 kN as per the limitation of the actuator capacity. Remarkable improvements were noted for both the ultimate load and slab toughness. The depth of the crack at a load of 476.6 kN was about 180 mm. The SFRC slab continued to act as one specimen and was not separated into two pieces after the completion of the test. The deflection profiles along the length of the slab at different loading steps are presented in Figure 6.18. The deflection is almost uniform during the initial stages of the static test. After that, higher deflection is observed between the two loading lines and their surroundings. No significant change in deflection increase was noted during testing.

Specimen A-SP-U

A plain concrete slab was tested monotonically with a loading span of 1.0 metres. The thickness of the plain concrete slab was 250 mm. The failure of the slab was determined by the formation of one fracture line. The load versus central deflection during the test is shown in Figure 6.19. The plain concrete slab showed a brittle failure when a maximum load equal to 467.6 kN was reached. This ultimate load capacity was used to determine the fatigue loading range for the remaining specimens for Series A.

The deflection at different locations and loading steps is presented in Figure 6.20. As can be seen from the figure, the deflection increase is almost uniform along the length of the slab during the test up to the peak load. This reflects the support response of the springs. However, it is evident that the deflection is at a slope increasing from East to the West. This is due to the fact that the reaction floor of the laboratory is not perfectly flat and there is a decreasing slope of 9 mm towards the Southwest. The springs, shown in Figure 6.8, were placed to generate an increasing slope of 11.2 mm towards the Southwest levelling the specimen. In the end, the specimen was placed on an increasing slope of about 2.2 mm towards the Southwest corner. Consequently, higher load tends to applied at the West side of the specimen; leading to higher deflection; accordingly, crack formation at the West end of the specimen as can be seen from Figure 6.20. The load versus maximum measured deflection, which occurred at the interior West side of the loading system, is presented in Figure 6.19. The crack passed through strain gauges placed at the concrete surface. The reading of the strain gauges reinforces the brittle failure mode of plain concrete slab under static loading as shown in Figure 6.21. At failure, the specimen was completely separated into two distinct pieces, as seen in Figure 6.22.

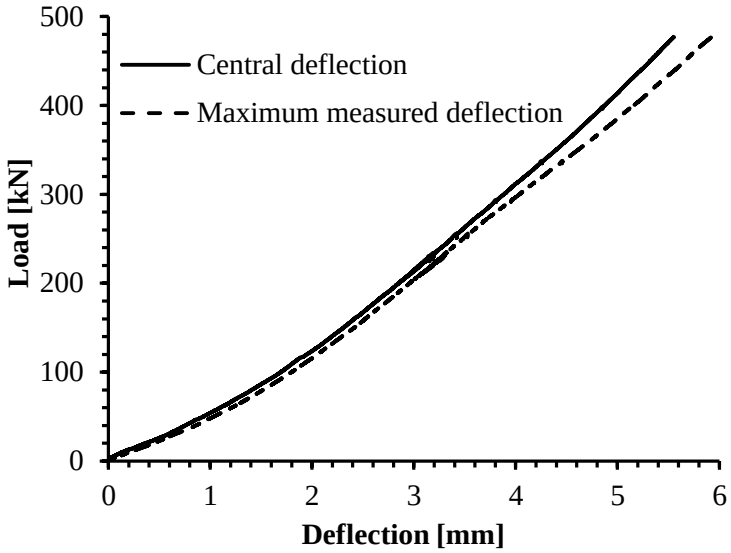

Figure 6.15 – Load versus deflection during static loading for slab A-SF-U.

Figure 6.16 – Crack development after the completion of the static test.

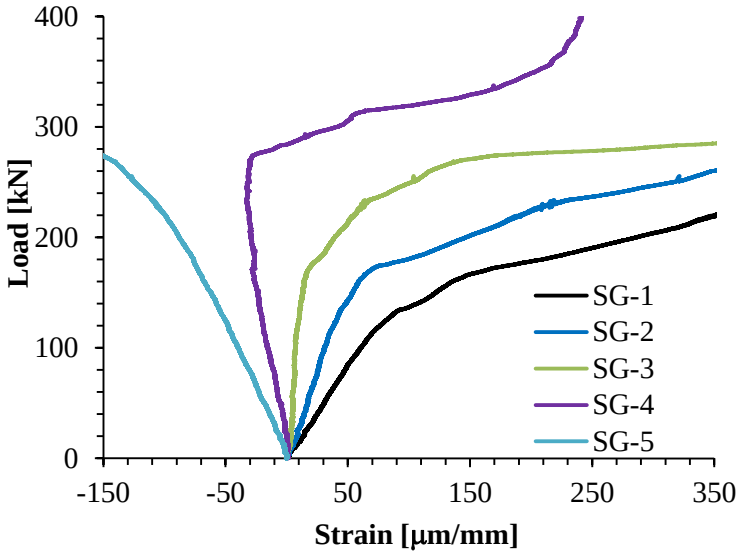

(a)

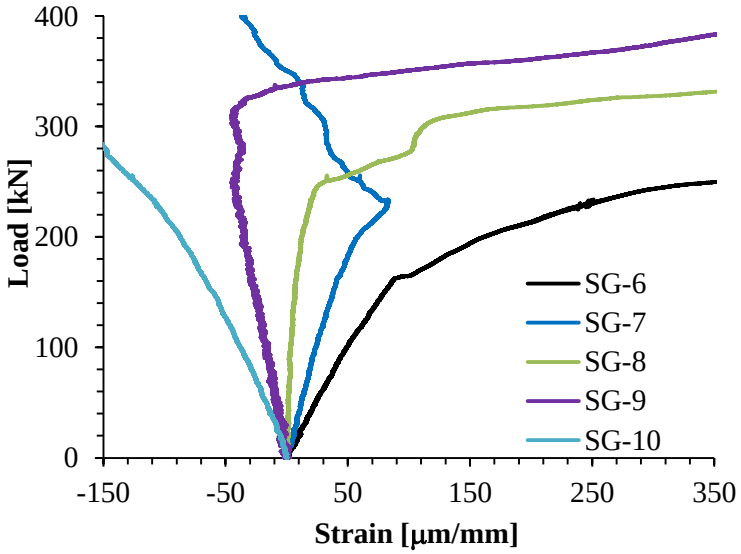

(b)

Figure 6.17 – Concrete surface strains taken across the depth of slab A-SF-U.

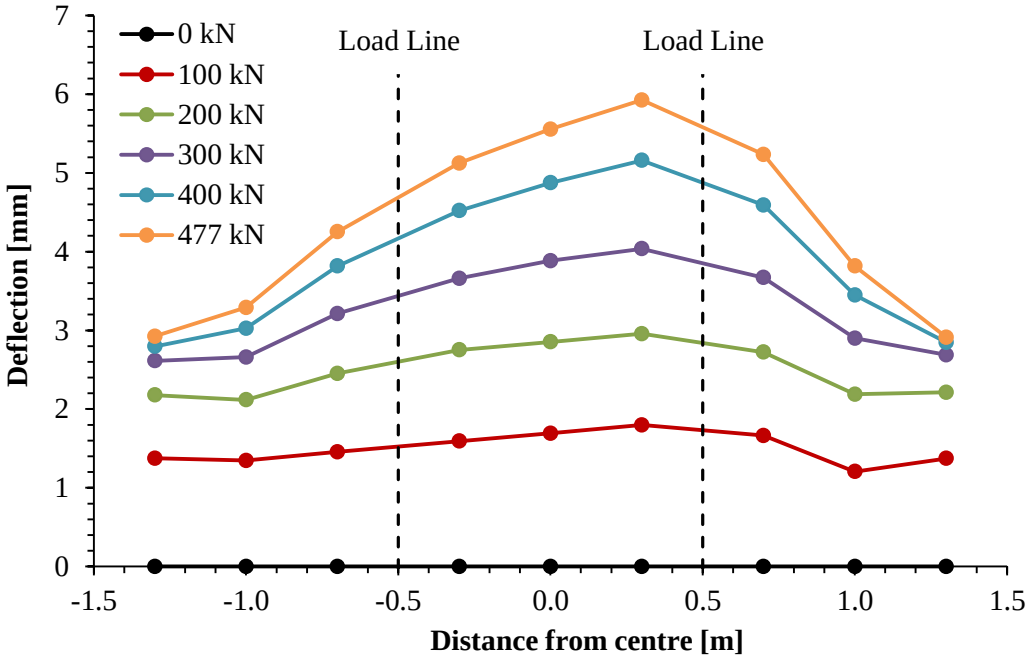

Figure 6.18 – Deflections measured along the length of slab A-SF-U during the static test.

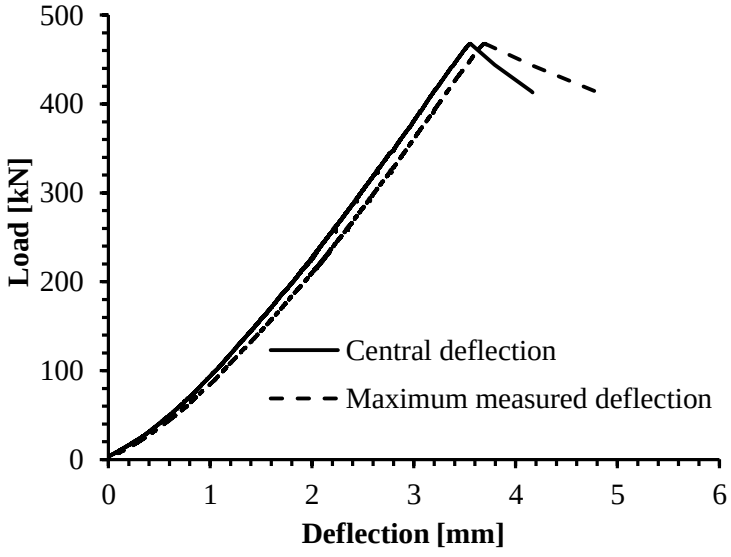

Figure 6.19 – Load versus deflection during static loading for slab A-SP-U.

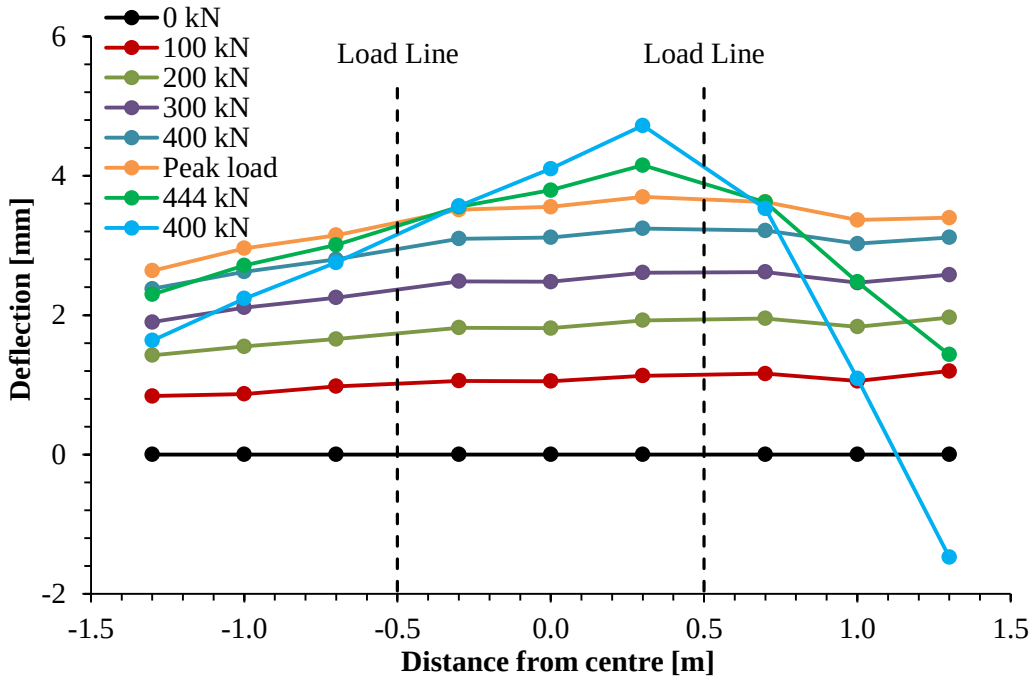

Figure 6.20 – Deflections measured along the length of slab A-SP-U during the static test.

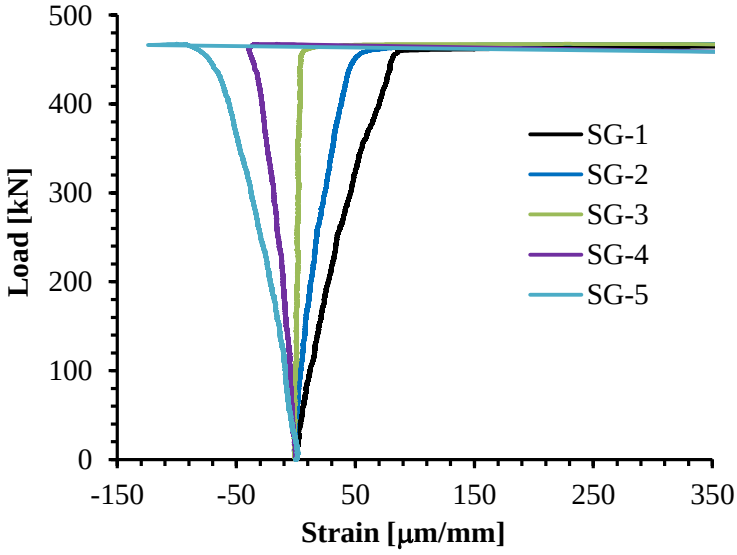

Figure 6.21 – Concrete surface strains taken across the depth of slab A-SP-U.

Figure 6.22 – Specimen A-SP-U after failure.

Specimen B-SP-U

Specimen B-SP-U was a plain concrete slab with a loading span of 2.3 metres and a thickness of 250 mm. It was loaded statically until the formation of a fracture line across the width at a load of 215.7 kN. This ultimate load capacity was used to determine the fatigue loading range for the remaining specimens of Series B. The crack formed almost at the centre of the slab. Load versus central deflection is plotted in Figure 6.23.

For slab B-SP-U, initially the central deflection increased up to 1.13 mm at the peak load; then it reduced to -0.58 mm at failure. A brittle failure mode was noted for the plain concrete slab and the specimen was unable to carry any further load after the formation of the crack and the load was transferred to the support system. The deflection profile along the 3.0 metres length of the slab can be seen in Figure 6.24 at various loading intervals. The deflection profile of the slab was approximately uniform along the length of the slab up to the peak load. Again, the brittle failure mode is evident from the deflection profile as soon as a crack was formed across the width of the slab.

Figure 6.25 presents the strain gauges readings during the static loading. It is evident from the figure that as soon as a crack formed, it propagated quickly across the depth of

the slab indicating that the slab was not capable of carrying any load after the formation of the crack. After the completion of testing, the specimen was completely separated into two parts as can be seen from Figure 6.26.

Specimen B-SF-U

Static loading was applied on a SFRC slab with a loading span of 2.3 metres and 200 mm thickness. A crack formed at a load of 175.4 kN as indicated by the concrete stain gauges and shown in Figure 6.27. After the formation of cracking, testing was paused and the crack width was measured at different locations across the thickness and at the surface of the slab using an optical microscope. The crack width at the surface was measured at two different locations along the width of the slab and it was found to be 0.40 mm and 0.32 mm, as presented in Figure 6.28. From Figure 6.29, it can be seen that the initial crack widths across the depth of the slab were 0.32 mm and 0.14 mm at depths of 20 mm and 100 mm, respectively. The crack was formed up to a depth of 170 mm.

After the initial crack width measurements, gauges were installed for continuous crack width measurement and testing was continued. As can be seen from Figures 6.28 and 6.29, the crack width increased at a steady rate to reach an average crack width of 1.77 mm at a load of 490.4 kN at the specimen's surface. The crack width at depths of 20 mm, 100 mm and 180 mm was found to be 1.40 mm, 0.78 mm and 0.12 mm, respectively. After the completion of testing, and given a formation of a crack with a crack mouth of 1.77 mm, the two parts of the specimens remained connected to each other and the slab was removed from the test set-up as one solid specimen.

The load versus central deflection curve during the static test is presented in Figure 6.30. The central deflection at the cracking load (175.4 kN) was 0.81 mm. Soon after crack stabilisation, the central deflection reached 0.03 mm. After that, the deflection decreased steadily as higher load is applied to reach -0.54 mm at 490.4 kN.

The deflection profiles along the length of the slab, at various loading steps, are presented in Figure 6.31. The deflection profile of the slab was approximately uniform along the length of the slab up to the cracking load; before cracking the deflection increased as higher load was applied. After cracking, the central deflection, and its surroundings, decreased with higher loads, while the edge deflections continued to increase. The addition of fibres resulted in a substantial increase in displacement, indicating the improvement in toughness.

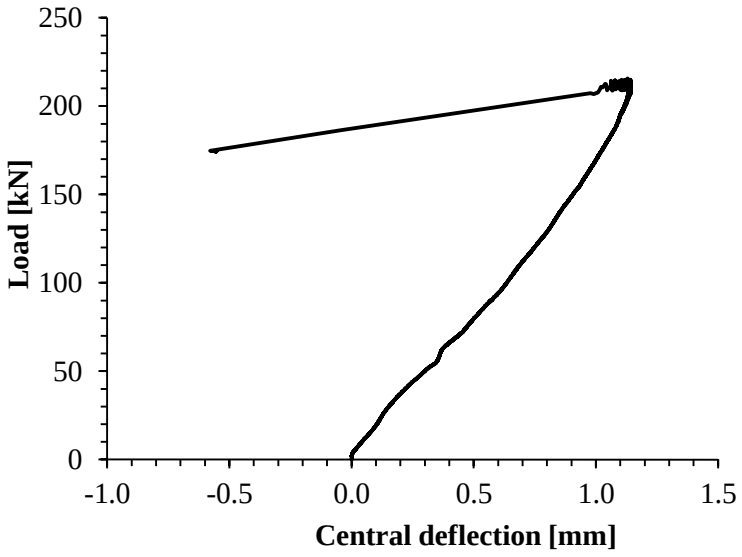

Figure 6.23 – Load versus deflection during static loading for slab B-SP-U.

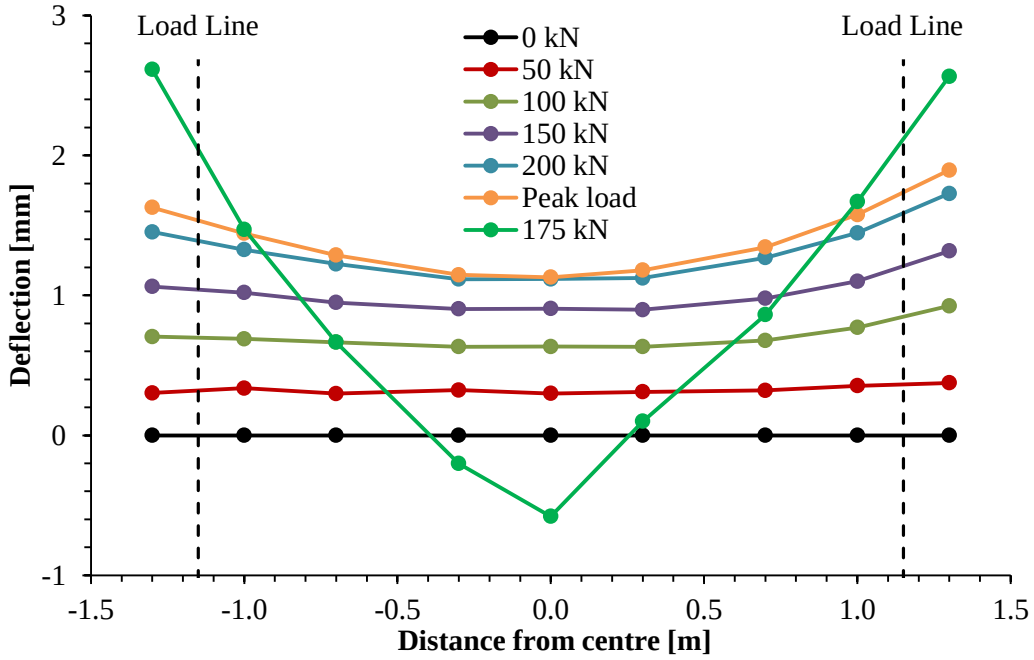

Figure 6.24 – Deflections measured along the length of slab B-SP-U during the static test.

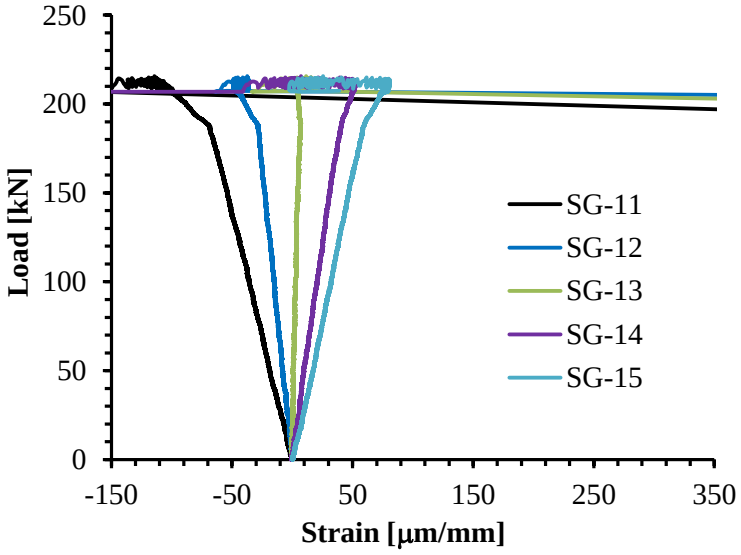

Figure 6.25 – Concrete surface strains taken across the depth of slab B-SP-U.

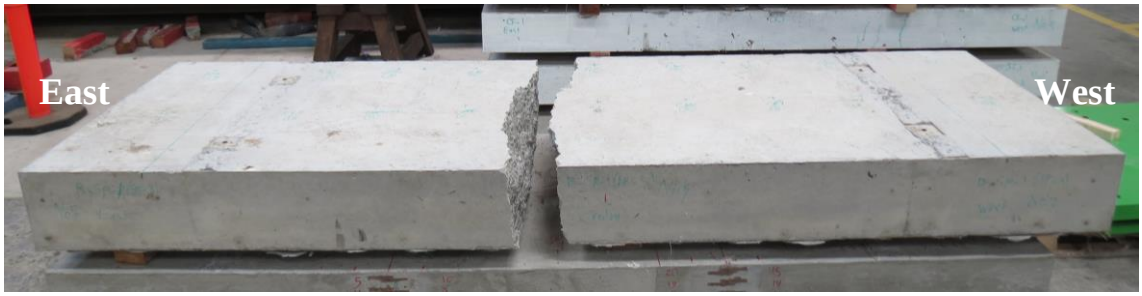

Figure 6.26 – Specimen B-SP-U after failure.

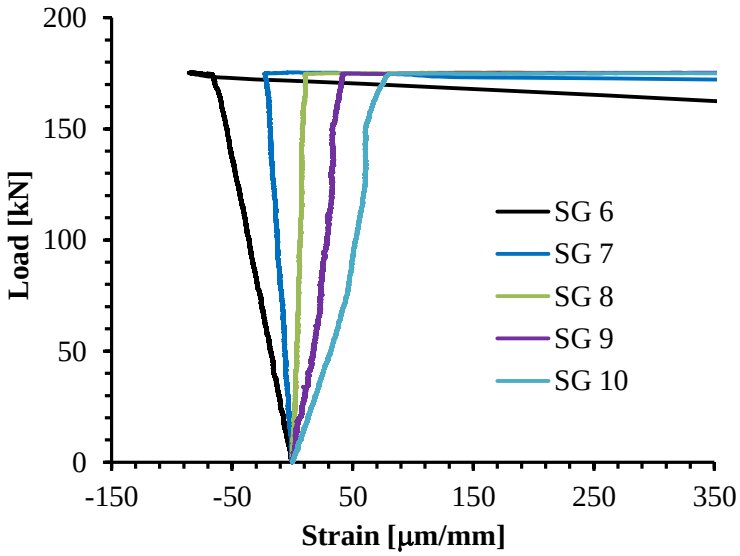

Figure 6.27 – Concrete surface strains taken across the depth of slab B-SF-U.

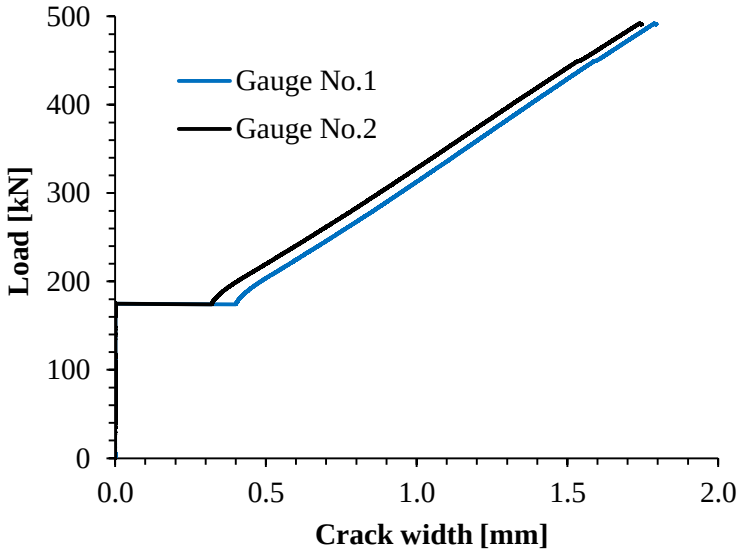

Figure 6.28 – Crack width development at the surface of slab B-SF-U during static test.

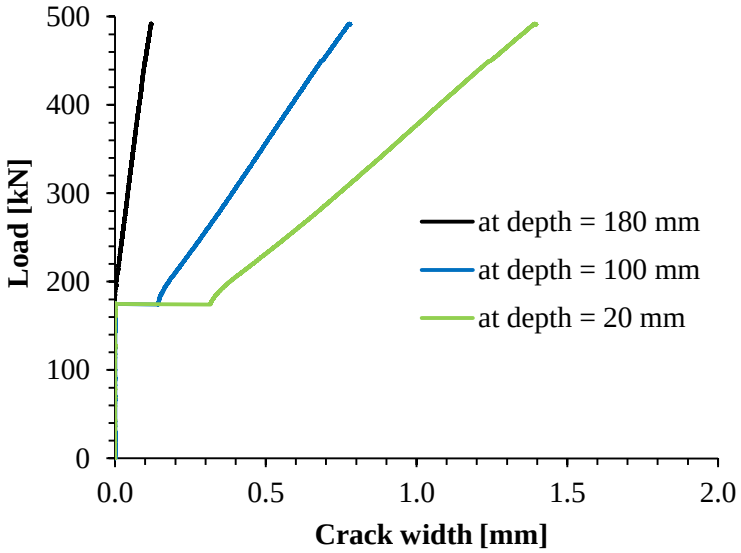

Figure 6.29 – Crack width development across the depth of slab B-SF-U during static test.

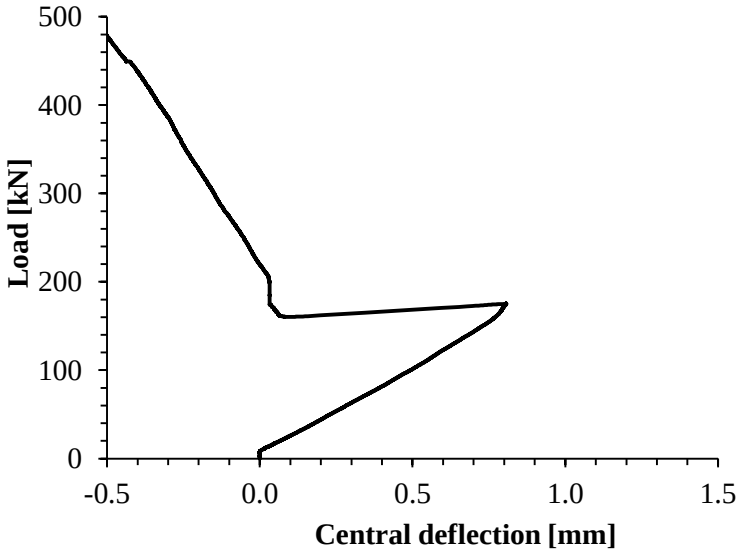

Figure 6.30 – Load versus deflection during static loading for slab B-SF-U.

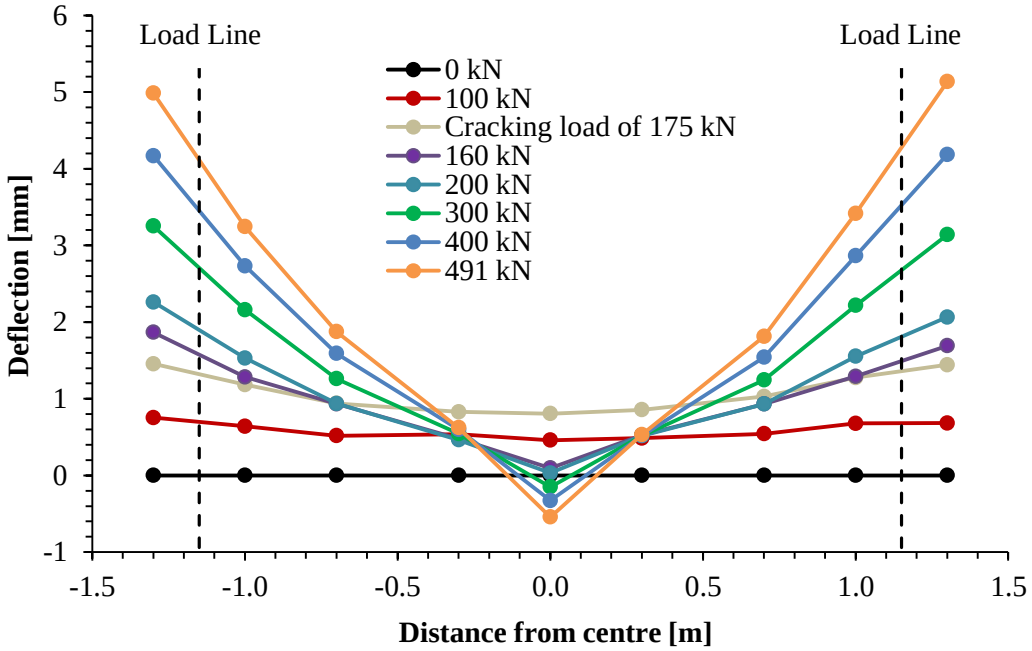

Figure 6.31 – Deflections measured along the length of slab B-SF-U during the static test.

6.4. Fatigue Lives and Failure Modes

The fatigue lives for the tested slabs are presented in Table 6.4. In total, four specimens were tested under cyclic loading; one thick plain concrete slab and three thinner SFRC ones. All the specimens that were uncracked prior to fatigue testing were loaded with a maximum load level of 70%, except one specimen was pre-cracked before the application of cyclic loading with 50% upper load level.

For the specimens tested with a loading span of 1.0 metres, the fracture line formed at one of the loading regions resulting in positive bending moment. The crack formed at the centre of the slabs tested with 2.3 metres loading span length. All the SFRC had a fatigue life greater than three million cycles. The higher toughness of the thinner SFRC resulted in longer fatigue life compared with thicker plain concrete slabs which had a brittle failure mode.

Table 6.4 – Fatigue lives for tested specimens.

Specimen ID	Loading span, *S* [mm]	Slab's thickness, *h* [mm]	Pre-cracked	Fibre content	Max load	No. of cycles
A-CP-U	1000	250	No	0	70%	323
A-CF-U	1000	200	No	30 kg/m^3	70%	> 3 million
B-CF-U	2300	200	No	30 kg/m^3	70%	> 3 million
B-CF-C	2300	200	Yes	30 kg/m^3	50%	> 5 million

6.5. Fatigue Test Results

One Plain and three SFRC slabs were tested under cyclic loading. The individual test results and failure mode of each specimen are shown together with a discussion of the test results.

Specimen A-CP-U

Specimen A-CP-U was a control specimen, which was a plain concrete slab with a depth of 250 mm and a loading span of 1.0 metres. The slab was loaded monotonically up to the minimum testing load of 80 kN and was then cycled between 17.3% (82 kN) and 73.1% (342 kN) of the static cracking load of specimen A-SP-U at a frequency of 1.25 Hz using a sine loading waveform. The failure of the slab occurred at 323 cycles by the formation of a crack at the West loading line.

The mid-span deflection of slab A-CP-U at both maximum and minimum loads is presented in Figure 6.32. The maximum measured deflection at the West end of slab A-CP-U is shown in Figure 6.33. In the first cycle, the mid-span deflections of specimen A-CP-U at maximum and minimum loads were 2.48 mm and 0.92 mm, respectively, then it can be seen that the central deflection increased slowly for the first 321 cycles with maximum and minimum deflections of 2.60 mm and 1.03 mm, respectively. A

rapid increase in central deflection was subsequently observed possibly due to the formation of a crack at the West end resulting in failure with fatigue life of 323 cycles. The maximum and minimum central deflections at 323 cycles were 3.21 mm and 1.36 mm, respectively. The curve of the maximum measured deflection at the West load line versus number of cycles followed the same pattern as the central deflection.

The load-deflection curves at various cycle intervals during fatigue loading for slab A-CP-U are presented in Figures 6.34 and 6.35 for mid-span and maximum measured deflection, respectively. The stiffness of the slab was almost constant for the first 321 cycles with minimal permanent deflection, indicating elastic behaviour; however, a remarkable reduction in the modulus was observed during cycle 322 together with substantial permanent deflection at the un-loading stage of cycle 322. As the slab is fully supported, the contribution of the subgrade can be observed with the load-deflection curve of cycle 323.

The deflection measurements obtained along the slab, at different cycle intervals, are given in Figures 6.36 and 6.37 for maximum and minimum load levels, respectively. The deflection was almost uniform for the first 321 cycles. The sharp increase in deflection is noted between and next two the loading lines, together with significant decrease in deflection at the edges of the slab at failure, which indicates lifting of the slab's ends. The deflection at the West end was -0.45 mm at the minimum load at 322 cycles.

Strain gauges were placed at different locations across the depth of the slab. The crack passed through the strain gauges as can be seen from Figure 6.38. The strain data of gauges 1 to 5 across the thickness of slab A-CP-U are shown in Figure 6.39. Figures 6.40 and 6.41 present the readings of strain gauges (SGs) 1 to 5 across the thickness of the specimen taken at the maximum and minimum loads, respectively. It is clear from the figures that the crack started to form around 290 cycles at a depth of 30 mm and then expanded through the depth of the slab to lead to failure at cycle 323.

All observations indicate a brittle failure mode for the plain concrete slab under fatigue. As soon as a crack is formed, no further loads can be applied; the concrete slab was completely separated into two pieces after the completion of the test, as can be seen from Figure 6.42.

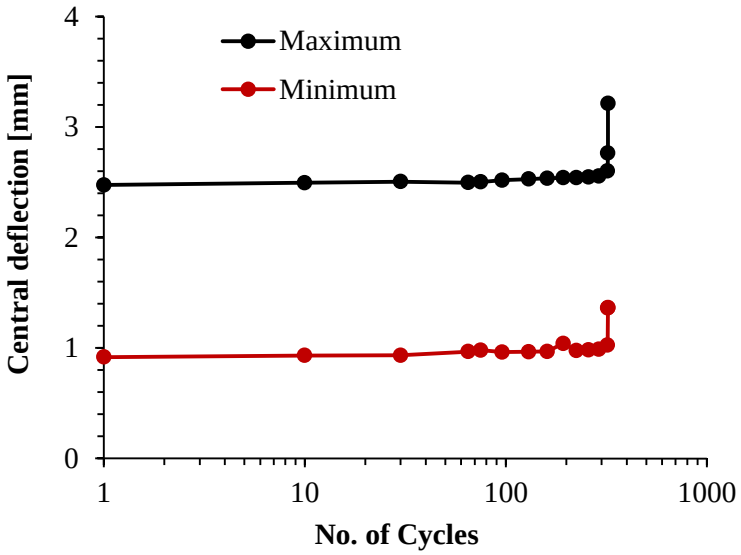

Figure 6.32 – Mid-span deflection versus number of cycles for slab A-CP-U.

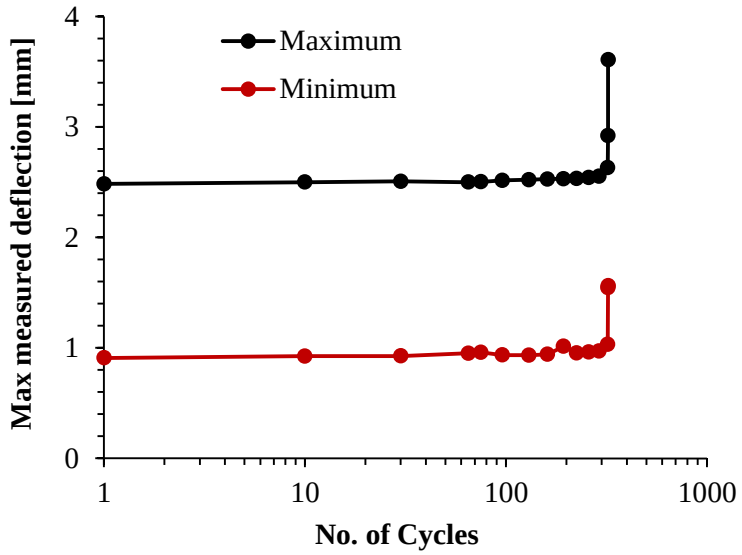

Figure 6.33 – Maximum measured deflection versus number of cycles for slab A-CP-U.

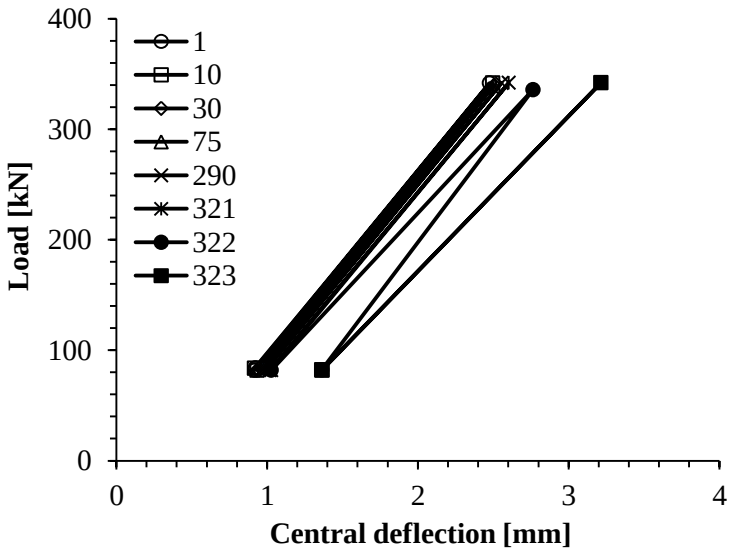

Figure 6.34 – Load versus mid-span deflection at various cycle intervals for slab A-CP-U.

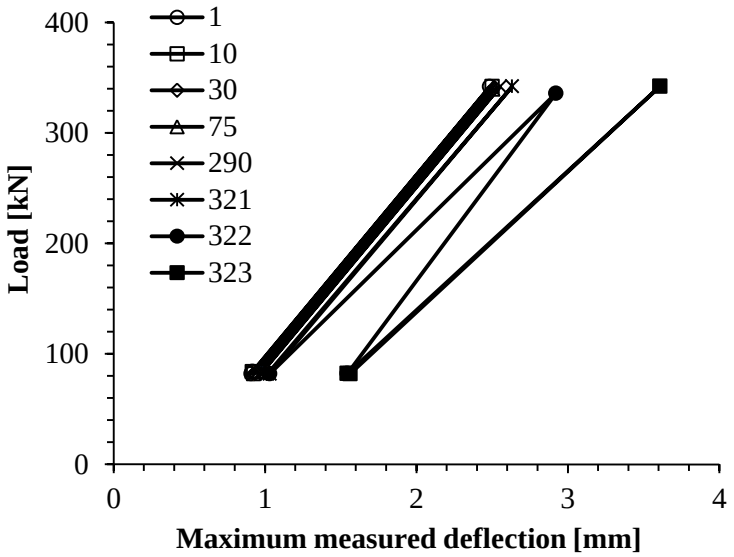

Figure 6.35 – Load versus maximum measured deflection at various cycle intervals for slab A-CP-U.

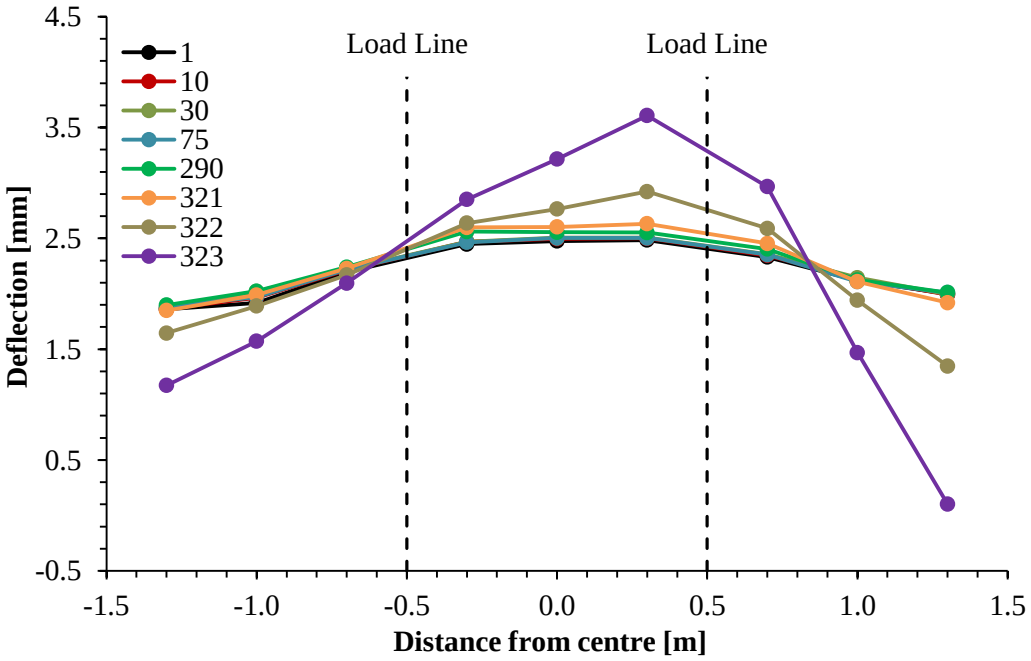

Figure 6.36 – Deflection measurements along slab A-CP-U taken at the maximum load of 342 kN.

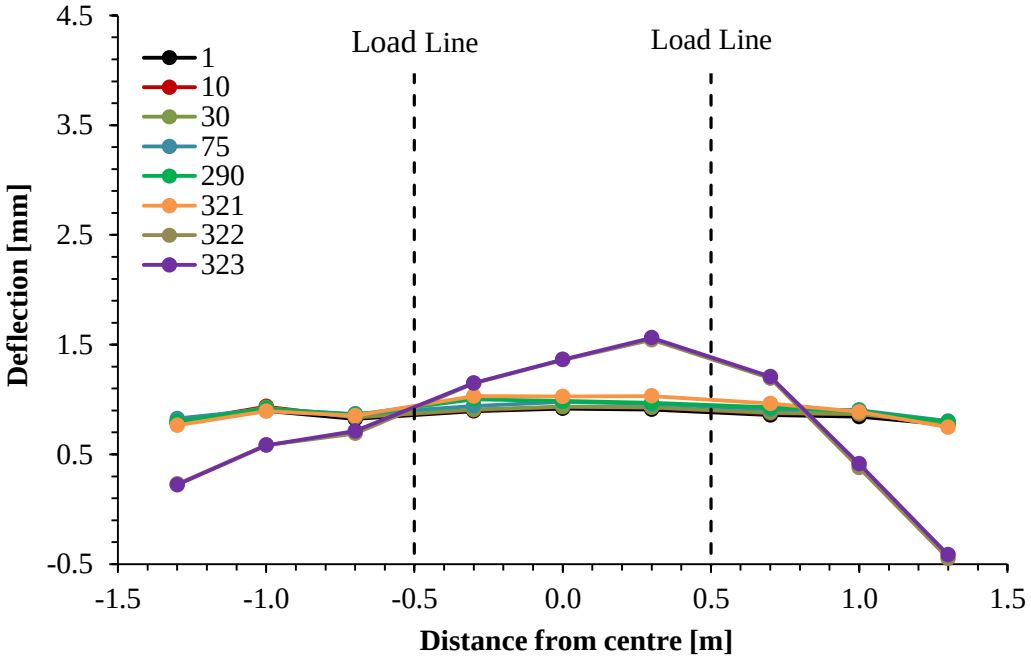

Figure 6.37 – Deflection measurements along slab A-CP-U taken at the minimum load of 82 kN.

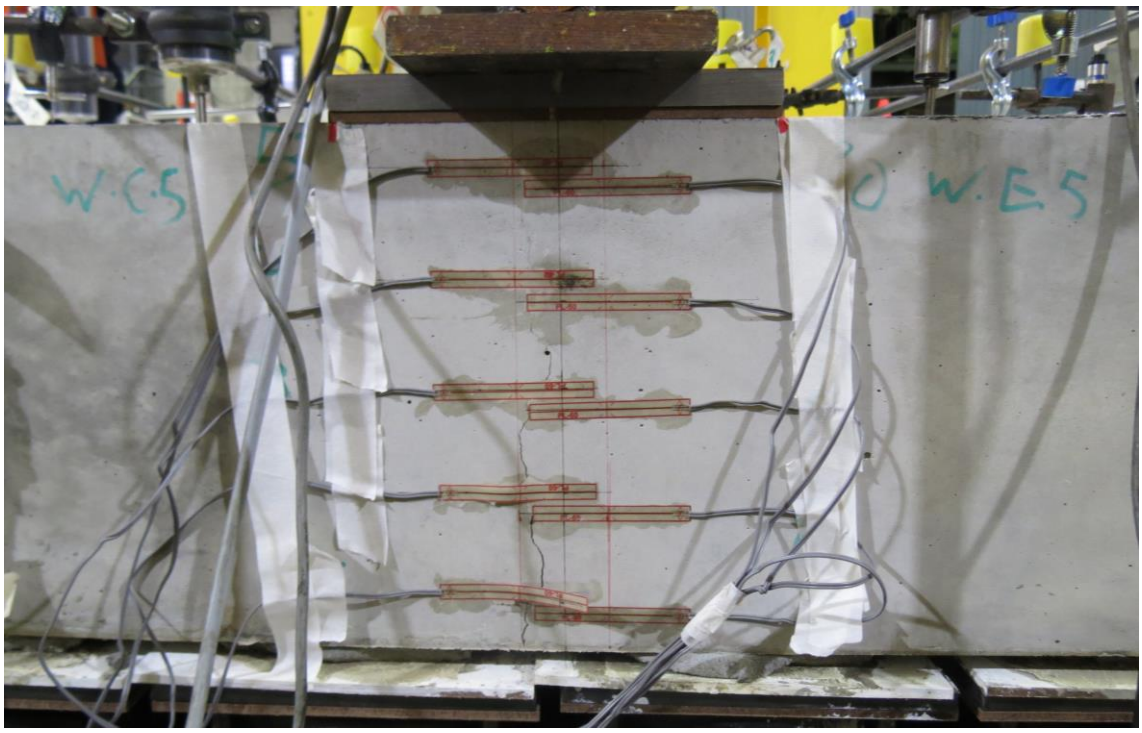

Figure 6.38 – Crack formation in slab A-CP-U.

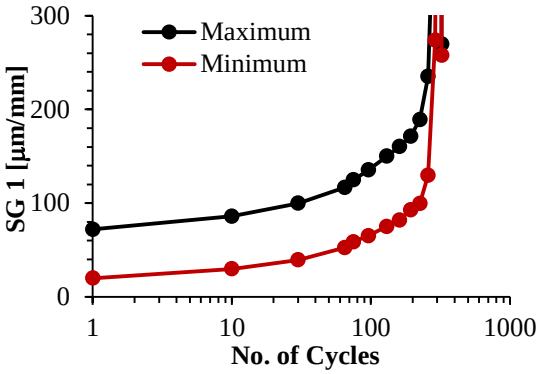

(a)

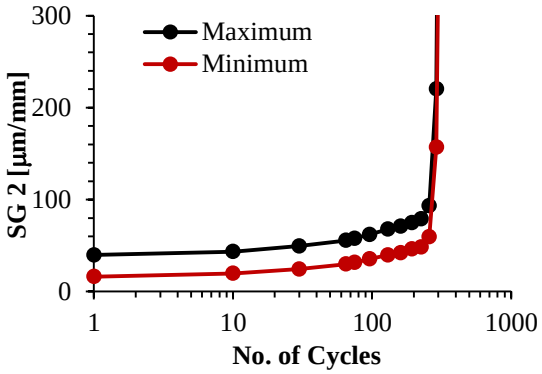

(b)

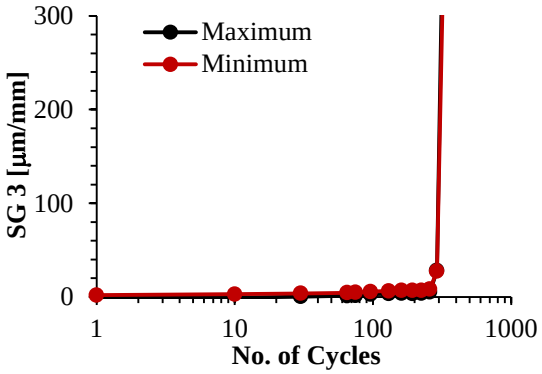

(c)

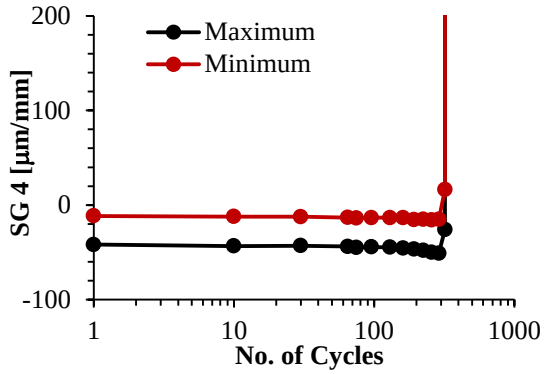

(d)

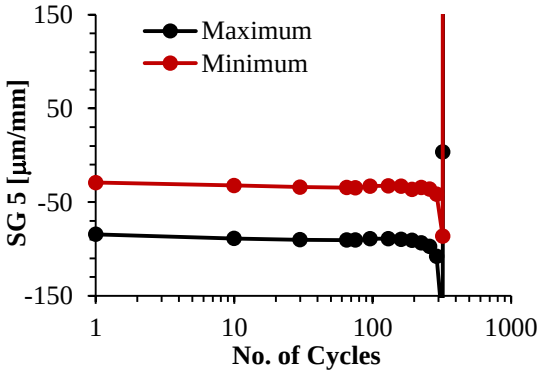

(e)

Figure 6.39 – Strain data versus the number of cycles at depth: (a) 30 mm; (b) 80 mm; (c) 130 mm; (d) 180 mm; (e) 230 mm.

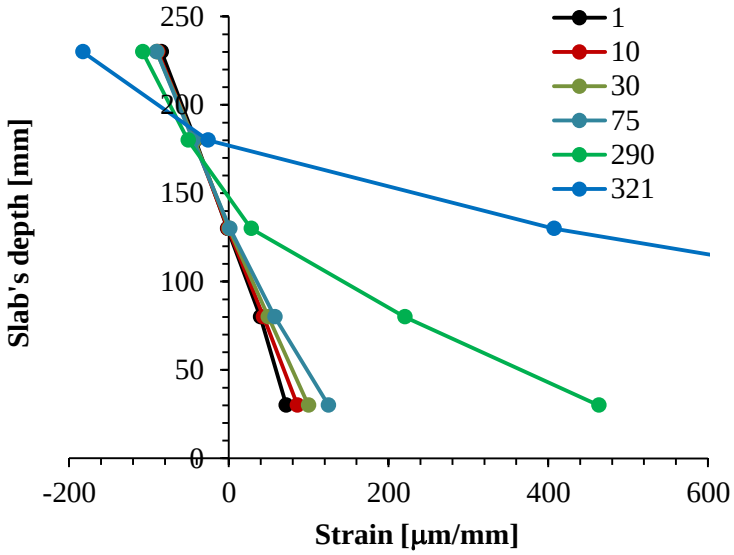

Figure 6.40 – Strain data of gauges 1 to 5 across the thickness of slab A-CP-U taken at the maximum load of 342 kN.

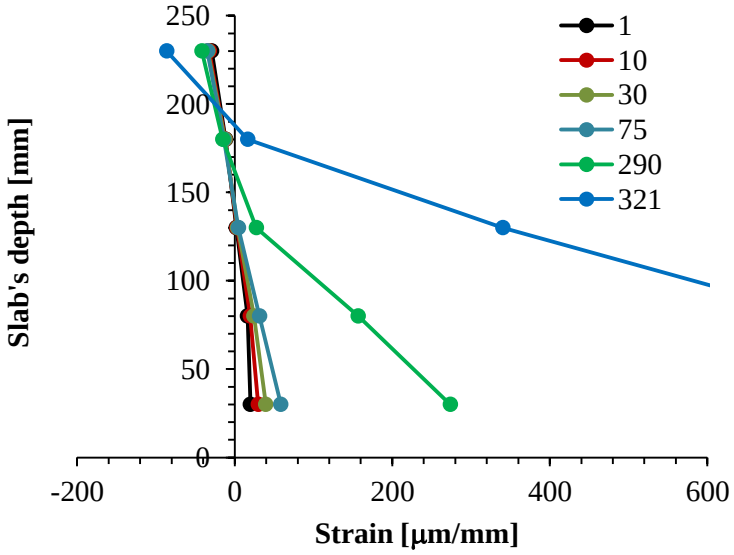

Figure 6.41 – Strain data of gauges 1 to 5 across the thickness of slab A-CP-U taken at the minimum load of 82 kN.

Figure 6.42 – Specimen A-CP-U after failure.

Specimen A-CF-U

Specimen A-CF-U was a SFRC slab with a total depth of 200 mm and a loading span of 1.0 metres. The specimen was cycled between 17.3% (81 kN) and 73.4% (343 kN) of the static cracking load of specimen A-SP-U at a frequency of 1.25 Hz. The readings of strain gauges 6 to 10 versus the number of cycles are presented in Figure 6.43. The strain data of gauges 6 to 10 across the thickness of slab A-CF-U taken at the maximum and minimum load levels are shown in Figures 6.44 and 6.45, respectively. During the first monotonic loading up to 80 kN, no cracks were initiated. After 1,796 cycles, a crack developed at the West load line, as can be seen from Figure 6.43(a – c). The crack tip was located at a depth of 135 mm from the slab's base as can from Figure 6.44. The strain at a depth of 135 mm was zero at 1,796 cycles. The crack propagation continued until the crack tip reached 175 mm.

During different intervals of testing, crack developments were marked using a felt tip pen (see Figure 6.46) and the crack widths were measured using an optical microscope at the end of fatigue testing at the upper load level. The crack widths were measured at depths of 20 mm, 60 mm, 100 mm, 140 mm and 180 mm and they were 0.06 mm, 0.28 mm, 0.32 mm, 0.52 mm and 0.80 mm, respectively.

The central deflection of the slab at both maximum and minimum loads as well as the maximum measured deflection is shown Figures 6.47 and 6.48. At the first cycle, the maximum and minimum central deflections were 2.72 mm and 1.05 mm, respectively. This was followed by a steady increase in deflection for the first 289,105 cycles to reach a deflection of 3.11 mm and 1.39 mm at the maximum and minimum loads, respectively. After this, the deflection rate accelerated to have maximum and minimum deflections of 3.46 mm and 1.70 mm, respectively, at 3 million cycles. Similar pattern was noted for the maximum measured deflection during the fatigue loading of A-CF-U as can be seen from Figure 6.48. It is clear from both figures (Figures 6.47 and 6.48), that the formation of the crack, at 1,796 cycles, did not affect the rate of deflection

increase which supports the superior performance of SFRC pavements compared to those of plain concrete.

The deflection at the West edge of the slab is presented in Figure 6.49. The maximum and minimum deflections at the first cycle were 2.49 mm and 1.14 mm, respectively. The deflections remained almost constant for the first 1,796 cycles, until the formation of a crack at the loading line. After that, the deflections decreased at a steady rate to reach at 289,105 cycles 1.09 mm and 0.77 mm at maximum and minimum loads, respectively. This was followed by an accelerated rate of deflection decrease to reach maximum and minimum deflections of 0.69 mm and -0.11 mm, respectively, at 2 million cycles. The rate of deflection decrease was reduced slightly again to reach 0.67 mm and -0.16 mm at the maximum and minimum loads, respectively, at 3 million cycles. At about 1,250,000 cycles, the deflection at the minimum load became negative, which indicates lifting of the West edge. This means if the slab was continuous, a crack would likely have formed at this end. This shows the capability of SFRC to redistribute load, indicating the high ductility and toughness SFRC pavements compared to plain concrete and longer fatigue life.

The load-deflection curves during fatigue loading for both central and maximum measured deflection, taken at different number of cycles, are presented in Figures 6.50 and 6.51. It is clear from both figures that the modulus of the loading and unloading curves remained almost constant during the test. However, there is a permanent deflection of 0.74 mm and 1.12 mm for central and maximum measured deflection, respectively, during 3 million cycles of loading. This indicates the higher toughness and ductility of SFRC slabs as well as the integrity of SFRC slab during the test.

The deflection measured along the length of the specimen remained almost unchanged for the first 7,500 cycles, as shown in are presented in Figures 6.52 and 6.53, at maximum and minimum load levels, respectively. After that, the deflection started to increase between and next to the loading lines and to decrease at the edges of the slab.

At 1,724,100 cycles, it was noted that the deflection to the right of the West loading line increased. This indicates load redistribution from the cracked region (left side of the West loading line) to the adjacent one to form a constant moment region. Again, this supports the increased toughness of the SFRC slabs under fatigue loading.

After the completion of 3 million loading cycles, the fatigue test was stopped. The specimen was unloaded back to zero load. Following that, a displacement controlled monotonic load was applied at a rate of 0.12 mm/min until a load of 492.7 kN was reached; as the limit capacity of the actuator is 500 kN. Load versus central deflection during the static test is presented in Figure 6.54. It is clear from the figure that there is a permanent deflection of 0.58 mm after 3 million cycles of fatigue loading with an upper load level of 73.4%. During the static test, the stiffness of the specimen and the rate of deflection increase remained unchanged during the test. No reduction in load bearing capacity was observed. This indicates that SFRC maintained its slab action after 3 million cycles of cyclic loading. The addition of SFRC resulted in higher ultimate bearing capacity and increased toughness. At the conclusion of the test, the SFRC slab was handled as a solid, one piece, specimen and was not separated into two pieces.

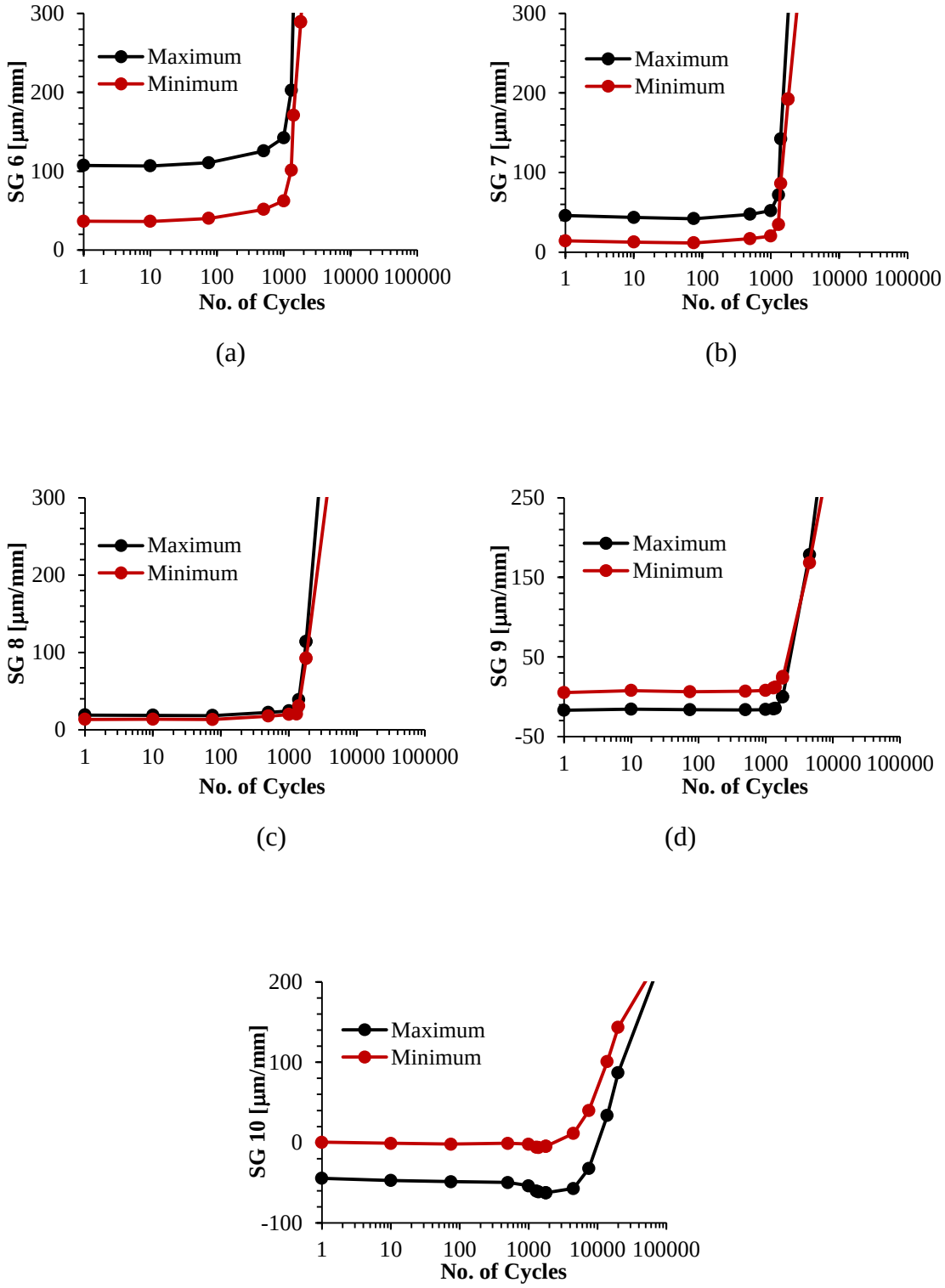

Figure 6.43 – Strain data versus the number of cycles at depth: (a) 15 mm; (b) 55 mm; (c) 95 mm; (d) 135 mm; (e) 175 mm.

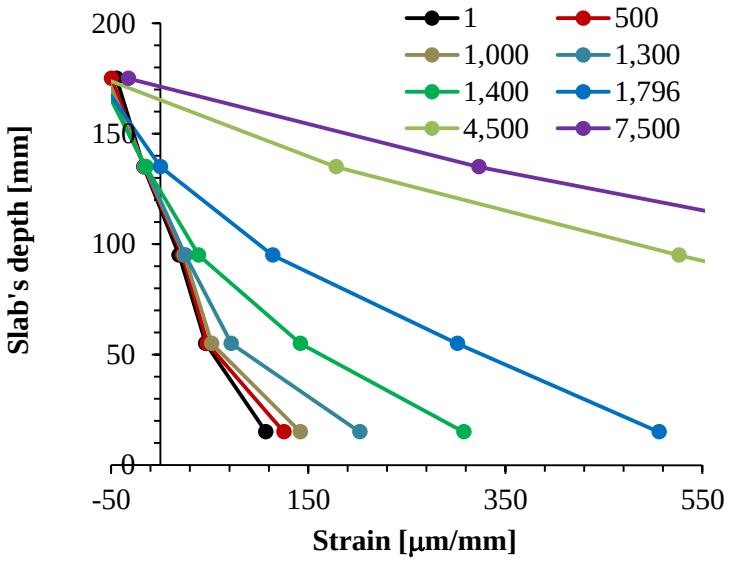

Figure 6.44 – Strain data of gauges 6 to 10 across the thickness of slab A-CF-U taken at the maximum load of 343 kN.

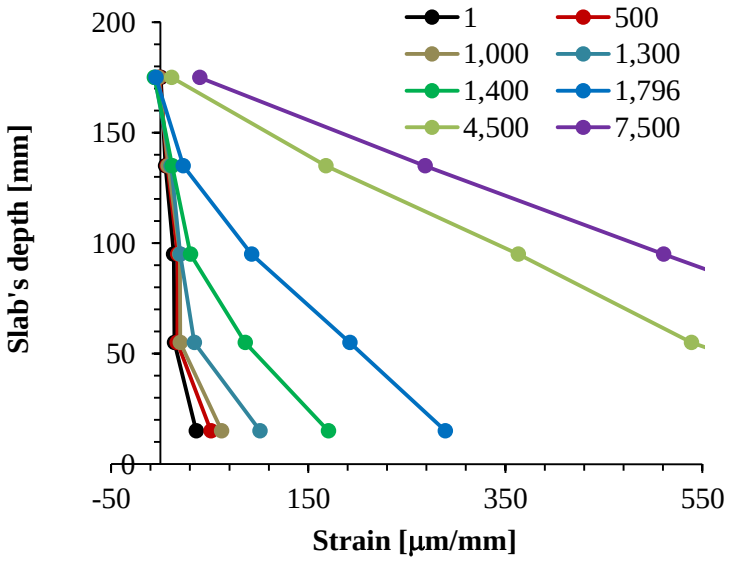

Figure 6.45 – Strain data of gauges 6 to 10 across the thickness of slab A-CF-U taken at the minimum load of 81 kN.

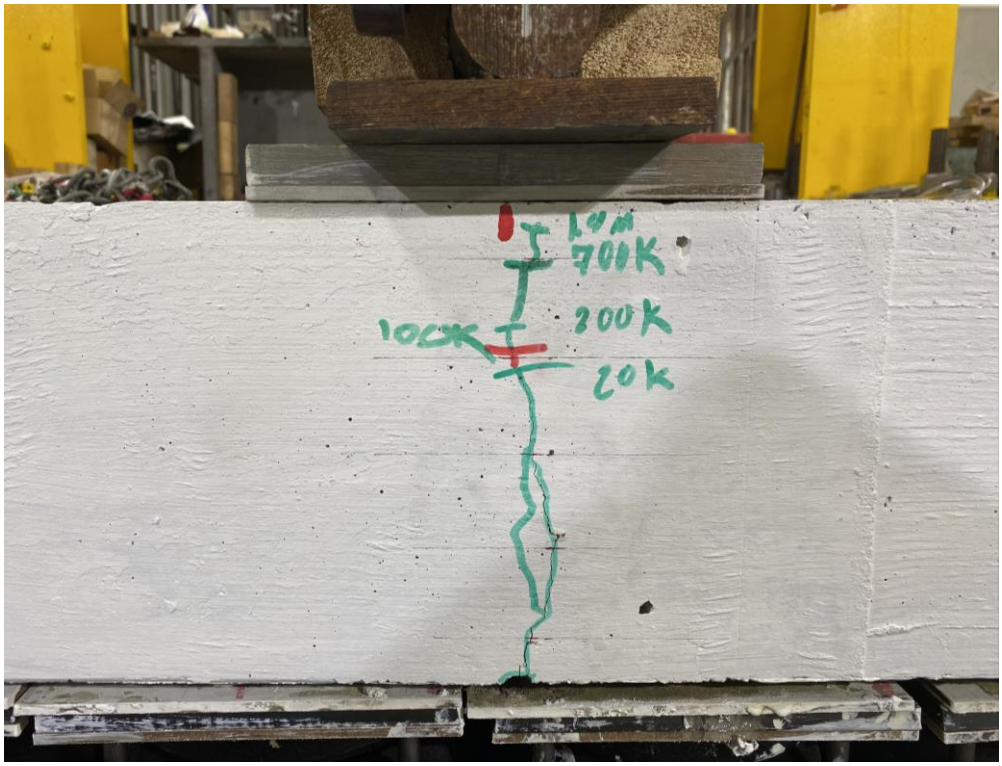

Figure 6.46 – Crack pattern of slab A-CF-U after 3 million cycles.

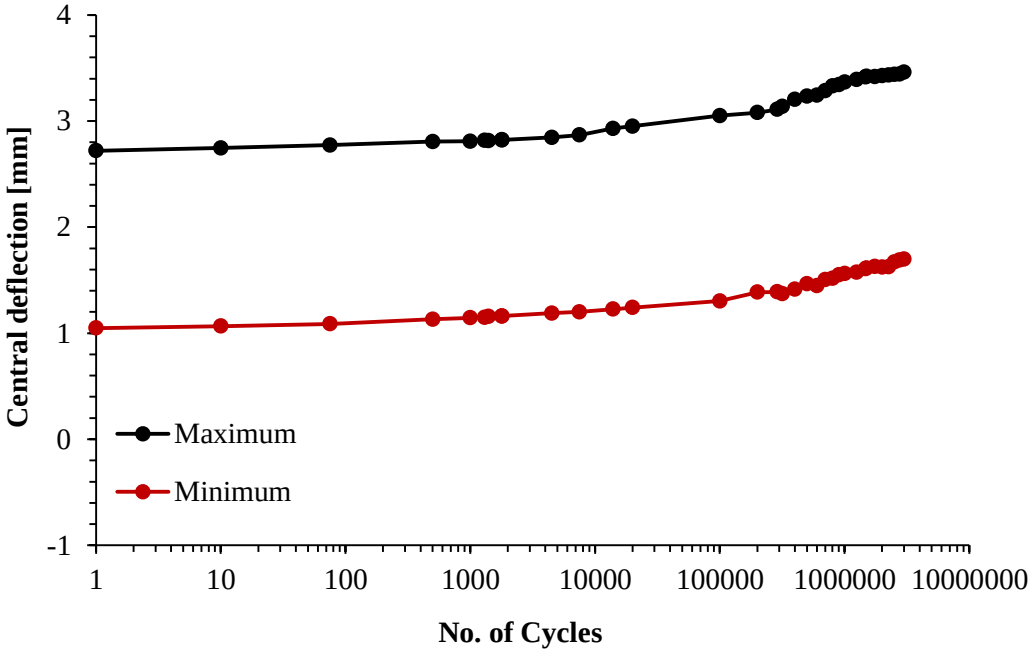

Figure 6.47 – Central deflection versus number of cycles for slab A-CF-U.

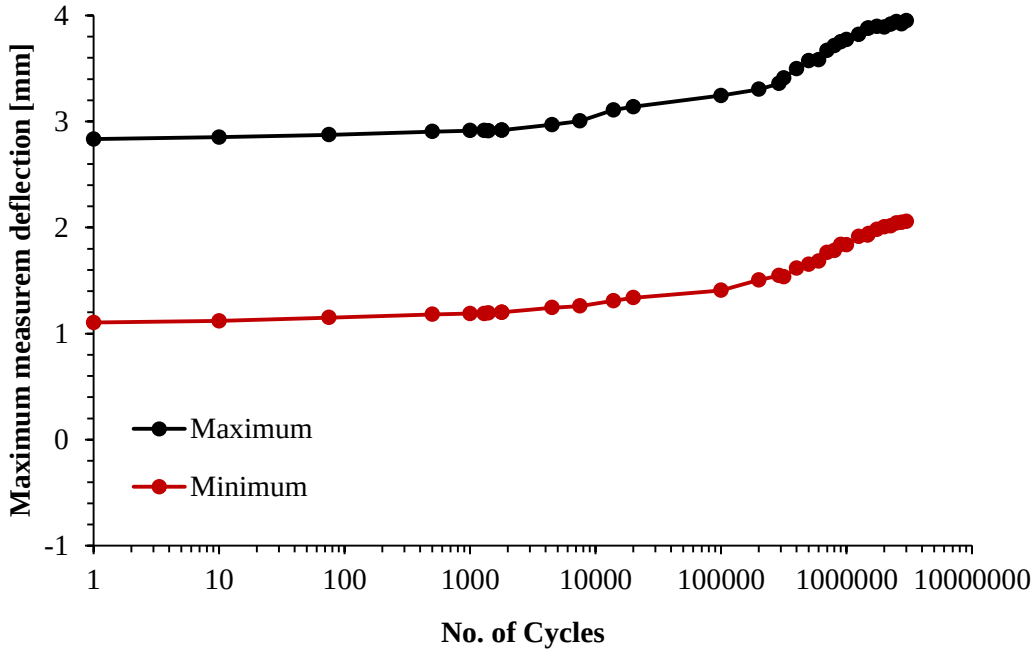

Figure 6.48 – Maximum measured deflection versus number of cycles for slab A-CF-U.

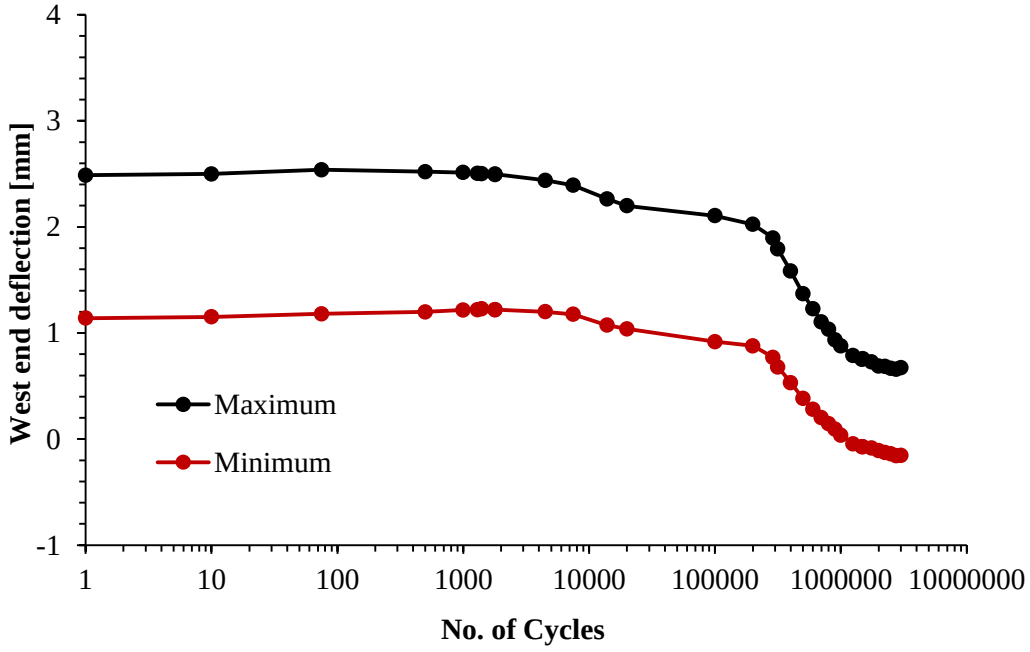

Figure 6.49 – Deflection of the West end versus number of cycles for slab A-CF-U.

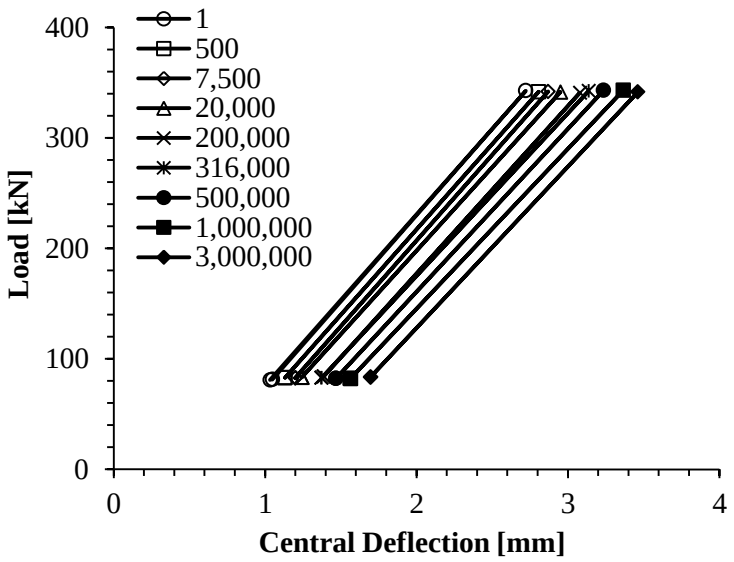

Figure 6.50 – Load versus central deflection at various cycle intervals for slab A-CF-U.

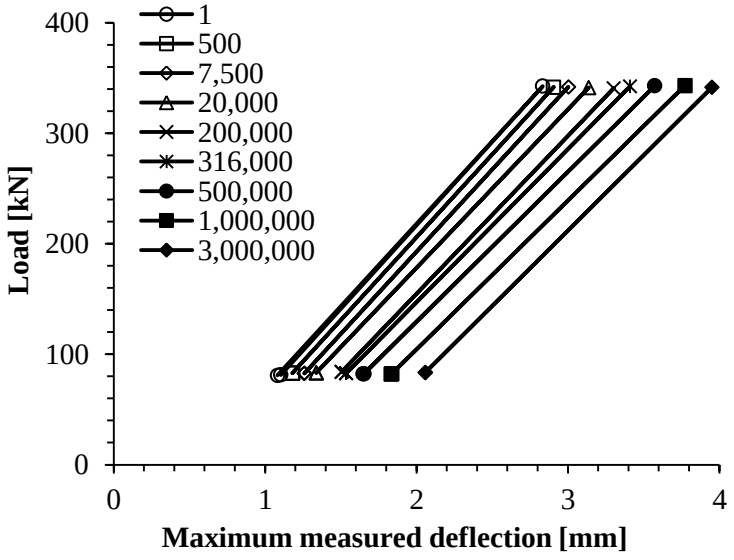

Figure 6.51 – Load versus maximum measured deflection at various cycle intervals for slab A-CF-U.

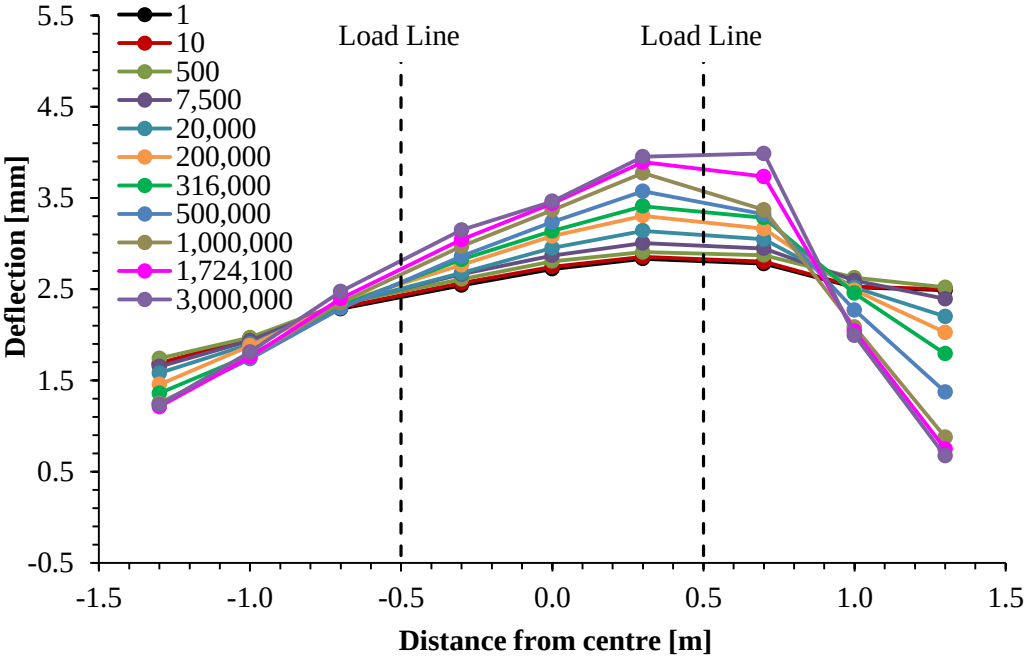

Figure 6.52 – Deflection measurements along slab A-CF-U taken at the maximum load of 343 kN.

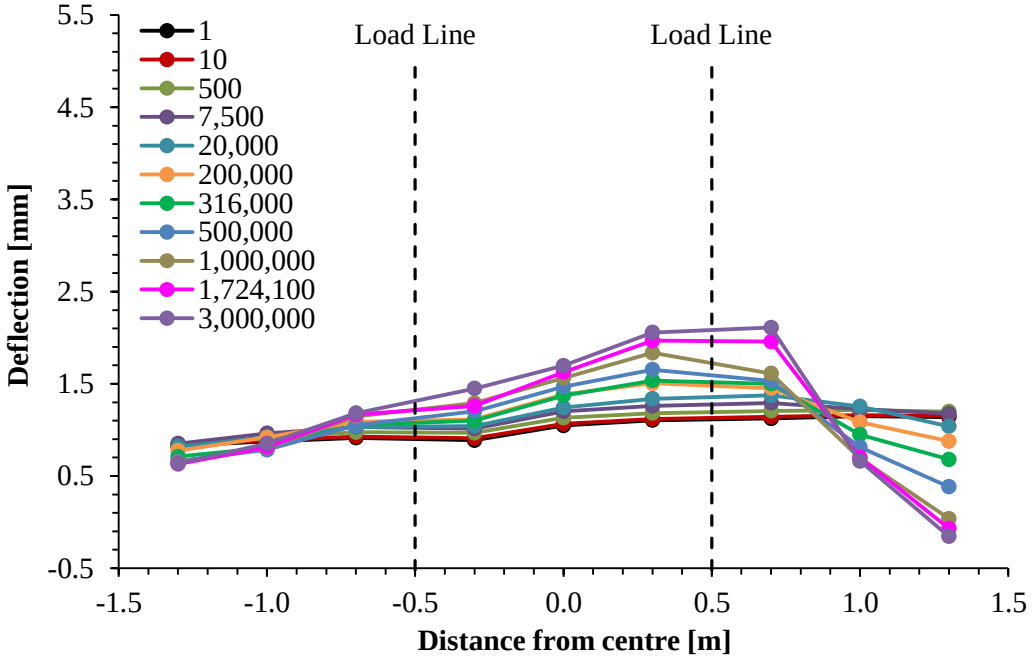

Figure 6.53 – Deflection measurements along slab A-CF-U taken at the minimum load of 81 kN.

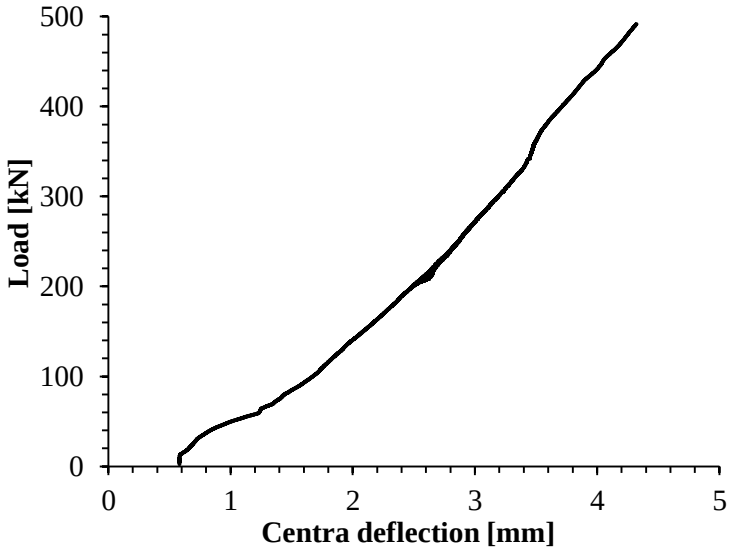

Figure 6.54 – Load versus deflection during static loading for slab A-CF-U.

Specimen B-CF-U

Specimen B-CF-U is a SFRC slab with a total depth of 200 mm and a loading span of 2.3 metres. The specimen was loaded monotonically up to the minimum testing load of 36 kN and was then cycled between 17.4% (37.5 kN) and 72.3% (156 kN) of the static cracking load of specimen B-SP-U at a frequency of 1.5 Hz using a sine loading waveform up to 2.0 million cycles. After 2.0 million cycles, the load range increased by a factor of two for a further one million loading cycles; that is a range of 77.2 kN and 311.6 kN. The upper end of this range represents a load equivalent to 144.5% of the capacity of the statically tested plain concrete control slab B-SP-U.

Figure 6.55 presents the crack width development versus the number of cycles at the slab's surface. The propagation of the crack width across the thickness of the slab is shown in Figure 6.56. A crack was formed at cycle 98,334 about the mid-span of the slab. After the formation of cracking, testing was paused and the crack width was measured at different locations across the thickness and at the surface of the slab using an optical microscope. The crack width at the surface was measured at two locations along the width of the slab and it was found to be 0.24 mm and 0.26 mm, as presented

in Figure 6.55. From Figure 6.56, it can be seen that the initial crack widths across the depth of the slab were 0.16 mm, 0.08 mm and 0.01 mm at depths of 20 mm, 100 mm and 180 mm, respectively. The crack was formed up to a depth of 180 mm. After crack width measurement, gauges were installed and testing was continued.

As can be seen from Figures 6.55 and 6.56, the crack width increased at a steady rate to reach an average maximum crack width of 0.95 mm at the specimen's surface; while the maximum crack width at depths of 20 mm, 100 mm and 180 mm was found to be 0.74 mm, 0.41 mm and 0.01 mm, respectively, at 2.0 million cycles. As the applied load was magnified by a factor of two, the crack width significantly enlarged. At cycle 2,000,001, the maximum average surface crack width became 1.65 mm and across the depth the maximum crack widths were 1.32 mm, 0.73 mm and 0.05 mm at depths of 20 mm, 100 mm and 180 mm, respectively. After that, the crack width continued to increase slowly to reach 1.55 mm, 0.88 mm and 0.11 mm at the upper load level at depths of 20 mm, 100 mm and 180 mm, respectively, at 3 million cycles. Similarly, the average maximum surface crack width increased steadily to reach 1.90 mm at 3 million loading cycles. The SFRC slab after the completion of test was handled as a solid one specimen which was not broken into two pieces.

The central deflection of the slab at both maximum and minimum loads is shown Figure 6.57. At the first cycle, the maximum and minimum central deflections were 0.78 mm and 0.26 mm, respectively. This was followed by a slow increase in deflection to reach 0.90 mm and 0.30 mm maximum and minimum deflections, respectively, prior to crack formation. Soon after crack formation, the maximum and minimum deflection sharply dropped to 0.19 mm and -0.13 mm, respectively. The negative deflection indicates lifting of the mid-span of the slab at the minimum load. After that, the deflection continued to decrease steadily to reach a deflection of -0.22 mm and -0.29 mm at the maximum and minimum loads, respectively, at 2 million cycles. Following that, a significant reduction in mid-span deflection was noticed due to higher

load application. The maximum and minimum deflections dropped to -0.45 mm and -0.50 mm, respectively. After 3 million of cycles, the deflections at maximum and minimum loads were -0.63 mm (same deflection). Interestingly, as higher number of cycles was applied the minimum and maximum central deflections approach the same value. This indicates that the fibres controlled the growth of fatigue crack and that the slab maintained its integrity throughout the test.

The deflection at the West edge of the slab versus the number of cycles is presented in Figure 6.58. The maximum and minimum deflections at the first cycle were 1.39 mm and 0.47 mm, respectively. Similarly to the central deflection, a slow increase in deflection was observed to reach 1.56 mm and 0.61 mm at the upper and lower loads, respectively. The maximum and minimum deflections after cracking jumped to 1.93 mm and 0.86 mm, respectively. Following the crack formation, the deflection increased at a steady rate to reach maximum and minimum deflections of 2.37 mm and 1.18 mm, respectively, at 2 million loading cycles. As higher fatigue loading is applied, the maximum and minimum deflections increased to 3.99 mm and 1.76 mm, respectively. At the end of the test, the deflections at the upper and lower loads were 4.22 mm and 2.02 mm, respectively.

The deflection profiles measured along the length of the specimen are presented in Figures 6.59 and 6.60 at maximum and minimum loads, respectively. The deflection profiles remained almost unchanged for the first 90,000 cycles of the test. After that, the central deflection decreased and the edge deflections increased due to crack formation.

At the second stage of testing (after 2 million cycles) significant central deflection reduction and edge deflection increase was observed due to the application of the higher load. It is important to mention over here that if a detailed a attention is paid to the central and edge deflections at maximum and minimum loads in the figures; as previously noted, that the central deflection at the maximum and minimum loads approach the same deflection value as higher number of cycles are applied. However,

the edge deflections continue to increase. This indicates that the fibres controlled the growth of fatigue crack and that the slab maintained its integrity throughout the test. This results in a substantial increase in total displacement, indicating the improvement in toughness. This also indicates that load redistribution mechanism from the cracked region to the adjacent ones is valid in SFRC slabs.

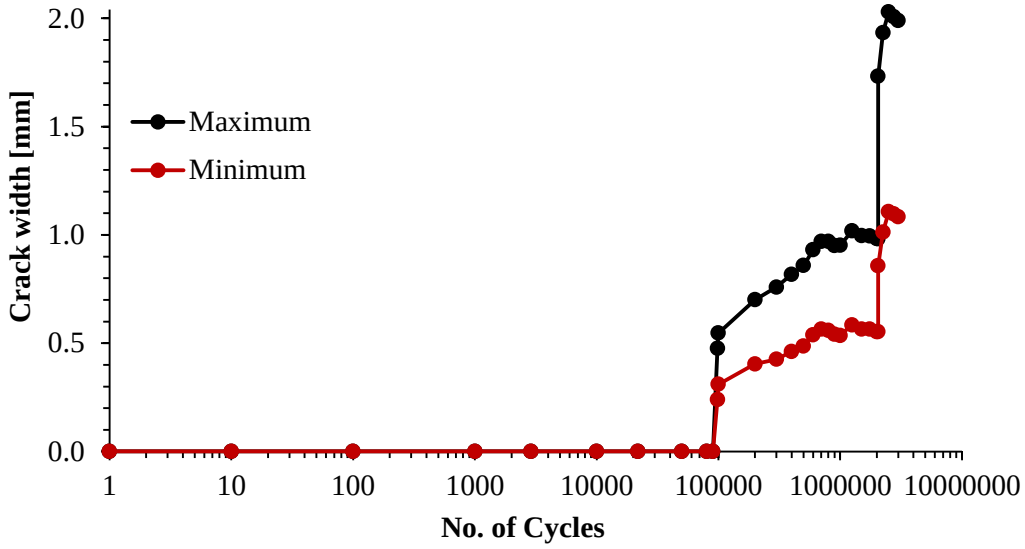

(a)

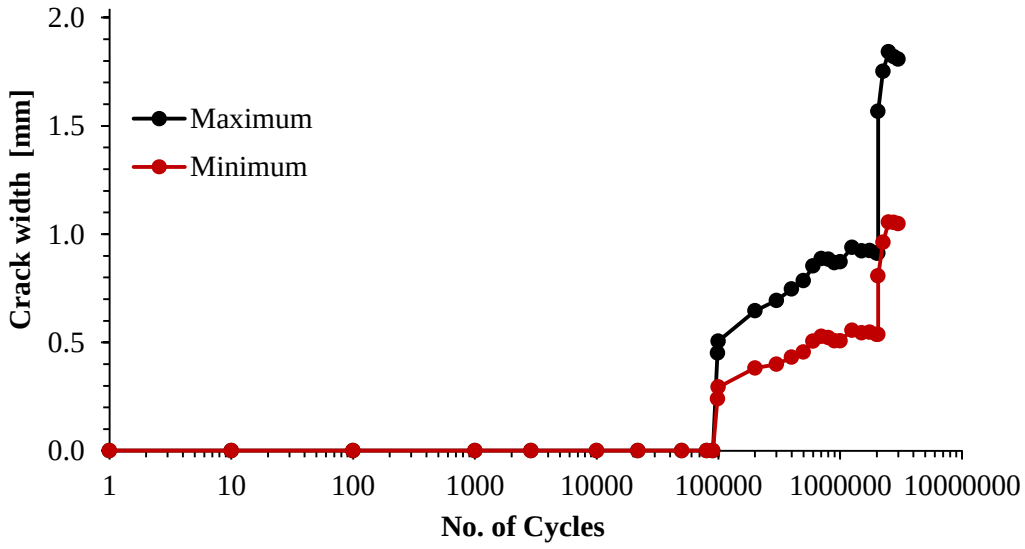

(b)

Figure 6.55 – Crack width development versus number of cycles at the slab's surface: (a) gauge No. 1; (b) gauge No. 2.

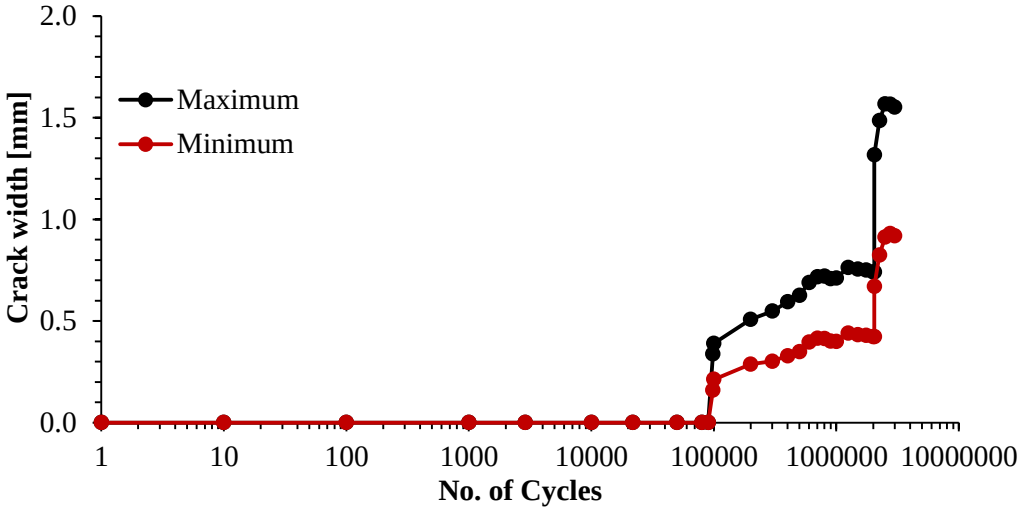

(a)

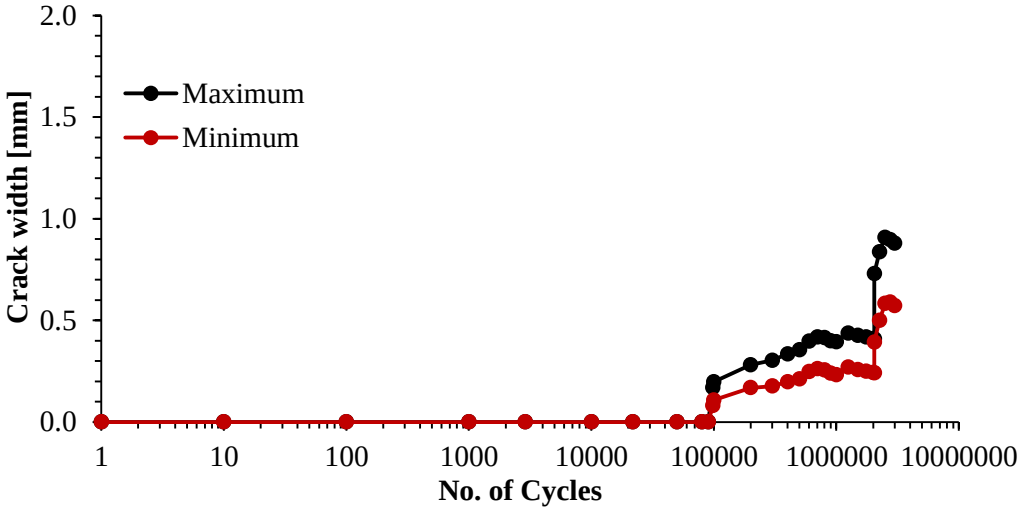

(b)

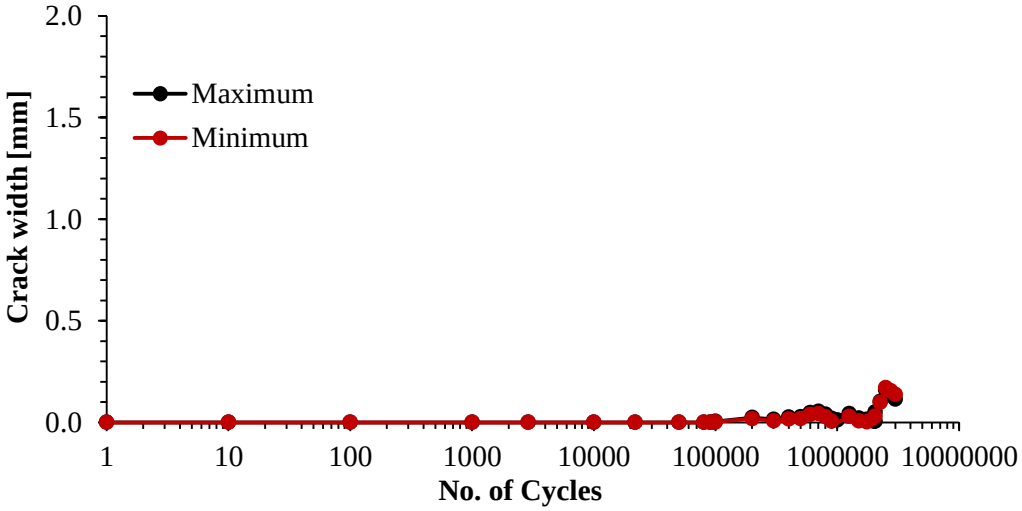

(c)

Figure 6.56 – Crack width development versus number of cycles at depth: (a) 20 mm; (b) 100 mm; (c) 180 mm.

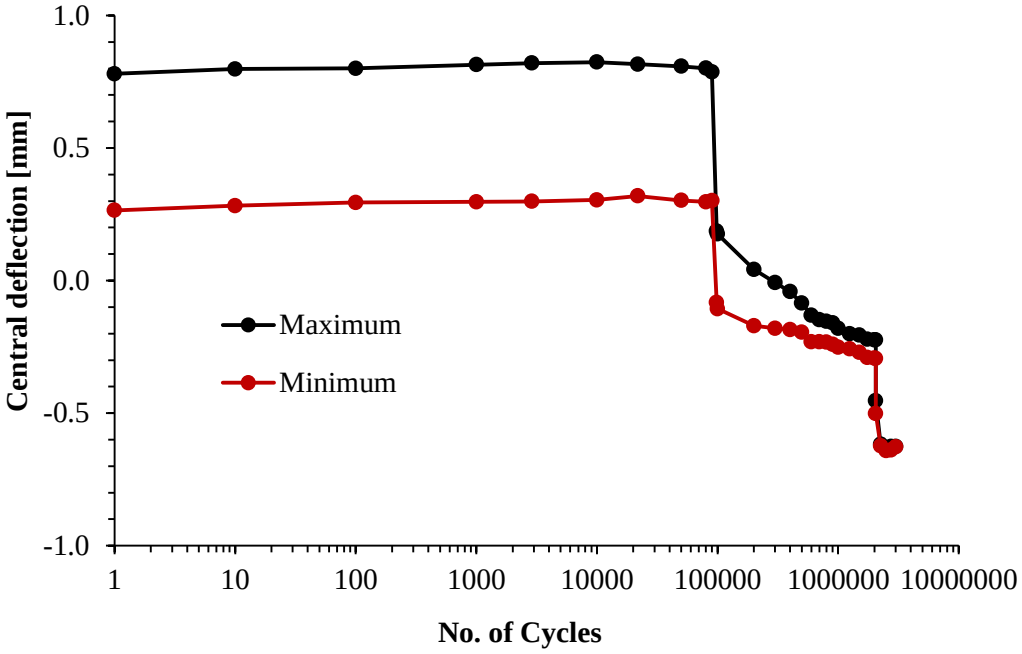

Figure 6.57 – Central deflection versus number of cycles for slab B-CF-U.

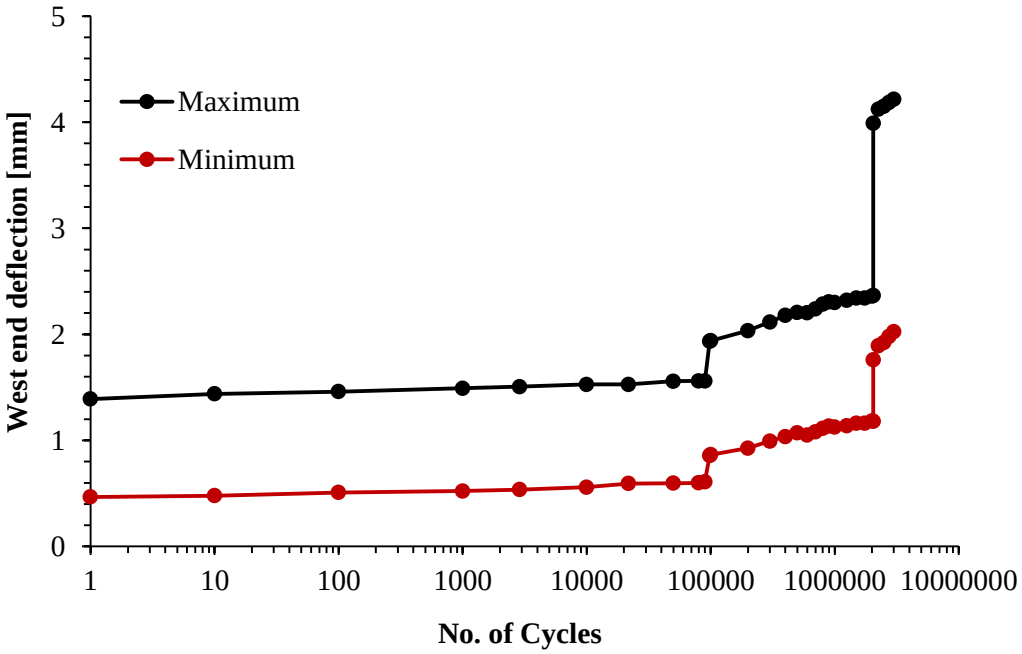

Figure 6.58 – Deflection of the West end versus number of cycles for slab B-CF-U.

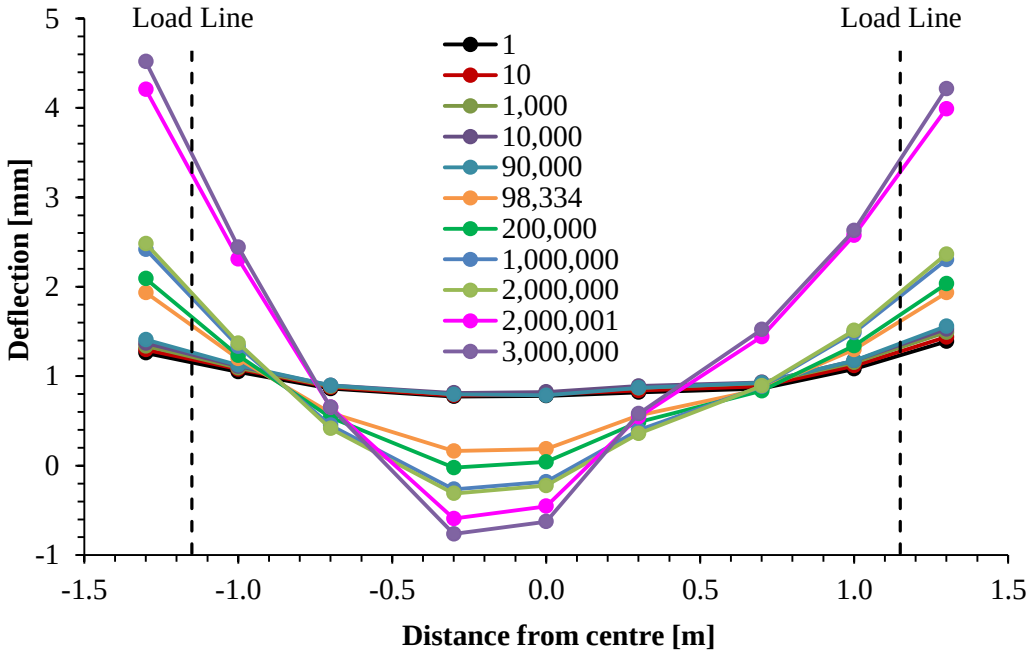

Figure 6.59 – Deflection measurements along slab B-CF-U taken at the maximum load.

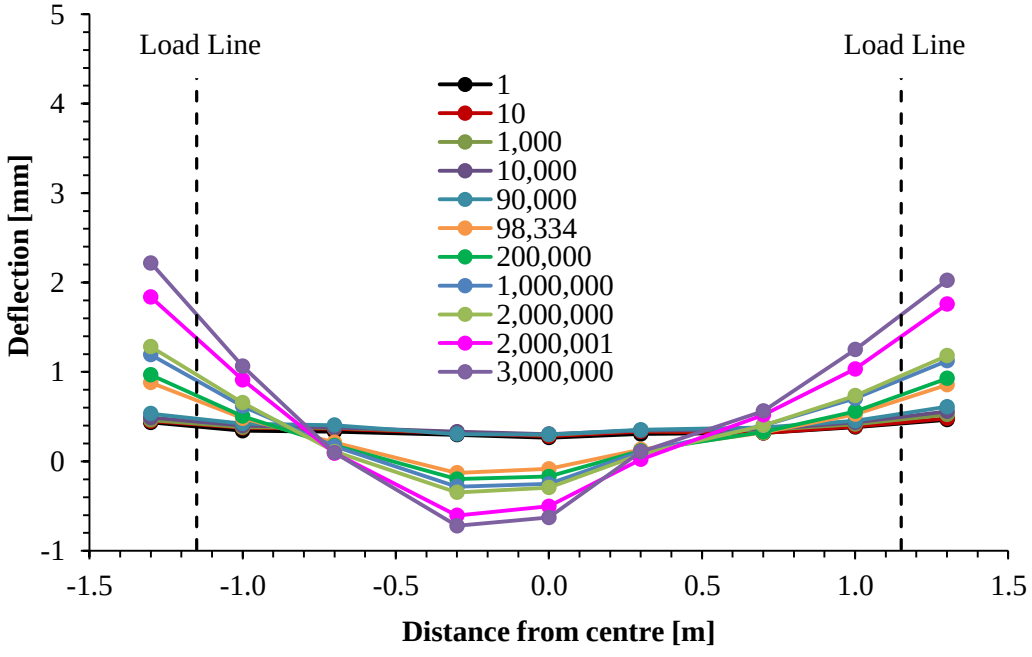

Figure 6.60 – Deflection measurements along slab B-CF-U taken at the minimum load.

Specimen B-CF-C

Specimen B-CF-C was a pre-cracked SFRC slab with a loading span of 2.3 metres and a thickness of 200 mm. It was loaded monotonically at a rate of 0.12 mm/min until a crack was developed, after which cyclic loading between 16.3% (35.2 kN) and 50.5% (109 kN), of the of the static cracking load of specimen B-SP-U, was applied at a frequency of 2.5 Hz using a sine loading waveform to determine the residual fatigue resistance.

A crack formed at a load of 165.4 kN (see Figure 6.61) as indicated by the concrete stain gauges and shown in Figure 6.62. After cracking, testing was paused and the specimen was unloaded to 34 kN. At this stage the crack width was measured at different locations across the thickness and at the surface of the slab using an optical microscope. The crack width at the surface was measured at two locations along the width of the slab and it was found to be 0.14 mm and 0.15 mm. The initial crack widths across the depth of the slab were 0.10 mm and 0.04 mm at depths of 20 mm and 100 mm, respectively. The crack was formed up to a depth of 130 mm. Figure 6.63 presents the load versus central deflection during the initial monotonic loading. It is observed from the figure that the load increases linearly up to cracking load with a central deflection of 0.76 mm. Following that, a crack was developed about the mid-span of the slab and the central deflection dropped to 0.45 mm.

After the formation of the crack, fatigue testing was commenced. The central deflection versus the number of cycles at both maximum and minimum loads is presented in Figure 6.64. At the first load cycle, specimen B-CF-C had minimum and maximum deflections of 0.17 mm and -0.04 mm, respectively. This was followed by almost constant deflection for the first 10,000 cycles. After this, a steady decrease in deflection was observed to reach 0.02 mm and -0.10 mm at the upper and lower load levels, respectively, at 5 million cycles.

The deflection at the West end of the slab versus the number of cycles is presented in Figure 6.65. The maximum and minimum deflections at the first cycle were 1.30 mm and 0.68 mm, respectively. Similarly to the central deflection, a negligible change in deflection was observed for the first 10,000 cycles. After that, a slow increase in deflection was recorded to reach 1.51 mm and 0.92 mm at the maximum and minimum loads, respectively, at 5 million loading cycles.

The load-deflection curves during fatigue loading for both central and the West end deflections, taken at various cycle intervals, are presented in Figures 6.66 and 6.67, respectively. It is observed in Figure 6.66 that the stiffness of the specimen slowly reduced for the first 10,000 cycles, and then a significant stiffness reduction is observed in cycle intervals from 10,000 to 1,000,000 cycles, together with evident permanent central deflection. This is due to the crack propagation across the depth of the specimen and coinciding with a significant opening of the crack. Interestingly, after crack stabilisation, the stiffness of the mid-span section remained approximately constant with negligible change until the completion of five million cycles indicating the substantial engagement of fibres in controlling and bridging the growth of fatigue crack and maintaining the integrity of the slab throughout the test. The stiffness of the specimen at the West end (uncracked section) remained approximately constant with inducing higher increments of permeant deflections with higher number of cycles, as seen from Figure 6.67. This means that the load was redistributed to the edge of the specimens and a higher total deflection would be the resultant at failure.

The deflection measurements obtained along the slab, at different cycle intervals, are given in Figures 6.68 and 6.69 for maximum and minimum loads, respectively. It is clear from both figures, that the central deflection and its surroundings decreased as higher number of cycles were applied. To the contrary, the deflections surrounding the loading lines increased with higher number of cycles. It is worthy of mention that the

reduction of central deflection and its surrounding was slower than the deflection increase at the edges.

Figure 6.70 presents the crack width development versus the number of cycles at the slab's surface. The propagation of the crack width across the thickness of the slab is shown in Figure 6.71. At the first cycle, the maximum average crack width at the specimen's surface was 0.20 mm. The maximum crack widths across the depth of the slab were 0.15 mm, 0.06 mm and zero at depths of 20 mm, 100 mm and 180 mm, respectively, at the first cycle. This was followed by a negligible change in crack width development for the first 10,000 loading cycles, consistently with the observation seen in central deflection in Figure 6.64. Next, noticeable and steady increase in crack width enlarging was recorded up to 1,000,000 cycles to reach maximum and minimum average crack width at the specimen's surface of 0.35 mm and 0.24 mm, respectively. The maximum crack width at depths of 20 mm, 100 mm and 180 mm was found to be 0.25 mm, 0.13 mm and 0.01 mm, respectively. This explains the dramatic change in the stiffness of the specimen at the centreline observed in Figure 6.66.

After one million loading cycles, negligible crack width enlarging was recorded until the completion of the fatigue test. A negligible noise in range of ±0.02 mm was noted with the crack widths after one million cycles due to slight temperature change between day and night as testing was undertaken continuously 24 hours a day (including weekends).

During different intervals of testing, crack developments were marked using a felt tip pen (see Figure 6.72). The crack was formed up to a depth of 175 mm approximately. After the conclusion of the test, the SFRC slab was handled as a solid one specimen and was not separated into two pieces.

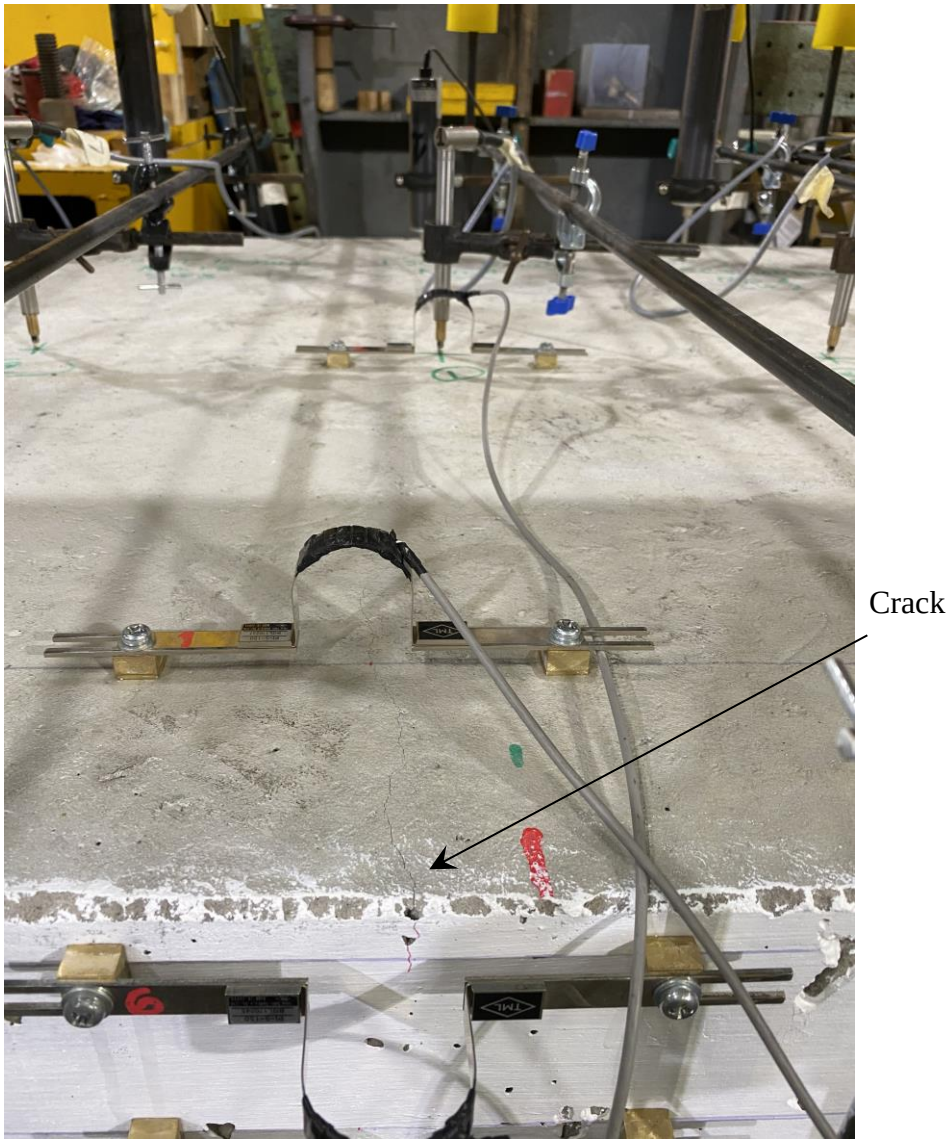

Figure 6.61 – Crack development during the initial monotonic loading.

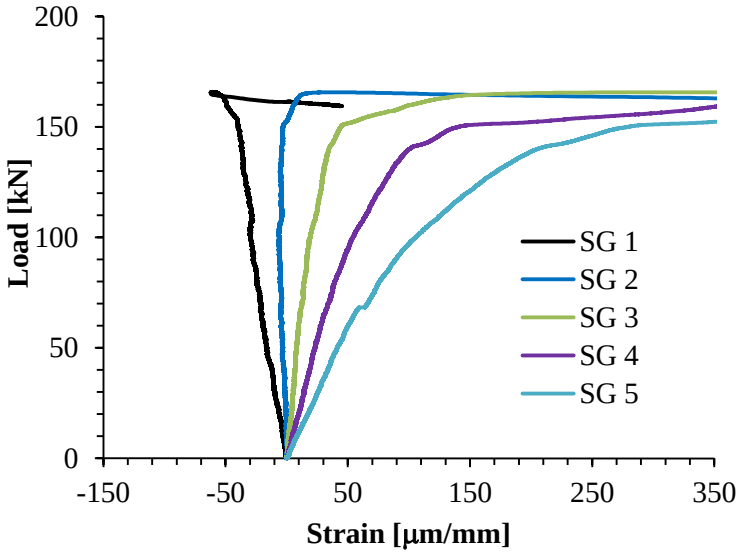

Figure 6.62 – Concrete surface strains taken across the depth of slab B-CF-C.

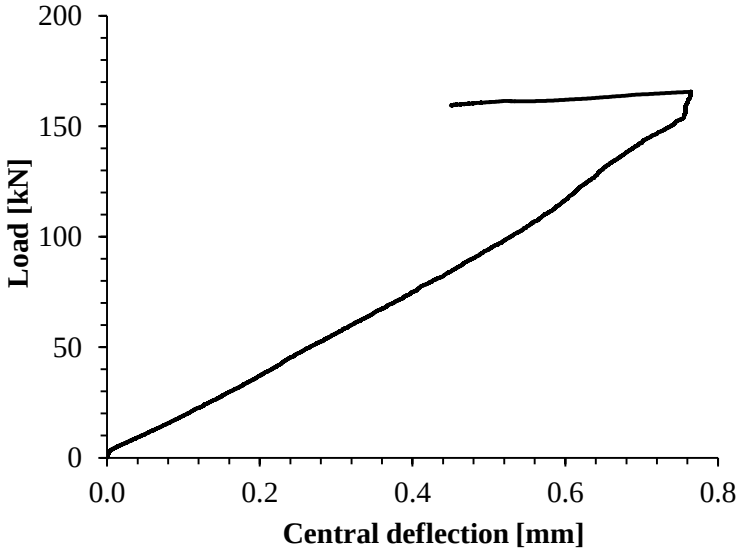

Figure 6.63 – Load versus deflection during initial monotonic loading of slab B-CF-C.

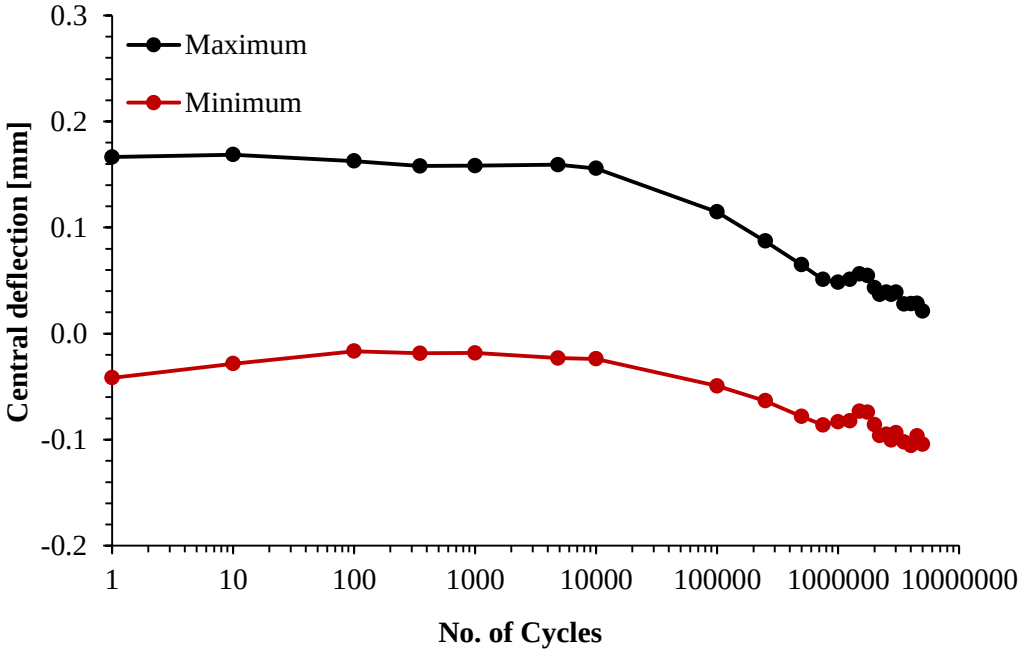

Figure 6.64 – Central deflection versus number of cycles for slab B-CF-C.

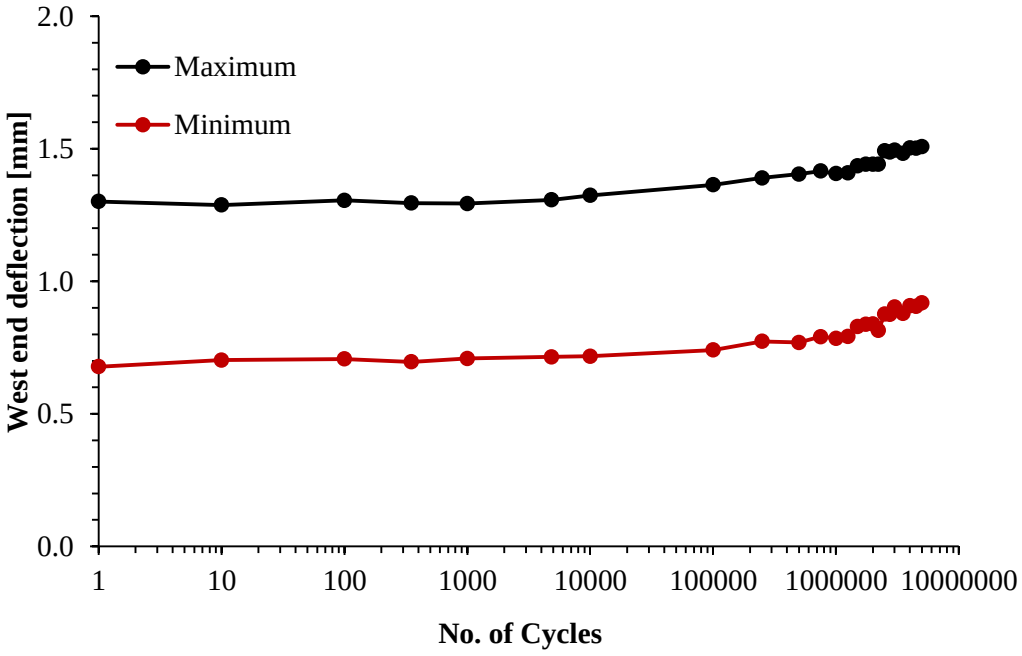

Figure 6.65 – Deflection of the West end versus number of cycles for slab B-CF-C.

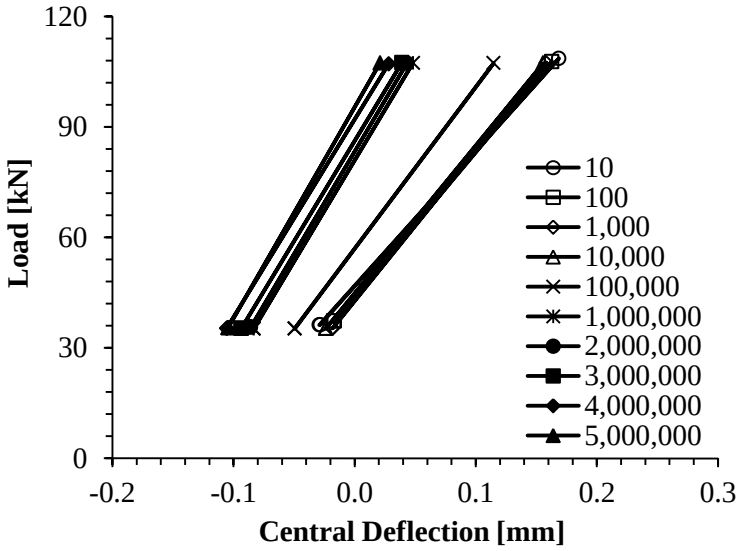

Figure 6.66 – Load versus central deflection at various cycle intervals for slab B-CF-C.

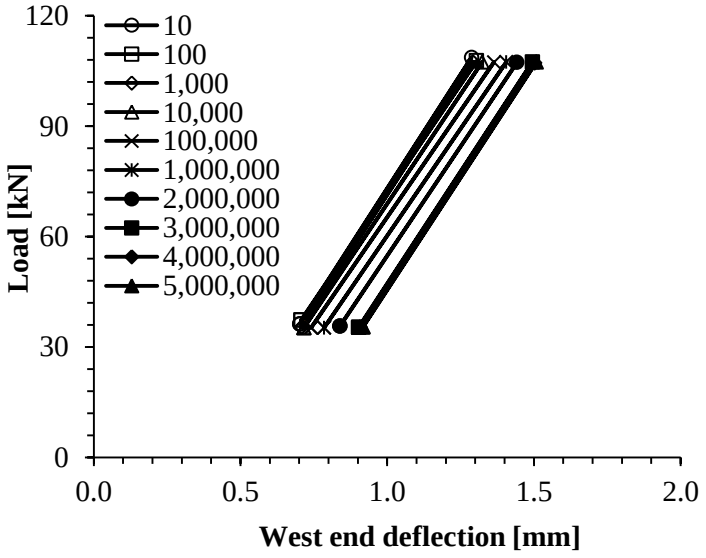

Figure 6.67 – Load versus the West end deflection at various cycle intervals for slab B-CF-C.

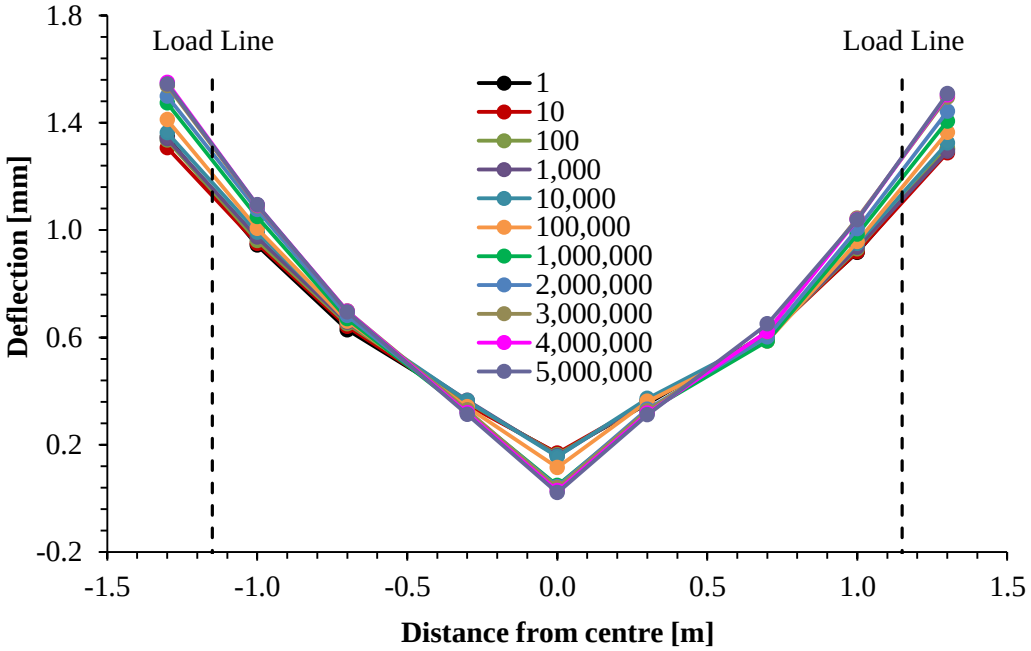

Figure 6.68 – Deflection measurements along slab B-CF-C taken at the maximum load of 109 kN.

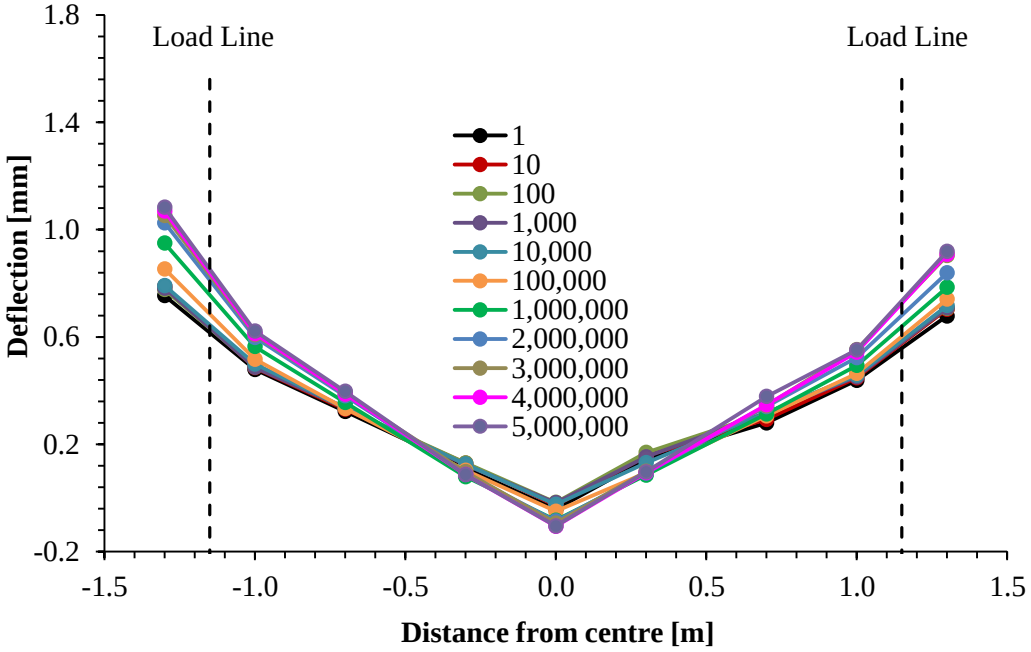

Figure 6.69 – Deflection measurements along slab B-CF-C taken at the minimum load of 35.2 kN.

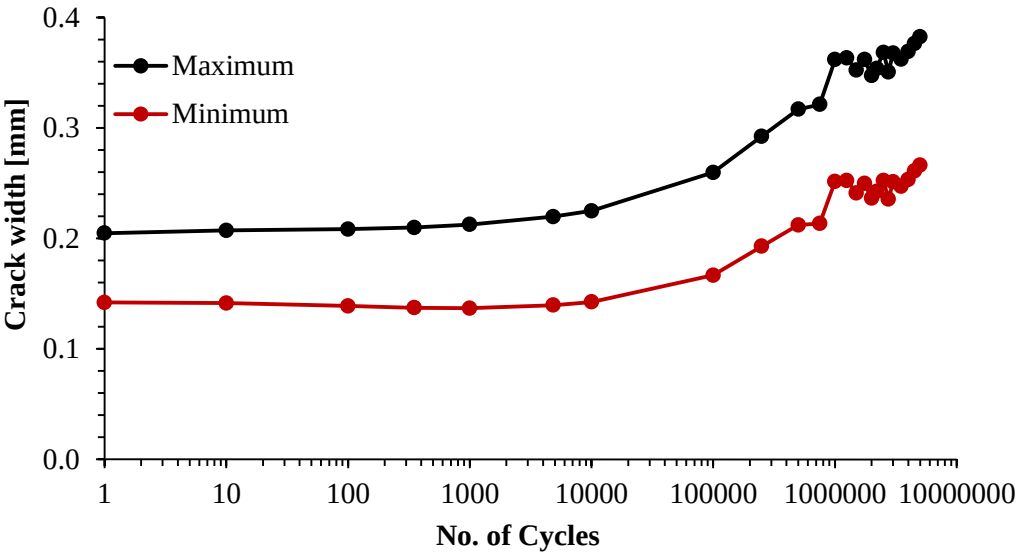

(a)

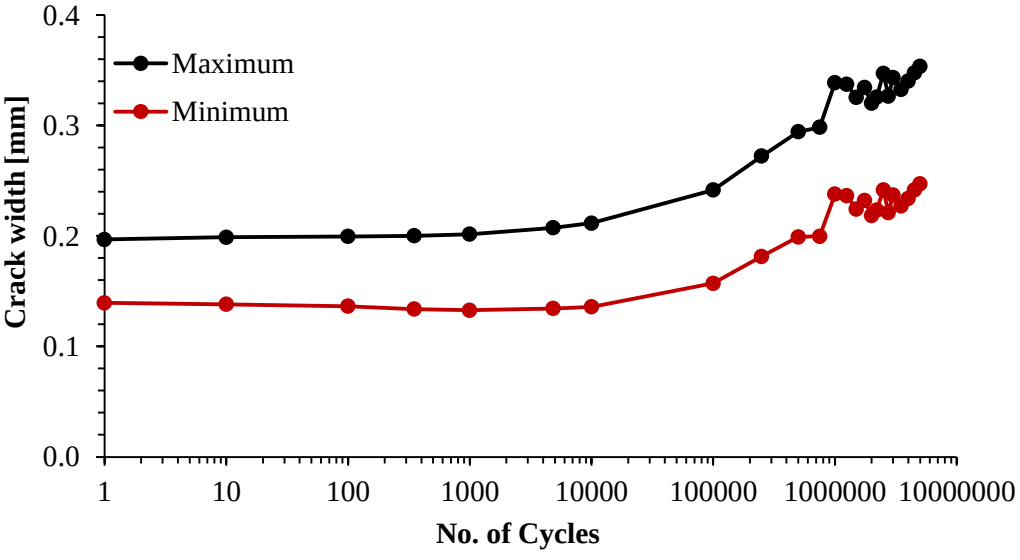

(b)

Figure 6.70 – Crack width development versus number of cycles at the slab's surface: (a) gauge No. 1; (b) gauge No. 2.

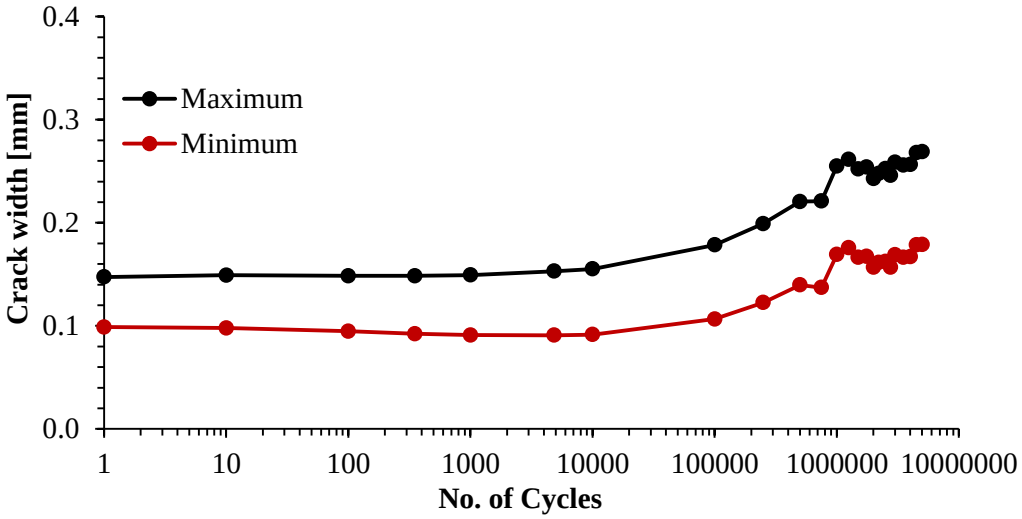

(a)

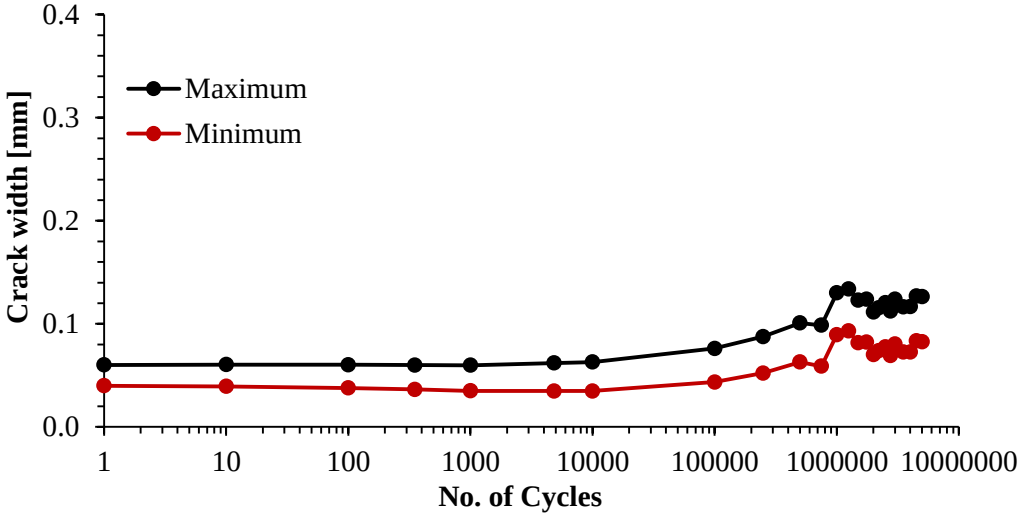

(b)

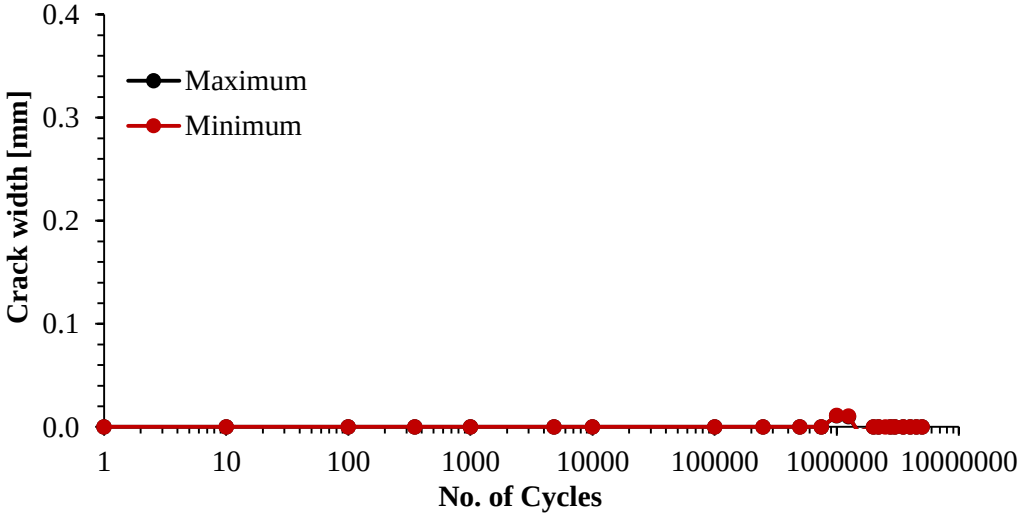

(c)

Figure 6.71 – Crack width development versus number of cycles at depth: (a) 20 mm; (b) 100 mm; (c) 180 mm.

Figure 6.72 – Crack pattern of slab B-CF-C after 5 million cycles.

6.6. Comparison between the Performance of Plain and SFRC Pavements

A comparison between the central and maximum measured deflections versus number of cycles for slabs A-CP-U and A-CF-U at the maximum load level are shown in Figures 6.73 and 6.74, respectively. Both slabs, A-CP-U and A-CF-U, were uncracked and cycled between 17% and 73% of the static cracking load of specimen A-SP-U at a frequency of 1.25 Hz using a sine loading waveform. The only difference was the 20% reduced thickness for the SFRC slab as opposed to the plain concrete one; i.e. 250 mm and 200 mm thickness for A-CP-U and A-CF-U, respectively.

It is evident from Figures 6.73 and 6.74 that the SFRC slab had initially higher deflection due to its reduced depth. It was observed that as soon as a crack formed, the

deflection of the plain concrete slab increased sharply; contrastingly, the rate of deflection increase remained unchanged during the 3 million fatigue test despite a crack was developed at 1,796 cycles for the SFRC slab. This indicates that a relatively low content of 4D 55/60 steel fibres (0.38%) effectively enhanced the load-carrying capacity of the reduced thickness slab and increased the toughness. Also, this elaborates that SFRC maintained its slab action before and after crack formation and the load can be increased until failure occurs. This supports the superior performance of SFRC pavements compared to those of thicker plain concrete.

Figure 6.75 presents the deflection of the West end versus number of cycles for slabs A-CP-U and A-CF-U at the maximum load level. As soon as a crack was formed through the plain concrete slab, the edges of the slab lifted and the slab was unable to carry any further load. This highlights the brittle failure mode of the thicker plain concrete slab as opposed to the slow rate of change in the deflection of the thinner SFRC slab. In addition to that, the stabilisation in the deflection rate of SFRC after one million cycles of loading indicates the capability of SFRC to redistribute load. This means that if the slab was continuous, another crack would likely have been observed at the edge of the slab, indicating the high toughness SFRC pavements compared to plain concrete and longer fatigue life in its cracked manner.

The deflection profiles measured along slabs A-CP-U and A-CF-U taken at the maximum load level and after post-fatigue static test of A-CF-U are compared in Figure 6.76. Figure 6.77 shows the deflection measurements taken at the lower load level. From both figures, it is clear that the deflection profiles of the thinner SFRC slab after 3 million of cycles, and even after post-fatigue static loading to 492 kN are higher than the thicker plain concrete slab (A-CP-U). The fibre reinforced slab has a substantially larger displacement, indicating the improvement in toughness. Moreover, comparing the shape of the deflection profiles of the plain and SFRC slabs, it can be seen that the deflection profile of plain concrete slab has one maximum deflection to the

left of the West load line. In contrast, the deflection values, adjacent the West line load from both sides, are almost constant in the deflection profile of SFRC slab. This indicates load redistribution from the cracked region to the adjacent one to form a constant moment region. Again, this demonstrates the increased toughness of the SFRC slab under cyclic loading.

Figure 6.78 presents the static test results of two thinner SFRC slabs (A-SF-U and A-CF-U), together with that of the thicker plain concrete slab (A-SP-U), all tested with a 1.0 metres loading span. Slab A-CF-U was tested to 3 million cycles with a maximum load level of 73% prior to conducting the static test, it is recognised that steel fibres effectively enhanced the load-carrying capacity of the reduced thickness slab and increased the toughness. Accordingly, no reduction in load bearing capacity was observed. Note the slight difference in stiffness of the grouted SFRC (A-CF-U) to the un-grouted specimen (A-SF-U).

A comparison between the deflection profiles along the statically tested slabs B-SP-U and B-SF-U, with 2.3 metres loading span, is shown in Figure 6.79. It can be seen that the deflection profiles of both plain and the thinner SFRC was approximately uniform up to cracking load. The brittle failure mode of the plain concrete slab was foreshadowed by a significant change in central and edge deflections. In contrast, the performance of the SFRC slab was ductile. A post-cracking load of 250 kN, higher than the cracking load, was needed to reach an edge deflection approximately equivalent to that of the edge of the thicker plain concrete at failure. Moreover, a post-cracking load of 491 kN was required to approach a central deflection in the thinner SFRC equivalent to that of the plain concrete slab at failure. It is also observed that at a post-cracking load of 491 kN the SFRC slab had substantially higher edge deflections compared to the thicker plain concrete slab. This means that steel fibres controlled and bridged the growth of the crack and this led a substantial increase in deflection, indicating the improvement in toughness.

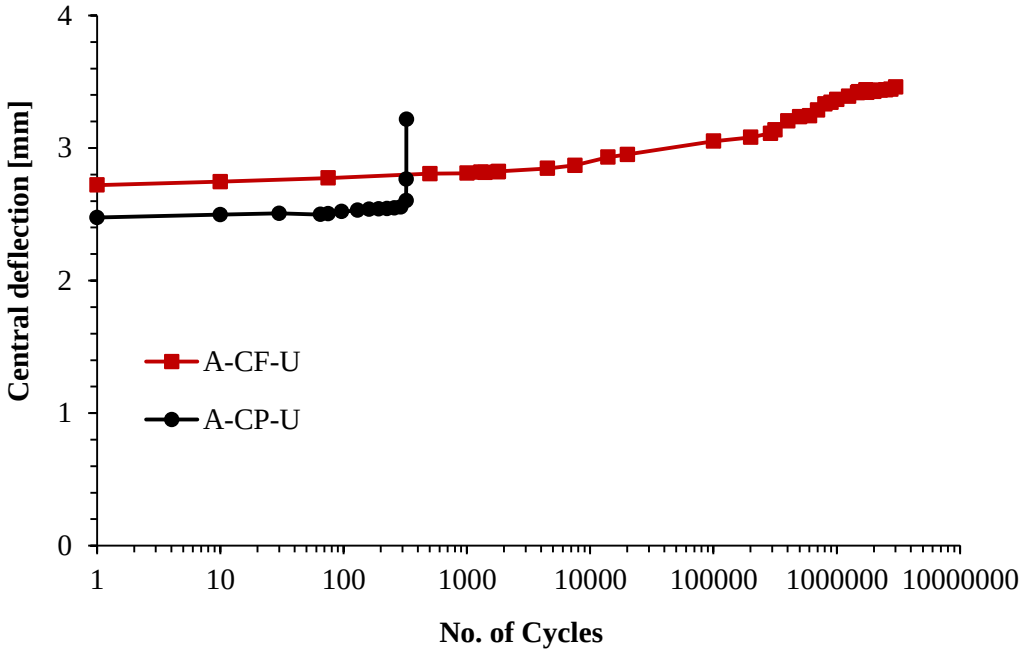

Figure 6.73 – Comparison between the central deflections versus number of cycles for slabs A-CP-U and A-CF-U at the maximum load level.

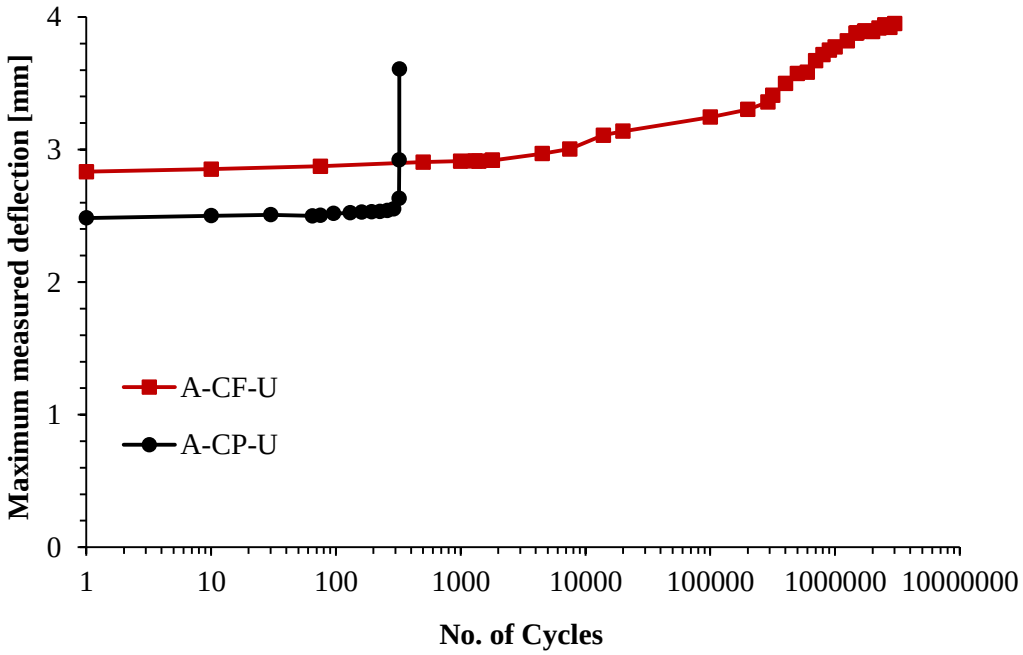

Figure 6.74 – Comparison between the maximum measured deflections versus number of cycles for slabs A-CP-U and A-CF-U at the maximum load level.

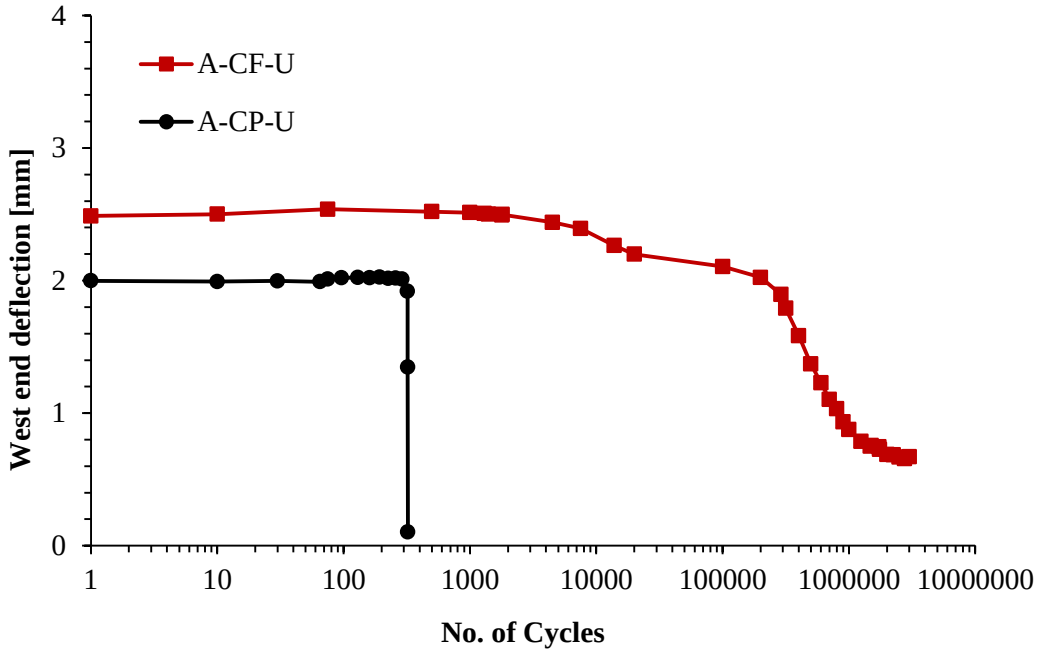

Figure 6.75 – Comparison between the West end deflections versus number of cycles for slabs A-CP-U and A-CF-U at the maximum load level.

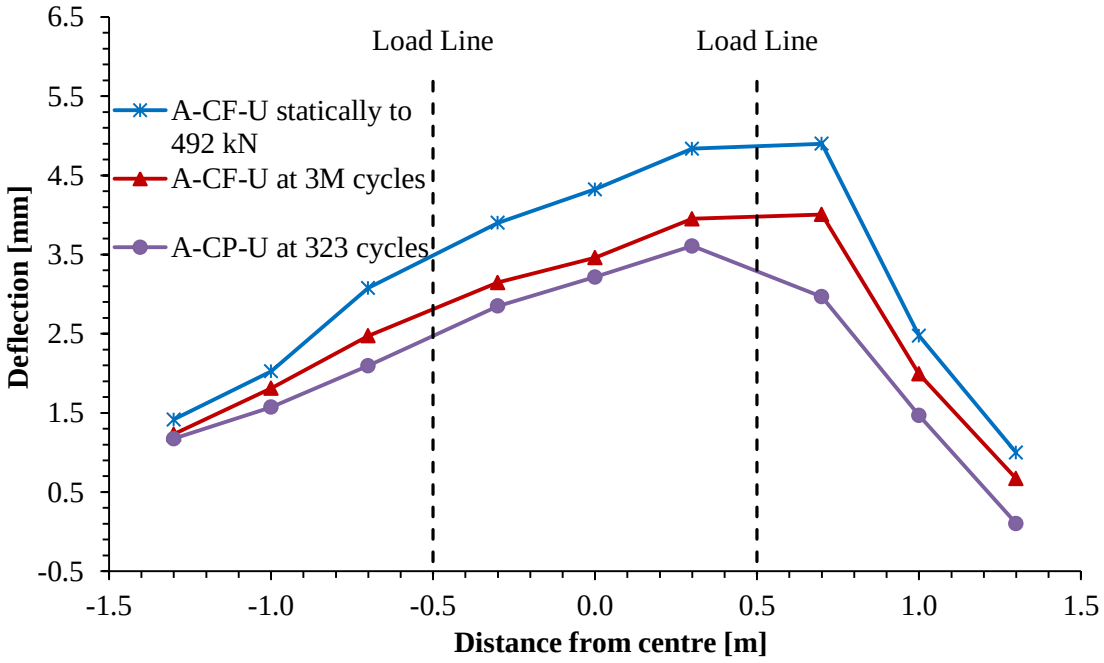

Figure 6.76 – Comparison between the deflection measurements along slabs A-CP-U and A-CF-U taken at the maximum load level and after static test of A-CF-U.

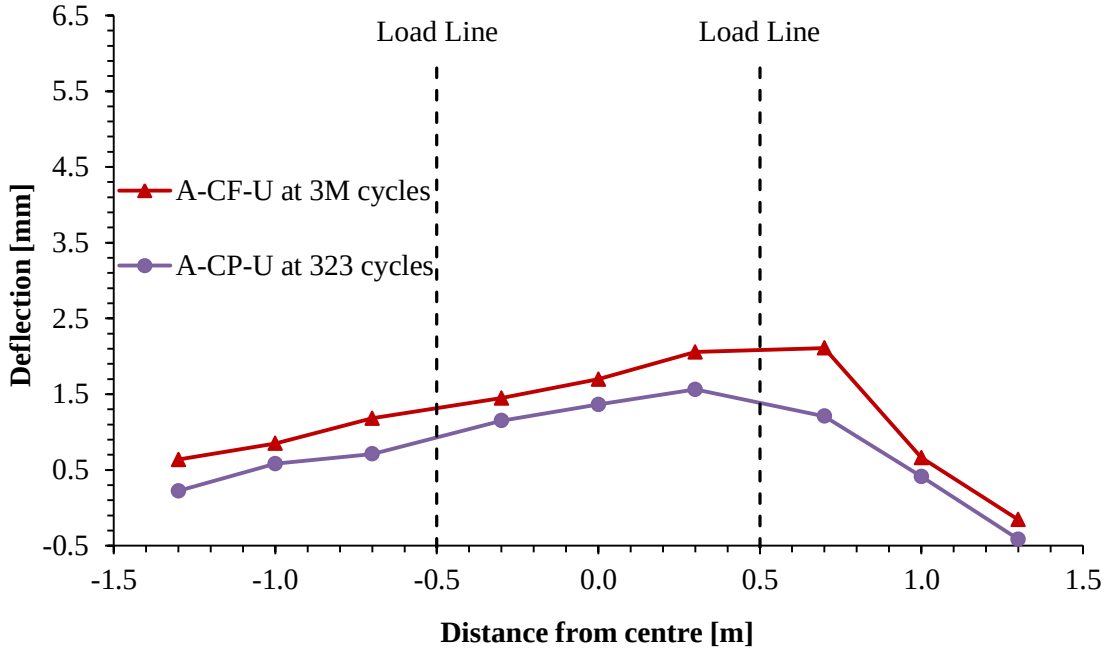

Figure 6.77 – Comparison between the deflection measurements along slabs A-CP-U and A-CF-U taken at the minimum load level.

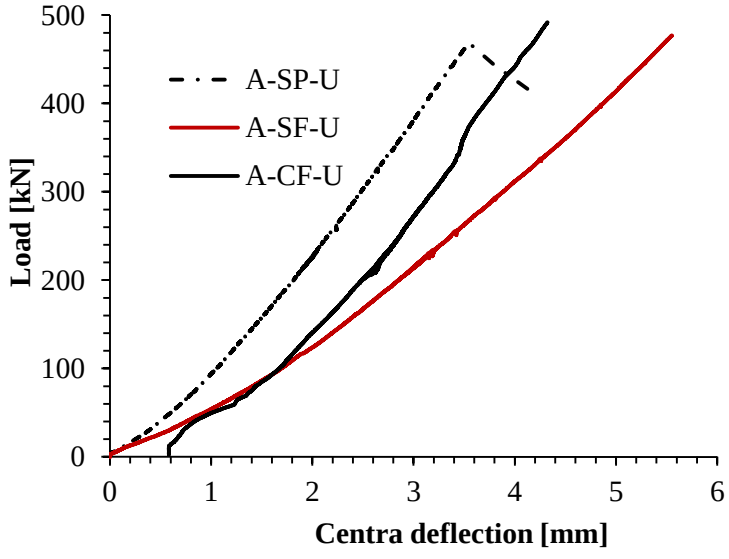

Figure 6.78 – Comparison between A-SP-U, A-SF-U and A-CF-U.

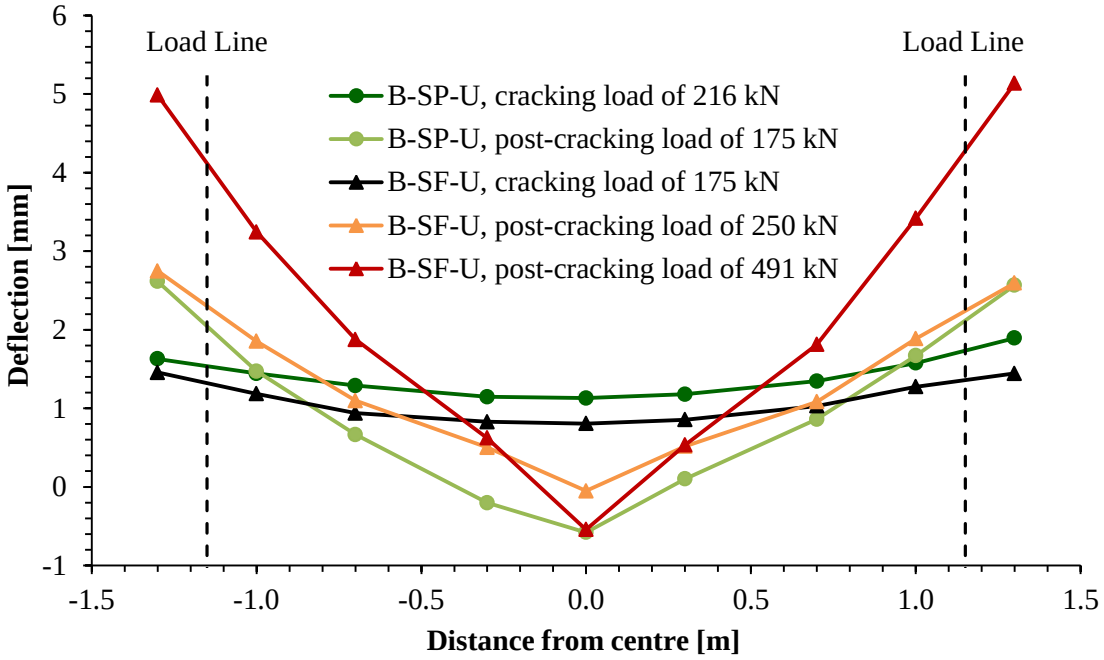

Figure 6.79 – Comparison between the deflection measurements along slabs B-SP-U and B-SF-U.

6.7. Concluding Remarks

Eight large scale plain and SFRC slab specimens were designed, cast and tested under static and cyclic loading to demonstrate the effectiveness of steel fibres in reducing the thickness of pavements. The thickness of SFRC slabs was reduced by 20% to those of plain concrete (thickness of plain concrete slabs = 250 mm; thickness of SFRC slabs = 200 mm). Two types of fatigue test were performed, the first on uncracked specimens at 70% maximum loading and the second on a pre-cracked slab at 50% maximum loading. The experimental results show that:

- plain concrete slabs fail in a brittle mode immediately following the formation of the dominant crack;
- thinner SFRC pavements can carry higher load repetition of currently constructed plain concrete pavements with excellent serviceability performance in terms of crack width prorogation and deflection development;

- a relatively low content of 4D 55/60 steel fibres (0.38%) effectively enhances the load-carrying capacity of pavements and increases toughness;
- fibres control the growth of the fatigue crack and the SFRC slab maintains its integrity throughout fatigue loading;
- higher energy dissipates at small crack openings for small volume of fibres; and
- large scale testing and indeterminacy of structure allows maximising the benefit of utilising SFRC as the mechanism of load redistribution is valid.

In conclusion, the current Austroads Guide to Pavement Technology has a provision for using SFRC pavements; however, the design methodology is based on elastic behaviour. The addition of steel fibres to concrete enhances the post-cracking tensile strength, provides significant ductility and increases toughness. As a result, the use of elastic theory for designing SFRC is overly conservative and non-economic. To obtain a more realistic estimation of the load bearing capacity of SFRC, a plastic analysis method may be considered in the design approach of SFRC pavements. This will ensure that the material characteristic of SFRC is taken into account. Consequently, the thickness of SFRC pavement can be reduced and the joint spacing may be increased when comparing with a conventional unreinforced pavement. Furthermore, the maintenance requirement would be less. As a result, the design of SFRC pavement may offer considerable economic benefits.

Chapter 7 CONCLUSIONS AND RECOMMENDATIONS

7.1. Conclusions

Portland cement concrete is a widely utilised material in construction such as industrial pavements, roadways, parking areas, airport runways and bridge projects. Heavy wheel loads and high traffic volumes over time have required the design of thicker pavements. In rigid pavements, the thickness is frequently governed by the applied traffic loads, rather than the stresses due to temperature and moisture gradients. Traffic axel loadings mainly lead to flexure and shear of concrete member; these loads are repetitive for millions of cycles throughout the structure's service life. This continuous bending of the concrete structure leads to the development of microcracks, which continue to propagate over time, due to repetitive loading, resulting in fatigue damage and failure. By including fibres in concrete, the main objective is to bridge cracks once they form and, in doing so, improve the post-cracking behaviour of the otherwise brittle concrete material.

A literature review presented in Chapter 2 shows that there is potential that the addition of steel fibres improves that the fatigue performance of concrete pavements. However, there is a lack of realistic test programs representative of the failure mode of pavements in practice. The lack of reasonably sized test specimens and load application casts doubt on the transfer of the results of such tests to full scale structures and in the development of models suitable for design of full scale structures. In this study, efforts have been taken to improve upon this situation through the development of a comprehensive testing methodology.

In this dissertation, two major focusses are examined. Detailed assessment of SFRC at material level through testing three series of round panel tests under fatigue loading, presented in Chapters 3 and 5, together with an enhanced model for determining the $\sigma-$

w relationship for SFRC in Chapter 4. The second focus has been the close examination of the large scale performance of thinner SFRC pavements under fatigue loading with the emphasis on the contribution and effectiveness of steel fibres in controlling and bridging the crack development process in thinner SFRC pavements compared with currently constructed plain concrete ones. Major research outcomes and conclusions of each of these main dissertation components are described.

In Chapter 3, an extensive experimental investigation was conducted on three series round panels cast and tested using three different SFRC mix designs, together with a series of matched direct uniaxial tension and prism bending tests were also undertaken to provide comprehensive material characterisation data. In total, tests were conducted on eighteen dog-bones, thirty six prisms and twenty seven round panels. The round panels were tested with different load levels. Fatigue test was performed on either uncracked or pre-cracked specimens where a micro-cracked fracture process zone is present; this investigated the role of concrete strength and the effectiveness of steel fibres on fatigue behaviour. Experimental results showed that fibres improve the fatigue life and performance of concrete and result in higher energy dissipation for all the load levels and fibre types considered in this study. It was reported that post-fatigue static test results match the monotonic curves with a good agreement. The limitations of round panel test when long fibres are used were discussed and the requirement for a 3D orientation correction factor when considering thick applications was raised.

Following the experimental investigation of three SFRC mixes which display softening behaviour in uniaxial tension testing, in Chapter 4, an enhanced and efficient inverse analysis procedure is derived for determining the $\sigma - w$ relationship for SFRC from both notched and un-notched prism bending tests. The model is developed from existed models and enhanced by determining more accurately the depth to the neutral axis from the extreme compressive fibre at a specified CMOD or deflection, depending on the test type. The model is validated against the data obtained from direct tension tests for the

three SFRC mixes carried out in this study and found to fall well within the range of scatter of the collected data. When a prism test is in transition from strain softening to strain hardening behaviour occurs, the model breaks down and limits are applied to the model such that: (i) the residual stress at a crack opening displacement greater than 0.5 mm ($w > 0.5$) must be smaller or equal to that at COD = 0.5 mm ($f_{0.5}$); and (ii) the residual tensile is limited to the tensile strength of the matrix without fibres (f_{ct}).

In Chapter 5, the deviation of failure planes in round panel tests is discussed and related to the variation in post-cracking material properties. It is concluded that a variation of as little as 13 percent in local material distributions within the panel can change the mode of failure from a three-fracture line pattern to a single-fracture-line pattern. Based on a normal distribution fit to data, the probability that a single-fracture-line governs, as opposed to a three-fracture-line mode, is 10.7%.

Also in Chapter 5, the effectiveness of SFRC on fatigue behaviour is investigated in terms of cyclic creep curves and Wöhler diagrams. It is shown that the provision of fibres controls both the crack opening range (minimum crack width to maximum) and the crack opening increment per cycle and provides resistance to fatigue. There are three stages to cracking: stage 1 initiation; stage 2 propagation; and stage 3 acceleration to failure. Fibres are most significant in the second stage of crack growth during fatigue loading. The effectiveness of steel fibres is greater for high cycle fatigue range and tends to maximise with fatigue load levels lower than 50% of the specimen capacity.

Based on the measurements and observations of the round panel tests, a constitutive model is developed, in Chapter 5, for SFRC for post-cracking fatigue damage that occurs during cyclic loading loops. The model is verified against the available test data. The model is shown to be capable of predicting the overall cyclic fatigue loading response of SFRC. The model is also able to capture the change in the COD, the

stiffness development with increasing load cycles, and the number of load cycles to failure.

In the final component of this study (Chapter 6), the hypothesis that thinner SFRC pavements can carry the same or higher numbers of load repetitions of those of currently constructed plain concrete ones, with minimum maintenance requirements is investigated. In total, eight large scale plain and SFRC slab specimens were designed, cast and tested under static and cyclic loading to demonstrate the effectiveness of steel fibres in reducing the thickness of pavements. The thickness of SFRC slabs was reduced by 20% to those cast with plain concrete. Uncracked specimens were tested with 70% maximum load level and a pre-cracked slab was loaded with 50% upper load level. The slabs were loaded in such a way to simulate the crack patterns and failure mode of pavements in practice. The experimental results showed that plain concrete slabs fail in a brittle mode immediately after the formation of the dominant crack. In spite of that, fibres controlled the growth of the fatigue crack and the SFRC slab maintained its integrity throughout fatigue loading. Additionally, a relatively low content of 4D 55/60 steel fibres (0.38%) effectively enhanced the load-carrying capacity of pavements, increased toughness and dissipated higher energy at small crack openings. The test results indicate the importance of large scale testing and indeterminacy of structure in maximising the benefit of utilising SFRC as the mechanism of load redistribution is applicable.

In conclusion, the pavement tests demonstrated that 20% thinner SFRC pavements can carry higher number of load repetition of those of currently constructed plain concrete ones, with excellent serviceability performance in terms of crack width propagation and deflection development.

7.2. Recommendations for Future Research

From the outcomes of this study, a number of recommendations can be made towards future research:

- In Chapters 3 and 5, it was observed that steel fibres improved the fatigue performance of concrete. This study is mainly conducted at two load levels and the only variable is fibre type. In order to draw *S-N* curve, testing needs to be conducted for different load levels. Further testing is also recommended with varying fibre volumes, different types of fibres and uncracked and pre-cracked panels. Additionally, the need for more tests on pre-cracked concrete subjected to high cycle fatigue loading is identified for further calibration of the model developed in Chapter 5.
- The models presented in this thesis (in Chapters 4 and 5) are limited to strain softening SFRC and further development work is needed for hardening SFRC.
- The experimental program in Chapter 6 only investigates the performance of eight plain and SFRC pavements where one type of fibres is used and tested with 70% load level (except one pre-cracked specimen tested with 50% maximum load level). This study is considered the first of its type to investigate the performance of SFRC pavements under high cycle fatigue loading. The need for further test data is identified to examine the effect of several variables; for example, variable amplitude loading (i.e. various magnitude and load sequence) different load levels, variety of supporting system stiffness, fibre type and content. Specimens with further reduced thickness can also be investigated. In addition to that, the influence of structural fibres in reducing joint faulting or other joint deteriorations needs to be investigated.
- The effect of stresses induced due to temperature and moisture gradients were beyond the scope of this research; however, these stresses do influence the overall performance of SFRC pavements and this influence should be addressed.

- One of the major concerns with cracked SFRC pavements in service is the effect of water filling the cracks. As it is addressed in this study, steel fibres control and bridge the crack opening range; this means that there is a tendency for a crack to open and close under cyclic loading. The effect of the water filling partially or completely the crack opening and the stresses developed as the crack tends to close must be addressed.
- From this research project, a clear fatigue failure of SFRC pavements is not observed; thus, no definition of failure could be determined. Instead, increased toughness and higher load-carrying capacity are noted, together with controlled crack propagation and deflection development. This means that the failure of SFRC pavement can be defined by its serviceability performance rather than its ultimate capacity. Thus, it is recommended to define the fatigue failure of SFRC pavements by setting limits for the allowable crack width and deflection. Also, plastic analysis may be considered in the development of design procedures for SFRC pavements.
- Punching shear strength for SFRC pavements supported on an elastic foundation were not studied in this research and require further investigation.
- Lastly, further research should place emphasis on developing finite element model capable of conducting parametric studies on the fatigue response of the SFRC pavements. The model can be validated with the limited test data from Chapter 6, and as more experimental results become available, the model can be refined and developed further. Afterwards, a parametric study may be undertaken to examine the effect of variables, such varying stiffness of the support system, slab thickness, the influence of humidity and temperature gradients, fibre contents and types, load level, influence of variable amplitude loading … etc.

REFERENCE

Aas-Jakobsen, K. (1970) *Fatigue of concrete beams and columns*, Division of Concrete Struc. Norwegian Institute of Technology.

AASHTO (1993) *AASHTO Guide for Design of Pavement Structures*, American Association of State Highway Transportation Officials.

ACI (1992) *Guide for Concrete Floor and Slab Construction* (ACI 360R-92), American Concrete Institute, Farmington Hills.

ACI Commitee 544 (2009) *State-of-the-Art Report on Fiber Reinforced Concrete*, American Concrete Institute, Farmington Hills.

American Concrete Pavement Association (ACPA) (1999) *Database of State DOT Concrete Pavement Practices*, American Concrete Pavement Association.

Alani, A., Beckett, D. and Khosrowshahi, F. (2012) 'Mechanical behaviour of a steel fibre reinforced concrete ground slab', *Magazine of Concrete Research*, 64(7), 593-604.

Alani, A. M., Rizzuto, J., Beckett, D. and Aboutalebi, M. (2014) 'Structural behaviour and deformation patterns in loaded plain concrete ground-supported slabs', *Structural Concrete*, 15(1), 81-93.

Amin, A. and Foster, S. J. (2016) 'Predicting the flexural response of steel fibre reinforced concrete prisms using a sectional model', *Cement and Concrete Composites*, 67, 1-11.

Amin, A., Foster, S. J., Gilbert, R. I. and Kaufmann, W. (2017) 'Material characterisation of macro synthetic fibre reinforced concrete', *Cement and Concrete Composites*, 84, 124-133.

Amin, A., Foster, S. J. and Muttoni, A. (2015) 'Derivation of the σ-w relationship for SFRC from prism bending tests', *Structural Concrete*, 16(1), 93-105.

AS1012.9 (1999) *Methods of Testing Concrete - Determination of the compressive strength of concrete specimens*, Standards Australia.

AS 1012.10 (2000) *Methods of Testing Concrete - Determination of indirect tensile strength of concrete cylinders (Brazil or splitting test)*, Standards Australia.

AS 1012.11 (2000) *Methods of Testing Concrete. - Determination of the modulus of rupture*, Standards Australia.

AS1012.17 (1997) *Methods of Testing Concrete - Determination of the static chord modulus of elasticity and Poisson's ratio of concrete specimens*, Standards Australia.

AS3600 (2018) *Concrete structures*, Standards Australia.

Association Française de Génie Civil (AFGC) (2002) *Ultra high performance fibre-reinforced concretes: Interim recommendations*, SETRA Reference F2011.

ASTM C1550 (2012) *Standard test method for flexural toughness of fiber reinforced concrete (using centrally loaded round panel)*, ASTM International, West Conshohocken, PA.

ASTM C1609/1609M (2006) *Standard method for flexural performance of fiber reinforced concrete (using beam with third-point loading)*, ASTM International, West Conshohocken, PA.

Austroads (2009) *Guide to Pavement Technology. Part 1: Introduction to Pavement Technology*, Australia: Austroads.

Austroads (2012) *Guide to Pavement Technology. Part 2: Pavement Structural Design*, Australia: Austroads.

Aveston, J. and Kelly, A. (1973) 'Theory of multiple fracture of fibrous composites', *Journal of Materials Science*, 8(3), 352-362.

Awad, M. E. (1971) *Strength and deformation characteristics of plain concrete subjected to high repeated and sustained loads*, University of Illinois Engineering Experiment Station. College of Engineering. University of Illinois at Urbana-Champaign.

Ballatore, E. and Bocca, P. (1997) 'Variations in the mechanical properties of concrete subjected to low cyclic loads', *Cement and Concrete Research*, 27(3), 453-462.

Banthia, N., Chokri, K. and Trottier, J. F. (1995) 'Impact tests on cement-based fiber reinforced composites', *ACI Special Publication*, 155, 171-188.

Barker, W. R. (1981) 'Introduction to a rigid pavement design procedure', in *Proceedings of the 2nd International Conference on Concrete Pavement Design*, Purdue University.

Barman, M. (2014) *Joint performance characterization of bonded concrete overlay* [Doctoral dissertation], Department of Civil and Environmental Engineering, University of Pittsburgh.

Barman, M. and Hansen, B. (2018) *Comparison of Performances of Structural Fibers and Development of a Specification for Using Them in Thin Concrete Overlays*, Final Report. Minnesota Department of Transportation, St. Paul.

Barnett, S. J., Lataste, J. F., Parry, T., Millard, S. G. and Soutsos, M. N. (2010) 'Assessment of fibre orientation in ultra high performance fibre reinforced concrete and its effect on flexural strength', *Materials and Structures*, 43(7), 1009-1023.

Batson, G., Ball, C., Bailey, L., Landers, E. and Hooks, J. (1972) 'Flexural fatigue strength of steel fibre reinforced concrete beams', *ACI Journal*, 69(11), 673-677.

Beckett, D. (1990) 'Comparative tests on plain, fabric reinforced and steel fibre reinforced concrete ground slabs', *Concrete*, 24(3), 43-45.

Beckett, D. (1999) 'Comer and edge loading on concrete industrial ground floors reinforced with steel fibers', *Concrete*, 33(3), 22-24.

Bekaert (1999) *Steel Fibers for the Pre-cast Industry*, Bekaert NV. Dramix Technical Pamphlet.

Bernard, E. S. (2000) 'Behaviour of round steel fibre reinforced concrete panels under point loads', *Materials and Structures*, 33(3), 181-188.

Bernard, E. S. and Xu, G. G. (2008) 'The effect of radial crack locations on load resistance in C1550 panel tests', *Journal of ASTM International*, 5(10), 1-14.

Bischoff, P. H., Valsangkar, A. J. and Irving, J. (2003) 'Use of fibers and welded-wire reinforcement in construction of slabs on ground', *Practice Periodical on Structural Design and Construction*, 8(1), 41-46.

Bischoff, P. H., Valsangkar, A. J. and Irving, J. A. (1996) 'Experimental study of concrete floor slabs on grade', in *Proceedings of the Canadian Society for Civil Engineering Annual Conference*, Canada, 273-82.

Bright, J. K. and Mays, J. R. (1996) 'Cellular rigid pavement', *Journal of Transportation Engineering*, 122(5), 381-387.

Cachim, P. B. (1999) *Experimental and numerical analysis of the behaviour of structural concrete under fatigue loading with applications to concrete pavements* [Doctoral dissertation], unpublished thesis University of Porto.

Cachim, P. B., Figueiras, J. A. and Pereira, P. A. (2002) 'Fatigue behavior of fiber-reinforced concrete in compression', *Cement and Concrete Composites*, 24(2), 211-217.

CEB (1988) *Fatigue of concrete structures, state of the art report*, CEB Bulletin D'information No. 188, Comité Euro-International du Béton, Lausanne.

Chang, D. I. and Chai, W. K. (1995) 'Flexural fracture and fatigue behavior of steel-fiber-reinforced concrete structures', *Nuclear Engineering and Design*, 156(1), 201-207.

Chao, S. H., Cho, J. S., Karki, N. B., Sahoo, D. R. and Yazdani, N. (2011) 'FRC performance comparison: uniaxial direct tensile test, third-point bending test, and round panel test', *Special Publication*, 276, 1-20.

Chen, S. (2004) 'Strength of steel fibre reinforced concrete ground slabs', *Proceedings of the Institution of Civil Engineers: Structures and Buildings*, 157(2), 157-163.

Cornelissen, H. A. W. (1984) 'Fatigue failure of concrete in tension', *HERON*, 29(4).

Cornelissen, H. A. W. and Reinhardt, H. W. (1984) 'Uniaxial tensile fatigue failure of concrete under constant-amplitude and programme loading', *Magazine of Concrete Research*, 36(129), 216-226.

Crepps, R. B. (1923) 'Fatigue of mortar', in *American Society for Testing Materials Proceeding*, 329-340.

Darter, M. I. (1977) *Design of a zero-maintenance plain jointed concrete pavement, volume one-development of design procedures*, Washington, DC: Federal Highway Administration.

Darter, M. I. (1988) *A Comparison Between Corps of Engineers and ERES Consultants, Inc. Rigid Pavement Design Procedures*, Technical Report Prepared for the United States Air Force SAC Command. Savoy, IL.

Darter, M. I. and Barenberg, E. J. (1977) *Design of Zero-Maintenance Plain Jointed Concrete Pavement, Volume 1: Development of Design Procedures*, Report FHWA-RD-77-III, FHWA, U.S. Department of Transportation,

Delatte, N. J. (2014) *Concrete pavement design, construction, and performance*, CRC Press.

de Montaignac, R., Massicotte, B., Charron, J. P. and Nour, A. (2012) 'Design of SFRC structural elements: post-cracking tensile strength measurement', *Materials and Structures*, 45(4), 609-622.

de Oliveira e Sousa, J. L. A., Gettu, R. and Barragán B. E. (2002) 'Inverse analysis of the notched beam response for determining the σ-w curve for plain and fiber reinforced concretes', *Anales de Mecánica de la Fractura*, 19, 393-398.

di Prisco, M., Colombo, M. and Dozio, D. (2013) 'Fibre-reinforced concrete in fib Model Code 2010: principles, models and test validation', *Structural Concrete*, 14, 342-361.

di Prisco, M., Plizzari, G. and Vandewalle, L. (2009) 'Fibre reinforced concrete: new design perspectives', *Materials and Structures*, 42(9), 1261-1281.

Domenichini, L. and Marchionna, A. (1981) 'Influence of stress range on plain concrete pavement fatigue design', in *Proceedings of the 2nd International Conference on Concrete Pavement Design*, held at Purdue University, 55-65.

Dupont, D. and Vandewalle, L. (2005) 'Distribution of steel fibres in rectangular sections', *Cement and Concrete Composites*, 27(3), 391-398.

Elsaigh, W. A. (2001) *Steel fibre reinforced concrete ground slabs* [Master's dissertation], unpublished thesis University of Pretoria.

Elsaigh, W. A. and Kearsley, E. P. (2002) 'Effect of steel fibre content on properties of concrete', *Journal of Concrete/ Beton, South Africa*, 102, 8-12.

Elsaigh, W. A. M. H. (2008) *Modelling the behaviour of steel fibre reinforced concrete pavements* [Doctoral dissertation], unpublished thesis University of Pretoria.

EN 14651 (2007) *Test method for metallic fibre concrete – measuring the flexural tensile strength (Limit of Proportionality (LOP), residual)*, European Committee for Standardization.

Falkner, H., Huang, Z. and Teutsch, M. (1995) 'Comparative study of plain and steel fiber reinforced concrete ground slabs', *Concrete International*, 17(1), 45-51.

Falkner, H. and Teutsch, M. (1993) *Comperative investigations of plain and steel fibre reinforced industrial ground slabs*, Germany: Institut Für Baustoffe, Massivbau und Brandschutz (IBMB).

Falkner, H., Teutsch, M. and Klinkert, H. (1997) *Load bearing capacity and deformation of dynamically loaded plain and steel fibre reinforced concrete road pavements*, iBMB University Brunswick.

Ferrara, L. and Meda, A. (2006) 'Relationships between fibre distribution, workability and the mechanical properties of SFRC applied to precast roof elements', *Materials and Structures*, 39(4), 411-420.

Finney, E. A. and Oehler, L. T. (1959) 'Final report on design project', Michigan Test Road, in *Highway Research Board Proceedings*.

Foster, S. J. (2006) 'Limited rotation CMM model for FE analysis of RC membranes', *Progress in Mechanics of Structures and Materials, 19th Australasian Conference on the Mechanics of Structures and Materials*, Christchurch, New Zealand, 177-183.

Foster, S. J. (2017) 'FRC design according to the draft Australian bridge code', *Special Publication*, 310, 29-40.

Foster, S., Htut, T. and Ng, T. (2013) 'High performance fibre reinforced concrete: fundamental behaviour and modelling', in *Proceedings of the 8th International Conference on Fracture Mechanics of Concrete and Concrete Structures (FraMCoS)*, 69-78.

Foster, S. J., Agarwal, A. and Amin, A. (2018) 'Design of steel fiber reinforced concrete beams for shear using inverse analysis for determination of residual tensile strength', *Structural Concrete*, 19(1), 129-140.

Gao, L. and Hsu, C. T. T. (1998) 'Fatigue of concrete under uniaxial compression cyclic loading', *Materials Journal*, 95(5), 575-581.

Germano, F. and Plizzari, G. A. (2012) 'Fatigue behaviour of SFRC under bending', in *Proceedings of Eighth RILEM International Conference on Fibre Reinforced Concrete*, 19-21.

Germano, F., Tiberti, G. and Plizzari, G. (2016) 'Post-peak fatigue performance of steel fiber reinforced concrete under flexure', *Materials and Structures*, 49(10), 4229-4245.

Grzybowski, M. and Meyer, C. (1993) 'Damage accumulation in concrete with and without fiber reinforcement', *ACI Materials Journal*, 90(6).

Hatt, W. K. (1925) 'Fatigue of concrete', *in Highway Research Board Proceedings*, National Research Council, 47-60.

Heath, A. C., Roesler, J. R. and Harvey, J. T. (2003) 'Modeling longitudinal, corner and transverse cracking in jointed concrete pavements', *International Journal of Pavement Engineering*, 4(1), 51-58.

Hiller, J. E. (2007) *Development of mechanistic-empirical principles for jointed plain concrete pavement fatigue design* [Doctoral dissertation], unpublished thesis University of Illinois.

Hoel, L. A. and Short, A. J. (2006) *The Engineering of the Interstate Highway System*, Washington, DC: Transportation Research Board.

Holmen, J. O. (1979) *Fatigue of concrete by constant and variable amplitude loading* [Doctoral thesis], Norwegian Institute of Technology, University of Trondheim.

Holmen, J. O. (1982) 'Fatigue of concrete by constant and variable amplitude loading', *ACI Special Publication*, 75, 71-110.

Hordijk, D. A. (1991) *Local approach to fatigue of concrete* [Doctoral thesis], Delft University of Technology.

Hordijk, D. A. and Reinhardt, H. W. (1993) 'Numerical and experimental investigation into the fatigue behavior of plain concrete', *Experimental Mechanics*, 33(4), 278-285.

Horii, H., Shin, H. C. and Pallewatta, T. M. (1992) 'Mechanism of fatigue crack growth in concrete', *Cement and Concrete Composites*, 14(2), 83-89.

HRB (1962) *The AASHO Road Test - Report 5, Pavement Research, Special Report 61E*, Washington, DC: Highway Research Board, National Research Council.

Hsu, T. T. C. (1981) 'Fatigue of plain concrete', *ACI Journal, Journal Proceedings*, 78(4), 292-305.

Hsu, T. T. C. (1984) 'Fatigue and microcracking of concrete', *Materials and Structures*, 17(97), 51-54.

Htut, T. N. S. (2010) *Fracture processes in steel fibre reinforced concrete* [Doctoral thesis], The University of New South Wales, Sydney, Australia.

Htut, T. N. S. and Foster, S. J. (2010) 'Unified model for mixed mode fracture of steel fiber reinforced concrete', in *Proceedings of Fracture Mechanics of Concrete and Concrete Structures–High Performance, Fiber Reinforced Concrete, Special Loadings and Structural Applications*, 23-28.

Huang, Y. H. (1993) *Pavement analysis and design*, Pearson/Prentice Hall.

Huang, Y. H. (2004) *Pavement design and analysis*, Pearson/Prentice Hall.

JCI-S-002 (2003) *Method of test for load-displacement curve of fiber reinforced concrete by use of notched beam*, Japanese Concrete Institute Standards.

Jiang, Y. and Tayabji, S. (1998) 'Mechanistic evaluation of test data from long-term pavement performance jointed plain concrete pavement test sections', *Transportation Research Record: Journal of the Transportation Research Board*, 1517(1629), 32-40.

Johnston, C. D. (1985) 'Toughness of steel fiber reinforced concrete', *Steel Fiber Concrete*, 333-360.

Johnston, C. D. and Zemp, R. W. (1991) 'Flexural fatigue performance of steel fiber reinforced concrete-influence of fiber content, aspect ratio, and type', *Materials Journal*, 88(4), 374-383.

Kabir, R. (2015) *Numerical study of structural responses of rigid and flexible pavements under heavy vehicles' loading* [Master's Thesis], unpublished thesis Michigan Technological University.

Kearsley, E. P. and Elsaigh, W. (2003) 'Effect of ductility on load-carrying capacity of steel fibre reinforced concrete ground slabs', *Journal of the South African Institution of Civil Engineering*, 45(1), 25-30.

Kesler, C. E. (1953) 'Effect of speed of testing on flexural fatigue strength of plain concrete', in *Highway Research Board Proceedings*, 251-258.

Khaloo, A. R. and Kim, N. (1997) 'Influence of concrete and fiber characteristics on behavior of steel fiber reinforced concrete under direct shear', *ACI Materials Journal*, 94(6), 592-601.

Kim, J. K. and Kim, Y. Y. (1996) 'Experimental study of the fatigue behavior of high strength concrete', *Cement and Concrete Research*, 26(10), 1513-1523.

Kim, S. W., Kang, S. T., Park, J. J. and Ryu, G. S. (2008) 'Effect of filling method on fibre orientation and dispersion and mechanical properties of UHPC', In *Proceedings of second international symposium on ultra high performance concrete*, Kassel, Germany, 185-192.

Kitsutaka, Y. (1987) 'Fracture parameters by polylinear tension-softening analysis', *Journal of Engineering Mechanics*, 123(5), 444-450.

Klcriber, F. W. (1982) 'The Effects of air content, water-cement ratio, and aggregate type on the flexural fatigue strength of plain concrete', *ACI Special Publication*, 75, 111-132.

Knapton, J. (1999) *Single pour industrial floor slabs: Specification, design, construction and behaviour*, Thomas Telford.

Kolluru, S. V., O'Neil, E. F., Popovics, J. S. and Shah, S. P. (2000) 'Crack propagation in flexural fatigue of concrete', *Journal of Engineering Mechanics*, 126(9), 891-898.

Komloš, K., Babal, B. and Nürnbergerova, T. (1995) 'Hybrid fibre-reinforced concrete under repeated loading', *Nuclear Engineering and Design*, 156(1), 195-200.

Kooiman, A. G. (2000) *Modelling steel fibre reinforced concrete for structural design* [PhD Dissertation], Department of Structural and Building Engineering, Delft University of Technology, The Netherlands.

Krstulovic-Opara, N., Haghayeghi, A. R., Haidar, M. and Krauss, P. D. (1995) 'Use of conventional and high-performance steel-fiber reinforced concrete for bridge deck overlays', *ACI Materials Journal*, 92(6), 669-677.

Kwan, A. K. H., Ho, J. C. M. and Pam, H. J. (2002) 'Flexural strength and ductility of reinforced concrete beams', *Proceedings of the Institution of Civil Engineers: Structures and Buildings*, 152(4), 361-369.

Lee, G. G. and Foster, S. J. (2007) *Behaviour of steel fibre reinforced mortar III: variable engagement model II*, UNICIV report R-448, School of Civil & Environmental Engineering, The University of New South Wales, Australia.

Lee, G. G. and Foster, S. J. (2008) 'Modelling of shear-fracture of fibre-reinforced concrete', In *Tailor made concrete structures, fib symposium*, Amsterdam, The Netherlands, 19-22.

Lee, M. K. and Barr, B. I. G. (2004) 'An overview of the fatigue behaviour of plain and fibre reinforced concrete', *Cement and Concrete Composites*, 26(4), 299-305.

Lee, S. C., Cho, J. Y. and Vecchio, F. J. (2011) 'Diverse embedment model for steel fiber-reinforced concrete in tension: model development', *ACI Materials Journal*, 108(5), 516-525.

Li, V. C. and Matsumoto, T. (1998) 'Fatigue crack growth analysis of fiber reinforced concrete with effect of interfacial bond degradation', *Cement and Concrete Composites*, 20(5), 339-351.

Maeda, Y., Matsui, S., Shimada, I. and Kato, H. (1980a) *Deterioration and repairing of reinforced concrete slabs of highway bridges in Japan; part I: actual circumstances and causes of cracking*, 30, Japan: Osaka University.

Maeda, Y., Matsui, S., Shimada, I. and Kato, H. (1980b) *Deterioration and repairing of reinforced concrete slabs of highway bridges in Japan; part II: causes of cracking and stress analysis of cracked slabs*, 30, Japan: Osaka University.

Maeda, Y., Matsui, S., Shimada, I. and Kato, H. (1981) *Deterioration and repairing of reinforced concrete slabs of highway bridges in Japan; part III: inspection and reparing of cracked slabs*, 30, Japan: Osaka University.

Mallet, G. P. (1991) *Fatigue of Reinforced Concrete, State of the Art Review 2, Transport and Road Research Laboratory*, London: HMSO Publications.

Matsui, S., Sonoda, K., Okamura, H. and Okada, K. (1986) 'Concepts for Deterioration of Highway Bridge Decks and Fatigue Studies', in *International Symposium on Fundamental Theory of Reinforced and Prestressed Concrete*, China, 831-838.

McCall, J. T. (1958) 'Probability of fatigue failure of plain concrete', *ACI Joutnals, Journal Proceedings*, 55(8), 233-244.

Meda, A. and Plizzari, G. A. (2004) 'New design approach for steel fiber-reinforced concrete slabs-on-ground based on fracture mechanics', *ACI Structural Journal*, 101(3), 298-303.

Miller, J. S. and Bellinger, W. Y. (2003) *Distress identification manual for the long-term pavement performance program*, Washington, DC: Federal Highway Administration, United States Department of Transportation.

Minelli, F. and Plizzari, G. (2010) 'Fiber reinforced concrete characterization through round panel test-part I: experimental study', *Proceedings of the Fracture Mechanics of Concrete and Concrete Structures (FraMCoS-7): High Performance, Fiber Reinforced Concrete, Special Loadings and Structural Applications*, Jeju, Korea, 1451-1460.

Miner, M. A. (1945) 'Cumulative damage in fatigue', *Journal of Applied Mechanics*, 12(3), 159-164.

Moss, J. (2008) 'Pavement Flexural Fatigue Capacity, and the influence of Mix Charging Sequence', In *9th International Conference on Concrete Pavements International Society for Concrete Pavements Federal Highway Administration American Concrete Pavement Association*.

Mulheron, M., Kevern, J. T. and Rupnow, T. D. (2015) 'Laboratory fatigue and toughness evaluation of fiber-reinforced concrete', *Transportation Research Record*, 2508(1), 39-47.

Murdock, J. W. and Kesler, C. E. (1958) 'Effect of range of stress on fatigue strength of plain concrete beams', *ACI Journal, Journal Proceedings*, 55(8), 221-231.

Naaman, A. E. and Hammoud, H. (1998) 'Fatigue characteristics of high performance fibrereinforced concrete', *Cement and Concrete Composites*, 20(5), 353-363.

Ng, T. S., Htut, T. N. S. and Foster, S. J. (2012) *Fracture of steel fibre reinforced concrete–The unified variable engagement model*, UNICIV Report R-460, School of Civil and Environmental Engineering, The University of New South Wales, Sydney, Australia.

Oh, B. H. (1991) 'Cumulative damage theory of concrete under variable-amplitude fatigue loadings', *ACI Materials Journal*, 88(1), 41-48.

Older, C. (1924) 'Highway research in Illinois', *Transactions of the American Society of Civil Engineers*, 88(1), 1180-1222.

Øverli, J. (2014) 'Experimental and numerical investigation of slabs on ground subjected to concentrated loads', *Central European Journal of Engineering*, 4(3), 210-225.

Packard, R. G. and Tayabji, S. D. (1985) 'New PCA thickness design procedure for concrete highway and street pavements', in *Third International Conference on Concrete Pavement Design and Rehabilitation*.

Pansuk, W., Sato, H., Sato, Y. and Shionaga, R. (2008) 'Tensile behaviors and fiber orientation of UHPC', In *Proceedings of second international symposium on ultra high performance concrete*, Kassel, Germany, 161-168.

Parker, F., Barker, W. R., Gunkel, R. C. and Odom, E. C. (1979) *Development of a Structural Design Procedure for Rigid Airport Pavements*, Washington, DC: Federal Aviation Administration.

Parmentier, B., Vandewalle, L. and Van Rickstal, F. (2008) 'Evaluation of the scatter of the postpeak behaviour of fibre reinforced concrete in bending: a step towards reliability', in *7th international RILEM symposium on fibre reinforced concrete*, Chennai, India, 133-143.

Parvez, A. and Foster, S. J. (2014) 'Fatigue behavior of steel-fiber-reinforced concrete beams', *Journal of Structural Engineering*, 141(4), 04014117.

Paskova, T. and Meyer, C. (1997) 'Low-cycle fatigue of plain and fiber-reinforced concrete', *ACI Materials Journal*, 94(4), 273-285.

PCA (1984) *Thickness design for concrete highway and street pavements*, Portland Cement Association.

Perdikaris, P. C., Calomino, A. M. and Chudnovsky, A. (1986) 'Effect of fatigue on fracture toughness of concrete', *Journal of Engineering Mechanics*, 112(8), 776-791.

Planas, J., Guinea, G. V. and Elices, M. (1999) 'Size effect and inverse analysis in concrete fracture', *International Journal of Fracture*, 95, 367-378.

Plizzari, G. A., Cangiano, S. and Alleruzzo, S. (1997) 'The fatigue behaviour of cracked concrete', *Fatigue & Fracture of Engineering Materials & Structures*, 20(8), 1195-1206.

Plizzari, G. A., Cangiano, S. and Cere, N. (2000) 'Postpeak behavior of fiber-reinforced concrete under cyclic tensile loads', *Materials Journal*, 97(2), 182-192.

Raithby, K. D. (1979) 'Flexural fatigue behaviour of plain concrete', *Fatigue & Fracture of Engineering Materials & Structures*, 2(3), 269-278.

Raithby, K. D. and Galloway, J. W. (1974) 'Effects of moisture condition age, and rate of loading on fatigue of plain concrete', *ACI Special Publication*, 41, 15-35.

Ramakrishnan, V. and Lokvik, B. (1992) 'Flexural fatigue strength of fiber reinforced concretes', in *High Performance Fiber Reinforced Cement Composites: Proceedings of the International RILEM/ACI Workshop*, London, 271-287.

Rasmussen, R. O., Rogers, R. and Ferragut, T. R. (2011) *Continuously Reinforced Concrete Pavement: Design and Construction Guidelines*, Washington, DC: USDOT Federal Highways Administration.

RILEM (1984) 'Long term random dynamic loading of concrete structures', *Materials and Structures*, 17(97), 1-28.

Roelfstra, P. E. and Wittmann, F. H. (1986) 'Numerical method to link strain softening with failure of concrete', *Fracture Toughness and Fracture Energy of Concrete*, 163-175.

Roesler, J. and Barenberg, E. (1999a) 'Effect of static and fatigue cracking on concrete strain measurements', *Transportation Research Record: Journal of the Transportation Research Board*, 1684, 51-60.

Roesler, J. and Barenberg, E. (1999b) 'Fatigue and static testing of concrete slabs', *Transportation Research Record: Journal of the Transportation Research Board*, 1684, 71-80.

Roesler, J. R. (1998) *Fatigue of concrete beams and slabs* [Doctoral dissertation], unpublished thesis University of Illinois.

Roesler, J. R., Altoubat, S. A., Lange, D. A., Rieder, K. A. and Ulreich, G. R. (2006) 'Effect of synthetic fibers on structural behavior of concrete slabs-on-ground', *ACI Materials Journal*, 103(1), 3-10.

Roesler, J. R., Hiller, J. E. and Littleton, P. C. (2005) 'Large-scale airfield concrete slab fatigue tests', in *Eighth International Conference on Concrete Pavements*, 66-87.

Roesler, J. R., Lange, D. and Ulreich, G. (2003) *Fracture behavior of full-scale, fiber-reinforced concrete slabs*, Report prepared for WR Grace, Inc., University of Illinois, Urbana, IL.

Roesler, J. R., Lange, D. A., Altoubat, S. A., Rieder, K.-A. and Ulreich, G. R. (2004) 'Fracture of plain and fiber-reinforced concrete slabs under monotonic loading', *Journal of Materials in Civil Engineering*, 16(5), 452-460.

Rollins, R. S. (1986) *Field Performance of Fiber-Reinforced Concrete Airfield Pavements*, Army Engineer Waterways Experiment Station Vicksburg Ms Geotechnical Lab, Federal Aviation Administration, Washington.

Romualdi, J. P. and Mandel, J. A. (1964) 'Tensile strength of concrete affected by uniformly distributed closely spaced short lengths of wire reinforcement', *ACI Journal Proceedings*, 61(6), 657-671.

Saito, M. (1983) 'Direct tensile fatigue of concrete by the use of friction grips', *ACI Journal, Journal Proceedings*, 80(5), 431-438.

Saleh, M. F., Yeow, T., MacRae, G. and Scott, A. (2012) 'Effect of steel fibre content on the fatigue behaviour of steel fibre reinforced concrete', in *7th RILEM International Conference on Cracking in Pavements*, Springer, 815-825.

Schäfer, N., Gudžulić, V., Timothy, J.J., Breitenbücher, R. and Meschke, G. (2019) 'Fatigue behavior of HPC and FRC under cyclic tensile loading: Experiments and modeling', *Structural Concrete*, 20(4), 1265-1278.

Singh, S. P. and Kaushik, S. K. (2003), 'Fatigue strength of steel fibre reinforced concrete in flexure', *Cement and Concrete Composites*, 25(7), 779-786.

Singh, S. P., Goel, S., Lal, R. and Kaushik, K. (2004), 'Prediction of mean and design fatigue lives of steel fibrous concrete using S-N relationships', *Asian Journal of Civil Engineering (Building and Housing)*, 5(3-4), 175-190.

Sivagamasundari, R. and Kumaran, G. (2011) 'Experimental study on the behaviour of concrete one way slabs reinforced with GFRP reinforcements under constant and variable amplitude repeated loadings', *International Journal of Civil & Structural Engineering*, 2(2), 556-578.

Slowik, V., Plizzari, G. A. and Saouma, V. E. (1996) 'Fracture of concrete under variable amplitude fatigue loading', *Materials Journal*, 93(3), 272-283.

Smith, K. D. and Roesler, J. R. (2003) 'Review of fatigue models for concrete airfield pavement design', in *Airfield Pavements: Challenges and New Technologies, Proceedings of the Specialty Conference*, Las Vegas, NV, United states, American Society of Civil Engineers, 231-258.

Sorelli, L. G., Meda, A. and Plizzari, G. A. (2006) 'Steel fiber concrete slabs on ground: a structural matter', *ACI Structural Journal*, 103(4), 551-558.

Sparks, P. R. (1982) 'The influence of rate of loading and material variability on the fatigue characteristics of concrete', *Special Publication*, 75, 331-342.

Sparks, P. R. and Menzies, J. B. (1973) 'The effect of rate of loading upon the static and fatigue strengths of plain concrete in compression', *Magazine of Concrete Research*, 25(83), 73-80.

Stemland, H., Petkovic, G., Rosseland, S. and Lenschow, R. (1990) 'Fatigue of high strength concrete', *Nordic Concrete Research*, (9), 172-196.

Stroeven, P. (2009) 'Stereological principles of spatial modeling applied to steel fiber-reinforced concrete in tension', *ACI Materials Journal*, 106(3), 213.

Su, E. C. M. and Hsu, T. T. C. (1988) 'Biaxial compression datigue and the discontinuity of concrete', *Materials Journal*, 85(3), 178-188.

Suh, C., Lee, J., Fowler, D. and Stokoe II, K. (2005) 'Part 3: accelerated pavement testing: superaccelerated pavement testing on full-scale concrete slabs', *Transportation Research Record: Journal of the Transportation Research Board*, 1940, 109-124.

Tayabji, S. D., Ye, D. and Buch, N. (2013) *Precast Concrete Pavement Technology*, Report S2-R05-RR-1, Strategic Highway Research Program, Washington, DC: Transportation Research Board.

Tepfers, R. (1979) 'Tensile fatigue strength of plain concrete', *ACI Journals, Journal Proceedings*, 76(8), 919-934.

Tepfers, R. and Kutti, T. (1979) 'Fatigue strength of plain, ordinary, and lightweight concrete', in *ACI Jounals, Journal Proceedings*, 635-652.

Thompson, M. R. and Barenberg, E. J. (1992) *Calibrated Mechanistic Structural Analysis Procedure for Pavements-Phase 2*, Washington, DC: Transportation Research Board.

Titus-Glover, L., Mallela, J., Darter, M., Voigt, G. and Waalkes, S. (2005) 'Enhanced portland cement concrete fatigue model for streetpave', *Transportation Research Record: Journal of the Transportation Research Board*, (1919), 29-37.

Tran, V. N. G. (2003) *Constitutive modelling of fibre reinforced concrete and shotcrete* [Doctoral dissertation], University of Tasmania.

Tran, V. N., Bernard, E. S. and Beasley, A. J. (2005) 'Constitutive modeling of fiber reinforced shotcrete panels', *Journal of Engineering Mechanics*, 131(5), 512-521.

Uchida, Y., Kurihara, N., Rokugo, K. and Koyanagi, W. (1995) 'Determination of tension softening diagrams of various kinds of concrete by means of numerical analysis', In *Proceedings of the 2nd International Conference on Fracture Mechanics Concrete and Concrete Structures (FraMCoS-2)*, 17-30.

Van Ornum, J. L. (1903) 'The fatigue of cement products', *Transactions of the American Society of Civil Engineers*, 51(2), 443-445.

Van Ornum, J. L. (1907) 'The fatigue of concrete', *Transactions of the American Society of Civil Engineers*, 58(1), 294-320.

Vandewalle, L. and Dupont, D. (2003) *Bending test and interpretation*, RILEM Publication PRO: Bagneux, France, 31, 1-14.

Voo, J. Y. L. and Foster, S. J. (2003) *Variable engagement model for fibre reinforced concrete in tension*, UNICIV Report No. R-420, School of Civil and Environmental Engineering, The University of New South Wales, Australia.

Voo, J. Y. L. and Foster, S. J. (2004) 'Tensile-fracture of fibre-reinforced concrete: variable engagement model', In *6th International RILEM Symposium on Fibre Reinforced Concretes*, RILEM Publications SARL, Varenna, Italy, 875-884.

Voo, Y. L. and Foster, S. J. (2009) *Reactive powder concrete: analysis and design of RPC girders*, Lambert Academic Publishing.

Wei, S., Jianming, G. and Yun, Y. (1996) 'Study of fatigue performance and damage mechanism of steel fibre-reinforced concrete', *ACI Materials Journal*, 93(3), 206-211.

Williams, H. A. (1943) 'Fatigue Tests of Lightweight Aggregate Concrete Beams', *ACI Journals, Journal Proceedings*, 39, 441-448.

Yin, W. and Hsu, T. T. C. (1995) 'Fatigue behavior of steel fiber reinforced concrete in uniaxial and biaxial compression', *ACI Materials Journal*, 92(1), 71-81.

Zhang, B. (1998) 'Relationship between pore structure and mechanical properties of ordinary concrete under bending fatigue', *Cement and Concrete Research*, 28(5), 699-711.

Zhang, B., Phillips, D. V. and Wu, K. (1996) 'Effects of loading frequency and stress reversal on fatigue life of plain concrete', *Magazine of Concrete Research*, 48(177), 361-375.

Zhang, B., Phillips, D. V. and Wu, K. (1997) 'Further research on fatigue properties of plain concrete', *Magazine of Concrete Research*, 49(180), 241-252.

Zhang, J. and Stang, H. (1998) 'Fatigue performance in flexure of fiber reinforced concrete', *ACI Materials Journal*, 95(1), 58-67.

Zhang, J., Stang, H. and Li, V. C. (1999) 'Fatigue life prediction of fibre reinforced concrete under flexural load', *International Journal of Fatigue*, 21(10), 1033-1049.

Appendix A: EXPERIMENTAL DATA – ROUND PANEL TEST

Appendix Outline

A.1 Thicknesses and Dimensions of Specimens

A.2 Raw Round Panel Static Test Data

A.3 Raw Round Panel Fatigue Test Data

A.1 Thicknesses and Dimensions of Specimens

Specimen ID	Diameter					Thickness							
	1	2	3	**Mean**	**COV**	1	2	3	4	5	6	**Mean**	**COV**
A-1S-P	805	795	797	**799**	**0.01**	76.5	77.5	79.0	76.0	77.0	76.0	**77.0**	**0.01**
A-1S-F	799	799	799	**799**	**0.00**	80.7	79.0	73.6	72.8	77.4	82.6	**77.7**	**0.05**
A-2S-F	799	799	797	**798**	**0.00**	72.6	73.0	78.2	77.9	80.6	79.3	**76.9**	**0.04**
A-1C-F-U-60	797	799	798	**798**	**0.00**	80.3	80.4	77.8	79.3	75.7	76.9	**78.4**	**0.02**
A-1C-F-U-70	800	801	797	**799**	**0.00**	77.3	78.7	77.2	78.0	77.3	76.5	**77.5**	**0.01**
A-1C-F-C-60	797	800	797	**798**	**0.00**	77.7	76.5	73.6	73.2	74.8	74.0	**75.0**	**0.02**
A-2C-F-C-60	798	800	800	**799**	**0.00**	79.8	77.8	77.9	71.6	71.6	77.9	**76.1**	**0.05**
A-1C-F-C-40	797	798	800	**798**	**0.00**	78.9	78.0	75.6	78.2	83.2	81.7	**79.3**	**0.03**
A-2C-F-C-40	800	798	800	**799**	**0.00**	78.0	78.6	77.8	77.7	73.5	74.8	**76.7**	**0.03**
B-1S-F	800	797	800	**799**	**0.00**	80.5	78.0	75.2	77.9	76.8	77.7	**77.7**	**0.02**
B-2S-F	801	797	800	**799**	**0.00**	79.3	80.1	79.7	77.9	76.9	76.5	**78.4**	**0.02**
B-1C-F-U-70	801	797	799	**799**	**0.00**	85.0	84.1	81.5	82.6	79.9	80.6	**82.3**	**0.02**
B-2C-F-U-70	799	799	800	**799**	**0.00**	80.5	79.4	77.0	77.0	80.2	81.0	**79.2**	**0.02**
B-1C-F-C-60	800	800	797	**799**	**0.00**	82.6	80.0	80.1	80.1	80.7	82.0	**80.9**	**0.01**

Specimen ID	Diameter					Thickness							
	1	2	3	**Mean**	**COV**	1	2	3	4	5	6	**Mean**	**COV**
B-2C-F-C-60	798	799	801	**799**	**0.00**	83.5	79.4	80.6	79.1	80.5	81.2	**80.7**	**0.02**
B-3C-F-C-60	800	799	799	**799**	**0.00**	75.8	74.2	75.7	77.0	78.5	80.2	**76.9**	**0.03**
B-1C-F-C-40	801	797	796	**798**	**0.00**	74.9	75.2	78.1	77.9	74.9	74.7	**76.0**	**0.02**
B-2C-F-C-40	798	799	801	**799**	**0.00**	78.2	79.3	78.9	78.4	75.6	75.1	**77.6**	**0.02**
C-1S-F	800	801	798	800	0.00	80.3	77.3	75.6	78.6	79.0	79.8	**78.4**	**0.02**
C-2S-F	798	802	799	800	0.00	77.3	74.7	76.3	79.8	78.8	76.7	**77.3**	**0.02**
C-1C-F-U-70	799	797	801	799	0.00	80.9	80.6	76.2	76.0	81.0	81.9	**79.4**	**0.03**
C-2C-F-U-70	801	802	795	799	0.00	82.5	79.0	79.0	81.7	79.9	82.1	**80.7**	**0.02**
C-1C-F-C-60	801	798	799	799	0.00	77.2	78.3	81.6	79.5	80.4	79.8	**79.5**	**0.02**
C-2C-F-C-60	799	799	799	799	0.00	75.5	76.5	76.3	75.3	75.1	73.4	**75.4**	**0.01**
C-1C-F-C-50	797	803	798	799	0.00	83.6	80.6	82.5	81.5	79.7	77.9	**81.0**	**0.03**
C-2C-F-C-50	800	800	800	800	0.00	81.7	80.9	79.6	80.9	77.3	80.7	**80.2**	**0.02**
C-1C-F-C-40	801	798	802	800	0.00	77.9	78.4	78.2	76.1	77.7	77.0	**77.6**	**0.01**
Mean				**799**								**78.3**	
COV				**0.07%**								**2.39%**	

A.2 Raw Round Panel Static Test Data

Series A				
Specimen ID	***P′***	***P***	***W′***	***W***
	[kN]	**[kN]**	**[J]**	**[J]**
A-1S-F	31.2	29.1	479	455
A-2S-F	28.2	26.9	517	499
Mean	29.7	28.0	498	477
COV	0.07	0.06	0.05	0.07

Series B				
Specimen ID	***P′***	***P***	***W′***	***W***
	[kN]	**[kN]**	**[J]**	**[J]**
B-1S-F	28.6	26.7	519	493
B-2S-F	28.0	25.7	547	512
Mean	28.3	26.2	533	503
COV	0.01	0.03	0.04	0.03

Series C				
Specimen ID	***P′***	***P***	***W′***	***W***
	[kN]	**[kN]**	**[J]**	**[J]**
C-1S-F	33.2	30.3	308	288
C-2S-F	32.3	30.4	379	362
Mean	32.7	30.4	344	325
COV	0.02	0.00	0.15	0.16

Specimen A-1S-F

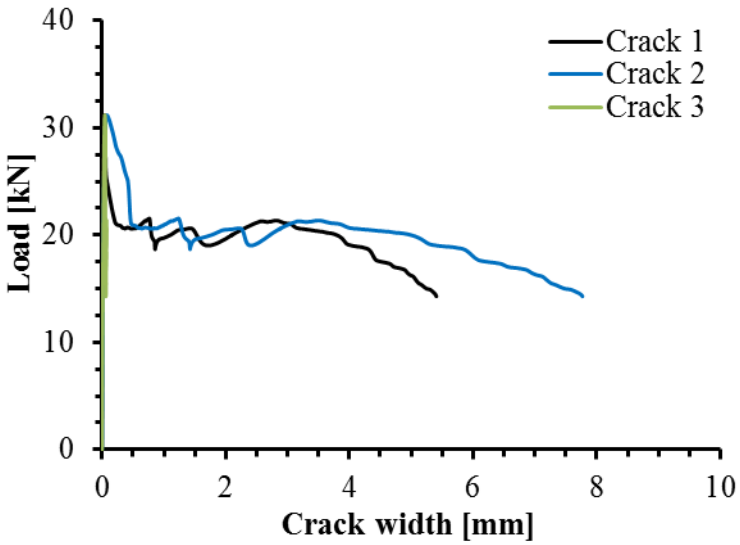

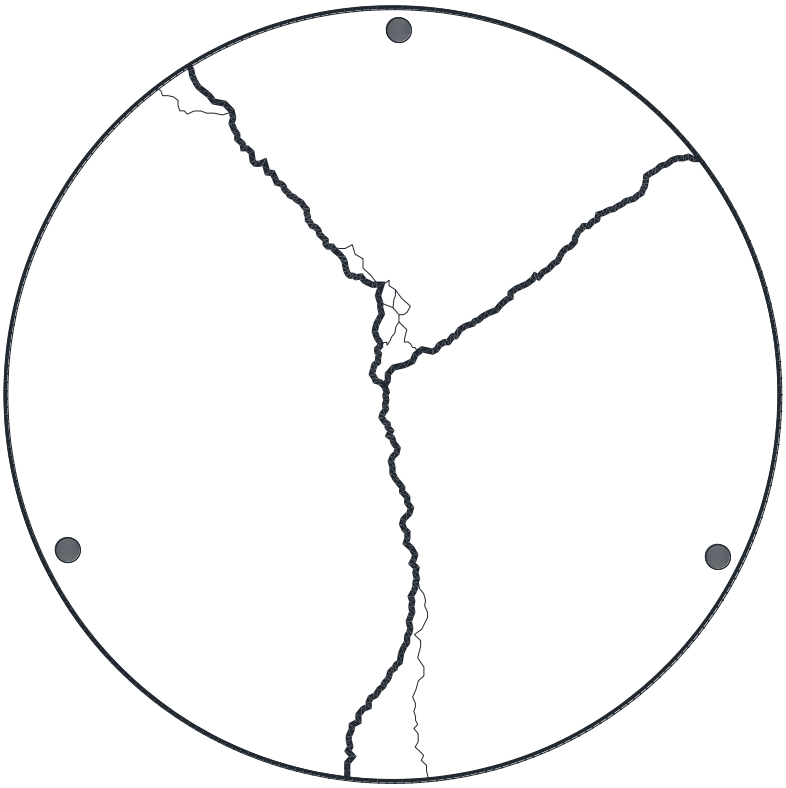

Specimen A-2S-F

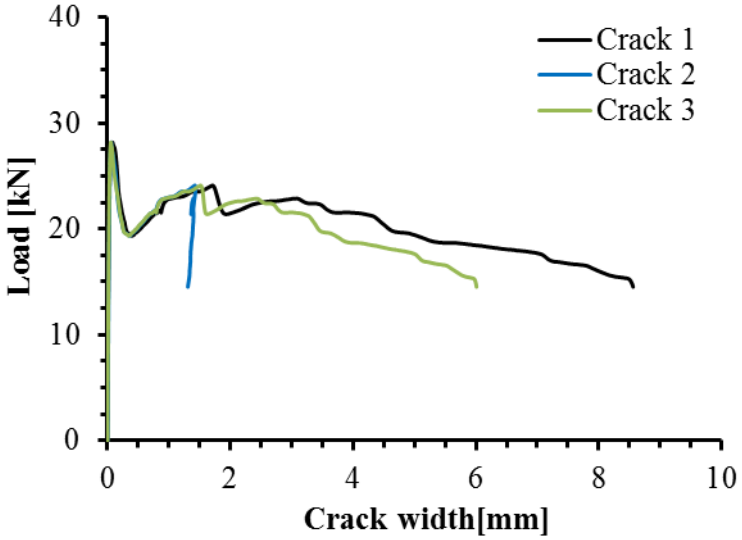

Specimen A-1S-P

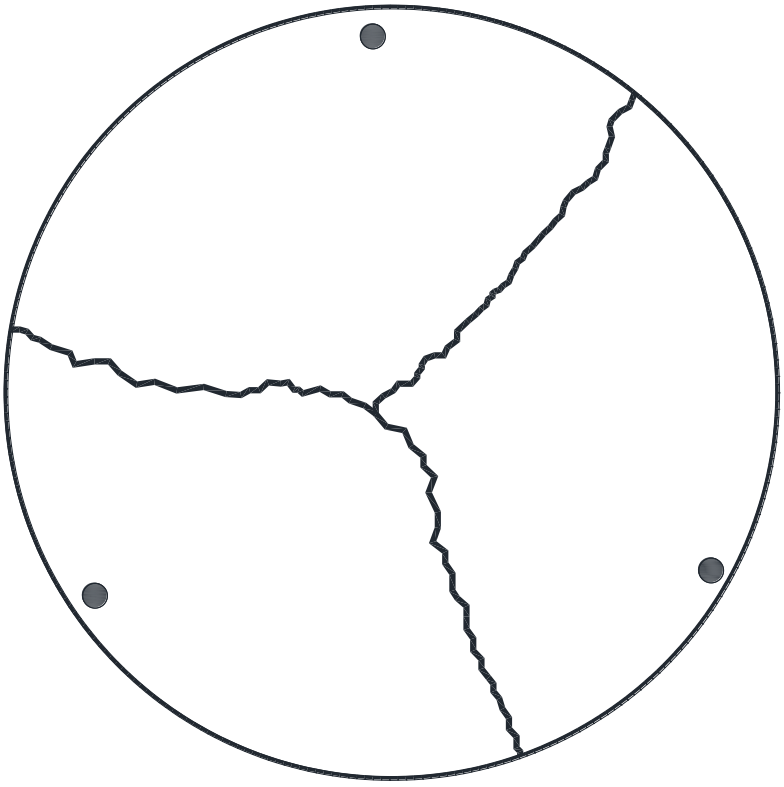

Specimen B-1S-F

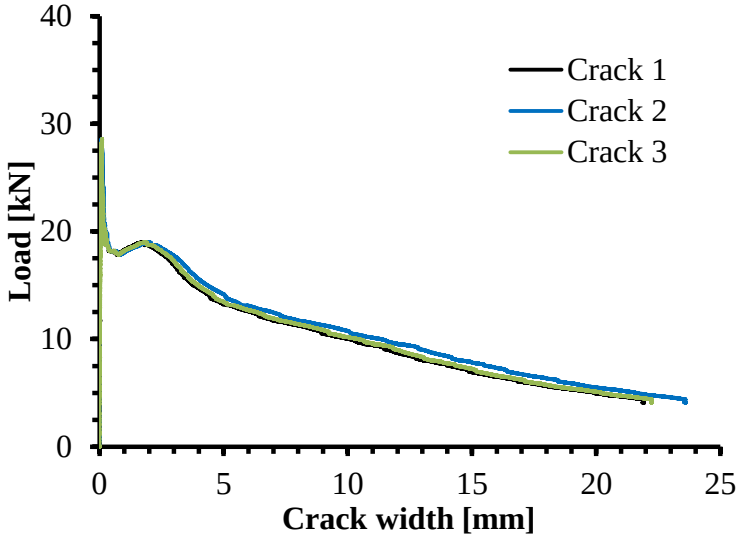

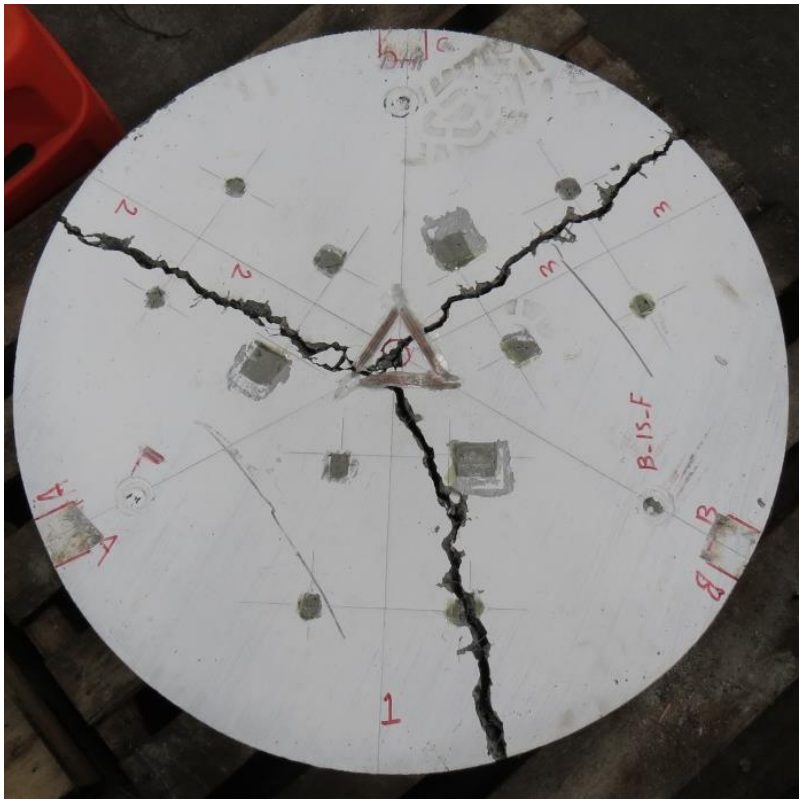

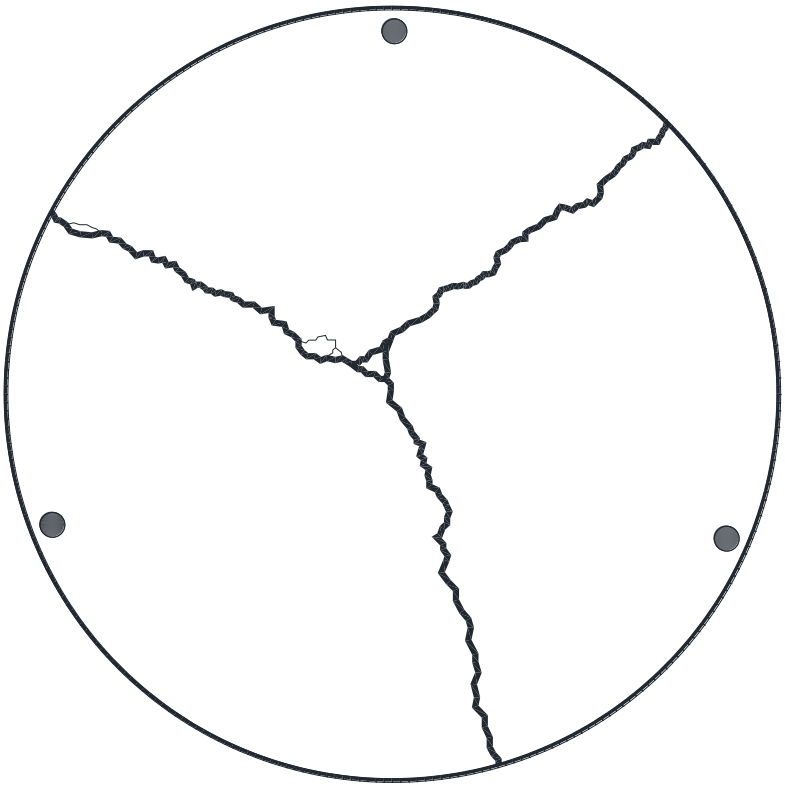

Specimen B-2S-F

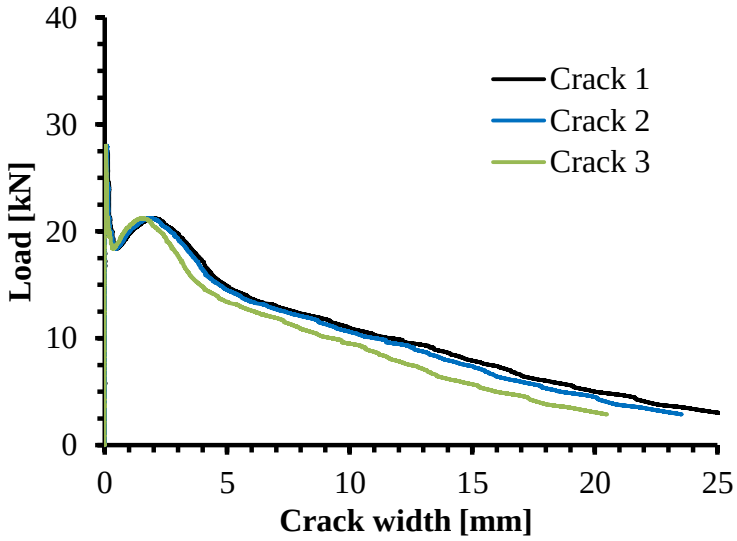

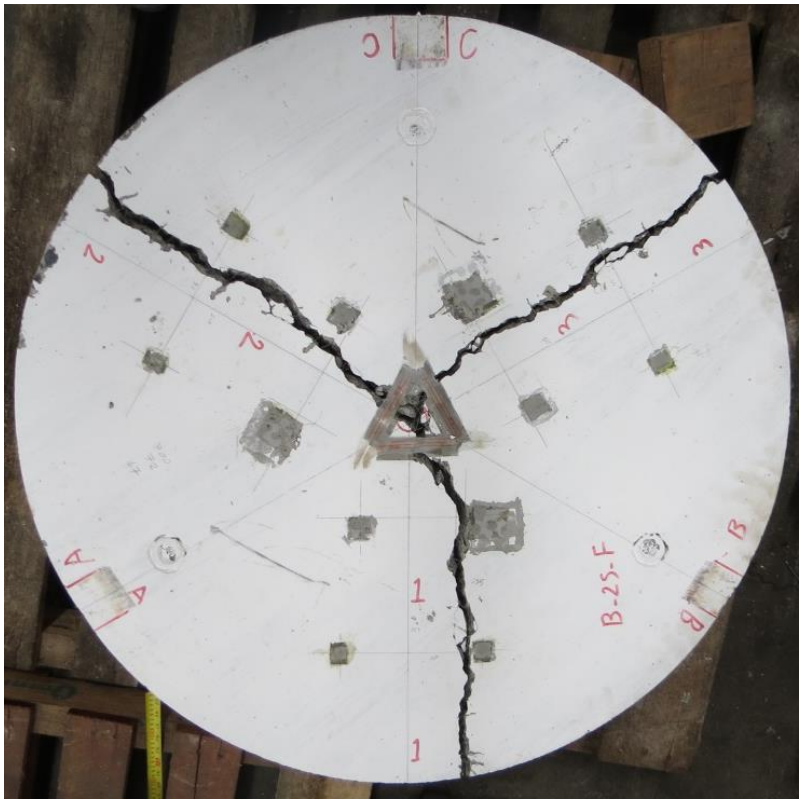
C
C
2
2
3
3
A
A
1
1
B-25-F
B
B

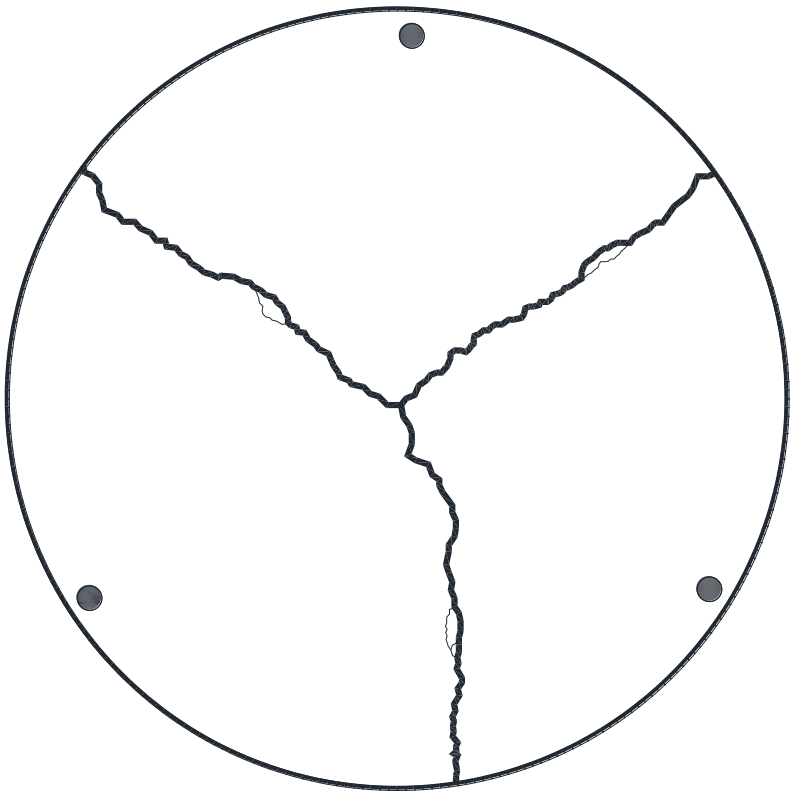

Specimen C-1S-F

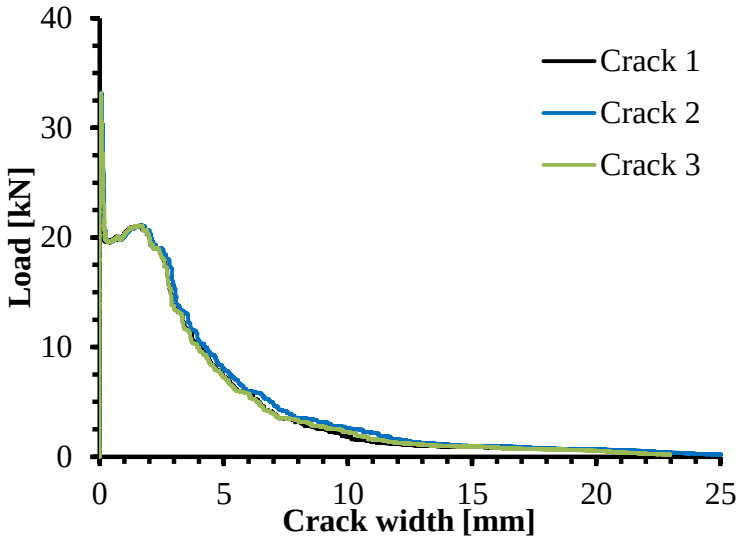

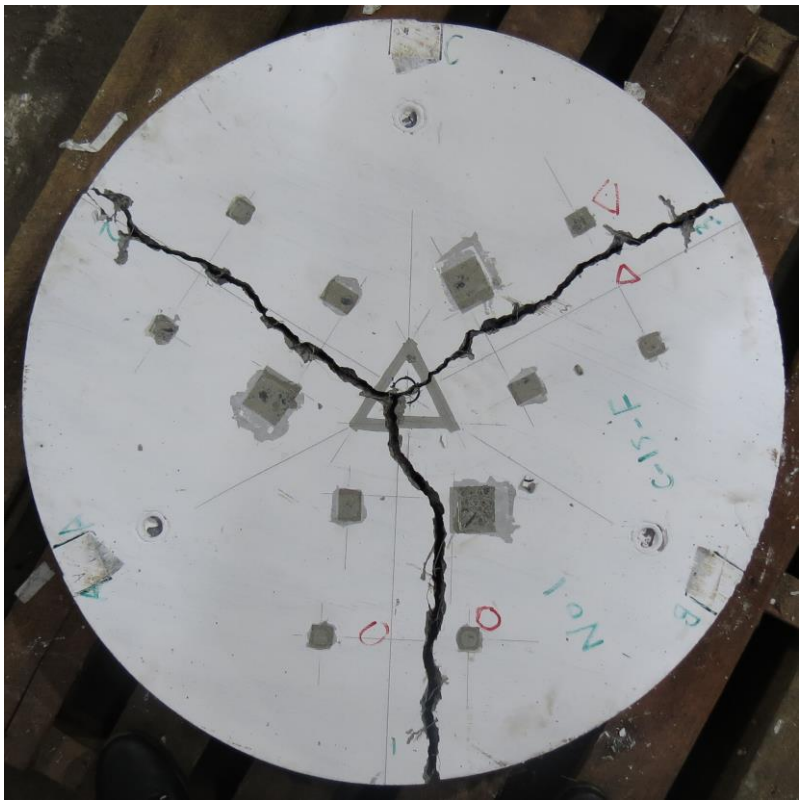

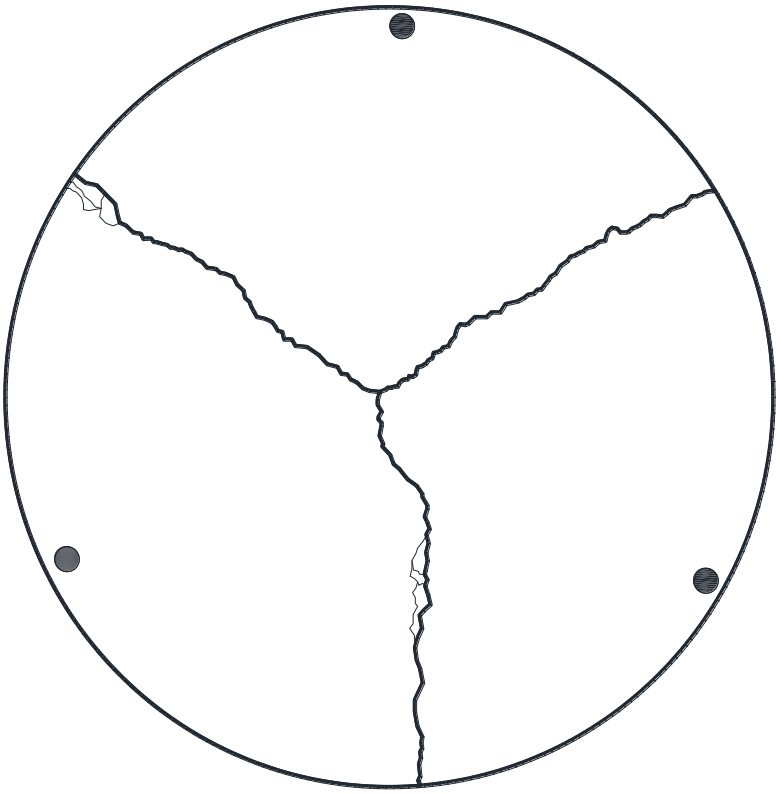

Specimen C-2S-F

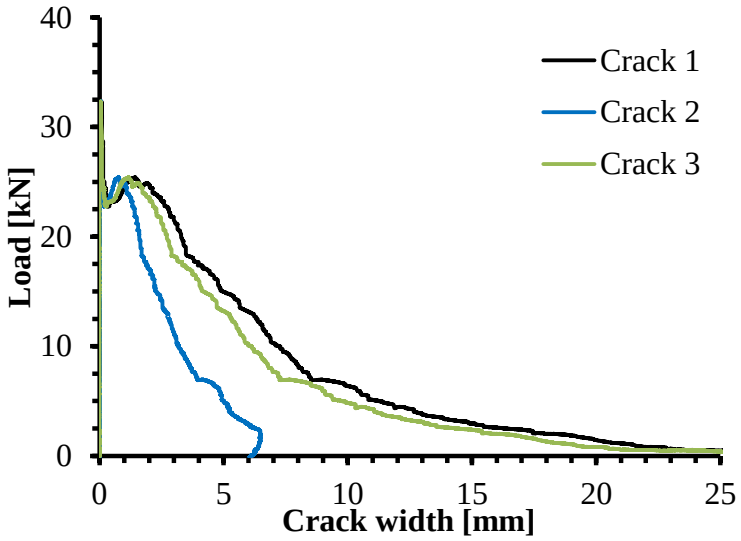

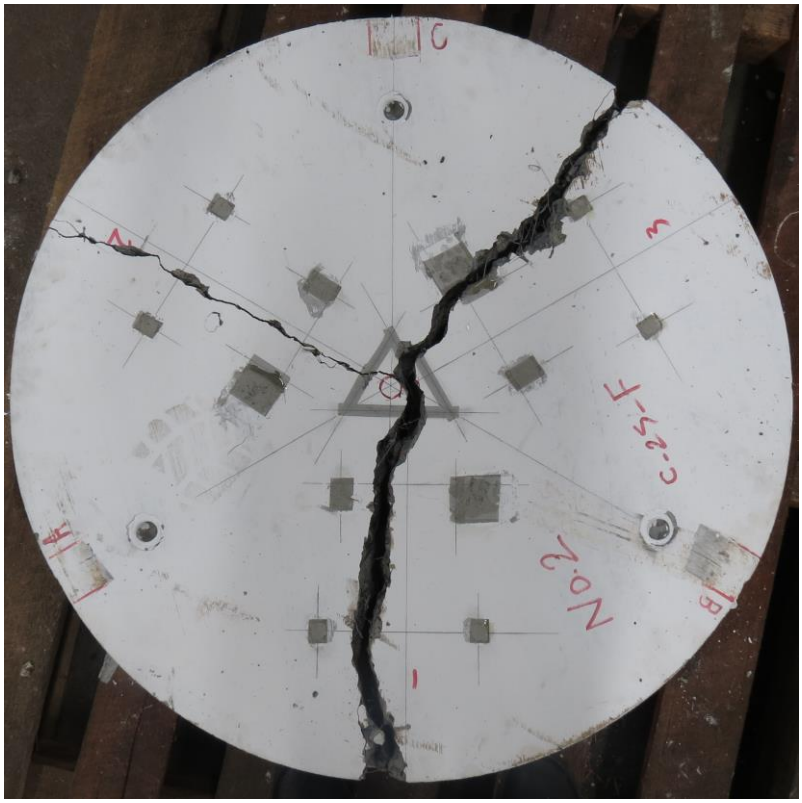
C
A
B
1
3
No.2
c.25-F

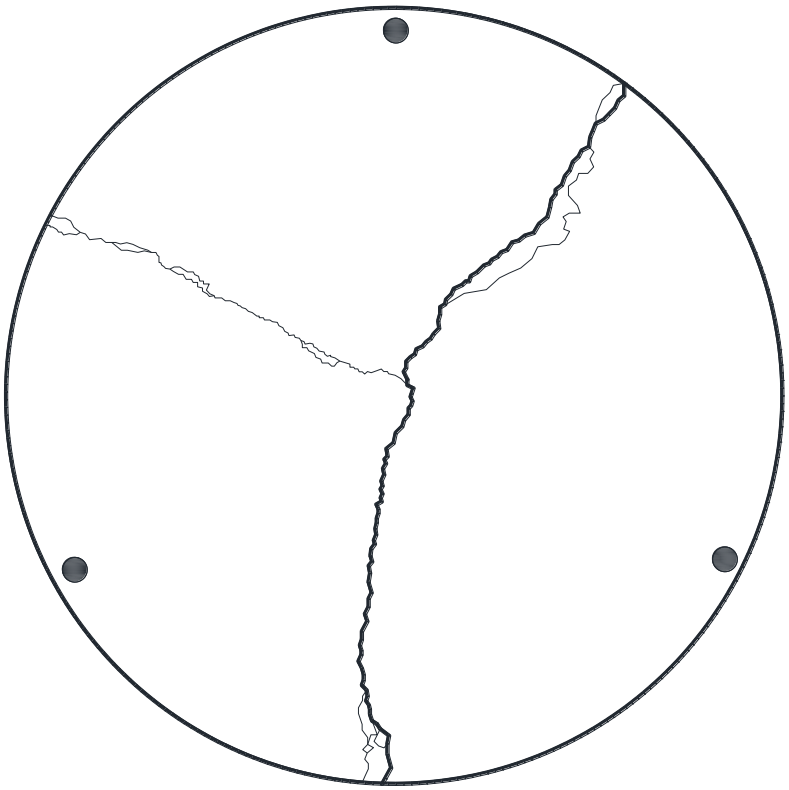

A.3 Raw Round Panel Fatigue Test Data

Specimen A-2C-F-C-60

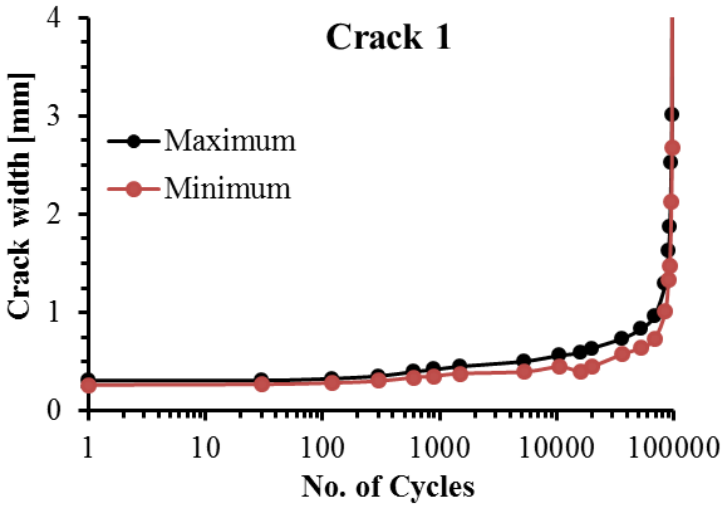

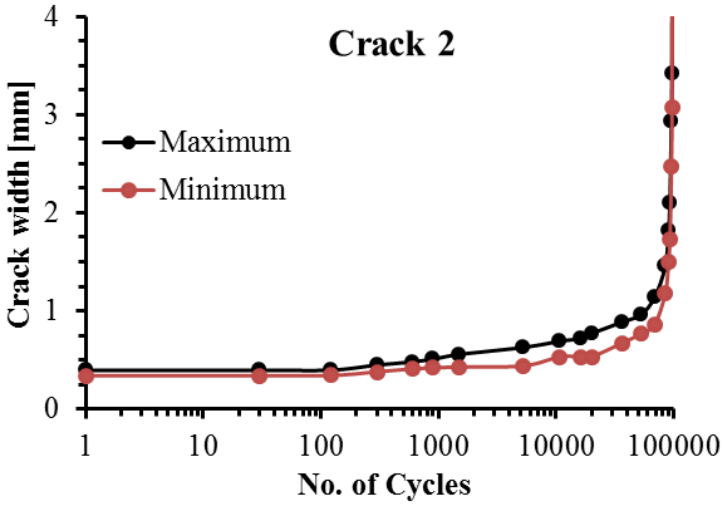

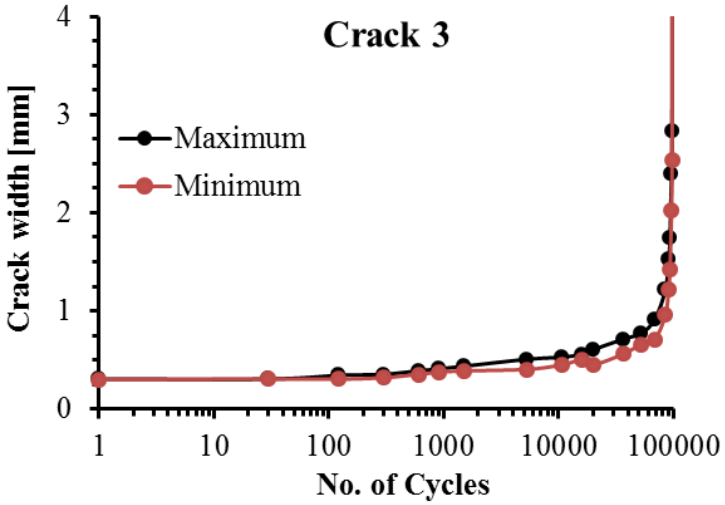

Specimen A-1C-F-C-40

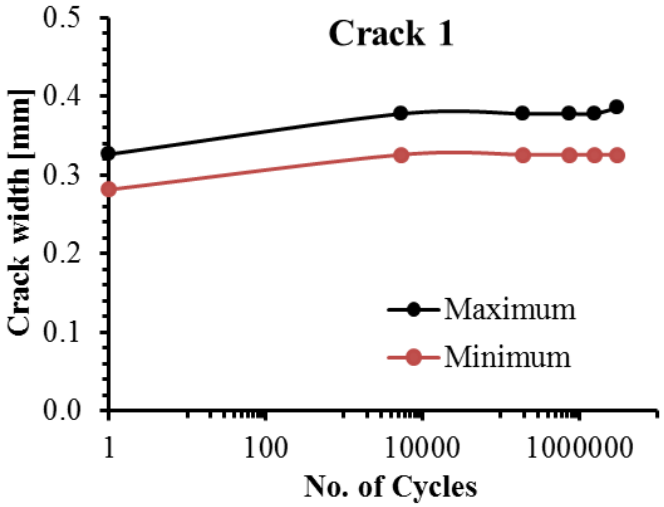

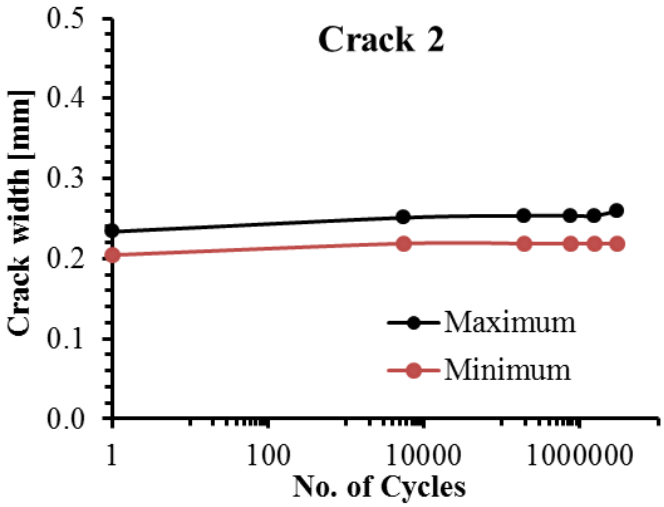

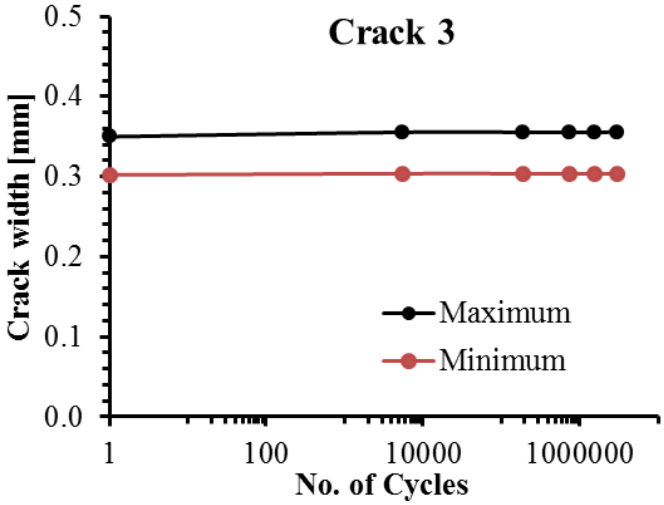

Specimen A-2C-F-C-40

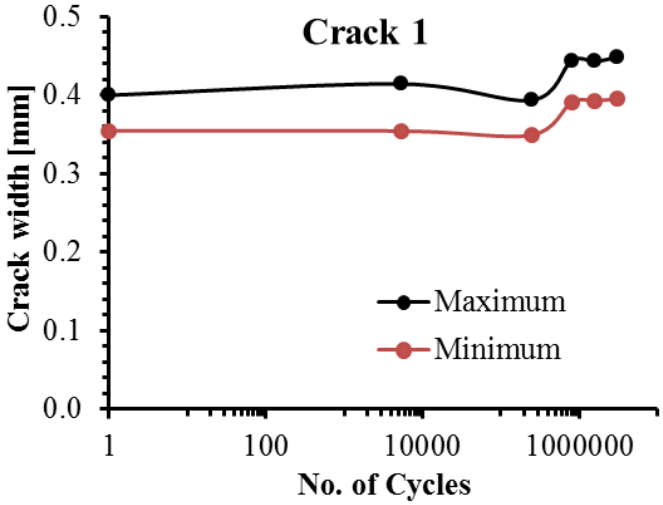

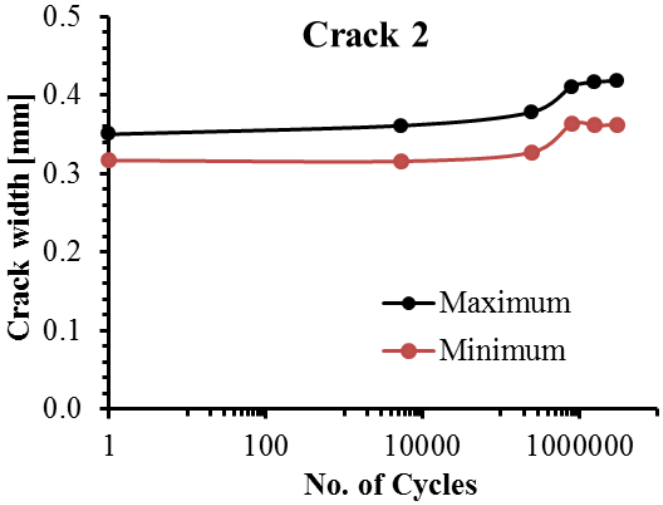

Specimen B-1C-F-U-70

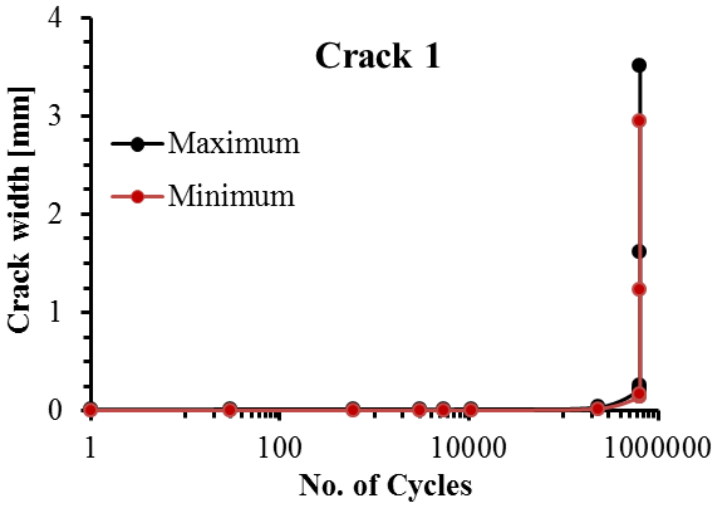

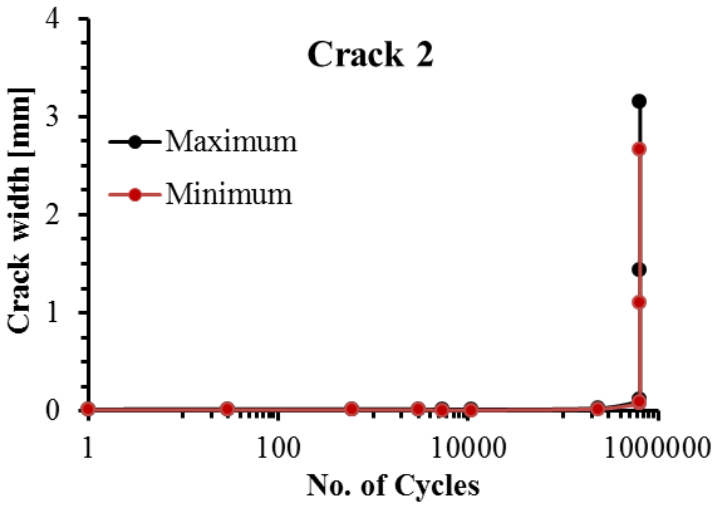

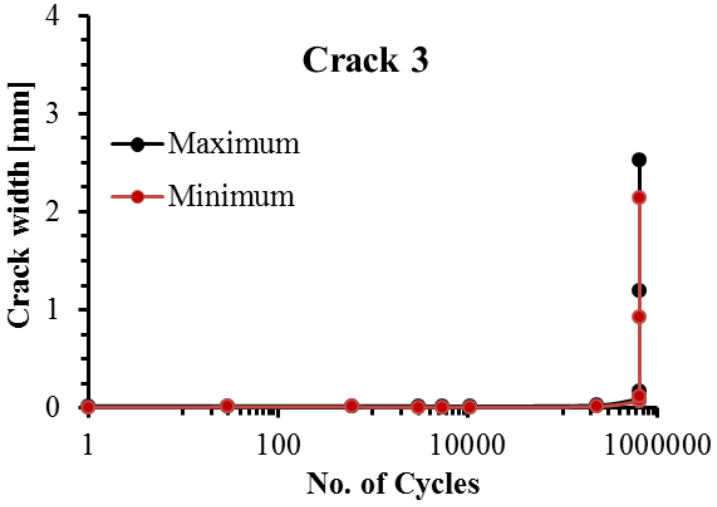

Specimen B-2C-F-U-70

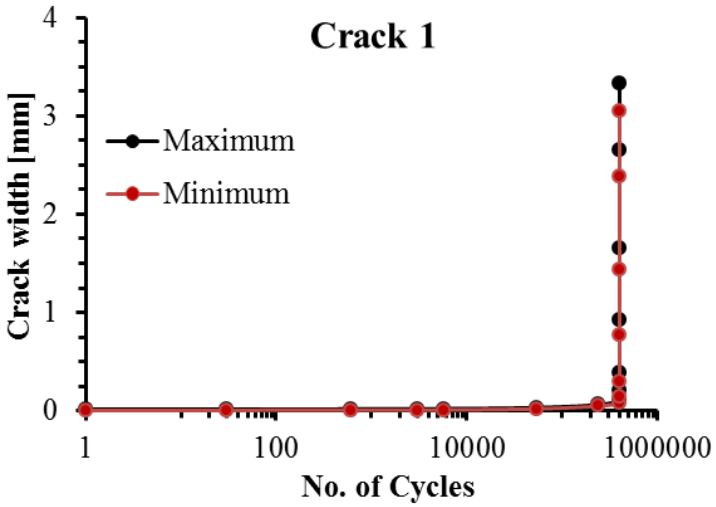

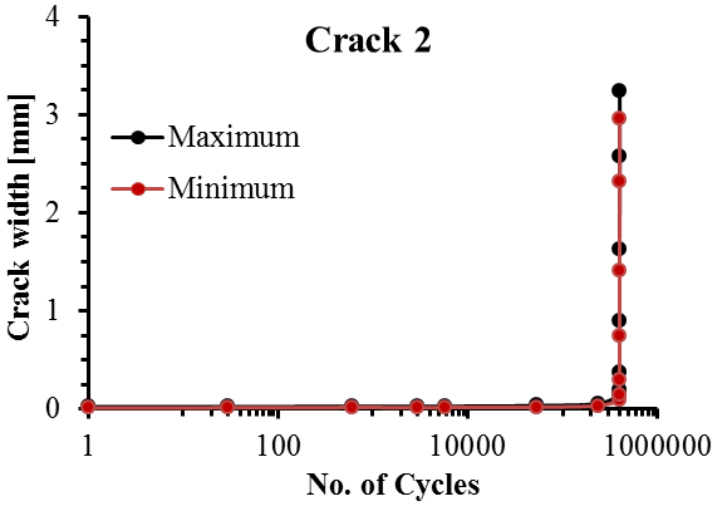

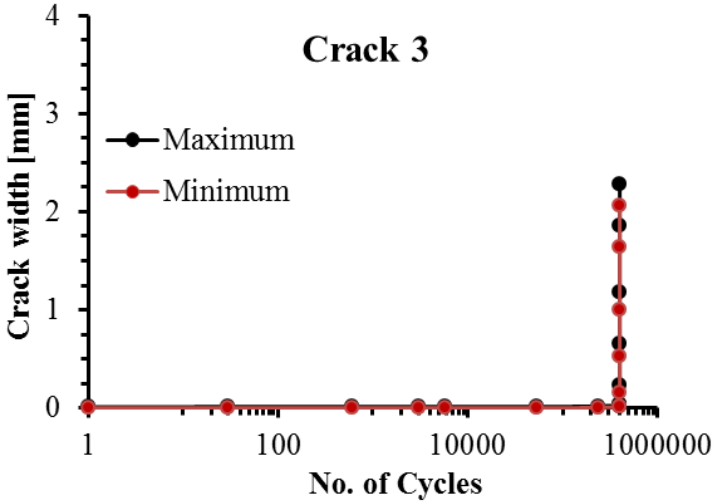

Specimen B-1C-F-C-60

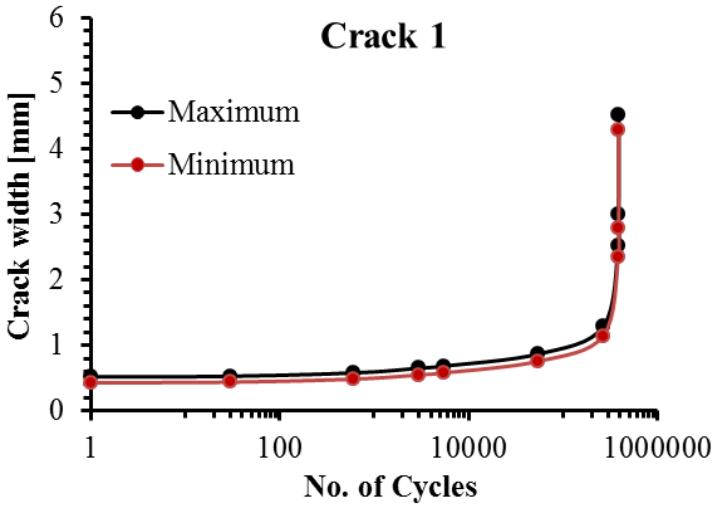

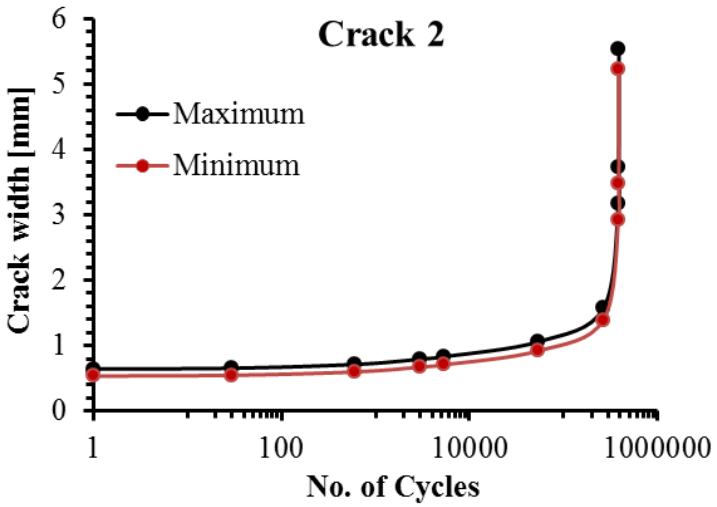

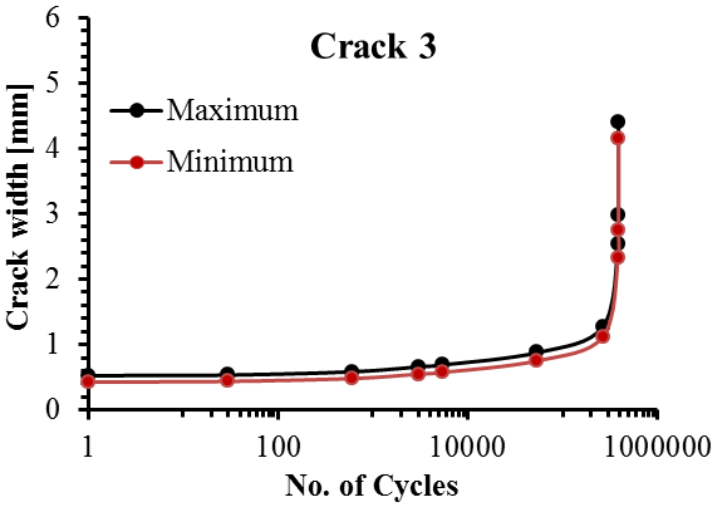

Specimen B-3C-F-C-60

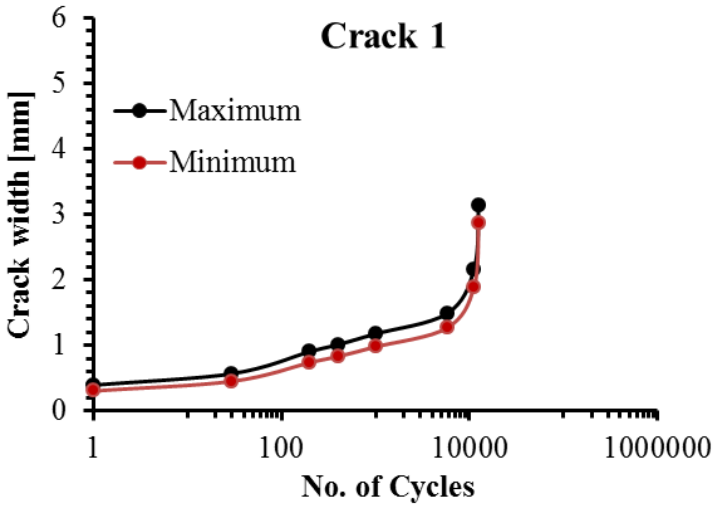

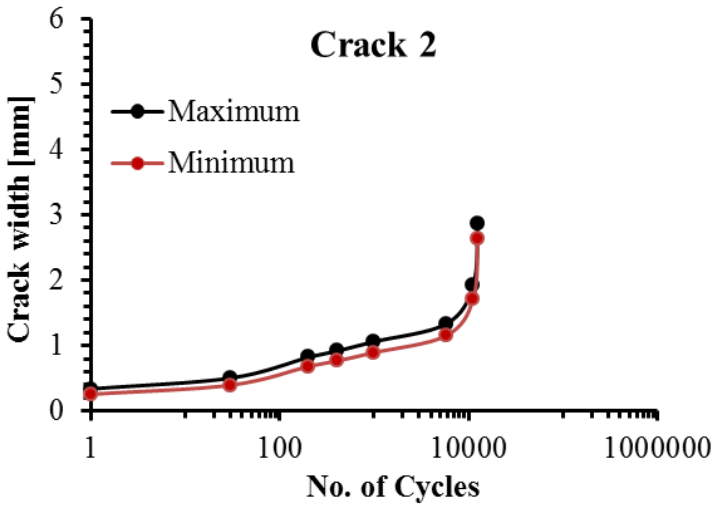

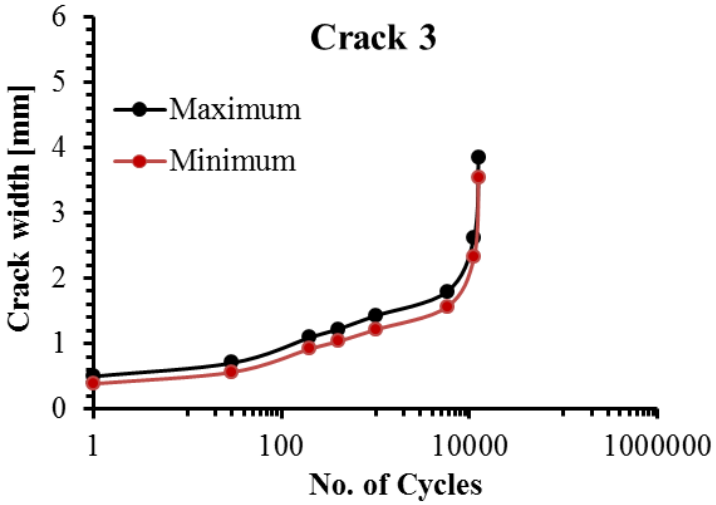

Specimen B-1C-F-C-40

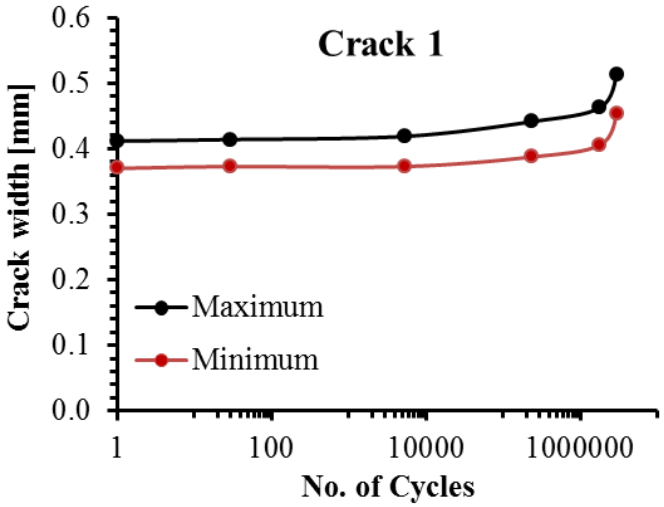

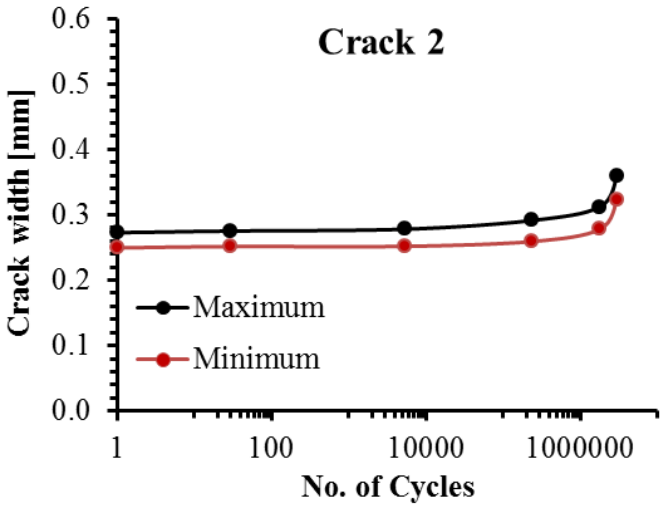

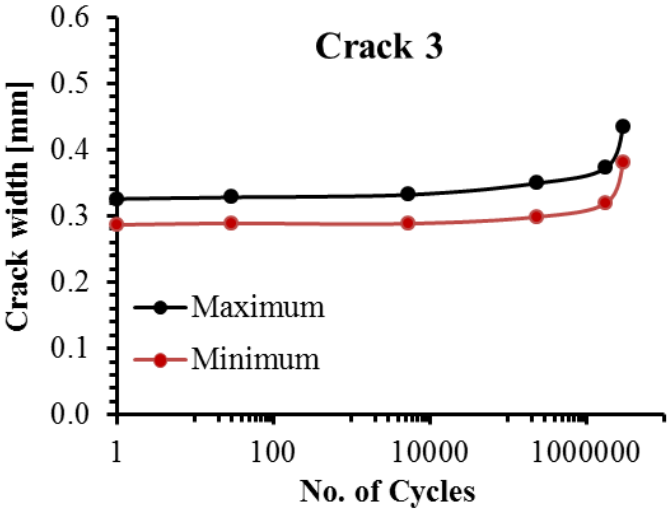

Specimen B-2C-F-C-40

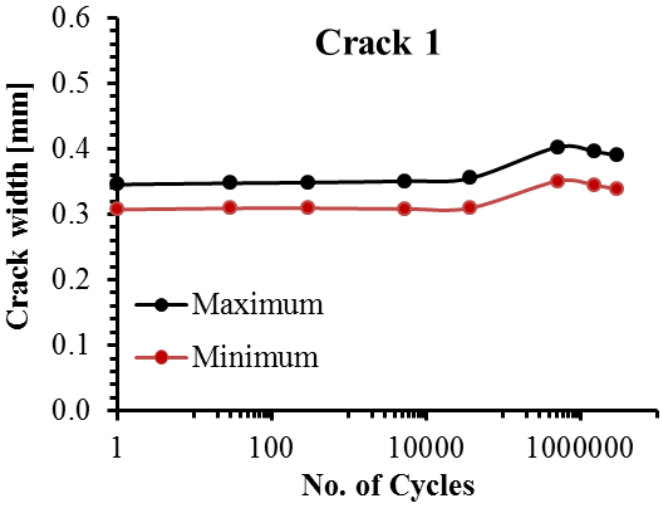

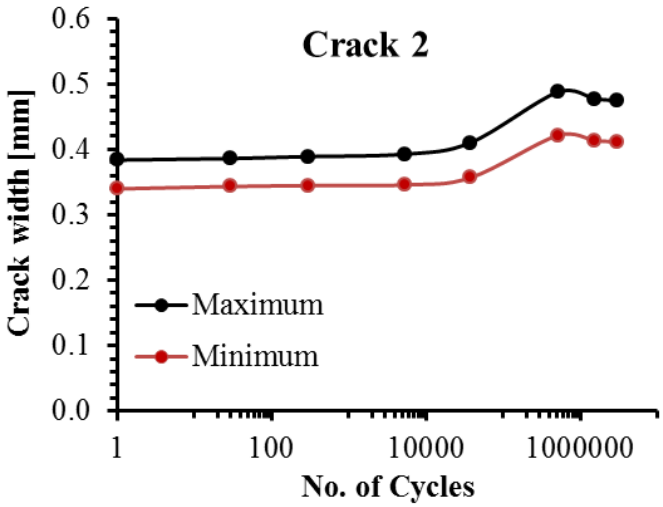

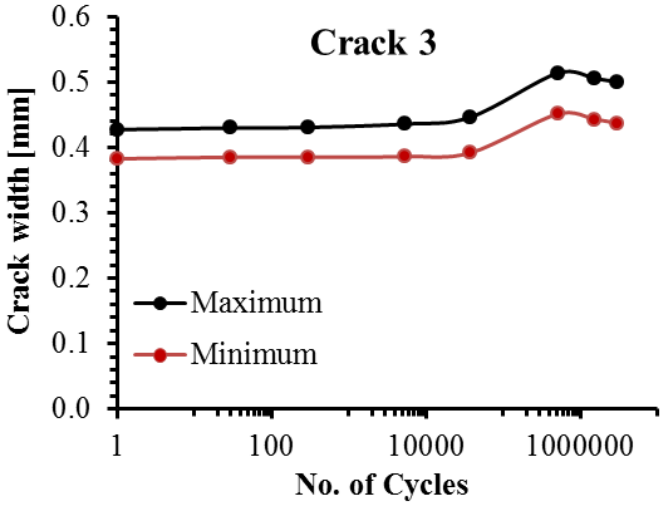

Specimen C-2C-F-U-70

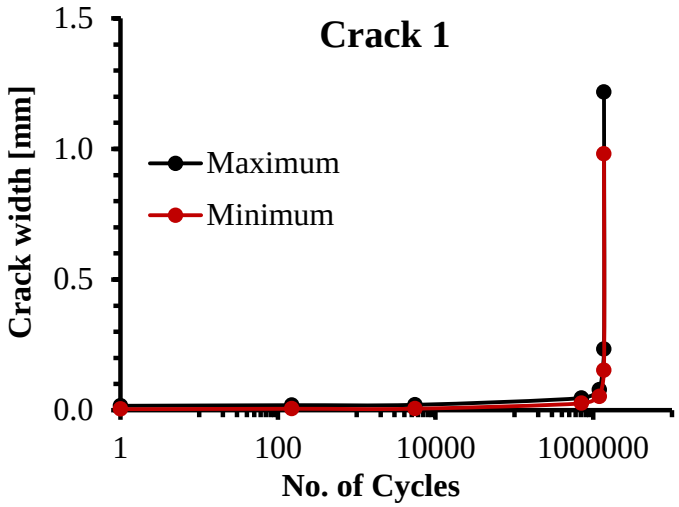

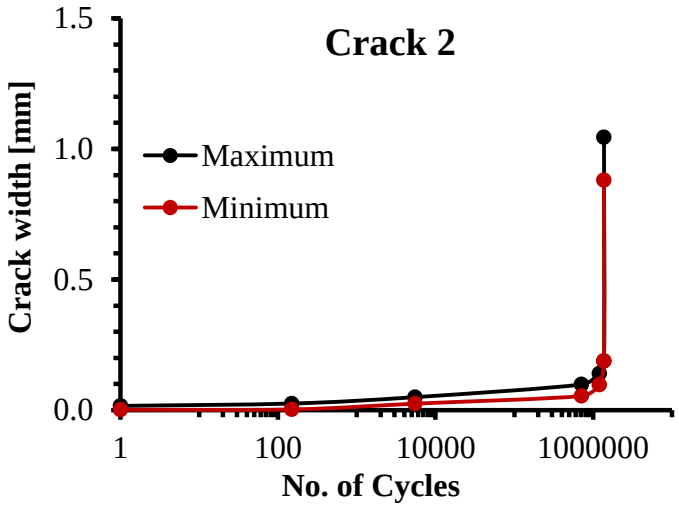

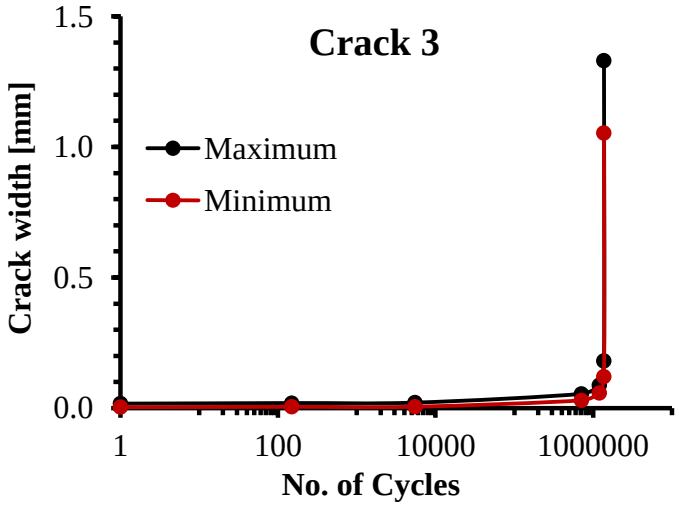

Specimen C-2C-F-C-60

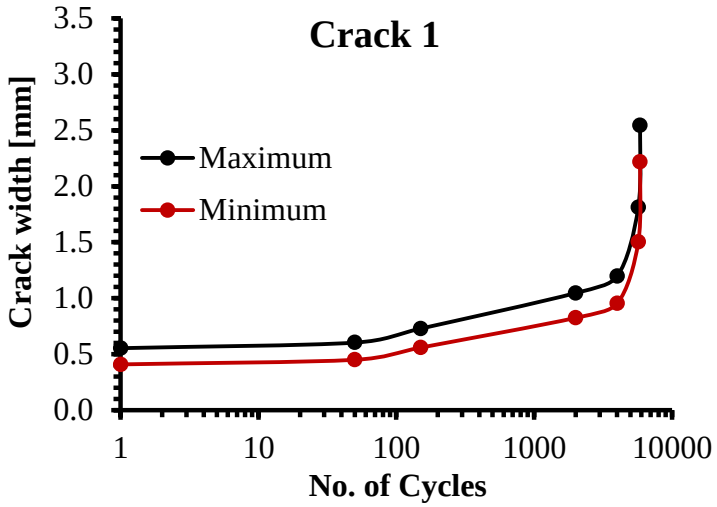

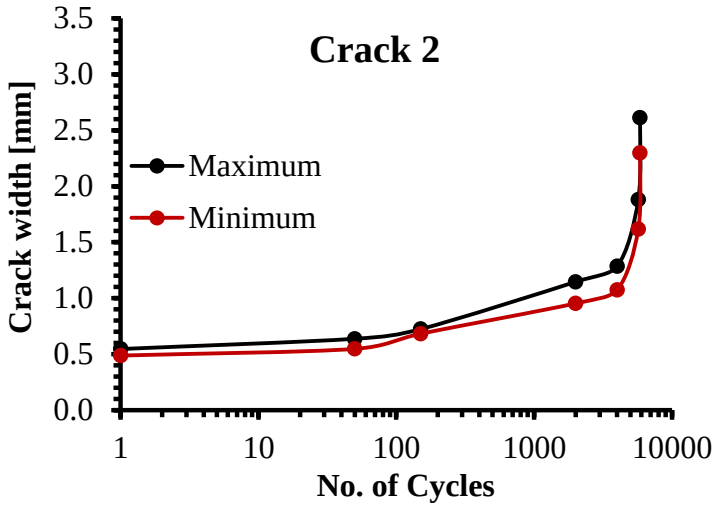

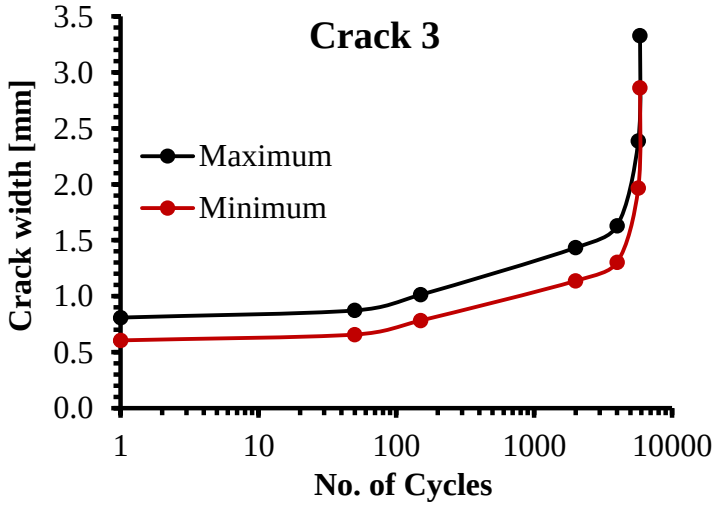

Specimen C-1C-F-C-40

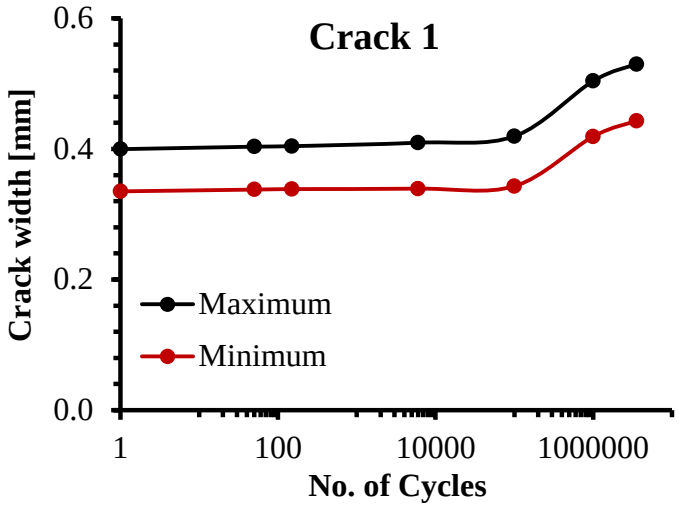

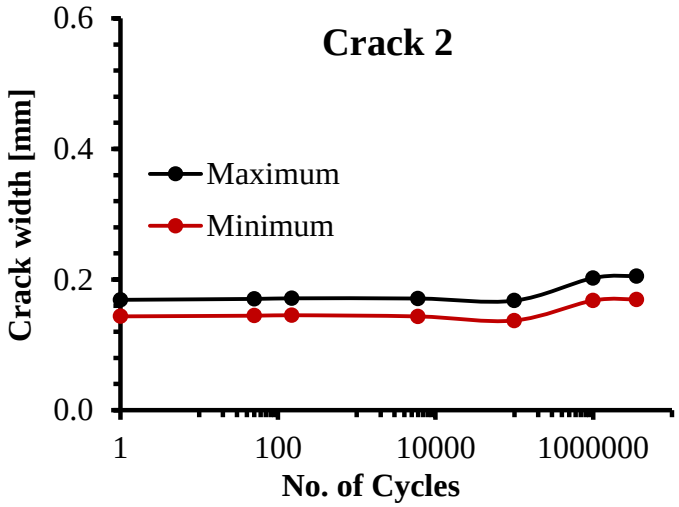

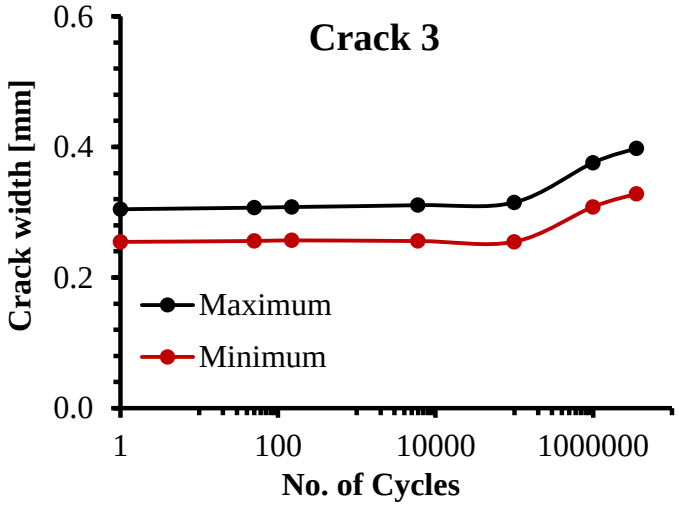

Specimen C-1C-F-C-50

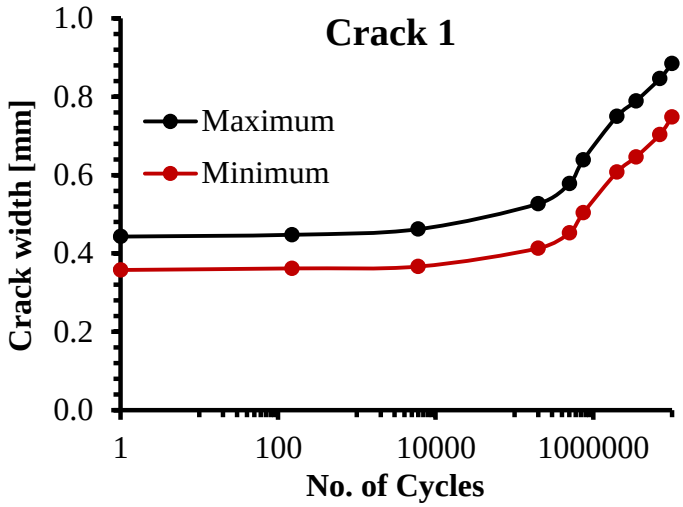

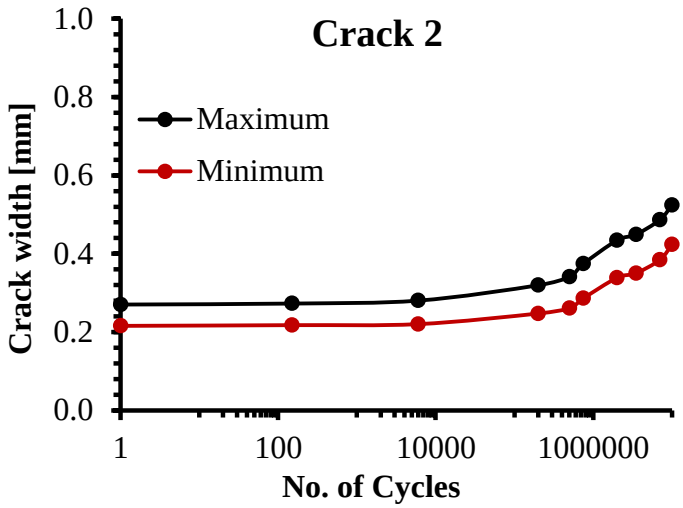

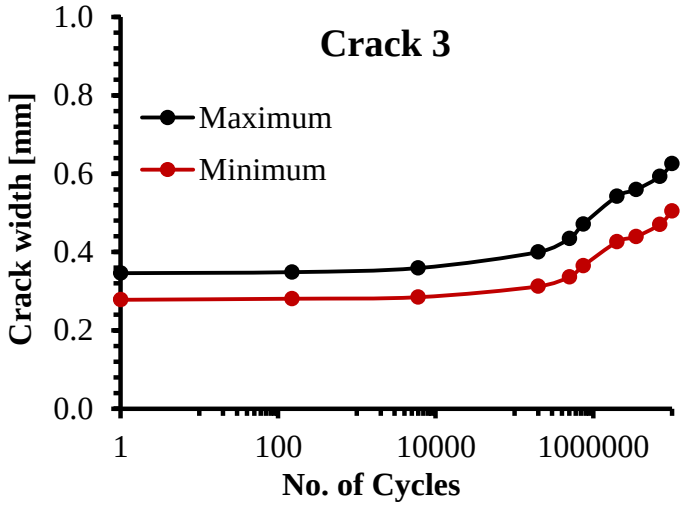

Specimen C-2C-F-C-50

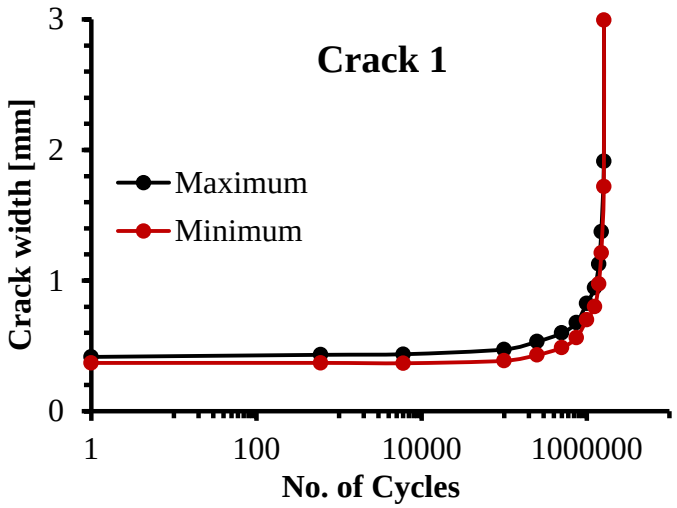

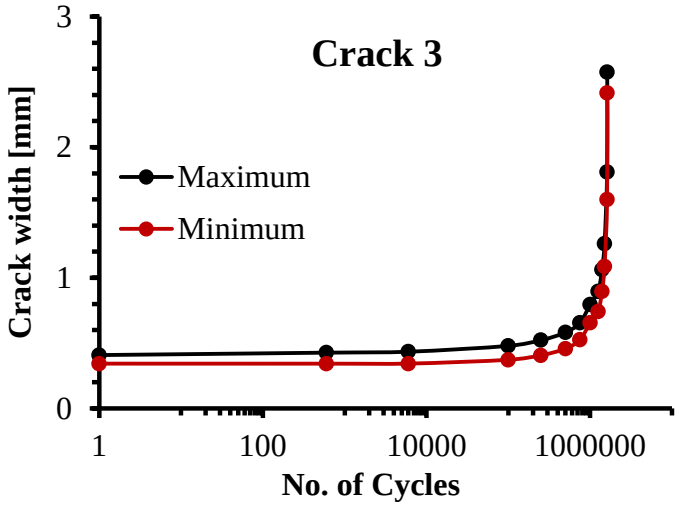

Appendix B: EXPERIMENTAL DATA – UNIAXIAL TENSION TEST

Appendix Outline

B.1 Raw Uniaxial Tension Test Data

B.2 Crack Distribution and Failure Mode of Dogbone Specimens

B.3 Number of Fibres Crossing Failure Plane of Uniaxial Tension Test

B.1 Raw Uniaxial Tension Test Data

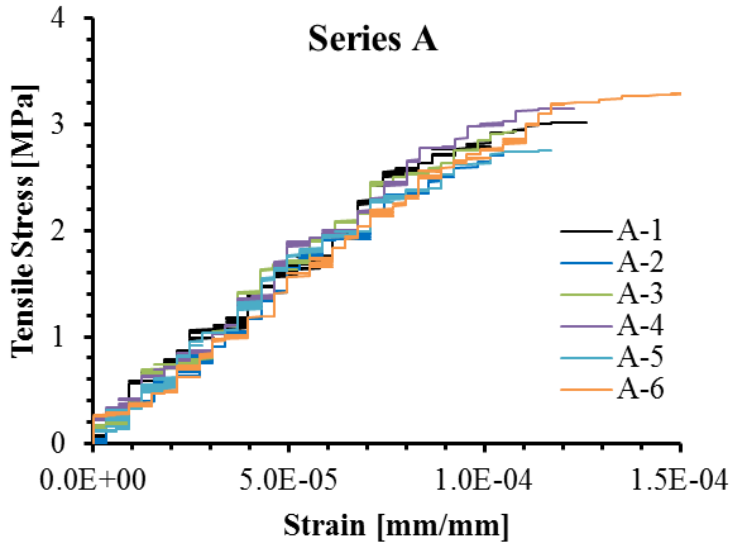

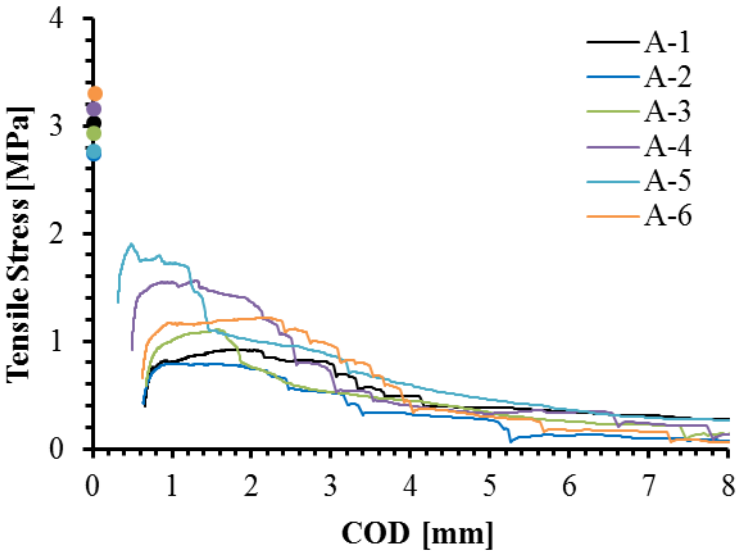

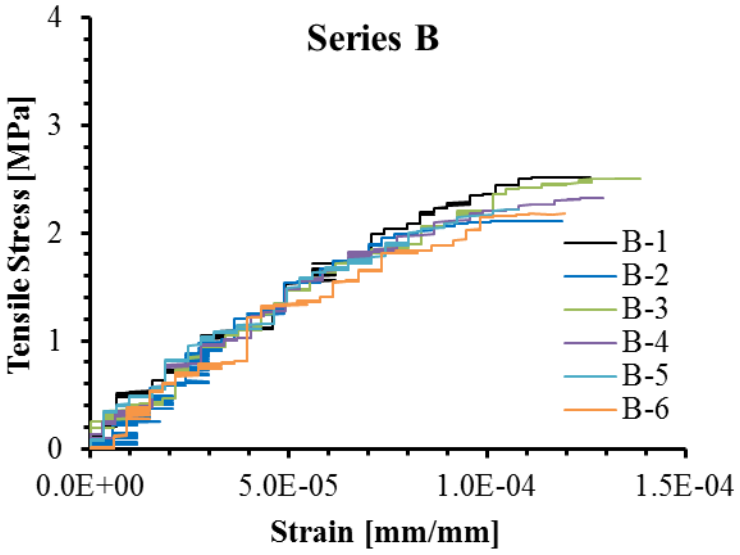
Series B
Tensile Stress [MPa]
Strain [mm/mm]
0
1
2
3
4
0.0E+00
5.0E-05
1.0E-04
1.5E-04
B-1
B-2
B-3
B-4
B-5
B-6

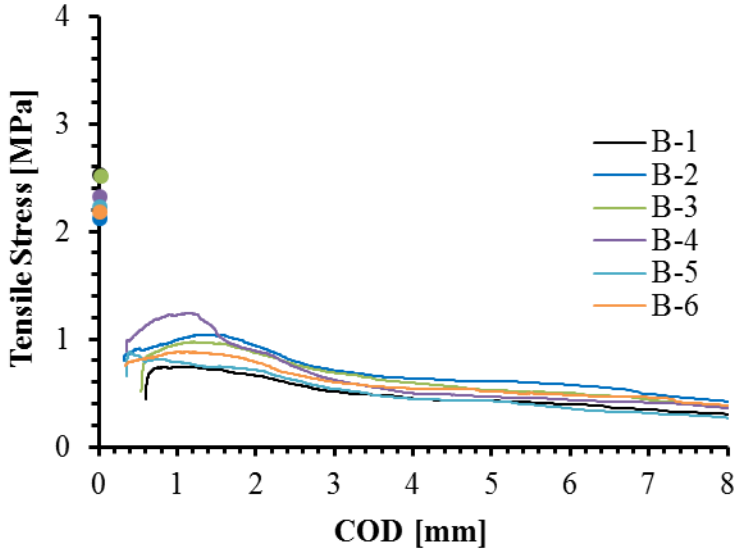
Tensile Stress [MPa]
COD [mm]
0
1
2
3
4
5
6
7
8
B-1
B-2
B-3
B-4
B-5
B-6

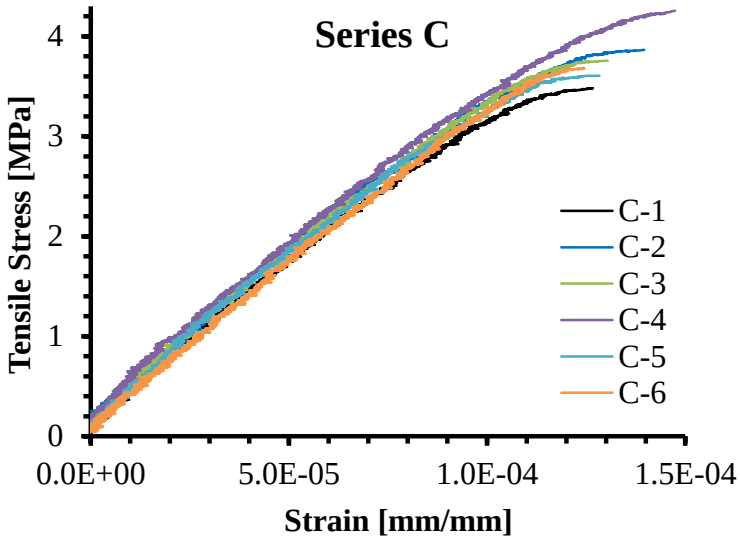
Series C
Tensile Stress [MPa]
Strain [mm/mm]
0
1
2
3
4
0.0E+00
5.0E-05
1.0E-04
1.5E-04
C-1
C-2
C-3
C-4
C-5
C-6

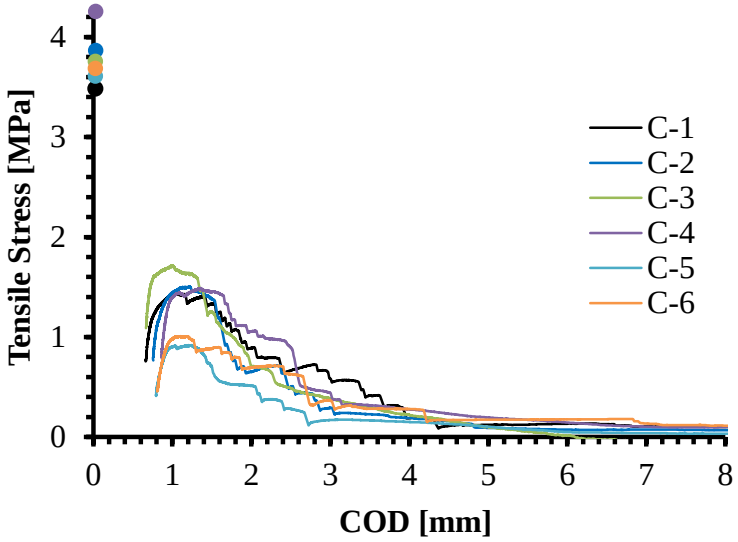

Series A					
Specimen ID	f_{ct}	ε_t ($\times 10^{-4}$)	E_t	$f_{0.5}$	$f_{1.5}$
	[Mpa]	**[mm/mm]**	**[Gpa]**	**[Mpa]**	**[Mpa]**
A-1	3.02	1.26	30.5	-	0.89
A-2	2.73	1.05	28.8	-	0.78
A-3	2.93	1.08	29.1	-	1.09
A-4	3.15	1.23	29.1	1.01	1.47
A-5	2.76	1.17	29.4	1.89	1.10
A-6	3.29	1.51	25.9	-	1.17
Mean	**2.98**	**1.22**	**28.8**	**1.45**	**1.08**
COV	**0.07**	**0.14**	**0.05**	**0.43**	**0.22**

Series B					
Specimen ID	f_{ct}	ε_t (×10^{-4})	E_t	$f_{0.5}$	$f_{1.5}$
	[MPa]	**[mm/mm]**	**[GPa]**	**[MPa]**	**[MPa]**
B-1	2.52	1.26	22.9	-	0.71
B-2	2.11	1.19	26.3	0.91	1.03
B-3	2.50	1.39	21.1	-	0.95
B-4	2.32	1.24	24.4	1.07	1.06
B-5	2.22	1.08	22.9	0.85	0.74
B-6	2.18	1.20	22.9	0.81	0.86
Mean	**2.31**	**1.23**	**23.4**	**0.91**	**0.89**
COV	**0.07**	**0.08**	**0.06**	**0.13**	**0.16**

Series C					
Specimen ID	f_{ct}	ε_t (×10^{-4})	E_t	$f_{0.5}$	$f_{1.5}$
	[MPa]	**[mm/mm]**	**[GPa]**	**[MPa]**	**[MPa]**
C-1	3.48	1.27	30.1	-	1.33
C-2	3.86	1.40	30.7	-	1.38
C-3	3.76	1.30	31.4	-	1.25
C-4	4.25	1.47	32.8	-	1.45
C-5	3.61	1.28	31.0	-	0.70
C-6	3.68	1.24	31.3	-	0.89
Mean	**3.77**	**1.33**	**31.2**	**-**	**1.16**
COV	**0.07**	**0.07**	**0.03**	**-**	**0.26**

B.2 Crack Distribution and Failure Mode of Dogbone Specimens

A-1

A-2

A-3

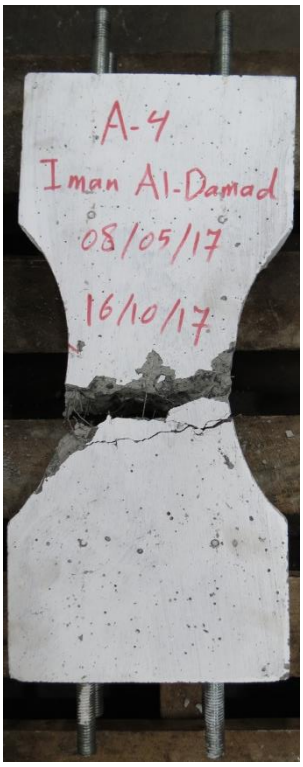

A-4

A-5

A-6

B-1

B-2

B-3

B-4

B-5

B-6

C-1

C-2

C-3

C-4

C-5

C-6

B.3 Number of Fibres Crossing Failure Plane of Uniaxial Tension Test

Series A			
Specimen ID	$N_{f,exp}$	$N_{f,theory}$	$N_{f,exp}/N_{f,theory}$
A-1	33	50	0.67
A-2	38	50	0.76
A-3	51	51	0.99
A-4	51	50	1.03
A-5	47	52	0.91
A-6	43	50	0.85
Mean	**44**	**50**	**0.87**
COV	**0.17**	**0.02**	**0.16**

Series B			
Specimen ID	$N_{f,exp}$	$N_{f,theory}$	$N_{f,exp}/N_{f,theory}$
B-1	85	140	0.61
B-2	98	136	0.72
B-3	100	138	0.72
B-4	121	142	0.85
B-5	100	140	0.72
B-6	92	141	0.65
Mean	**99**	**139**	**0.71**
COV	**0.12**	**0.01**	**0.12**

Series C			
Specimen ID	$N_{f,exp}$	$N_{f,theory}$	$N_{f,exp}/N_{f,theory}$
C-1	43	44	0.98
C-2	32	44	0.73
C-3	45	44	1.01
C-4	36	44	0.82
C-5	34	43	0.79
C-6	37	44	0.84
Mean	**38**	**44**	**0.86**
COV	**0.14**	**0.01**	**0.13**

Appendix C: EXPERIMENTAL DATA – PRISM BENDING TEST

Appendix Outline

C.1 Raw EN 14651 Notched Prism Test Data

C.2 Crack Distribution and Failure Mode of EN 14651 Notched Prisms Specimens

C.3 Load-Strain Curves for EN 14651 Notched Prism Bending Tests

C.4 Raw ASTM C1609 Un-notched Prism Test Data

C.5 Crack Distribution and Failure Mode of ASTM C1609 Un-notched Prisms Specimens

C.6 Load-Strain Curves for ASTM C1609 Un-notched Prism Bending Tests

C.7 Raw JCI-S-002 Notched Prism Test Data

C.8 Crack Distribution and Failure Mode of JCI-S-002 Notched Prisms Specimens

C.1 Raw EN 14651 Notched Prism Test Data

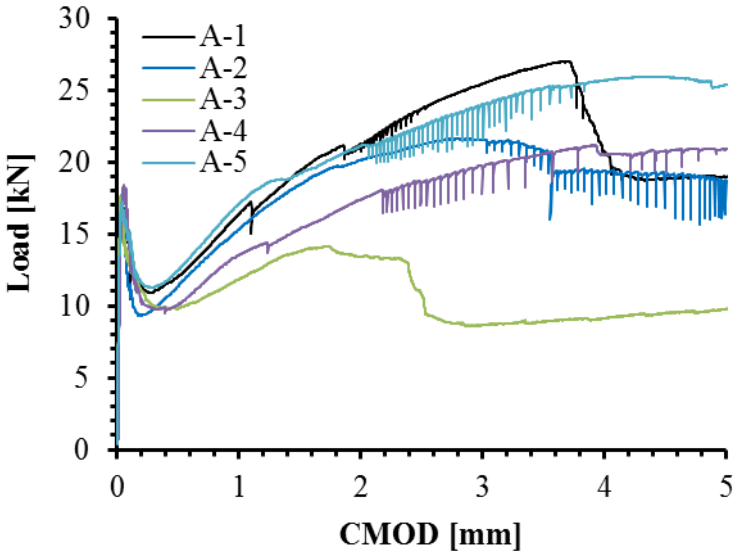

Specimen ID	f_{R1}	f_{R2}	f_{R3}	f_{R4}	$f^{f}_{ct,L}$
	[MPa]	**[MPa]**	**[MPa]**	**[MPa]**	**[MPa]**
A-1	3.67	5.90	7.22	8.14	5.38
A-2	3.50	5.68	6.53	6.40	5.45
A-3	3.01	4.23	3.31	2.73	5.39
A-4	3.10	4.72	5.70	6.32	5.65
A-5	3.89	5.99	7.03	7.85	5.39
Mean	**3.43**	**5.30**	**5.96**	**6.29**	**5.45**
COV	**0.11**	**0.15**	**0.27**	**0.34**	**0.02**

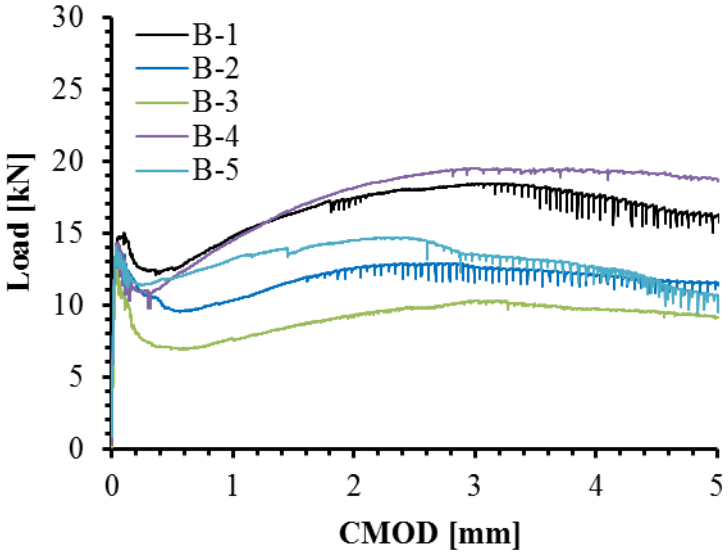

Specimen ID	f_{R1}	f_{R2}	f_{R3}	f_{R4}	$f^{f}_{ct,L}$
	[MPa]	**[MPa]**	**[MPa]**	**[MPa]**	**[MPa]**
B-1	3.62	4.71	5.19	5.20	4.22
B-2	2.96	3.58	3.95	3.79	4.05
B-3	2.08	2.55	2.92	2.97	3.72
B-4	3.55	4.98	5.69	5.76	4.27
B-5	3.53	4.08	4.36	3.92	4.21
Mean	**3.15**	**3.98**	**4.42**	**4.33**	**4.10**
COV	**0.21**	**0.24**	**0.24**	**0.26**	**0.05**

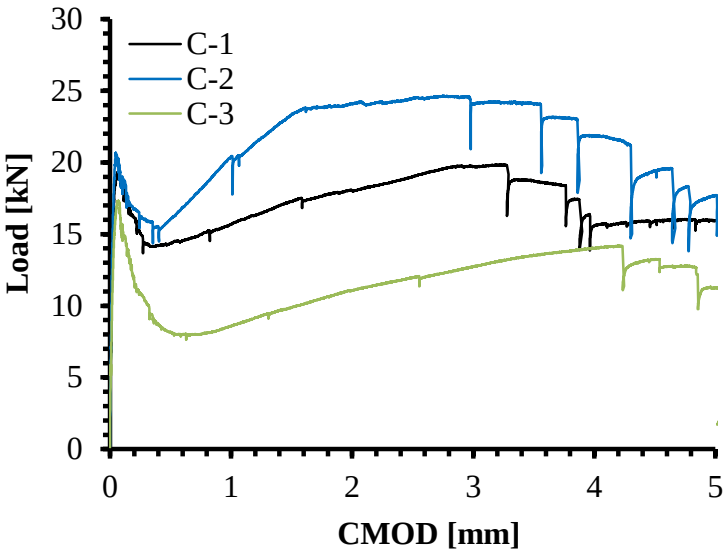

Specimen ID	f_{R1}	f_{R2}	f_{R3}	f_{R4}	$f^{f}_{ct,L}$
	[MPa]	**[MPa]**	**[MPa]**	**[MPa]**	**[MPa]**
C-1	4.34	5.21	5.74	5.66	5.79
C-2	4.55	6.61	6.93	6.82	5.85
C-3	2.62	3.16	3.84	4.34	5.31
Mean	**3.84**	**4.99**	**5.50**	**5.60**	**5.65**
COV	**0.28**	**0.35**	**0.28**	**0.22**	**0.05**

C.2 Crack Distribution and Failure Mode of EN 14651 Notched Prisms Specimens

A-1

A-2

A-3

A-4

A-5

B-1

B-2

B-3

B-4

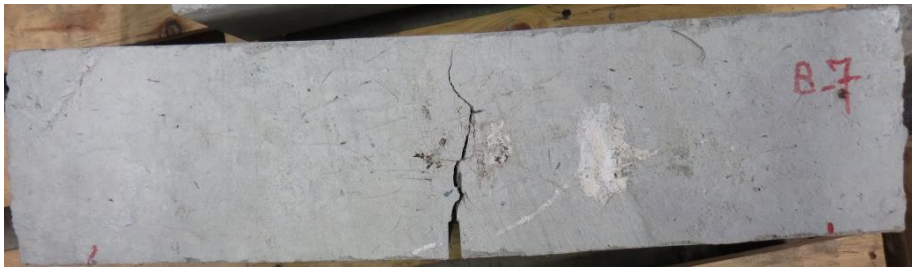

B-5

C-1

C-2

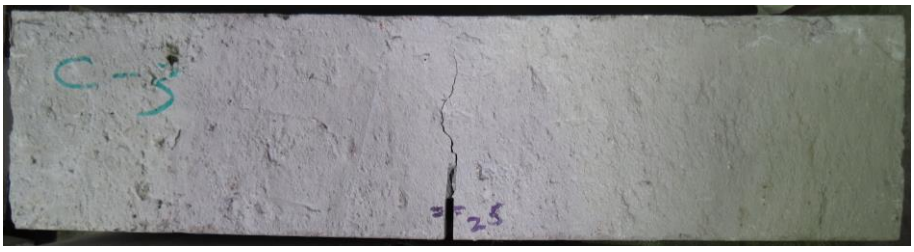

C-3

C.3 Load-Strain Curves for EN 14651 Notched Prism Bending Tests

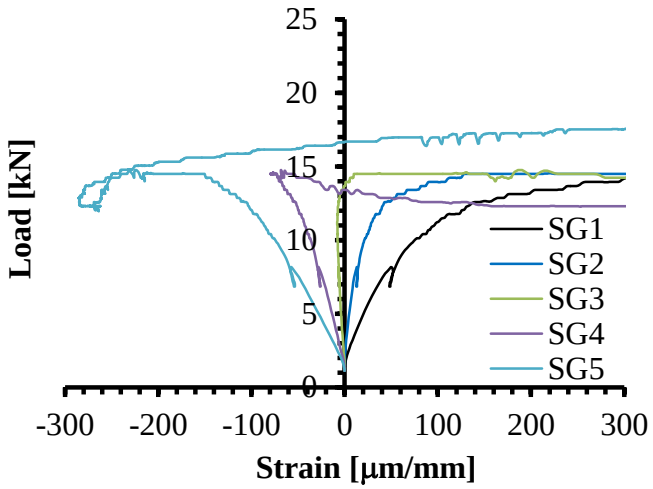

B-1

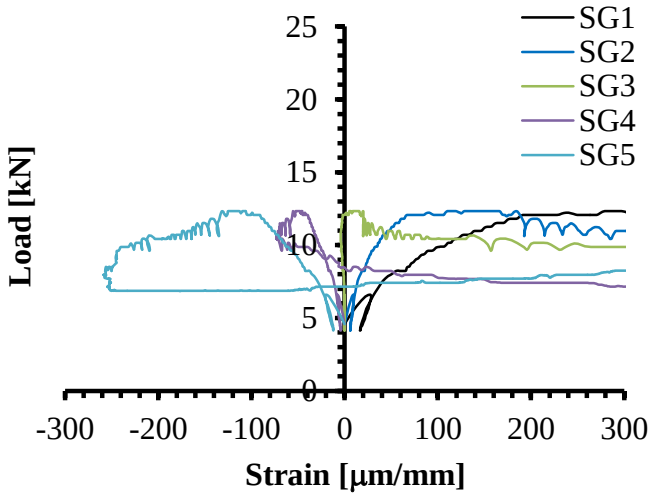

B-3

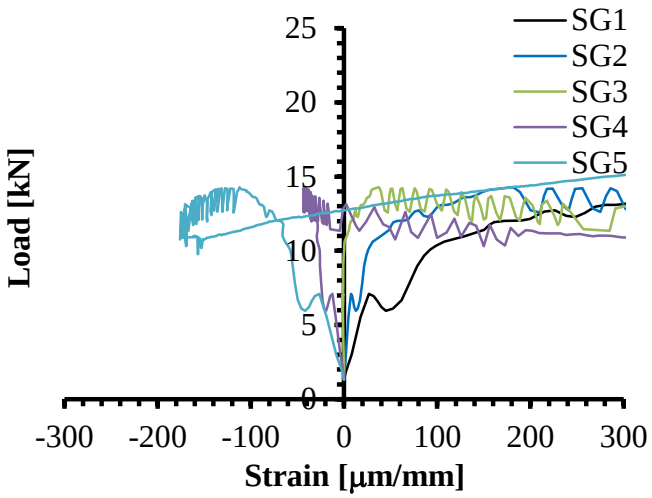
SG1
SG2
SG3
SG4
SG5
25
20
15
10
5
0
Load [kN]
-300
-200
-100
0
100
200
300
Strain [μm/mm]

B-4

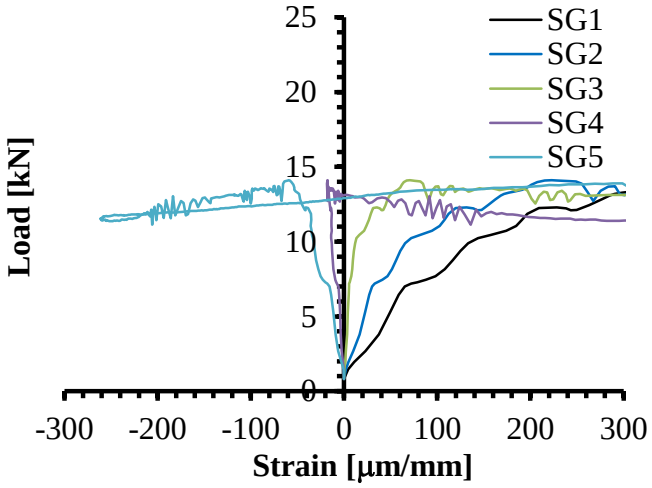
SG1
SG2
SG3
SG4
SG5
25
20
15
10
5
0
Load [kN]
-300
-200
-100
0
100
200
300
Strain [μm/mm]

B-5

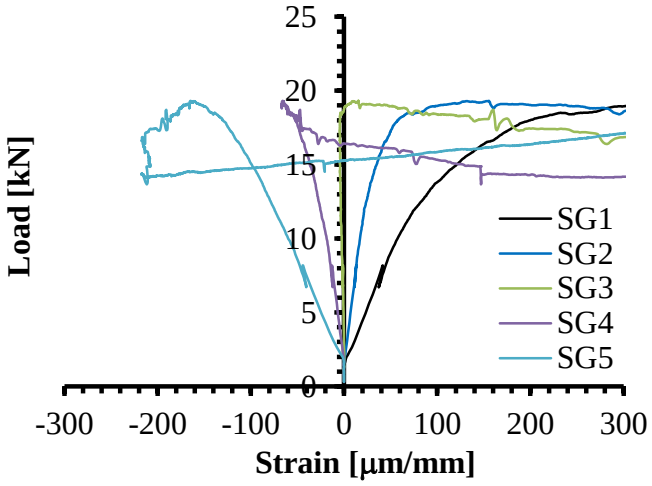
SG1
SG2
SG3
SG4
SG5
25
20
15
10
5
0
Load [kN]
-300
-200
-100
0
100
200
300
Strain [μm/mm]

C-1

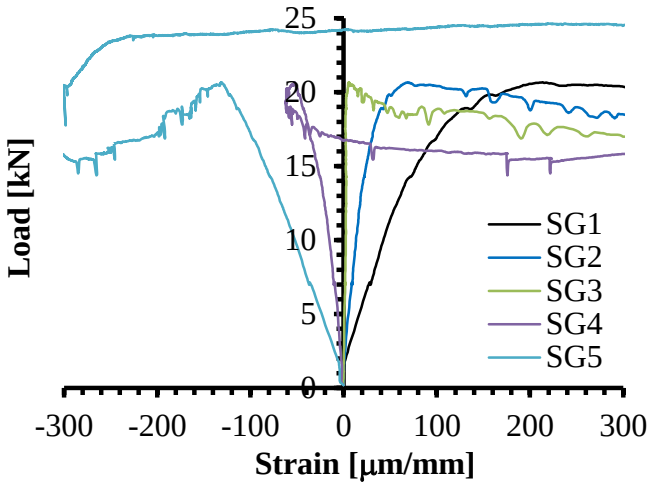
25
20
15
10
5
0
Load [kN]
-300
-200
-100
0
100
200
300
Strain [μm/mm]
SG1
SG2
SG3
SG4
SG5

C-2

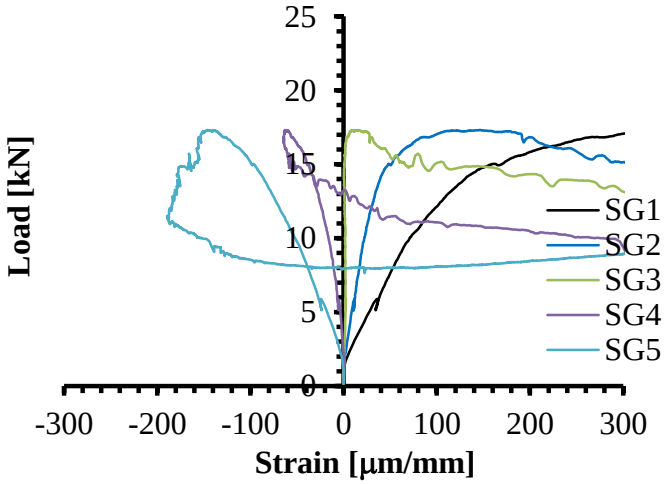
25
20
15
10
5
0
Load [kN]
-300
-200
-100
0
100
200
300
Strain [μm/mm]
SG1
SG2
SG3
SG4
SG5

C-3

C.4 Raw ASTM C1609 Un-notched Prism Test Data

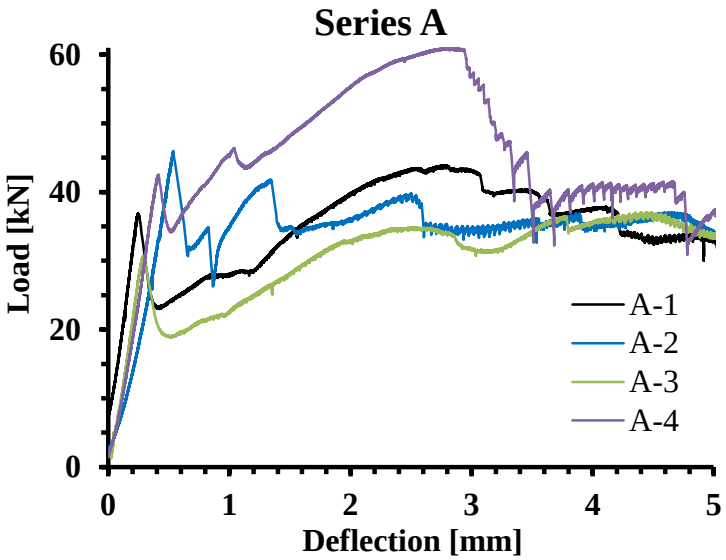

Specimen ID	P_P	δ_P	P_1	δ_1	P^D_{600}	P^D_{150}	f_P	f_1	f^D_{600}	f^D_{150}	T^D_{150}	R^D_{150}
	[kN]	[mm]	[kN]	[mm]	[kN]	[kN]	[MPa]	[MPa]	[MPa]	[MPa]	[Joule]	%
A-1	43.9	2.82	36.9	0.25	26.9	43.1	5.4	4.6	3.3	5.3	101.7	0.09%
A-2	45.9	0.54	45.9	0.54	33.0	34.6	5.7	5.7	4.1	4.3	100.5	0.07%
A-3	37.1	4.45	30.6	0.28	21.0	31.7	4.7	3.9	2.7	4.0	81.8	0.09%
A-4	61.0	2.80	42.5	0.41	40.2	56.8	7.5	5.3	5.0	7.0	139.8	0.11%
Mean	47.0	2.65	39.0	0.37	30.3	41.6	5.8	4.9	3.8	5.2	105.9	0.09%
COV	0.21	0.61	0.17	0.36	0.27	0.27	0.21	0.16	0.26	0.26	0.23	0.17

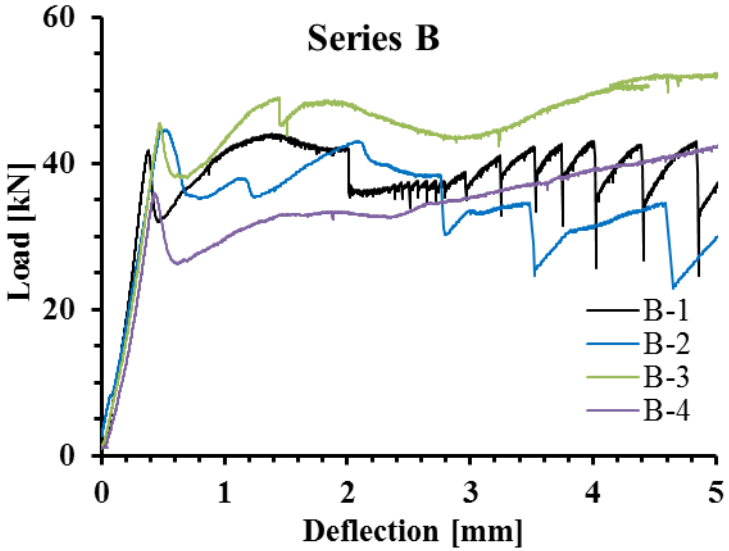

Specimen ID	P_P	δ_P	P_1	δ_1	P^D_{600}	P^D_{150}	f_P	f_1	f^D_{600}	f^D_{150}	T^D_{150}	R^D_{150}
	[kN]	[mm]	[kN]	[mm]	[kN]	[kN]	[MPa]	[MPa]	[MPa]	[MPa]	[Joule]	%
B-1	44.1	1.39	41.8	0.38	37.4	37.5	5.5	5.2	4.7	4.7	110.9	0.09%
B-2	44.6	0.51	44.6	0.51	35.5	33.1	5.4	5.4	4.3	4.0	107.1	0.08%
B-3	52.4	5.11	45.5	0.47	38.9	43.8	6.3	5.5	4.7	5.3	123.5	0.09%
B-4	42.8	5.30	35.9	0.43	27.3	35.4	5.3	4.5	3.4	4.4	89.2	0.08%
Mean	46.0	3.08	41.9	0.45	34.8	37.4	5.6	5.2	4.3	4.6	107.7	0.09%
COV	0.09	0.81	0.10	0.12	0.15	0.12	0.08	0.09	0.14	0.11	0.13	0.06

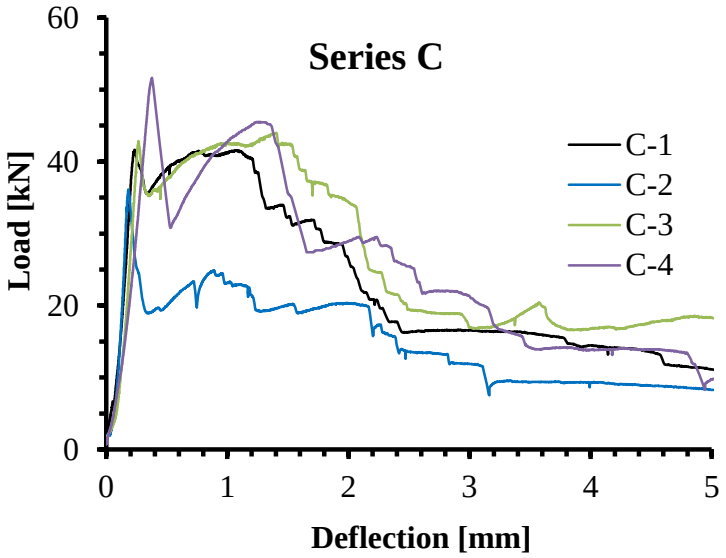

Specimen ID	P_P	δ_P	P_1	δ_1	P^D_{600}	P^D_{150}	f_P	f_1	f^D_{600}	f^D_{150}	T^D_{150}	R^D_{150}
	[kN]	[mm]	[kN]	[mm]	[kN]	[kN]	[MPa]	[MPa]	[MPa]	[MPa]	[Joule]	%
C-1	41.7	0.23	41.7	0.23	41.4	16.6	5.2	5.2	5.1	2.1	87.2	0.07%
C-2	36.1	0.18	36.1	0.18	20.2	11.9	4.6	4.6	2.6	1.5	56.3	0.05%
C-3	44.0	1.40	42.8	0.27	41.1	17.0	5.7	5.5	5.3	2.2	95.5	0.07%
C-4	51.7	0.38	51.7	0.38	37.6	21.3	6.6	6.6	4.8	2.7	94.1	0.06%
Mean	43.4	0.55	43.1	0.27	35.1	16.7	5.5	5.5	4.4	2.1	83.3	0.06%
COV	0.15	1.05	0.15	0.31	0.29	0.23	0.15	0.15	0.29	0.23	0.22	0.15

C.5 Crack Distribution and Failure Mode of ASTM C1609 Un-notched Prisms Specimens

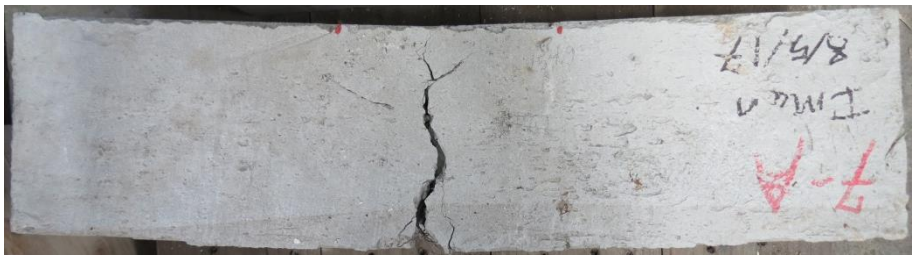

A-1

A-2

A-3

A-4

B-1

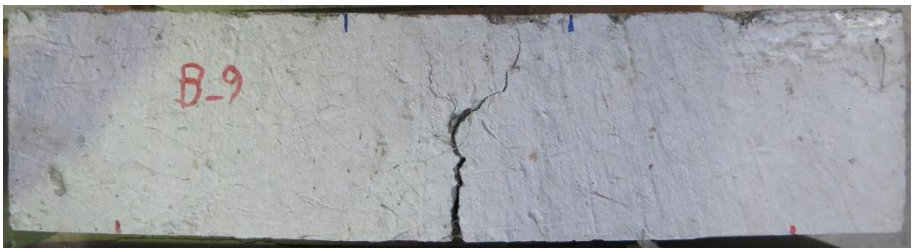

B-2

B-3

B-4

C-1

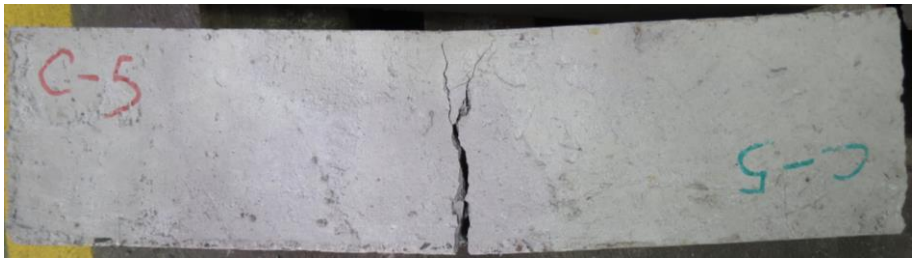

C-2

C-3

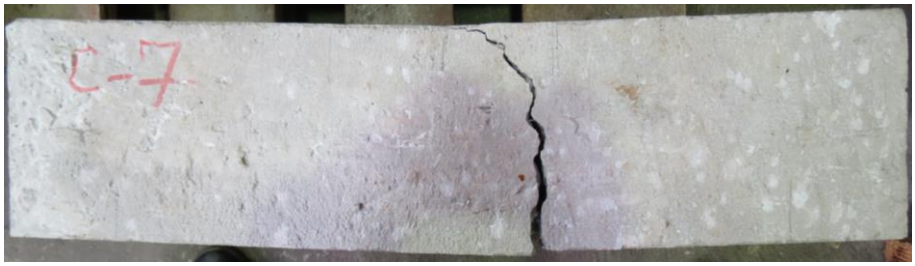

C-4

C.6 Load-Strain Curves for ASTM C1609 Un-notched Prism Bending Tests

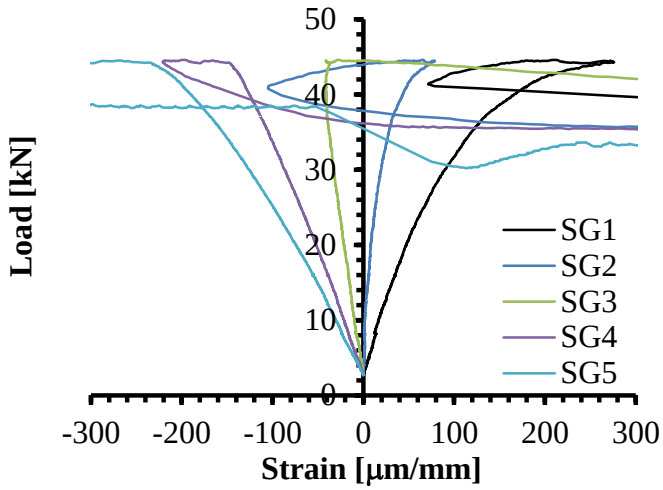

B-2

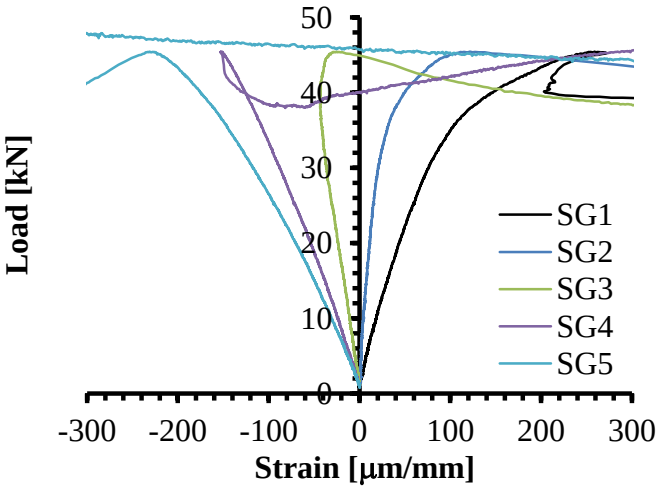

B-3

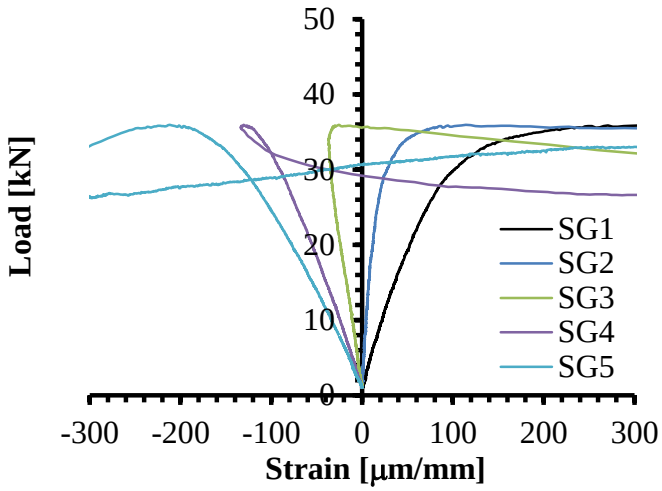
Load [kN]
50
40
30
20
10
0
-300
-200
-100
0
100
200
300
Strain [μm/mm]
SG1
SG2
SG3
SG4
SG5

B-4

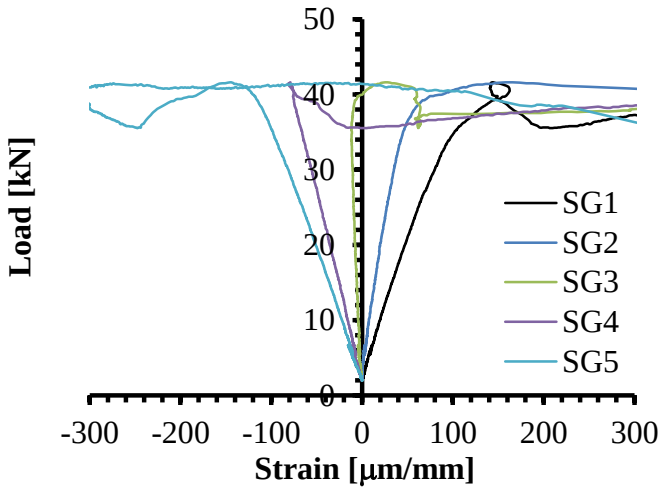
Load [kN]
50
40
30
20
10
0
-300
-200
-100
0
100
200
300
Strain [μm/mm]
SG1
SG2
SG3
SG4
SG5

C-1

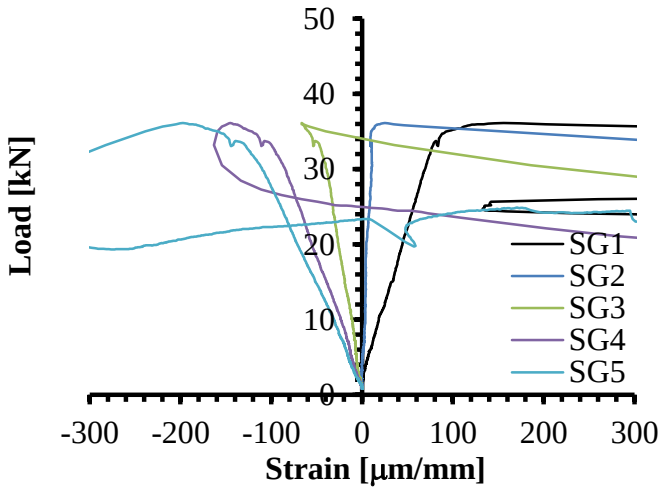
Load [kN]
50
40
30
20
10
0
-300
-200
-100
0
100
200
300
Strain [μm/mm]
SG1
SG2
SG3
SG4
SG5

C-2

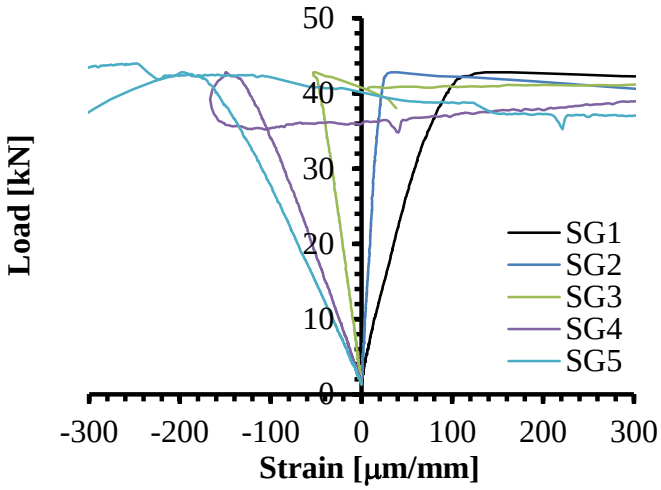
Load [kN]
50
40
30
20
10
0
-300
-200
-100
0
100
200
300
Strain [μm/mm]
SG1
SG2
SG3
SG4
SG5

C-3

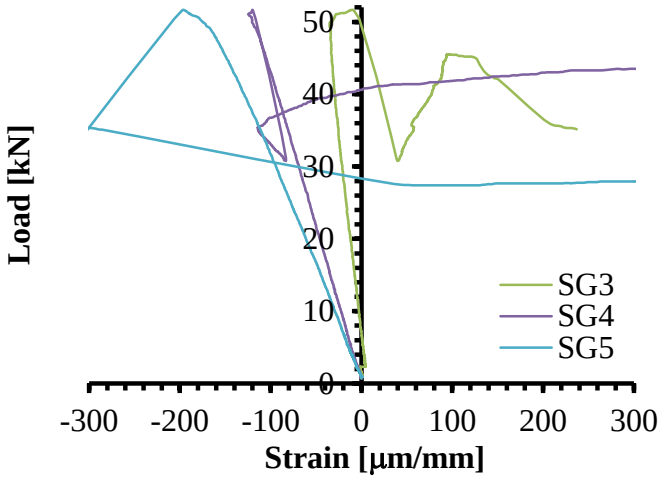
Load [kN]
50
40
30
20
10
0
-300
-200
-100
0
100
200
300
Strain [μm/mm]
SG3
SG4
SG5

C-4

C.7 Raw JCI-S-002 Notched Prism Test Data

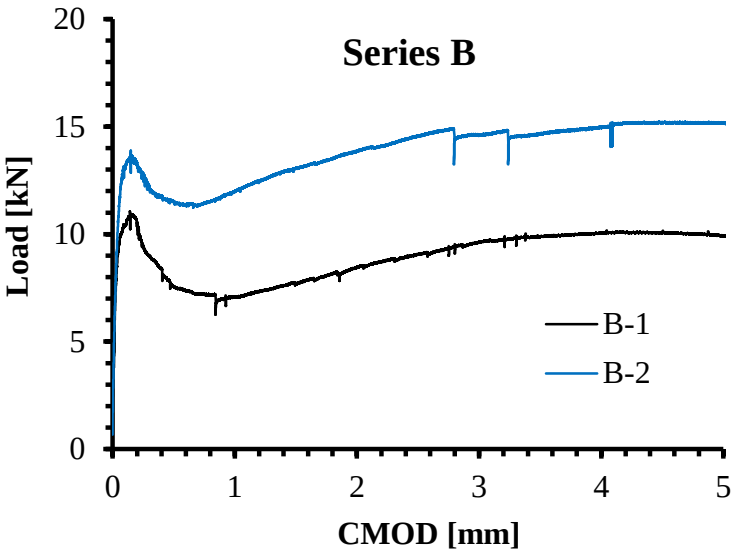

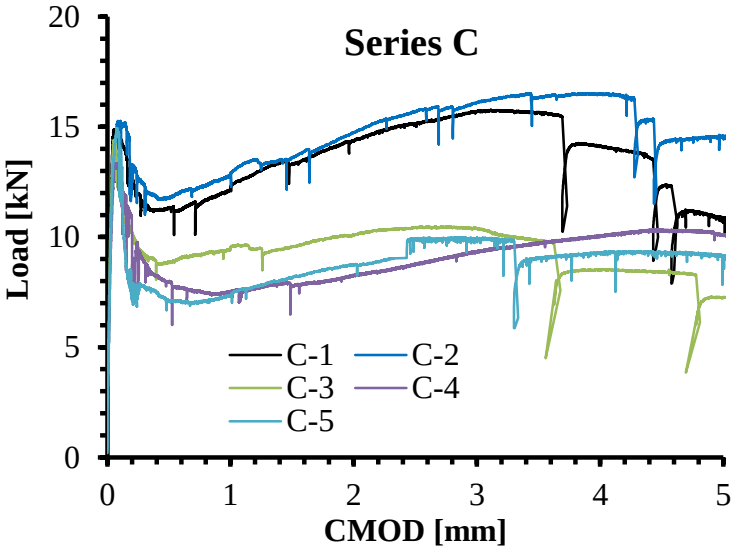

C.8 Crack Distribution and Failure Mode of JCI-S-002 Notched Prisms Specimens

A-1

B-1

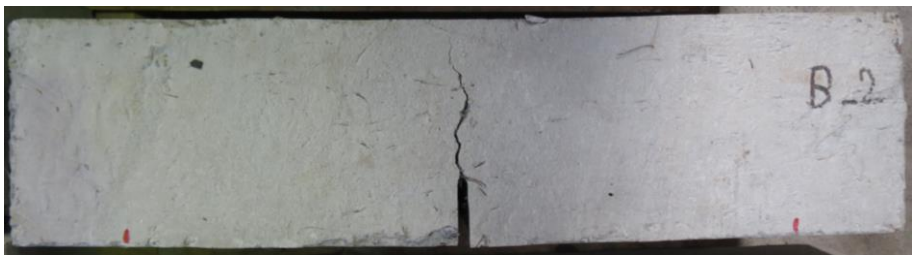

B-2

C-1

C-2

C-3

C-4

C-5

Appendix D: INVERSE ANALYSIS – PRISM BENDING TEST

Appendix Outline

D.1 Inverse Analysis of EN 14651 Notched Prism Test Data

D.2 Inverse Analysis of ASTM C1609 Un-notched Prism Test Data

D.3 Simplified Inverse Analysis Model of EN 14651 Notched Prism Test Data

D.4 Simplified Inverse Analysis Model of ASTM C1609 Un-notched Prism Test Data

D.1 Inverse Analysis of EN 14651 Notched Prism Test Data

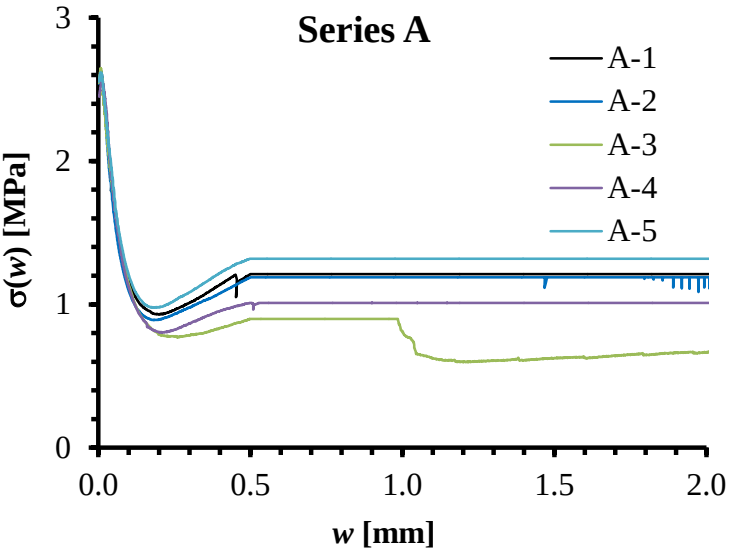

Specimen ID	$f_{0.5}$	$f_{1.5}$
	[MPa]	[MPa]
A-1	1.21	1.21
A-2	1.19	1.19
A-3	0.90	0.62
A-4	1.01	1.01
A-5	1.32	1.32
Mean	**1.13**	**1.07**
COV	**0.15**	**0.25**

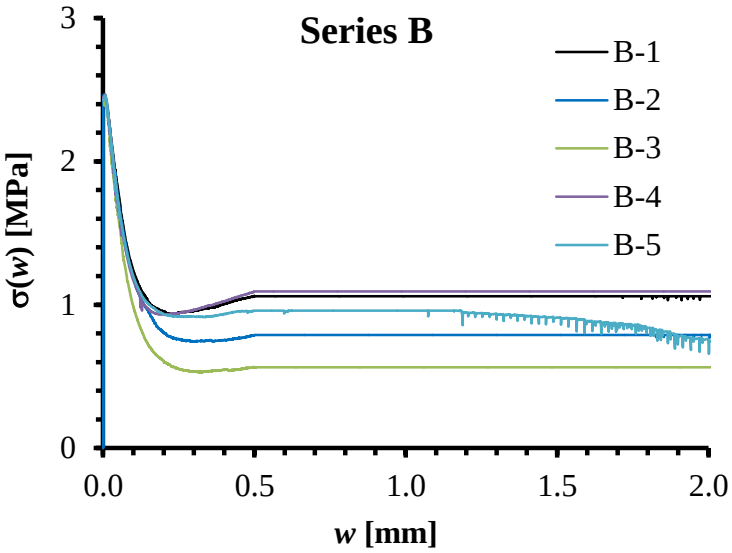

Specimen ID	$f_{0.5}$	$f_{1.5}$
	[MPa]	[MPa]
B-1	1.06	1.06
B-2	0.79	0.79
B-3	0.56	0.56
B-4	1.09	1.09
B-5	0.96	0.91
Mean	0.89	0.88
COV	0.24	0.24

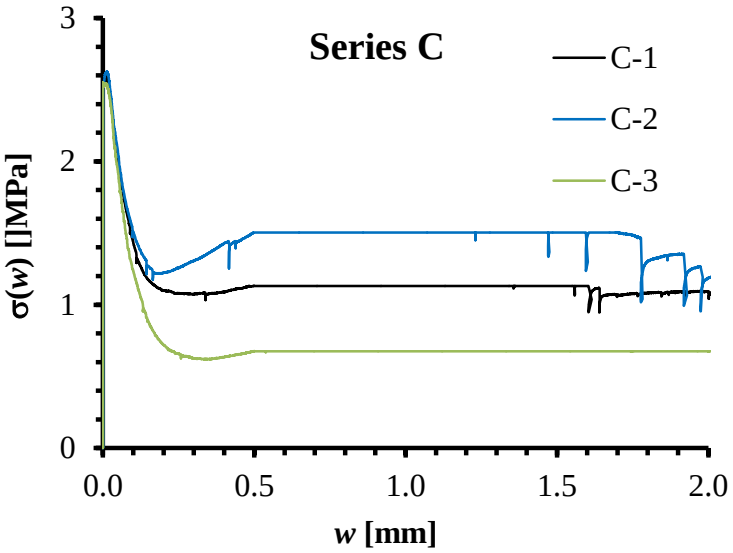

Specimen ID	$f_{0.5}$	$f_{1.5}$
	[MPa]	[MPa]
C-1	1.13	1.13
C-2	1.50	1.50
C-3	0.68	0.68
Mean	**1.10**	**1.10**
COV	**0.38**	**0.38**

D.2 Inverse Analysis of ASTM C1609 Un-notched Prism Test Data

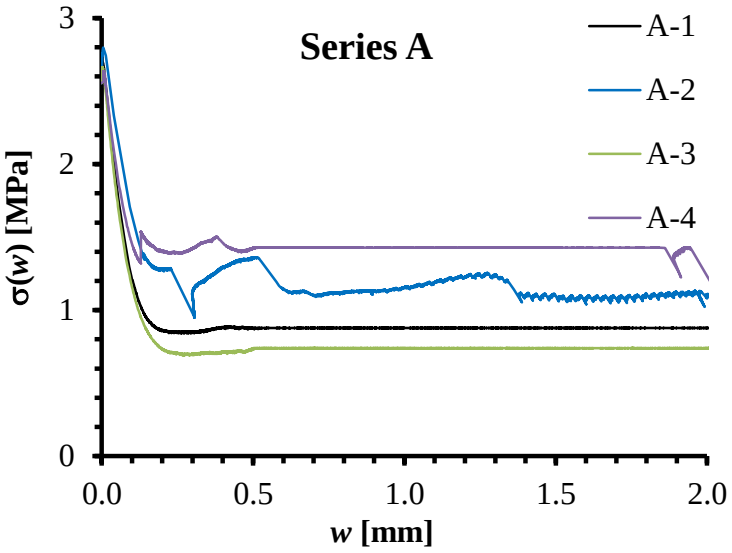

Specimen ID	$f_{0.5}$	$f_{1.5}$
	[MPa]	[MPa]
A-1	0.88	0.88
A-2	1.36	1.11
A-3	0.74	0.74
A-4	1.43	1.43
Mean	**1.10**	**1.04**
COV	**0.31**	**0.29**

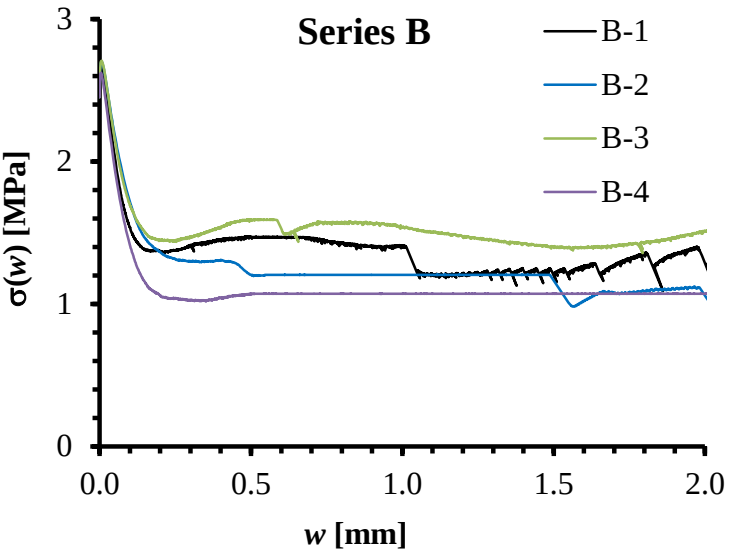

Specimen ID	$f_{0.5}$	$f_{1.5}$
	[MPa]	[MPa]
B-1	1.47	1.21
B-2	1.20	1.20
B-3	1.59	1.40
B-4	1.07	1.07
Mean	**1.33**	**1.22**
COV	**0.18**	**0.11**

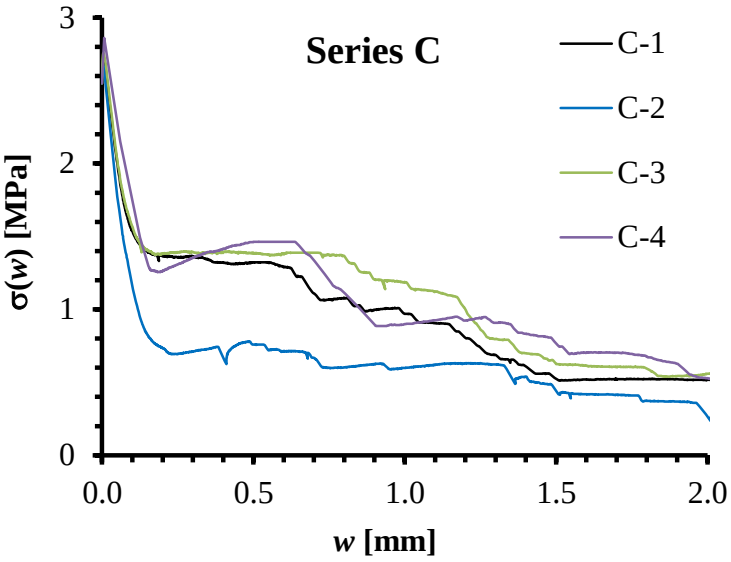

Specimen ID	$f_{0.5}$	$f_{1.5}$
	[MPa]	[MPa]
C-1	1.32	0.53
C-2	0.76	0.45
C-3	1.39	0.63
C-4	1.46	0.78
Mean	**1.23**	**0.60**
COV	**0.26**	**0.24**

D.3 Simplified Inverse Analysis Model of EN 14651 Notched Prism Test Data

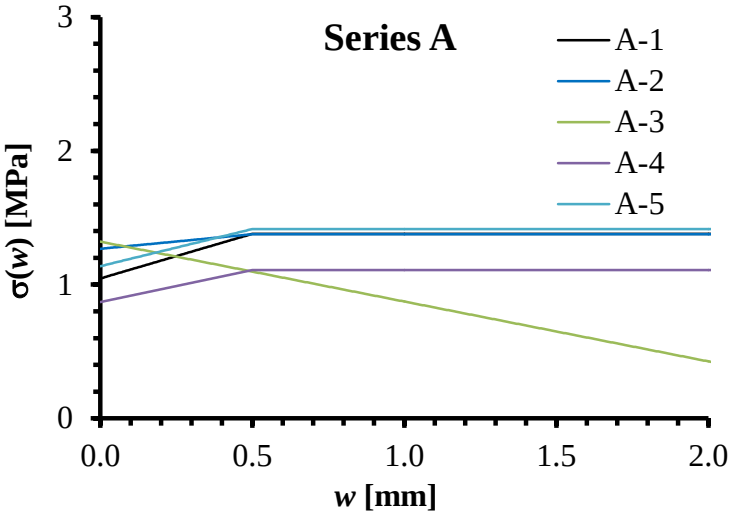

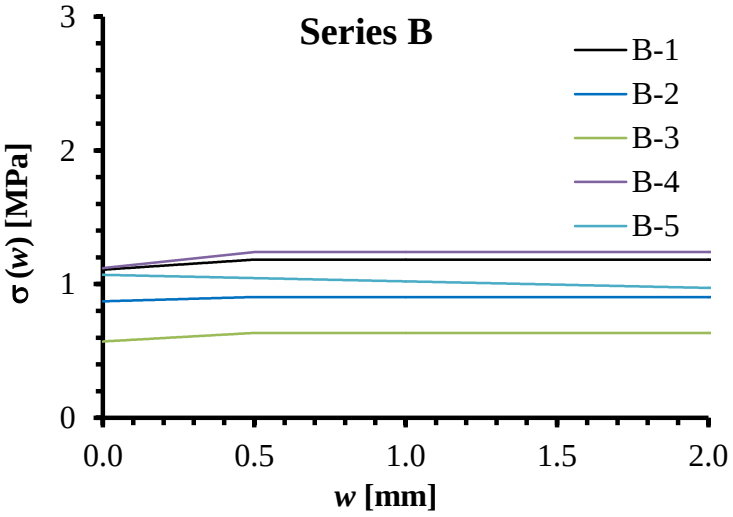

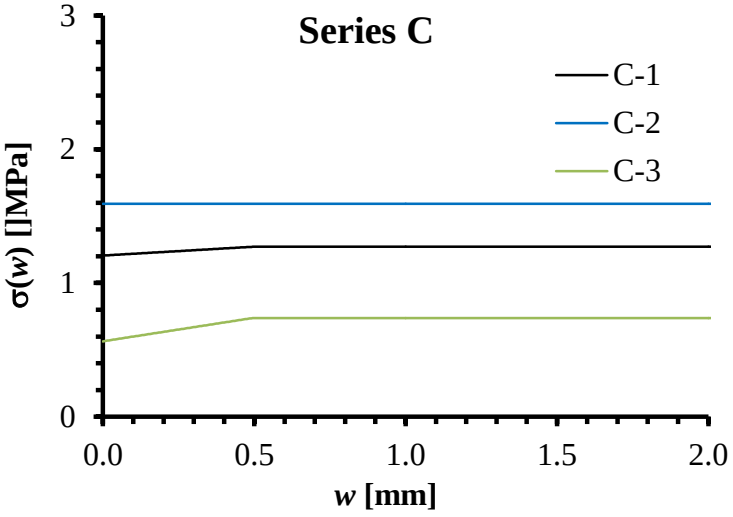

D.4 Simplified Inverse Analysis Model of ASTM C1609 Un-notched Prism Test Data